Technical Report
TR-22-07
September 2023

Task Force on Engineered Barrier System (EBS)

Task 9 FEBEX in situ test – Final Report

Antonio Gens
Jordi Alcoverro
Masataka Sawada
Klaus-Peter Kröhn
Giulia M Ghiadistri
Lidija Zdravkovic
David M Potts
Aikaterini Tsiampousi
Teklu Hadgu
Thomas Dewers
Steven Gomez
Edward Matteo
Ola Kristensson
Milan Hokr
Petr Rálek
Jiří Landa
Ilona Hančilová
Alfonso Rodríguez-Dono

SVENSK KÄRNBRÄNSLEHANTERING AB

SWEDISH NUCLEAR FUEL
AND WASTE MANAGEMENT CO

Box 3091, SE-169 03 Solna
Phone +46 8 459 84 00
skb.se

~~SVENSK~~ KÄRNBRÄNSLEHANTERING

ISSN 1404-0344
SKB TR-22-07
ID 1979514

September 2023

Task Force on Engineered Barrier System (EBS)

Task 9 FEBEX in situ test – Final Report

Antonio Gens[1], Jordi Alcoverro[2], Masataka Sawada[3], Klaus-Peter Kröhn[4], Giulia M Ghiadistri[5], Lidija Zdravkovic[5], David M Potts[5], Aikaterini Tsiampousi[5], Teklu Hadgu[6], Thomas Dewers[6], Steven Gomez[6], Edward Matteo[6], Ola Kristensson[7], Milan Hokr[8], Petr Rálek[8], Jiří Landa[8], Ilona Hančilová[8], Alfonso Rodríguez-Dono[1]

1 Universitat Politècnica de Catalunya
2 International Center for Numerical Methods in Engineering
3 Central Research Institute of Electric Power Industry
4 Gesellschaft für Anlagen- und Reaktorsicherheit
5 Imperial College London
6 Sandia National Laboratories
7 Clay Technology AB
8 Technical University of Liberec

Executive summary

Task 9 of SKB's Engineered Barrier System Task Force (EBS TF) is devoted to the numerical analysis of the FEBEX in situ experiment, a full-scale heating test performed at the Grimsel Test Site (GTS) in Switzerland. The Task goals are the enhancement of the understanding of the EBS THM behaviour during the transient phase, the detailed examination of the evolution of the state of the barrier, and the validation and improvement of the numerical capabilities of the participating modelling teams.

The FEBEX experiment involves the installation of two heaters that simulate nuclear waste canisters surrounded by an engineered barrier made up of compacted blocks. The test was placed at the end of a tunnel specifically excavated for the test in the GTS. The experiment is temperature-controlled in such a way that the maximum temperature in the bentonite is maintained at 100 °C over the entire testing period. During the test, the bentonite barrier is subject to natural hydration from the granitic host rock. An intensive monitoring system has provided continuous information on key parameters and variables throughout. The FEBEX test is a long-term experiment spanning a total heating period of 18.15 years. The test underwent two dismantling events. The partial first one took place five years after the start of heating and involved the removal of one of the heaters and of the corresponding part of bentonite barrier. The second dismantling occurred at the end of the experiment and it involved the removal of all remaining test components. The state of the barrier was fully characterised at each dismantling event.

The modelling teams and computer codes involved in Task 9 were:

- Central Research Institute of Electric Power Industry, Japan (CRIEPI)
  - Computer code: LOSTUF
- Gesellschaft für Anlagen- und Reaktorsicherheit, Germany (GRS)
  - Computer code: COMSOL and VIPER
- Imperial College, London, UK (ICL)
  - Computer code: ICFEP
- Sandia National Laboratories, US (SNL)
  - Computer code: PFLOTRAN
- Svensk Kärnbränslehantering AB - Clay Technology, Sweden (SKB-CT)
  - Computer code: CODE_BRIGHT
- Technical University of Liberec, Czech Republic (TUL)
  - Computer code: COMSOL
- Universitat Politècnica de Catalunya, Spain (UPC)
  - Computer code: CODE_BRIGHT

CRIEPI, ICL, SKB-CT, TUL and UPC performed coupled THM analyses whereas GRS and SNL carried out coupled TH calculations. Given the characteristics of the experiment, 2D axisymmetric domains have been used in most simulations; in addition, one team adopted a 3D geometry whereas another team used a 1D axisymmetric geometry for the hydraulic problem. Only one team incorporated the gap between the barrier and the rock.

All the teams were supplied with the same information on the properties of the FEBEX bentonite and of the rock in the GTS; the teams were given freedom for interpreting the data and for selecting appropriate constitutive laws and associated parameters. Consequently, there were differences in the parameters and relationships selected by the teams. Overall, the Task incorporated a variety of approaches, formulations, computer codes, constitutive laws and parameters thus providing a wider perspective to Task 9.

The formulations used involved the solution of energy and mass balance equations as well as the equilibrium equation, if the mechanical problem was considered. In most cases, Fourier's law characterized thermal conduction and Darcy's law characterized hydraulic advection. The dependence of thermal and hydraulic conductivity on degree of saturation was generally incorporated in the formulations while

some form of the Van Genuchten expression was adopted by most teams to define the water retention relationship. A variety of mechanical constitutive laws were selected for the analyses; two teams used an elastic formulation coupled to a specific swelling term, two teams used different versions of the elastoplastic Barcelona Basic Model (BBM) and one team employed an elastoplastic double structure model (IC-DSM).

Thermal variables (heater power and the temperature field) were generally well reproduced by the numerical models. In particular, the increase of heating power with time, consequence of the barrier saturation increase was picked up by several teams. The progressive hydration of the barrier was captured by all models although a number of differences between calculations and observations could be observed when examining the results in detail. For instance, the drying of the bentonite close to the heater was frequently underestimated. Also, the role of vapour migration in the early stages of the test was demonstrated. In general, models tended to underestimate the level of saturation at the end of the test. The assessment of the simulation of the development of swelling pressures was hampered by uncertainties about the reliability of the measurements. All THM models, however, provided reasonable outcomes in terms of evolution and final values of radial and axial total stresses.

The first dismantling showed a highly non-homogenous state of the barrier in terms of dry density while it was also observed that a large proportion of the bentonite was in an unsaturated state, except in the barrier zones close to the rock. The results of the numerical models were consistent with observations.

The second dismantling demonstrated that after 18.15 years the bentonite barrier had become basically saturated, particularly in the narrower sections where the heater was located except in a narrow zone close to the heaters where degree of saturation was, in any case, quite high as well. It also revealed that the distribution of dry density had not varied since the first dismantling. The outcome of most numerical THM models was consistent with those observations although full confirmation of this agreement would require the continuation of the modelling until reaching a comparable level of barrier saturation.

In conclusion, it can be stated that the numerical analyses performed have been able to represent adequately the global TH and THM behaviour of a bentonite barriers as displayed in a long-term non-isothermal large-scale experiment. The overall observations concerning the evolution of heater power, the temperature field at different times, the progress of hydration, the development of stresses in the bentonite and the state of the barrier at first and final dismantling have been, on the whole, satisfactorily reproduced by the models. This provides strong support to the view that the most important processes and their mutual interactions appear to be incorporated in an appropriate manner in the numerical models. It can also be concluded that the goals established at the outset comprising the advancement of the understanding of the THM EBS behaviour during the transient phase, the examination of the evolution of the state of the barrier and the validation and improvement of the numerical capabilities of the participating modelling teams have been achieved.

Sammanfattning

Task 9 i SKB:s Engineered Barrier System Task Force (EBS TF) ägnades åt en numerisk analys av FEBEX in situ-experiment, ett fullskaligt värmetest utfört i Grimsel Test Site (GTS) i Schweiz. Målen var att förbättra förståelsen för THM-beteendet av barriärsystemet under den transienta fasen, en detaljerad förståelse för utvecklingen av barriärens tillstånd och validering och förbättring av den numeriska kapaciteten hos de deltagande modelleringsteamen.

FEBEX-experimentet innefattade en installation av två värmare som simulerar kärnavfallsbehållare omgiven av en barriär bestående av komprimerade bentonitblock. Testet placerades i änden av en tunnel vilken borrades ut speciellt för testet i GTS. Experimentet var temperaturstyrt på ett sådant sätt att maximal temperatur i bentoniten hölls vid 100 °C under hela försökets driftsperiod. Under testet vattenmättades bentonitbarriären naturligt från det granitiska berget.

Ett intensivt övervakningssystem gav kontinuerlig information om nyckelparametrar och variabler genom hela försöket. FEBEX-testet var ett långsiktigt experiment som spände över en total uppvärmningsperiod på 18,15 år. Testet genomgick två brytningssteg. Det första ägde rum fem år efter starten av uppvärmningen och innebar en demontering av en av värmarna och av motsvarande del av bentonitbarriären. Den andra brytningen skedde i slutet av experimentet och den innebar att alla återstående testkomponenter avlägsnades. Barriärens tillstånd karakteriserades fullt ut vid varje brytningssteg.

Modelleringsteamen och datormodellerna som var involverade i uppgiften var:

- Central Research Institute of Electric Power Industry, Japan (CRIEPI)
  - Computer code: LOSTUF
- Gesellschaft für Anlagen- und Reaktorsicherheit, Germany (GRS)
  - Computer code: COMSOL and VIPER
- Imperial College, London, UK (ICL)
  - Computer code: ICFEP
- Sandia National Laboratories, US (SNL)
  - Computer code: PFLOTRAN
- Svensk Kärnbränslehantering AB - Clay Technology, Sweden (SKB-CT)
  - Computer code: CODE_BRIGHT
- Technical University of Liberec, Czech Republic (TUL)
  - Computer code: COMSOL
- Universitat Politècnica de Catalunya, Spain (UPC)
  - Computer code: CODE_BRIGHT

De formuleringar som användes involverade både lösningen av energi- och massbalansekvationer såväl som jämviktsekvationer, när det mekaniska problemet beaktades. I de flesta fall användes Fouriers lag för värmeledning och Darcys lag för hydraulisk advektion. Beroendet av termisk och hydraulisk konduktivitet på mättnadsgrad inkorporerades i allmänhet i formuleringarna medan någon form av Van Genuchtens uttryck användes av de flesta team för att definiera vattenretentionsrelationen. En mängd olika mekaniska konstitutiva lagar valdes ut för analyserna; två team använde en elastisk formulering kopplad till vilken en specifik svällningsterm kopplades, två team använde olika versioner av elastoplastisk Barcelona Basic Model (BBM) och ett team använde en elastoplastisk dubbelstrukturmodell (IC-DSM).

Termiska variabler (värmarens effekt och temperaturfältet) reproducerades i allmänhet väl av de numeriska modellerna. I synnerhet kunde ökningen av värmeeffekten med tiden och dess konsekvens för barriärens mättnadsökning plockas upp av flera team. Den progressiva vattenmättnaden av barriären fångades av alla modeller även om ett antal skillnader mellan beräkningar och observationer kunde observeras när man granskade resultaten i detalj. Till exempel var torkningen

av bentoniten nära värmaren ofta underskattad. Betydelsen av ångmigration i de tidiga stadierna av testet demonstrerades också. I allmänhet tenderade modellerna att underskatta nivån av mättnad i slutet av testet. Bedömningen av precisionen i simuleringen av utvecklingen av svälltrycket försvårades av osäkerheter om experimentella mätningarnas tillförlitlighet. Alla THM-modeller gav dock rimliga utfall i termer av utveckling och slutvärden för radiella och axiella totalspänningar.

Den första brytningen visade ett mycket icke-homogent tillstånd i barriären i termer av torrdensitet och det också observerades att en stor del av bentoniten var i ett omättat tillstånd, förutom i zonerna nära berget. I det fallet så överensstämde resultaten från de numeriska modellerna med observationerna. Vid den andra brytningen visade det sig att bentonitbarriären efter 18,15 år hade blivit i princip helt mättad, särskilt i de smalare sektionerna där värmaren var placerad, förutom i en smal zon nära värmarna där mättnadsgraden i alla fall var ganska hög. Det visade sig också att fördelningen av torrdensitet inte hade ändrats sedan den första brytningen. Resultaten från de flesta numeriska THM-modellerna överensstämde med dessa observationer, även om full validering av denna överensstämmelse skulle kräva en fortsättning av modelleringen tills en jämförbar nivå av barriärmättnad hade uppnåtts. Sammanfattningsvis kan det konstateras att de numeriska analyser som gjorts har kunnat representera det globala TH- och THM-beteendet hos en bentonitbarriär i ett icke-isotermiskt storskaligt experiment på ett adekvat sätt. De övergripande observationerna rörande värmarens utveckling, effekt, temperaturfältet vid olika tidpunkter, vattenmättnadens framsteg, utvecklingen av spänningar i bentoniten och barriärens tillstånd vid den första och slutliga demonteringen har på det hela taget varit tillfredsställande representerade av modellerna. Detta ger starkt stöd för uppfattningen att de flesta viktiga processer och deras kopplade interaktioner tycks vara inkorporerade på ett lämpligt sätt i de numeriska modellerna. Man kan också dra slutsatsen att de fastställda målen som omfattade främjandet av förståelsen av THM EBS-beteendet under den transienta fasen, undersökningen av utvecklingen av barriärens tillstånd och validering och förbättring av numeriska förmågan hos de deltagande modelleringsteamen har uppnåtts.

Contents

1 Introduction

The SKB Engineered Barrier System Task Force (EBS TF) was created in May 2004 by the Äspö HRL International Joint Committee with the long-term objective of developing general and effective tools for the advanced coupled TH, THM, THC and THMC analysis of buffer and backfill behaviour. The activities of the Task Force have been steered by SKB throughout its existence. Since its inception, the work of the Task Force has developed without breaks; 32 Task Force meetings have been held so far to report and discuss the progress achieved. The activity of the EBS TF is structured in a series of tasks; generally, several of them run concurrently. 13 different Tasks have been undertaken by the TF so far.

This document reports the outcome of Task 9, a Task focused on the numerical analysis of the FEBEX in situ test, a full-scale heating experiment performed at the Grimsel Test Site (GTS). Waste canisters are simulated by means of two heaters surrounded by an engineered barrier composed of bentonite blocks. It is a temperature-controlled non-isothermal test where the barrier undergoes natural hydration from the host rock. The experiment included two dismantling operations, a partial one after 5 years of heating and a final one after a total of 18.15 years of heating.

Tasks 9 involves the numerical modelling of the FEBEX experiment by seven different teams using a variety of formulations and computer codes. The modelling undertaken in this Task does not constitute a blind prediction exercise as test observations were available to the modelling teams during the Task. Also, opportunities were provided to improve the analyses after comparison with observations and discussion of the results.

The objectives of the Task are:

- To enhance understanding of the THM EBS behaviour during the transient phase.
- To study the state of the engineered barrier at two different stages of its evolution.
- To improve the predictive capabilities and validate the performance of coupled TH and THM formulations and associated codes.
- To develop (or to enhance) constitutive relationships for the thermal, hydraulic and mechanical behaviour of the bentonite.
- To compare the performance of different formulations, numerical codes and constitutive laws.

The Task is organized in two stages; Stage 1 runs from the start of heating to the first partial dismantling while Stage 2 covers the period from the first dismantling to the final dismantling at the end of the test.

The Report is structured as follows. The basic concept, installation, and operation of the experiment as well as the two dismantling events are described first, followed by a presentation of the Task structure, specifications and modelling teams. The main features of the formulations and the analyses of the different modelling teams are then outlined. For each of the two stages of the Task, the results of the numerical analyses performed by the different teams are then presented and compared with the experiment monitoring data. The description of each modelling stage closes with a section containing a number of summary comments. An additional section is devoted to the evolution of the state of the bentonite barrier between the two dismantling events and to the capability of the numerical model to reproduce it. The final section provides an overview and a series of concluding remarks. The report is complemented with a number of Annexes containing relevant information of the Task. They include the specifications for the two Task stages and the final reports submitted by the various modelling teams.

It should be noted that, although care has been taken to incorporate all suggestions from the members of the modelling teams, the opinions and comments contained in this report are the responsibility of the lead author alone.

2 The FEBEX experiment

2.1 Concept and installation

The initial aim of the FEBEX in situ test was to provide a full-scale physical simulation of the Spanish AGP-Granito reference concept for the disposal of spent fuel and High Level radioactive waste (HLW). The concept envisaged placing the waste-containing canisters in horizontal drifts surrounded by an engineered barrier made up of compacted bentonite. Thus, the test involved placing two heaters in the centre of a horizontal tunnel, simulating waste packages, surrounded by a buffer of compacted bentonite blocks (Figure 2-1).

The experiment was initiated in 1995 and the final dismantling was completed in 2015. The total heating time was 18.15 years and a partial dismantling involving the removal of one of the heaters was performed after 5 years of heating thus allowing a direct observation of the state of the bentonite barrier at an intermediate stage. The experiment has been associated with a number of international projects as illustrated in the timeline shown in Figure 2-2. Only an abridged description of the test is given here; additional information is provided in the specifications of Stage 1 (Annex A).

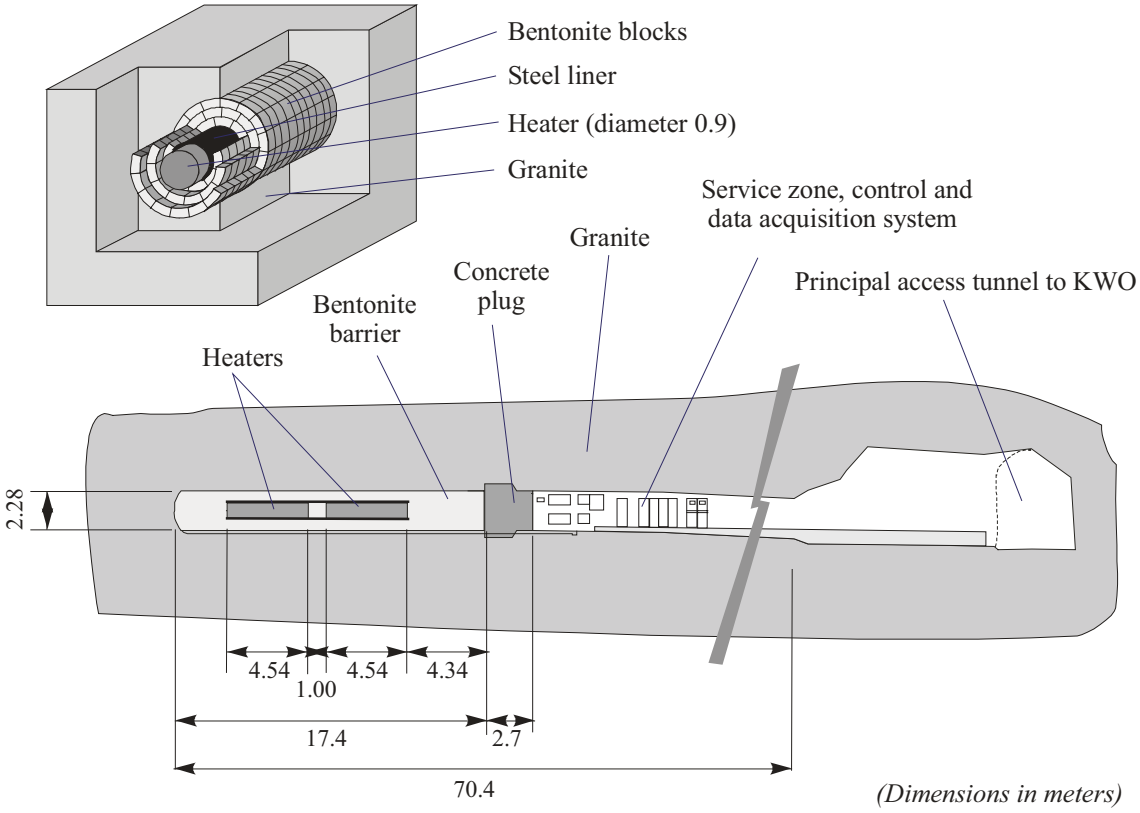

Figure 2-1. *Layout of the FEBEX in situ test (ENRESA 2000).*

Figure 2-2. *Timeline of the FEBEX experiment.*

The FEBEX test was performed at the Grimsel Test Site (GTS), an underground laboratory located in the Swiss Alps (Figure 2-3). To install the test, a purpose-built 2.28 diameter and 70.4 m long tunnel was excavated with a Tunnel Boring Machine (TBM) (Figure 2-4). The host rock is a good-quality granite, containing, a lamprophyre dyke in the test zone. The tunnel location is shown in Figure 2-5. The test area occupied the final 17.4 metres of the tunnel.

Figure 2-3. *Location and surroundings of the Grimsel Test Site (1. Test Site; 2. Juchlistock; 3. Lake Räterichsboden; 4. Lake Grimsel; 5. Rhone Valley).*

Figure 2-4. *Excavation of the FEBEX experiment tunnel.*

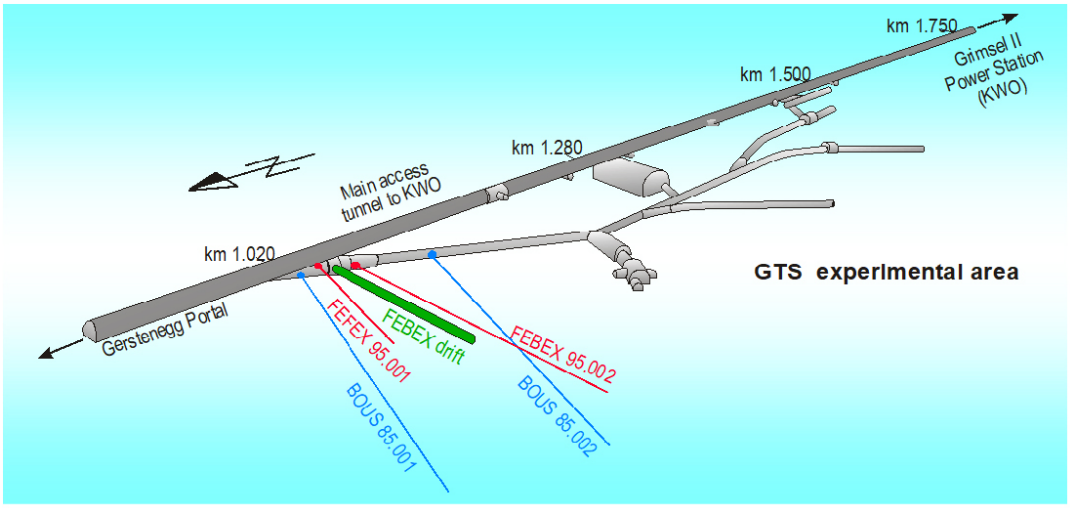

Figure 2-5. *Location of the FEBEX tunnel at the Grimsel Test Site. Associated exploration boreholes are also shown (ENRESA 2006a).*

The general layout of the experiment is shown in Figure 2-6. The heaters are 4.54 m long and 0.90 m diameter and have a power of 4 300 W; the dimensions are selected to simulate the canister design of the disposal concept. The installation of the heaters was assisted by the previous placing of a 15 mm-thick perforated steel liner (Figure 2-7). The empty space of the tunnels was filled by compacted bentonite blocks to form the engineered barrier (Figure 2-8). A total of 5 331 blocks were used in the installation of the experiment. The thickness of the barrier in the zone corresponding to the location of the heaters is 69 cm. The barrier was constructed manually. Finally, the test area was sealed with a 2.7 m-long concrete plug (Figure 2-6).

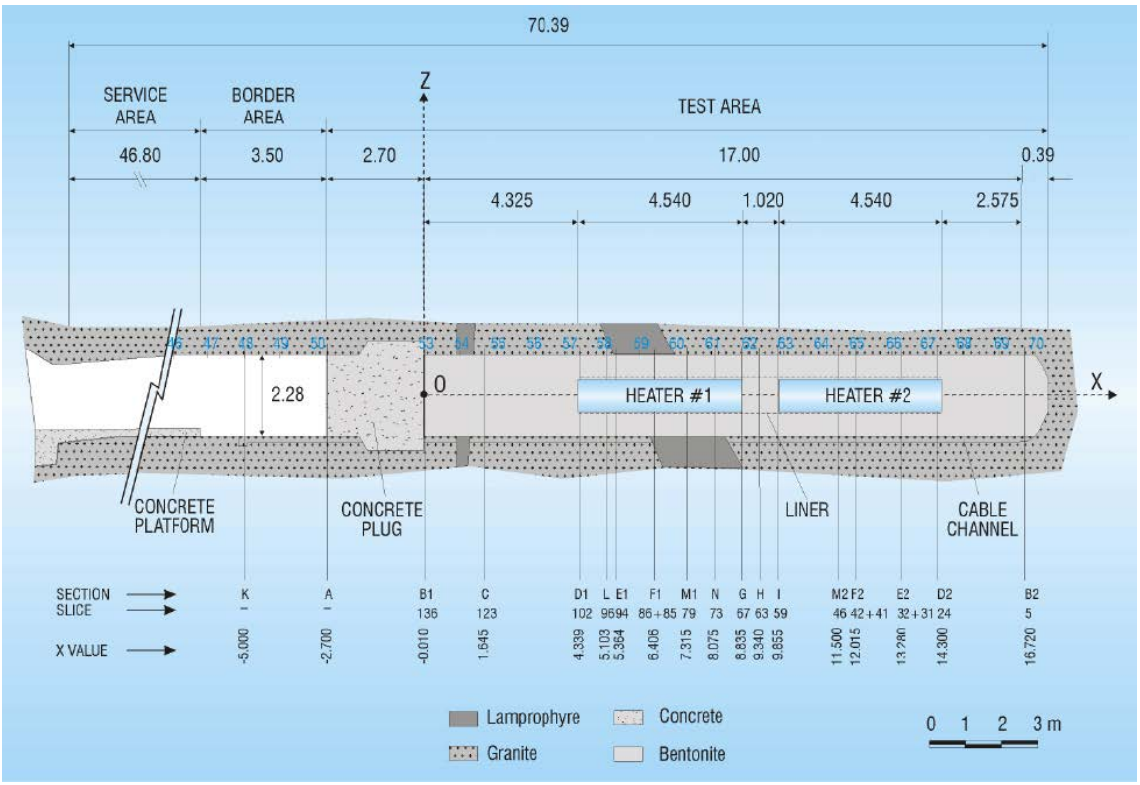

Figure 2-6. *General layout of the FEBEX test (Bárcena et al. 2003).*

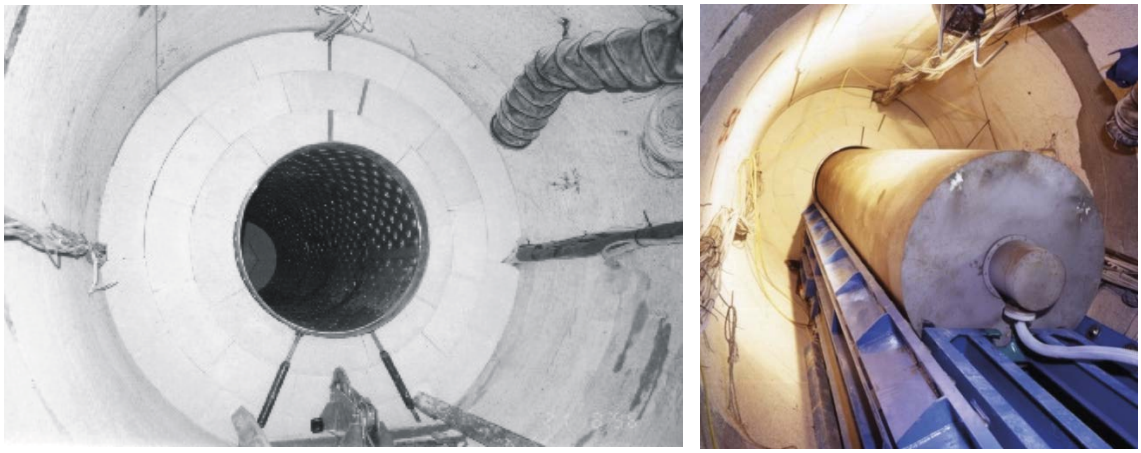

Figure 2-7. *Left: Perforated liner, Right: insertion of a heater (ENRESA 2000).*

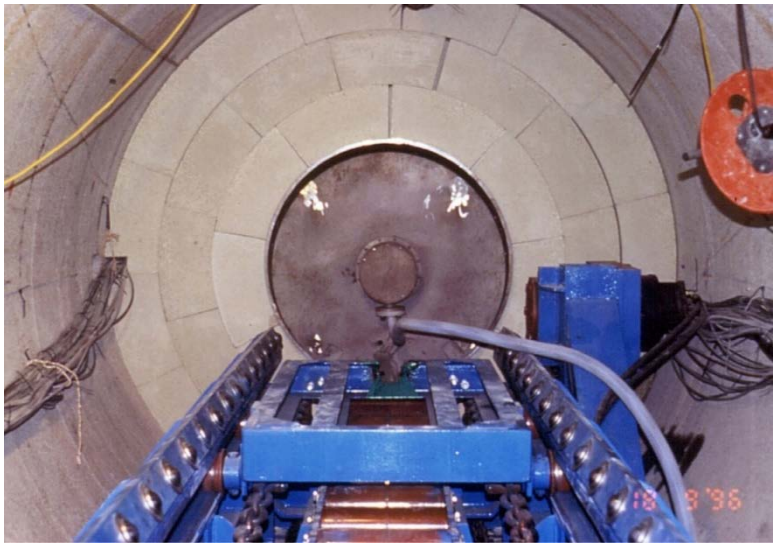

Figure 2-8. *Compacted bentonite blocks barrier surrounding one heater (ENRESA 2000).*

The bentonite was quarried in the volcanic zone of Serrata de Níjar in southern Spain. It has a smectite content in the range of 88–96 %, with small and variable quantities of accessory minerals such as quartz, calcite and feldspars. The cation exchange capacity is 100–102 meq/100 g (42 % Ca, 33 % Mg, 23 % Na, 2 %K). The ranges of the liquid and plastic limits are 98–106 and 50–56, respectively. The material will be called FEBEX bentonite in the following. The bentonite blocks were compacted to a dry density of 1.7 g/cm^3 at an average water content of 14.4 %. Because there were small gaps between blocks, and between the clay barrier and the rock, the overall dry density of the emplaced barrier was 1.60 g/cm^3. Full details on the thermo-hydro-mechanical properties of the FEBEX bentonite are provided in Annex A.

A total of 632 sensors were installed in the clay barrier, the surrounding rock, the heaters and the service zone to monitor the THM behaviour of the test. Only the test observations made in the barrier and heaters are considered in this benchmark. The main parameters measured in the bentonite barrier were temperature, relative humidity and total normal stresses with sensors emplaced in the sections shown in Figure 2-9. A typical instrumentation layout section is presented in Figure 2-10. The power applied to the two heaters was also monitored.

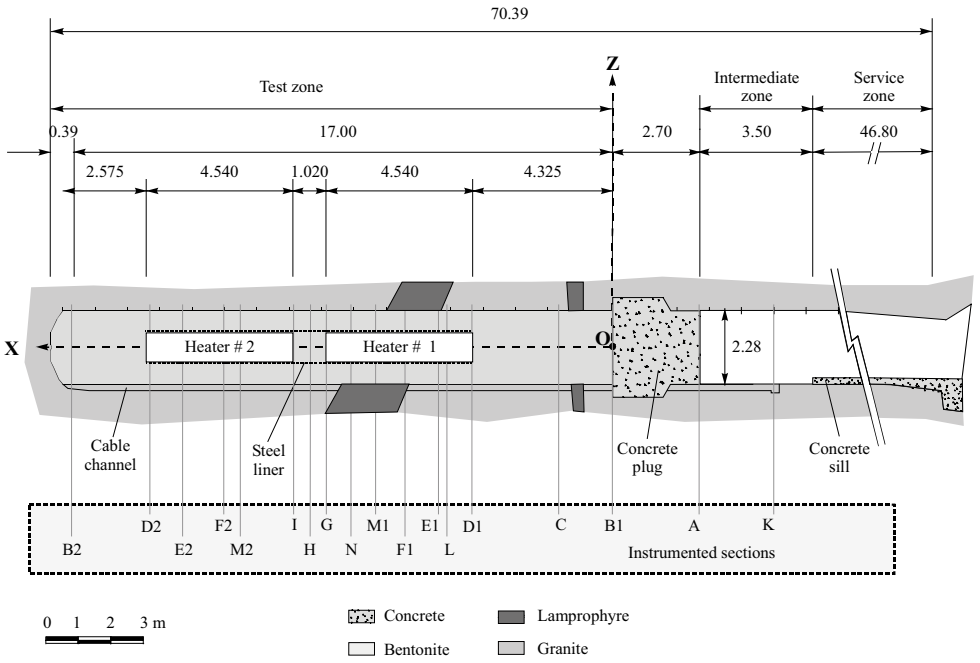

Figure 2-9. *Instrumented sections in the engineered barrier(ENRESA 2006a).*

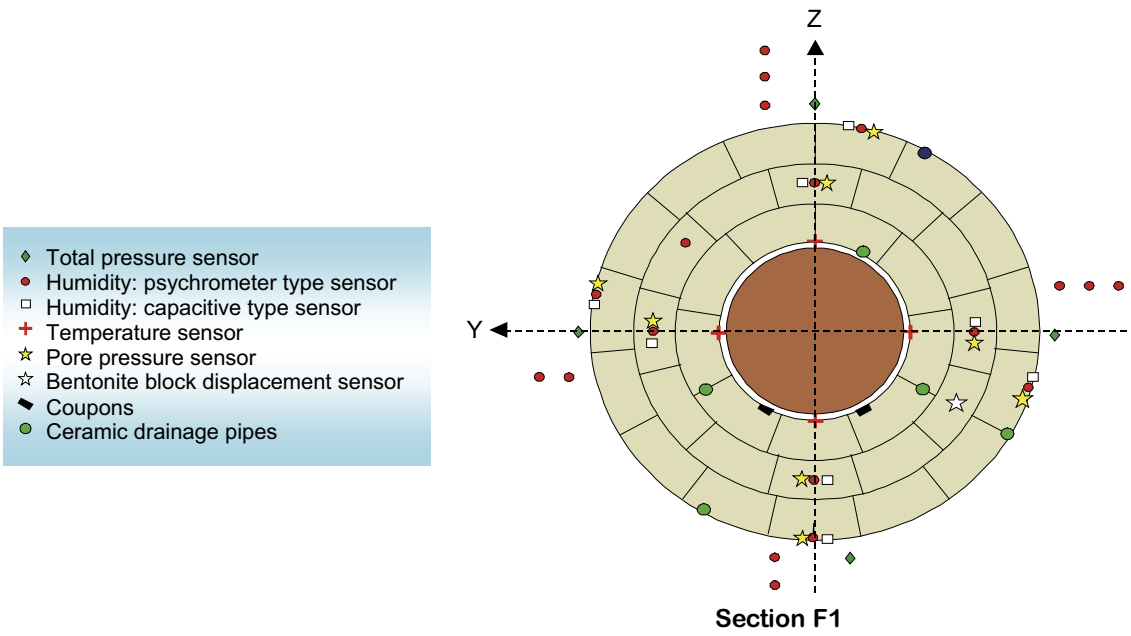

Figure 2-10. *Instrumentation layout of section F1.*

2.2 Operation and dismantling

The operation of the test included an installation phase, two heating phases and two dismantlings, a partial one and a final one. Heating phase 1 involved two operating heaters whereas in heating stage 2 there was only one heater. Table 2-1 shows the dates of major test operations.

The heating stage of the experiment started on the 27th February 1997. This is taken as day zero to define a common time scale. The sequence of the initial heating stage was as follows:

- A constant power of 1 200 W per heater was applied during an initial period of 20 days in order to determine the thermal response of the system and adjust the control algorithms.
- During the next 33 days, the power was increased to 2 000 W in each heater and maintained constant until reaching the specified maximum temperature of 100 °C on the surface of the steel liner.
- On 21st April 1997 (day 53), the system was transferred to temperature control maintaining a maximum temperature of 100 °C on the liner/bentonite contact surface. From then on, the heater power was automatically adjusted to keep this condition.

Full details of the design, installation and operation of the experiment are presented in ENRESA (2000). The full instrumentation records are collected in Martínez et al. (2016)

Table 2-1. Dates of relevant events of the FEBEX experiment.

Phase	Description	Date	Days
Installation	Start of tunnel excavation	25/09/95	−521
	End of tunnel excavation	30/10/95	−486
	Start of test installation	01/07/96	−241
	End of test installation	15/10/96	−135
Heating 1	Heaters #1 and #2 switched on. Power: 1 200 W/heater	27/02/97	0
	Heaters #1 and #2. Power: 2 000 W/heater	19/03/97	20
	Heaters #1 and #2 transferred to temperature control	21/04/97	53
	Heater #1 switched off	28/02/02	1 827
Partial/ First dismantling	Start of plug demolition	02/04/02	1 860
	Excavation of bentonite up to heater #1	29/05/02	1 917
	Extraction of heater #1	19/06/02	1 938
	End of bentonite excavation	19/07/02	1 968
Heating 2	Shotcrete of second plug (inner part)	25/07/02	1 974
	Shotcrete of second plug (outer part)	27/06/03	2 311
	Start of bentonite coring through the plug	17/02/15	6 564
Final dismantling	Start of the demolition of the second plug (outer part)	07/04/15	6 613
	Heater #2 switched off	20/04/15	6 626
	Start of the demolition of the second plug (inner part)	27/04/15	6 633
	Excavation of bentonite up to heater #2	18/05/15	6 654
	Excavation of bentonite up to the centre of heater #2	24/05/15	6 660
	Excavation of bentonite to the end of heater #2	30/05/15	6 666
	Excavation of bentonite to the end of the tunnel and extraction of heater #2	04/06/15	6 671
	End of dismantling	20/07/15	6 717

After 5 years of heating, a partial dismantling operation was performed (Barcena et al. 2003, ENRESA 2006b). Heater #1 was switched off and, after excavation of the bentonite surrounding it, it was extracted and removed. Only the bentonite slices corresponding to the end 1 m of the heater were left in place and the resulting void filled with a dummy cylinder. The remaining experiment was sealed with a new shotcrete plug built in two stages. A few new instruments were installed prior to the construction of the plug measuring temperature, total pressure, relative humidity, mass water content, plug displacements and gas flow. Heater #2 was kept functioning throughout the dismantling operations using the same maximum 100 °C criterion as before. The experiment configuration after this first dismantling is shown in Figure 2-11. Figure 2-12 shows the state of the barrier after 5 years of heating and a view of the extraction of heater #1.

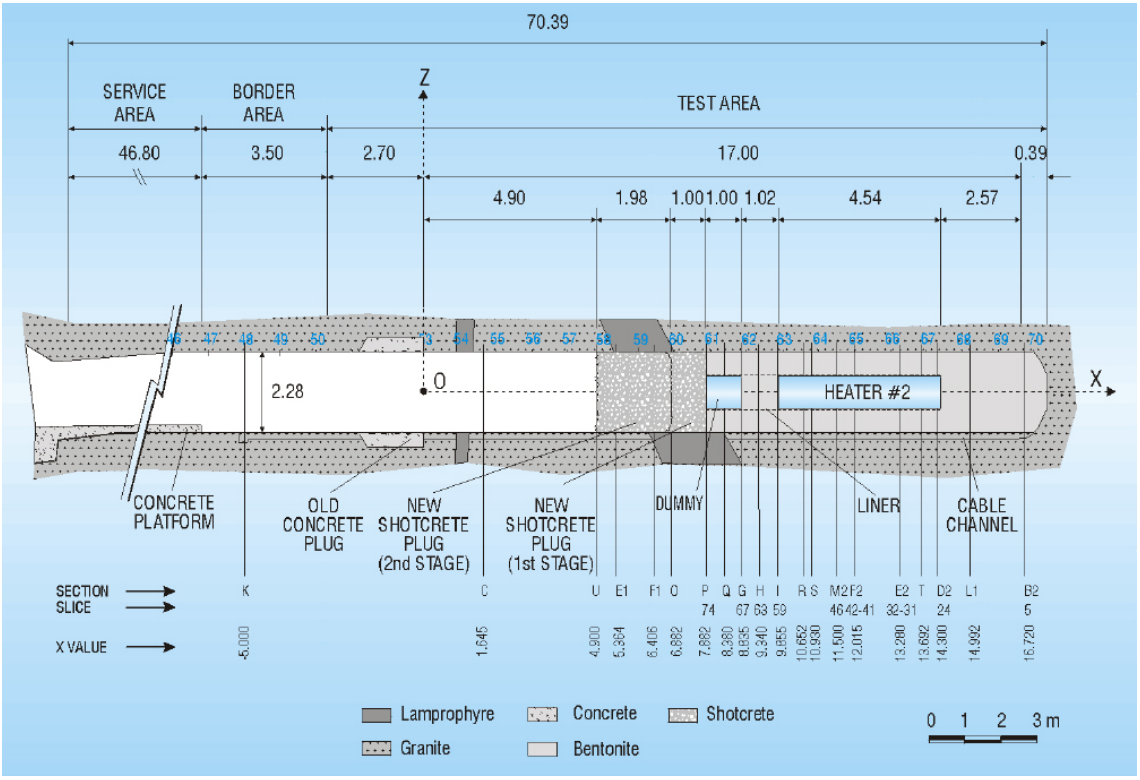

Figure 2-11. *Test configuration after the first dismantling (ENRESA 2006a).*

Figure 2-12. *Left: State of the barrier after 5 years of heating. Right: Extraction of heater #1 during the first dismantling (Barcena et al. 2003).*

During the dismantling, the bentonite was intensively sampled in the sections indicated in Figure 2-13. Of special interest for this benchmark are the determinations of dry density, water content and degree of saturation using samples extracted from sections 8, 9, 10, 11, 13, 14, 15, and 16, located in the zone between the concrete plug and the heater, and from sections 18, 20, 22, 27, 29 and 31 located in the region of the heater. Sampling points were arranged in a radial pattern (Figure 2-14). The determinations of those parameters were performed in a field laboratory located in the FEBEX experimental area.

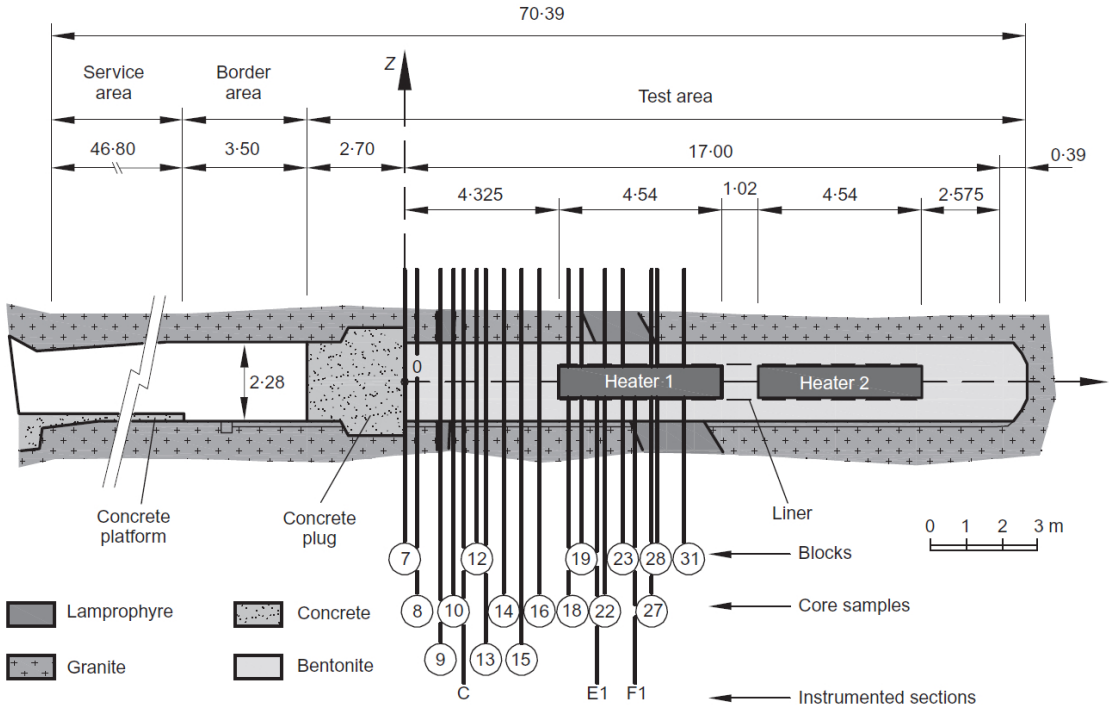

Figure 2-13. *Location of sampling sections (Barcena et al. 2003).*

Figure 2-14. *Bentonite sampling during the first dismantling (Barcena et al. 2003).*

Heater #2 was switched off on the 20 April 2015, 18.15 years after the start of heating. Throughout all this time the maximum temperature in the liner/bentonite contact was maintained at 100 °C. Immediately afterwards, the final dismantling of the experiment was undertaken (García-Siñériz et al. 2016, Villar et al. 2016) involving the demolition of the second plug, the excavation of the bentonite and the extraction of the remaining heater (Figure 2-15). The bentonite was again intensely sampled in the sections shown in Figure 2-16. Water content, dry density and degree of saturation were measured from samples extracted from sections 37, 39, 43, 45, 49, 52, 56, 58 and 61. Again, to ensure the quality of the results, the determinations were performed in a field laboratory on site. An example of one of the sections is shown in Figure 2-17 left. An interesting observation was that, at the time of final dismantling, the bentonite had flowed through the holes of the liner creating a number of bulges as shown in Figure 2-17 right.

Figure 2-15. *Extraction of Heater 2 during final dismantling (García-Siñériz et al. 2016).*

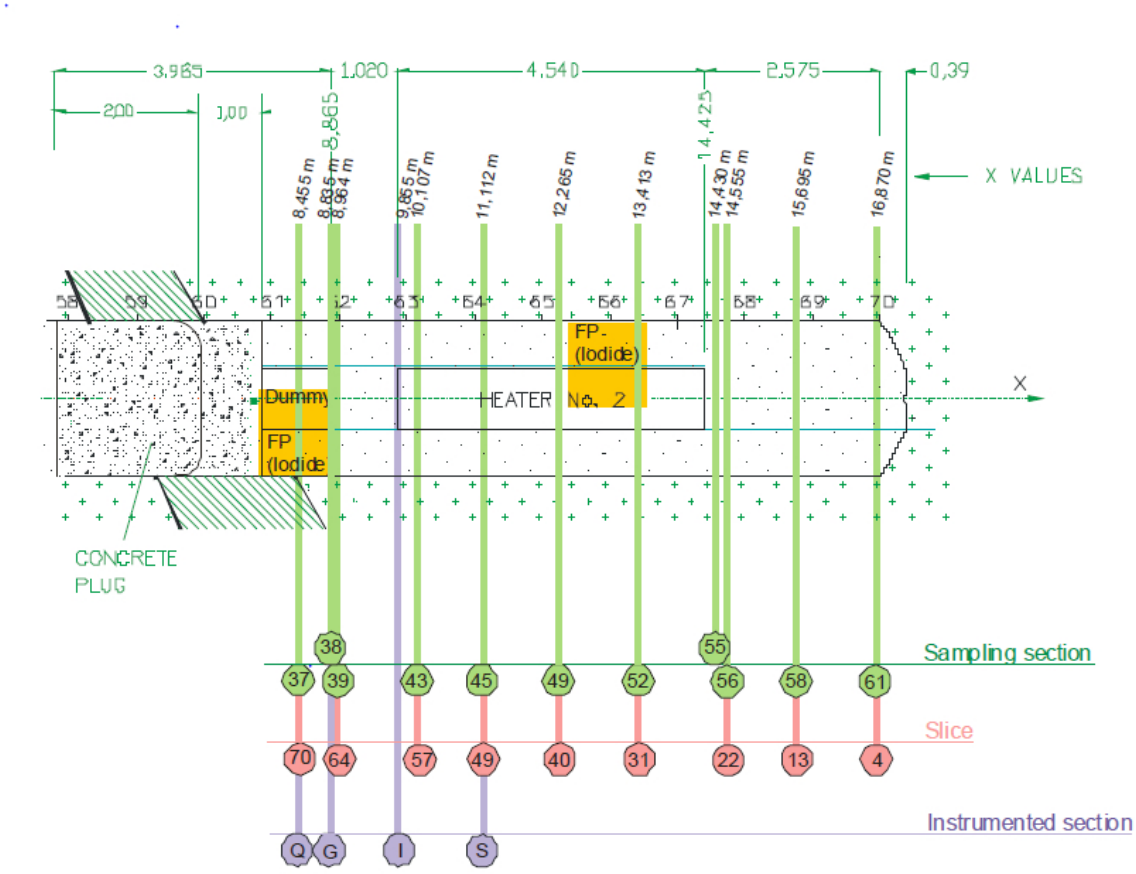

Figure 2-16. *Location of the sampling sections of the final dismantling (Villar et al. 2017).*

Figure 2-17. *Left: Example of sampling section. Right: Bentonite bulges inside the liner (García-Siñériz et al. 2016).*

3 Organization of the Task

3.1 Task structure and specifications

The Task was structured in two successive stages:

- Stage 1 involving the stages of installation, heating 1 and first dismantling.
- Stage 2 involving the stages of heating 2 and final dismantling.

The specifications for Stage 1 are in Annex A. The specifications include a detailed account of the FEBEX test and information on the FEBEX bentonite. The description of the experiment covered the following items:

- Geology and hydrogeology of the Grimsel Test Site
- Properties of the rocks at the Grimsel Test Site
- Geology and hydrogeology of the FEBEX drift area
- Configuration of the FEBEX tunnels and associated boreholes
- Description of the excavation of the FEBEX tunnel
- Bentonite blocks used in the experiment
- Description of the heating system
- Description of the instrumentation
- Description of the concrete plug
- Test start-up procedure
- Heating control and test operation
- Description of the first dismantling

The information on the FEBEX bentonite comprised the following points:

- Origin of the bentonite
- General properties and porosity
- Mechanical, hydraulic and thermal parameters
- Additional tests for the derivation of parameters
- Thermo-hydraulic vapour migration test
- Oedometer tests under controlled suction at different temperatures
- Tests on bentonite joints
- Tests in CIEMAT thermohydraulic cell

The specifications also included the modelling results requested. They refer to both operational test observations and dismantling data. Regarding the operational data, the following parameters were demanded:

- Evolution of the power in each of the two heaters
- Distributions of temperature on three cross-sections and two axial segments
- Evolution of temperature in three cross-sections
- Distributions of relative humidity in four cross-sections
- Evolution of relative humidity in four cross-sections
- Evolution of total pressure at four locations (three radial stresses, one axial stress)

With respect to the first dismantling data, radial distributions of dry density, mass water content and degree of saturation were required for three sections, two in the zone of the heater and one outside.

Stage 2 specifications (Annex B) provided information on the configuration and operation of the experiment after the first dismantling, and on the final dismantling. The requested results again involved operational test observations and the final dismantling data. The required results of the analyses for the operational test data included:

- Evolution of the power of the remaining heater
- Distributions of temperature in one cross-section and two axial segments
- Distributions of relative humidity in one cross-section
- Evolution of relative humidity in one cross-section
- Evolution of total pressure at five locations (three radials stresses and two axial stresses)

In addition, radial distributions of dry density, mass water content and degree of saturation at four cross-sections corresponding to the final dismantling were requested for comparison with observations. Two cross-sections were in the heater zone and two outside. One cross-section (61), close to the end of the tunnel, had an unusually low initial value of dry density due to the difficulty of fitting the blocks in the curved surface at the end of the drift. The observations of this section are therefore not representative of the overall behaviour of the tunnel.

3.2 Modelling teams

Seven modelling teams participated in the benchmark. They are (in alphabetic order):

- Central Research Institute of Electric Power Industry, Japan (CRIEPI)
- Gesellschaft für Anlagen- und Reaktorsicherheit, Germany (GRS)
- Imperial College, London, UK (ICL)
- Sandia National Laboratories, US (SNL)
- Svensk Kärnbränslehantering - Clay Technology, Sweden (SKB-CT)
- Technical University of Liberec, Czech Republic (TUL)
- Universitat Politècnica de Catalunya, Spain (UPC)

The team from Sandia National Laboratories joined the Task at a later stage than the other teams. In the following, the teams will be referred to by the acronyms shown in brackets in the above list.

4 Features of the numerical analyses

This section is based on the information provided by the modelling teams in their Final Reports. The reports are incorporated as Annexes C to I. They generally contain a description of the formulation used, the thermal, hydraulic and mechanical constitutive laws, the computer code employed, the parameters adopted, the main characteristics of the calculations carried out (including the domain geometry and discretization) and a presentation and a discussion of selected results. Some teams include important supplementary information such as sensitivity analyses or additional simulations. Only the most salient features of the reports are summarised in this section.

4.1 Central Research Institute of Electric Power Industry, Japan (CRIEPI)

CRIEPI has used a coupled T-H-M formulation extended to include a partially saturated thermo-hydro-elastic medium. Three phases were considered, solid, liquid, and gas but the gas pressure was assumed constant and equal to atmospheric in the calculations. Vapour transport is due to molecular diffusion driven by a gradient in the vapour concentration (Fick's law), while the advection of vapour with the bulk gas flow is neglected. The resulting equations are solved in a fully coupled manner using the in-house computer code LOSTUF.

The mechanical constitutive law is isotopic elastic with the addition of a bentonite-swelling model in which the maximum swelling strain of bentonite is expressed as a function of the mean stress as derived from Komine and Ogata (2004). Swelling strain is related to the change of suction by a power law although a linear relationship has been used in the base case. Figure 4-1 shows a scheme of the bentonite swelling model and the associated numerical strategy.

Other features of the constitutive laws adopted are:

- Specific heat and coefficient of thermal expansion dependent on temperature
- Thermal conductivity dependent on degree of saturation
- Vapour diffusion dependent on degree of saturation and tortuosity
- Intrinsic permeability dependent on dry density (or porosity)
- Van Genuchten expression adopted for the water retention curve
- Cubic law for the dependency of relative permeability with degree of saturation

A 2D axisymmetric analysis domain has been used that takes into account the presence of the access drift and the concrete plug. The size of the analysis domain is 120 m in the axial direction and 50 m in the radial direction. The mesh incorporates 7 017 nodes and 6 940 linear quadrilateral elements (Figure 4-2). The number of elements across the bentonite barrier is 6 in the heater section, and 10 in the no-heater section. The lamprophyre and fracture zone are considered with a higher permeability. CRIEPI performed a groundwater analysis in order to determine the initial water pressure field for the THM calculations (Figure 4-3). The ventilation and isothermal hydration stages of the experiment were included in the analyses and the various stages of the dismantling operations were carefully reproduced in the THM simulations.

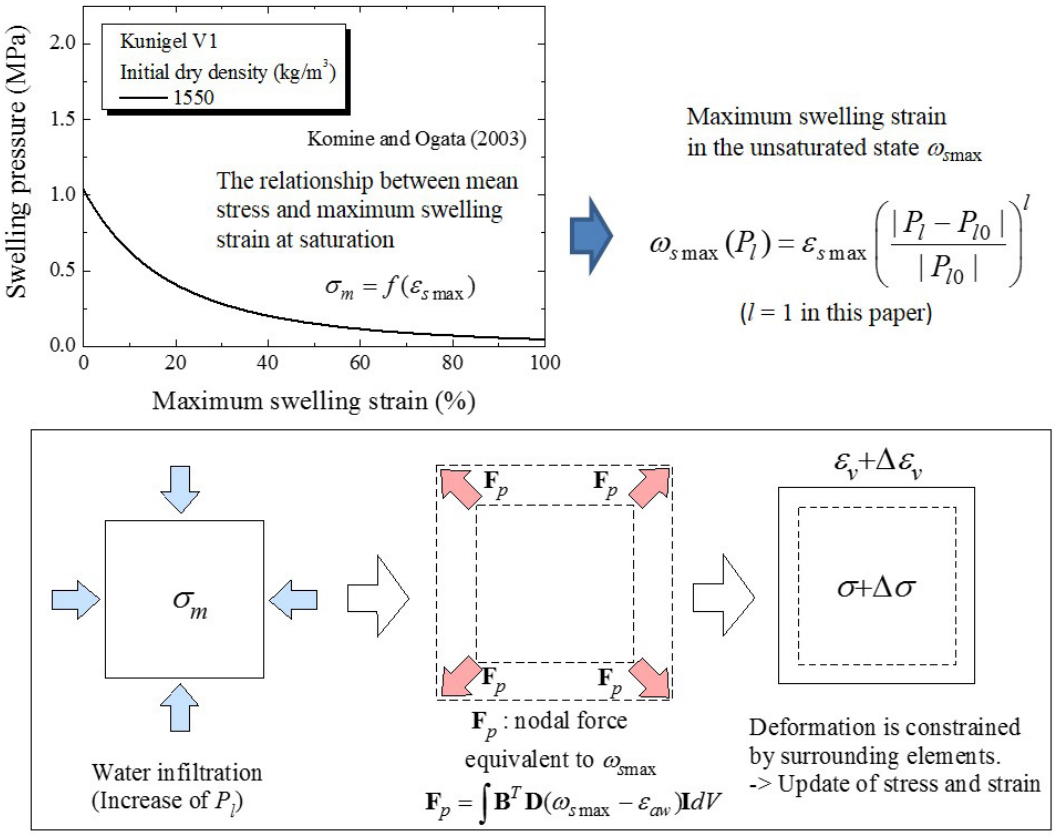

Figure 4-1. *Bentonite swelling model and associated numerical algorithm.*

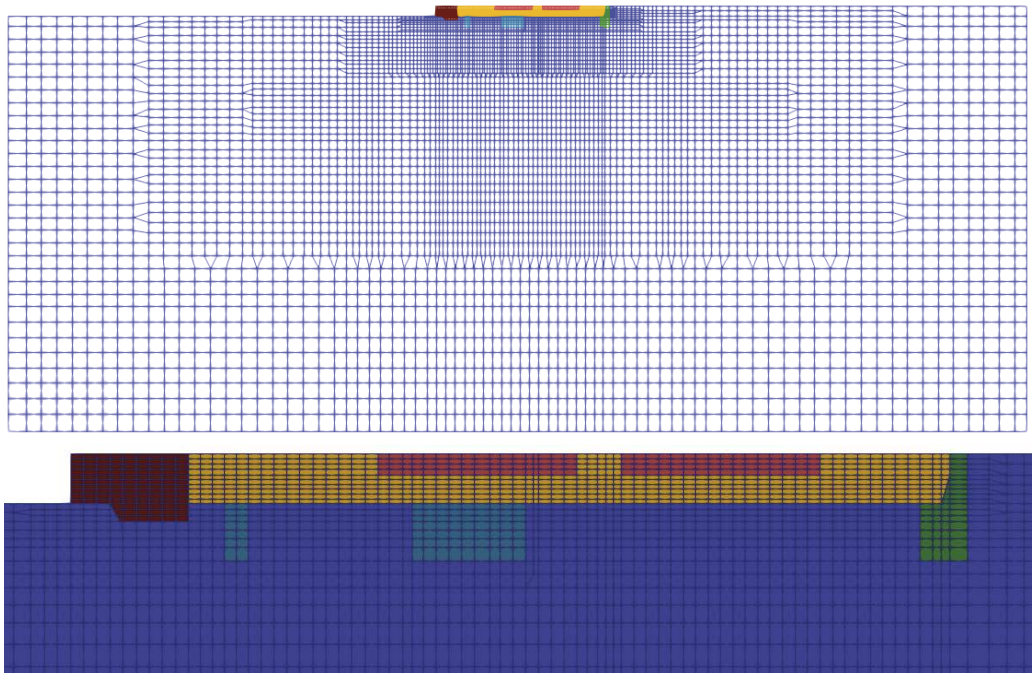

Figure 4-2. *Finite element mesh.*

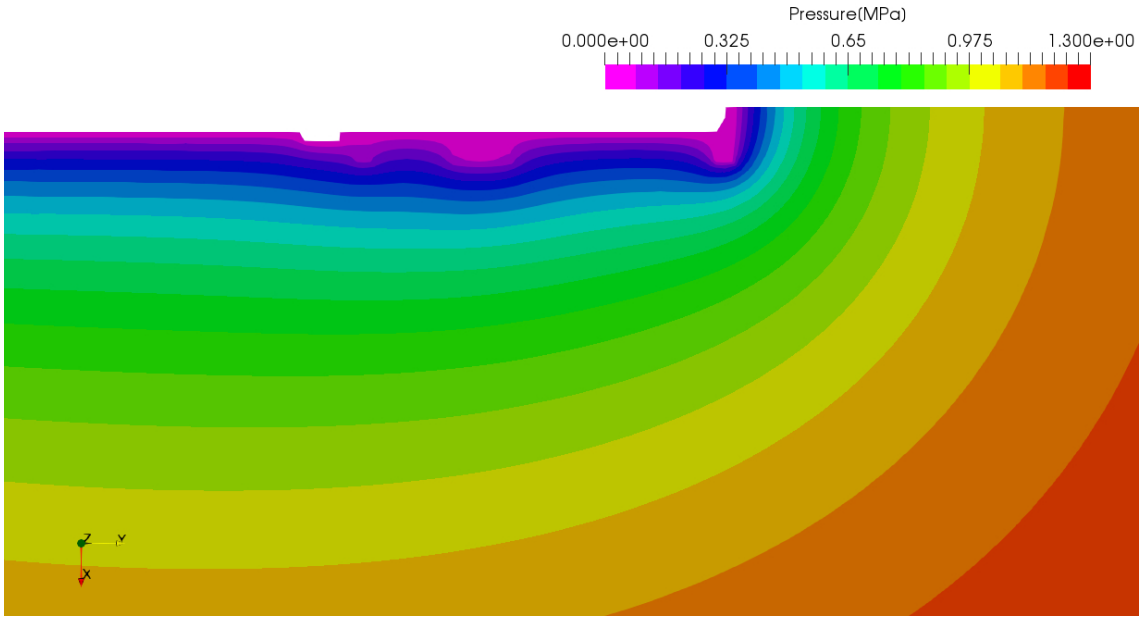

Figure 4-3. *Water pressure distribution after one year of analysis.*

CRIEPI also performed a series of sensitivity analyses varying rock permeability, bentonite permeability, Young's modulus and Poisson's ratio and the coefficient of the relationship relating swelling strains and suction. An example of the results is shown in Figure 4-4 where it can be observed that increasing the bentonite permeability by an order of magnitude has an important effect on the saturation of the barrier and, as a consequence, a noticeable effect on the computed heater power. Following a suggestion of the Task coordinator, CRIEPI also extended the Stage 1 analysis to 100 years to examine long-term effects. This simulation allowed the estimation of the time for full saturation as 44 years, approximately. Surprisingly, the prediction of the distribution of dry density changed significantly now showing a higher value close to the rock (Figure 4-5).

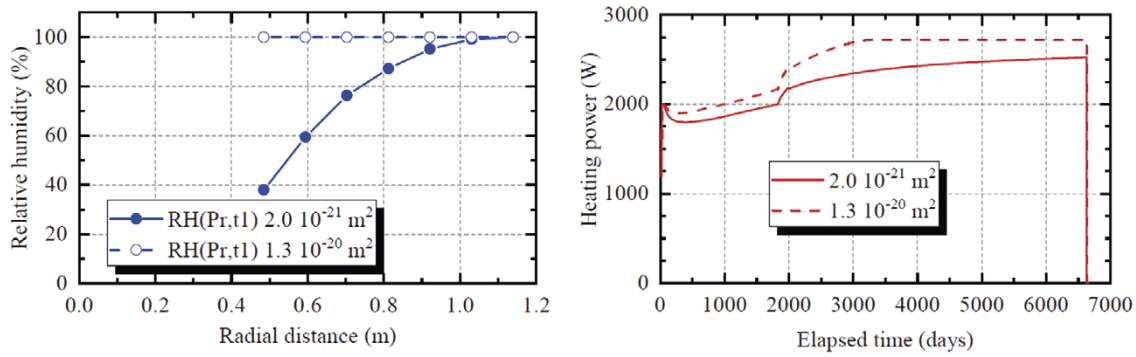

Figure 4-4. *Effect of bentonite permeability. Left: distribution of relative humidity. Right: heater power.*

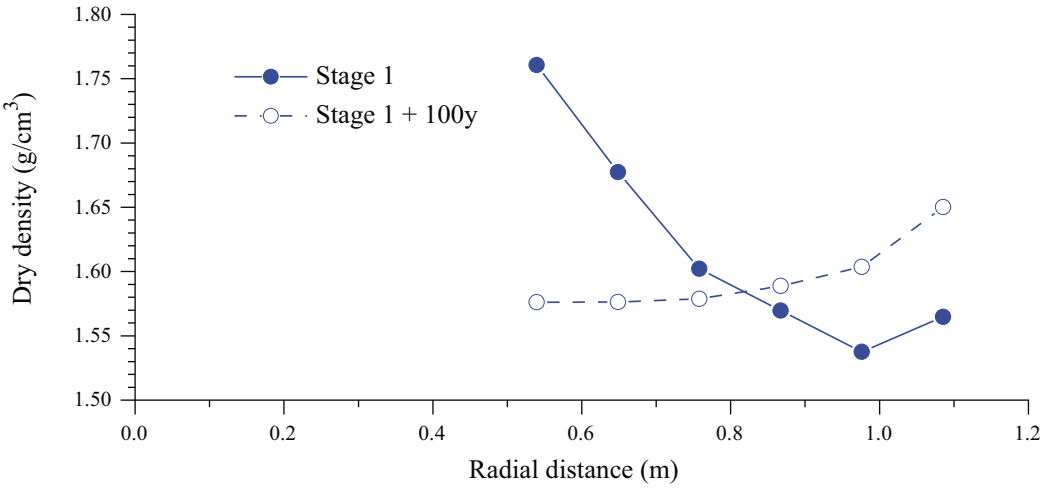

Figure 4-5. *Distribution of dry density: Stage 1 and Stage 1 + 100 years.*

4.2 Gesellschaft für Anlagen- und Reaktorsicherheit, Germany (GRS)

GRS addressed the thermal and hydraulic problem but did not incorporate the mechanical aspects. The thermal calculations are done first with an axisymmetric 2D-Model and the resulting temperature fields are used as input for the calculation of the non-isothermal water uptake. The influence of water flow on the temperature field is neglected. For stage 2, the changes in the system due to excavation and renewed plugging are neglected; heater #1 is simply switched off at the end of stage 1. Rock permeability is assumed high enough to provide as much water as the bentonite can take up at any particular moment. Modelling included the isothermal period of 135 days between installation and begin of heating

A 2D axisymmetric analysis domain, 50 m long and 45 m radius, is used for solving the thermal problem (Figure 4-6). The mesh has 37 943 linear triangular elements and 13 484 nodes. The computer code employed for the heater flow problem is COMSOL.

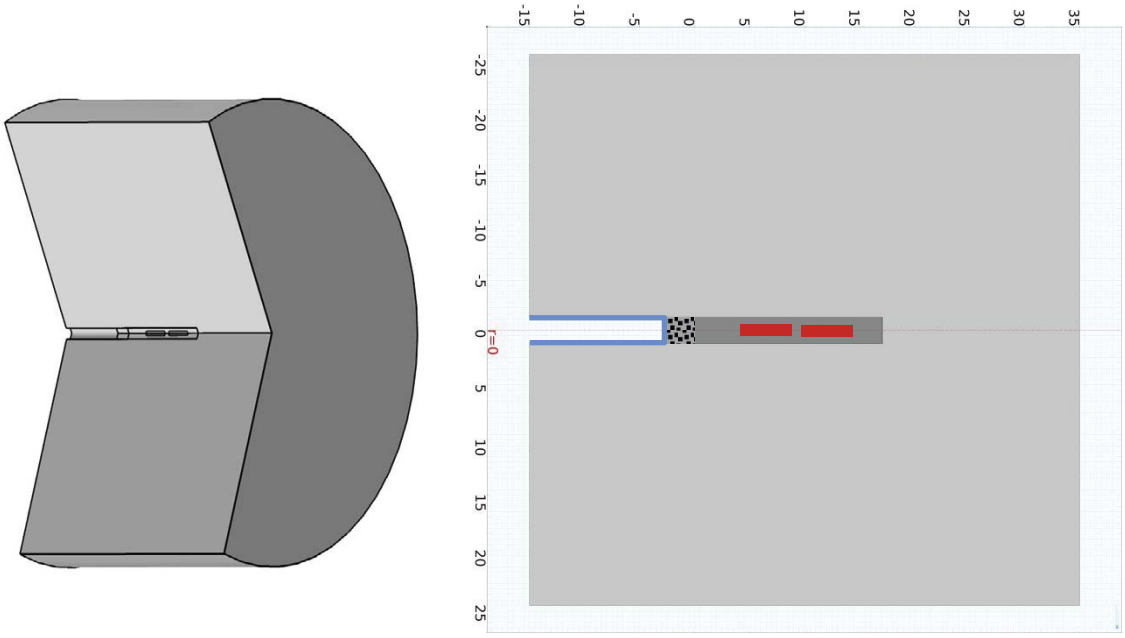

Figure 4-6. *Analysis domain for the thermal problem; left: full model in 3D, right: Cut-out in 2D.*

The conceptual background of the code used to simulate the water uptake process, VIPER, is based on a double-continuum model which is composed of the intergranular pore space and the interlamellar space of the clay grains. The balance equations are set up for water vapour in the pore space and for hydrated water in the interlamellar space. In each balance equation, only one migration process is considered, vapour diffusion in the pore space and diffusion of hydrated water in the interlamellar space (using Fick's law in both cases). There is an instantaneous exchange of water between these two spaces using an adsorption isotherm. Non-isothermal problems are solved by using pre-determined transient temperature fields as input.

The key temperature-dependent isotherm is based on an isotherm established for the FEBEX test (Villar et al. 2005) modified to account for the effects of temperature and relative humidity based on data from MX-80 bentonite (Kröhn 2011). The resulting family of curves is shown in Figure 4-7 where it can be noted that the maximum influence of temperature lies in the range of 70 % relative humidity.

Taking advantage of symmetry conditions, the hydraulic problem is addressed with a 1D axisymmetric geometry involving only the bentonite barrier. The two cross sections complying with the symmetry conditions are modelled: section C (without heater), 114 cm long, and section F2 (with heater), 69 cm long. 100 elements (and 101 nodes) are used in both cases.

Some features of the constitutive laws adopted are:

- Specific heat and thermal conductivity of the bentonite are constant
- Vapour diffusion dependent on temperature
- Diffusion of interlayer water dependent on temperature and water content
- Intrinsic permeability does not enter in the formulation
- Isotherms establish a temperature-dependent relationship between water content and relative humidity

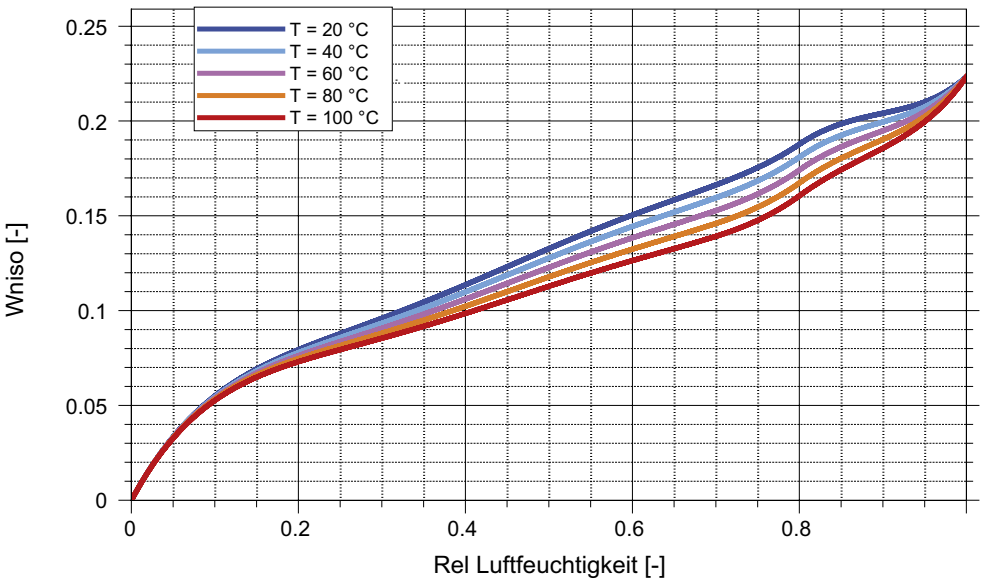

Figure 4-7. *Temperature-dependent isotherm for confined FEBEX-bentonite (Kröhn 2010). Relationship between water content and degree of saturation.*

4.3 Imperial College, London, UK (ICL)

ICL uses a fully coupled thermo-hydro-mechanical formulation implemented in the bespoke computer code ICFEP (Potts and Zdravkovic 1999). Full details are given in Cui et al. (2018).

The mechanical behaviour of the bentonite is simulated by the Imperial College Double Structure Model (IC DSM), (Ghiadistri et al. 2018, Ghiadistri 2019). The IC DSM uses the concept of double porosity present in the structure of a compacted clay (Figure 4-8). One level of porosity is the void space between the clay aggregates, defined as macro- or inter-aggregate porosity and the second level of porosity is the void space within an aggregate, defined as micro- or intra-aggregate porosity. The interaction between the two levels of structure upon saturation of compacted clays contributes to their swelling potential. The model is defined in terms of net stresses and equivalent suction that is the excess of suction over the air entry value of the clay. Interaction functions define the interplay between the two porosity levels, their value depends on the location of the current stress state with respect to the yield surface (Figure 4-9).

Other features of the constitutive laws used are:

- Specific heat and thermal conductivity are constant
- Vapour transport not considered in the analysis
- Intrinsic permeability independent of dry density (or porosity)
- Van Genuchten expression adopted for the water retention curve
- The dependence of hydraulic conductivity with suction is defined by a linear variation between two specified value of suction

A 2D axisymmetric geometry has been used in the analyses (Figure 4-10). It includes the entire FEBEX drift, comprising the concrete plug and the surrounding host rock, both behind the tunnel face and around the tunnel walls. The axis of the drift coincides with the axis of symmetry. The mesh employs 2016 8-noded quadrilateral elements. There are 10 elements across the thickness of the bentonite buffer in sections of the drift where the heater is also present and 16 elements where sections comprise bentonite only. Tunnel excavation, installation of the experiment and dismantling operations have been simulated in the analyses.

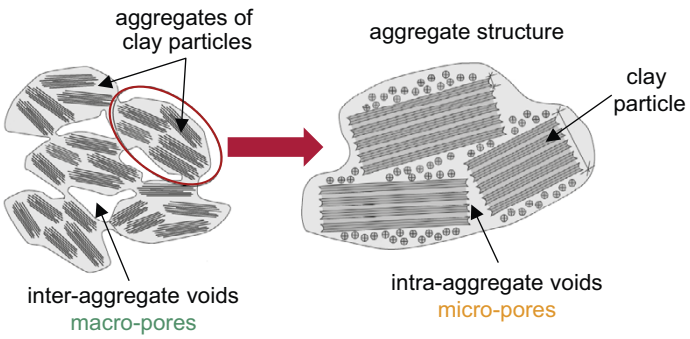

Figure 4-8. *Conceptual illustration of a double-porosity structure in compacted clays.*

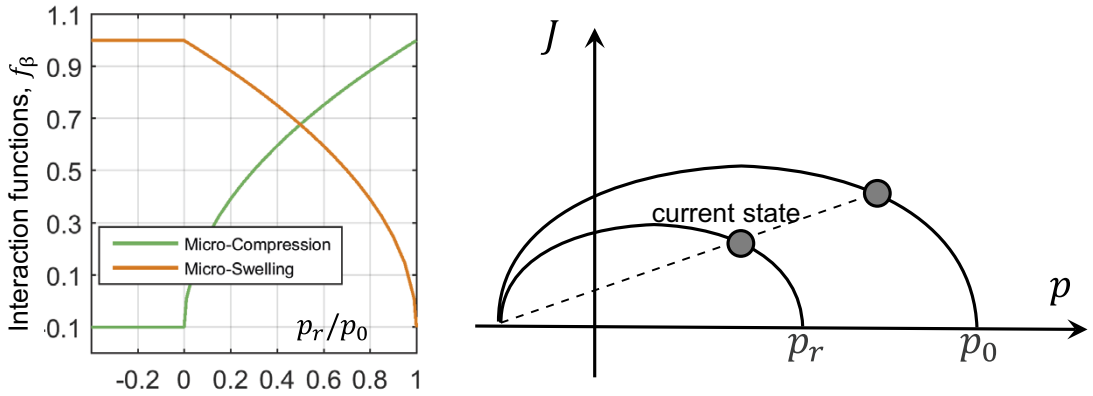

Figure 4-9. *Left: interaction functions, Right: Relationship between the current stress state and the yield surface.*

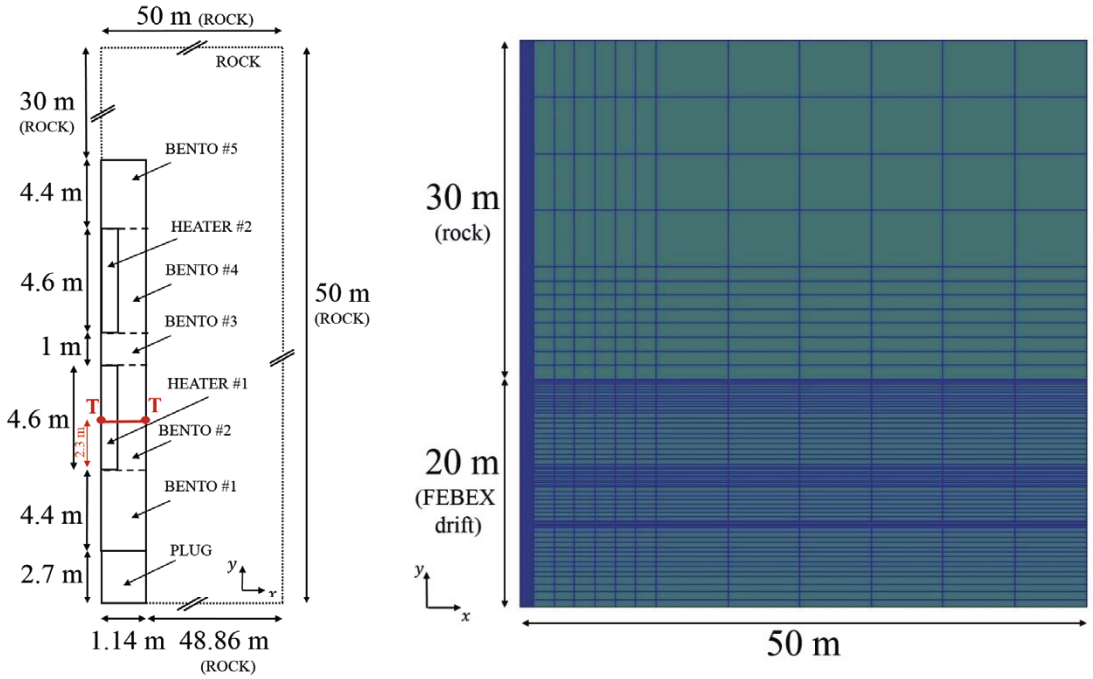

Figure 4-10. *Analysis domain and finite element mesh.*

4.4 Sandia National Laboratories (SNL)

SNL has performed coupled TH analyses based on a general formulation that prescribes mass and energy conservation in a three-phase, three-species porous medium. Vapour transport is due to molecular diffusion driven by a gradient in the vapour concentration (Fick's law). Local phase equilibrium is assumed throughout. Mechanical aspects are not incorporated in the calculations. The calculations were carried out using the code PFLOTRAN in a high-performance computing environment involving 160 processors.

Some other relevant features of analyses are:

- Thermal conductivity dependent on degree of saturation
- Vapour diffusion dependent on degree of saturation and tortuosity
- Gas diffusion coefficient is a function of temperature and pressure
- Intrinsic permeability is constant
- Van Genuchten expression adopted for the water retention curve and relative permeability

A 3D geometry with axisymmetric meshing has been used as analysis domain (Figure 4-11) with dimensions 60 m long, 20 m wide and 40 m high. Mesh details for Stages 1 and 2 are shown in Figure 4-12 and Figure 4-13, respectively. The mesh for Stage 1 contains 125 824 grid blocks. The buffer is represented by a total of 4 096 grid blocks (elements), with 46 grid blocks (elements) across the bentonite barrier. The mesh size for Stage 2 is 329 828 grid blocks and includes a total of 1 052 grid blocks (elements) across the bentonite barrier. In Stage 2, modelling is performed for 18 years with Heater 2 operating only to obtain reasonable initial conditions for the Stage 2 modelling. This strategy removes the contributions of Heater 1 for Stage 2. The stages of tunnel excavation and ventilation lasting a total of 120 days have been considered in the analyses.

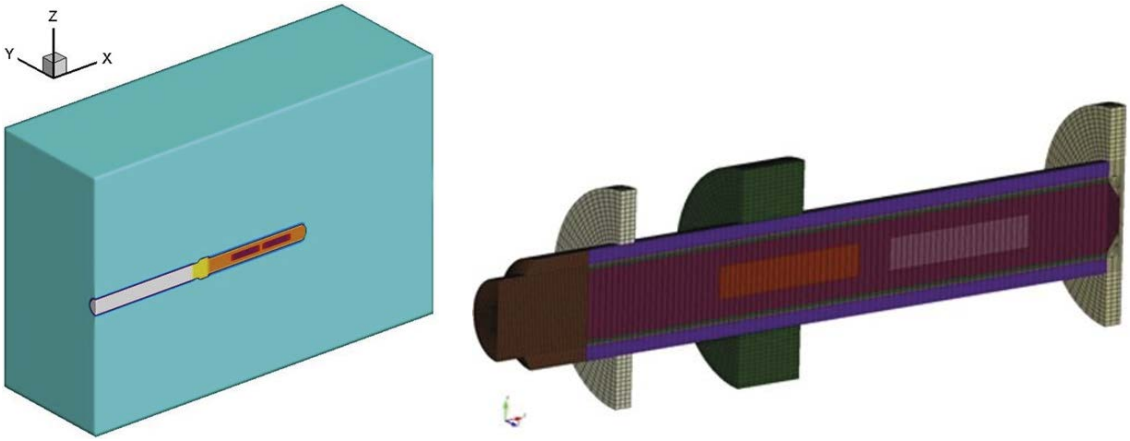

Figure 4-11. *3D modelling domain with axisymmetric meshing.*

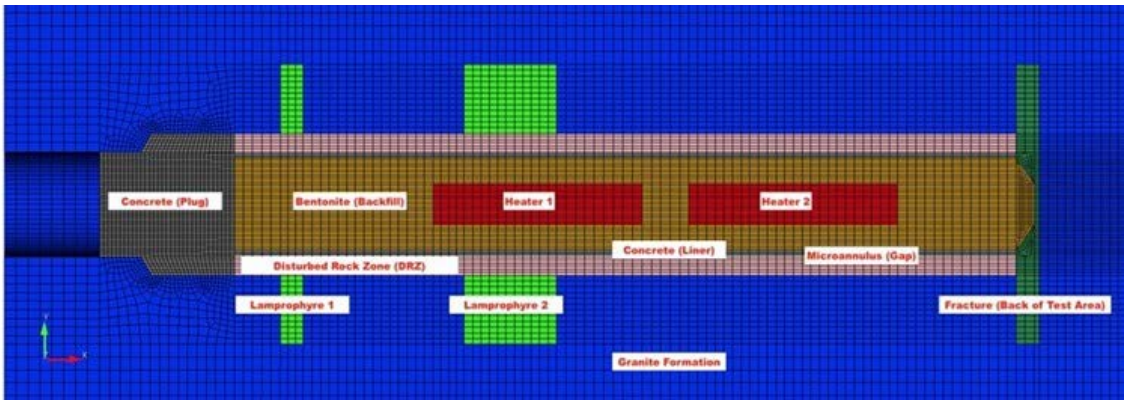

Figure 4-12. *Mesh cross-section for Stage 1 modelling.*

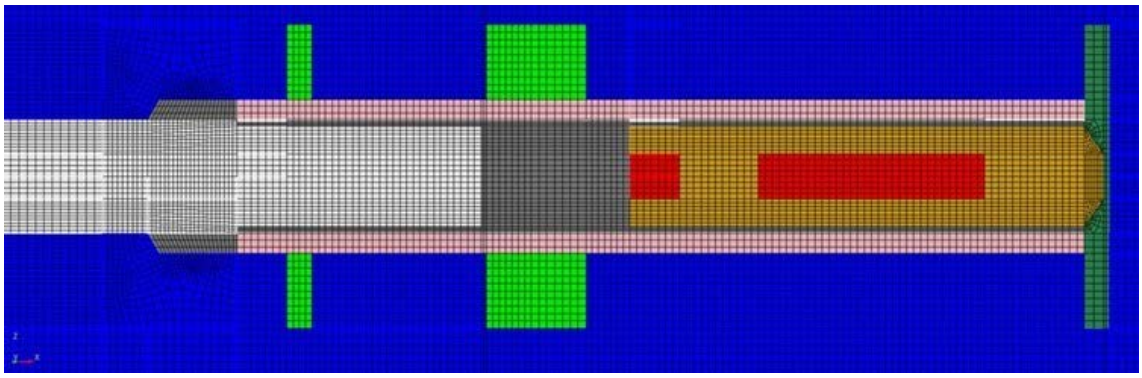

Figure 4-13. *Mesh cross-section for Stage 2 modelling.*

4.5 Svensk Kärnbränslehantering AB - Clay Technology (SKB-CT)

SKB-CT adopted a fully coupled THM formulation with their associated constitutive laws. Vapour migration is caused by molecular diffusion driven by a gradient in vapour concentration (Fick's law). A constant gas pressure is assumed throughout the analysis. The calculations have been performed with the computer code CODE_BRIGHT.

The constitutive laws adopted exhibit the following characteristics:

- Specific heat is constant
- Coefficient of thermal expansion is zero
- Thermal conductivity dependent on degree of saturation
- Vapour diffusion dependent on degree of saturation and tortuosity
- Intrinsic permeability dependent on dry density (or porosity)
- Van Genuchten expression adopted for the water retention curve
- Cubic law for the dependency of relative permeability on degree of saturation
- A modified version of the Barcelona Basic Model (BBM) is adopted for the bentonite mechanical constitutive law

A 2D axisymmetric domain (100 m long and 100 m radius) has been used in the calculations and it is illustrated in Figure 4-14. Note that the mesh actually used in the analyses was finer with 18 elements across the bentonite barrier in the zones without a heater. The mesh used linear quadrilateral elements in the inner part of the model and liner triangular elements in the outer part (rock); the total number

of nodes was 7 244. In contrast to all other teams, SKB-CT included a gap between the barrier and the rock. In this way the actual initial dry density of the blocks could be specified in the computations while at the same time achieving the final overall density of the barrier. A bilinear elastic model was adopted to represent the behaviour of the gap.

To facilitate the mechanical representation and to improve the numerical performance, a volume of rock material was removed at the end of the buffer and replaced by empty space. Longitudinal displacements were prevented at the barrier boundary in contact with the gap.

Prescribed temperature was not used as the thermal boundary conditions, instead the measured heater power was applied to the heater surface. Also, a hydraulic line source, with a liquid pore pressure of 0.1 MPa, was introduced close (0.5 m) to the tunnel surface. The adoption of this hydraulic boundary condition allowed full water access to the buffer and was based on reports of a highly permeable and water bearing host rock in the experiment. An isothermal hydration phase of 135 days was included in the analyses. The removal of material during dismantling was not considered in order to limit the complexity of the model. It should be noted that the modelling results provided by this team considered the start of the isothermal hydration phase as time zero, i.e. 135 days before the beginning of the heating.

The SKB-CT team performed calculations to check the effect of the presence of the liner (Figure 4-15) and sensitivity analyses varying parameters of the mechanical constitutive model.

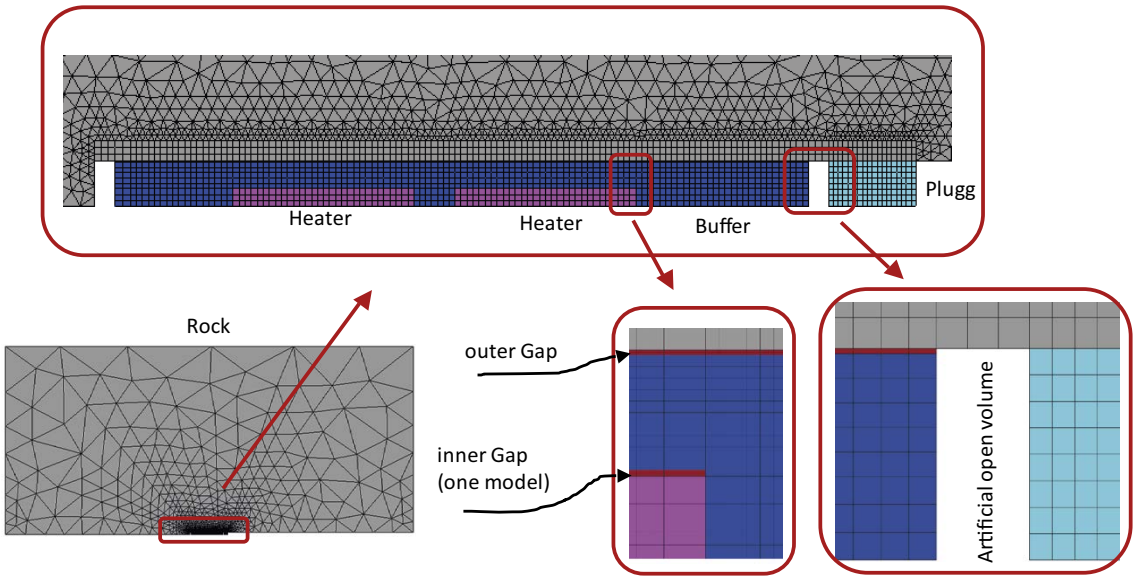

Figure 4-14. *2D axisymmetric analysis domain.*

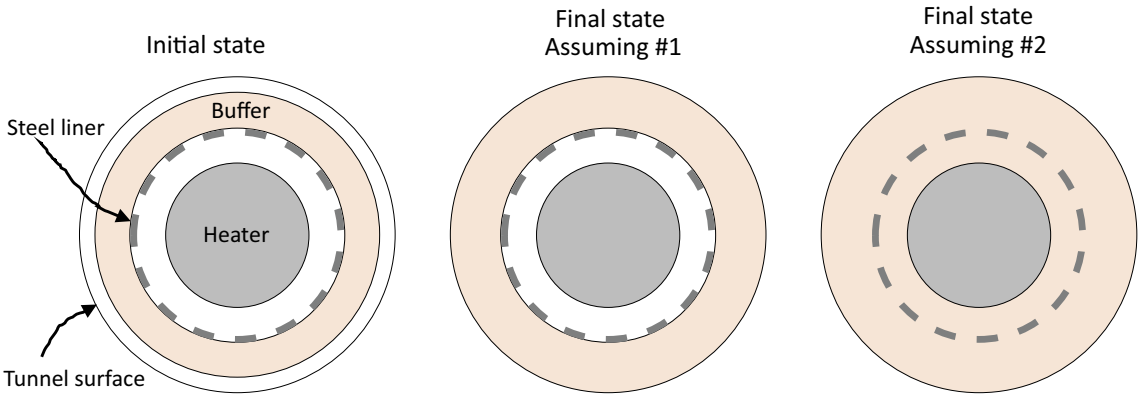

Figure 4-15. *Initial and final barrier states depending on the liner assumption. #1 The steel liner is a perfect barrier for the clay. #2 The steel liner is not a barrier for the clay.*

4.6 Technical University of Liberec (TUL)

TUL performed a coupled thermo-hydraulic (TH) modelling of the experiment using a 2D axisymmetric domain. It is 35 m long and 12 m in radius. Richard's equation is used as the hydraulic governing equation. The results of the TH analysis are then introduced in the mechanical problem, so the coupling is one-directional, TH towards M but not vice versa. The computer code COMSOL was used in the calculations.

Some relevant features of the constitutive laws adopted are:

- Specific heat dependent on temperature
- No thermal expansion considered
- Thermal conductivity dependent on degree of saturation
- Vapour diffusion dependent on degree of saturation and tortuosity
- Intrinsic permeability dependent on dry density (or porosity)
- Van Genuchten expression adopted for the water retention curve
- Cubic law for the dependency of relative permeability with degree of saturation
- Non-linear elasticity plus a swelling term in the bentonite mechanical constitutive model

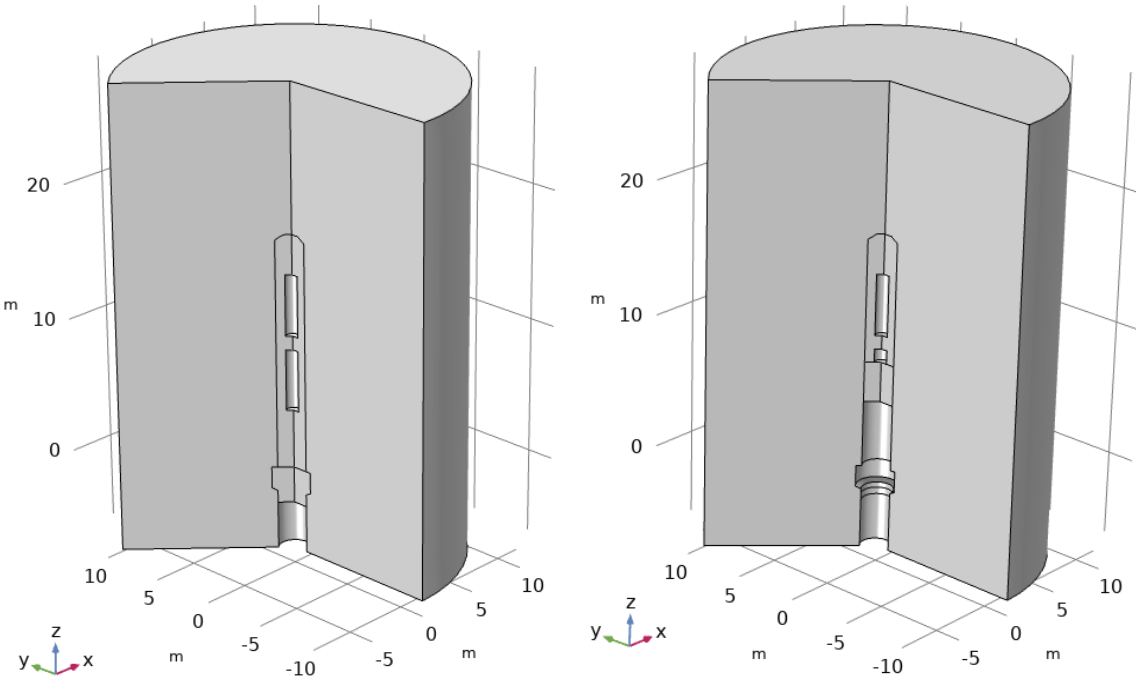

Figure 4-16. *Analysis domain. Left: Stage 1. Right: Stage 2.*

Two different discretizations are used for Stages 1 and 2 as shown in Figure 4-17 and Figure 4-18. The Stage 1 mesh has 9 396 nodes, 18 372 linear triangular elements and 16 elements between heater and rock whereas the Stage 2 mesh has 3 744 nodes, 7 220 linear triangular elements and 10 elements between heater and rock. No installation of isothermal phase before the start of heating was considered.

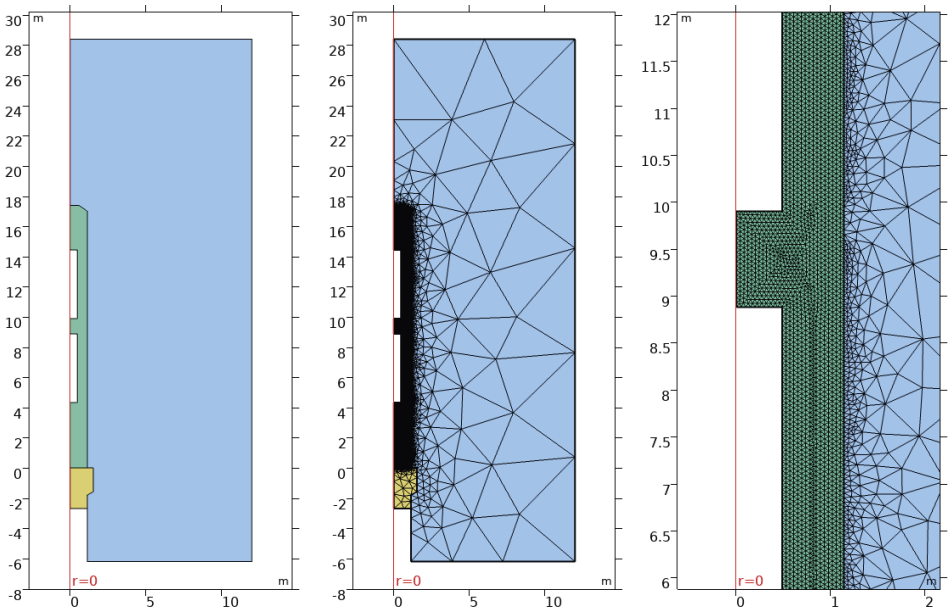

Figure 4-17. *Stage 1 mesh.*

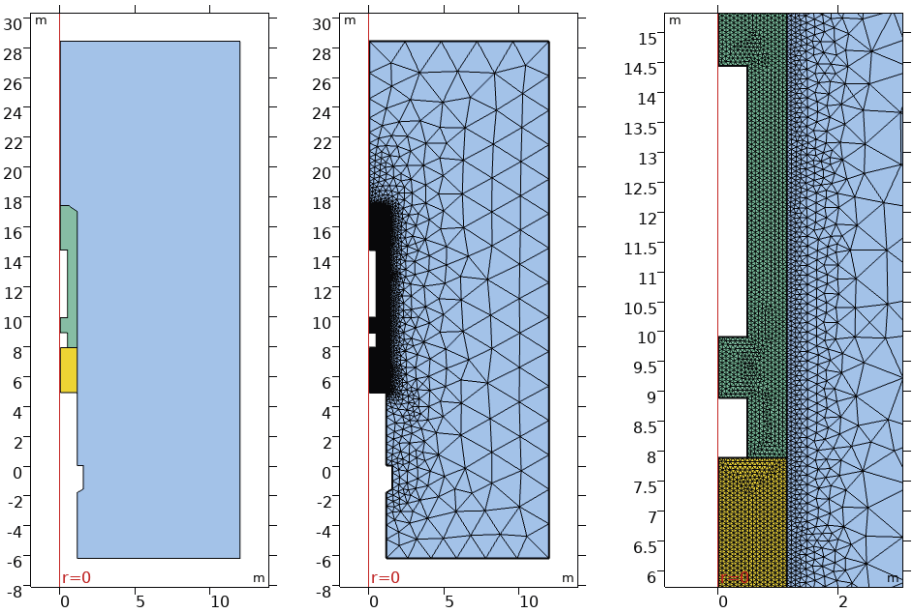

Figure 4-18. *Stage 2 mesh.*

4.7 Universitat Politècnica de Catalunya (UPC)

A coupled THM formulation has been used by UPC as the basis for the modelling of the experiment. The analysis domain is 2D axisymmetric, 31.2 m long and 30 m in radius. Vapour migration is caused by molecular diffusion driven by a gradient in vapour concentration (Fick's law). A constant gas pressure is assumed throughout the analysis. CODE_BRIGHT is the computer code employed in the calculations.

Regarding the constitutive relationships, the following should be noted:

- Specific heat and linear thermal expansion coefficient are constant
- Thermal conductivity dependent on degree of saturation
- Vapour diffusion dependent on degree of saturation and tortuosity
- Intrinsic permeability dependent on dry density (or porosity)
- Van Genuchten expression adopted for the water retention curve
- Cubic law for the dependency of relative permeability with degree of saturation
- The Barcelona Basic Model (BBM) has been adopted for the mechanical constitutive law of the bentonite

The Finite Element mesh used in the analysis is depicted in Figure 4-19. It is composed of 3 049 linear quadrilateral elements and 3 139 nodes; there are 10 elements across the barrier between heater and rock. Tunnel excavation and installation over a 200 days period have been introduced in the analyses.

UPC also carried out a number of sensitivity analyses exploring the effects of the variation of a number of variables. Specifically, the following are reported:

- Influence of intrinsic permeability on final degree of saturation, final dry density and final water content
- Effect of initial porosity on final degree of saturation, final dry density and final water content
- Effect of bentonite thermal conductivity and intrinsic permeability on heating power

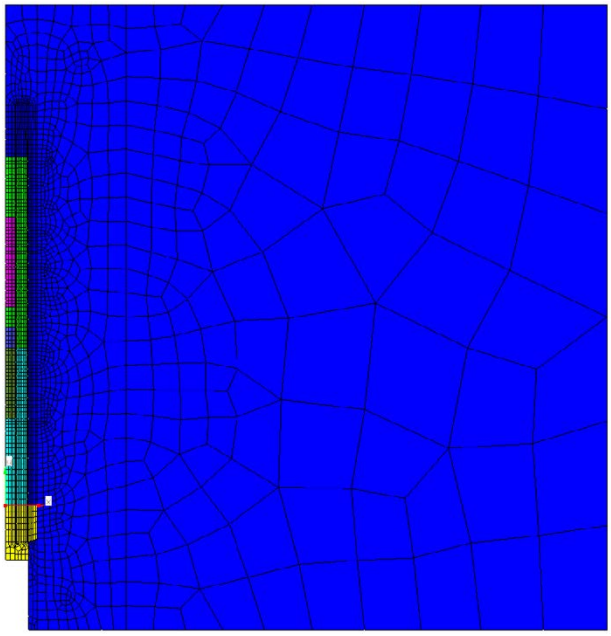

Figure 4-19. *Finite element mesh.*

The sensitivity analyses enhance the understanding of the system. For instance, it is interesting to note that intrinsic permeability affects, as expected, the final degree of saturation (Figure 4-20) but has a negligible effect on the final distribution of dry density (Figure 4-21). Also, the analyses demonstrate the effects of initial porosity, intrinsic permeability and, of course, thermal conductivity on computed heater power (Figure 4-22).

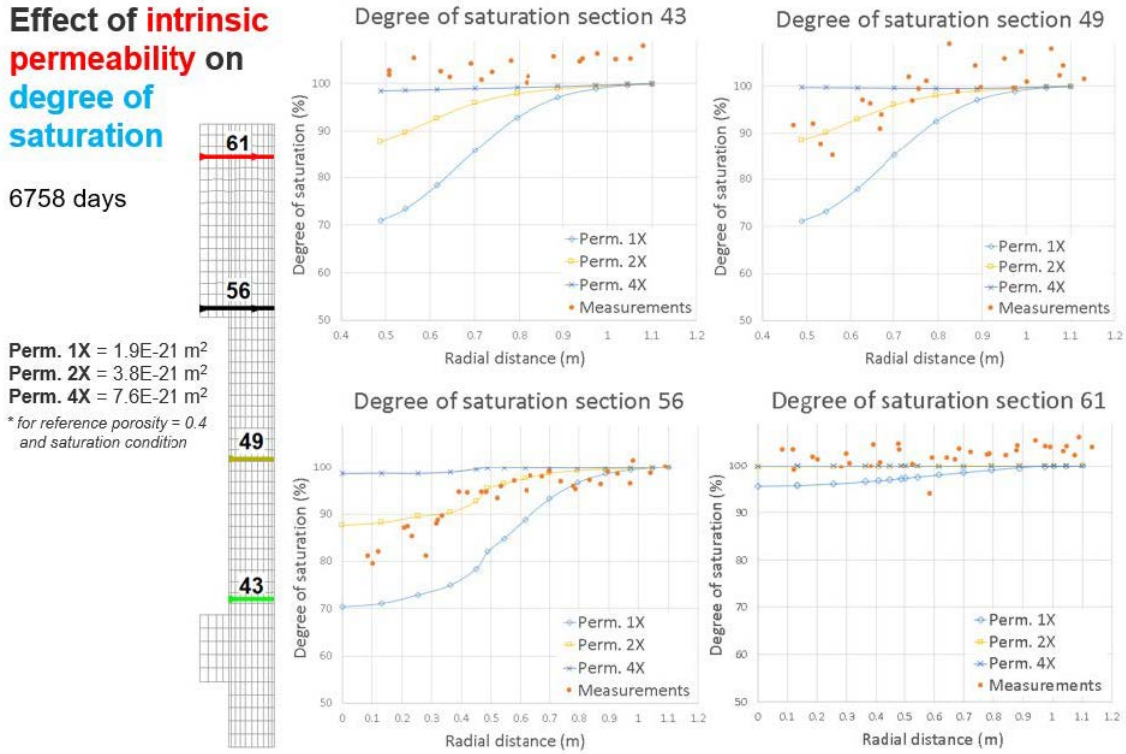

Figure 4-20. *Effect of intrinsic permeability on final degree of saturation.*

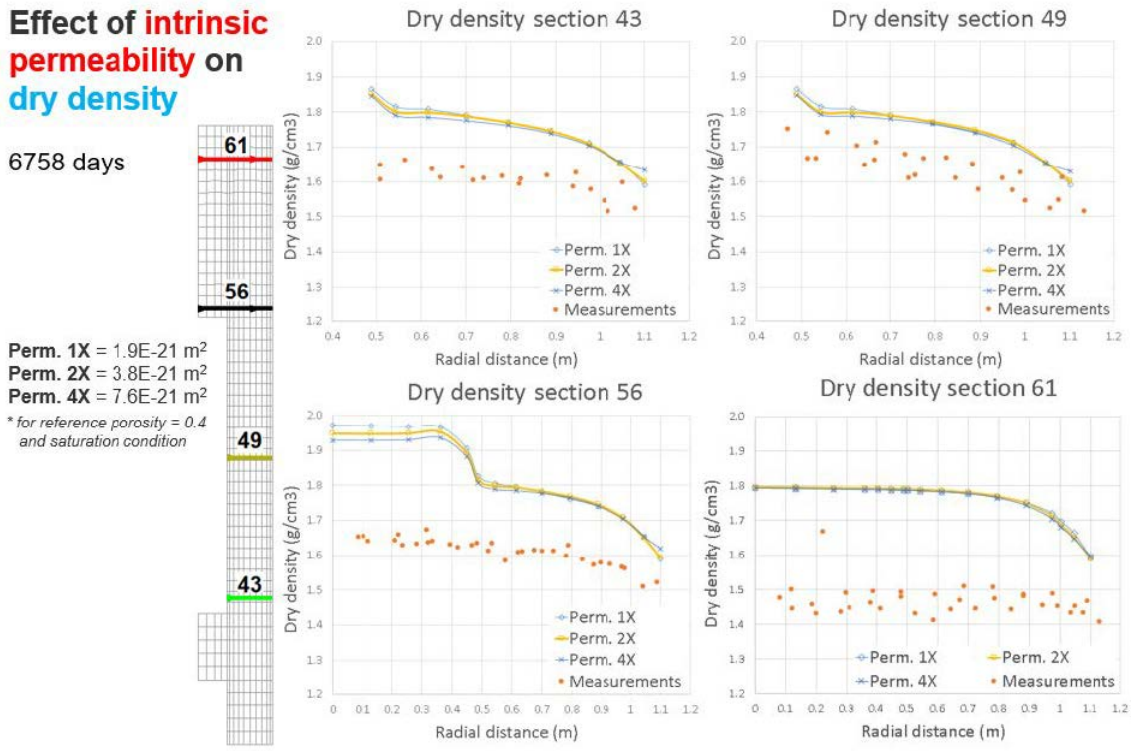

Figure 4-21. *Effect of intrinsic permeability on final dry density.*

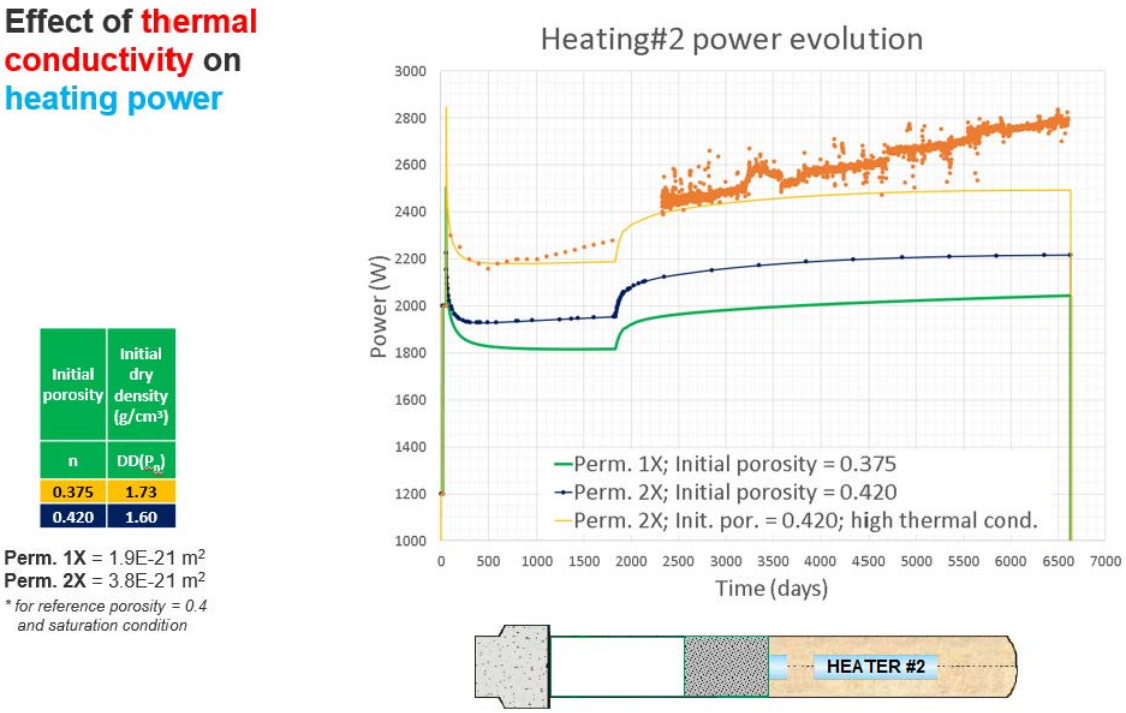

Figure 4-22. *Effect of thermal conductivity and initial porosity on heating power.*

4.8 Summary

The main features of the analyses carried out by the different modelling teams are collected in Table 4-1. Five teams carried out thermo-hydro-mechanical (THM) analyses, four of them fully coupled and one (TUL) with a one-directional coupling from thermo-hydraulic (TH) to mechanical. A team (SNL) used a fully coupled TH formulation and another one (GRS) assumed one-directional coupling from thermal to hydraulic. The coupling between mechanical and thermal aspects is not significant and the mechanical effects on the hydraulic results is also limited; therefore, TH analyses can produce relevant results. However, TH calculations cannot provide results regarding the development of stresses in the barrier or distributions of dry density.

All the formulations are based on the solution of equations of mass balance, energy balance and, in the case of THM analyses, the equilibrium equation (conservation of momentum). Although several formulations include a gas/air equation, all teams have assumed that gas pressure is constant and equal to atmospheric. Six different computer codes have been used providing a broad perspective of numerical approaches. Because of the characteristics of the case analysed, most teams have adopted a 2D axisymmetric geometry. The exception is SNL that used a 3D geometry (with axisymmetric meshing) for solving the mechanical problem and GRS that used a 1D geometry (two different sections) as a basis for modelling. Most teams considered, in different ways, the initial stages of excavation, installation and isothermal hydration.

Table 4-1. Main features of the analyses.

Team	Coupling	Computer code	Geometry	Domain dimensions
CRIEPI	THM (fully coupled)	LOSTUF	2D axisymmetric	120 m long 50 m radius
GRS	T > H	COMSOL (T) VIPER (H)	2D axisymmetric (T) 1D axisymmetric (H)	50 m long, 45 m radius (T) 0.69–1.14 m long (H)
ICL	THM (fully coupled)	ICFEP	2D axisymmetric	50 m long 50 m radius
SNL	TH (fully coupled)	PFLOTRAN	3D	60 m long 40 m high 20 m wide
SKB-CT	THM (fully coupled)	CODE_BRIGHT	2D axisymmetric	100 m long 100 m radius
TUL	TH > M	COMSOL	2D axisymmetric	35 m long 12 m radius
UPC	THM (fully coupled)	CODE_BRIGHT	2D axisymmetric	31.2 m long 30 m radius

TH: thermo-hydraulic, THM: thermo-hydro-mechanical.

There are a number of similarities in the constitutive models used by the different teams (Table 4-2). Thus, all teams except one consider the variation of thermal conductivity (the basic parameter in Fourier's law) with degree of saturation. Also, all teams except one incorporate vapour transport in their analyses. Vapour migration is generally accounted for by Fick's law driven by vapour pressure or concentration gradients and it is affected by the gas degree of saturation and modified by a tortuosity factor. Advective liquid flow where considered is always assumed to be governed by a generalised Darcy's law. The variation of intrinsic permeability with porosity is also taken into account by all teams except one. It should be noted that there is no permeability in the GRS formulation since it is assumed that there is no advective liquid water flow in the pores. The strong dependence of hydraulic permeability on degree of saturation is considered by all the teams, often using a cubic dependence. ICL expresses the variation of hydraulic conductivity in the unsaturated range in terms of suction. The retention curve is generally stated using a form of the Van Genuchten equation except by GRS that uses isotherms at different temperatures as key building blocks of their formulation.

Table 4-2. Constitutive models.

Team	Thermal conductivity variable	Vapour Transport considered	Intrinsic perm. variable	Retention curve	Mechanical constitutive model
CRIEPI	Yes[1]	Yes[2]	Yes[3]	VG	Linear elastic + swelling term
GRS	No	Yes[2]	N/A	Isotherms	N/A
ICL	No	No	Yes[3]	VG	IC DSM
SNL	Yes[1]	Yes[2]	No	VG	N/A
SKB-CT	Yes[1]	Yes[2]	Yes[3]	VG	Modified BBM
TUL	Yes[1]	Yes[2]	Yes[3]	VG	Non-linear elastic + swelling term
UPC	Yes[1]	Yes[2]	Yes[3]	VG	BBM

[1] Thermal conductivity depends on degree of saturation.

[2] Vapour transport depends on degree of saturation and tortuosity.

[3] Intrinsic permeability dependent on dry density (porosity).

BBM: Barcelona Basic Model, IC DSM: Imperial College Double Structure Model, VG: Van Genuchten.

N/A: not applicable.

There is also variety in the mechanical constitutive models employed by the teams that have performed THM analyses. Two teams use elastic (linear and nonlinear) models with an additional swelling term. The other three teams use elastoplastic models that explicitly address the behaviour of the bentonite in the unsaturated regime. Two of the teams adopted somewhat different versions of the Barcelona Basic Model (BBM). Only ICL has employed a double structure (double porosity) elastoplastic model.

The main initial conditions of the bentonite barrier assumed by the modelling teams are listed in Table 4-3. It can be noted that most teams used an initial dry density of 1.6 g/cm^3 that corresponds to the installation average dry density considering the constructions technological voids. SKB-CT used the bentonite block density (1.7 g/cm^3) because they incorporated a gap in the analysis representing the effect of the voids. ICL used an intermediate value of 1.65 g/cm^3. The initial water content ranges from 11.0 to 16.0 which is somewhat surprising as the initial water content of the blocks, about 14.4 %, is well established. This may be due to having derived water content from the initial suction and the adopted retention curve. In this respect, the range of initial suctions (or relative humidity) is rather narrow.

Table 4-3. Initial conditions in the bentonite barrier.

Team	Initial dry density (g/cm^3)	Initial porosity	Initial water content (%)	Initial degree of saturation (%)	Initial suction (MPa)	Initial relative humidity (%)
CRIEPI	1.60	0.39	11.3	47.7	135	35.8
GRS	1.60	0.23	11.0	N/A	N/A	37.9
ICL	1.65	0.39	12.2	50.0	120	40.0
SNL	1.60	0.375	15.2[1]	65.0	N/P	N/P
SKB-CT	1.70	0.378	14.4	64.7	124.9	40.0
TUL	1.60	0.407	14.2	55.9	120	41.2
UPC	1.61	0.42	16.0	65.0	135	34.0

[1] Derived from degree of saturation.

N/A: not applicable. N/P: not provided.

The main thermal properties of bentonite and rock are shown in Table 4-4. The dry and saturated thermal conductivities are all rather similar except for the teams that use a constant value. The initial values are also similar but for ICL and CRIEPI that adopt a rather low value compared to the other teams. There also differences regarding the bentonite solid specific heat although this parameter has a quite limited influence on results. There is general agreement in the rock thermal parameters.

Table 4-4. Main thermal parameters.

Team	Bentonite initial thermal conduct. (W/mK)	Bentonite initial sat. thermal conduct. (W/mK)	Bentonite initial dry thermal conduct. (W/mK)	Bentonite solid specific heat (J/kg K)	Rock thermal conduct. (W/mK)	Rock specific heat (J/kg K)
CRIEPI	0.677	1.259	0.571	749.1	3.34	920
GRS	1.000	1.000	1.000	800.0	3.30	850
ICL	0.550	N/A	N/A	870.0	3.20	920
SNL	1.160	1.300	0.600	1 091.0	3.30	793
SKB-CT	0.919	1.259	0.571	1 091.0	3.80	920
TUL	0.936	1.280	0.500	1 125.5	3.30	920
UPC	1.080	1.400	0.600	1 000.0	4.00	793

Finally, the main hydraulic, mechanical and thermomechanical parameters for bentonite and rock are collected in Table 4-5. The differences between the initial values of intrinsic permeability (or hydraulic conductivity) are approximately within an order of magnitude except for SNL that used a higher constant value. The same range of differences are present in the saturated hydraulic conductivity. There is more variation concerning the rock permeability reaching spanning than two orders of magnitude.

It is not possible to compare individual parameters of the mechanical constitutive laws as they correspond to quite different formulations. However, all teams performing mechanical analyses were asked to provide values of the swelling pressure that would be obtained in an isochoric oedometer test starting from the initial conditions of the analyses. They are shown in Table 4-5 where it can be observed that they range from 5.2 to 13.3 MPa, a quite significant variation. There are also differences in the linear thermal expansion coefficient but the effects of this parameter on results is very minor.

Table 4-5. Main hydraulic, mechanical and thermomechanical parameters for bentonite and rock.

Team	Bentonite initial permeab. (m^2)	Bentonite Initial hydraulic conduct. (m/s)	Bentonite initial saturated hydraulic conduct. (m/s)	Rock intrinsic saturated permeab. (m^2)	Bentonite initial swelling pressure* (MPa)	Bentonite linear thermal expansion coeff. (K^{-1})
CRIEPI	0.2×10^{-21}	0.17×10^{-14}	1.59×10^{-14}	5×10^{-19}	7.82	Variable[1]
GRS	N/A	N/A	N/A	N/A	N/A	N/A
ICL	1.0×10^{-21}	0.8×10^{-14}	10.0×10^{-14}	1.33×10^{-19}	9.00	6.5×10^{-6}
SNL	2.1×10^{-21}	N/P	N/P	1.26×10^{-19}	N/A	N/A
SKB-CT	0.3×10^{-21}	0.3×10^{-14}	1.1×10^{-14}	1×10^{-17}	13.3	0
TUL	0.7×10^{-21}	0.7×10^{-14}	4.0×10^{-14}	1×10^{-17}	5.2	0
UPC	3.0×10^{-21}	2.3×10^{-14}	4.0×10^{-14}	0.8×10^{-17}	5.7	7.8×10^{-6}

[1] Linear thermal expansion coefficient (K^{-1}) = $-0.118 \times 10^{-4} + 6.5 \times 10^{-6}$ T.

N/A. not applicable, N/P: not provided.

5 FEBEX test – Modelling results and observations

In this section, the results of the different teams are plotted and compared with the experiment observations. Section 5.1 refers to the Stage 1 operation and first dismantling and Section 5.2 concerns Stage 2 operation and final dismantling. Finally, Section 5.3 explored the evolution of the barrier between the first and the final dismantling.

The results provided by the different modelling teams are indicated by the codes and symbols listed in Table 5-1. In all cases, the modelling results correspond to the final contribution submitted by each team. It should be noted that, in the case of the SK1 results, there is a 135-days offset in the time scale, i.e. time zero corresponds to the end of the construction stage. Note that the experiment observations are denoted as CIM and the symbol is a black circle.

Table 5-1. Codes and symbols of the modelling teams.

Modelling team	Code	Symbol
Central Research Institute of Electric Power Industry (CRIEPI)	CRP	■
Gesellschaft für Anlagen- und Reaktorsicherheit (GRS)	GRS	◆
Imperial College London (ICL)	ICL	●
Sandia National Laboratories (SNL)	SNL	▲
Svensk Kärnbränslehantering AB-Clay Technology (SKB-CT)	SK1	□
Technical University of Liberec (TUL)	TUL	×
Universitat Politècnica de Catalunya (UPC)	UPC	◇
Experiment observations	CIM	●

5.1 Stage 1: test operation and first dismantling

5.1.1 Test operation

The instrumented sections in Stage 1 of the experiment sections (K to B2) are shown in Figure 5-1. Temperatures, relative humidity and total stresses in the bentonite barrier were measured throughout. The requested results correspond to the sections shown in Figure 5-2 (temperatures), Figure 5-3 (relative humidity) and Figure 5-4 (total stresses). Relative humidity results have been requested for points in section C located in the cooler zone where the increase of temperature is very limited (less than 5 °C) to be compared with the hotter sections across the heaters. Heater power was also measured throughout the experiment.

The comparison between model results and observations are shown in the following Figures:

- Heater power (Figure 5-5 and Figure 5-6)
- Distributions of temperature (Figure 5-7 to Figure 5-8)
- Evolution of relative humidity (Figure 5-9 to Figure 5-10)
- Distribution of relative humidity (Figure 5-11 to Figure 5-12)
- Evolutions of total stress (Figure 5-13 to Figure 5-14)

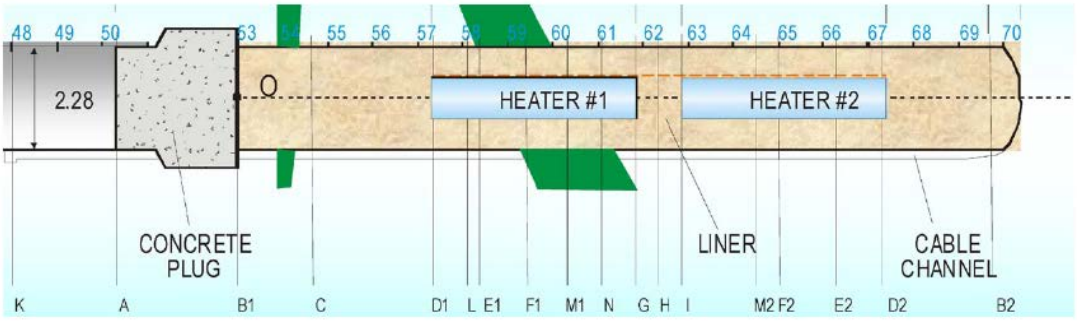

Figure 5-1. *Location of the barrier monitoring sections in the FEBEX test.*

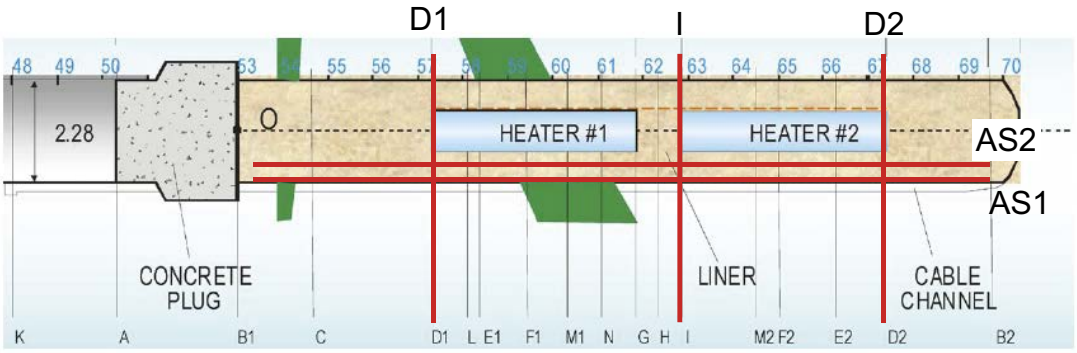

Figure 5-2. *Location of the monitoring sections where temperature modelling results have been requested.*

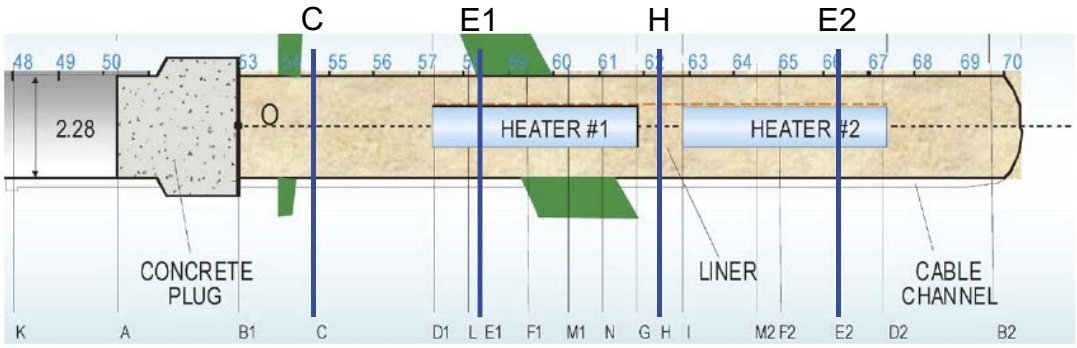

Figure 5-3. *Location of the monitoring sections where relative humidity modelling results have been requested.*

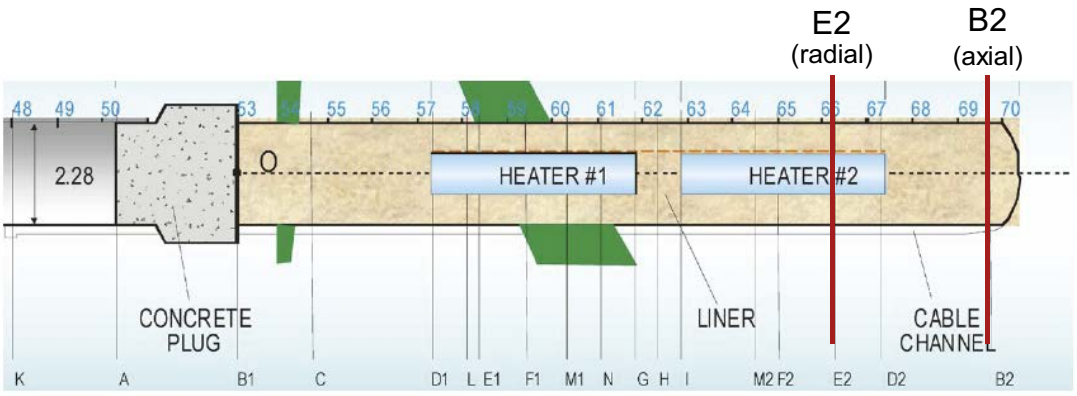

Figure 5-4. *Location of the monitoring sections where total stress modelling results have been requested.*

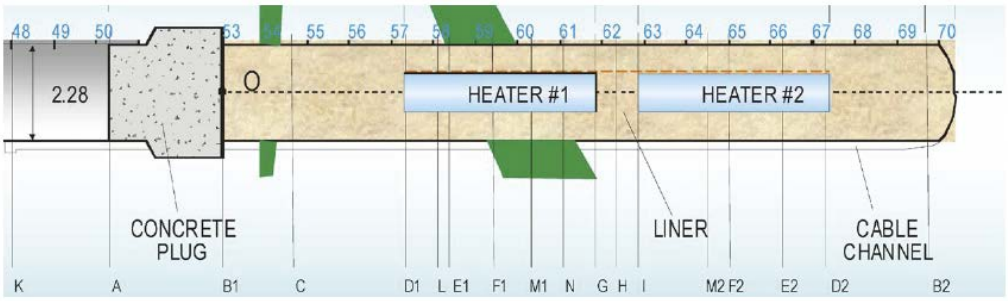

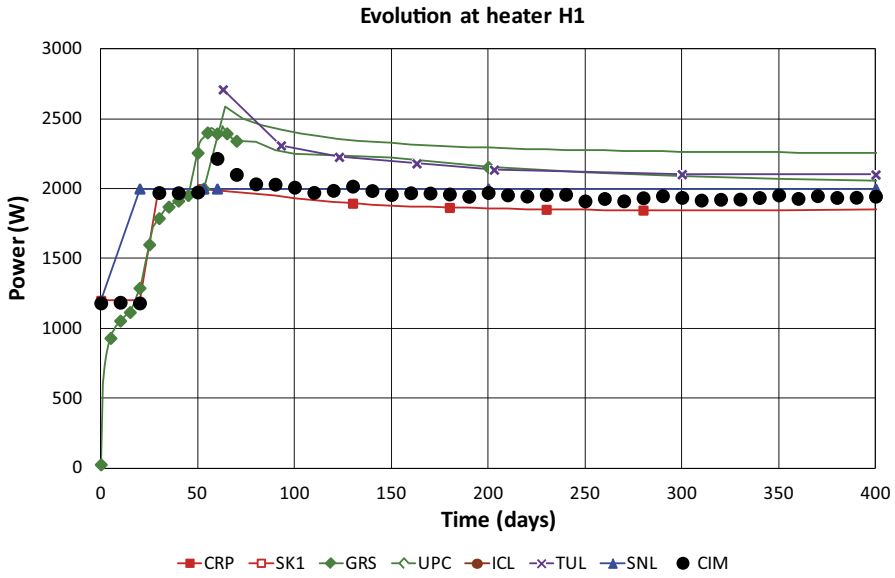

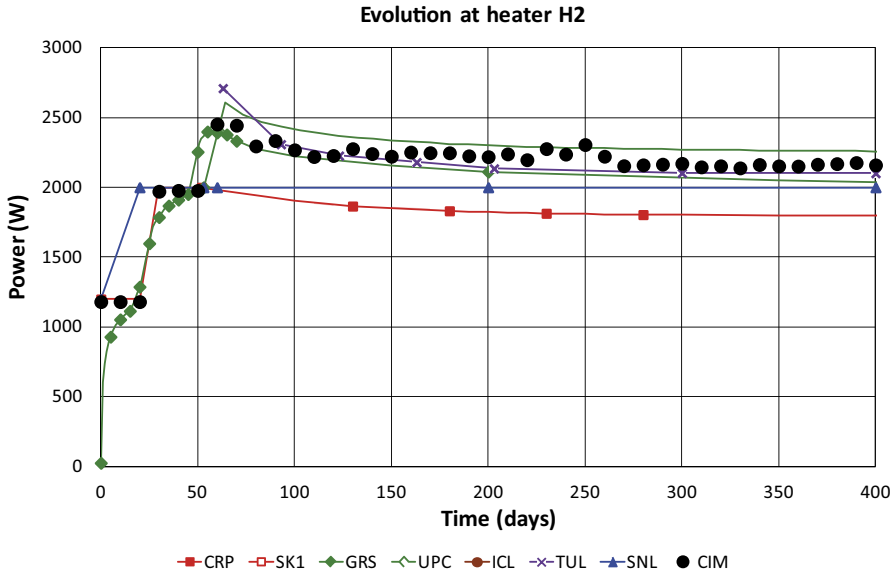

Figure 5-5. *Modelling results vs observations (CIM) for the first 400 days. Evolution of heater power.*

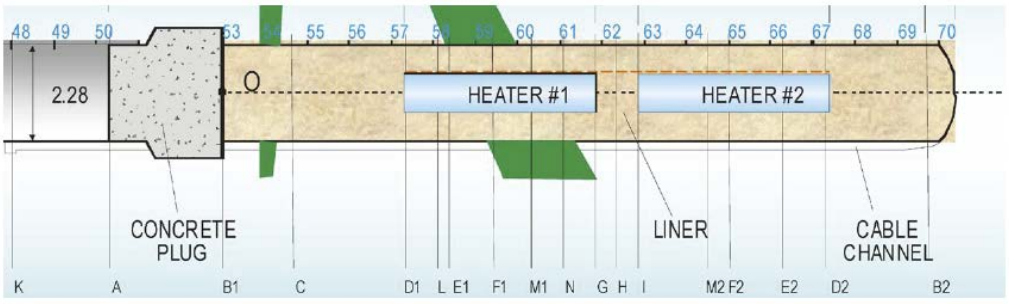

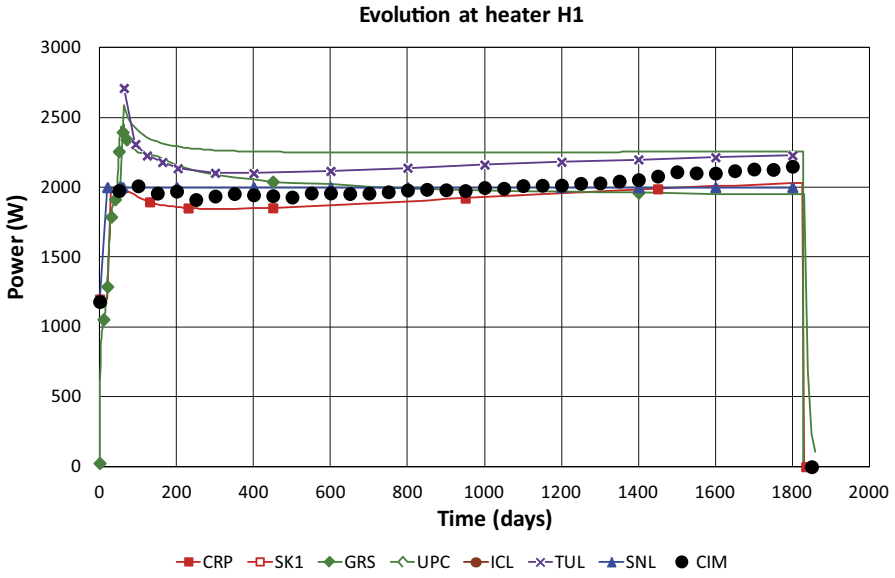

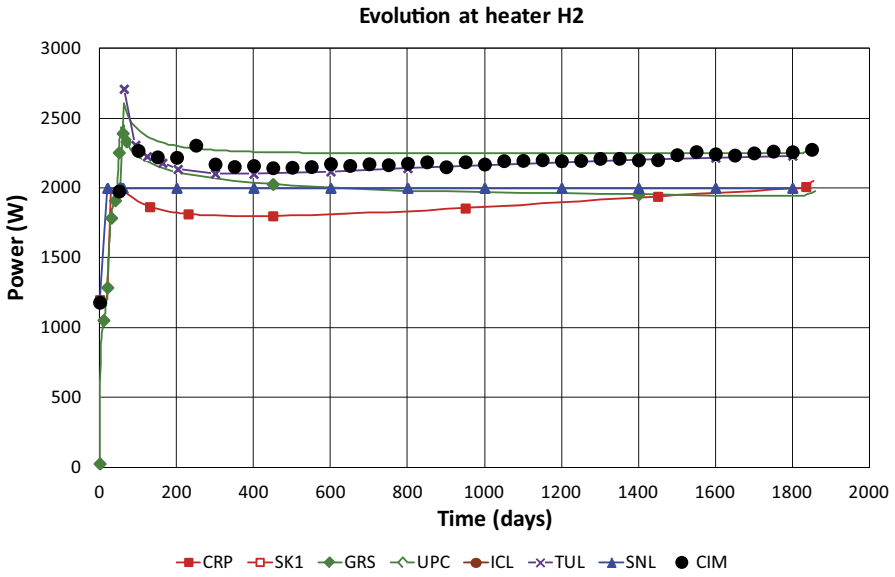

Figure 5-6. *Modelling results vs observations (CIM) up to first dismantling. Evolution of heater power.*

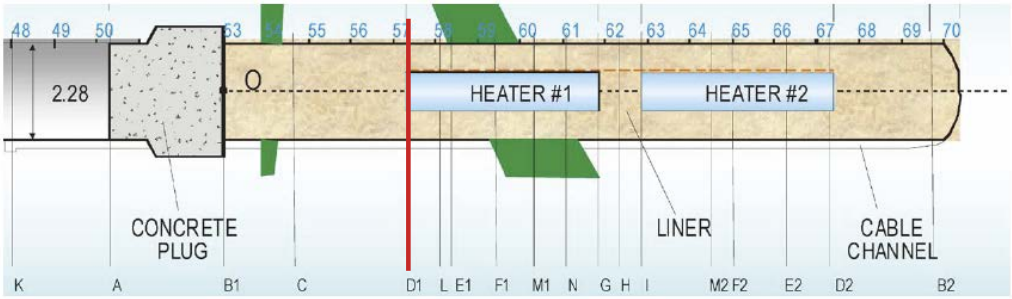

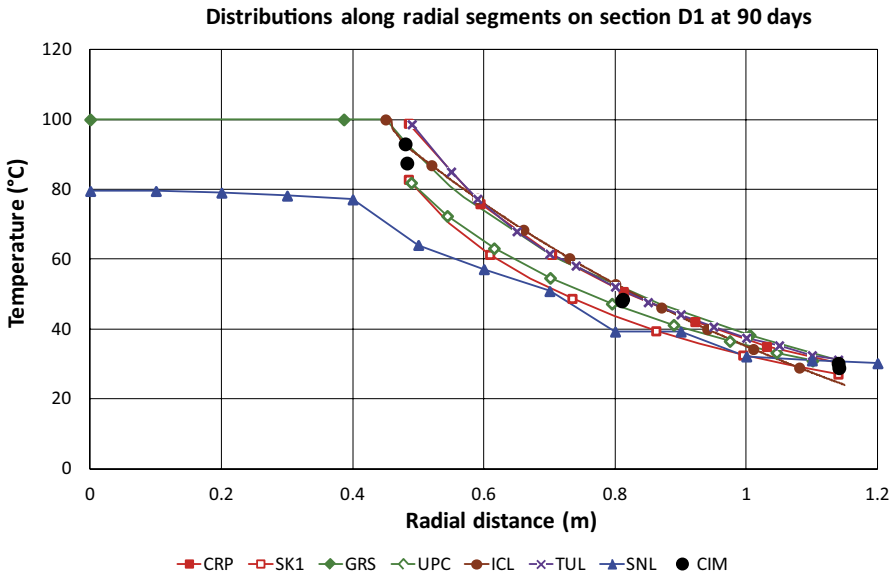

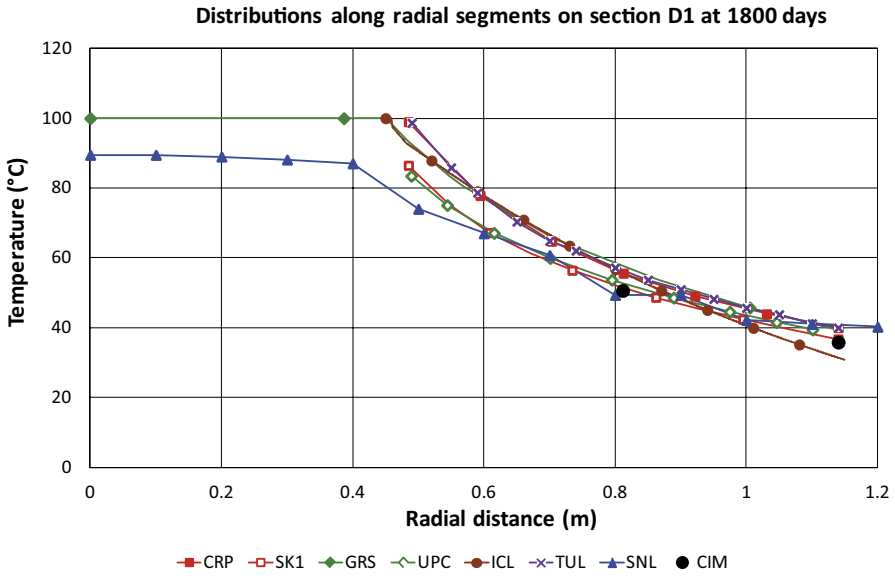

Figure 5-7. *Modelling results vs observations (CIM) at 90 days and at 1800 days. Distribution of temperatures in section D1.*

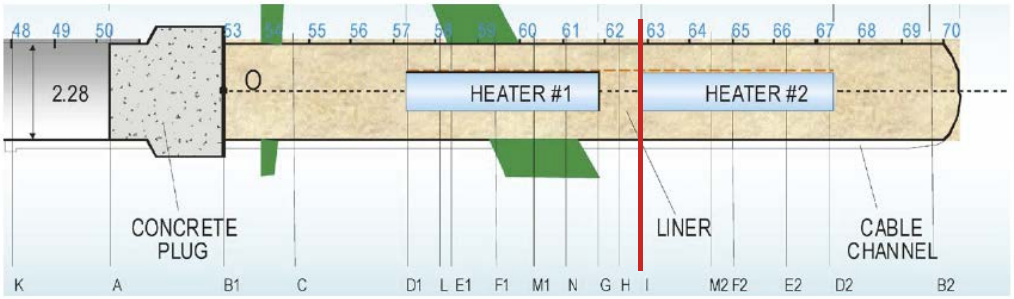

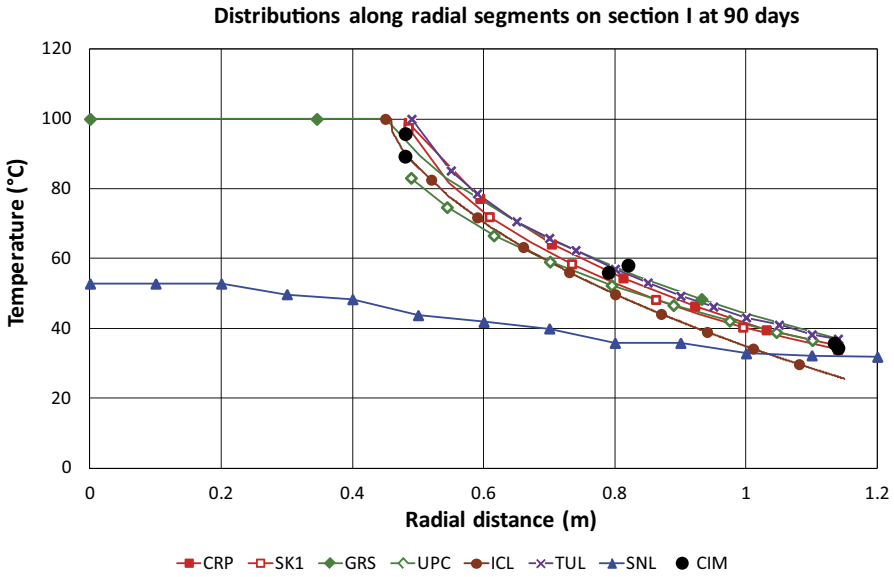

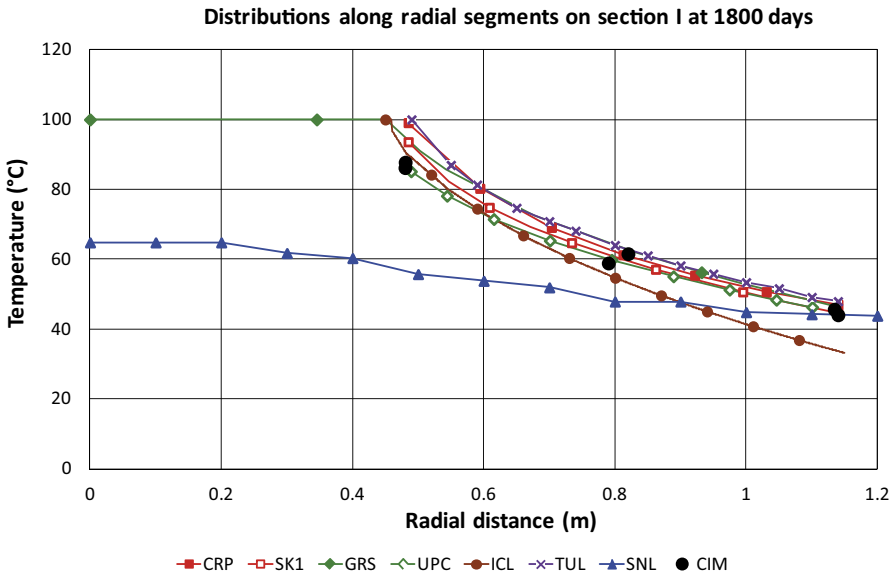

Figure 5-8. *Modelling results vs observations (CIM) at 90 days and at 1 800 days. Distribution of temperatures in section I.*

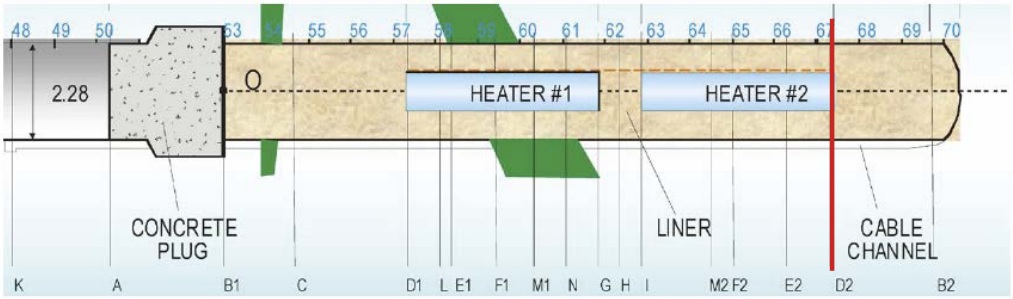

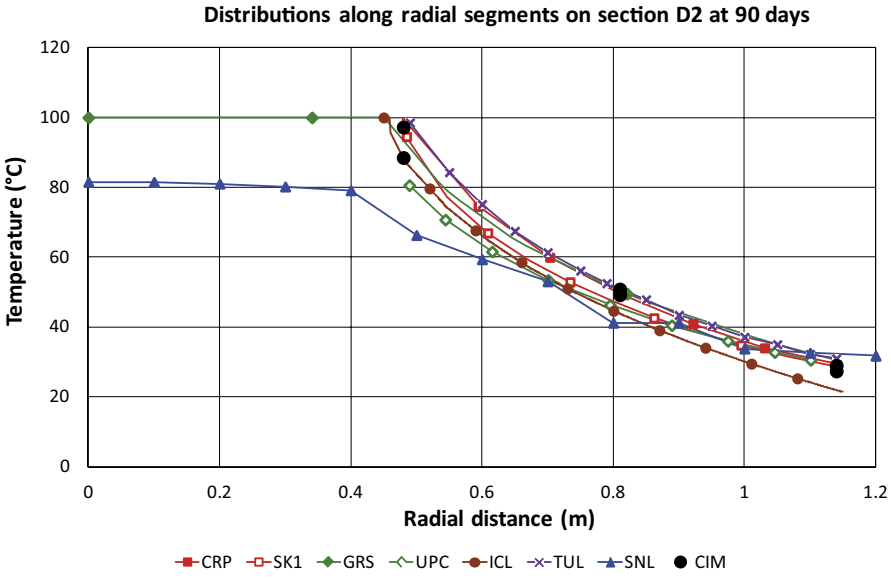

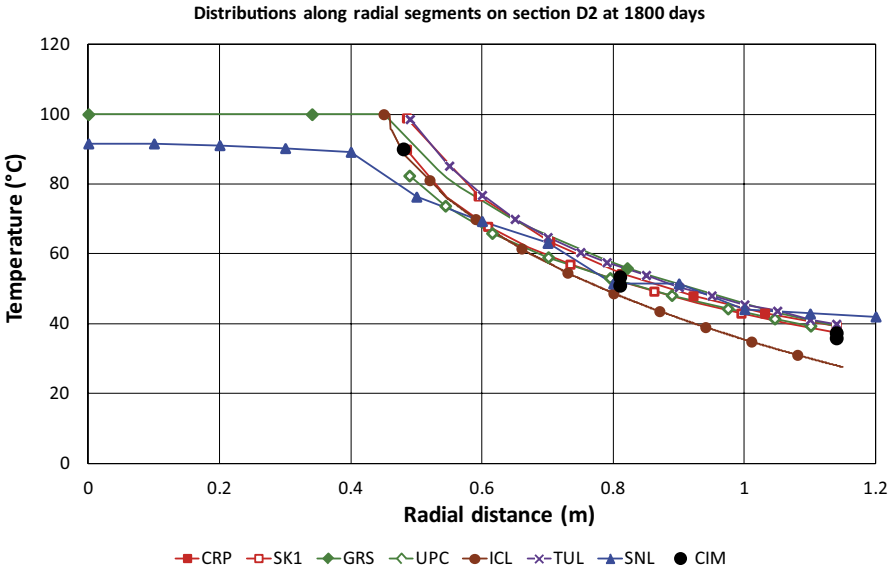

Figure 5-9. *Modelling results vs observations (CIM) at 90 days and at 1 800 days. Distribution of temperatures in section D2.*

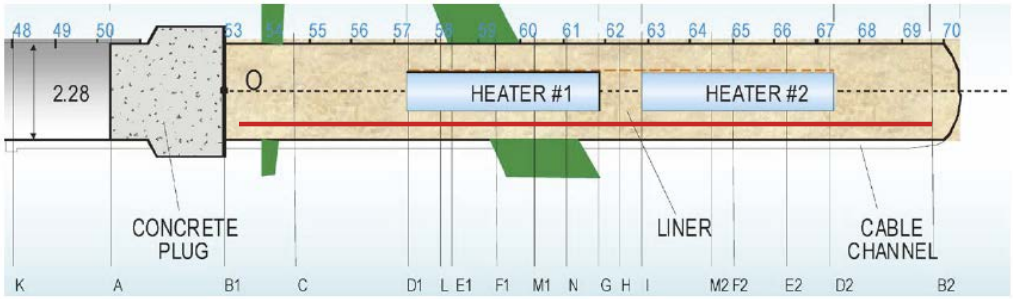

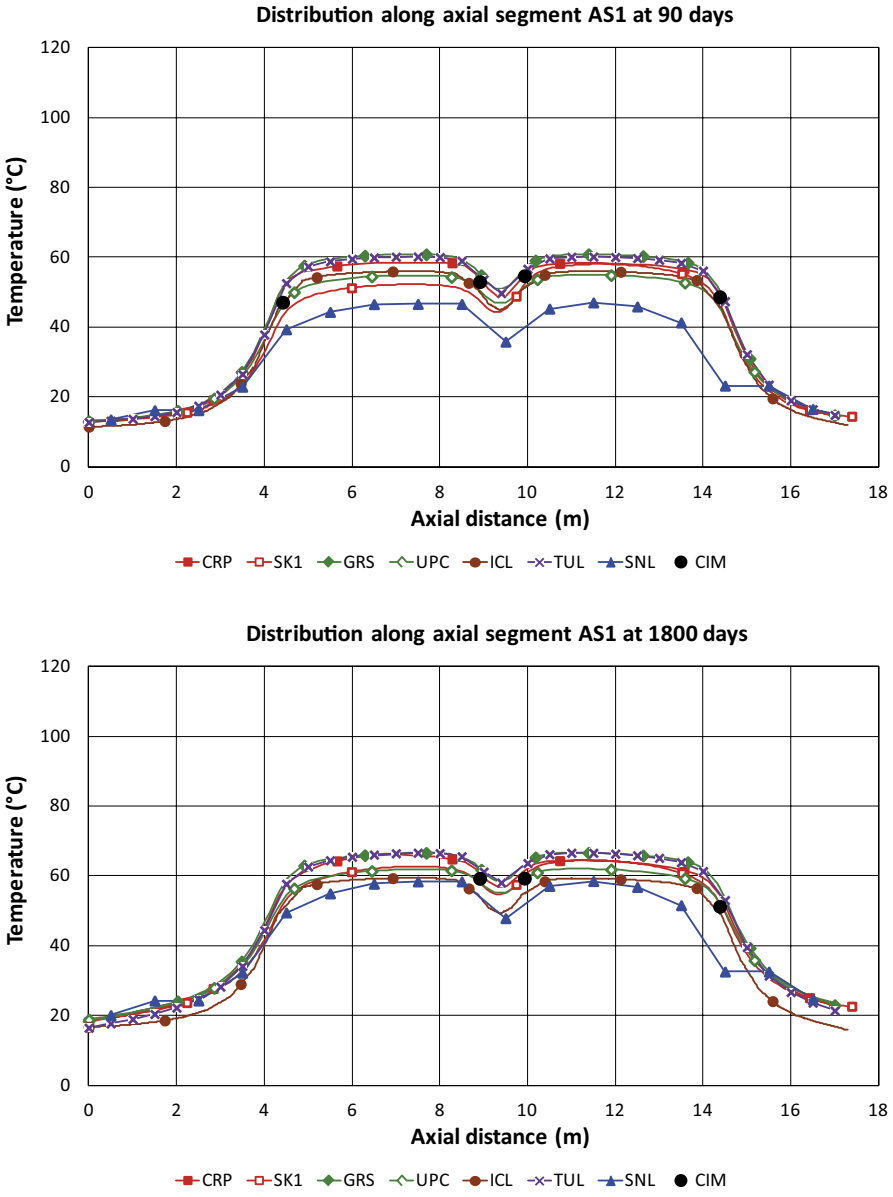

Figure 5-10. *Modelling results vs observations (CIM) at 90 days and at 1 800 days. Distribution of temperatures along segment AS1 (intermediate).*

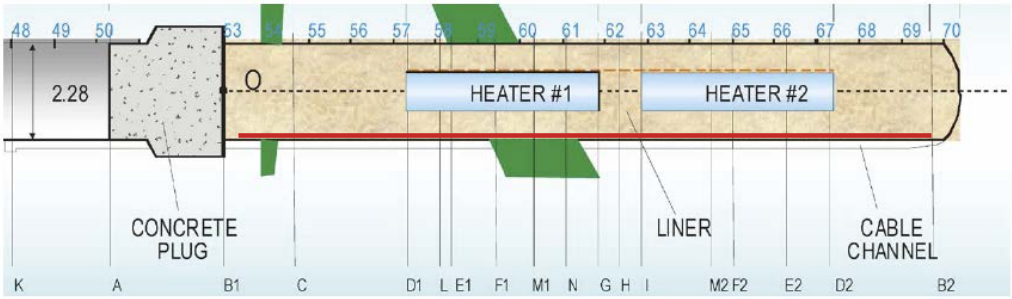

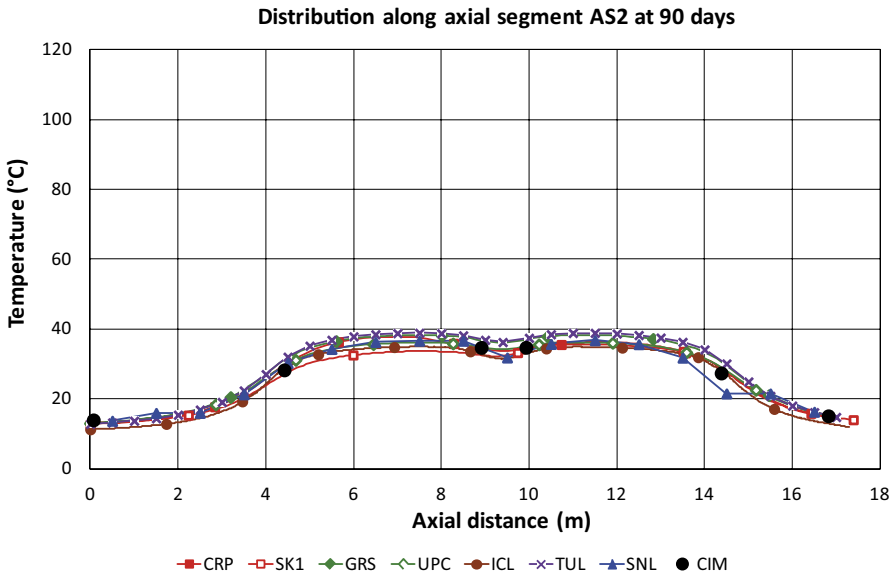

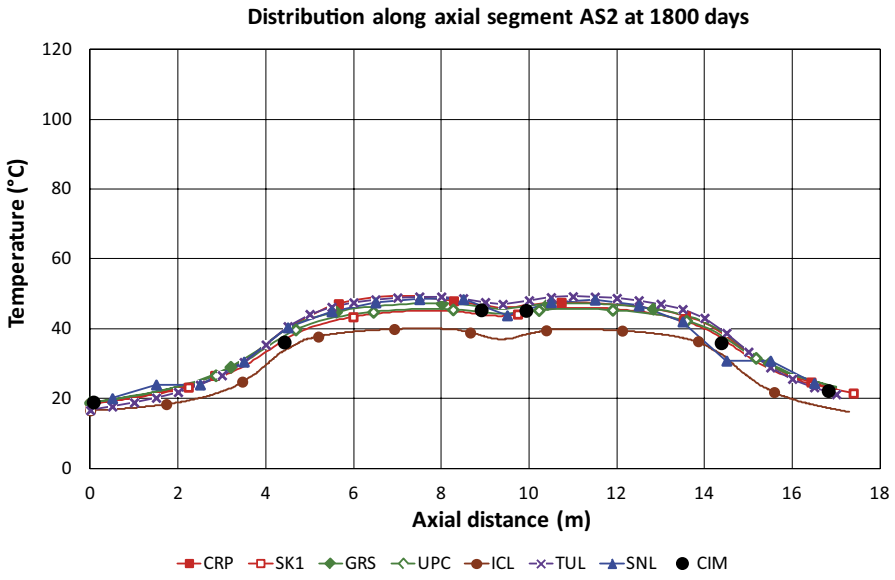

Figure 5-11. *Modelling results vs observations (CIM) at 90 days and at 1 800 days. Distribution of temperatures along segment AS2 (close to the rock).*

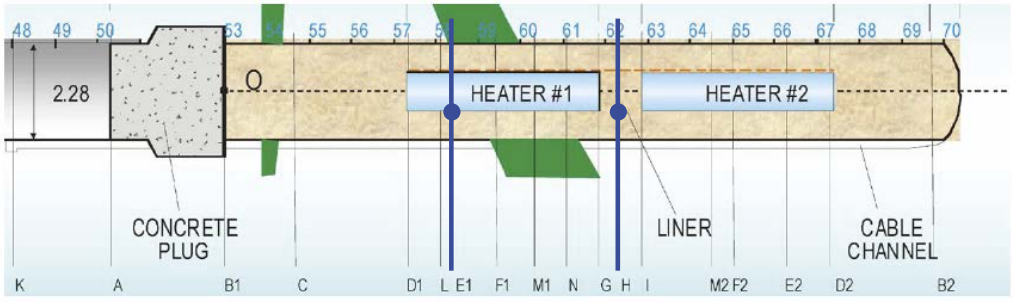

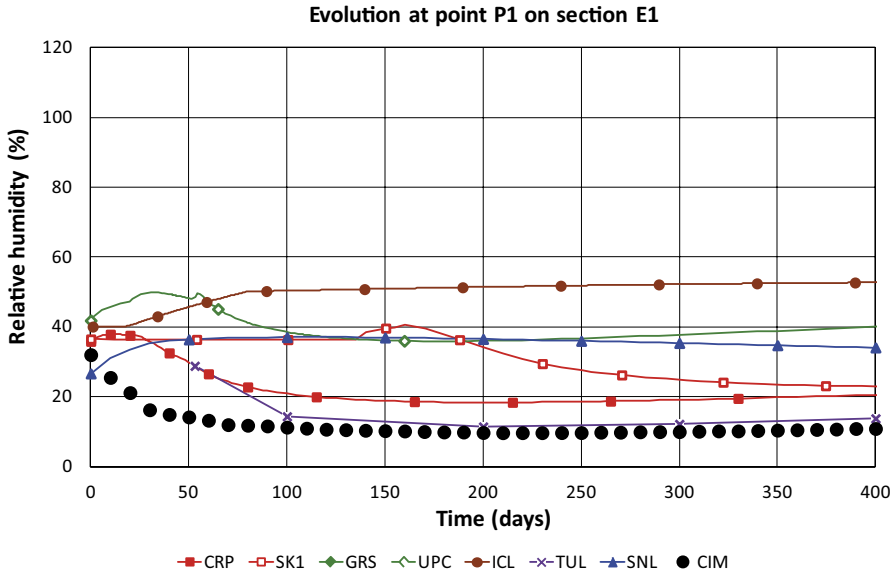

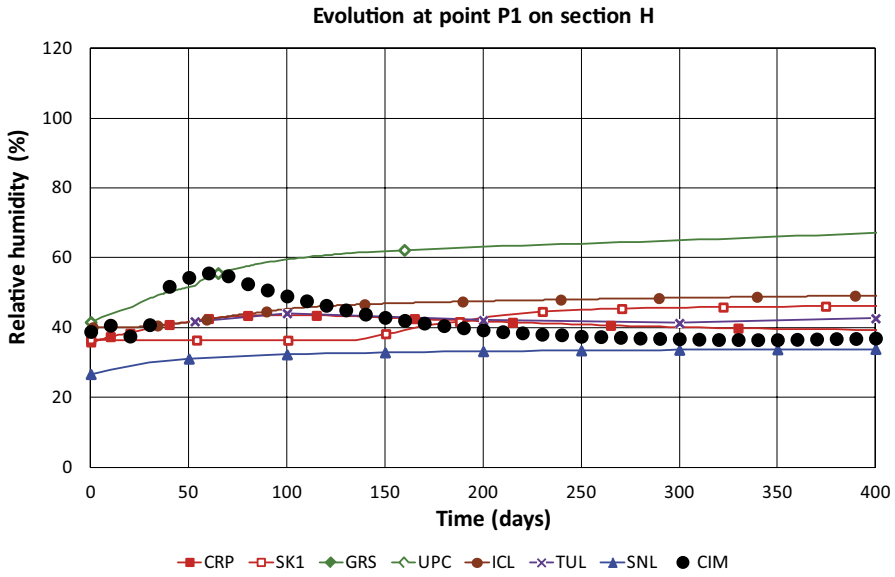

Figure 5-12. *Modelling results vs observations (CIM) up to 400 days. Evolution of relative humidity at points P1 (close to the heater) in sections E1 and H.*

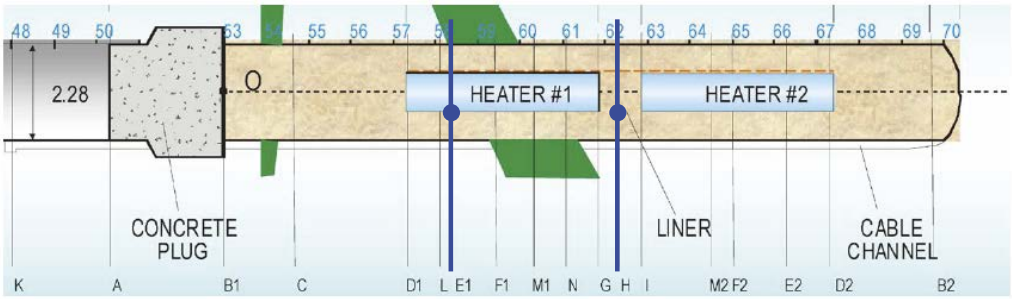

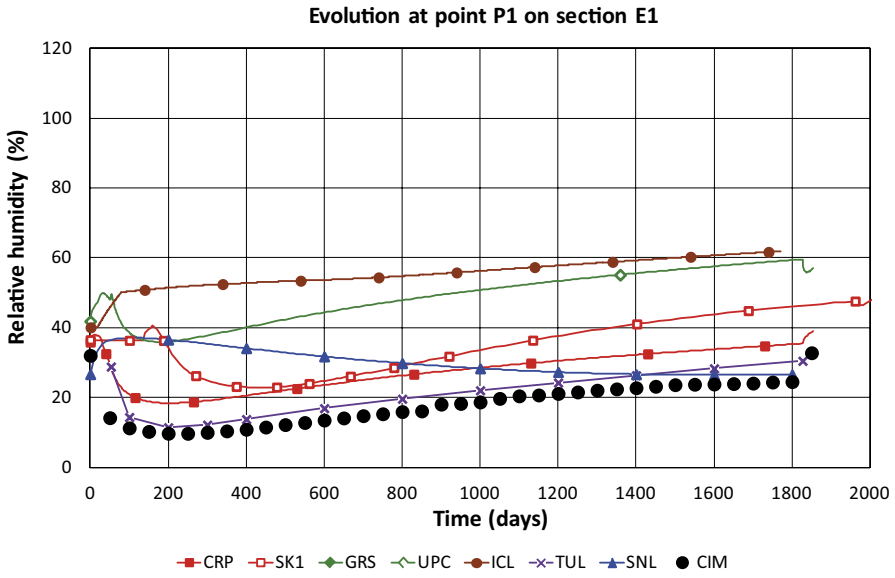

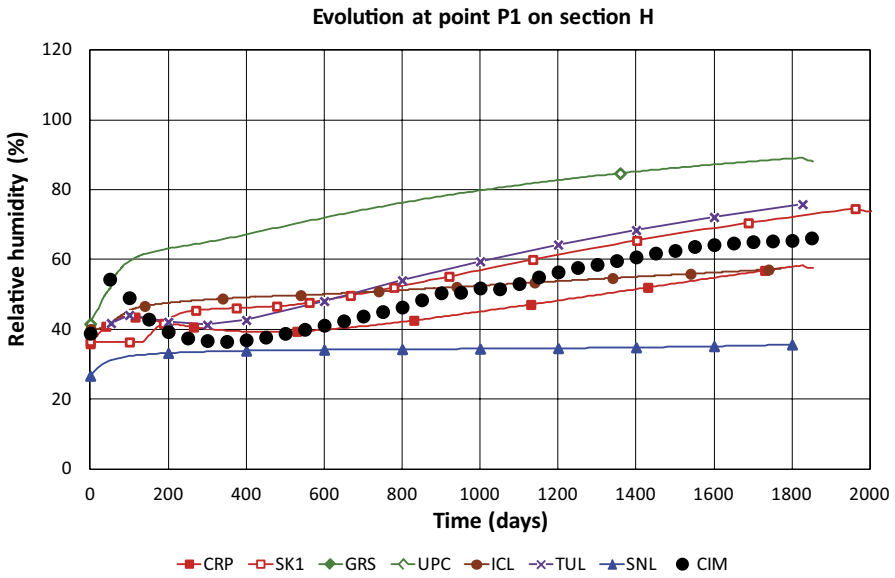

Figure 5-13. *Modelling results vs observations (CIM) up to first dismantling. Evolution of relative humidity at points P1 (close to the heater) in sections E1 and H.*

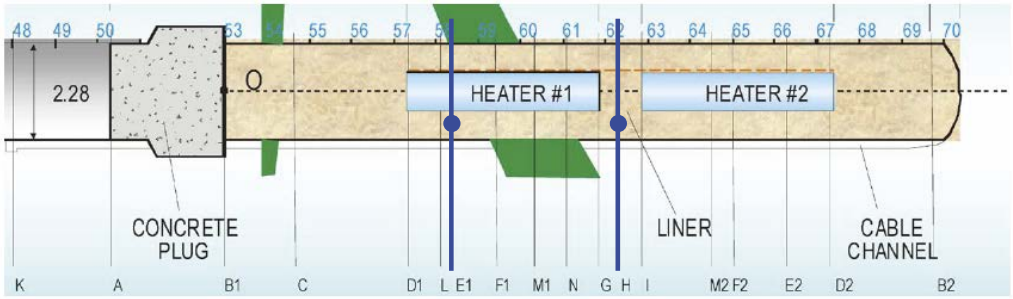

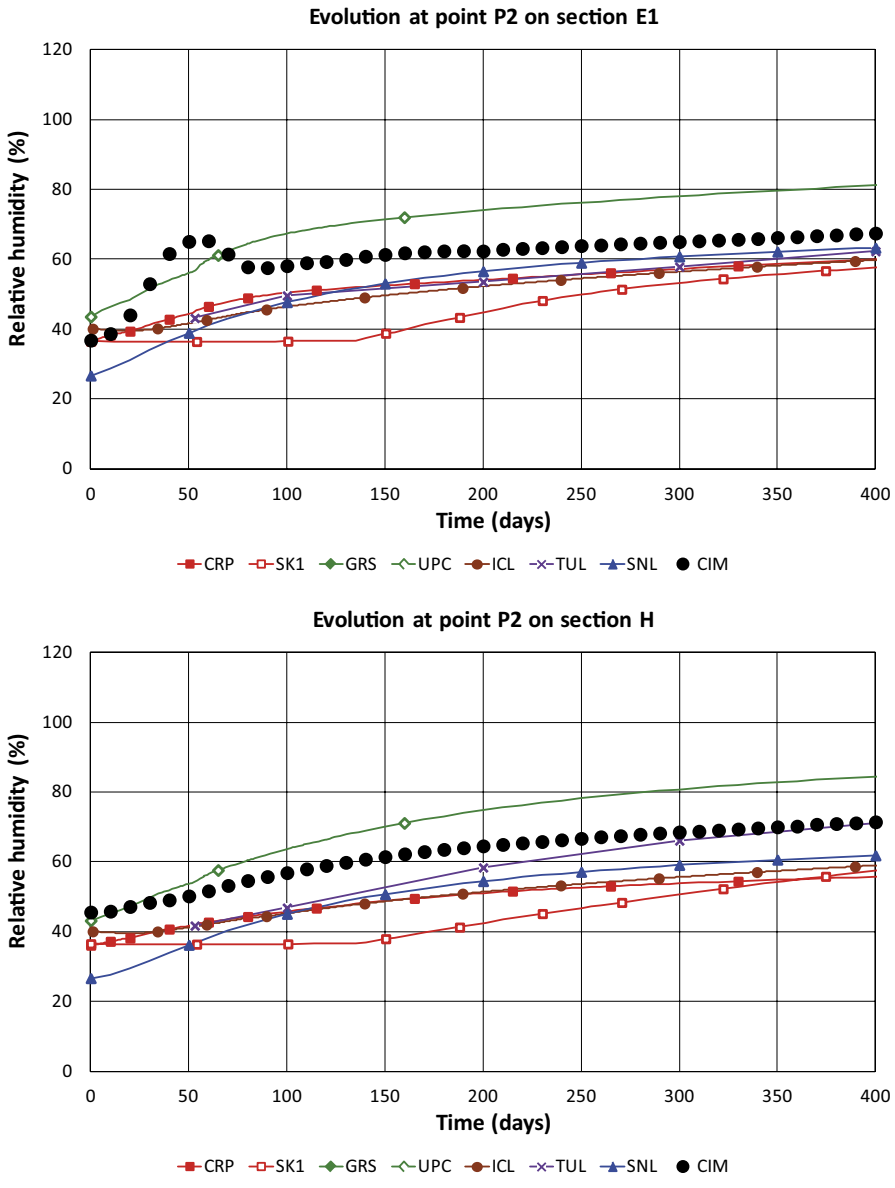

Figure 5-14. *Modelling results vs observations (CIM) up to 400 days. Evolution of relative humidity at points P2 (intermediate) in sections E1 and H.*

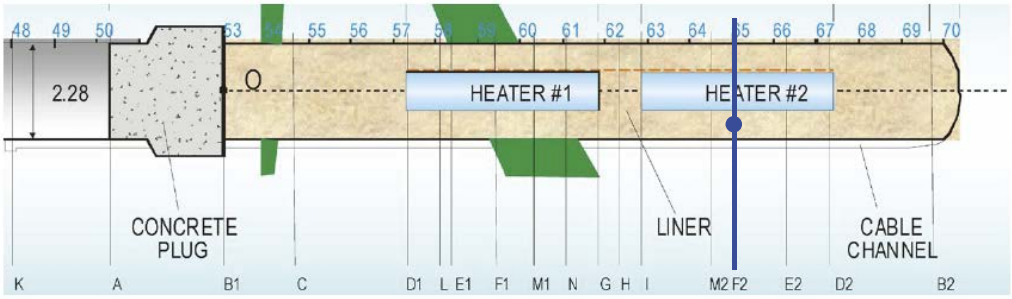

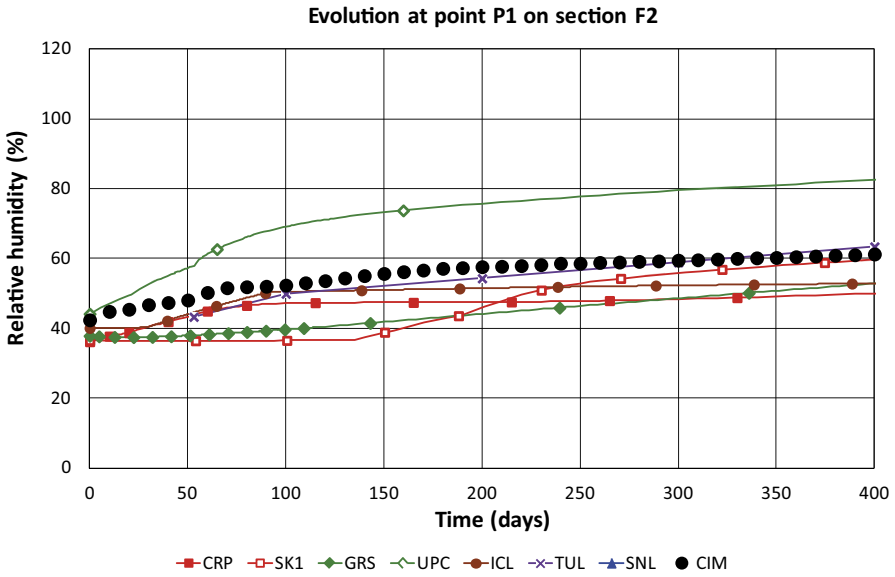

Figure 5-15. *Modelling results vs observations (CIM) up to 400 days. Evolution of relative humidity at point1 P1 (intermediate) in section F2.*

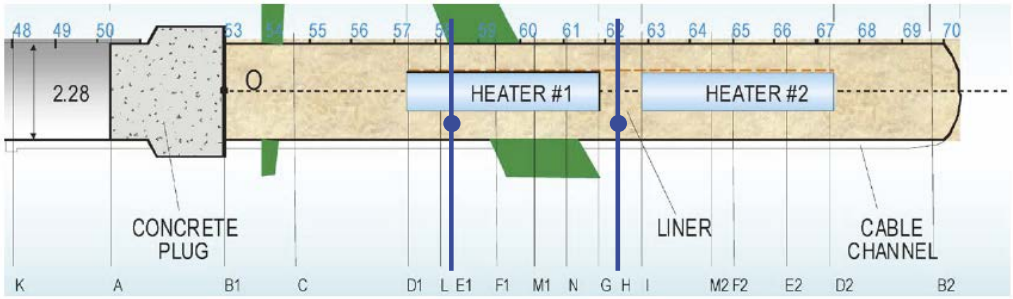

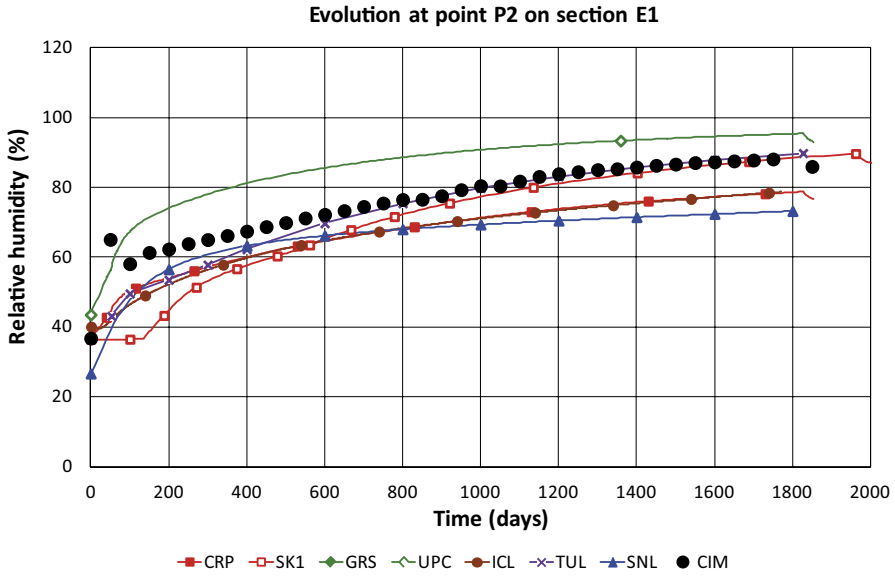

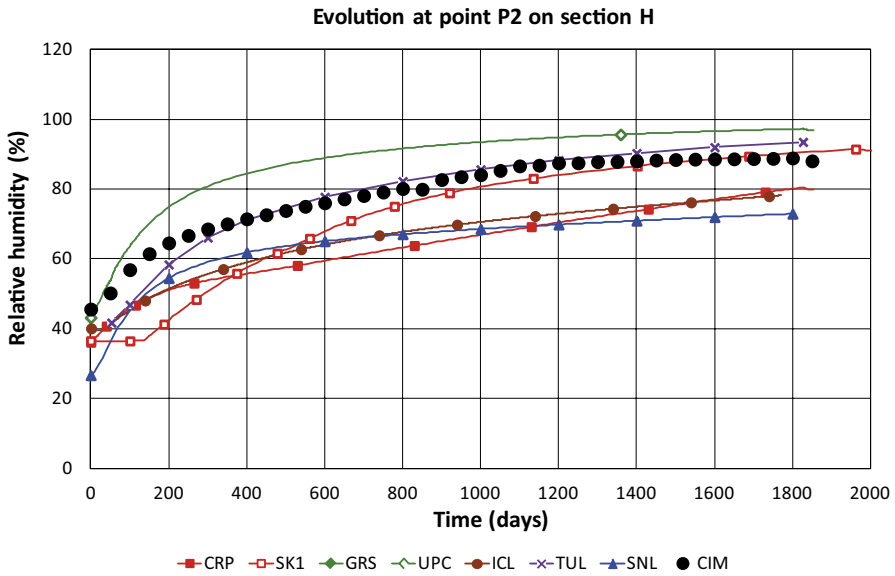

Figure 5-16. *Modelling results vs observations (CIM) up to first dismantling. Evolution of relative humidity at points P2 (intermediate) in sections E1 and H.*

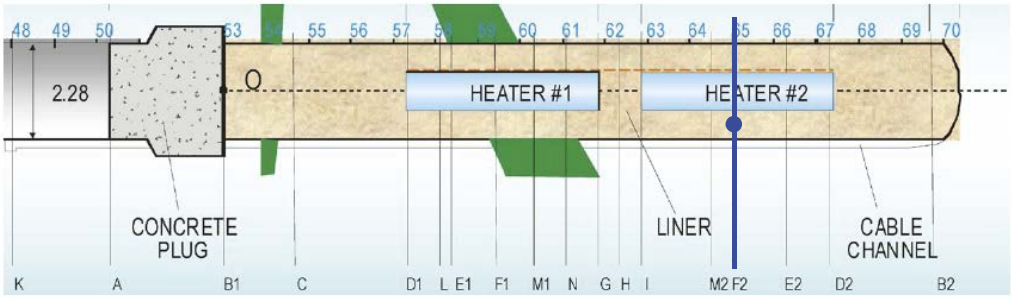

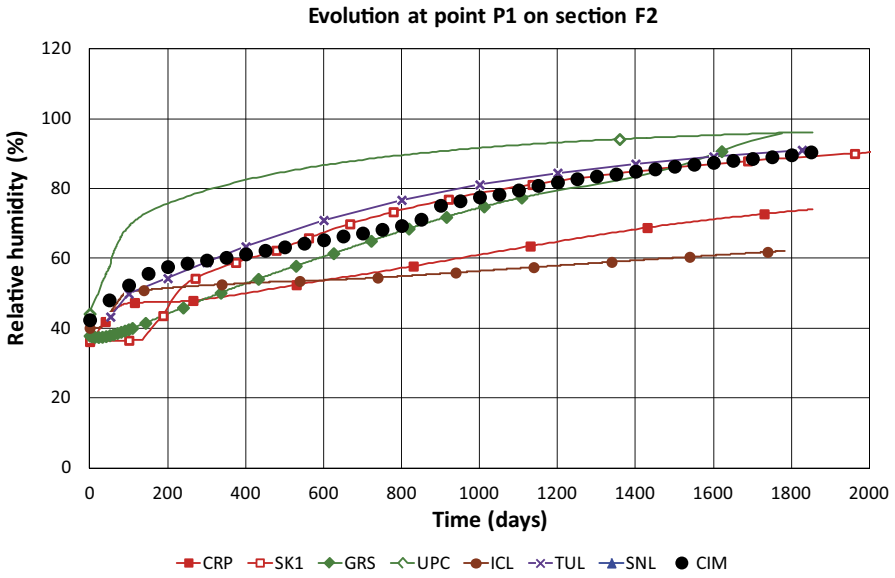

Figure 5-17. *Modelling results vs observations (CIM) up to first dismantling. Evolution of relative humidity at point P1 (intermediate) in section F2.*

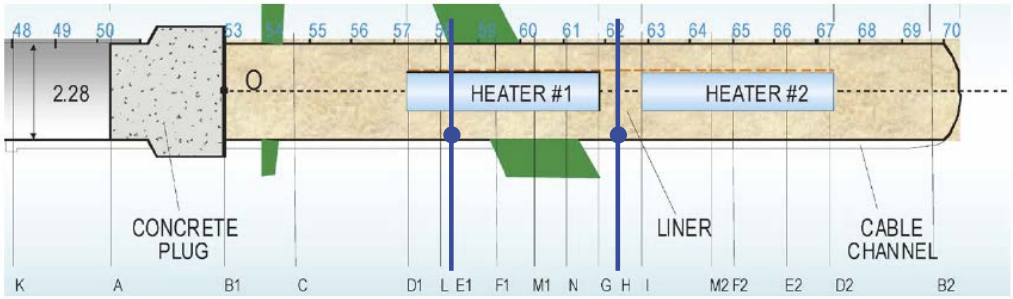

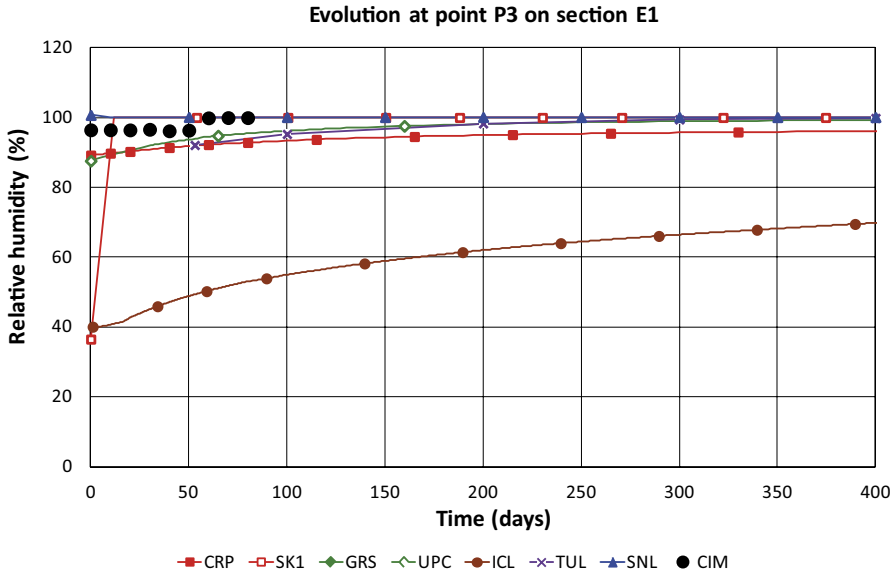

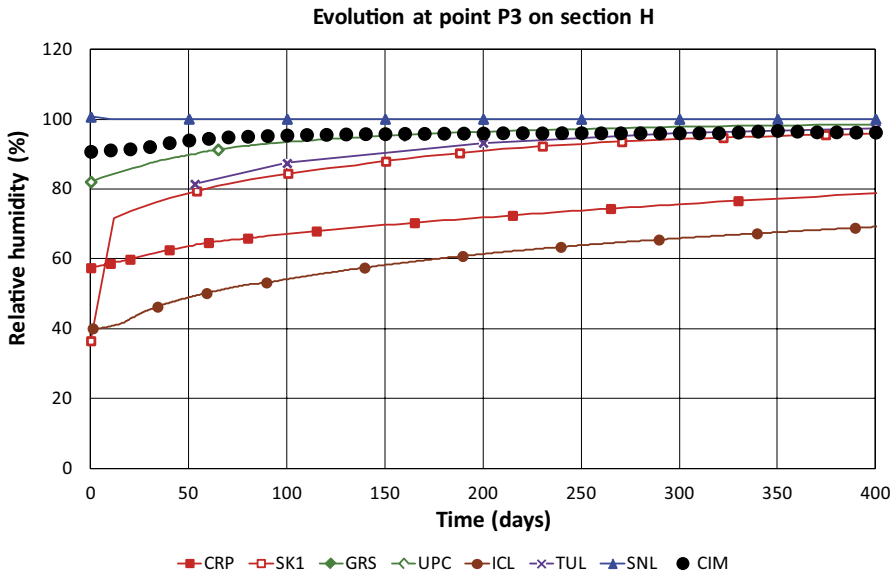

Figure 5-18. *Modelling results vs observations (CIM) up to 400 days. Evolution of relative humidity at points P3 (close to the rock) in sections E1 and H.*

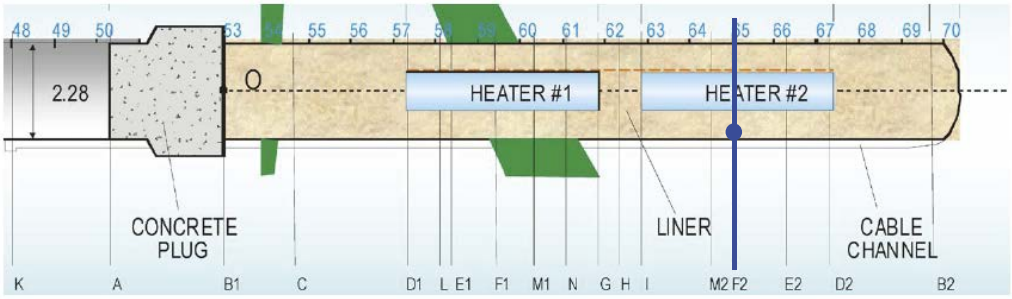

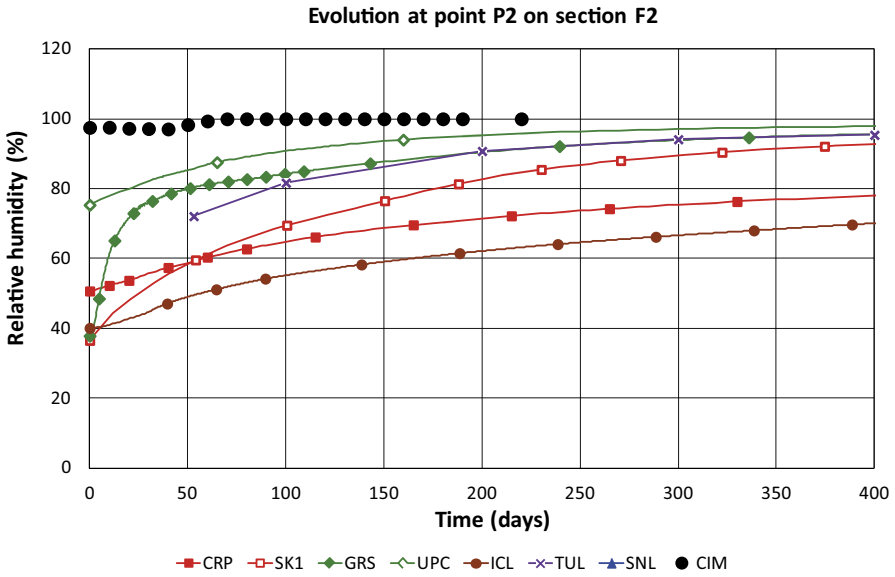

Figure 5-19. *Modelling results vs observations (CIM) up to 400 days. Evolution of relative humidity at point P2 (close to the rock) in section F2.*

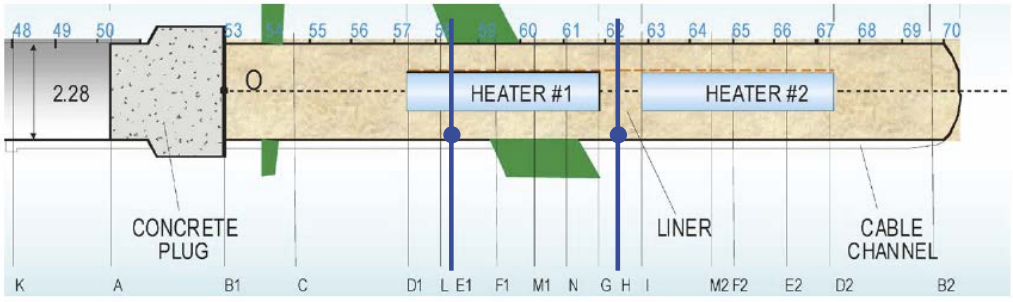

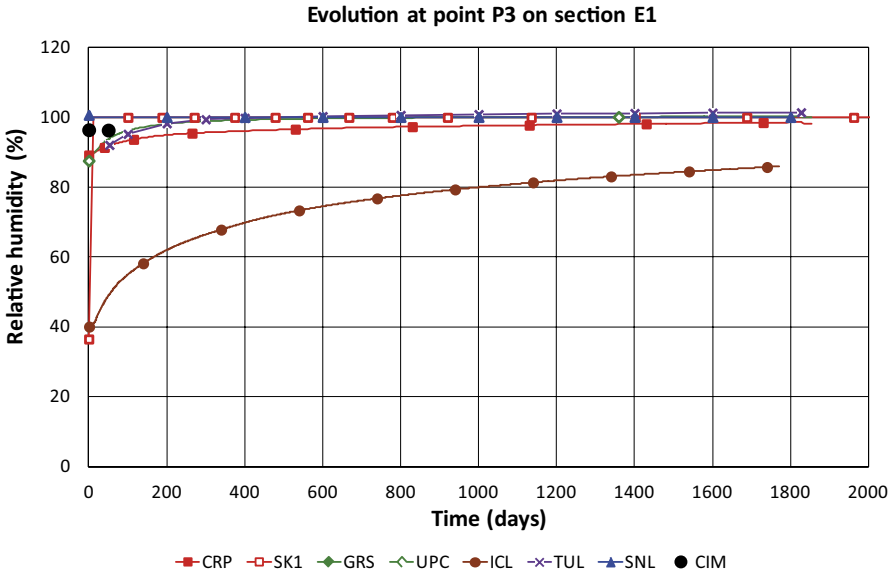

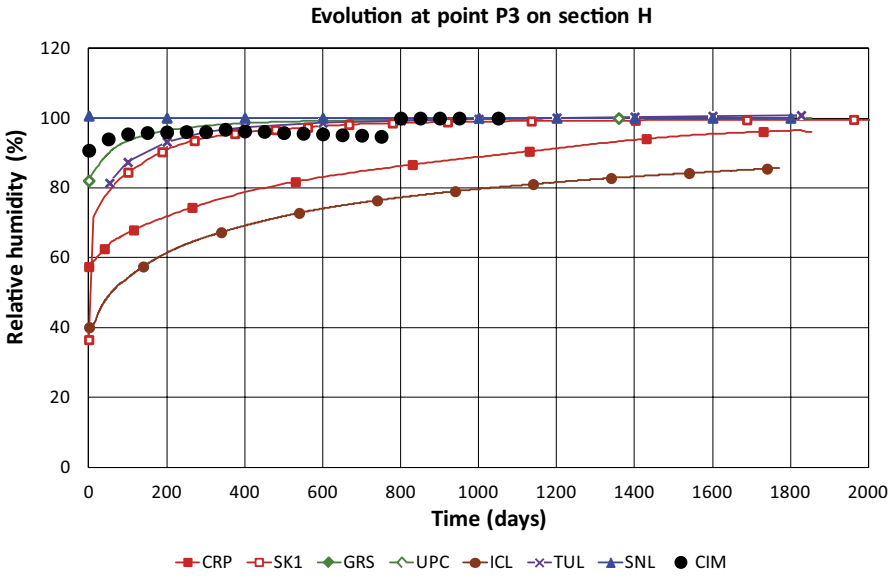

Figure 5-20. *Modelling results vs observations (CIM) up to first dismantling. Evolution of relative humidity at points P3 (close to the rock) in sections E1 and H.*

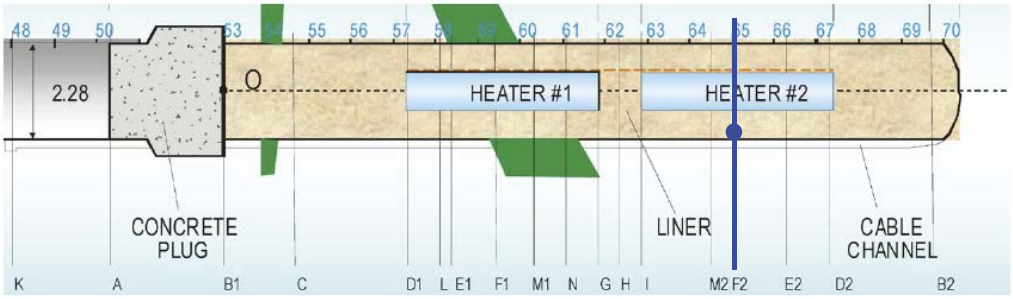

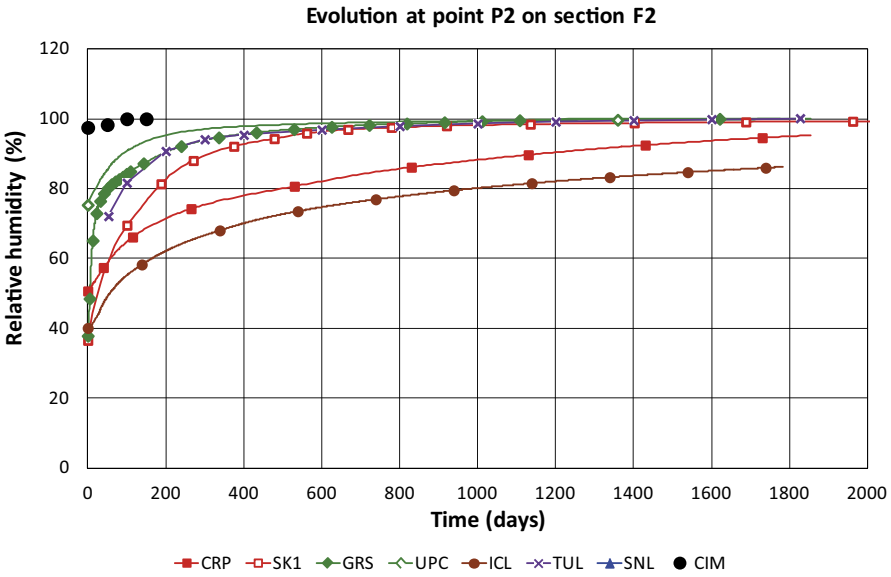

Figure 5-21. *Modelling results vs observations (CIM) up to first dismantling. Evolution of relative humidity at point P2 (close to the rock) in section F2.*

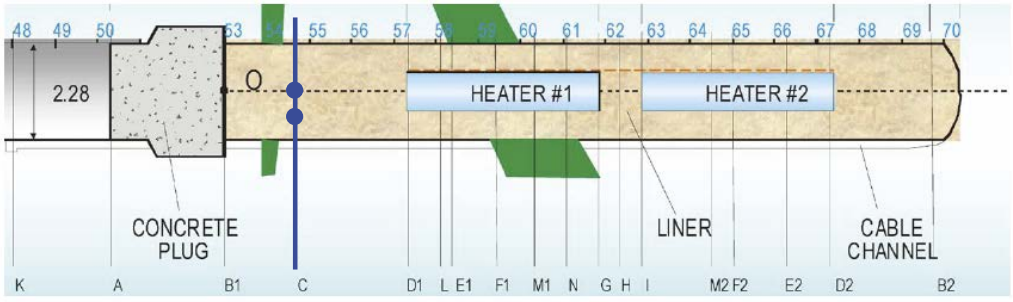

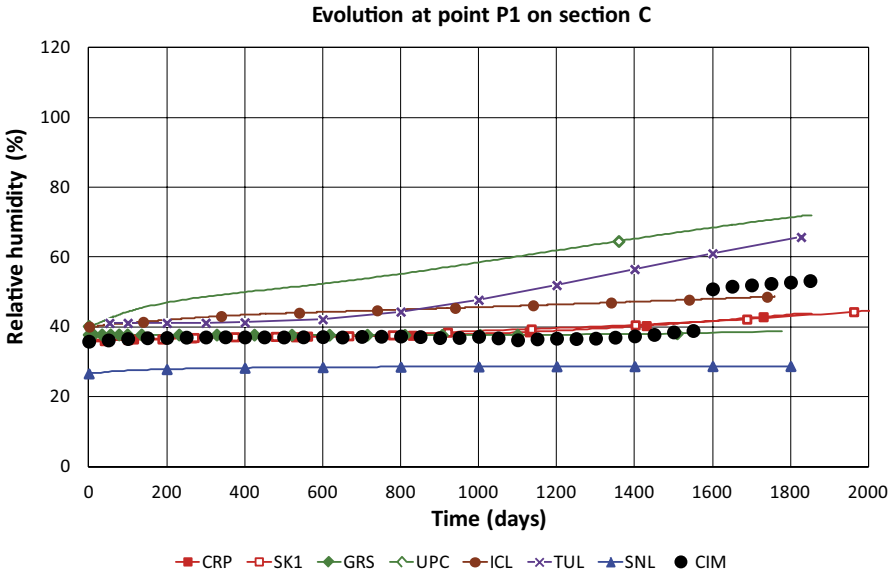

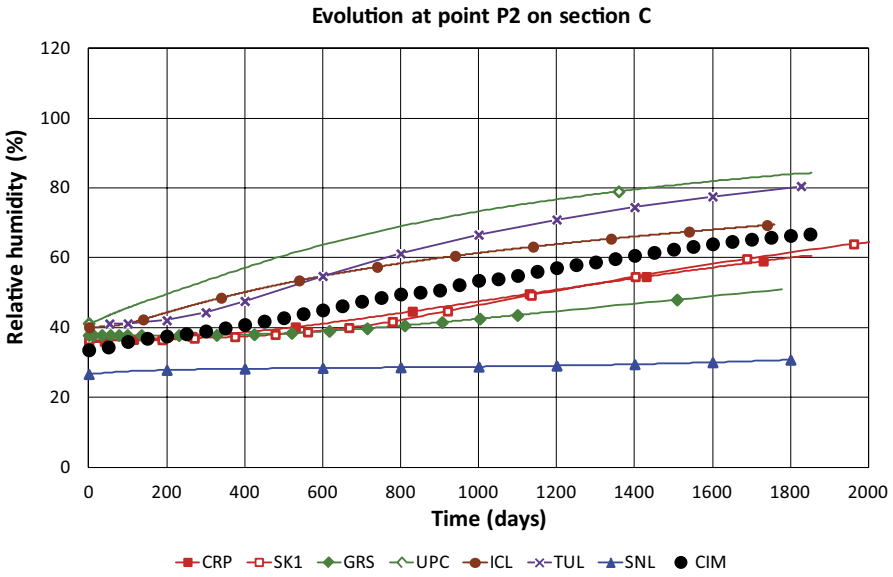

Figure 5-22. *Modelling results vs observations (CIM) up to first dismantling. Evolution of relative humidity at points P1 (tunnel axis) and P2 (intermediate) in section C.*

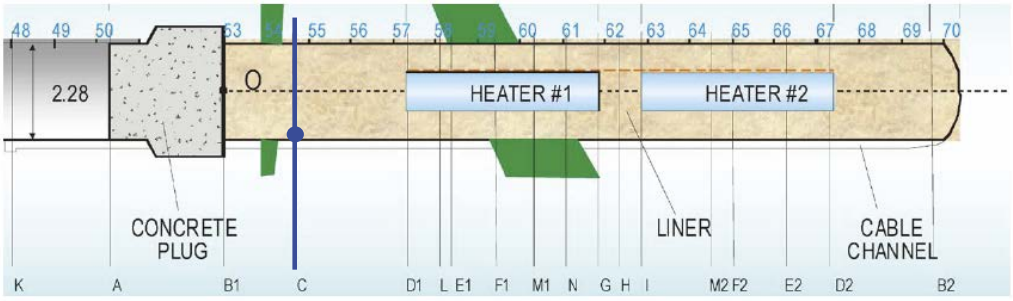

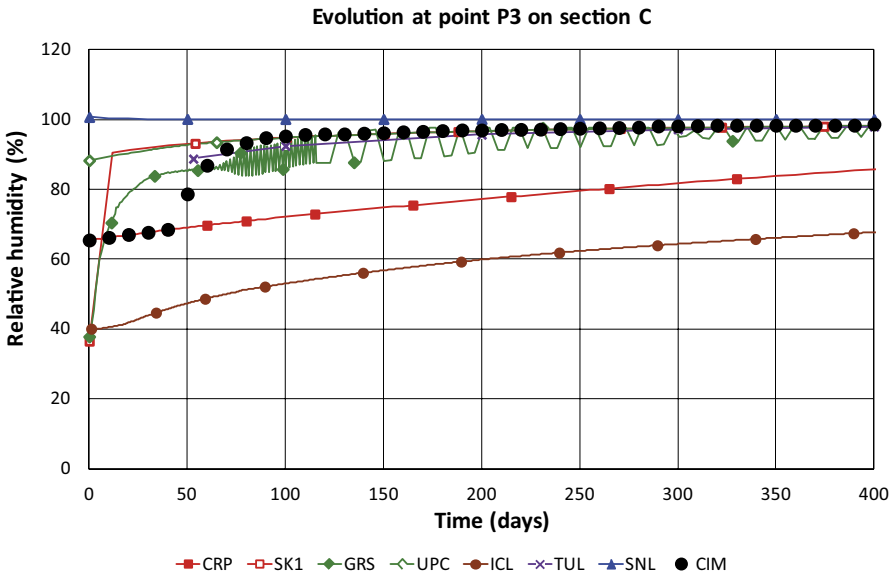

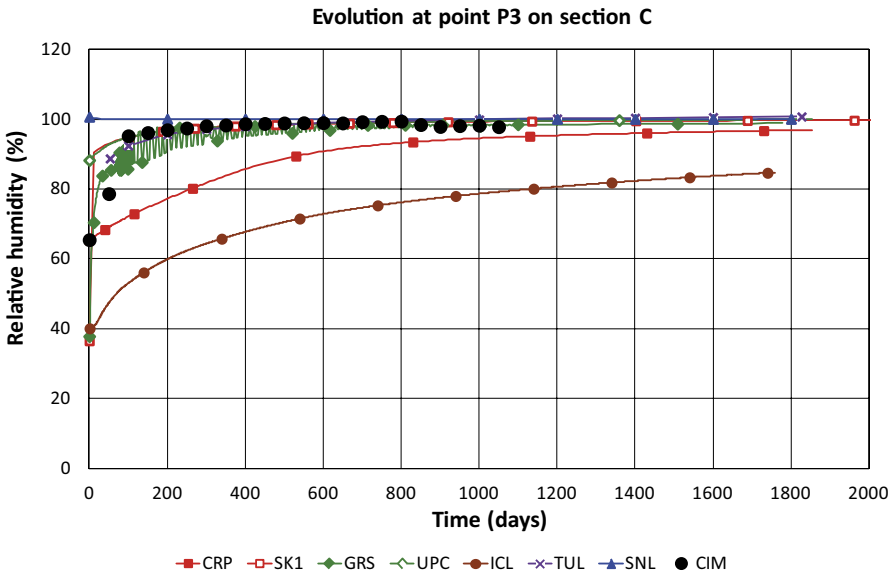

Figure 5-23. *Modelling results vs observations (CIM) up to 400 days and first dismantling. Evolution of relative humidity at point P3 (close to the rock) in section C.*

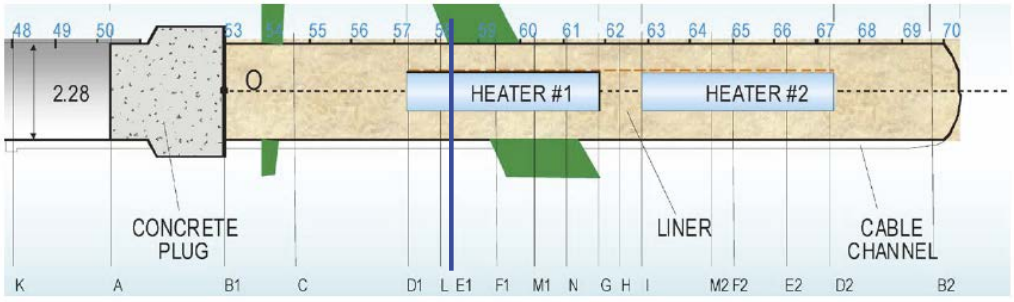

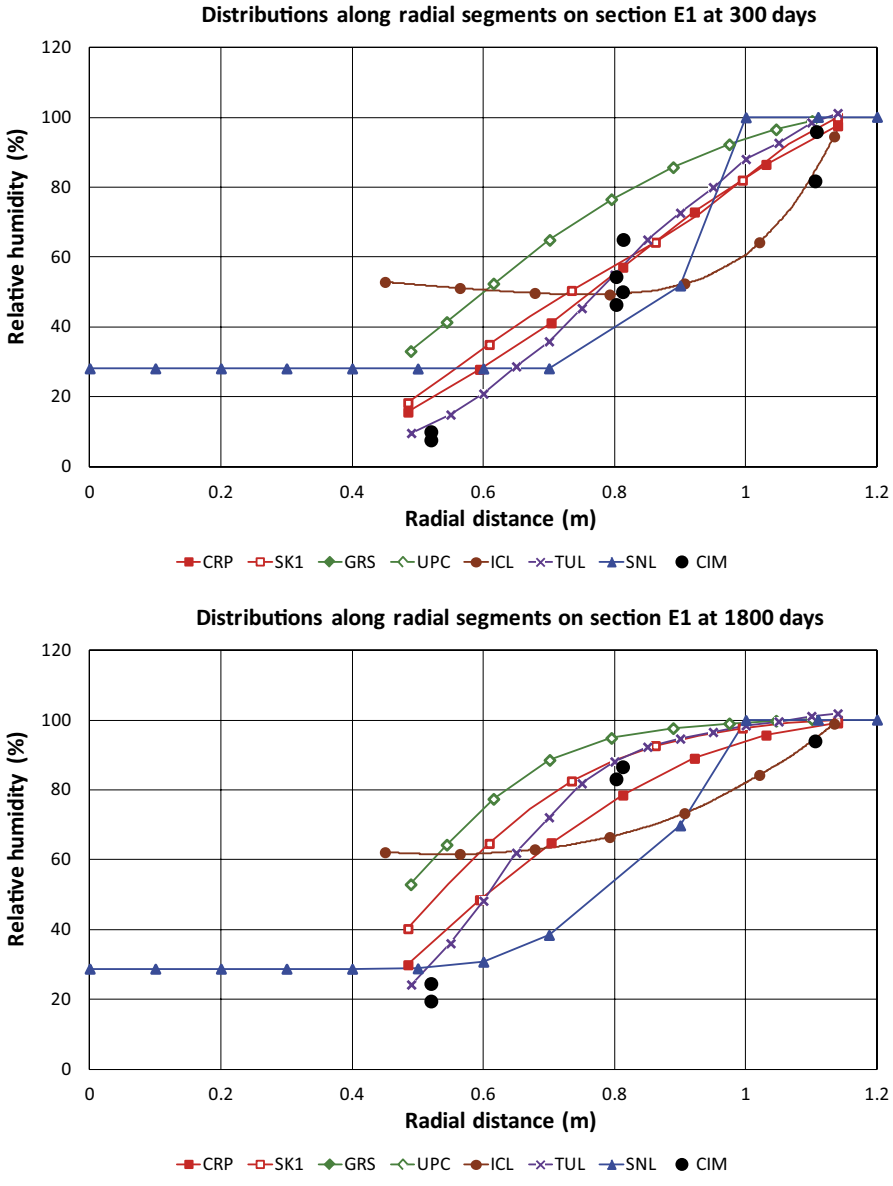

Figure 5-24. *Modelling results vs observations (CIM) at 300 days and at first dismantling. Distribution of relative humidity in section E1.*

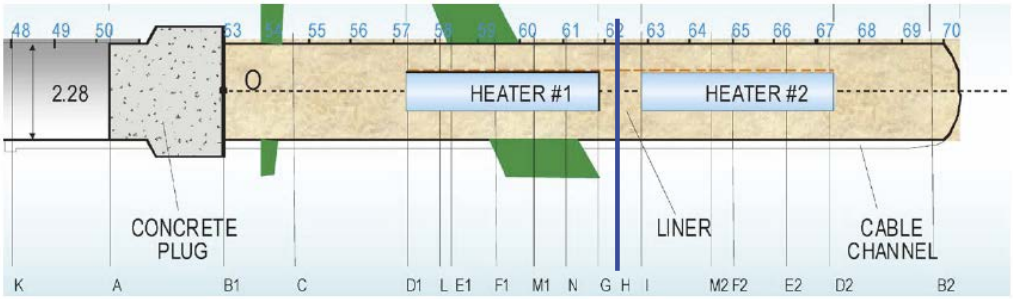

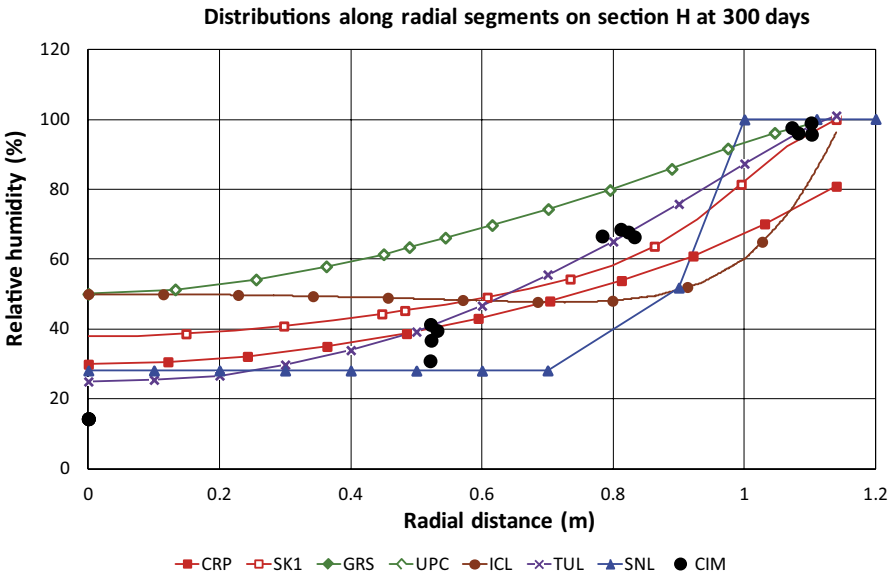

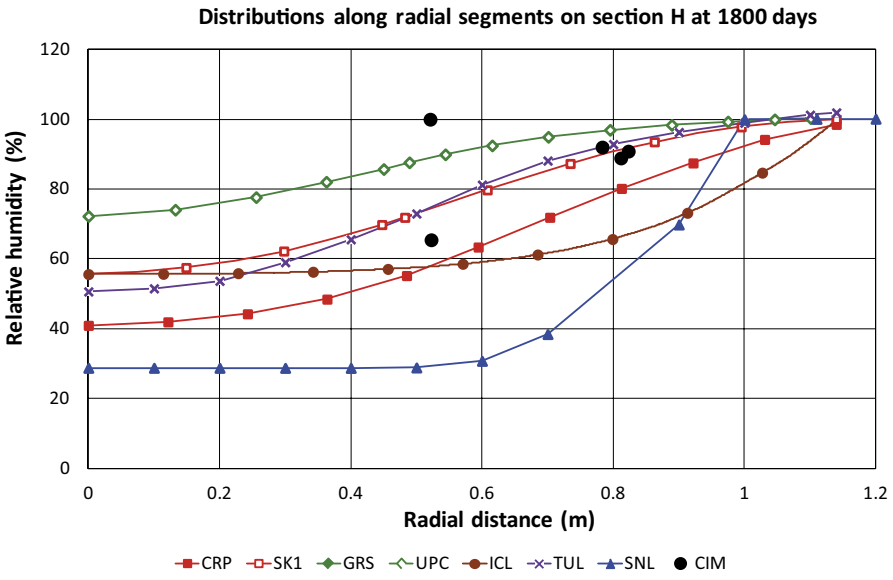

Figure 5-25. *Modelling results vs observations (CIM) at 300 days and at first dismantling. Distribution of relative humidity in section H.*

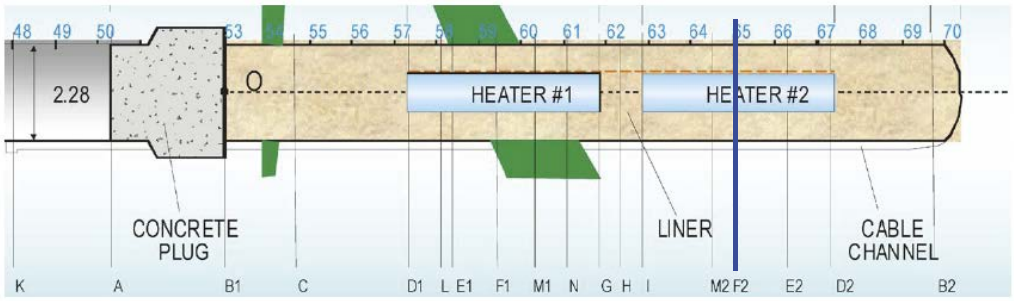

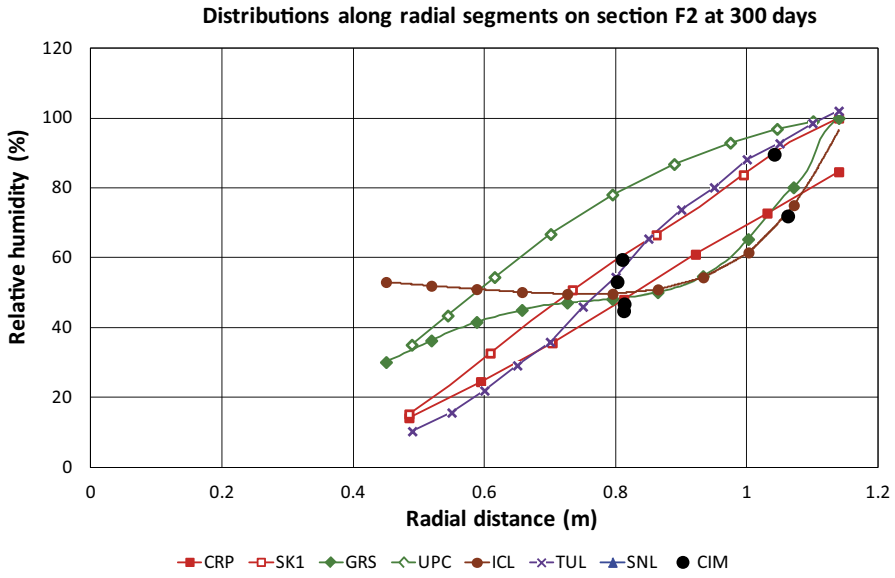

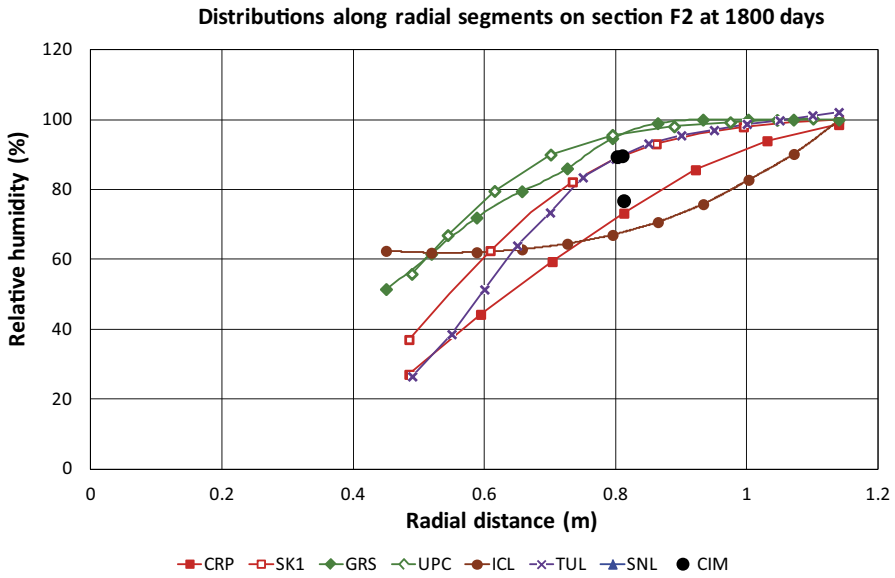

Figure 5-26. *Modelling results vs observations (CIM) at 300 days and at first dismantling. Distribution of relative humidity in section F2.*

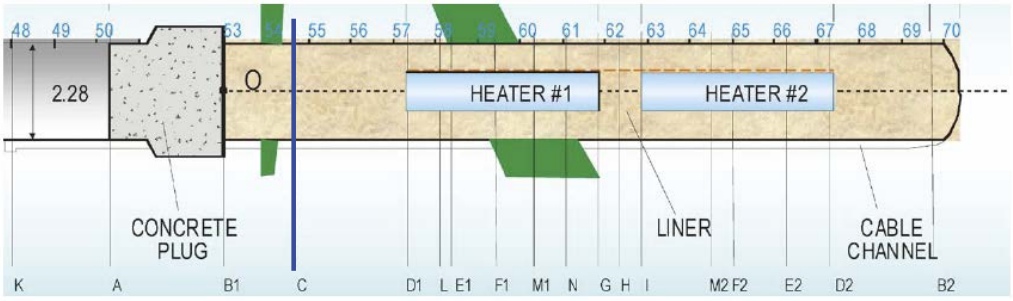

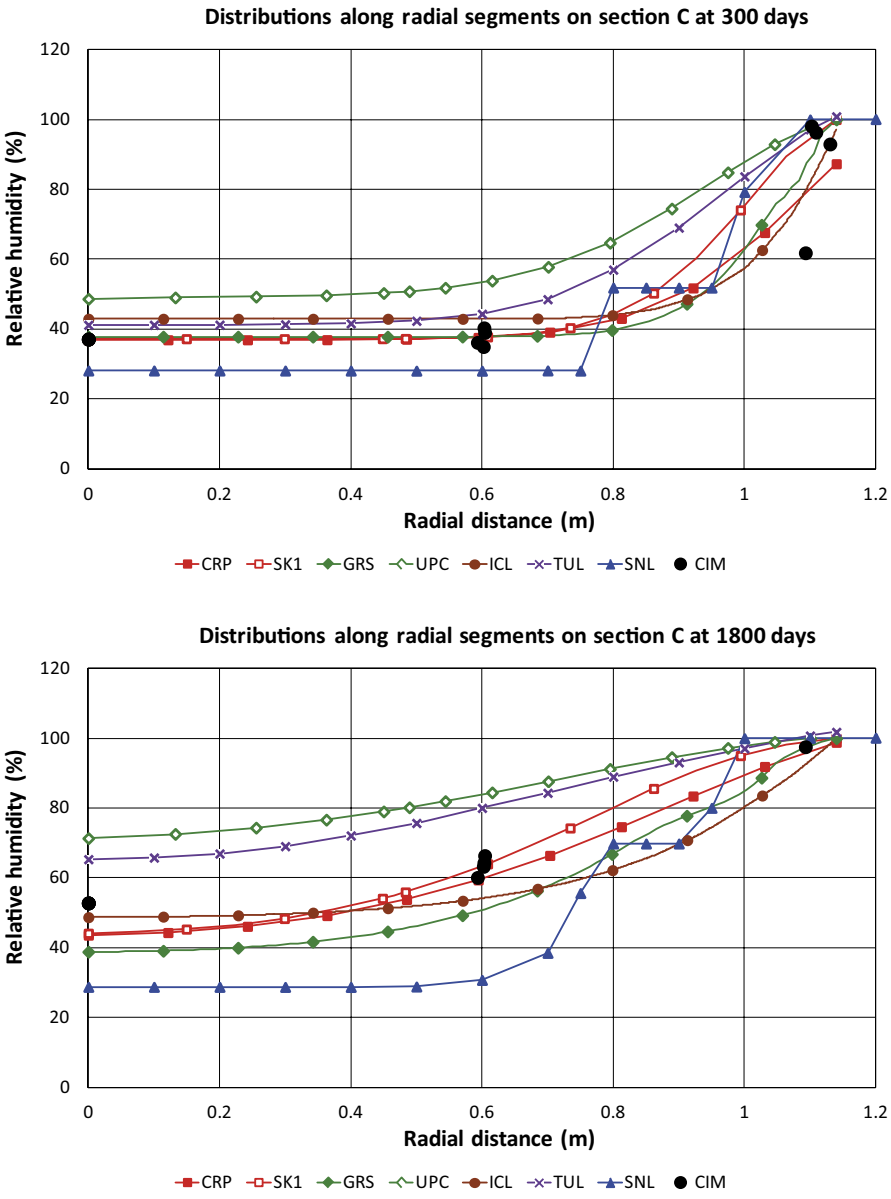

Figure 5-27. *Modelling results vs observations (CIM) at 300 days and at first dismantling. Distribution of relative humidity in section C.*

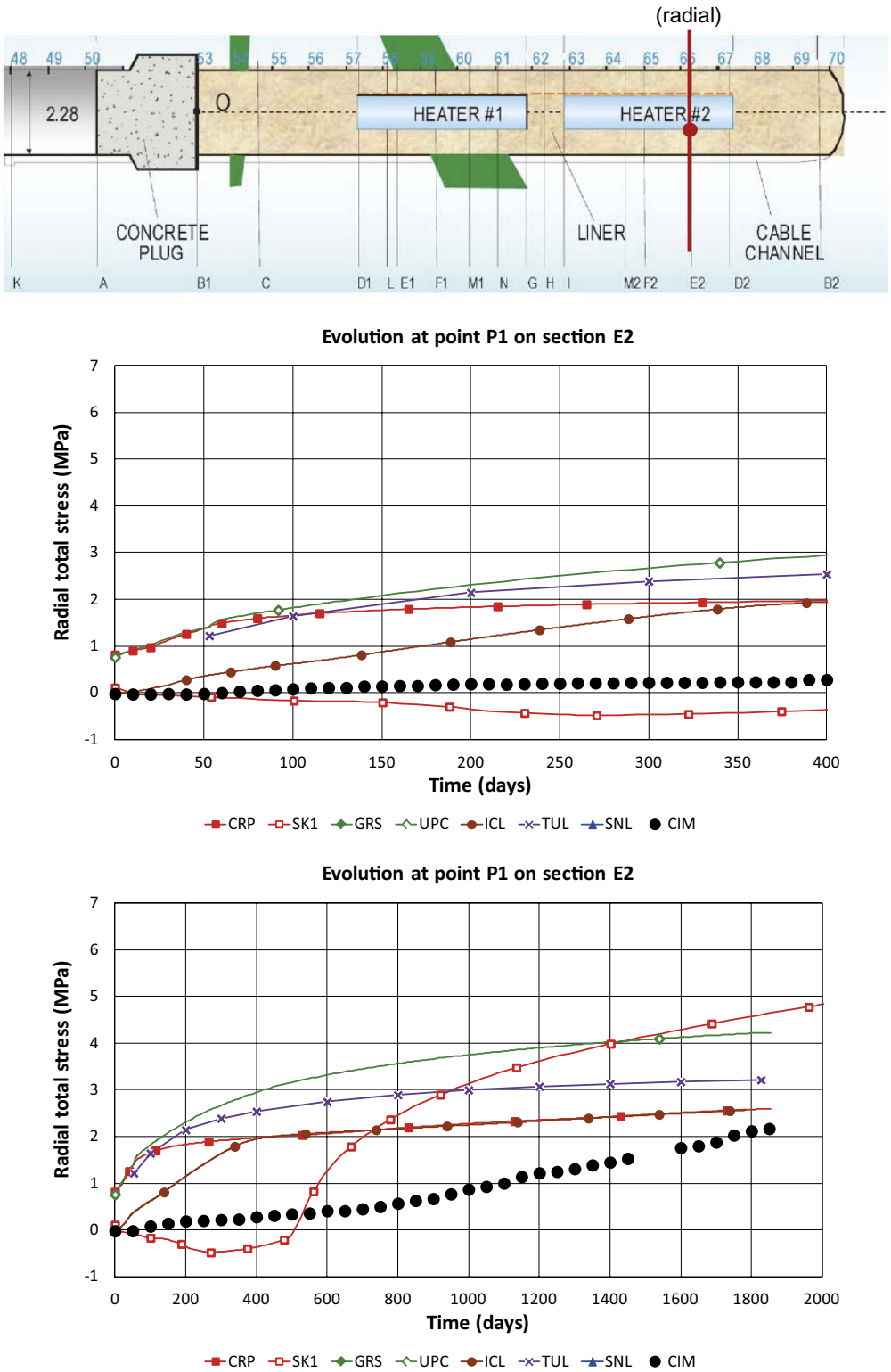

Figure 5-28. *Modelling results vs observations (CIM) up to 400 days and up to first dismantling. Evolution of radial stresses in point P1 (close to the heater) in section E2.*

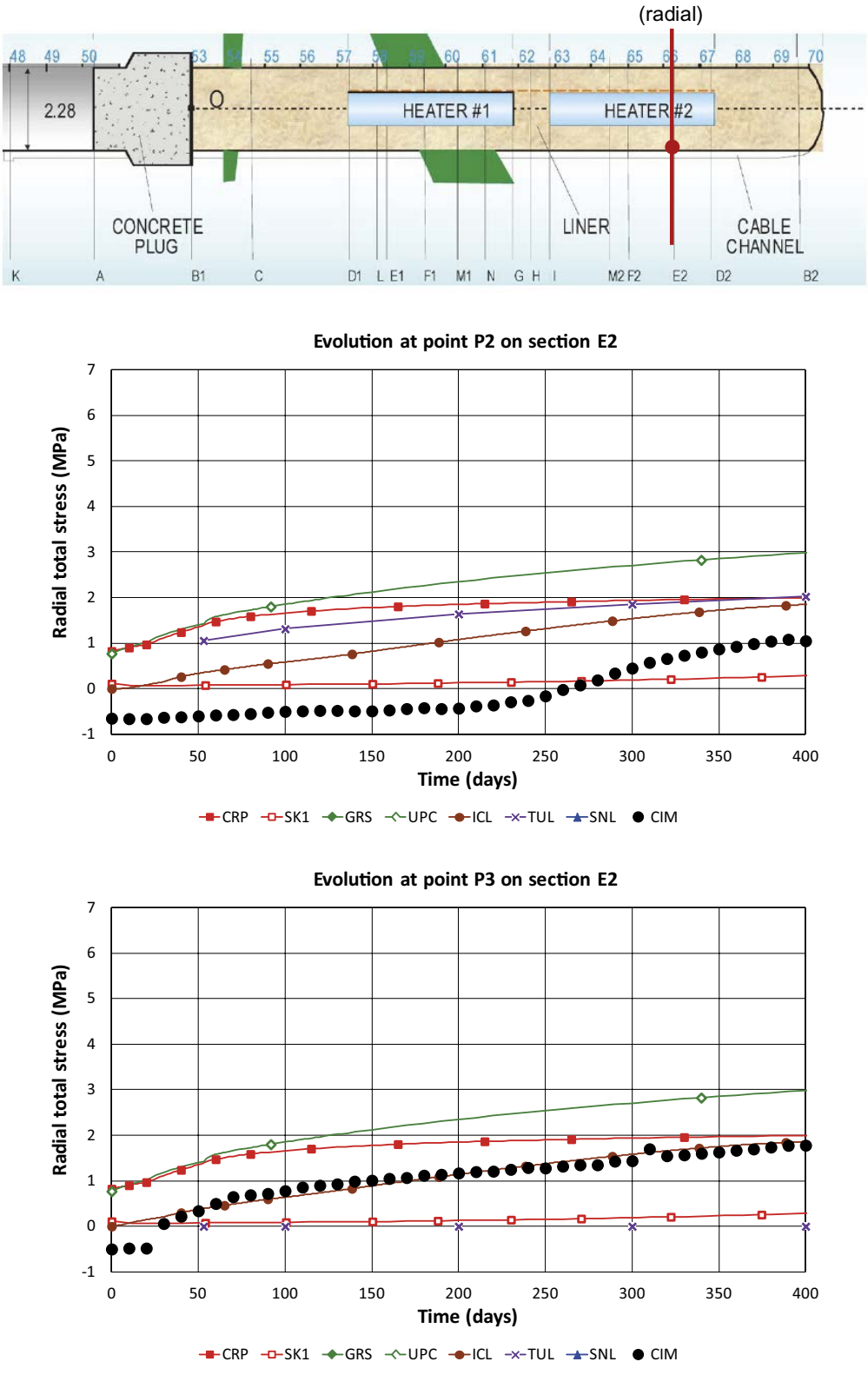

Figure 5-29. *Modelling results vs observations (CIM) up to 400 days. Evolution of radial stresses in points P2 and P3 (close to the rock) in section E2.*

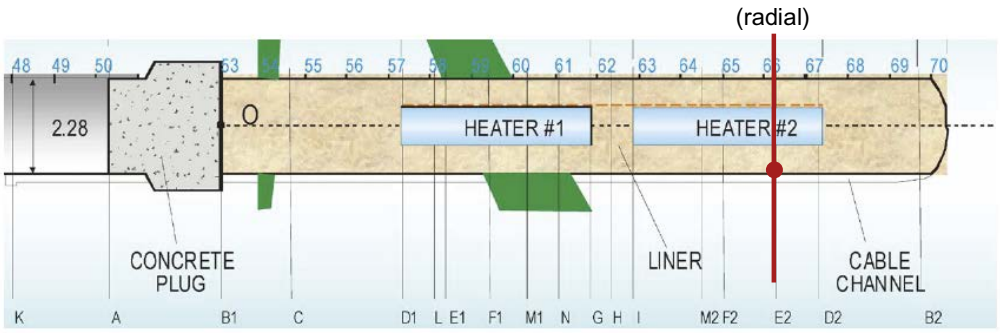

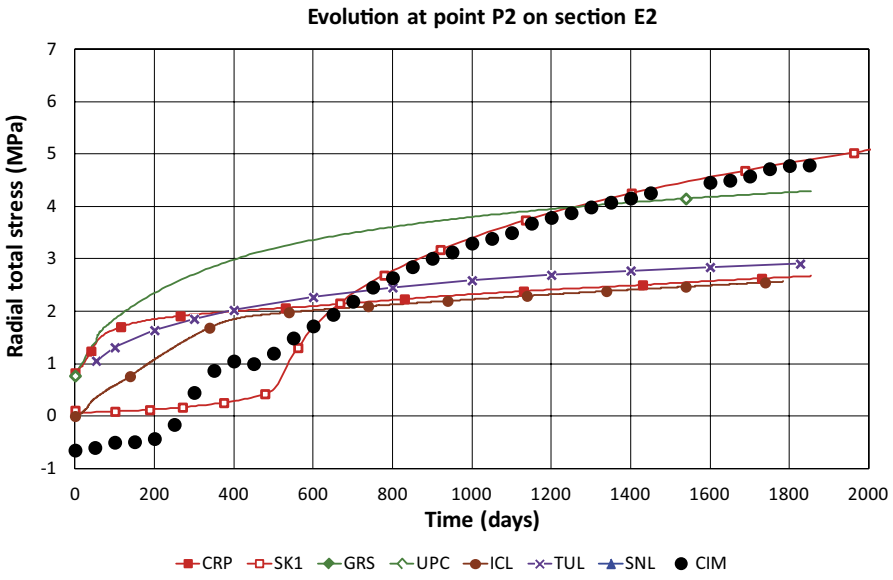

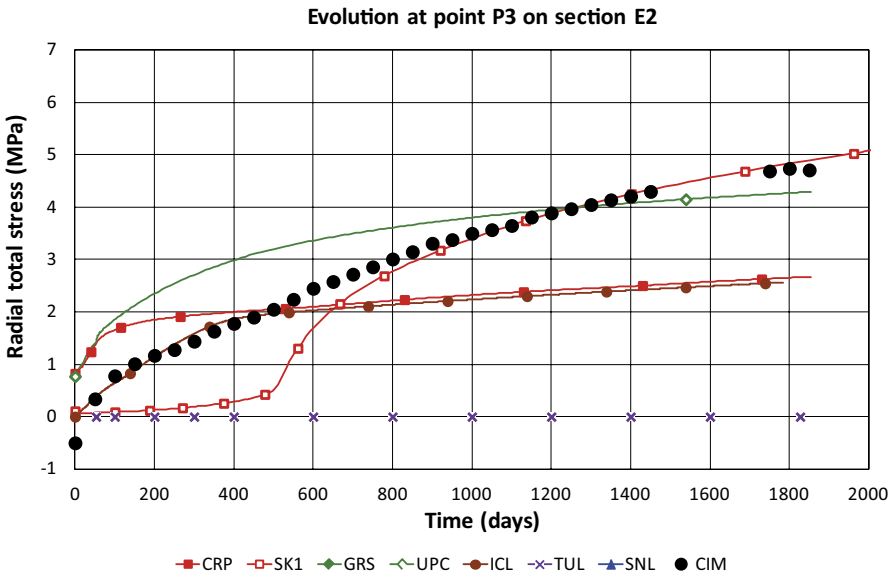

Figure 5-30. *Modelling results vs observations (CIM) up to first dismantling. Evolution of radial stresses in points P2 and P3 (close to the rock) in section E2.*

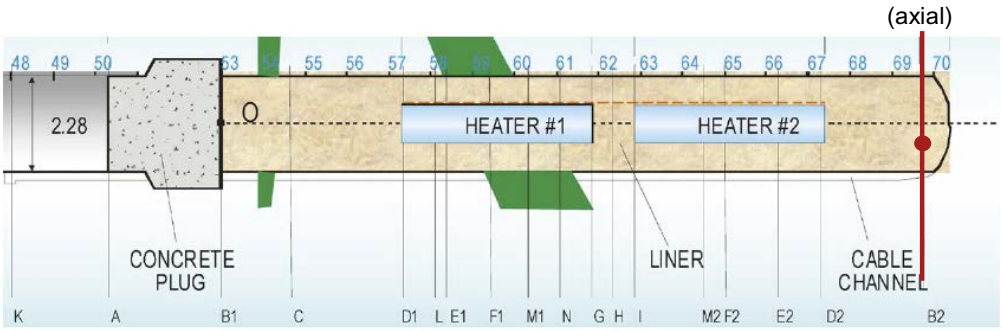

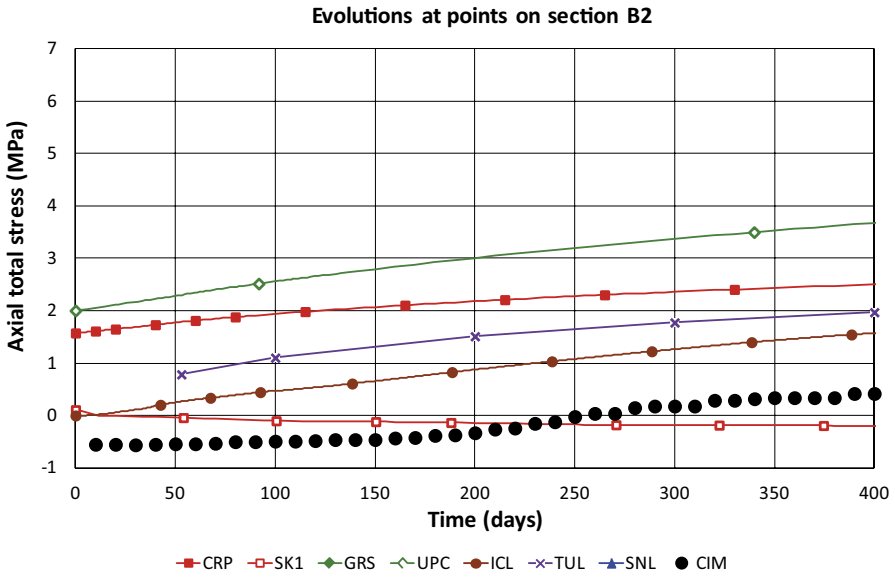

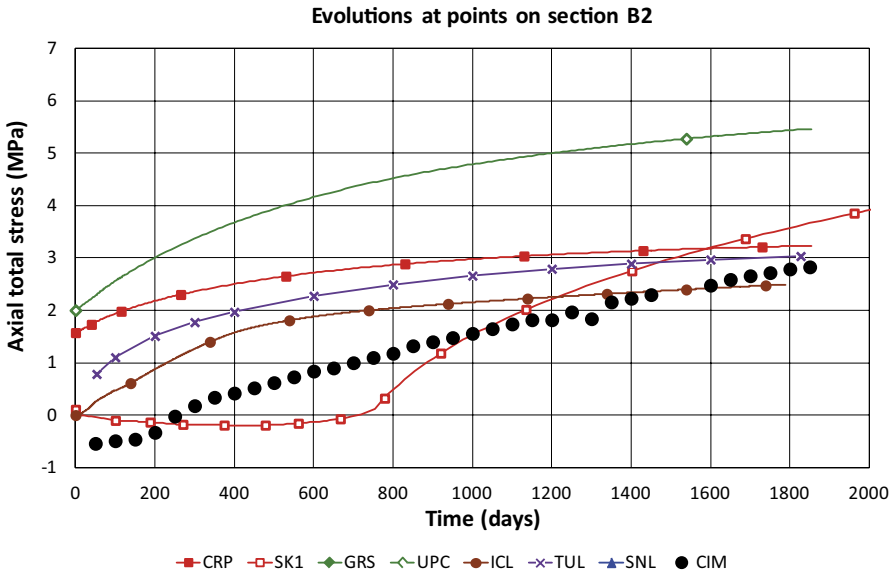

Figure 5-31. *Modelling results vs observations (CIM) up to 400 days and up to first dismantling. Evolution of axial stresses in point P1 (intermediate) in section B2.*

5.1.2 First dismantling

As indicated above, a large number of samples were extracted during dismantling as the successive bentonite sections were being removed. Dry density and mass water content were measured immediately after extraction. The results of the modelling for the distributions of dry density, mass water content and degree of saturation were requested for sections 15, 27 and 31 (Figure 5-32). Two of the sections (27 and 31) correspond to the zone surrounding the heater whereas the third one (15) corresponds to a cooler zone. Because the experimental results exhibited a practically axisymmetric pattern and the modelling teams have used an axisymmetric geometry, the observations along all the different radii in a section have been plotted together. The comparisons of the dismantling data with modelling results are shown from Figure 5-33 to Figure 5-38.

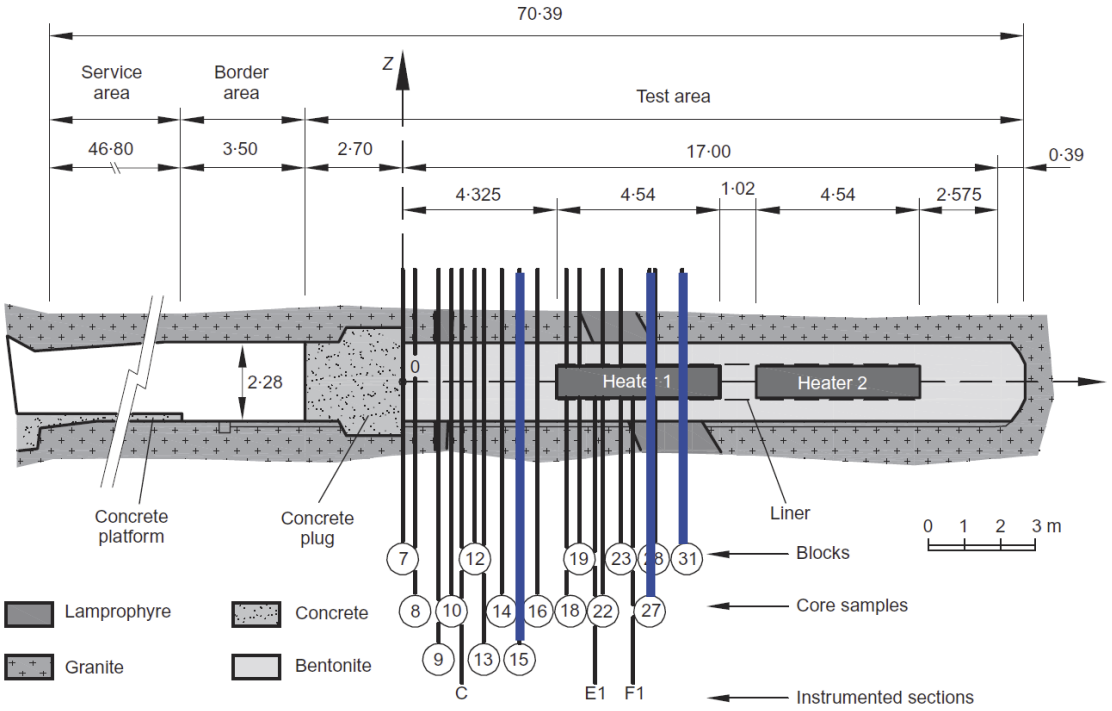

Figure 5-32. *Bentonite sections for which modelling results were requested.*

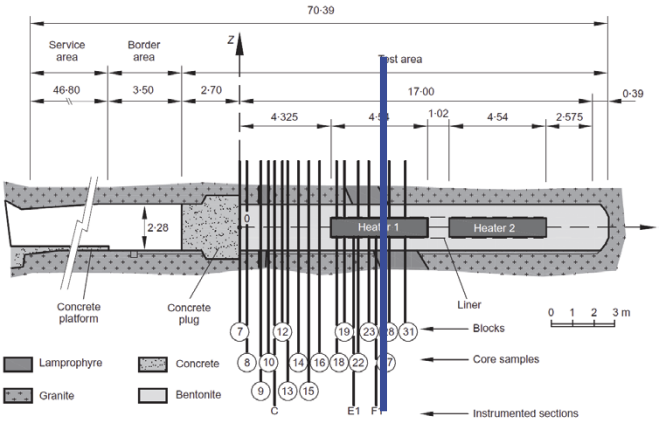

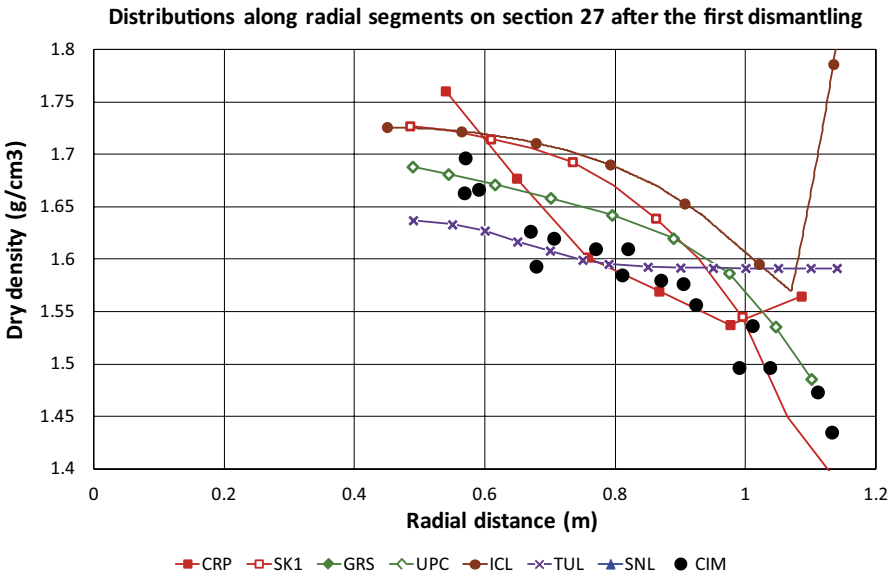

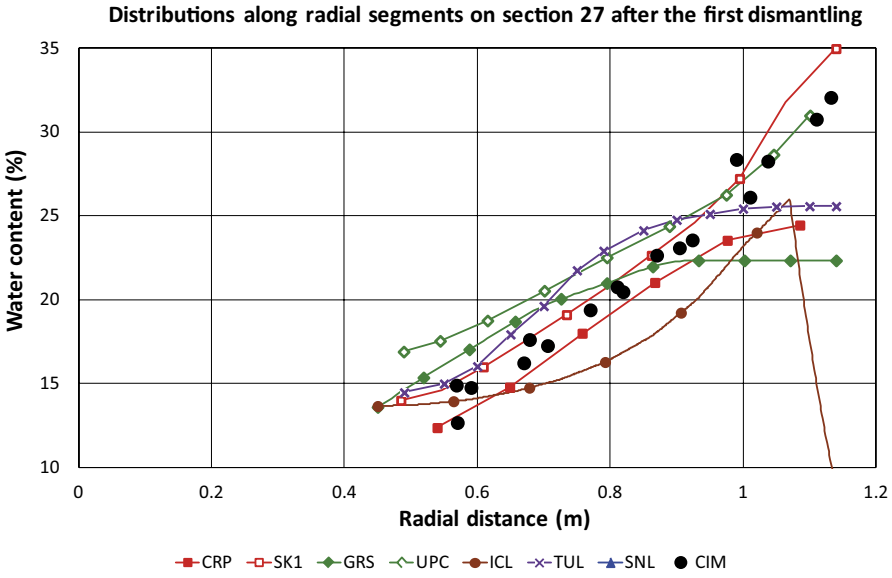

Figure 5-33. *Modelling results vs observations (CIM). Distributions of dry density and mass water content after first dismantling. Section 27.*

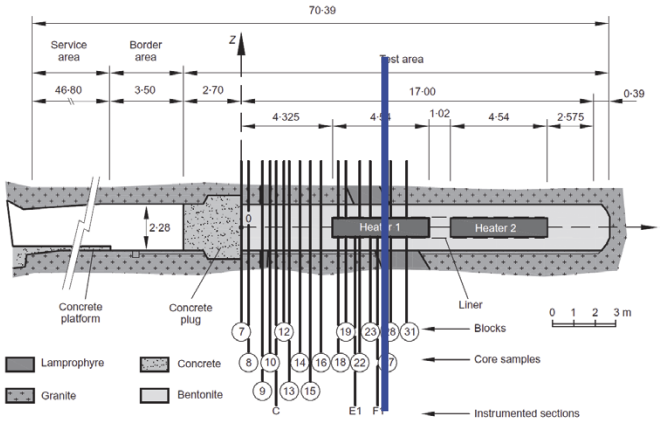

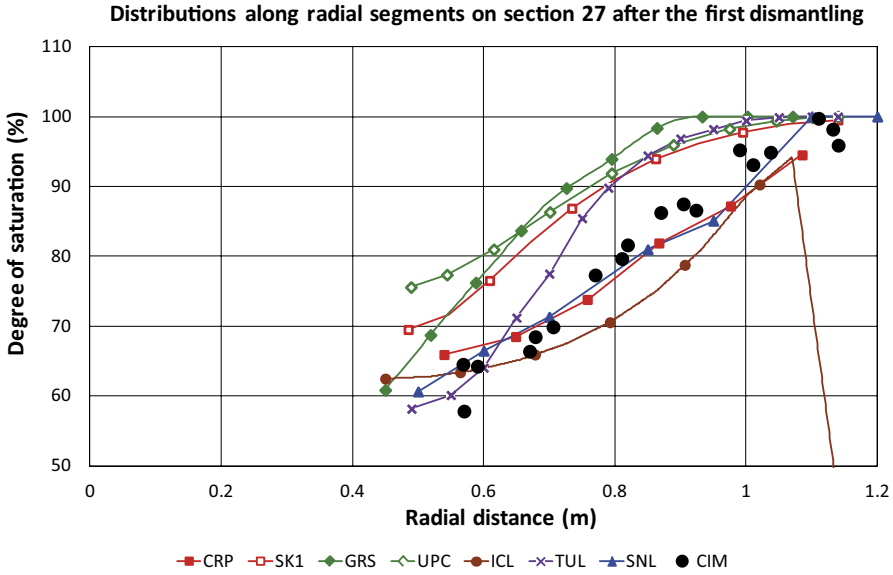

Figure 5-34. *Modelling results vs observations (CIM). Distribution of degree of saturation after first dismantling. Section 27.*

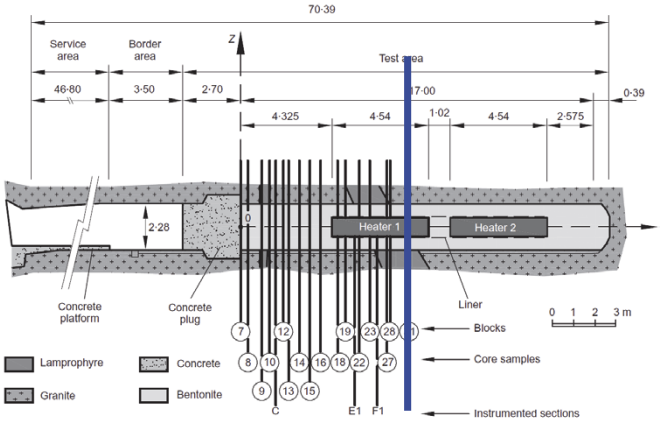

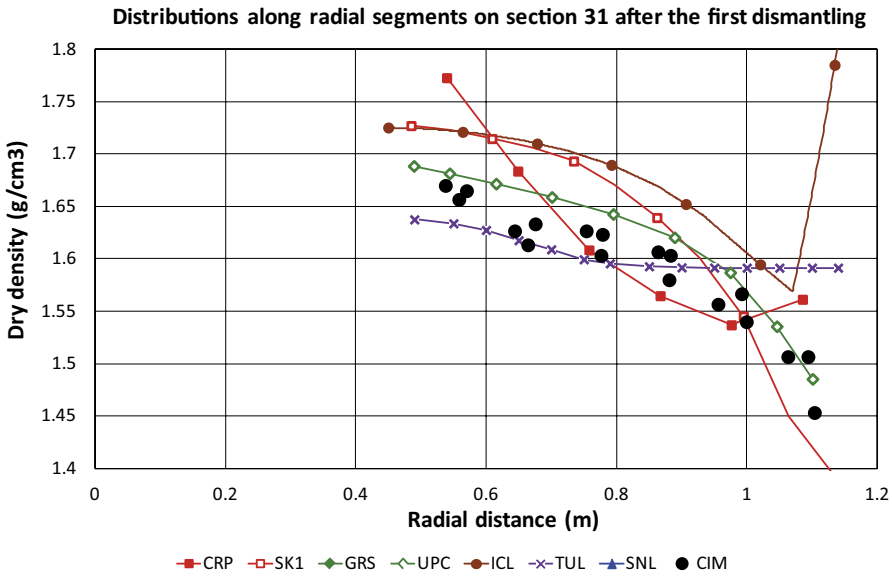

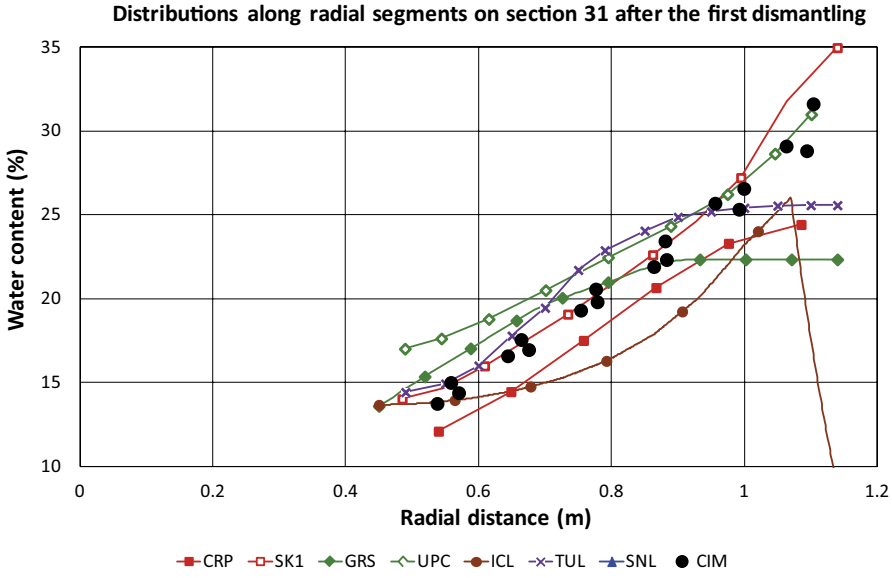

Figure 5-35. *Modelling results vs observations (CIM). Distributions of dry density and mass water content after first dismantling. Section 31.*

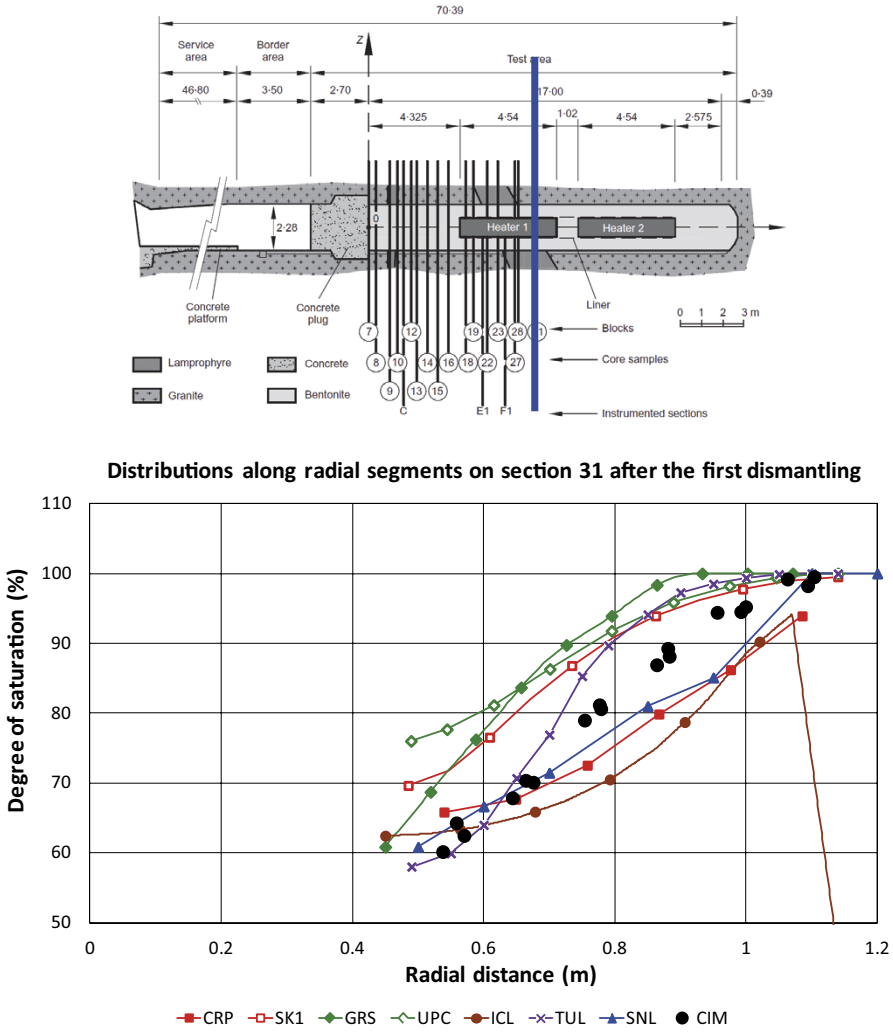

Figure 5-36. *Modelling results vs observations (CIM). Distribution of degree of saturation after first dismantling. Section 31.*

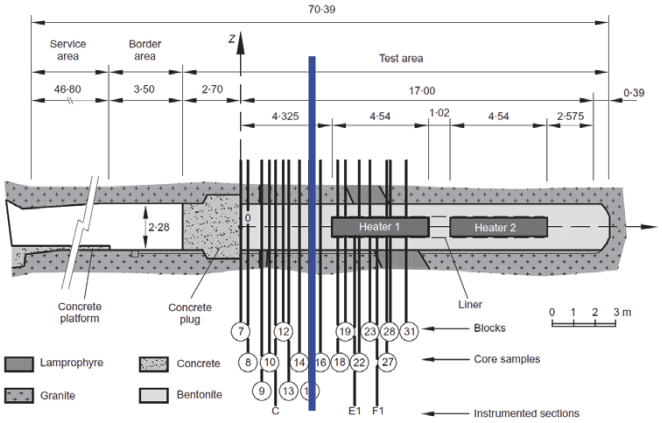

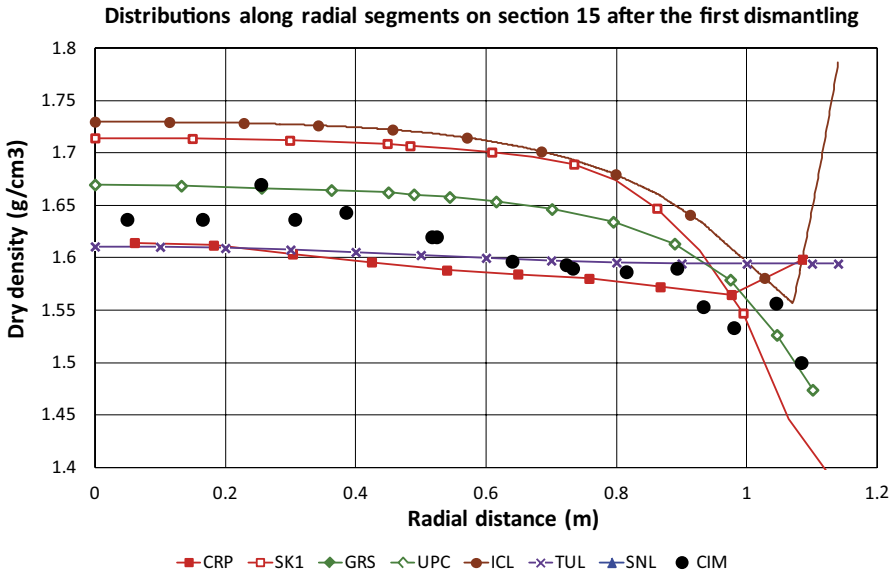

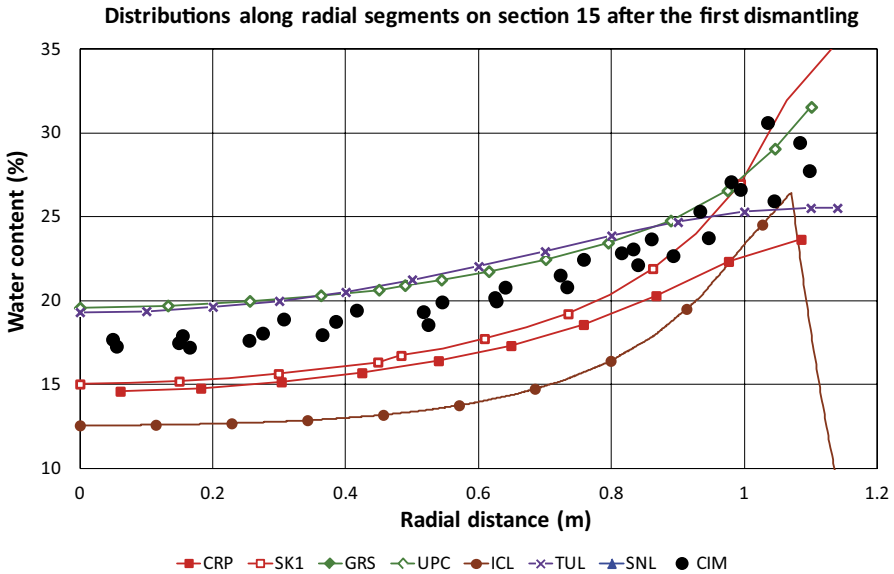

Figure 5-37. *Modelling results vs observations (CIM). Distributions of dry density and mass water content after first dismantling. Section 15.*

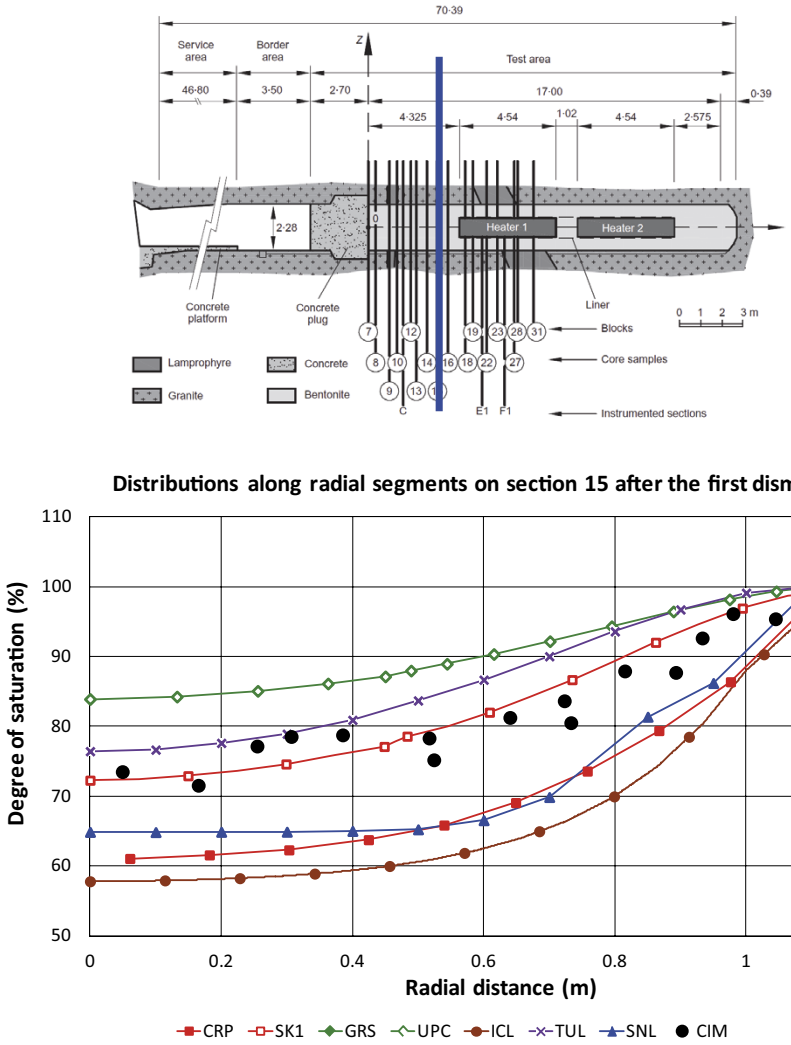

Figure 5-38. *Modelling results vs observations (CIM). Distribution of degree of saturation after first dismantling. Section 15.*

5.1.3 Summary comments

Heater power observations are plotted in Figure 5-5 (for the first 400 days) and Figure 5-6 (up to first dismantling). It can be observed that the power of heater #2 is about 10 % higher than that of heater #1; the reason for this difference is unknown. It is also apparent that, once the initial heating protocol is completed, the power required to maintain he maximum temperature at 100 °C increases steadily throughout this operational stage due to the progressive hydration of the barriers that enhances its thermal conductivity.

The same figures show also the results of the calculations of five teams. SKB-CT did not computer heater power but used the measured values as thermal boundary condition and it is not included in the figure. ICL did not provide heater power results and SNL applied a constant power throughout. It can be observed that all the teams that computed heater power obtained practically the same result for the two heaters indicating that their different location with respect to the plug and the open gallery is not the reason for the observed power difference. Another possibility would be a different thermal conductivity of the rock in the two zones but there was no indication of significant variation in the rock physical characterises along the length of the experiment.

Figure 5-5 and Figure 5-6 show that computed results bracket the heater power observations, the degree of agreement depends on whether either heater 1 or heater 2 is considered. The highest prediction is obtained by UPC and the lowest one by CRIEPI consistent with the fact that they use the highest and lowest thermal conductivity values, respectively. It is also interesting to note that the results of

CRIEPI, TUL and UPC show the increase of heating power with time consequence of the rise in degree of saturation of the bentonite. GRS reports a reduction of heating power with time because it assumes a constant thermal conductivity.

The distributions of *temperatures* are shown in Figure 5-7 to Figure 5-9 in cross-sections and in Figure 5-10 and Figure 5-11 in longitudinal sections. It can be noted that there is a good general agreement between observed and computed values with most differences amounting to a few degrees. The differences seen in some of the SNL results are a consequence of using a 3D geometry; the necessarily coarser mesh sometimes fails to provide results in precisely the location of the requested points.

The measured and computed time evolutions of *relative humidity* are shown in Figure 5-12 to Figure 5-23 for times of 400 days (early evolution) and 1 800 days (end of the Stage 1). Sections E1 and F2 correspond to locations in front of the heaters whereas section H is situated between the two heaters. In addition to those hot sections, section C is located in the cooler zone of the experiment. All analyses model successfully the progressive hydration of the barrier located around the heaters reflected in an increase of relative humidity. Note that GRS only provided results for sections F2 and C because of the specific characteristics of their analysis.

Focusing first on the behaviour close to the heater (point P1, section E1; Figure 5-12 and Figure 5-13), most teams simulate the initial drying of the bentonite although they tend (except TUL) to underestimate the drop in relative humidity. The exception is ICL because vapour transport has not been incorporated in their analysis. This feature also leads to an overestimation of the subsequent hydration along with the prediction of UPC, in the latter case because of using a higher hydraulic conductivity. After a small rise in relative humidity SNL shows a small steady reduction, the progressive hydration after day 200 is not reflected in their model results.

The evolution of relative humidity in section H (between the heaters, Figure 5-12 and Figure 5-13) is more complex with an initial increase of relative humidity (due probably to the passage of a vapour front), followed by some drying and subsequent hydration. This fluctuation does not appear to be reproduced in any model results. The pattern of predictions for this point after this initial period is similar to those provided for section E1.

Figure 5-14 to Figure 5-17 show the evolution of the relative humidity at an intermediate location of the barrier in sections E1, H and F2. The progressive hydration of the barrier at that location is reproduced by all teams although the rates of hydration differ. UPC tends to overestimate the progress of hydration and CRIEPI to underestimate it, a consequence of the values of intrinsic permeability adopted. Some of the underestimation of relative humidity by ICL is likely due to neglecting vapour transport. Due to heating, vapour will migrate from the inner to the intermediate and outer regions of the barrier increasing the hydraulic conductivity in those areas. That increase will not occur if vapour movement is neglected. The underestimation of hydration by SNL in some sections is more surprising, as they adopt a somewhat higher value of intrinsic permeability.

The same trends are apparent in the evolution of relative humidity in the locations close to rock (points P3 in section E1 and H, point P2 in section F2; Figure 5-17 to Figure 5-21). CRIEPI and ICL tend to underestimate the degree of hydration perhaps because they selected a lower intrinsic permeability for the rock. In the case of ICL, the lower initial relative humidity is attributed to the fact that the period of 135 days of hydration without heating was not incorporated in the analyses. It can be observed that the measurements indicate saturation earlier than the models but the sensors at those locations are more subject to local rock effects. SNL and UPC show the fastest hydration in this area probably due to their higher values of hydraulic conductivity.

In the cooler section C (Figure 5-22 and Figure 5-23), the bentonite occupies the whole tunnel section, so the progress of hydration in the inner part of the section is bound to be slower. Indeed, the relative humidity at the centre of the barrier has hardly increased at the end of the first five years of heating. The models predict in the central and intermediate zones of the barrier (Figure 5-22) a behaviour similar to that observed; the higher hydraulic permeability of TUL and UPC lead to a faster rate of hydration. Close to the rock (Figure 5-23), most models predict a very fast hydration similar to that observed. CRIPEI and ICL models yield a slower saturation probably related again to the lower permeability attributed to the rock. The initial lower value of relative humidity in the ICL case is attributed to the same reason indicated above. As thermal effects in this section are very limited. the potential effects of vapour migration are also very limited.

The same features of hydraulic behaviour can be recognized in the distributions of relative humidity at 300 days and at the end of Stage 1 plotted in Figure 5-24 to Figure 5-27 for the same cross-sections E1, H, F2 and C. The lack of drying and the small hydraulic gradient in the inner part due to the absence of vapour migration is readily apparent in Figure 5-24 and Figure 5-26. It should be also be noted that the initial relative humidity assumed by SNL (about 20 %) is lower than the range adopted by other teams (35 % – 40 %), thereby leading to a slower computed hydration progress.

The values of *total stresses* (Figure 5-28 to Figure 5-31) are always subject to a greater degree of uncertainties because of the inherent difficulties associated with their measurement (e.g. sensor seating, stress non-uniformities). Thus, the sensor at point P2 adjacent to the rock measures initially a negative value and it only starts increasing after day 250 whereas the sensor at point P3, in an equivalent location in the same section, shows an increase in readings from the beginning of the heating (Figure 5-29). The recorded total stresses at the end of the Stage for both sensors are close to 5 MPa (Figure 5-30). The sensor close to the heater at point P1 (Figure 5-28) also reacts late and it only reaches a stress of about 2 MPa but this may be a genuine effect of the high temperature that causes a contraction of the bentonite. Late reaction and a low value of total stress (about 3 MPa) are also observed in the axial stress sensor at section B2 (Figure 5-31); in this case a possible reason lies in the low density of the bentonite in that zone.

Only the five modelling teams carrying out THM analyses can provide total stresses results. All the teams indicate an increase in stresses as the experiment progresses in agreement with the monitoring observations. However, the pattern of development is often quite different. The evolution of the stresses computed by SKB-CT is very interesting. There is practically no change in the first 500 days (that correspond to 365 days after the start of heating because of the time-scale offset indicated previously) and, afterwards, the computed pressure picks up and follows a very realistic variation. It is likely that the gap of the SKB analyses does not close until around that time and it is only then that radial stresses can increase. At the end of the Stage, SKB-CT and UPC have developed stress values quite close to those observed whereas CRIEPI, ICL and TUL provide stress underestimations. All the models overestimate the radial stresses measured in the sensor close to the heater although CRIEPI and ICL only slightly. UPC overestimates the axial stress ins section B2 but the rest of the models yield results close to the observations at the end of the Stage. The computed values of radial total stress near the rock and close to the heater are very similar for all models in contrast with the measurements of the experiment. It is also interesting to note that the calculated values of total stresses are generally below the initial swelling pressures reported; this was foreseeable as full saturation is not expected to occur during Stage 1. In the case of SKB-CT, a computed stress value well below the initial swelling pressure is anticipated because the closure of the gap will lead to a lower final density of the barrier.

The observations of dry density, mass water content and degree of saturation obtained in the *first dismantling* are shown in Figure 5-33 to Figure 5-36 for heater sections 27 and 31 and in Figure 5-37 and Figure 5-38 for the full non-heater section 15. As expected, in the heater sections, there has been a reduction of dry density close to the rock and an increase close to the heater resulting in a non-homogeneous distribution. Dry density ranges from 1.45 to 1.7 g/cm^3, approximately. Since both the rock and the heater/liner are stiff, the average dry density is bound to remain approximately constant throughout. The water content range is 14 % – 32 % leading to a non-uniform distribution of degree of saturation between 60 % (close to the heater) and 100 % (near the rock). It is apparent that the barrier is still far away from full saturation. It is also interesting to note that the region close to the heater has gone back to the initial degree of saturation value after undergoing an initial drying.

Although there are quantitative differences between computed and observed dry density values, all teams reproduce distributions of dry density in sections 27 and 31 (heater sections) similar to those observed in the experiment. There is also a coincidence of the pattern of degree of saturation distribution computed and observed, in all cases models predict a largely unsaturated barrier. GRS, SKB-CT, TUL and UPC tend to overestimate the degree of hydration whereas some underestimation is obtained (at least for section 31) from the CRIEPI, ICL and SNL models. The explanation lies in the different hydraulic conductivities and in the effects of vapour migration. Also, the constant degree of saturation value obtained by GRS and TUL in the zone close to the rock is not borne out by the experimental observations. A consequence of introducing an outer gap in the analysis (SKB-CT) is that a quite low dry density and a high water content is predicted for the zone close to the rock. This computed gap effect is, however, larger than warranted by the test observations.

In the non-heater section 15 (Figure 5-37 and Figure 5-38), the dry density reduced close to the rock due to hydration and it is compensated by a slight increase in the central zone of the barrier. The same pattern is obtained by the models but the variation of dry density predicted is larger than observed. Only CRIEPI reports a nearly constant dry density across the section. Again, SKB-CT computes a lower dry density close to the rock because of the gap effect. Regarding hydration, the barrier has become saturated in the vicinity of the rock but has undergone a very limited increase toward the centre of the section. Again, the models yield a very similar distribution of degree of saturation; CRIEPI, ICL and SNL have underestimated the increase in saturation whereas UPC and TUL have overestimated it.

5.2 Stage 2: test operation and final dismantling

5.2.1 Test operation

The number of sensors available to provide measurements for comparison with modelling results after the first dismantling reduced significantly because many instruments have been removed when a part of the barrier was excavated but also because an increasing number of sensors failed as time passed. Consequently, only a limited set of modelling results were requested for the operational phase of this stage. They correspond to the sections indicated in Figure 5-39 (temperatures), Figure 5-40 (relative humidity) and Figure 5-41 (total stresses). The power of the remaining heater #2 was also required.

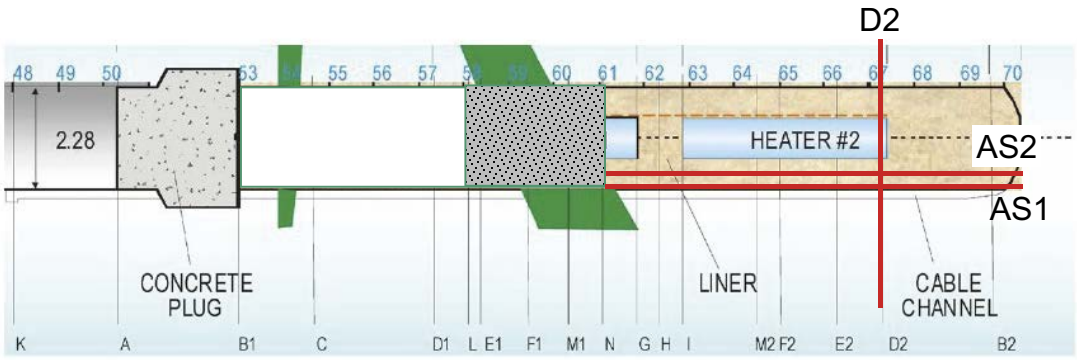

Figure 5-39. *Locations of the monitoring sections where temperature modelling results have been requested.*

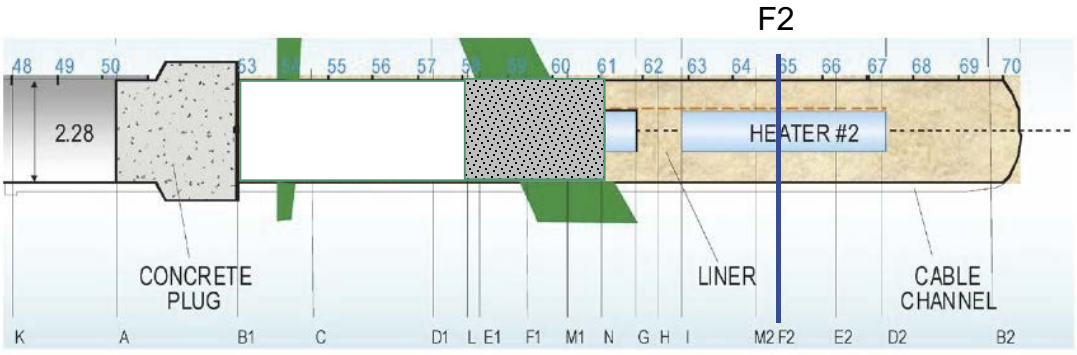

Figure 5-40. *Location of the monitoring section where relative humidity modelling results have been requested.*

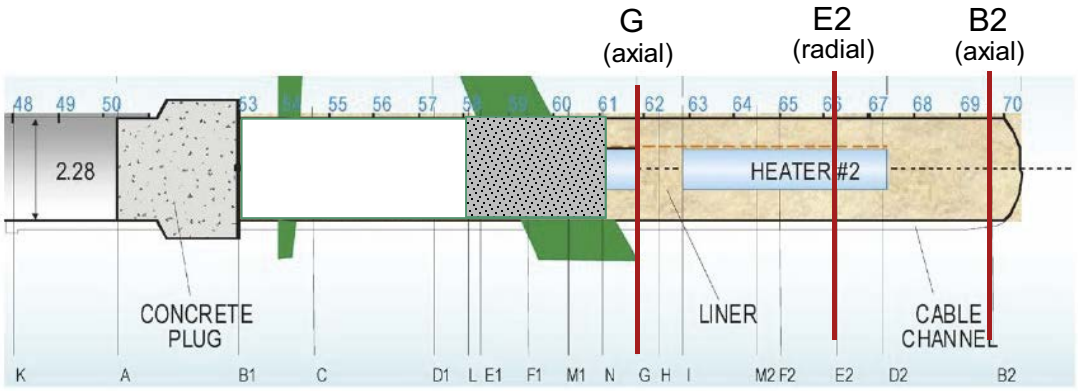

Figure 5-41. *Locations of the monitoring sections where total stresses modelling results have been requested.*

The comparison between observations and computed results for the operational phase of Stage 2 are shown in:

- Heater power (Figure 5-42)
- Distribution of temperatures (Figure 5-43 and Figure 5-44)
- Evolution of relative humidity (Figure 5-45)
- Evolution of total stresses (Figure 5-46 and Figure 5-47)

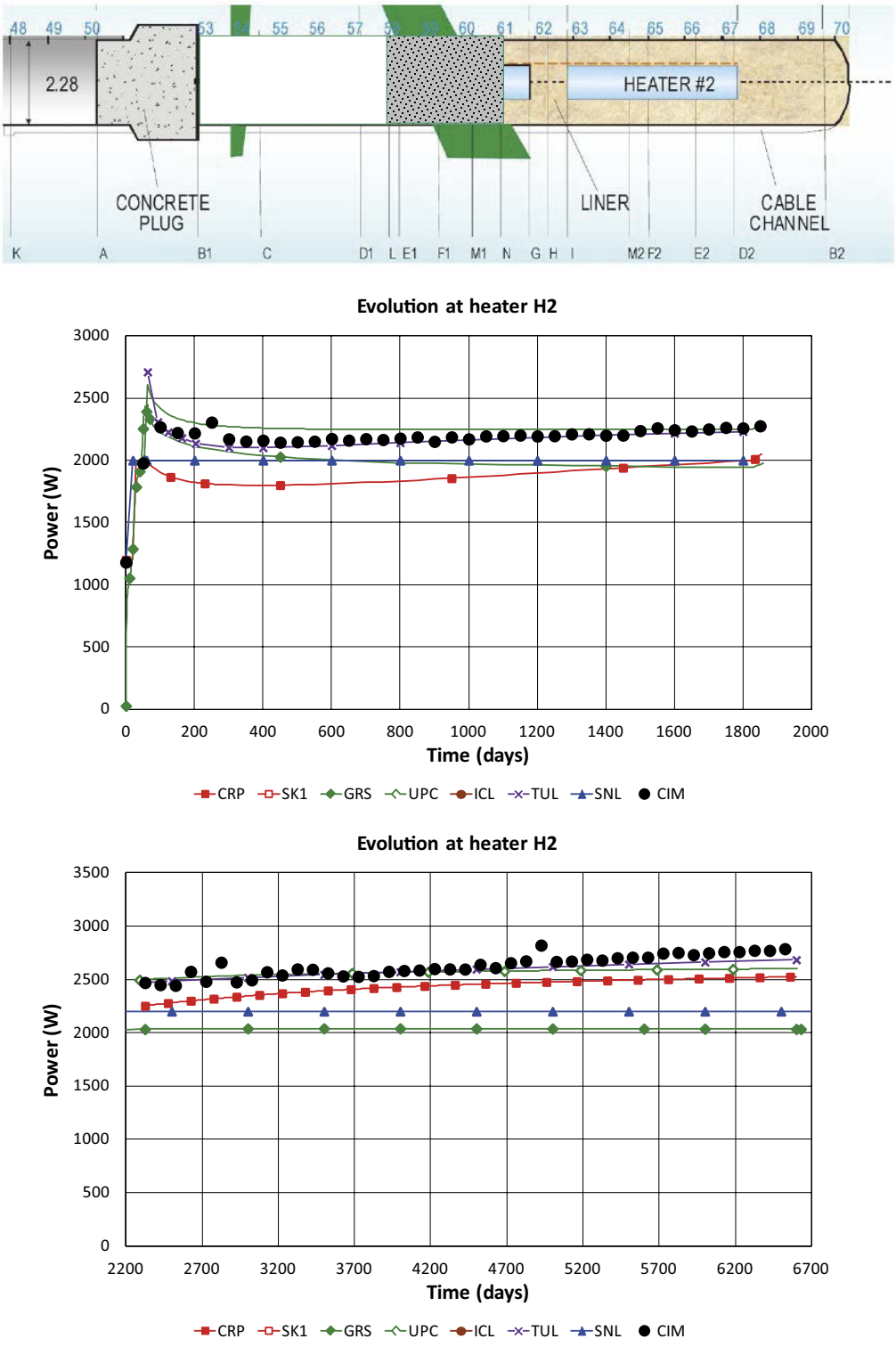

Figure 5-42. *Modelling results vs observations (CIM) up to first dismantling and after first dismantling. Evolution of heater #2 power.*

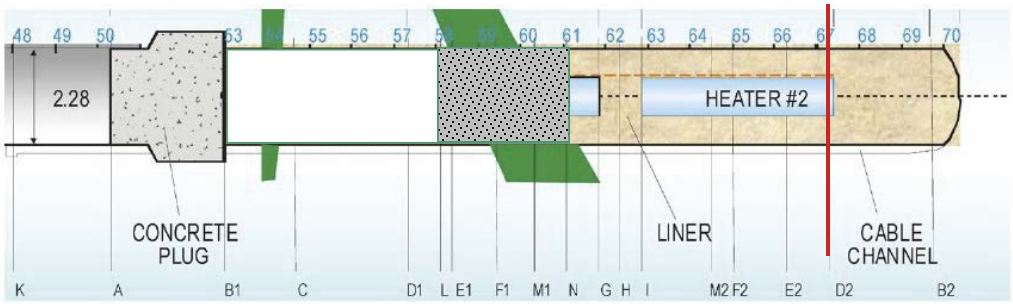

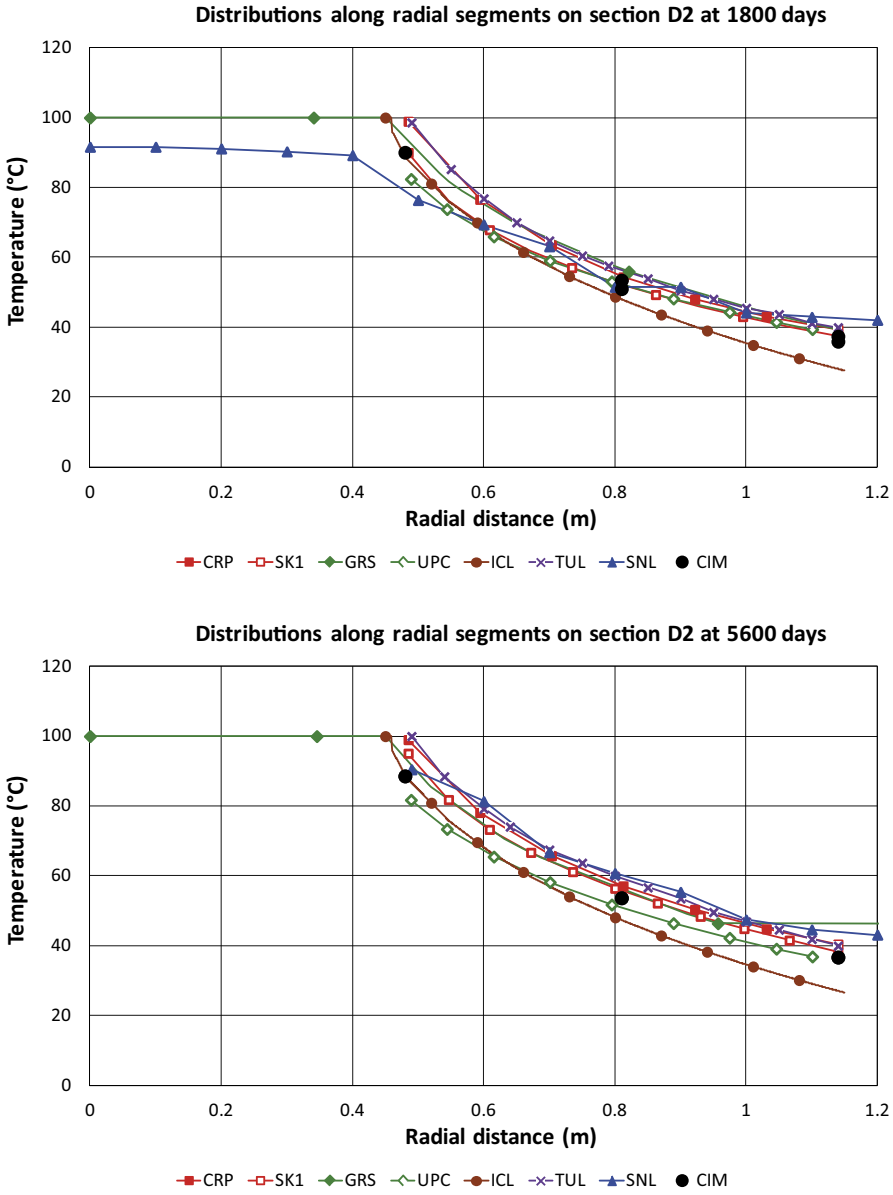

Figure 5-43. *Modelling results vs observations (CIM) at 1 800 days and 5 600. Distribution of temperatures in section D2.*

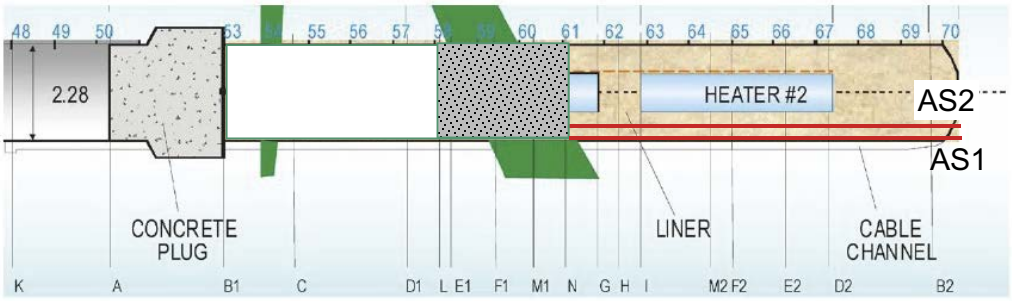

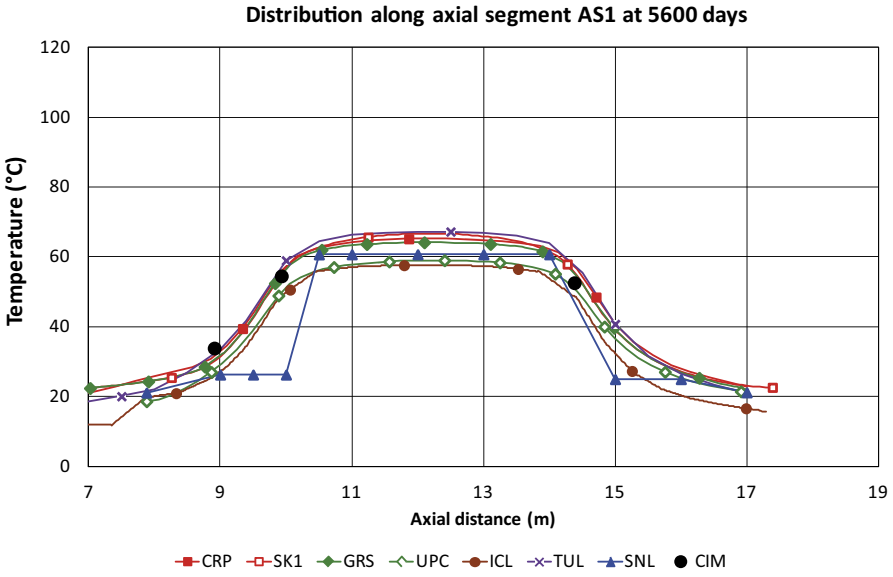

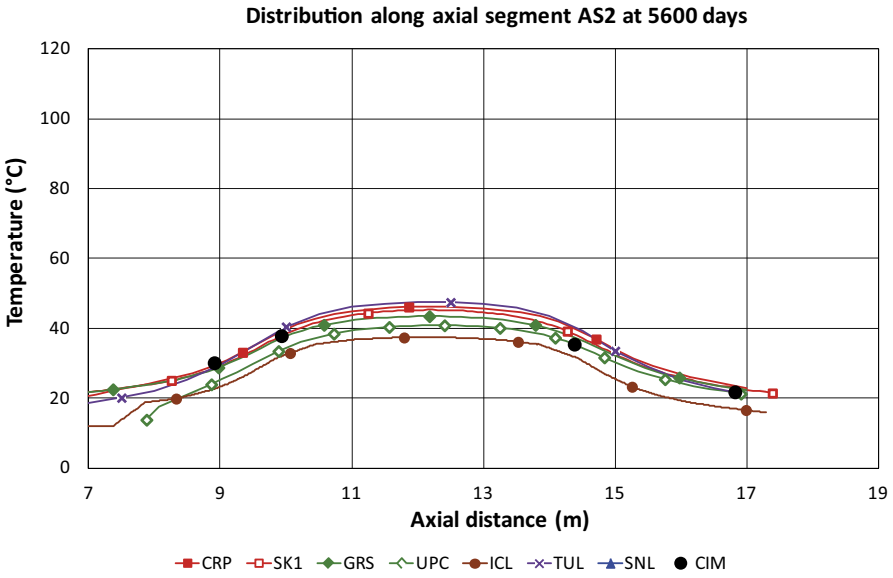

Figure 5-44. *Modelling results vs observations (CIM) at 5 600 days. Distribution of temperatures along segment AS1 (intermediate) and AS2 (close to the rock).*

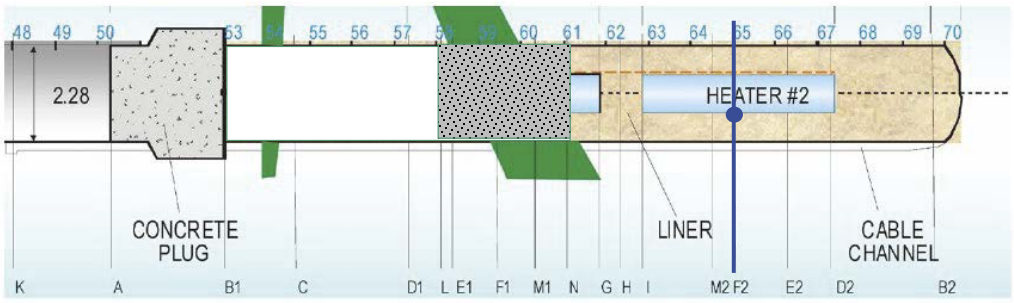

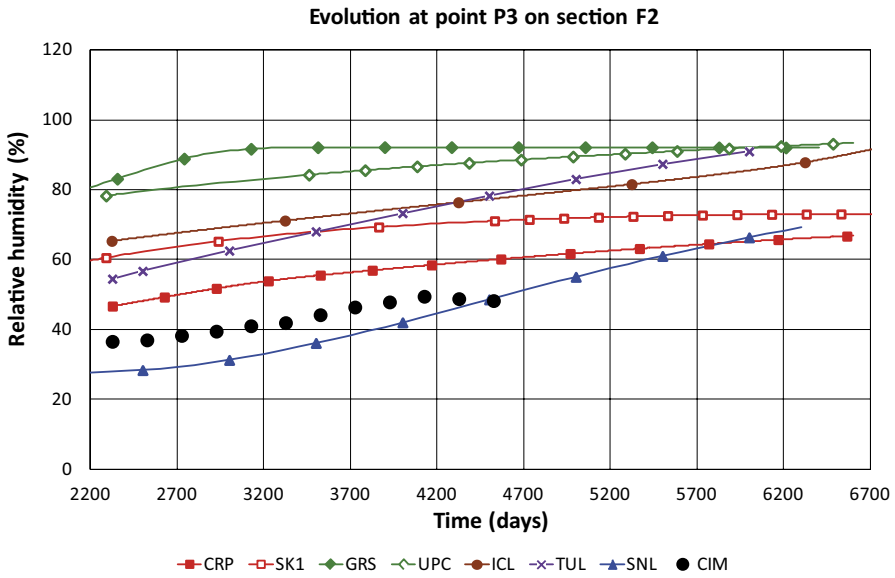

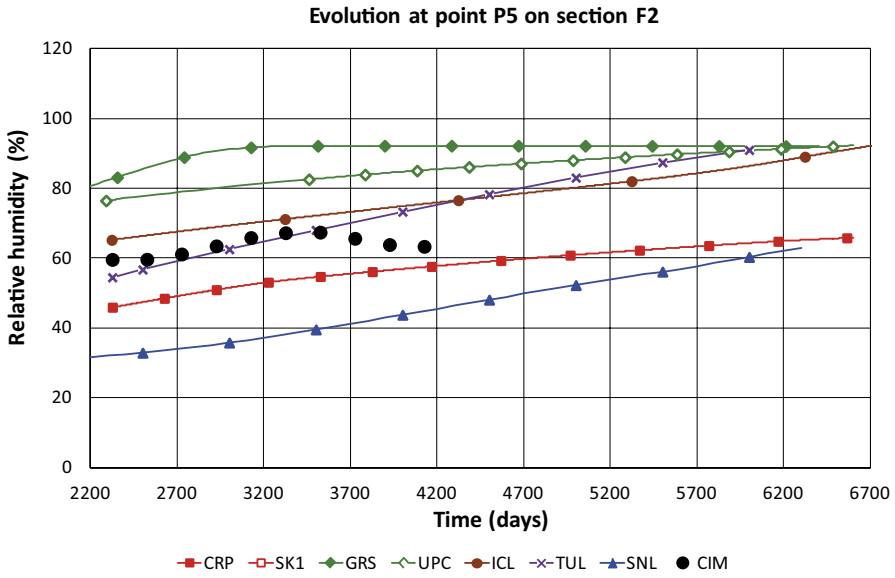

Figure 5-45. *Modelling results vs observations (CIM) after first dismantling. Evolution of relative humidity at points P3 and P5 (close to the heater) in section F2.*

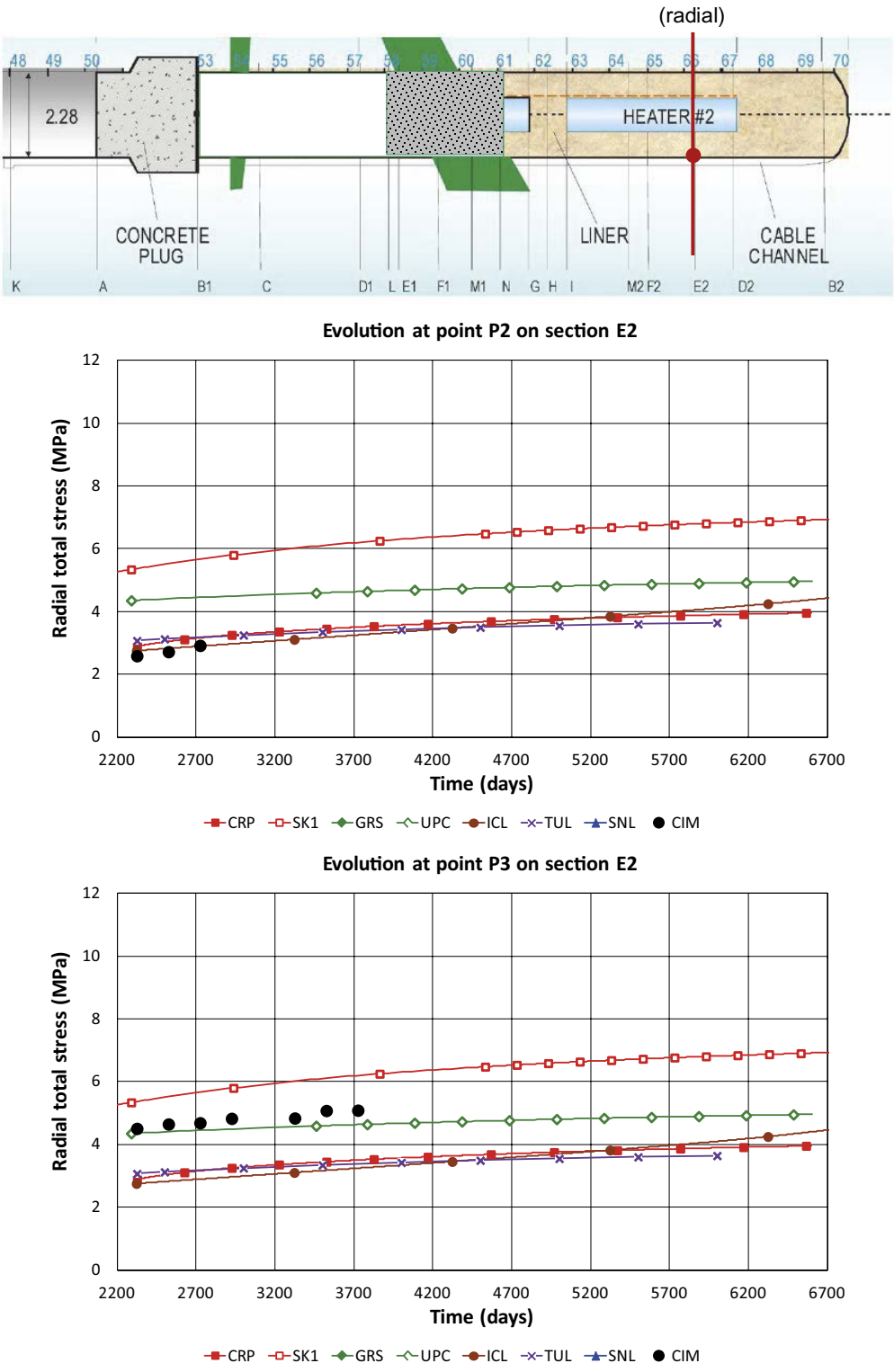

Figure 5-46. *Modelling results vs observations (CIM) after first dismantling. Evolution of radial stresses at points P2 and P3 (close to the rock) in section E2.*

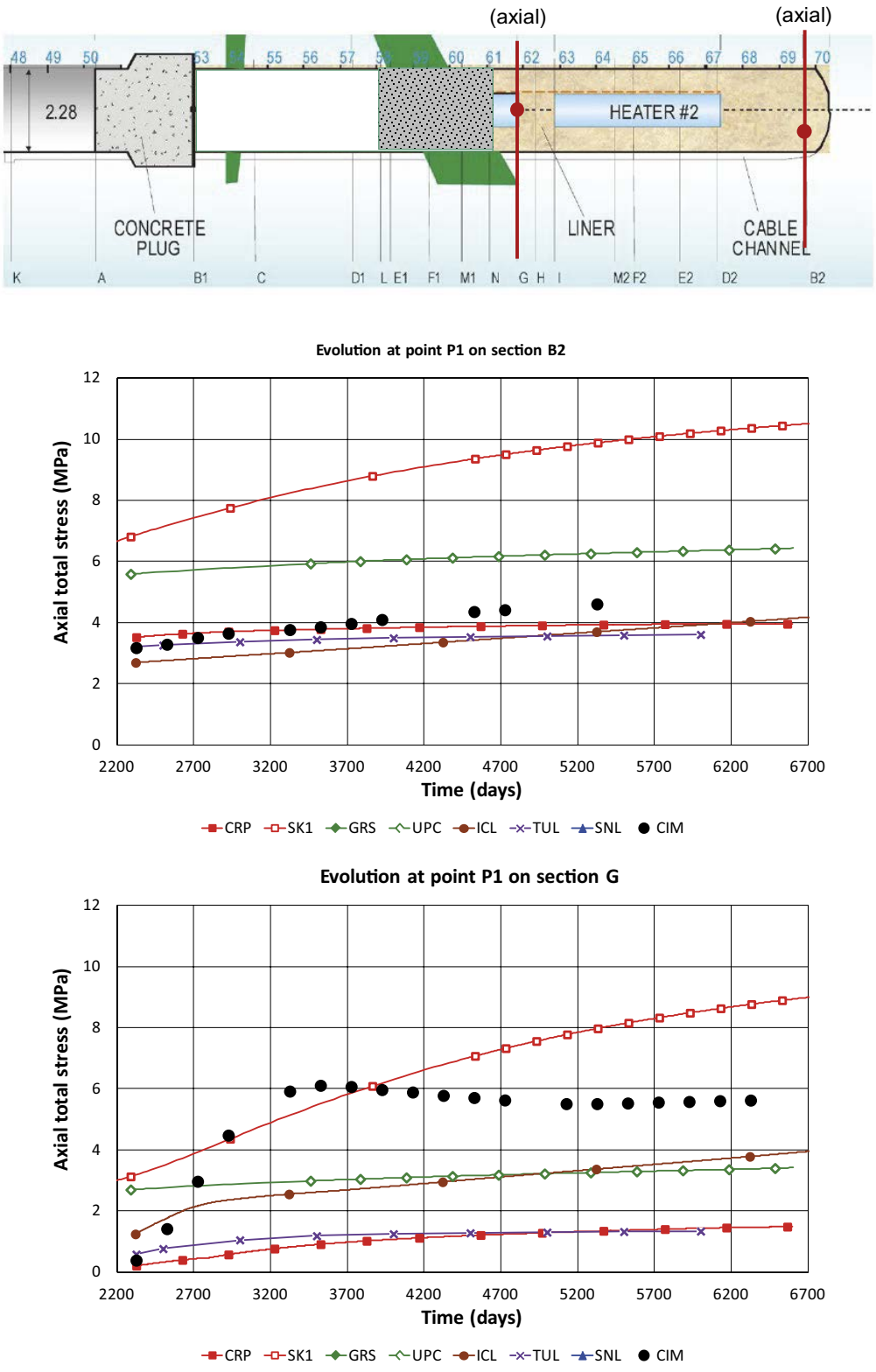

Figure 5-47. *Modelling results vs observations (CIM) after first dismantling. Evolution of axial stresses at points in sections B2 and G.*

5.2.2 Final dismantling

As in the first dismantling, dry density and mass water content were measured immediately after extracting the samples from the cross-sections shown in Figure 5-48. In this way, the state of the barrier at the end of the experiment could be determined directly. Modelling results of distributions of dry density, mass water content and degree of saturation were requested for sections 43, 49, 56 and 61 (Figure 5-48). Sections 43 and 49 correspond to bentonite zones around the heater and sections 56 and 61 involve the full section of the tunnel. It should be noted that section 61 had a low initial value of dry density because of installation constraints.

The comparison of the observed and computed distributions of dry density, mass water content and degree of saturation for sections 43, 49, 56 and 61 can be examined in Figure 5-49 to Figure 5-56. All the radial distributions have been plotted on the same graph because of the nearly axisymmetric nature of the observations.

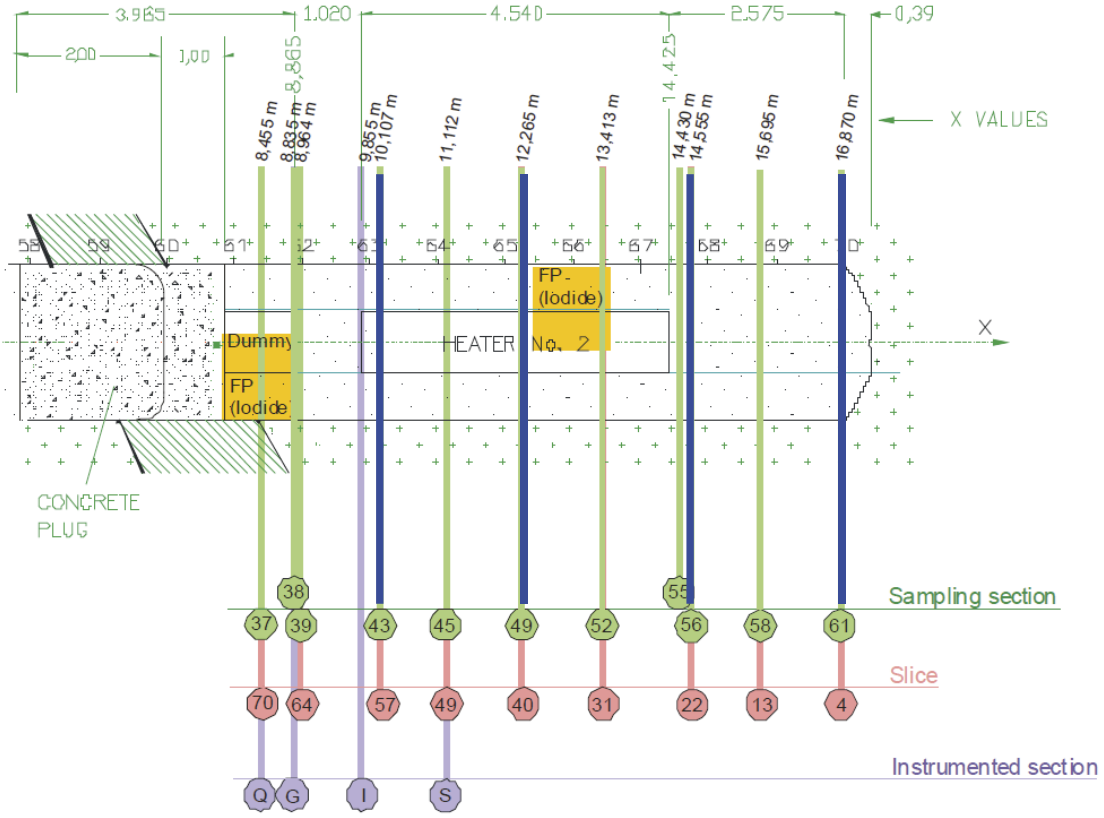

Figure 5-48. *Bentonite sections for which modelling results were requested.*

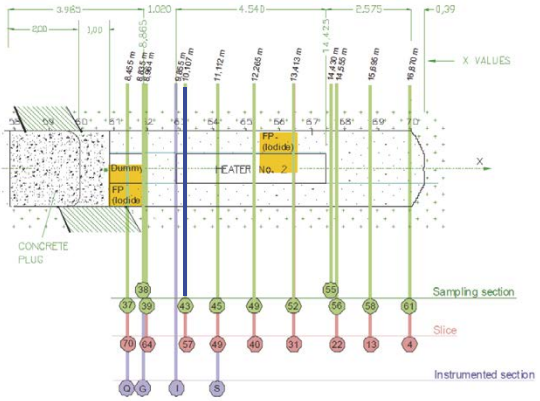

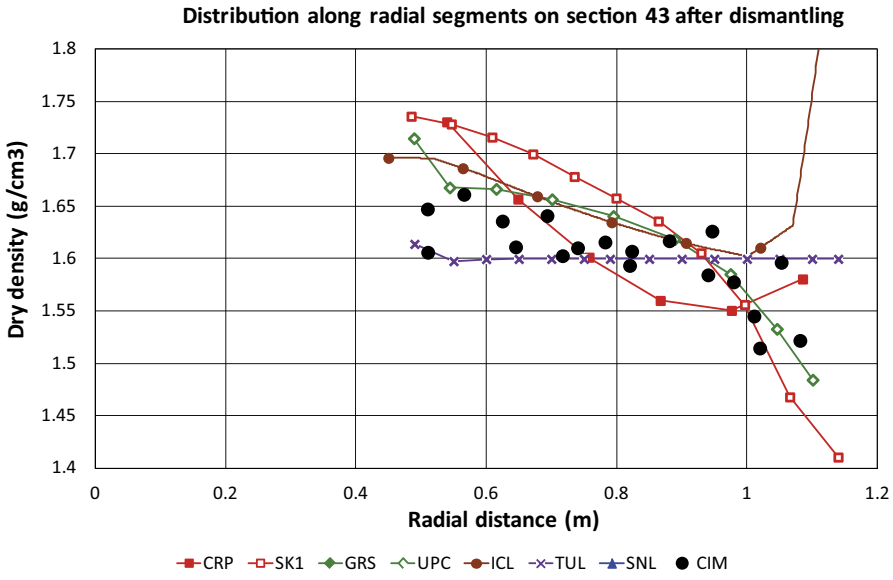

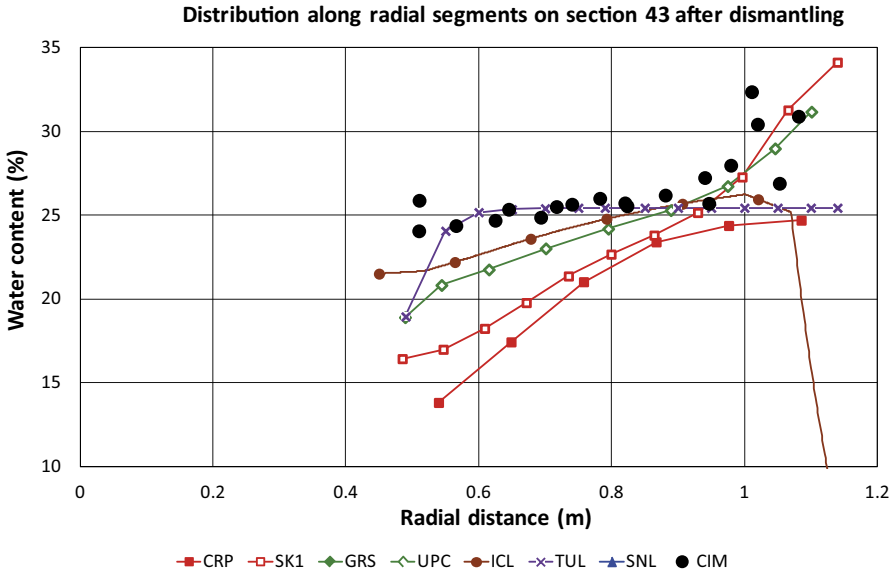

Figure 5-49. *Modelling results vs observations (CIM). Distributions of dry density and mass water content after final dismantling. Section 43.*

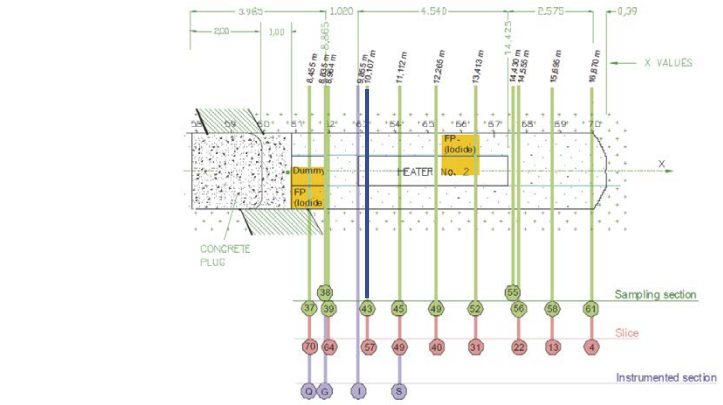

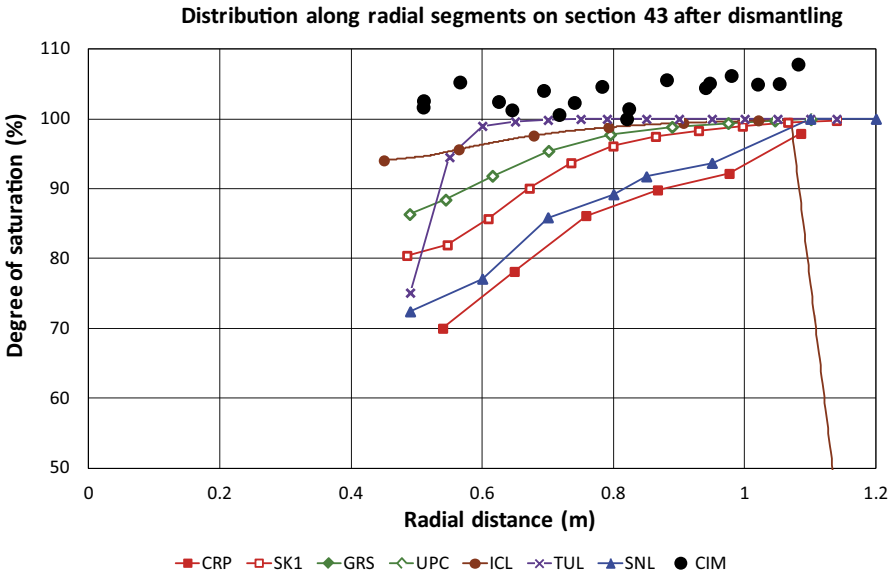

Figure 5-50. *Modelling results vs observations (CIM). Distributions of degree of saturation after final dismantling. Section 43.*

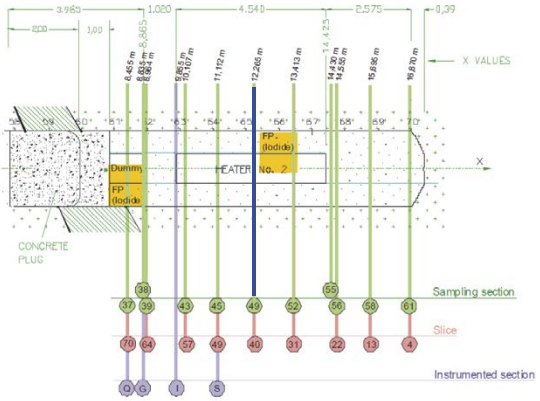

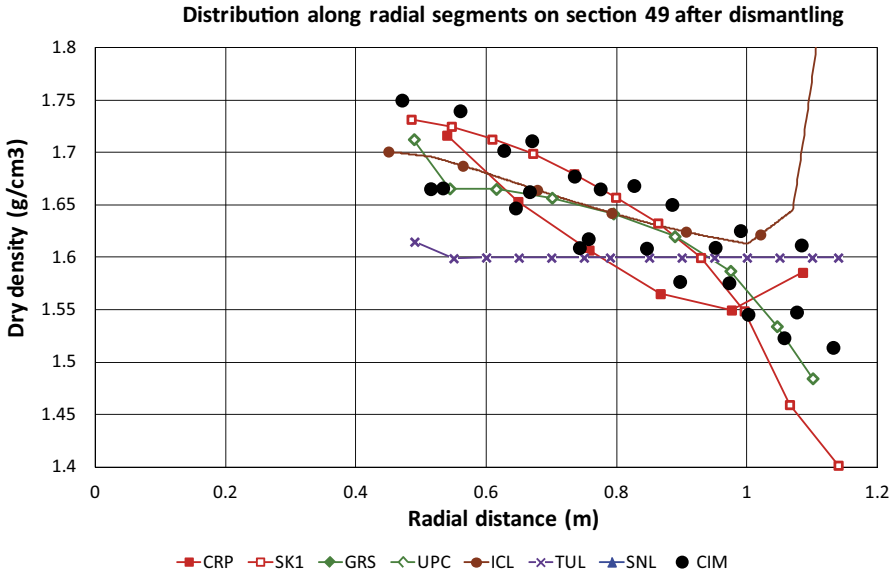

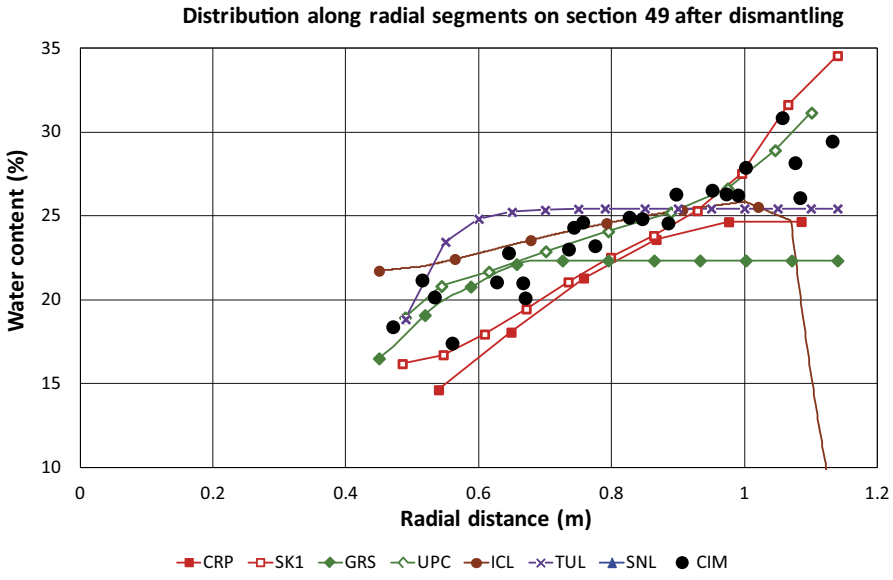

Figure 5-51. *Modelling results vs observations (CIM). Distributions of dry density and mass water content after final dismantling. Section 49.*

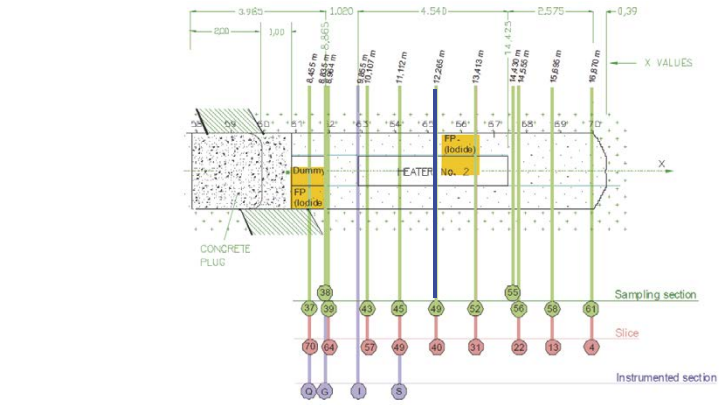

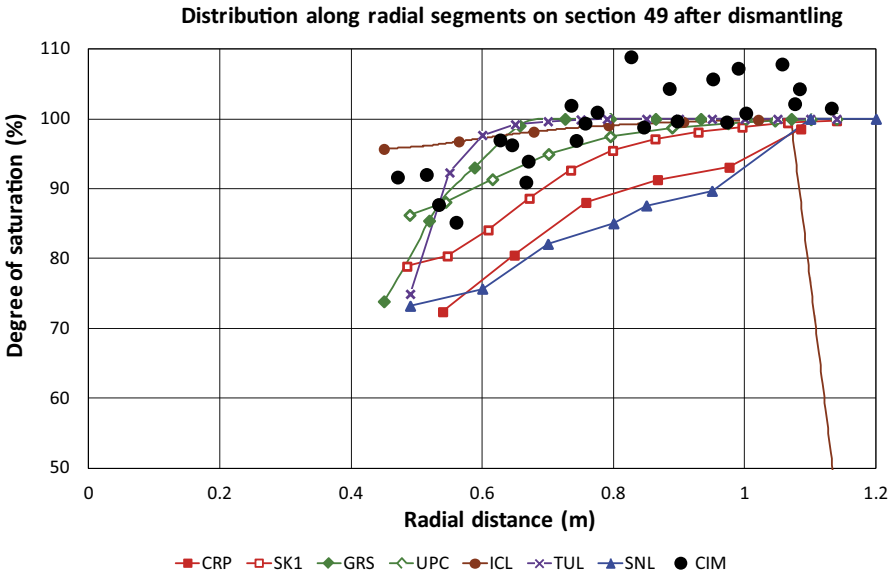

Figure 5-52. *Modelling results vs observations (CIM). Distributions of degree of saturation after final dismantling. Section 49.*

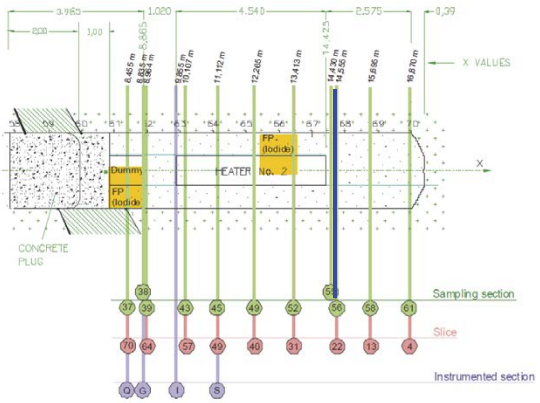

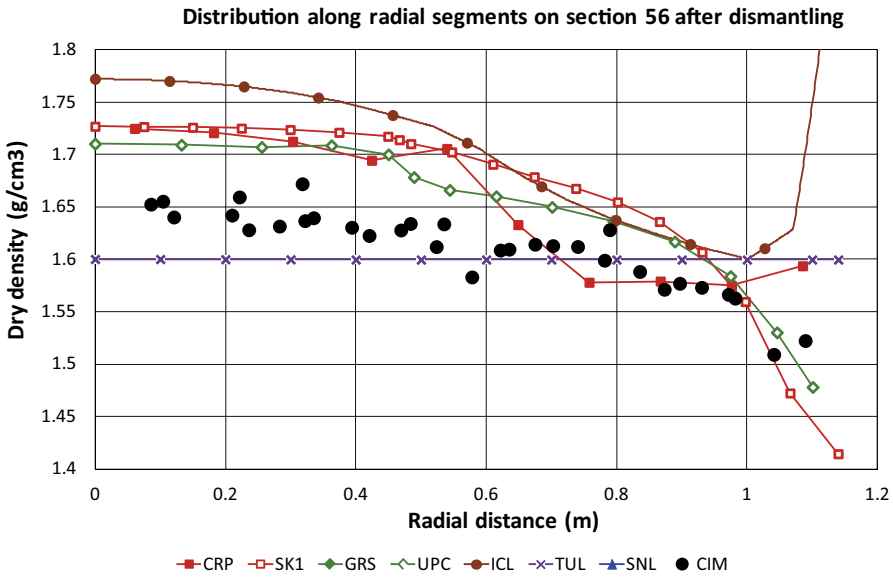

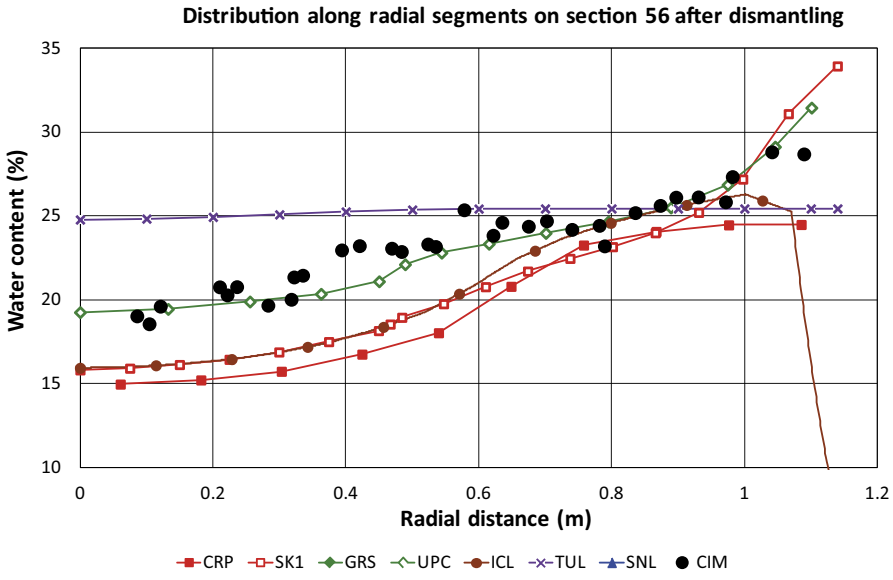

Figure 5-53. *Modelling results vs observations (CIM). Distributions of dry density and mass water content after final dismantling. Section 56.*

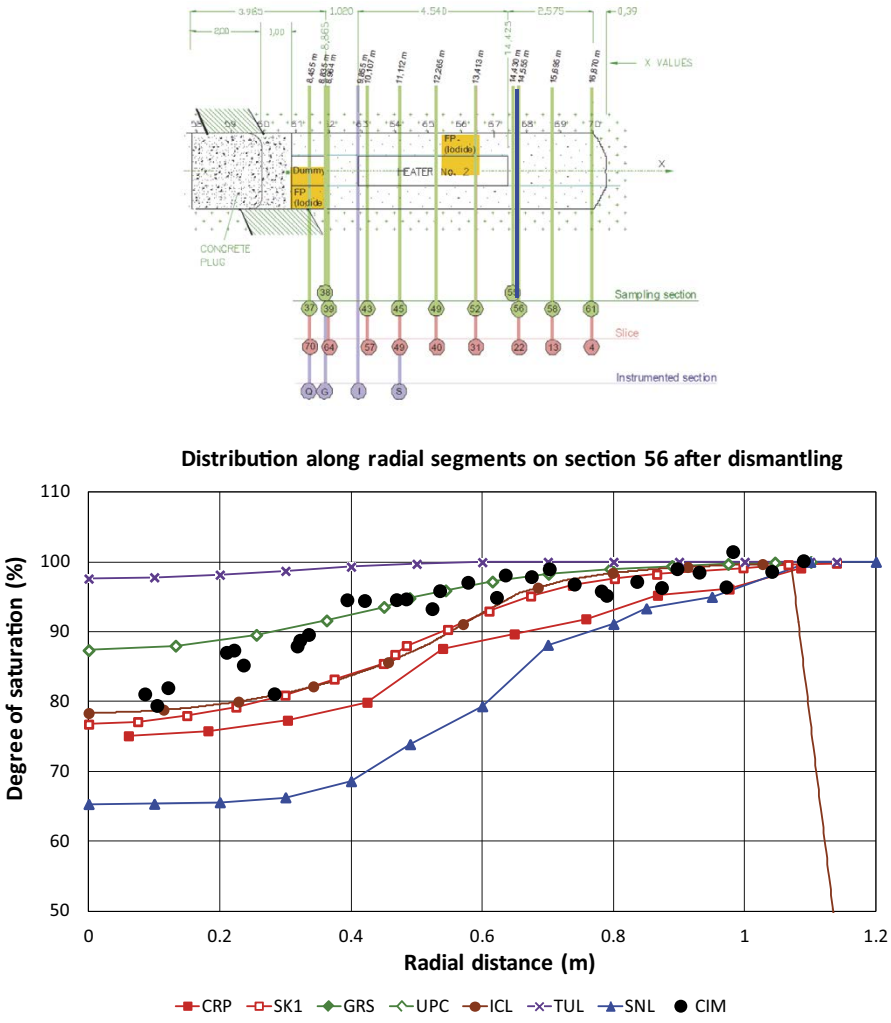

Figure 5-54. *Modelling results vs observations (CIM). Distributions of degree of saturation after final dismantling. Section 56.*

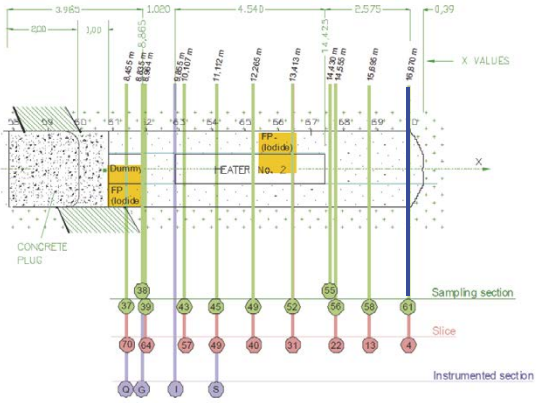

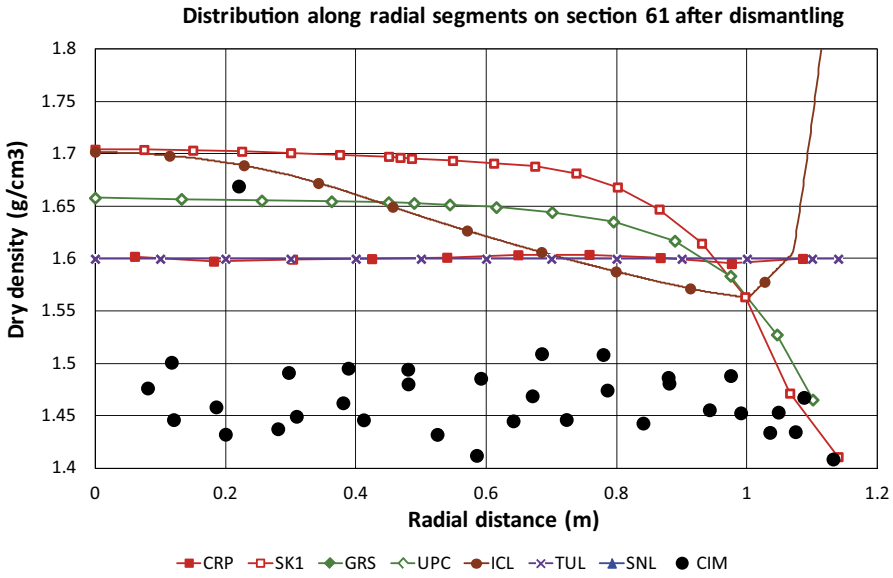

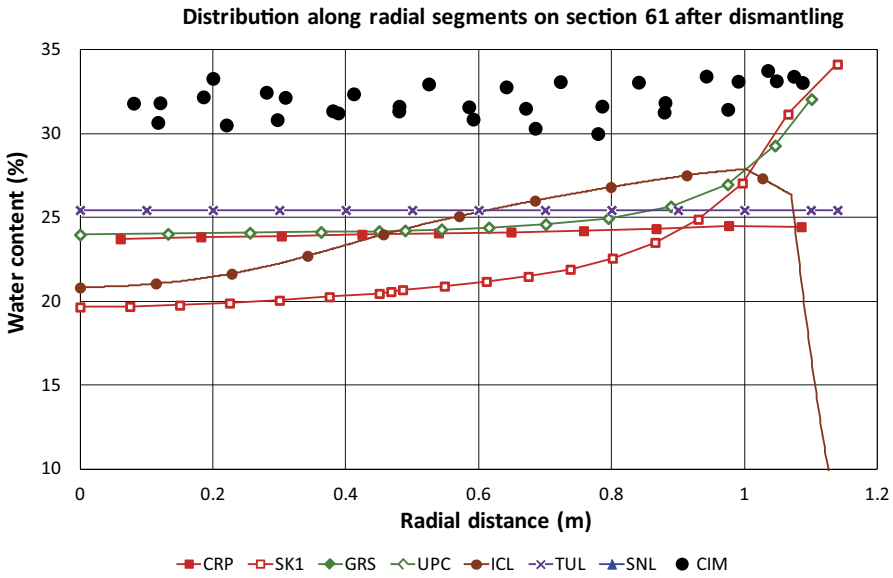

Figure 5-55. *Modelling results vs observations (CIM). Distributions of dry density and mass water content after final dismantling. Section 61.*

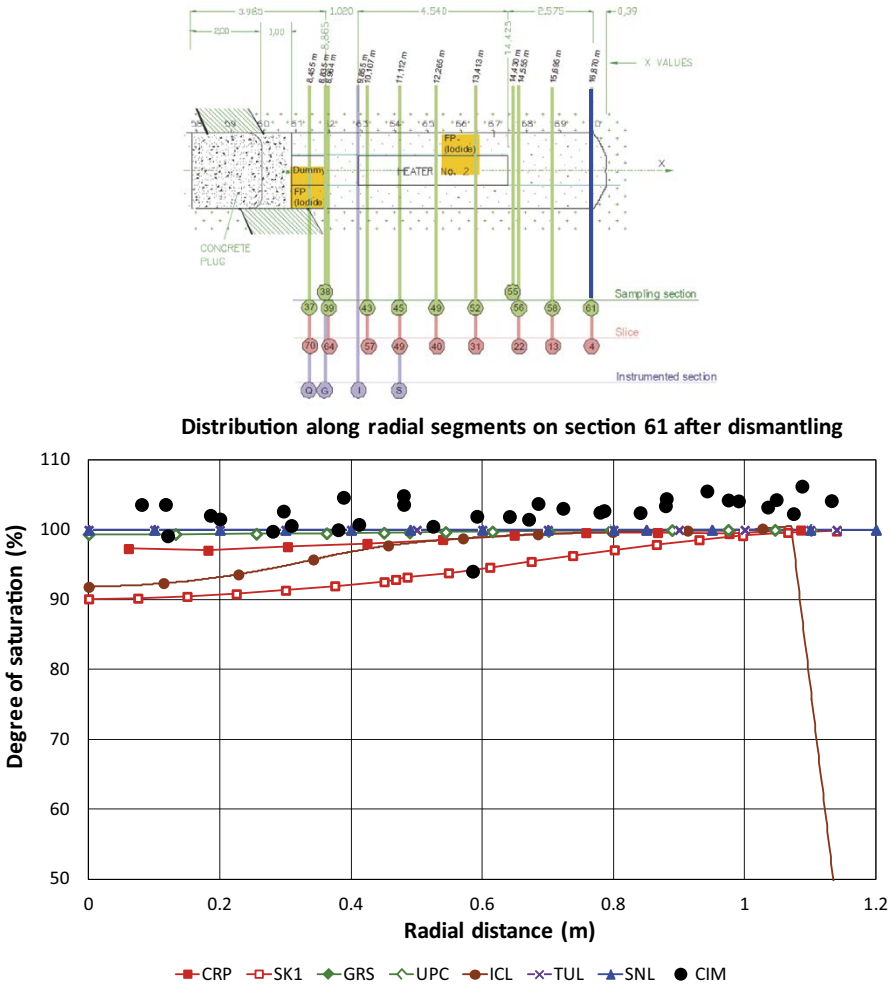

Figure 5-56. *Modelling results vs observations (CIM). Distributions of degree of saturation after final dismantling. Section 61*

5.2.3 Summary comments

The applied *heater 2 power* during Stage 2 is presented in Figure 5-42. For reference, the evolution of the power of the same heater 2 during Stage 1 is also shown in the same figure. It can be noted that there is a jump of about 10 % in the transition between the two stages to compensate for the absence of the first heater and to take into account the new configuration of the experiment. It is also noticeable that the power required to maintain the maximum temperature at 100 °C keeps increasing very gradually reflecting the progressively more saturated state of the barrier. It can also be observed that CRIEPI, TUL and UPC models provide a good agreement with the experiment. SNL apply a constant power.

The distributions of *temperatures* at days 1 800 (end of Stage 1) and 5 600 (end of Stage 2) in heater cross-section D2 are shown in Figure 5-43; temperatures are practically constant over this period. The distributions of temperatures along two longitudinal sections are displayed in Figure 5-44. The same figures demonstrate that the model results agree well with experimental observations.

The lack of sufficient working sensors makes it difficult to evaluate the reliability of the *relative humidity* monitoring data. For instance, sensors P3 and P5 in section F2, both located in equivalent locations close to the heater, provide quite different results (Figure 5-45). They also exhibit a slight increase with time until sensor failure. All model results also exhibit a progressive increase in relative humidity although at rather different rates.

Finally, data is also limited regarding the measurement of *total stresses*. The sensors monitoring total radial stresses close to the rock in section E2 (Figure 5-46) recorded a slight increase but they failed early on. Small increases in radial total stresses are also predicted by all the models. Computed final radial stress values range between 4 and 7 MPa approximately, values lower than their theoretical swelling pressures.

Figure 5-47 contains the information concerning axial stresses. The sensor in section B2 also failed but at a later time and showed a similar increase in stresses as the radial stress sensors. CRIEPI, ICL and TUL show good agreement with observations (including the gradual rise of stress with time) while SKB-CT and UPC overestimate the observations reaching values close to their theoretical swelling pressures. It should be noted that the stress readings of this sensor may be affected to some degree by the low density pf the barrier at the end of the tunnel. The axial stress sensor in section G was installed after the first dismantling, against the new shotcrete plug. The evolution of the measurements (Figure 5-47) illustrates the progressive development of swelling stresses until reaching an approximately constant value of 6 MPa, the highest stress recorded in the experiment. Models predict much lower values except SKB-CT that reaches a swelling pressure of about 9 MPa although this value includes the computed axial stress at the time when the inner plug where installed (about 3 MPa).

The distributions (observed and computed) of dry density, mass water content and degree of saturation measured after *final dismantling* are collected in Figure 5-49 to Figure 5-52 for two heater sections (43 and 49) whereas Figure 5-53 and Figure 5-54 contain the distributions for the non-heater section 56. The information regarding the low density section 61 is presented in Figure 5-55 and Figure 5-56.

The dismantling data shows that the heater sections are fully saturated (section 43) or nearly saturated (section 49). In spite of this, the distribution of dry density remains clearly non-homogenous with a significant gradient from the low values close to the rock to the high values in the vicinity of the heater. It can also be observed that most models underestimate the degree of saturation; ICL and TUL, however, predict a barrier saturation quite close to the observed. Again, the nearly constant water content values in the outer barrier zone of GRS and TUL do not correspond to the observed patterns. Regarding dry density, the computed distributions generally correspond well to the measured one apart from the constant distribution reported by TUL.

The outer part of the full non-heater section 56 is also fully saturated but the central part of the barrier is still unsaturated although with degree of saturation equal or higher than 80 %. A similar pattern is obtained by the different models although they exhibit quite a range of results. The distribution of dry density in this section is rather uniform except in the region close to the rock; the models (except TUL) tend to exhibit a much larger non-homogeneity across the section. The final dismantling of section 61 revealed that the barrier is fully saturated at that location and exhibits a homogenous dry density. Since no analyses incorporating the different initial dry density in this zone have been performed, comparisons with the modelling results are not relevant.

5.3 Evolution of the barrier between first and final dismantling

The fact that the FEBEX experiment involved two dismantling operations provides the opportunity to check what is the evolution of the state of the barrier and to examine how the models perform in this regard. It is of interest to note that, at the final dismantling, the barrier is saturated or close to saturation whereas in the first dismantling most of the bentonite was still unsaturated.

Of course, it is not feasible to compare the results of the same section. However, it has been observed that the behaviour of the test was quite uniform along the length of the experiment. In that case, there is the possibility of comparing sections whose location is approximately symmetric with respect to the centre of the experiment. Thus, the comparison of sections 31, 27 and 15 (first dismantling) with sections 43, 49 and 56 (final dismantling) may provide relevant information. The pairs 31/43 and 27/49 correspond to heater sections whereas the pair 27/49 refer to non-heater sections.

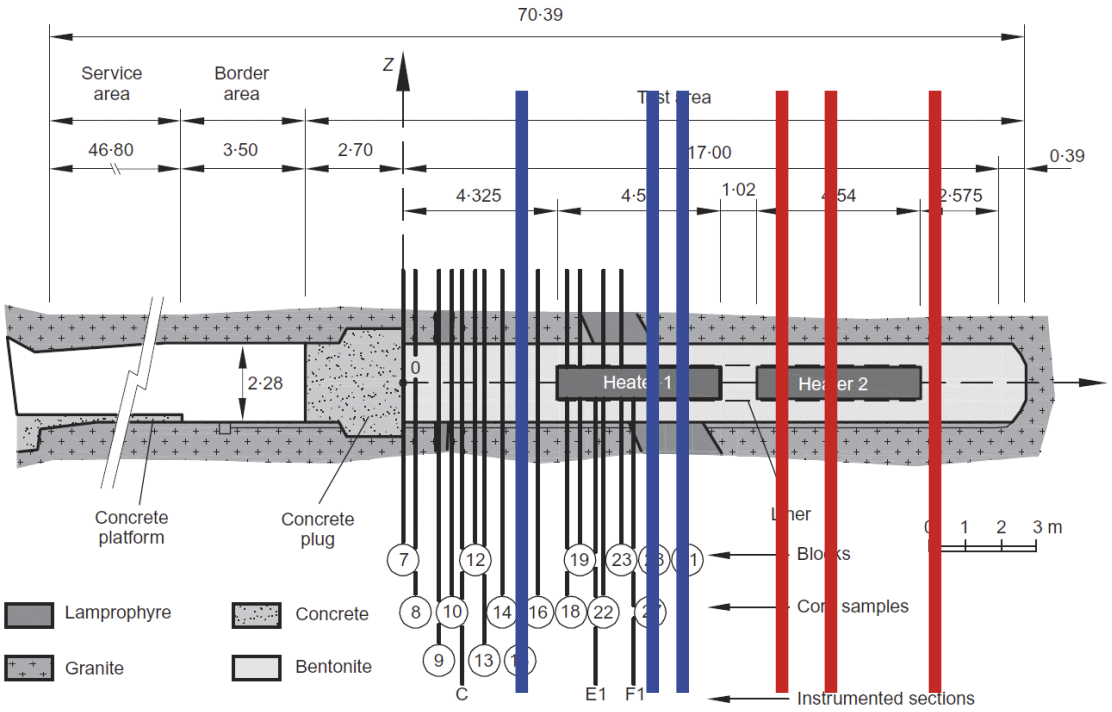

Figure 5-57. *Sections for comparing the state of the barrier at first and final dismantling.*

The observed distributions of dry density and degree of saturation at first dismantling and at final dismantling are plotted in Figure 5-58 to Figure 5-60 for the three sets of two sections. A clear pattern emerges. The barrier has hydrated very significantly between the two dismantling reaching a state either saturated or very close to saturation (i.e. degree of saturation above 90 %). Only in the full section 56 the central part of the barrier has not reached a quasi-saturated state but the degree of saturation is still above 80 %. In contrast, the distributions of dry density have barely changed between the two dismantlings. While there was a major dry density redistribution some time during the first five years of the experiment, it appears that this early dry density variation remained frozen in the subsequent stages of the test. As a result, the barrier exhibits a non-homogenous final state with a lower density close to the rock and a higher density close to the heater.

The corresponding plots of the model results are presented in Figure 5-61 to Figure 5-63 (CRIEPI), Figure 5-64 to Figure 5-66 (ICL), Figure 5-67 to Figure 5-69 (SKB-CT), Figure 5-70 to Figure 5-72 (TUL) and Figure 5-73 to Figure 5-75 (UPC). Only the models involving THM analyses can be considered here.

In the case of CRIEPI, there is practically no change in computed dry density between the two dismantling events for the heater sections (Figure 5-61 and Figure 5-62), in agreement with observations. This observation, however, should be set in the context of a limited increase in degree of saturation that leaves the final state of the section still far from full saturation. As a matter of fact, CRIEPI, very properly, continued the analysis of Stage 1 for 100 years more, achieving in this way a saturated stable state (Annex C). It was found that in the heater sections, full saturation resulted in a much more uniform dry density distribution (see Figure 4-5). This result may be related to the use of an elastic plus swelling term model but it is difficult to confirm as no other team performed a long-term calculation. In the no-heater section, there is an increase of dry density in the centre of the barrier after first dismantling that it is difficult to explain fully as it involves an increase of the average dry density (Figure 5-63). It may perhaps be related to the fact that those two sections are not at precisely the same distance with respect to the heater.

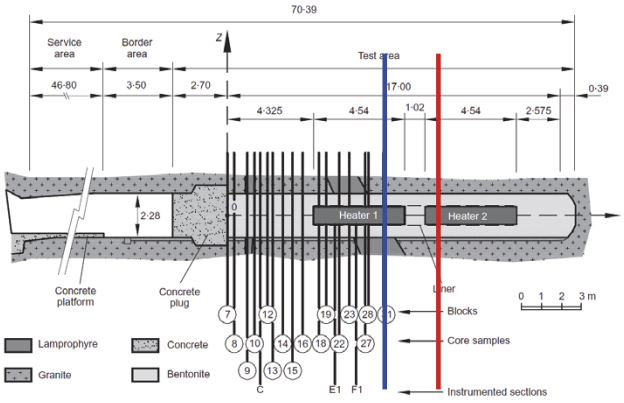

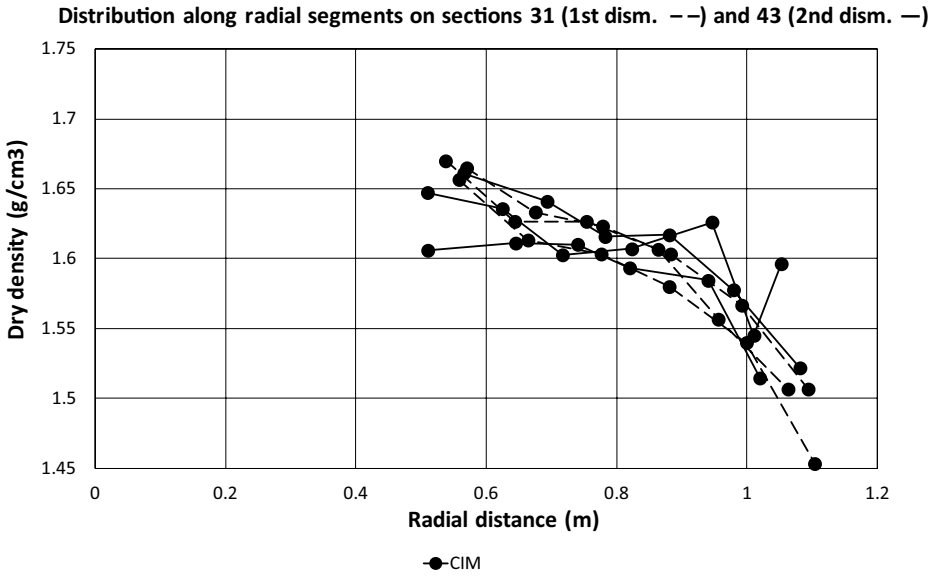

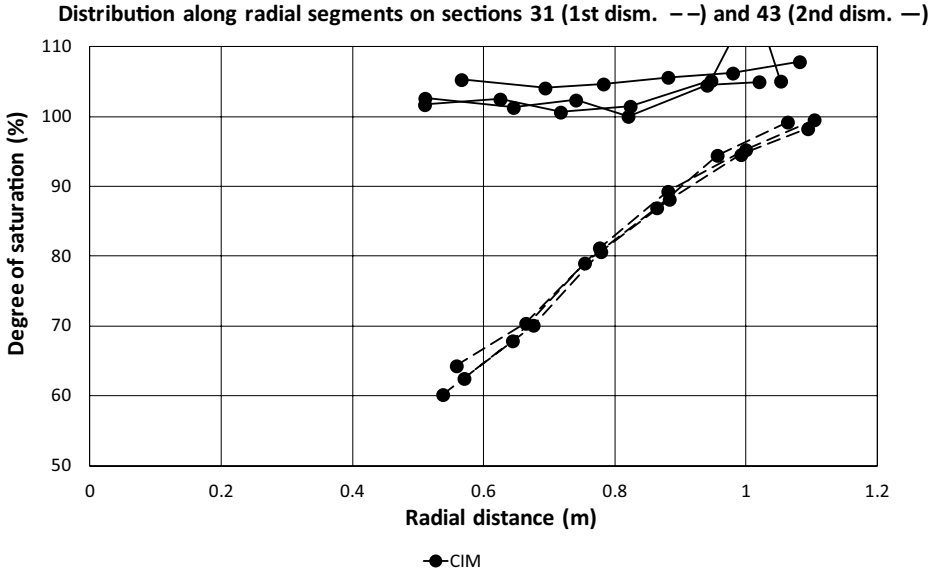

Figure 5-58. *Comparison of observed dry density and degree of saturation for sections 31 (dashed line, first dismantling) and 43 (continuous line, final dismantling).*

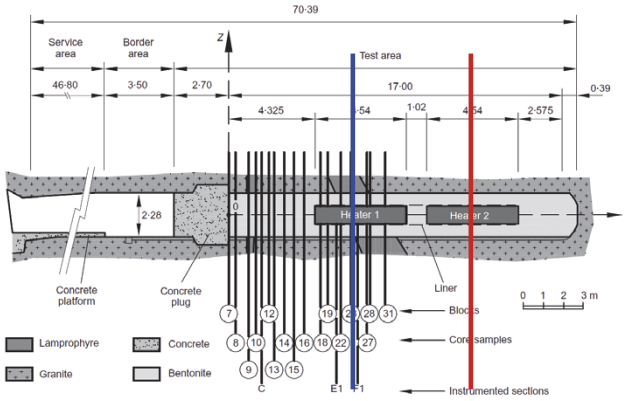

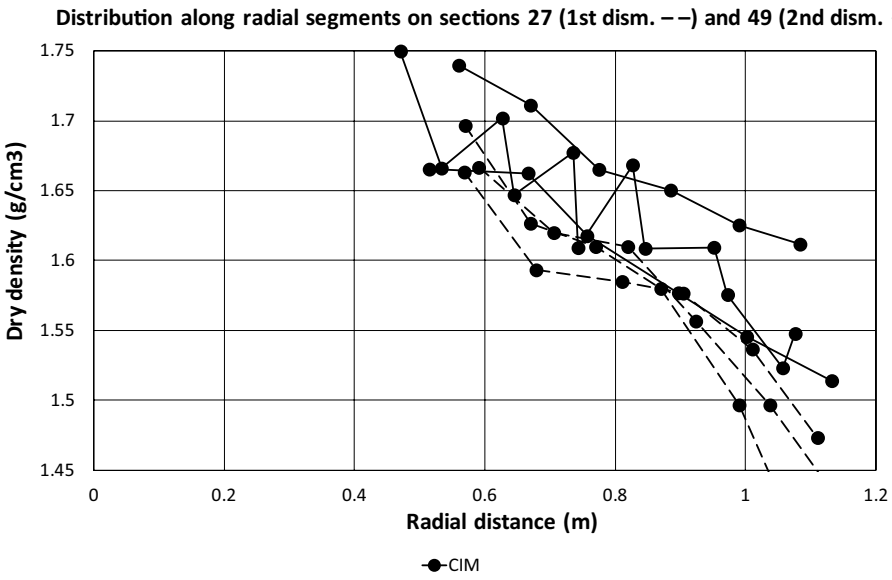

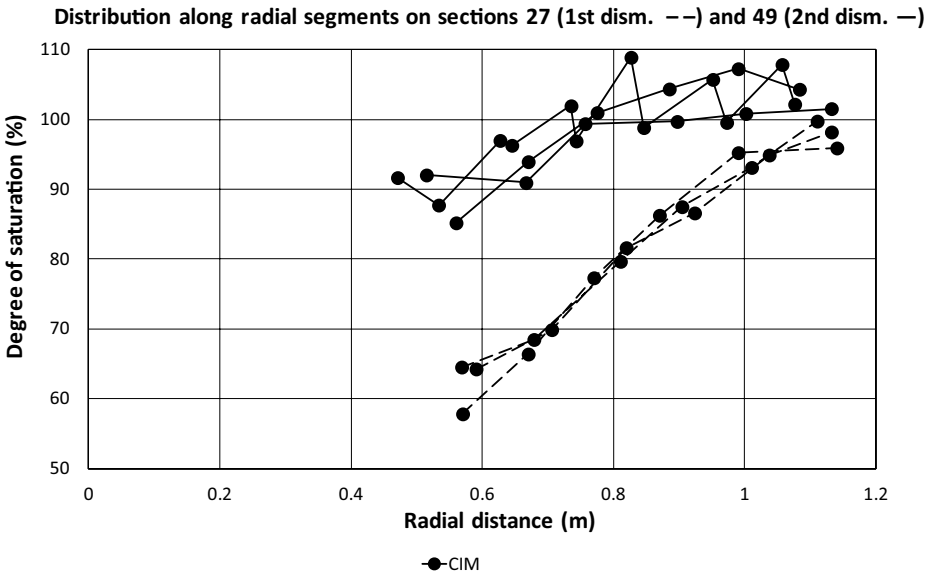

Figure 5-59. *Comparison of observed dry density and degree of saturation for sections 27 (dashed line, first dismantling) and 49 (continuous line, final dismantling).*

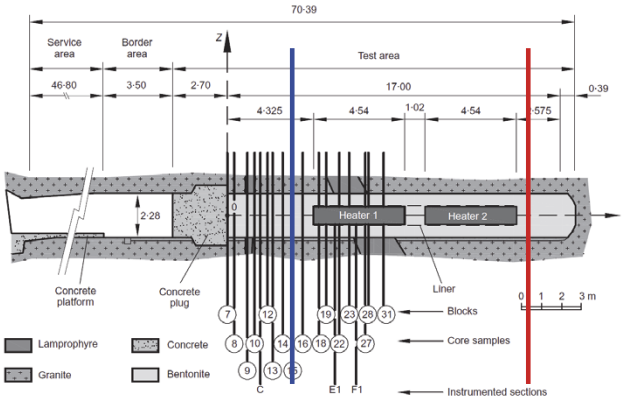

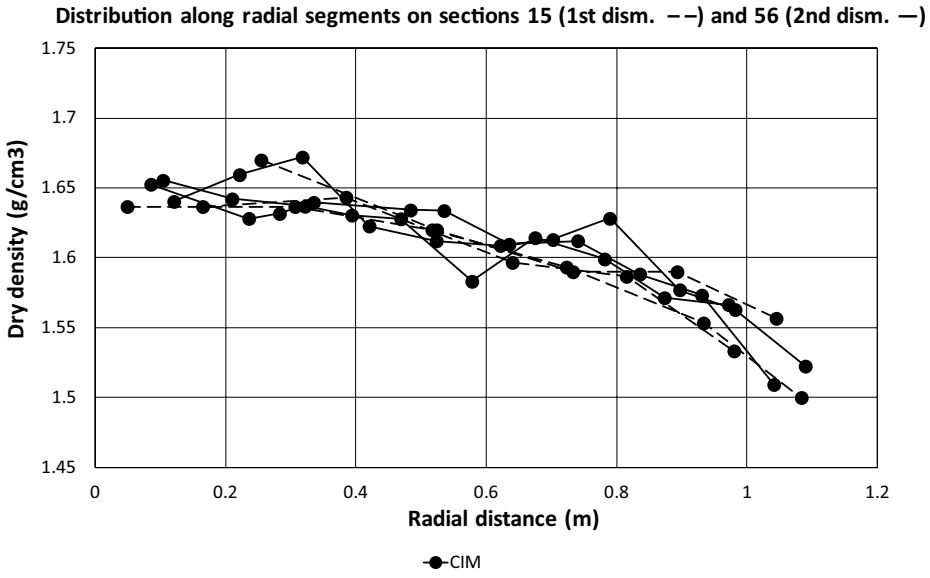

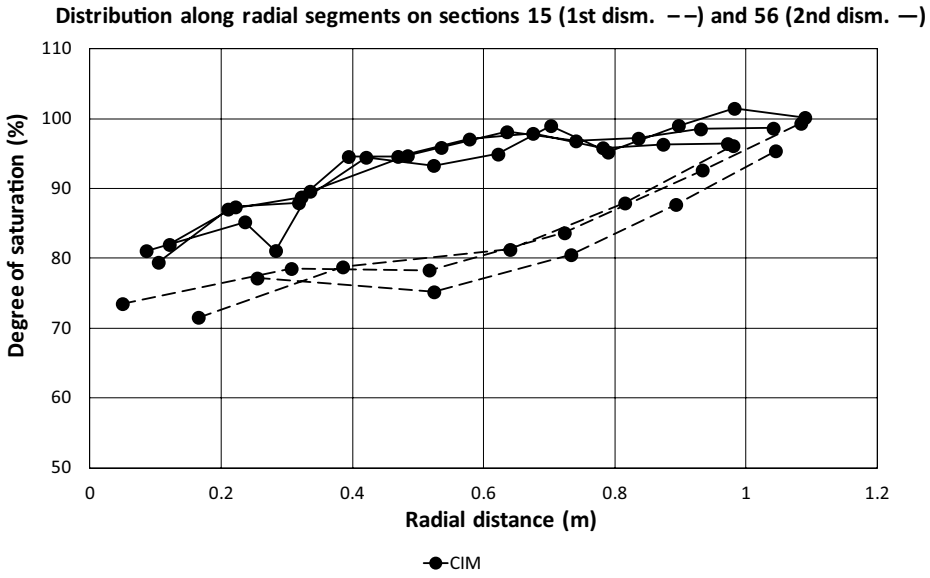

Figure 5-60. *Comparison of observed dry density and degree of saturation for sections 15 (dashed line, first dismantling) and 56 (continuous line, final dismantling).*

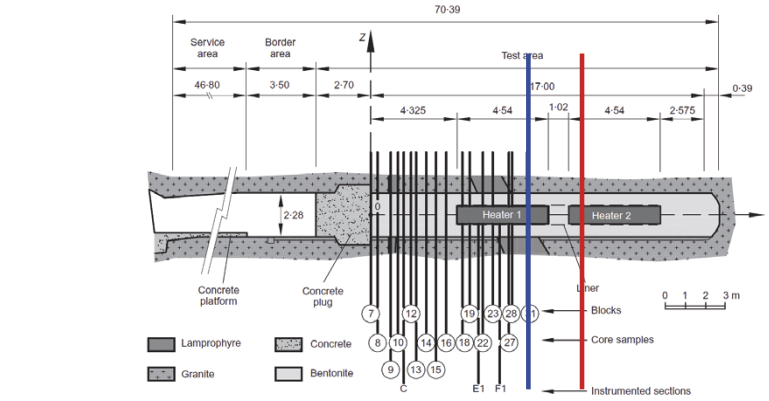

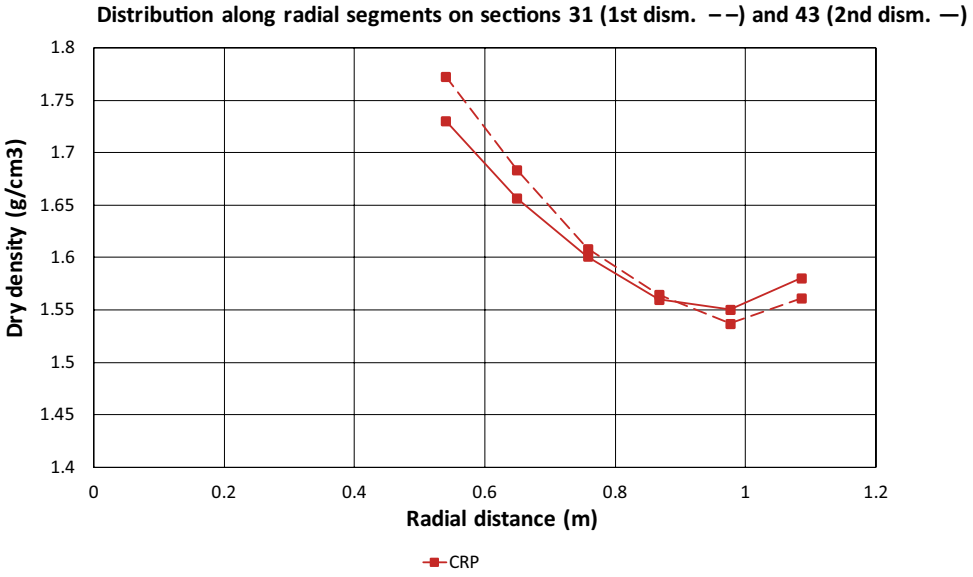

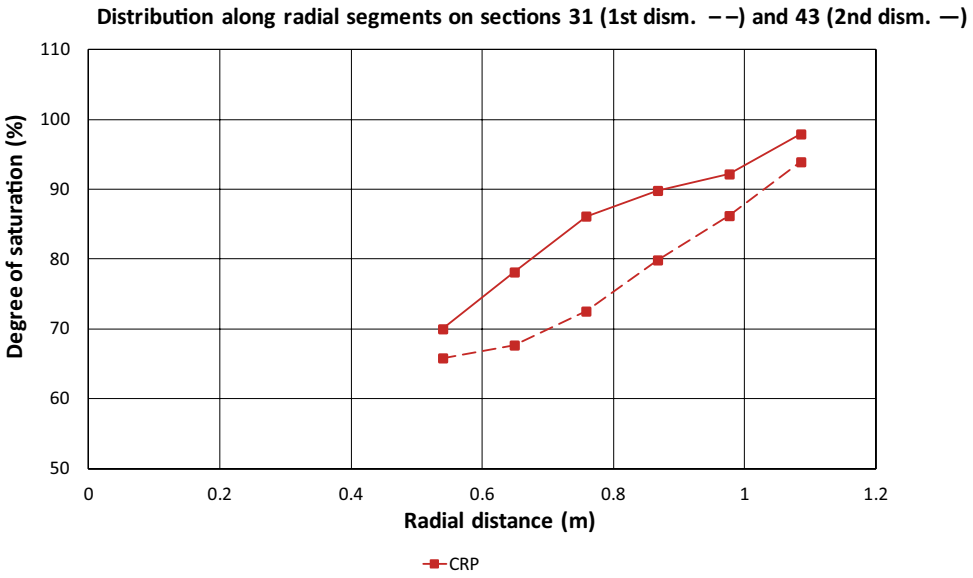

Figure 5-61. *Comparison of computed dry density and degree of saturation for sections 31 (first dismantling) and 43 (final dismantling). CRIEPI analysis.*

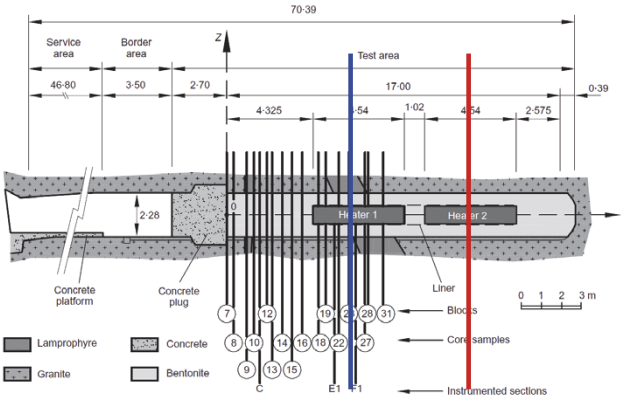

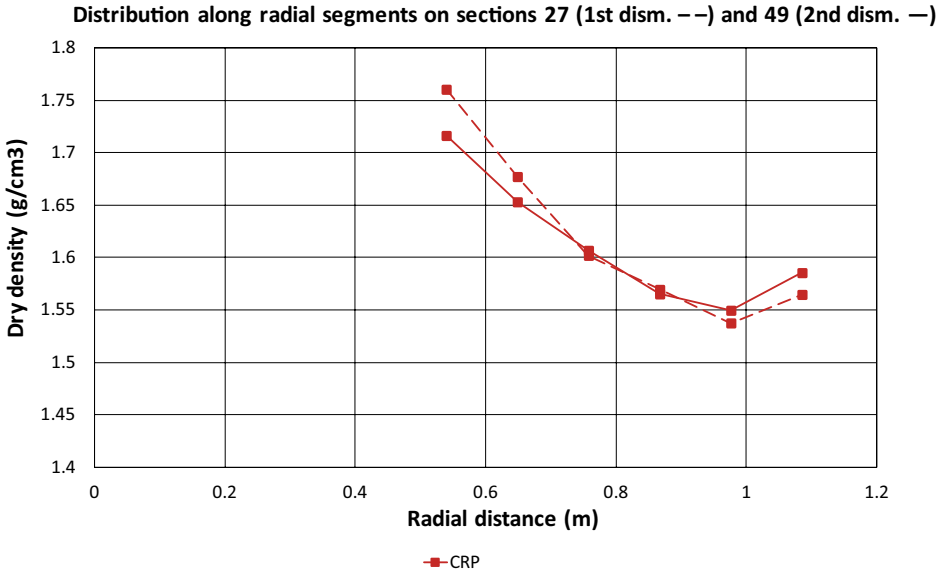

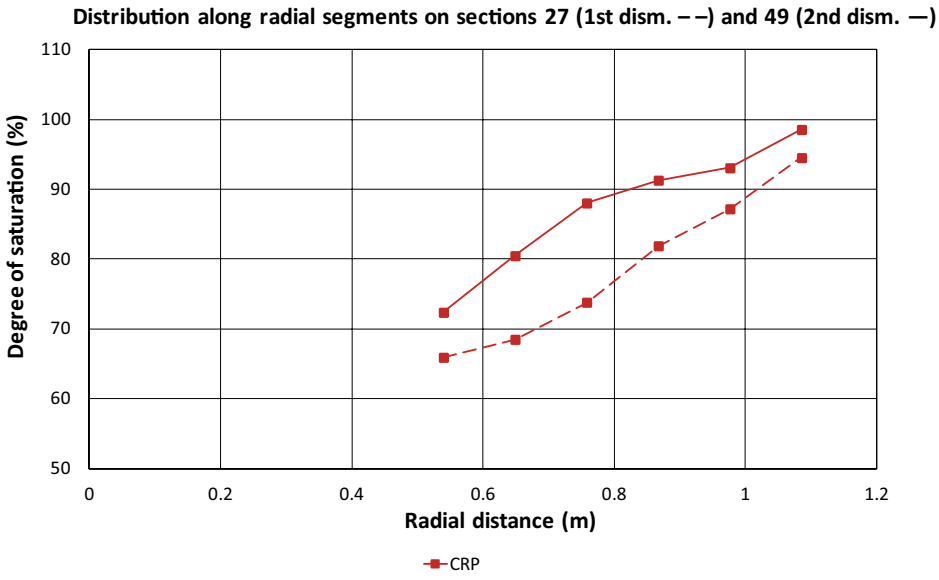

Figure 5-62. *Comparison of computed dry density and degree of saturation for sections 27 (first dismantling) and 49 (final dismantling). CRIEPI analysis.*

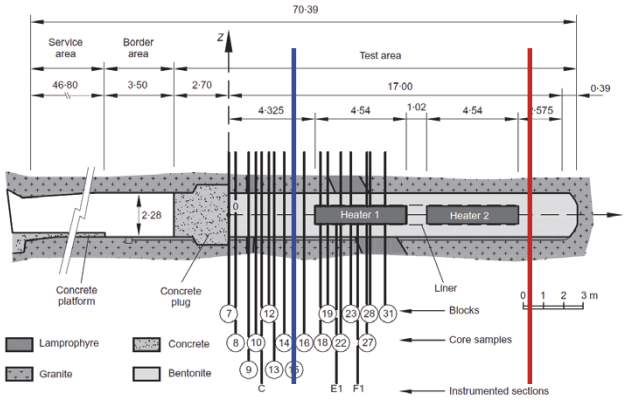

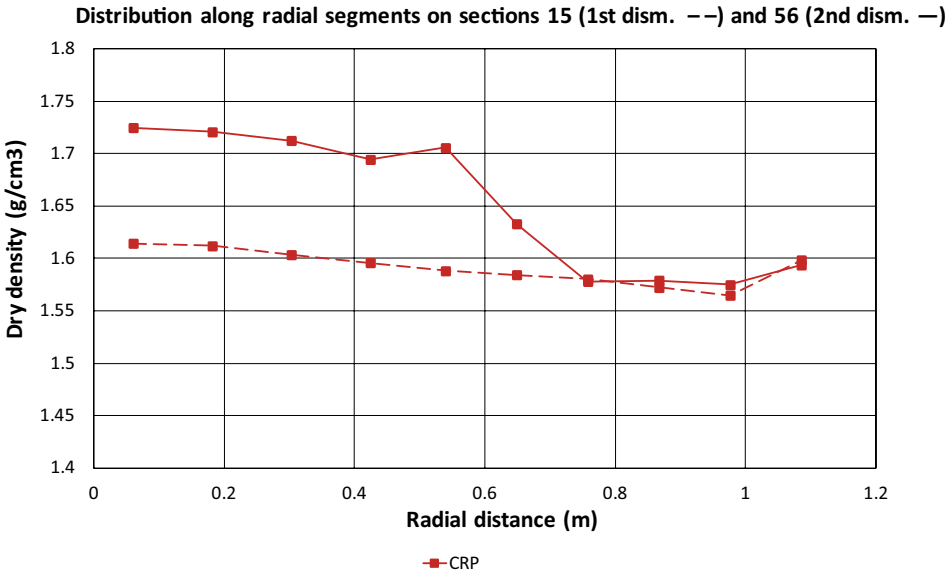

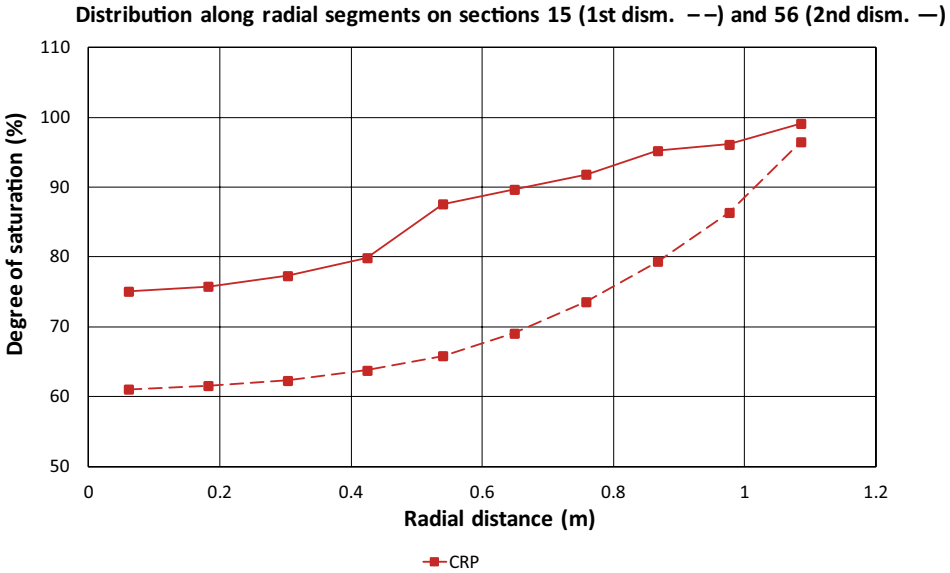

Figure 5-63. *Comparison of computed dry density and degree of saturation for sections 15 (first dismantling) and 56 (final dismantling). CRIEPI analysis.*

ICL reports a large increase of the degree of saturation in the heater sections that results in a quite small but not negligible change in dry density (Figure 5-64 and Figure 5-65). In the no-heater sections, the increase in degree of saturation is also quite large and it results in a reduction of dry density in the outer part of the barrier and an increase in the inner part (Figure 5-66). This is a plausible result, the swelling of the outer part of the barrier has compressed the central zone of the section that is still unsaturated. This dry density variation is not observed experimentally but the observed increase of degree of saturation between the two dismantling in the test is more limited than in the analysis.

In the case of the SKB-CT model, the variation of computed dry density between the two dismantling events in the heater sections is indeed negligible, in agreement with observations (Figure 5-67 and Figure 5-68). The interpretation of this result, however, is hampered by the fact that the increase in degree of saturation is also rather limited. It is unknown how the dry density distribution would change on reaching full saturation although SKB-CT uses an elastoplastic model that it is well suited to represent irreversible deformations. In this context, it is interesting to note that in the no-heater section, the computed variation of dry density is also very small while the change in degree of saturation is closer to that of the experiment (Figure 5-69). TUL results also show large increases in degree of saturations together with negligible changes in dry density both in the heater and no-heater sections (Figure 5-70 to Figure 5-72). However the computed distributions of dry density are very different from the observed ones in the two dismantlings suggesting that significant modifications are required in the mechanical constitutive model.

The results of UPC in the heater sections also show a negligible variation of dry density between the two dismantling events but again associated to a limited change in degree of saturation begging the question of what would be the final dry density distribution in case of reaching a fully saturated state (Figure 5-73 to Figure 5-74). The results are similar to those of SKB-CT; it may be relayed to the fact that the two teams use the same basic (though not identical) elastoplastic model. In the no-heater section UPC also obtains an increase of dry density in the inner pat of the barrier associated with a moderate increase of degree of saturation; in this case a result similar to CRIEPI's.

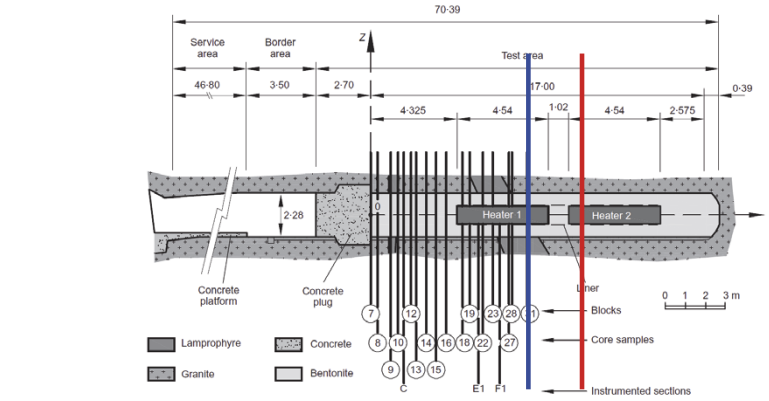

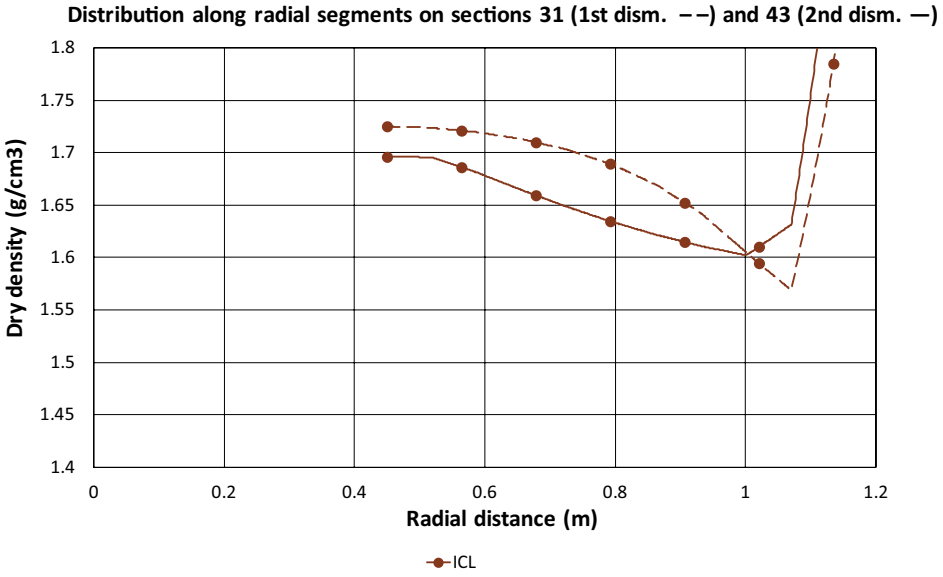

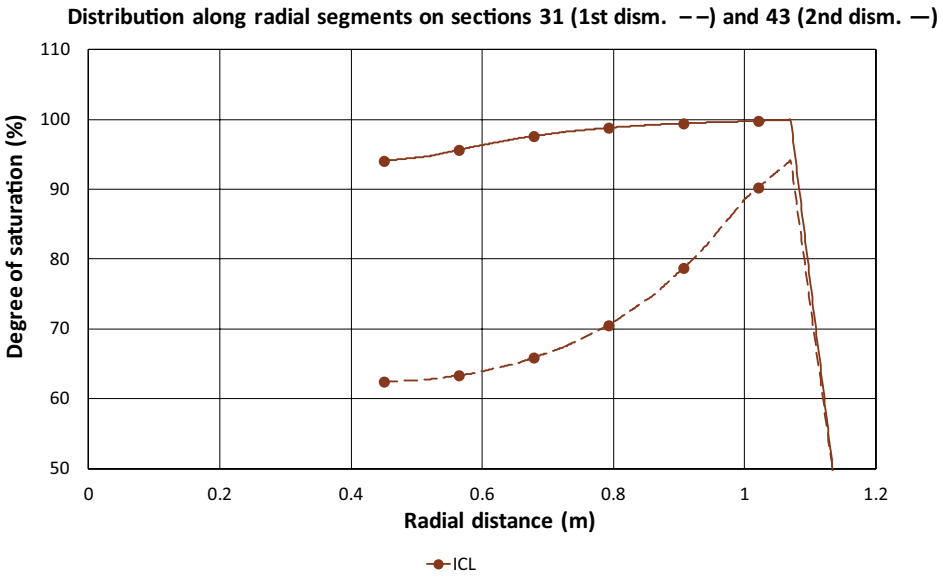

Figure 5-64. *Comparison of computed dry density and degree of saturation for sections 31 (first dismantling) and 43 (final dismantling). ICL analysis.*

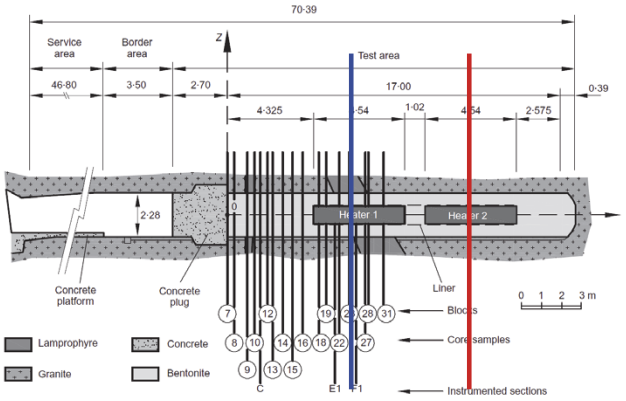

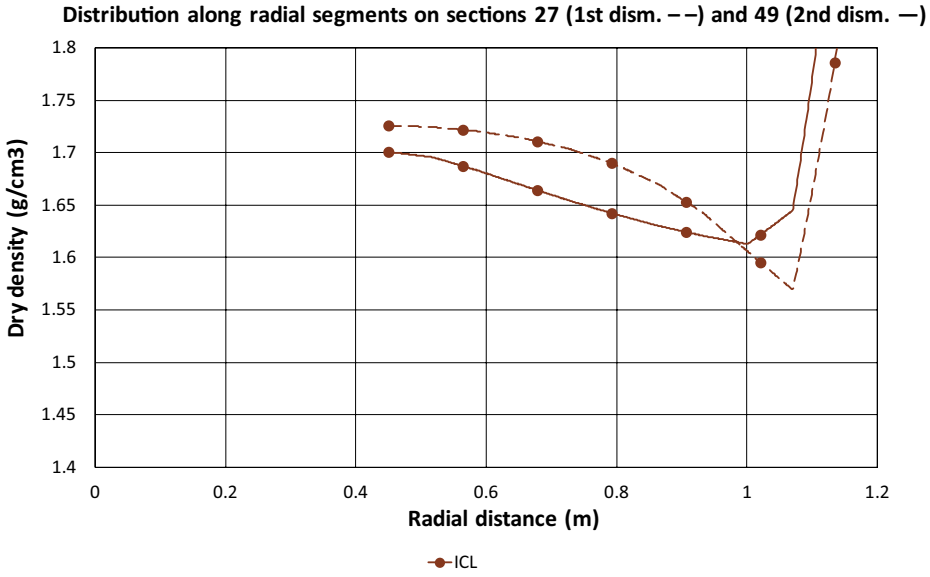

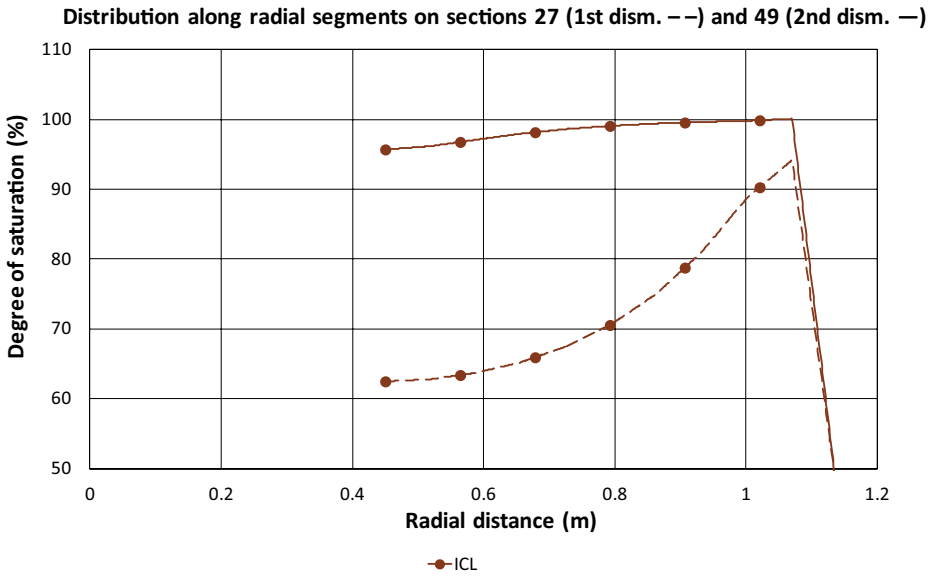

Figure 5-65. *Comparison of computed dry density and degree of saturation for sections 27 (first dismantling) and 49 (final dismantling). ICL analysis.*

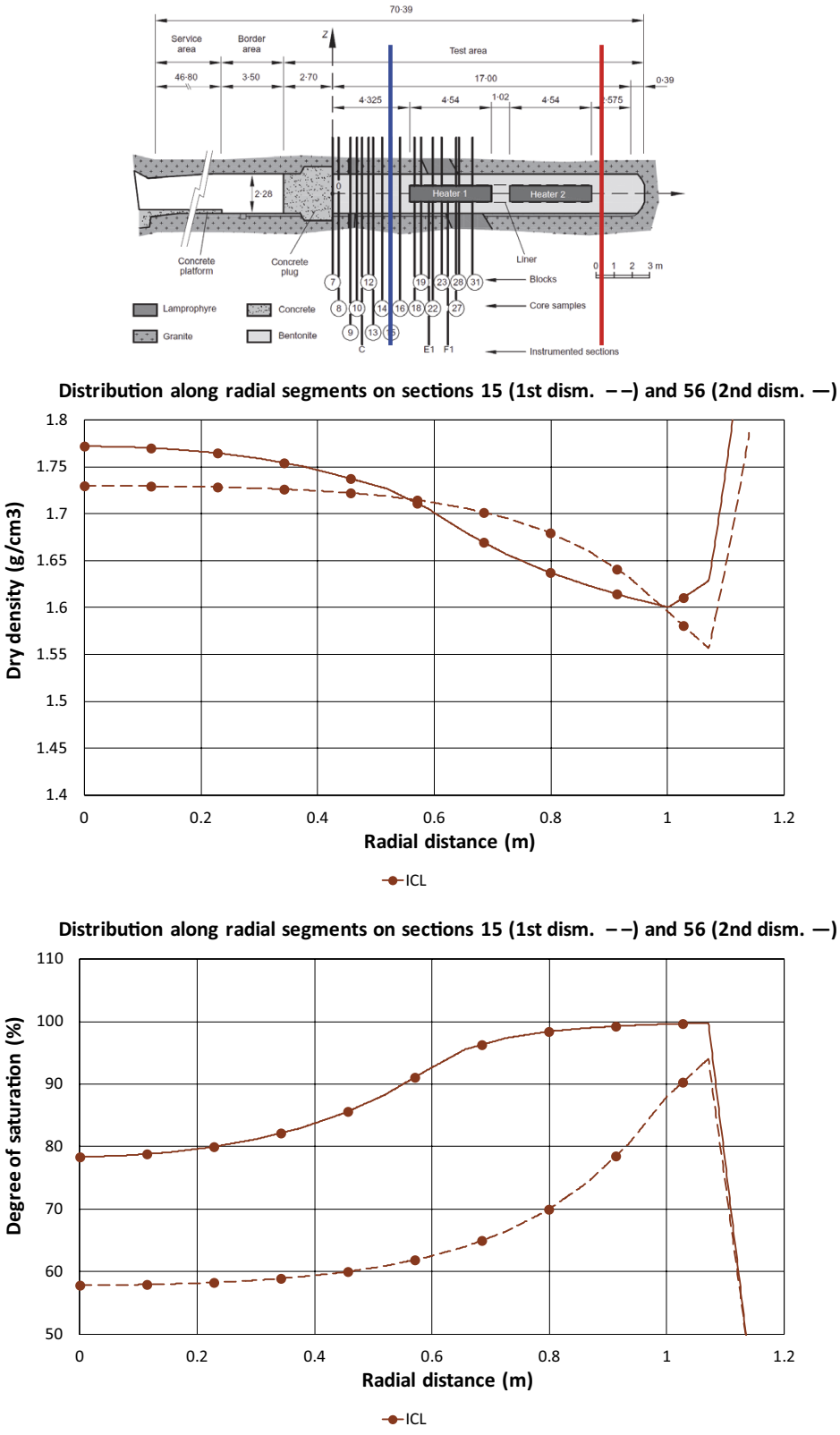

Figure 5-66. *Comparison of computed dry density and degree of saturation for sections 15 (first dismantling) and 56 (final dismantling). ICL analysis.*

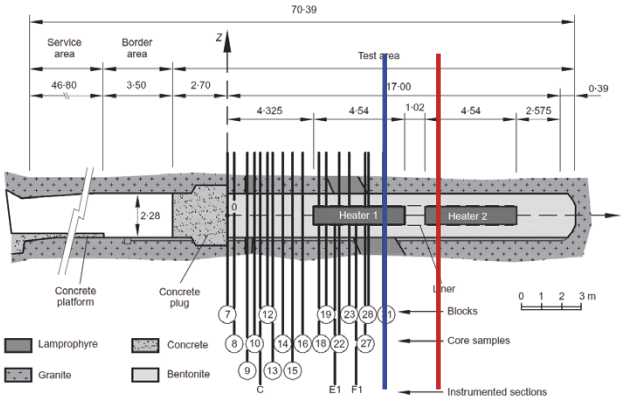

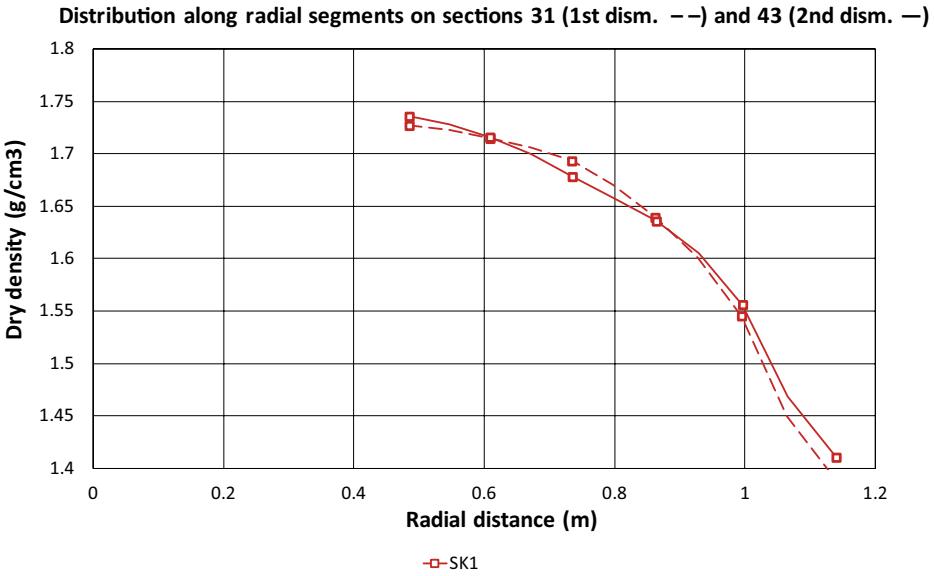

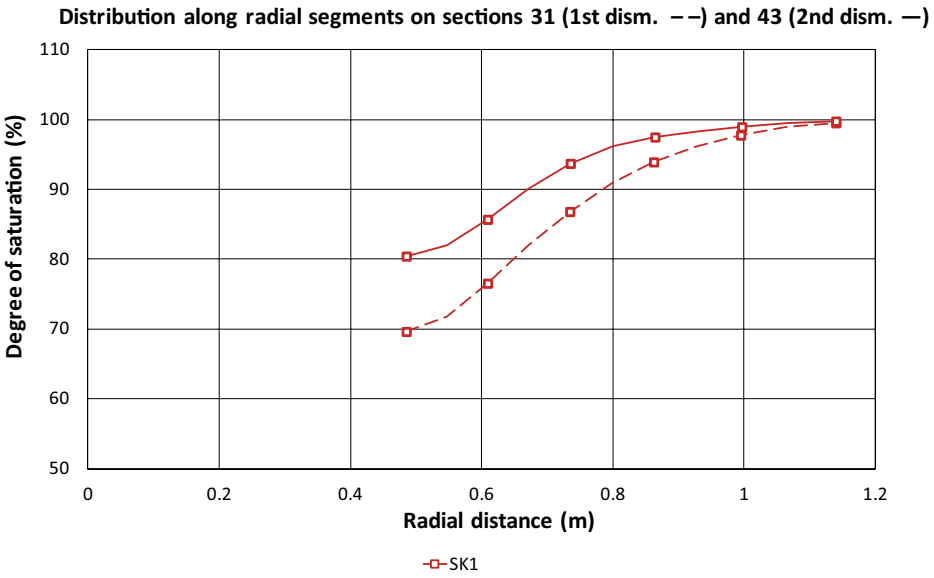

Figure 5-67. *Comparison of computed dry density and degree of saturation for sections 31 (first dismantling) and 43 (final dismantling). SKB-CT analysis.*

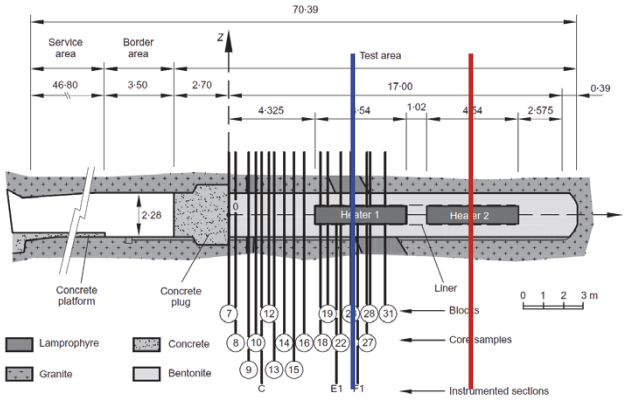

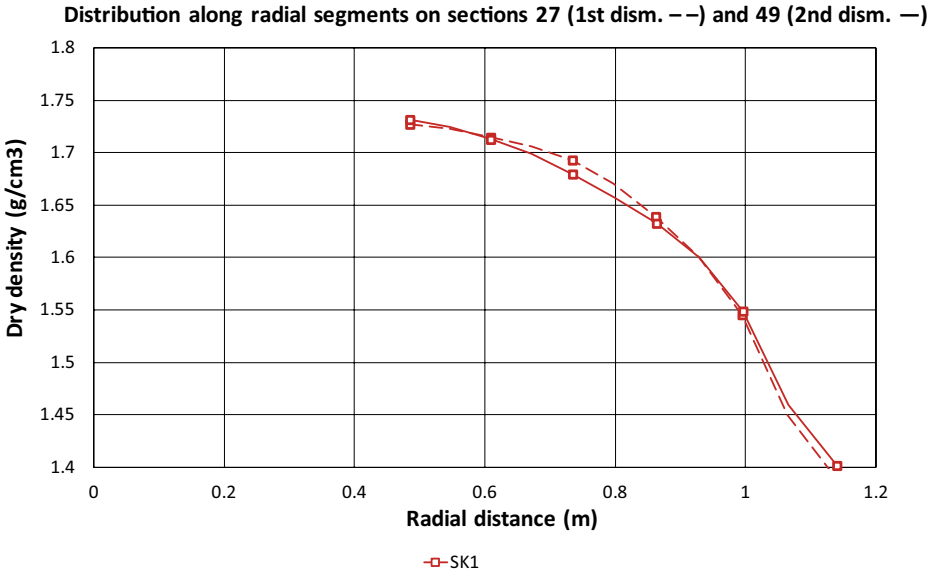

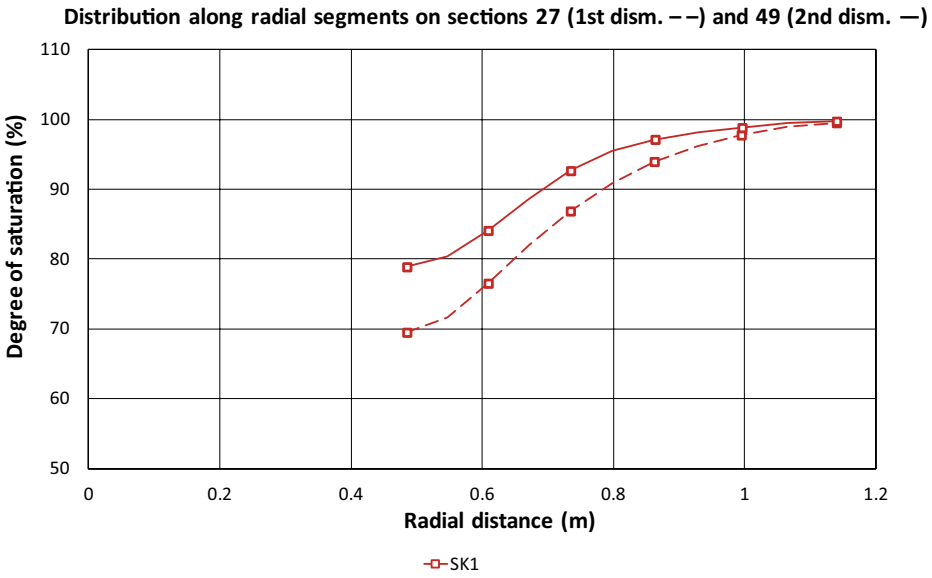

Figure 5-68. *Comparison of computed dry density and degree of saturation for sections 27 (first dismantling) and 49 (final dismantling). SKB-CT analysis.*

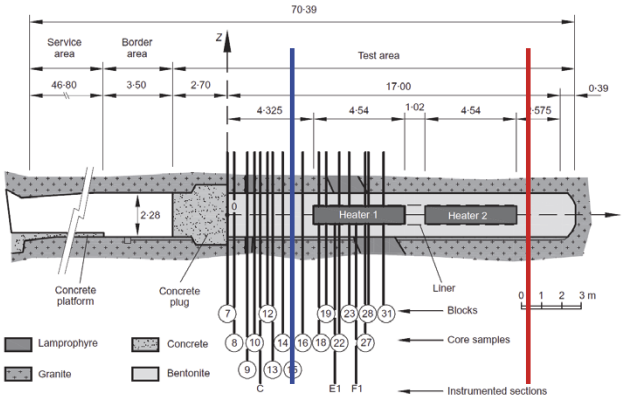

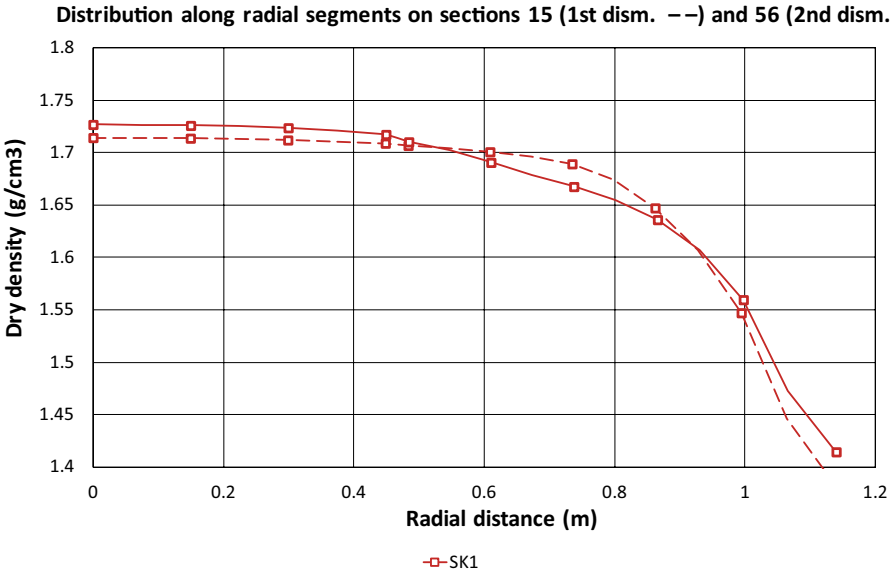

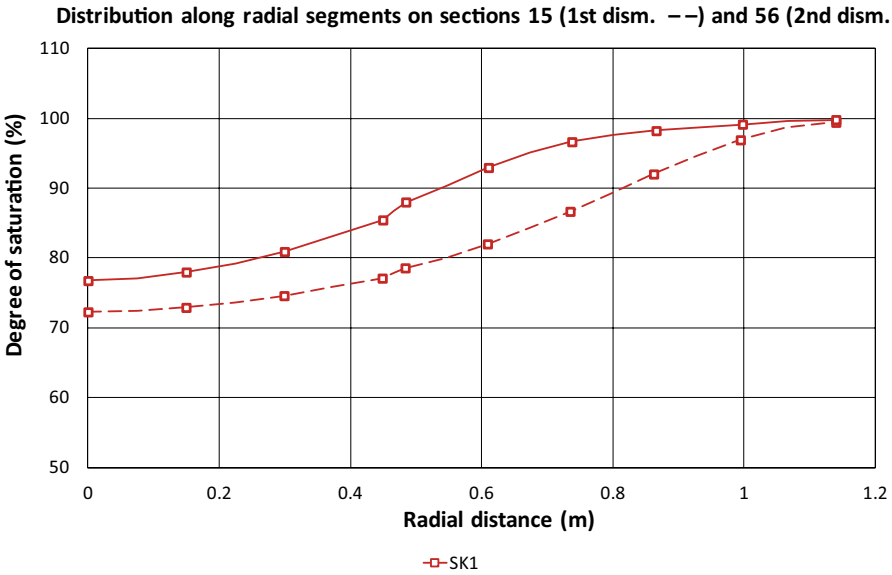

Figure 5-69. *Comparison of computed dry density and degree of saturation for sections 15 (first dismantling) and 56 (final dismantling). SKB-CT analysis.*

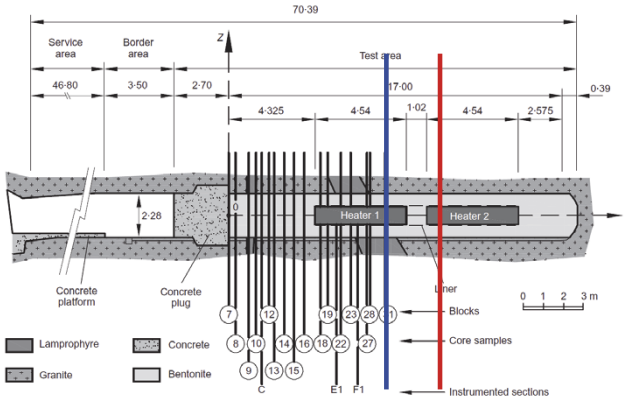

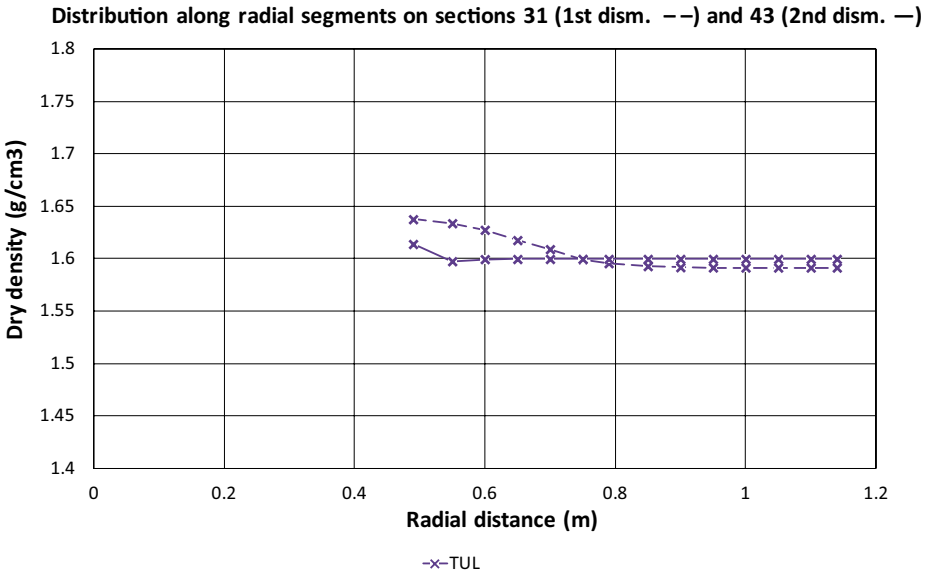

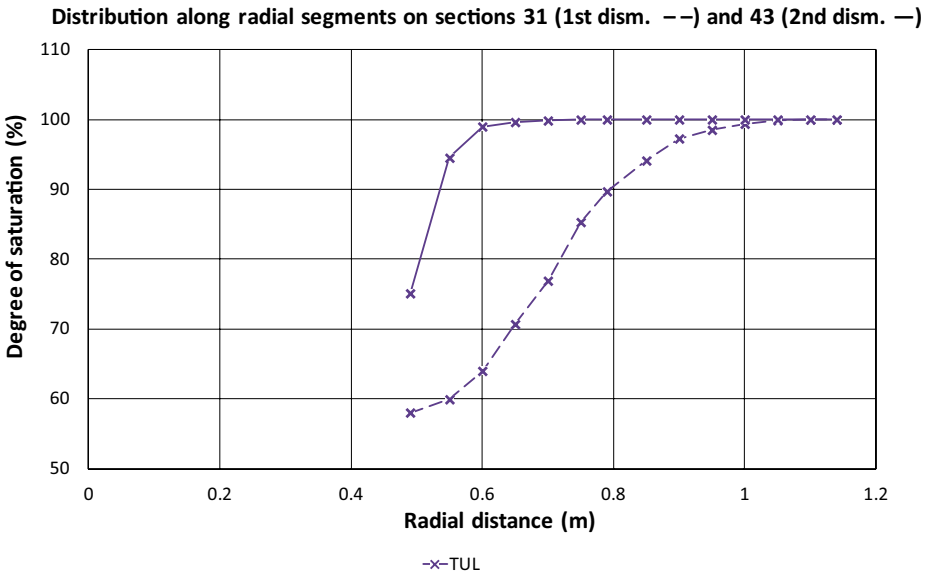

Figure 5-70. *Comparison of computed dry density and degree of saturation for sections 31 (first dismantling) and 43 (final dismantling). TUL analysis.*

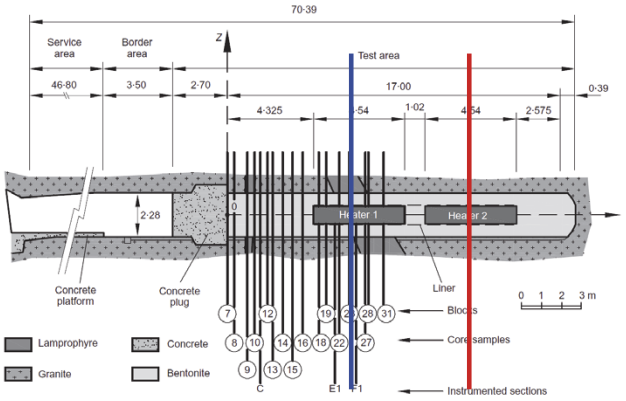

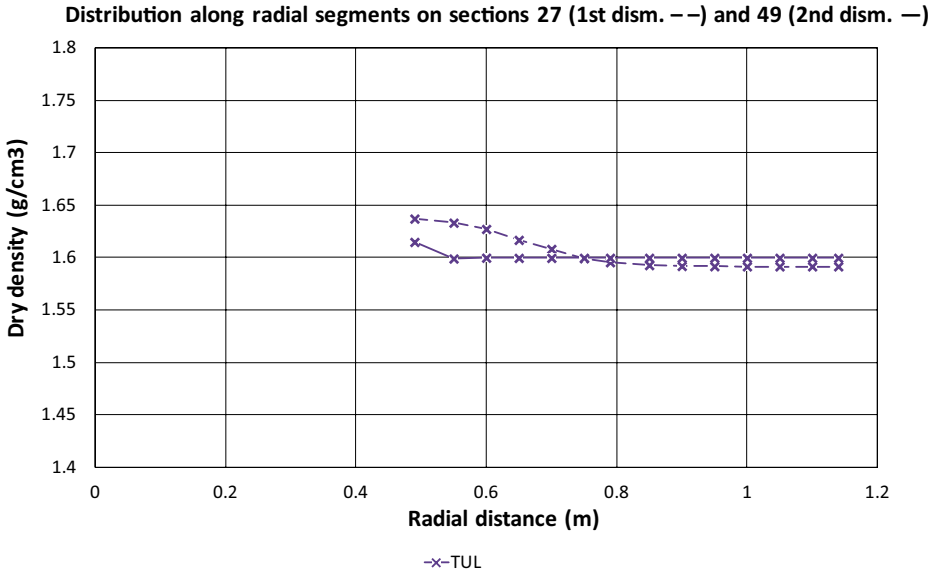

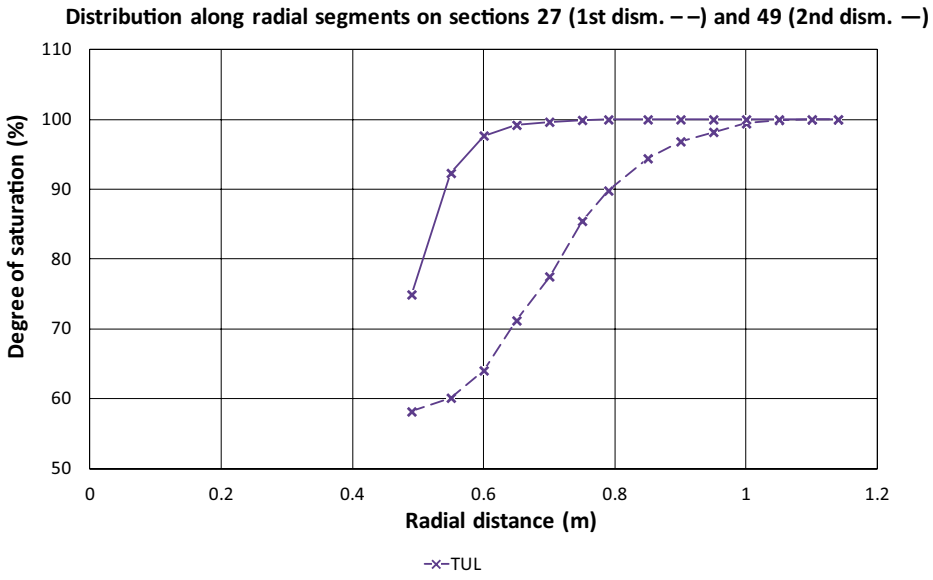

Figure 5-71. *Comparison of computed dry density and degree of saturation for sections 27 (first dismantling) and 49 (final dismantling). TUL analysis.*

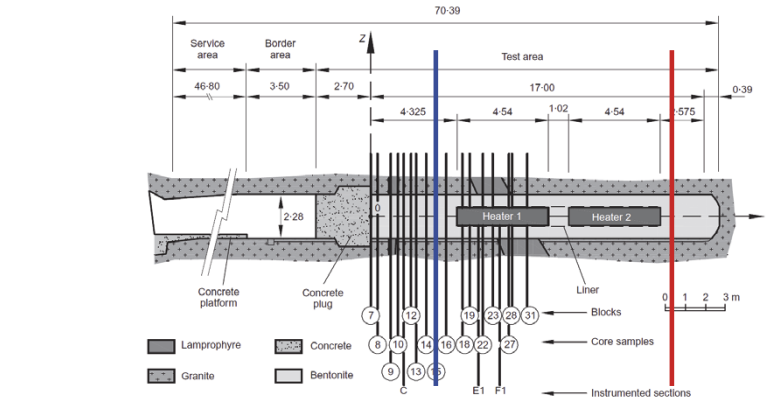

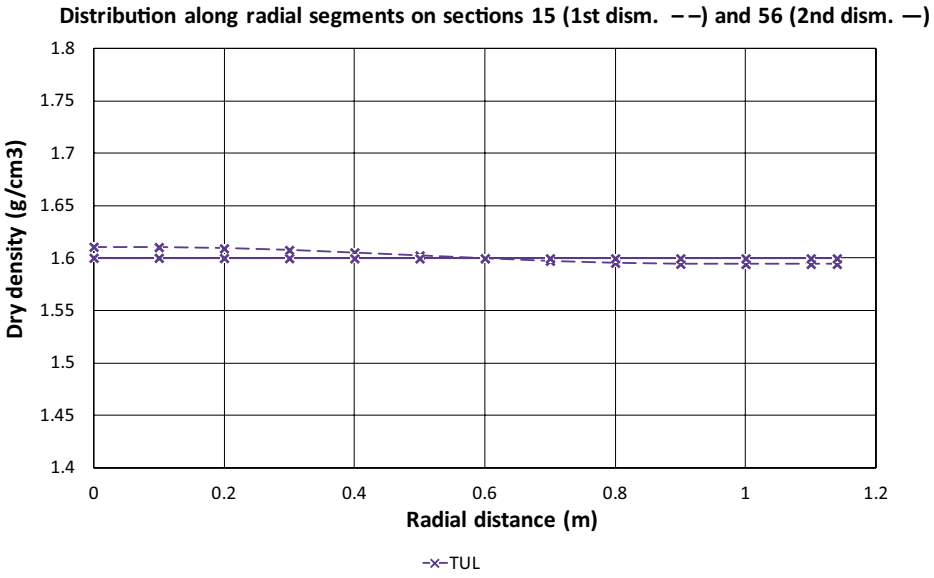

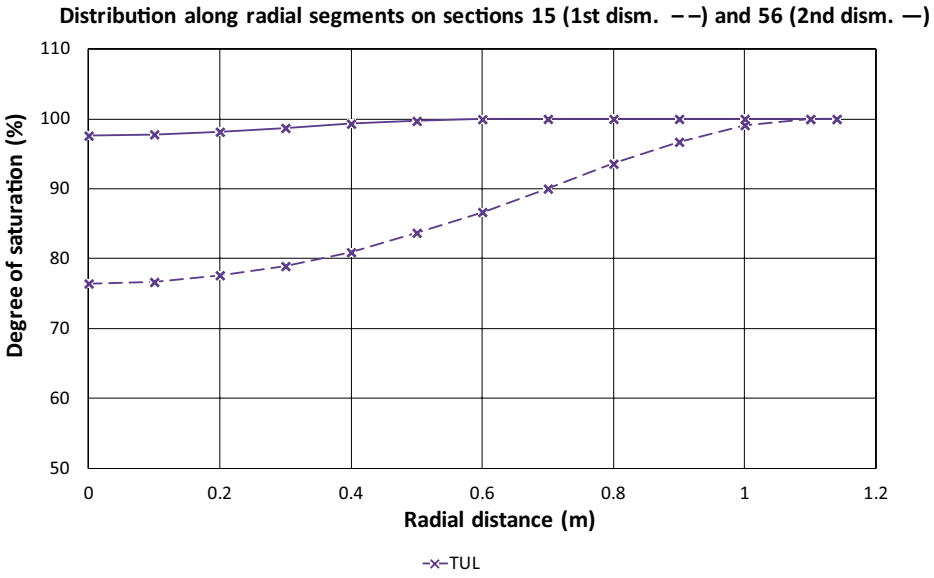

Figure 5-72. *Comparison of computed dry density and degree of saturation for sections 15 (first dismantling) and 56 (final dismantling). TUL analysis.*

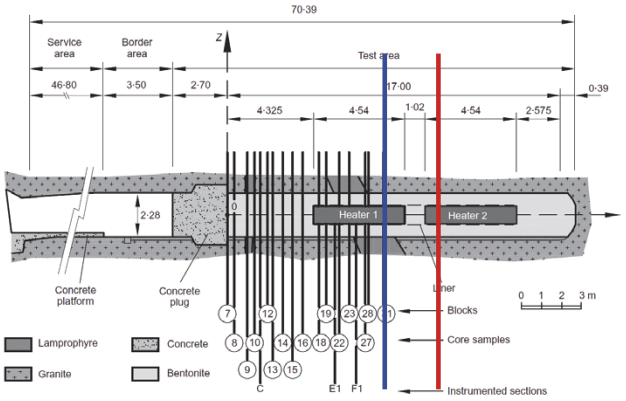

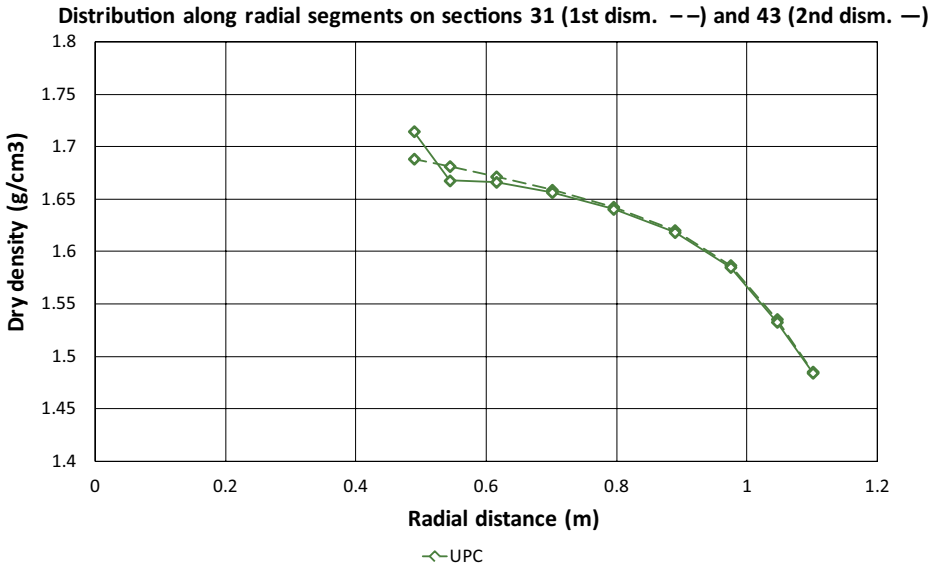

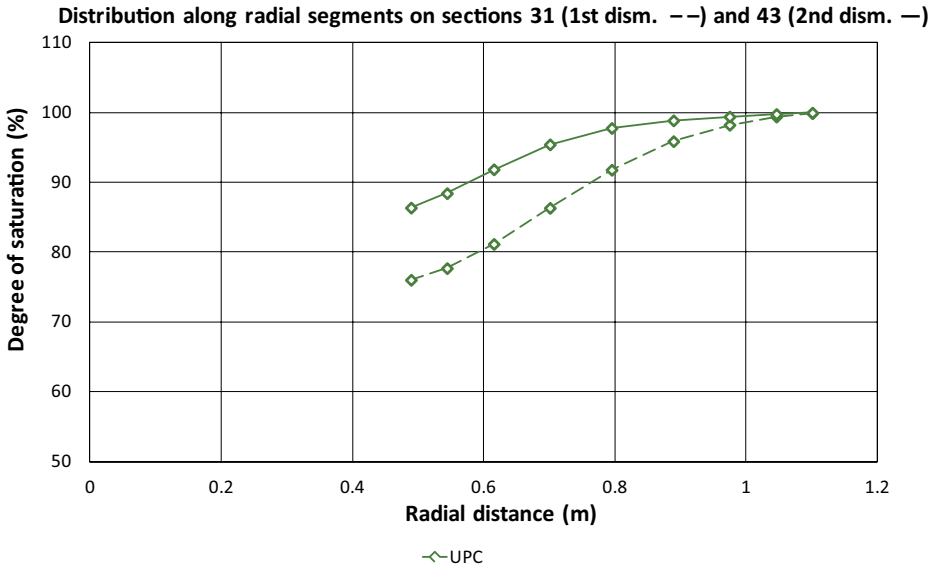

Figure 5-73. *Comparison of computed dry density and degree of saturation for sections 31 (first dismantling) and 43 (final dismantling). UPC analysis.*

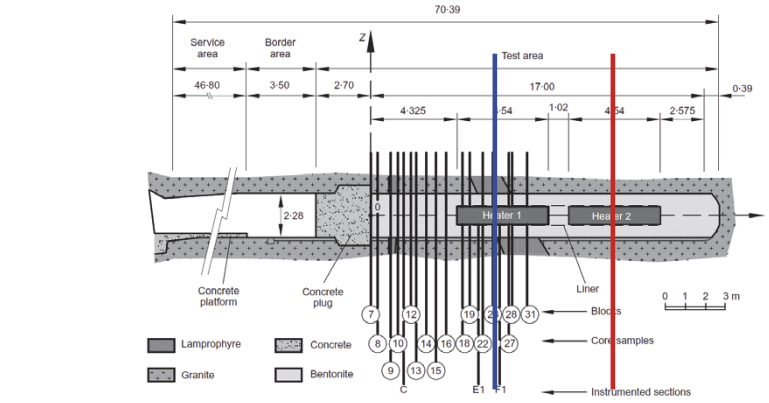

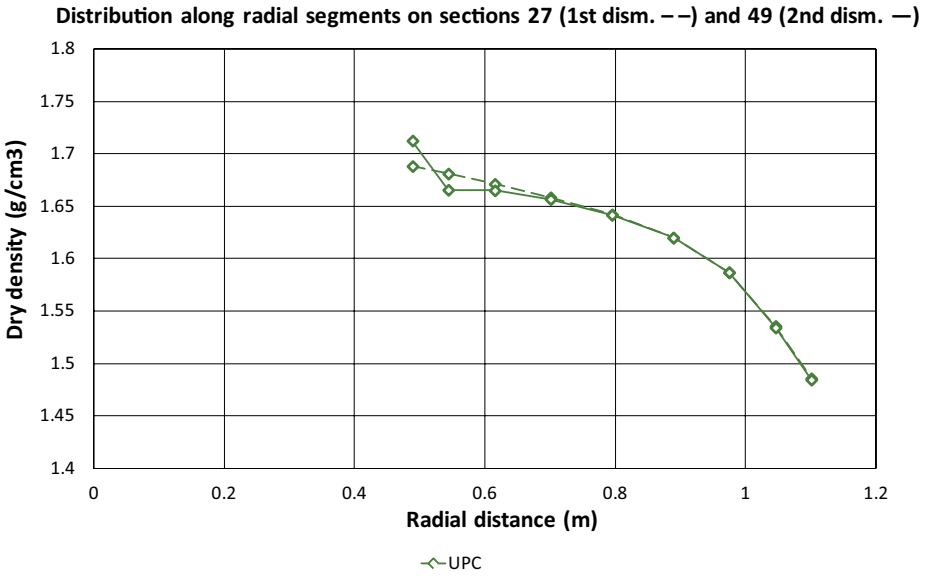

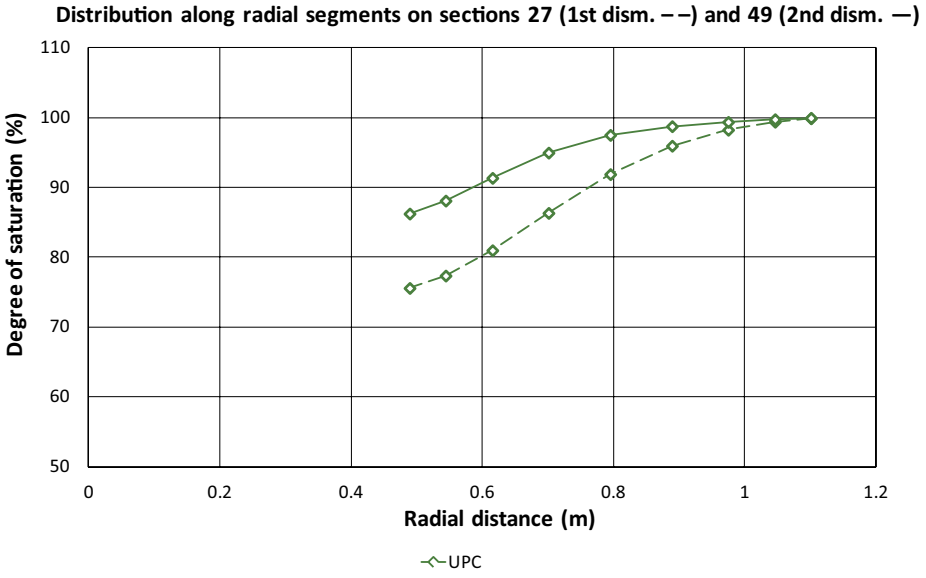

Figure 5-74. *Comparison of computed dry density and degree of saturation for sections 27 (first dismantling) and 49 (final dismantling). UPC analysis.*

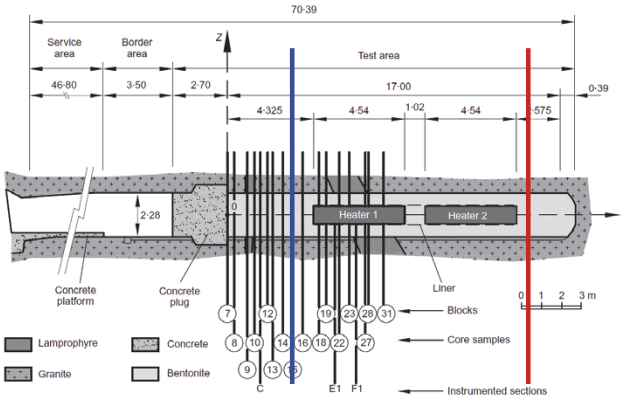

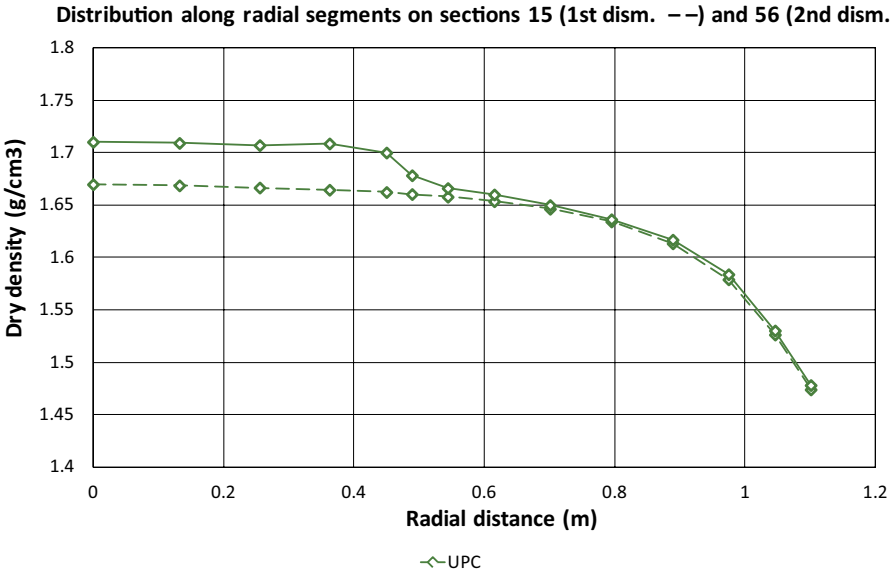

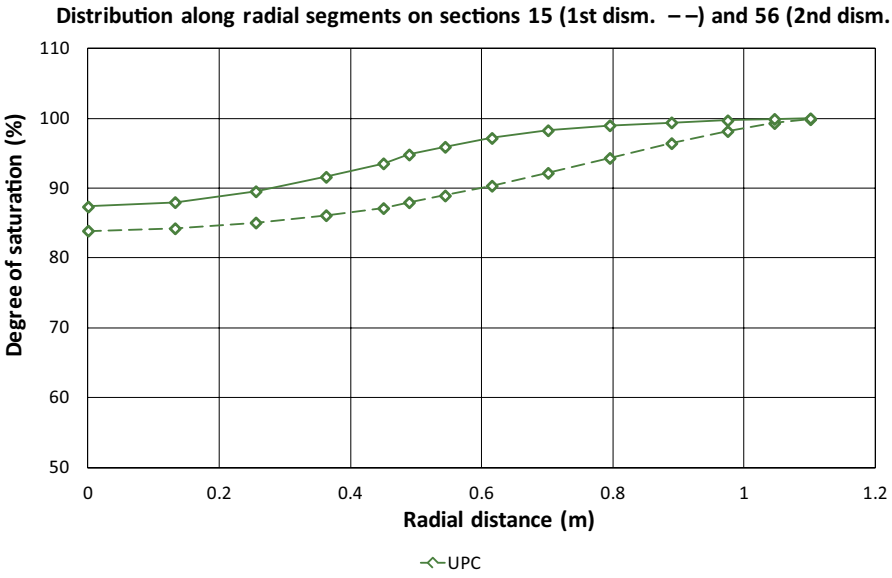

Figure 5-75. *Comparison of computed dry density and degree of saturation for sections 15 (first dismantling) and 56 (final dismantling). UPC analysis.*

6 Overview and concluding remarks

6.1 General

Seven modelling teams (CRIEPI, GRS, ICL; SNL; SKB-CT, TUL and UPC) using six different computed codes (CODE_BRIGHT, COMSOL, ICFEP, LOSTUF, PFLOTRAN and VIPER) have performed numerical analyses of the FEBEX test. The Task has been divided in two stages; Stage 1 included the first five years of heating and the first partial dismantling whereas Stage 2 involved the test operation until the end of heating and the final dismantling. Given the characteristics of the experiment, 2D axisymmetric domains have been used in nearly all the simulations; one team has adopted a 3D geometry whereas another team has used a 1D axisymmetric geometry for solving the hydraulic problem. Only SKB-CT has introduced explicitly a gap between the rock and the barrier as well as a hydraulic boundary condition close to the tunnel.

Five teams carried out THM analyses and two teams undertook TH analyses without the mechanical component. Generally, the formulations were fully coupled involving the solution of the corresponding energy and mass balance equations as well as the equilibrium equation, if the mechanical problem was considered. In two cases, there was one-directional coupling from the thermal to the hydraulic problem and from the TH problem to the mechanical. The missing back coupling did not appear to affect substantially the results obtained.

The thermal constitutive formulation was invariably based on Fourier's law; five of the seven modelling teams considered a thermal conductivity dependent on degree of saturation. Vapour migration driven by the gradients of vapour pressure or concentration (Fick's law) was considered by all teams except one. In most hydraulic formulations, liquid water flow is governed by Darcy's law with hydraulic conductivity dependent on degree of saturation and porosity (or dry density). All teams except one employed a Van Genuchten expression for the water retention curve. GRS adopted a different approach to the hydraulic problem based on a double-continuum model which is composed of the intergranular pore space and the interlamellar space of the clay grains; the movement of water is by vapour diffusion in the pore space and by diffusion of hydrated water in the interlamellar space.

A variety of mechanical constitutive laws have been used by the five teams performing THM analyses; two teams (CRIEPI and TUL) have used elastic (linear and nonlinear) models combined with an additional swelling term while SKB-CT and UPC have used different versions of the BBM elastoplastic model. ICL is the only team adopting a double structure elastoplastic model (IC DSM). None of those constitutive models introduce explicitly any effects of temperature on mechanical behaviour, the only thermomechanical effects considered by some teams was the inclusion of a thermal expansion coefficient. The absence of thermomechanical models does not appear to impair the performance and outcome of the analyses, at least for the level of temperatures of the FEBEX test.

Although all the teams were provided with the same information on the properties of the FEBEX bentonite and of the GTS rock, the modellers were given freedom of interpretation of the data when selecting appropriate constitutive laws and parameters. Not surprisingly, there were differences in the parameters and relationships selected by the different teams. Overall, the Task resulted in a wide variety of approaches, formulations, computer codes, constitutive laws and parameters being applied to the same well documented field case. In this way, a quite wide perspective was possible.

6.2 Results of the analyses

Generally, the four teams that provided thermal power results obtained a good reproduction of the power of the heaters required to maintain the maximum 100 °C temperature condition. The observed increase of power with time, a consequence of the progressive hydration of the barrier increasing its thermal conductivity, was also well captured. The jump increase of Heater 2 power after first dismantling is also modelled correctly. Observations showed that there is about a 10 % difference between the power values recorded in the two heaters. The origin of this difference is uncertain, and it is not obtained by any of the modelling teams. Temperatures are also generally well reproduced by all

the modelling teams. This result is not unexpected as the FEBEX test is temperature-controlled, but it is still helped by an adequate representation of the variation of thermal conductivity with degree of saturation, a feature incorporated in most formulations.

All the analyses reproduce the progressive hydration of the engineered barrier. The initial drying close to the heaters is obtained by all modelling teams that incorporate vapour transport in their formulations although the intensity of drying is generally underestimated. The consideration of vapour migration has proved necessary to simulate satisfactorily the early period of the test and, possibly, to follow closely the subsequent hydration. In general, the final degree of saturation in the barrier is somewhat underestimated by analyses. In some cases, it appears to be influenced by the adoption of a low permeability of the rock but the most important parameter in this respect is the bentonite hydraulic conductivity and its variation with degree of saturation.

Assessing the degree of agreement between computed and observed swelling pressures are hindered by uncertainties concerning the total stress measurements, especially during the initial part of the test. In any case, all teams performing THM analyses report stress increases with time and hydration with final values consistent with the observed order of magnitude of the stresses. In practically all cases, the computed final stress values are lower than the theoretical initial swelling pressures.

In the first dismantling, all teams predicted a saturated bentonite close to the rock and a quite unsaturated barrier in the rest of the section, in agreement with observations. Observations also revealed a quite non-homogenous barrier in terms of dry density with a low-density barrier close to the rock and a much higher bentonite density near the heaters. Generally, the THM models provided distributions exhibiting a pattern similar to the experimental one. In the cooler zone away from the heater, the progress of hydration was bracketed by the simulation results.

The second dismantling demonstrated that after 18.15 years the bentonite barrier had become basically saturated, particularly in the narrower sections where the heater was located except in a narrow zone close to the heaters where degree of saturation was, in any case, quite high as well. The level of hydration tended to be underestimated by the modelling but not by large amounts. Most THM teams also obtain a non-homogeneous distribution of dry density at the end of the test.

The model results concerning the evolution of dry density between the two dismantlings have also been examined. The measurements indicated that the distributions of dry density practically did not change between the two dismantling events; it was as though the initial heterogeneity had become frozen after the initial period of the test. Most THM models predicted a small or a negligible evolution of dry density in the second stage of the experiment but a more conclusive confirmation regarding this agreement with observations would require extending the analyses to full or quasi-full saturation.

6.3 Conclusion

Stepping back to gain a wider perspective of the ensemble of the Task, it must be stated that the numerical analyses performed have been able to represent adequately the global TH and THM behaviour of a rather complex long-term full-scale experiment. The overall observations concerning the evolution of heater power, the temperature field at different times, the progress of hydration, the development of stresses in the bentonite and the state of the barrier at the first and the final dismantling have been, on the whole, satisfactorily reproduced by the models. This strongly indicates that the most important processes and their interactions appear to be incorporated in an appropriate manner in the numerical models. Naturally, discrepancies can be observed on a closer comparison of the instrumentation data with modelling results; in fact, those differences provide valuable insights for further improvements of the formulations, constitutive laws and parameter selection. In conclusion, it can be stated that the Task goals of enhancing the understanding of the THM EBS behaviour during the transient phase, of examining the evolution of the state of the barrier and of validating and improving the numerical capabilities of the participating modelling teams have largely been achieved.

7 Acknowledgements

The work reported in this report constitutes Task 9 of the Engineered Barrier System (EBS) Task Force. The EBS Task Force is steered by SKB and receives funding from BMWi (Germany), CRIEPI (Japan), DOE/UFD (USA), NAGRA (Switzerland), NWS (UK), POSIVA (Finland), SKB (Sweden) and SÚRAO (Czech Republic).

The work of GRS in this Task was funded by the German Federal Ministry of Economics and Energy (BMWi) under contract No.s 02E11102 and 02E11647.

ICL team acknowledges the support of Nuclear Waste Services (formerly Radioactive Waste Management), UK, and Wood plc in funding the PhD research of Giulia Ghiadistri, during which the FEBEX analyses were undertaken.

The work of TUL was supported by Správa Úložišť RadioAktivních Odpadů (SÚRAO).

8 References

SKB's (Svensk Kärnbränslehantering AB) publications can be found at www.skb.se/publications.

AITEMIN, 2003. FEBEX Sensors Data Report No. 30 (In Situ Experiment). Project deliverable. AITEMIN D8-d. 70-AIT-L-6-07, Association for Research and Industrial Development of Natural Resources, Spain.

Alcoverro J, Alonso E E, 2001. Scientific bases of Code_Bright. UPC 70-UPC-L-1-001, 1–12, Technical University of Catalonia, Spain.

Alonso E E, Gens A, Josa A, 1990. A constitutive model for partially saturated soils. Géotechnique 40, No. 3, 405–430.

Alonso E E, Vaunat J, Gens A, 1999. Modelling the mechanical behaviour of expansive clays. Engineering Geology 54, No. 1-2, 173–183.

Alonso, E E, Alcoverro J, Coste F, Malinsky L, Merrien-Soukatchoff V, Kadiri I, Nowak T, Shao H, Nguyen T S, Selvadurai A P S, Armand G, Sobolik S R, Itamura M, Stone C M, Webb S W, Rejeb A, Tijani M, Maouche Z, Kobayashi A, Kurikami H, Ito A, Sugita Y, Chijimatsu M, Börgesson L, Hernelind J, Rutqvist J, Tsang C-F, H, Jussila P, 2005. The FEBEX benchmark test: case definition and comparison of modelling approaches. International Journal of Rock Mechanics and Mining Sciences Volume 42, Issues 5-6, 611–638.

Alonso E, Alcoverro J, 2005. The FEBEX test as a benchmark case for THM modelling: historical perspective and lessons learnt. In Alonso E, Ledesma A, (eds). Advances in understanding engineered clay barriers. London: Taylor & Francis, 3–19.

Amiguet J-L, 1985. Grimsel Test Site. Felskennwerte von intaktem Granit. Zusammenstellung felsmechanischer Laborresultate diverser granitischer Gesteine. Nagra NIB 85-08, National Cooperative for the Disposal of Radioactive Waste, Switzerland.

Amestoy P A, Duff I S, l'Excellent J-Y, Koster J, 2001. A fully asynchronous multifrontal solver using distributed dynamic scheduling. SIAM Journal on Matrix Analysis and Applications, 23 (1), 15–41.

Bárcena I, Fuentes-Cantillana J-L, García-Siñeriz J L, 2003. Dismantling of heater No. 1 at the FEBEX in situ test. Description of operations. ENRESA--09/03, Empresa Nacional de Residuos Radiactivos, Spain.

Bendito E, Pintado X, 2016. Monitoring of swelling pressure in bentonite. Environmental Geotechnics, 3:5, 334–345.

Blaheta R, Hasal M, Michalec Z, 2018. Decovalex 2019, Task D – Modelling the EB experiment: model formulation, implementation, results from 3D model. Appendix of SÚRAO Report No. 292/2018, Radioactive Waste Repository authority, The Czech Republic.

Brooks R H, Corey A T, 1964. Hydraulic Properties of Porous Media. Fort Collins: Colorado State University (Hydrology Papers 3).

Bräuer V, Kilger B, Pahl A, 1989. Grimsel Test Site. Engineering geological investigations for the interpretation of rock stress measurements and fracture flow tests. Nagra NTB 88-37E, National Cooperative for the Disposal of Radioactive Waste, Switzerland.

Börgesson L, Chijimatsu M, Fujita T, Nguyen T S, Rutqvist J, Jing L, 2001. Thermo-hydro-mechanical characterisation of a bentonite-based buffer material by laboratory tests and numerical back analysis. International Journal of Rock Mechanics & Mining Sciences 38, 95–104.

Börgesson L, Hernelind J, Ludvigsson J-E, 2004. Aspo Hard Rock Labolatory, DECOVALEX III, Task 1 Modelling of FEBEX in situ test, Coupled thermos-hydro-mechanical analysis of the buffer and the rock. SKB IPR-08-12, Svensk Kärnbränslehantering AB.

Cui W, Potts D M, Zdravkovic L, Gawecka K A, Taborda, D M G, 2018. An alternative coupled thermo-hydro-mechanical finite element formulation for fully saturated soils. Computers and Geotechnics, 94, 22–30.

Dueck A, 2004. Hydro-mechanical properties of a water unsaturated sodium bentonite – laboratory study and theoretical interpretation. PhD thesis. Department of Building and Environmental Technology, Lund University, Sweden.

Dueck A, Nilsson U, 2010. Thermo-Hydro-Mechanical properties of MX-80 Results from advanced laboratory tests. SKB TR-10-55, Svensk Kärnbränslehantering AB.

ENRESA, 2000. FEBEX project. Full-scale engineered barriers experiment for a deep geological repository for high level radioactive waste in crystalline host rock. Final report. Enresa 1/2000, Empresa Nacional de Residuos Radiactivos, Spain.

ENRESA, 2006a. Full-scale engineered barriers experiment. Updated Final Report 1994–2004. Publicación Técnica 05-0/2006, ENRESA, Madrid.

ENRESA, 2006b. Full-scale engineered barriers experiment. Final Report. Post-mortem bentonite analysis. Publicación Técnica 05-1/20, ENRESA, Madrid.

García-Siñeriz J L, Abós H, Martínez V, De la Rosa C, Mäder U, Kober F, 2016. FEBEX DP: Dismantling of heater 2 at the FEBEX "in situ" test. Description of operations. Arbeitsbericht NAB 16-11, National Cooperative for the Disposal of Radioactive Waste, Switzerland.

ENRESA, 2004. FEBEX II Project Final report on thermo-hydro-mechanical laboratory tests. ENRESA 10/2004, Empresa Nacional de Residuos Radiactivos, Spain.

Falk L, Magnusson K-Å, Olsson O, Ammann M, Keusen H R, Sattel, 1988. Grimsel Test Site. Analysis of radar measurements performed at the Grimsel Rock Laboratory in October 1985. Nagra NTB 87-13, National Cooperative for the Disposal of Radioactive Waste, Switzerland.

Fierz T, 1996. FEBEX Instrumentation of BOUS 85.001 and 85.002, FBX 95.001 and 95.002, and radial boreholes. Solexperts AG, Switzerland.

Finsterle S, Pruess K, 1995. Solving the estimation-identification problem in two-phase flow modelling. Water Resources Research, 31(4), 913–924.

Frieg B, Vomvoris S, 1994. Investigation of hydraulic parameters in the saturated and unsaturated zone of the ventilation drift. Nagra Technical Report 93-10, National Cooperative for the Disposal of Radioactive Waste, Switzerland.

García-Siñeriz J L, Abós H, Martínez V, De la Rosa C, Mäder U Kober F, 2016. FEBEX DP: Dismantling of heater 2 at the FEBEX "in situ" test. Description of operations. Nagra NAB 16-11, National Cooperative for the Disposal of Radioactive Waste, Switzerland.

Gens A, Alonso E E, 1992. A framework for the behaviour of unsaturated expansive clays. Canadian Geotechnical Journal, 29, No. 6, 1013–1032.

Gens A, Garcia-Molina A J, Olivella S, Alonso E, Huertas F, 1998. Analysis of a full scale in situ test simulating repository conditions. International Journal of Numerical and Analytical Methods in Geomechanics, 22(7), 515–48.

Gens A, Sanchez M, Guimaraes L, Do N, Alonso E E, Lloret A, Olivella S, Villar M V, Huertas F, 2009. A full-scale in situ heating test for high-level nuclear waste disposal: Observations, analysis and interpretation. Géotechnique 59(4) 377–399.

Gens A, 2018. Task Force on Engineered Barrier System (EBS). Task 1: Laboratory tests. SKB TR-14-24, Svensk Kärnbränslehantering AB.

Georgiadis K, Potts D M, Zdravkovic L, 2003. The influence of partial soil saturation on pile behaviour. Géotechnique, 53, No. 1, 11–25.

Georgiadis K, Potts D M, Zdravkovic L, 2005. Three-dimensional constitutive model for partially and fully saturated soils, International Journal of Geomechanics 5, No. 3, 244–255.

Ghiadistri G M, Potts D M, Zdravkovic L, Tsiampousi A, 2018. A new double structure model for expansive clays. In TC106 Conferences in Unsaturated Soils – 7th International Conference on Unsaturated Soils 2018, Hong Kong, 3–5 August 2018. London: International Society for Soil Mechanics and Geotechnical Engineering.

Ghiadistri G M, 2019. Constitutive modelling of compacted clays for applications in nuclear waste disposal. PhD thesis. Imperial College London, UK.

Guimerà J, Ortuño F, Vázquez E, Ruiz B, Martínez L, Carrera J, Meier P, 1996. Pulse tests at "in drift" boreholes. Performance and evaluation. UPC 70-UPC-L-0-1001, Technical University of Catalonia, Spain.

Guimerà J, Carrera J, Martínez L, Vázquez E, Ortuño F, Fierz T, Bülher C, Vives L, Meier P, Medina A, Saaltink M, Ruiz B, Pardillo J, 1998. FEBEX Hydrological characterization and modelling. UPC 70-UPC-M-0-1001, Technical University of Catalonia, Spain.

Hammond G E, Lichtner P C, Mills R T, 2014. Evaluating the Performance of Parallel Subsurface Simulators: An Illustrative Example with PFLOTRAN. Water Resources Research, 50 (1), 208–228. doi:10.1002/2012WR013483

Huertas F, Fariña P, Farias J, Garcıa-Siñeriz J L, Villar M V, Fernandez A M, Martín P L, Elorza, F J, Gens A, Sánchez M, Lloret A, Samper J, Martínez M A, 2006. Full-scale engineered barrier experiment. ENRESA 05-0/2006, Empresa Nacional de Residuos Radiactivos, Spain.

Häring M O, 1996. GTS/FEBEX: Supervision and interpretation of geophysical investigations Boreholes FBX95.001 and FBX95.002. Nagra NIB 96-14, National Cooperative for the Disposal of Radioactive Waste, Switzerland.

Josa A, Balmaceda A, Gens A, Alonso E E, 1992. An elastoplastic model for partially saturated soils exhibiting a maximum of collapse. In Owen D R J, Onate E, Hinton E (eds). Computational plasticity III. Vol. 1. Swansea: Pineridge Press, 815–826.

Keusen H R, Ganguin J, Schuler P, Buletti M, 1989. Grimsel Test Site. Geology. Nagra NTB 87-14E, National Cooperative for the Disposal of Radioactive Waste, Switzerland.

Komine, H, Ogata N, 2004. Predicting Swelling Characteristics of Bentonites. Journal of Geotechnical and Geoenvironmental Engineering, ASCE, 130 (8), 818–829. doi:0.1061/(ASCE)1090-0241(2004)130:8(818)

Kristensson O, Börgesson L, 2007. CRT – Canister Retrieval Test; EBS Task Force Assignments. SKB TR-14-19, Svensk Kärnbränslehantering AB.

Kröhn K-P, 2010. Simulating water uptake of compacted bentonite under non-isothermal conditions, decoupled from the mechanics and without feedback of hydraulics to heat transport. Applied Clay Science, 47, 28–35. doi:10.1016/j.clay.2008.06.004

Kröhn, K-P, 2011. Code VIPER – Theory and Current Status. Status report. FKZ 02 E 10548 (BMWi), Gesellschaft für Anlagen- und Reaktorsicherheit (GRS) mbH, GRS-269, Germany.

Kröhn K-P, 2017. Hydraulic Interaction of Engineered and Natural Barriers – Task 8b–8d, 8f of SKB. Summary report. GRS FKZ 02 E 10336, 02 E 10548, 02 E 10558, 02 E 11102, and 02 E 11213 (BMWi), Gesellschaft für Anlagen- und Reaktor-sicherheit, Germany.

Lanyon G W, Gaus I, Villar, M V, Martin P L, Gens A, García-Siñeriz J L, Bárcena I, 2013. Main outcomes and review of the FEBEX in situ test (GTS) and Mock-up after 15 years of operation. Nagra NAB 13-96, National Cooperative for the Disposal of Radioactive Waste, Switzerland.

Madaschi, A, Laloui L, 2018. EBS – Task Force: Task 7/ Gas Transport in Bentonite, Status Report 2017. Nagra NAB 18-03, National Cooperative for the Disposal of Radioactive Waste, Switzerland.

Man A, Martino J B, 2009. Thermal, Hydraulic, and Mechanical Properties of Sealing Materials. NWMO TR-2009-20, Nuclear Waste Management Organization, Canada.

Marcial D, Delage P, Cui Y J, 2008. Hydromechanical couplings in confined MX80 bentonite during hydration. In 1st European Conference on Unsaturated Soils, Durham, UK, 2–4 July 2008. Durham: CRC Press, 249–255.

Martinez M J, Stone C M, 2008. Considerations for developing models of multiphase flow in deformable porous media. SAND Report SAND2008-5887, Sandia National Laboratories, USA.

Martínez V, Abós H, García-Siñeriz J L, 2016. FEBEXe: Final Sensor Data Report (FEBEX "in situ" Experiment). Nagra NAB 16-19, National Cooperative for the Disposal of Radioactive Waste, Switzerland.

Matsuoka H, Nakai T, 1974. Stress-deformation and strength characteristics of soil under three different principal stresses. Proceedings of the Japan Society of Civil Engineers, 232, 59–70.

Meier P, Fernández P, Carrera J, Guimerà J, 1995. FEBEX – PHASE 1. Results of hydraulic testing in boreholes FBX 95.001, FBX 95.002, BOUS 85.001 and BOUS 85.002. Technical University of Catalonia, Spain.

Monroy R, Zdravkovic L, Ridley A, 2010. Evolution of microstructure in compacted London Clay during wetting and loading. Géotechnique, 60, No. 2, 105–119.

Nova R, 1988. Sinfonietta classica: an exercise on classical soil modelling. In Saada A, G. Bianchini (eds). Proceedings Symposium Constitutive Equations for Granular non- cohesive soils, Cleveland, Ohio, 22–24 July 1988. Balkema, Rotterdam, 501–519.

Nyambao, V P, Potts D M, 2010. Numerical simulation of evapotranspiration using a root water uptake model. Computers and geotechnics, 37, 175–186.

Olivella S, Carrera J, Gens A, Alonso, E E, 1994. Nonisothermal multiphase flow of brine and gas through saline media. Transport in Porous Media 15, 271–293. doi:10.1007/BF00613282

Olivella S, Gens A, Carrera J, Alonso E, 1996. Numerical formulation for a simulator 'CODE_ BRIGHT' for the coupled analysis of saline media. Engineering Computations, 13(7), 87–112.

Olivella S, Alonso E E, 2008. Gas flow through clay barriers. Géotechnique 58, 157–176.

Ortuño F, Carretero G, Martinez-Landa L, Carrera J, 2005. Hydraulic characterisation of the FEBEX granite: test performance and field interpretation. In Alonso E E, Ledesma A (eds). Advances in understanding engineered clay barriers. London: Taylor & Francis, 133–141.

Pahl A, Heusermann S, Bräuer V, Glöggler W, 1989. Grimsel Test Site. Rock stress investigations. Nagra NTB 88-39E, National Cooperative for the Disposal of Radioactive Waste, Switzerland.

Papafotiou A, Li C, Kober F, Qiao F, Ferrari A, Laloui L, Sanchez M, Gens A, Åkesson M, 2017. Pre-dismantling THM modelling of the FEBEX in situ experiment. Nagra NAB 16-022. National Cooperative for the Disposal of Radioactive Waste, Switzerland.

Pardillo J, Campos R, 1996. FEBEX – Grimsel Test Site (Switzerland) Considerations respect to the fracture distribution. CIMNE CIEM70-IMA-L-2-05, Centro de Investigaciones Energéticas, Medioambientales y Tecnológicas, Spain.

Pardillo J, Campos R, Gimerà J, 1997. Caracterización geológica de la zona de ensayo FEBEX (Grimsel-Suiza). CIMNE 70-IMA-M-2-01, Centro de Investigaciones Energéticas, Medioambientales y Tecnológicas, Spain.

Pintado X, Lloret A, 1997. THM laboratory tests in FEBEX Phase 3. UPC 70-UPC-L-3-01, Technical University of Catalonia, Spain.

Pintado X, Ledesma A, Lloret A, 2002. Back analysis of thermohydraulic bentonite properties from laboratory tests. Engineering Geology 64, 91–115.

Potts D M, Zdravkovic L, 1999. Finite element analysis in geotechnical engineering: theory. London: Thomas Telford.

Potts D M, Zdravković, 2001. Finite Element Analysis in Geotechnical Engineering: Application. Vol.2. London: Thomas Telford Services Limited.

Pusch R, Karnland O, Hökmark H, 1990. GMM – A general microstructural model for quantitative studies of smectite clays. SKB TR 90-43, Svensk Kärnbränslehantering AB.

Rodríguez-Dono A, Olivella S, Mokni N, 2020. Assessment of a high-level spent nuclear fuel disposal model. Journal of Environmental Geotechnics Volume 7(1), 1–17. https://doi.org/10.1680/jenge.18.00017

Romero Morales E, 1999. Characterisation and thermo-hydro-mechanical behaviour of unsaturated Boom Clay: an experimental study. PhD thesis. Technical University of Catalonia, Barcelona.

Roscoe K H, Schofield A N, 1963. Mechanical behaviour of an idealised 'wet' clay. In Proceedings of the 2nd European Conference on Soil Mechanics and Foundation Engineering, Wiesbaden, 15–18 October 1963. Essen: Deutsche Gesellschaft für Erd-und Grundbau, 47–54.

Roscoe K H, Burland J B, 1968. On the generalised stress-strain behaviour of 'wet' clay. In Heyman J (ed). Engineering Plasticity. Cambridge: Cambridge University Press, 535–609.

Samper J, Mon A, Montenegro L, 2018. A revisited thermal, hydrodynamic, chemical and mechanical model of compacted bentonite for the entire duration of the FEBEX in situ test. Applied Clay Science 160, 58–70.

Sanchez M, Gens A, do Nascimento Guimaraes L, Olivella S, 2005. A double structure generalized plasticity model for expansive materials. International Journal for Numerical and Analytical Methods in Geomechanics 29, 751–787.

Sanchez M, Gens A, 2006. FEBEX project: Final report on thermo-hydro-mechanical modelling. ENRESA Technical Publication 05-2/2006 Empresa Nacional de Residuos Radiactivos, Spain.

Sanchez M, Gens A, Olivella S, 2010. Effect of thermo-coupled processes on the behavior of a clay barrier submitted to heating and hydration. Anais da Academia Brasileira de Ciências, 82 (1), 153–168.

Sanchez M, Gens A, Guimaraes L, 2012. Thermal–hydraulic–mechanical (THM) behaviour of a large-scale in situ heating experiment during cooling and dismantling. Canadian Geotechnical Journal, 49(10), 1169–1195. https://doi.org/10.1139/t2012-076

Sanchez M, Gens A, Villar M V, Olivella S, 2016. Fully-coupled thermo-hydro-mechanical double-porosity formulation for unsaturated soils. International Journal of Geomechanics, 16(6).

Sawada M, Nishimoto S, Okada T, 2017. New rapid evaluation for long-term behavior in deep geological repository by geotechnical centrifuge – Part2: Numerical simulation of model tests in isothermal condition. Rock Mechanics and Rock Engineering, 50 (1), 159–169.

Schneebeli M, Flühler H, Gimmi T, Wydler H, Läser H-P, 1995. Measurements of water potential and water content in unsaturated crystalline rock. Water Resources Research, 31(8), 1837–1843.

Seiphoori A, Ferrari A, Laloui, L, 2014. Water retention behavior and microstructural evolution of MX-80 bentonite during wetting and drying cycles. Géotechnique 64(9), 721–734.

Smith P, 2003. Numerical analysis of infiltration into partially saturated soil slopes. PhD thesis. Imperial College London, UK.

Somerton W H, El-Shaarani A H, Mobarak S M, 1974. High temperature behavior of rocks associated with geothermal-type reservoirs. Paper SPE-4897. Paper presented at the SPE California Regional Meeting, San Francisco, California, April 1974. Proceedings of the 44th Annual California Regional Meeting of the Society of Petroleum Engineers, San Francisco, California April 4–5 1974. Richardson, TX: Society of Petroleum Engineers.

Svensson D, Dueck A, Nilsson U, Olsson S, Sandén T, Lydmark S, Jägerwall S, Pedersen K, Hansen S, 2011. Alternative buffer material. Status of the ongoing laboratory investigation of reference materials and test package 1. SKB TR-11-06, Svensk Kärnbränslehantering AB.

Tadikonda V B, 2014. Analytical model for 1-D contaminant diffusion through clay barriers. Environmental Geotechnics 1:4, 210–221.

Tang A M, Cui Y J, Barnel N, 2008. Thermo-mechanical behaviour of a compacted swelling clay. Géotechnique 58, No. 1, 45–54.

Toprak E, Olivella S, Pintado X, 2017. Coupled THM Modelling of engineered barriers for the final disposal of spent nuclear fuel isolation. In Norris S, Bruno J, Van Geet M, Verhoff E (eds). Radioactive Waste Confinement: Clays in Natural and Engineered Barriers. London: Geological Society, London, Special Publications 443, 235–251.

Toprak E, Olivella S, Pintado X, 2018. Modelling engineered barriers for spent nuclear fuel repository using a double-structure model for pellets. Journal of Environmental Geotechnics 7(1), 1–70.

Tsiampousi A, Zdravkovic L, Potts D M, 2013. A new Hvorslev surface for critical state type unsaturated and saturated constitutive models. Computers and Geotechnics, 48, 156–166.

UPC, 2018. Code_Bright User's Guide. Civil and Environmental Engineering Department. Barcelona: Technical University of Catalonia.

Van Genuchten R, 1978. Calculating the unsaturated hydraulic permeability conductivity with a new closed-form analytical model. Water Resources Research, 37(11), 21–28.

Van Genuchten M T, 1980. A closed-form equation for predicting the hydraulic conductivity of unsaturated soils. Soil Science Society of America Journal, 44, 892–898.

Vargaftik N B, 1975. Tables on the Thermophysical Properties of Liquids and Gases. 2nd ed. New York: John Wiley & Sons.

Villar M V, 2002. Thermo-hydro-mechanical characterisation of a bentonite from Cabo de Gata: A study applied to the use of bentonite as sealing material in high-level radioactive waste repositories. ENRESA Technical Publication 01/2002, Empresa Nacional de Residuos Radiactivos, Spain.

Villar M V, Lloret A, 2004. Influence of temperature on the hydro-mechanical behavior of a compacted bentonite. Applied Clay Science 26, 337–350.

Villar M V, 2005. MX-80 Bentonite. Thermo-Hydro-Mechanical characterisation performed at CIEMAT in the context of the Prototype Project. CIEMAT CIEMAT/DIAE/54540/2/04, Centro de Investigaciones Energéticas, Medioambientales y Tecnológicas, Spain.

Villar M V, Martín P L, Barcala J M, 2005. Infiltration test at isothermal conditions and under thermal gradient. CIEMAT CIEMAT/DMA/M2140/1/05, Centro de Investigaciones Energéticas, Medioambientales y Tecnológicas, Spain.

Villar, M V, Iglesias, R J, Abós H, Martínez V, De la Rosa C, Manchón M A, 2016. FEBEX-DP on-site analyses report. Arbeitsbericht NAB 16-12, National Cooperative for the Disposal of Radioactive Waste, Switzerland.

Villar M V, 2017. FEBEX-DP Post-mortem: THM/THG Analysis Report. NAB 16-17, National Cooperative for the Disposal of Radioactive Waste, Switzerland.

Villar M V, Iglesias R J, Garcia-Siñeriz J L, 2018. A Heterogeneous Bentonite Barrier after 18 Years Operation: Final Physical State of the Bentonite Barrier of the Febex in Situ Test. Journal of Environmental Geotechnics 7(2), 1–45.

Voborny O, Adank P, Hürlimann W, Vomvoris S, Mishra S, 1991. Grimsel Test Site. Modelling of groundwater flow in the rock body surrounding the underground laboratory. NAGRA NTB 91-03, National Cooperative for the Disposal of Radioactive Waste, Switzerland.

Walker W R, Sabey J D, Hampton D R, 1981. Studies of Heat Transfer and Water Migration in Soils. Final Report. DOE/CS/30139-T1. Department of Agricultural and Chemical Engineering, Colorado State University, USA.

Wang W, Rutqvist J, Görke U J, Birkholzer J T, Kolditz O, 2011. Non-isothermal flow in low permeable porous media: a comparison of Richards' and two-phase flow approaches. Environmental Earth Sciences, 62(6), 1197–1207.

Åkesson M, Börgesson L, Kristensson O, 2010. SR-Site data report. THM modelling of buffer, backfill and other system components. SKB TR 10-44, Svensk Kärnbränslehantering AB.

Appendix A

Specifications Stage 1 – Operational period until first dismantling

A1 Introduction

The Febex in situ test Task will be developed within the framework of the Engineered Barrier System (EBS) Task Force. The envisaged objectives of the task are:

- Enhance understanding of the THM EBS behaviour during the transient phase.
- Study the state of the engineered barrier at two different stages of its evolution. Observation of degree of homogenization.
- Improve the computational capabilities and validate the performance of coupled THM formulations and associated codes.
- Develop (or enhance) constitutive relationships of the bentonite: thermal, hydraulic and mechanical.
- Compare the performance of different formulations, numerical codes and constitutive laws.
- Examine other issues of potential interest such as: gap between dummy heater and bentonite, gap between rock and bentonite, swelling through liner grids, closure of joints between bentonite blocks.

A1.1 Test to be modelled

The FEBEX (Full-scale Engineered Barriers Experiment in Crystalline Host Rock) "in situ" test was a full-scale test conducted during 18.4 years in the Grimsel URL (Switzerland) managed by NAGRA. It was based on the ENRESA AGP Granito (Deep Geological Disposal, Granite) reference concept. A 70.4 m long drift with a circular section 2.28 m in diameter was excavated in the Grimsel granite. In the last 17.4 m of the gallery, two electrical heaters of dimensions and weight equivalent to those considered in the ENRESA and NAGRA concepts were emplaced and in the remaining space compacted bentonite blocks were emplaced. The test zone was closed with a concrete plug (see Figure A-1).

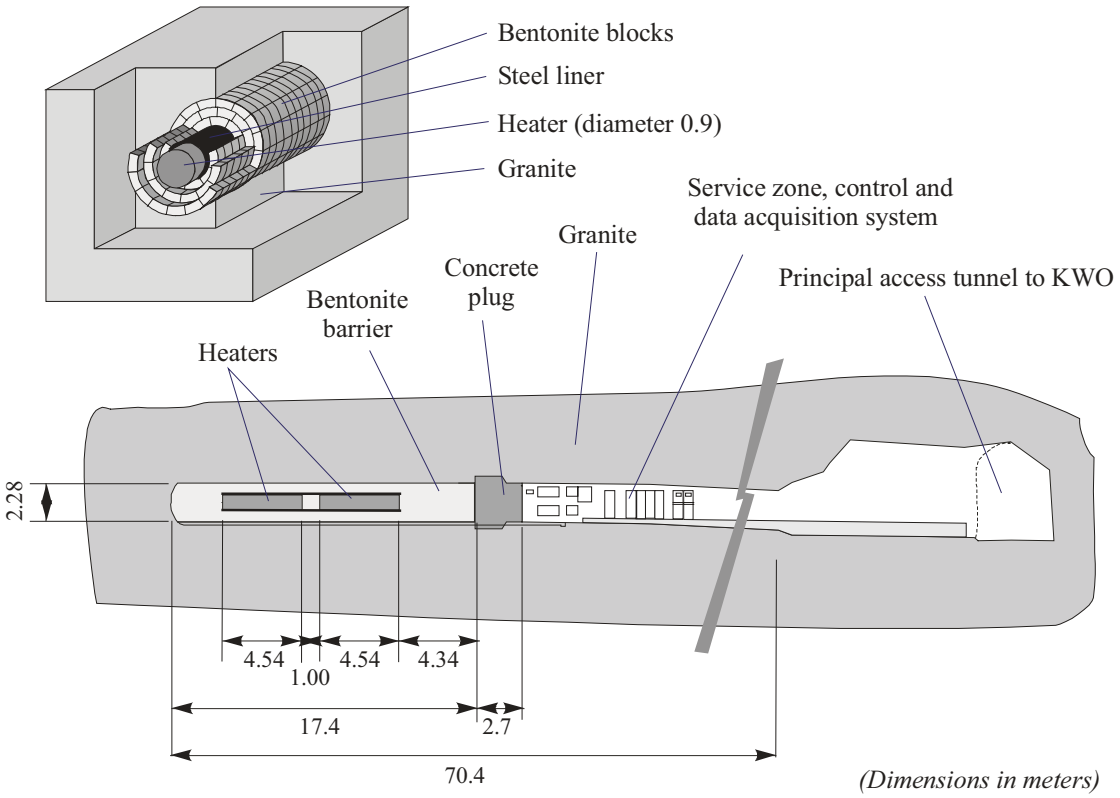

Figure A-1. *FEBEX "in situ" test layout (ENRESA 2000).*

The experiment was instrumented with sensors monitoring the thermo-hydro-mechanical processes taking place in the clay barrier and in the surrounding Grimsel granite. The experiment was in operation during 5.0 years. Thereafter, the outer heater was switched off and the outer half of the experiment was dismantled, whereby samples were taken from various points of the rock, the concrete and the bentonite buffer. During this first dismantling, the remaining half of the experiment, including the second heater, continued in operation. This remaining half of the experiment was in operation during 13.2 years more. Thereafter, the experiment was completely dismantled and, as before, samples from various points were taken. Table A-1 summarizes the dates of important events in the FEBEX in situ experiment.

Table A-1. Summary of important dates in the FEBEX in situ experiment.

Date	Event
25.09.1995	Start of tunnel excavation
30.10.1995	End of tunnel excavation
01.07.1996	Start of installation
15.10.1996	End of installation
27.02.1997	Heaters switch on (day 0)
28.02.2002	Heater #1 switch off
19.07.2002	End of first dismantling
20.04.2005	Heater #2 switch off
20.07.2015	End of dismantling

A1.2 Stages of the Task

The work to be performed in the Task has been divided into 2 stages:

- Stage 1: Operational period of the FEBEX experiment up to and including the dismantling of the first heater (5.0 years). The duration time should allow teams to become familiar with the problem and to develop/tune their formulations and codes for the FEBEX case.
- Stage 2: Operational period of the FEBEX experiment after the dismantling of the first heater up to and including the final dismantling of the test (13.2 years).

A1.3 Contents of the document

This document contains a detailed description of the Febex in situ test (the object of the Task) and a summary account of the properties of the Febex bentonite. The last section is devoted to the results demanded in the Task and it should be considered provisional until they are discussed with the modelling teams at the forthcoming EBS Task Force meeting. Once the set of requested results are agreed upon, the format specifications for the modelling output will be issued.

A2 The FEBEX in situ test

The purpose of the FEBEX (Full-scale Engineered Barriers Experiment) project was the study of the various processes occurring in the near field of a high activity radioactive waste storage. Specifically, three objectives were defined: (1) demonstration of the feasibility of the construction of engineered barriers, (2) study of the thermo-hydro-mechanical (THM) processes in the near field and (3) study of the thermo-hydro-geochemical (THG) processes in the near field. The FEBEX project had three main components, namely: (1) an “in situ” test in natural conditions and at real scale, (2) a mock-up test at near-to-real scale and (3) a series of laboratory tests to complement the information of the two large scale tests.

The first 3 phases of the FEBEX project started in 1994 and ended in 2007. During this period, the FEBEX in situ test was the research subject in 3 subsequent European research projects: FEBEX, FEBEX II and NF-PRO. The FEBEX in situ test was based on a ENRESA’s HLW disposal reference concept: AGP Granito (Deep Geological Disposal, Granite). A 70.4 m long drift with a circular section 2.28 m in diameter was excavated in the granite of the Grimsel Test Site using a TBM between the 25th of September 1995 and the 30th of October 1995. The geology and geohydrology of the rock

surrounding the drift were extensively investigated. The test area (see Figure A-2) occupied the last 17.4 m of the drift. Two electrical heaters with the same dimensions and weight as the canisters considered in the ENRESA and NAGRA concepts were horizontally placed along the axis of the drift and surrounded by highly compacted bentonite blocks. Due to water input from the host rock, the bentonite blocks will swell and provide an impervious sealing. A 2.70 m thick concrete plug isolated the test area. A total of 632 sensors were installed in the clay barrier, the surrounding rock, the heaters and the service zone to monitor the THM behaviour of the test.

The installation of the experiment was made between the 1st of July 1996 and the 15th of October 1996. The two heaters were switched on the 27th of February 1997 and 61 days later the temperature of 100 °C was reached on the heaters. Thereafter, the heating power was regulated so as to keep that temperature constant. On the 28th of February 2002, after 5.0 years of operation, the first heater was switched off, the concrete plug was demolished and the first 7.865 m of the test area were dismantled (see Figure A-3). The corresponding bentonite blocks and the first heater were extracted, a 1 m long dummy steel cylinder was emplaced to fill the void left by the extracted heater and a new 2.98 m thick shotcrete plug was emplaced in two stages, due to the need to install new instruments in the remaining part of the test. Samples taken from various points of the extracted bentonite blocks were analysed. This first dismantling of the experiment ended on the 19th of July 2002. During this dismantling, care was taken to cause a minimal disturbance to the section of the test corresponding to the second heater, which remained in operation at all times. The experiment continued in operation until the end of 2007.

As a continuation, the FEBEXe (extension) project started in 2008 and ended in 2014. Finally, as an additional continuation, the FEBEX-DP (dismantling project) project started in 2014 and it being completed. On 20th of April 2015, after 18.2 years of operation, the second heater was switched off, afterwards the shotcrete plug was demolished and the experiment was completely dismantled. Samples taken from various points of the removed bentonite blocks were analysed. This final dismantling of the experiment ended on the 20th of July 2015. A short overview video of the FEBEX-DP project, which includes images of the location of the Grimsel URL, the FEBEX drift excavation (25.09.1995 – 30.10.1995), the emplacement of FEBEX bentonite blocks (01.07.1996 – 15.10.1996) and the dismantling of the second heater (2015) is available at http://grimsel.com/gts-phase-vi/febex-dp/febex-dp-introduction (4 minutes, 27 seconds).

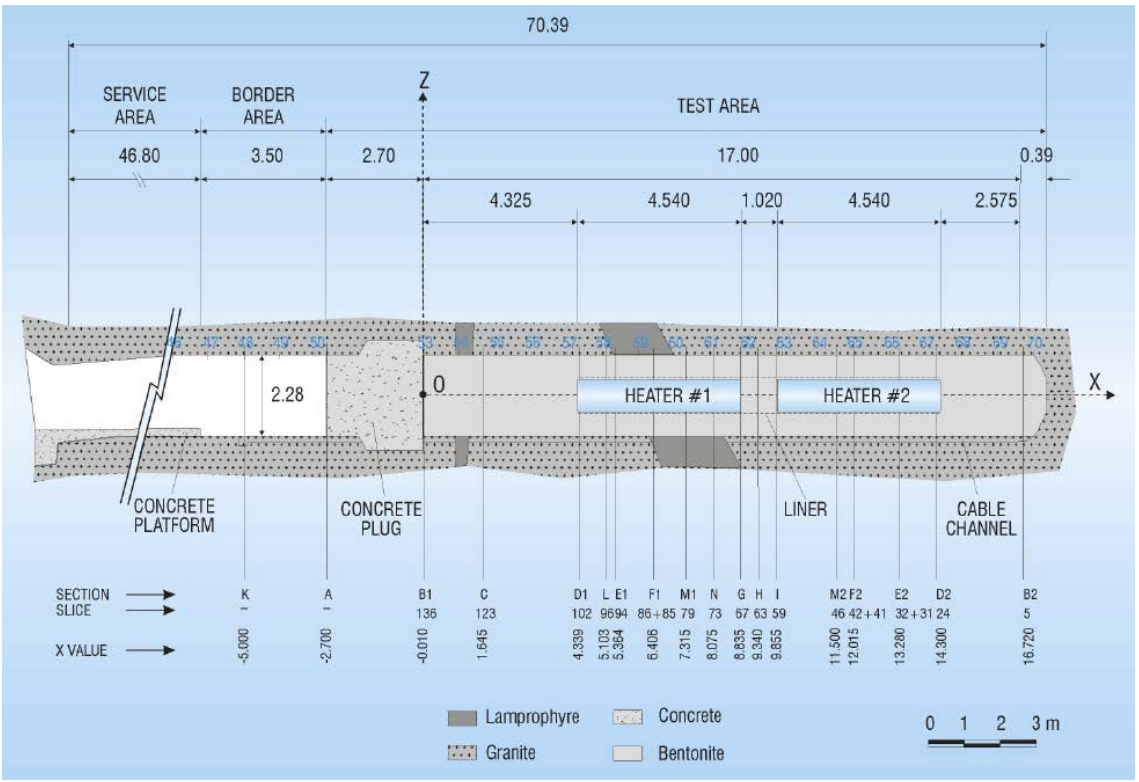

Figure A-2. *General layout of the FEBEX in situ test (Bárcena et al. 2003).*

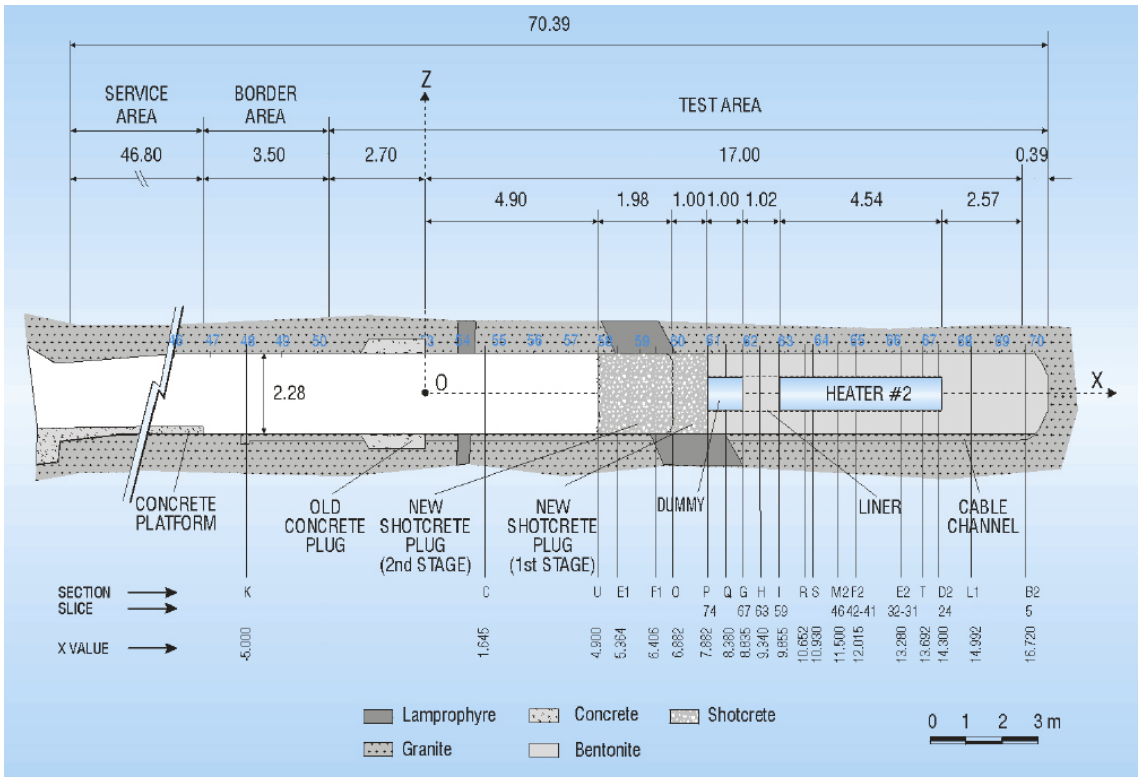

Figure A-3. *In situ test configuration after dismantling of heater #1 (Bárcena et al. 2003).*

A2.1 The FEBEX experiment at the Grimsel Test Site

The Grimsel Test Site is at an elevation of 1 730 m above sea level, around 450 m beneath the east flank of the Juchlistock mountain in the granitic rocks of the Aare Massif in central Switzerland (see Figure A-4 and Figure A-5). It is linked with the northern Grimsel Pass by a short approach road and a horizontal access tunnel around 1.2 km long leading to the Test Site itself. The Grimsel Test Site is operated by NAGRA, the Swiss agency for nuclear waste disposal.

The Grimsel Test Site is located in a tunnel system which branches off from the main access tunnel to the underground power station of the KWO (Kraftwerke Oberhasli AG). The GTS tunnel system consists of a laboratory tunnel with a total length of almost 1 000 m and a central building which houses the whole infrastructure such as offices, the ventilation plant, workshops and other installations (see Figure A-6). The laboratory tunnel has a diameter of 3.50 m and was excavated in 1983 in six months using a full-face tunnelling machine. Figure A-6 shows the location of the most important experiments which have been performed in the Grimsel Test Site, as well as the exploratory boreholes and the three 150 m long boreholes for the geophysical test field (US). Not shown in these figures are some 120 test-specific boreholes with an overall length of over 2 000 m.

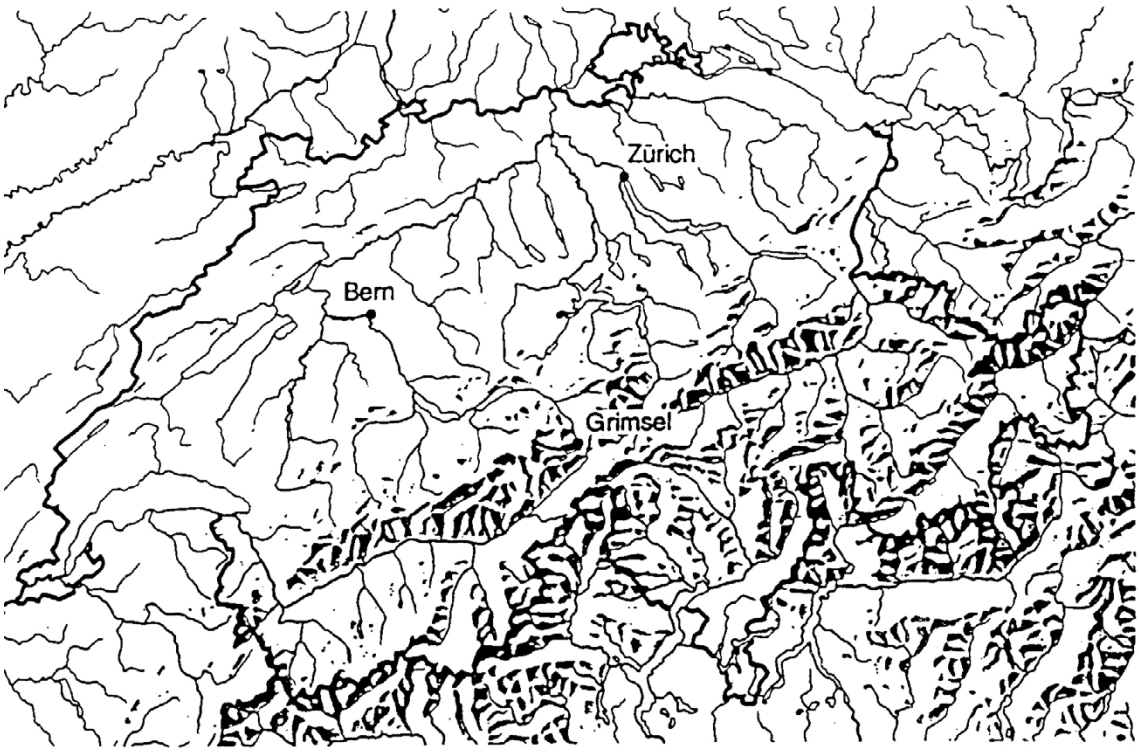

Figure A-4. *Location of Nagra's underground test facility at the Grimsel Pass in the Central Alps (Bernese Alps) of Switzerland (NAGRA).*

Figure A-5. *Grimsel Area (view looking West) (1. Test Site; 2. Juchlistock; 3. Lake Räterichsboden; 4. Lake Grimsel; 5. Rhone Valley) (NAGRA).*

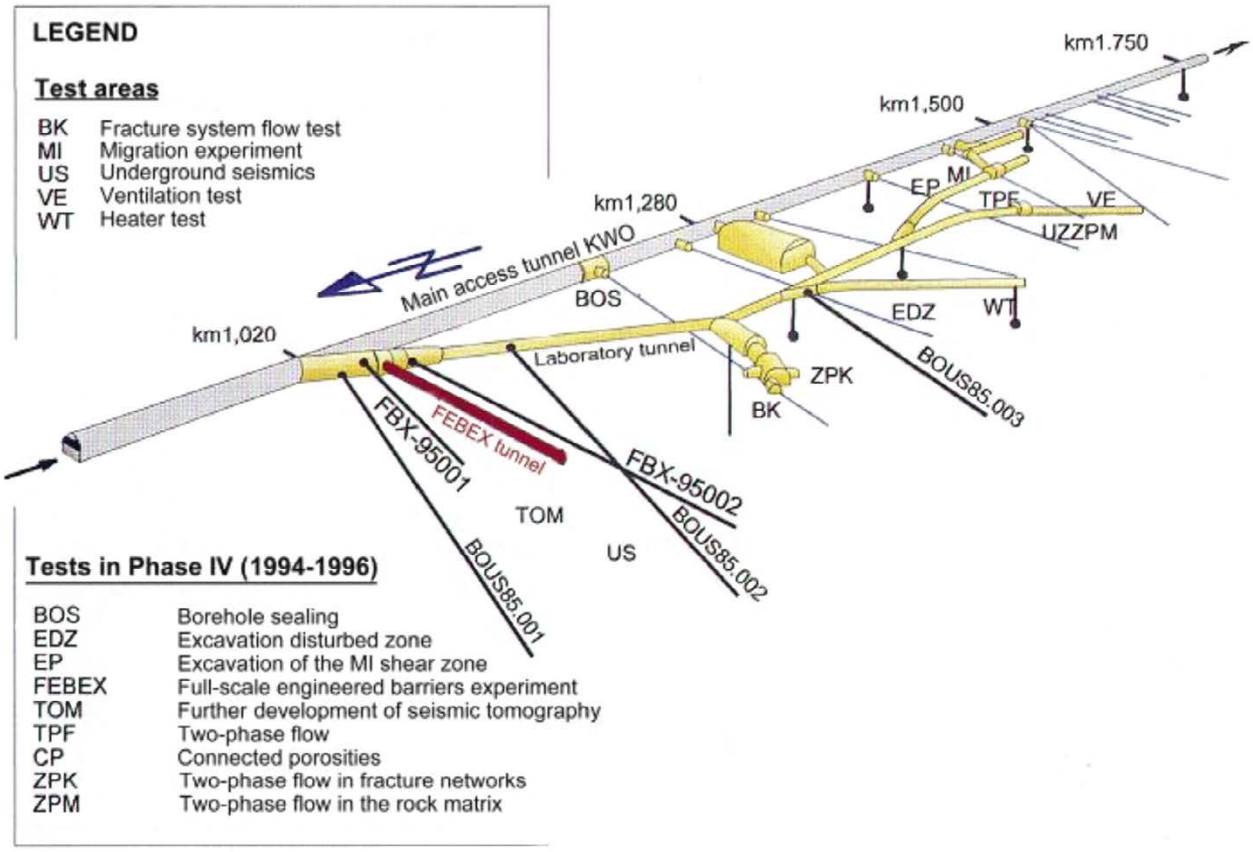

Figure A-6. *Location of tests performed at the Grimsel Test Site during Phase IV (1994–1996) (Pardillo et al. 1997).*

A2.1.1 Geology and hydrogeology of the Grimsel Test Site

Extensive geological and hydrogeological characterizations have been performed at the multiple experiments carried out and ongoing at the GTS. In October 1985, the Swedish Geological Co. conducted a radar reflection survey using the three boreholes of the US test area. The combination of radar results and geological information allowed to construct a geological model of the site, as explained in Falk et al. (1988). Geology of the area is documented in Keusen et al. (1989) which provides the general frame of the GTS in the context of the Swiss Alps. The GTS is excavated in a rock mass of intrusive nature. Most of this host rock is granite and granodiorite, which are affected by several tectonic episodes. These rocks are intruded by sets of lamprophyres and, to a lesser extent, by aplites. Keusen et al. (1989) found 12 possible discontinuity systems (see Figure A-7), from which the systems shown in Table A-2 were selected as those clearly existing.

Table A-2. Discontinuity systems shown to exist at the GTS (Keusen et al. 1989).

System	Comments
S_2	Main schistosity (azimuth strongly overlapping with S_1; the two systems cannot be separated on the basis of orientation alone)
S_1 and S_3	Equivalent system pair (conjugate)
S_4/K_4 and K_2/L_2	Equivalent system pair (+ orthogonal)
K_1 and K_3	Equivalent system pair (conjugate)
ZK	Tension joints

Based on Keusen et al. (1989) and on direct observations, Pardillo et al. (1997) suggest the following geological features as relevant for regional groundwater flow:

- Shear zones S_1 and S_2, of azimuth 140–150/80–90.
- Fracture zones and lamprophyre dykes, of azimuth 205–220/80.

Shear zones are of considerable thickness at the area (5 to 20 m). At the intersection with tunnels, they display major outflows indicating their relevance as preferential flow paths. Distribution of hydraulic parameters in the shear zone or whether the hydraulic conductivity tensor displays preferential directions is uncertain. Lamprophyre dykes have also considerable dimensions (thickness up to several meters), although their relevance as preferential flow paths is not so important as shear zones. A preferential flow path within these dykes is the contact surface between the lamprophyre and the host rock. Hence, it is not surprising to observe concentrated outflows at these surfaces at their intersections with the tunnels and drifts. Some of the thickest lamprophyres contain smaller fractures parallel to the main azimuth. These fractures enhance the hydraulic conductivity in this plane, but prevent groundwater flow in a normal direction to them. Thus, one would consider the hydraulic conductivity of these dykes as anisotropic. Both shear zones and lamprophyres are traceable from the tunnel daylights to surface outcrops. Figure A-8 shows the major geological features in a surface exposure, and the position of the GTS excavations. Figure A-9 shows the general geological model of the Grimsel Test Site. Figure A-10 correlates the surface outcrops and the intersections of the tunnels. The FEBEX drift which is located at the Northern end of the GTS, is bounded by two main shear zones according to Figure A-8 and Figure A-10.

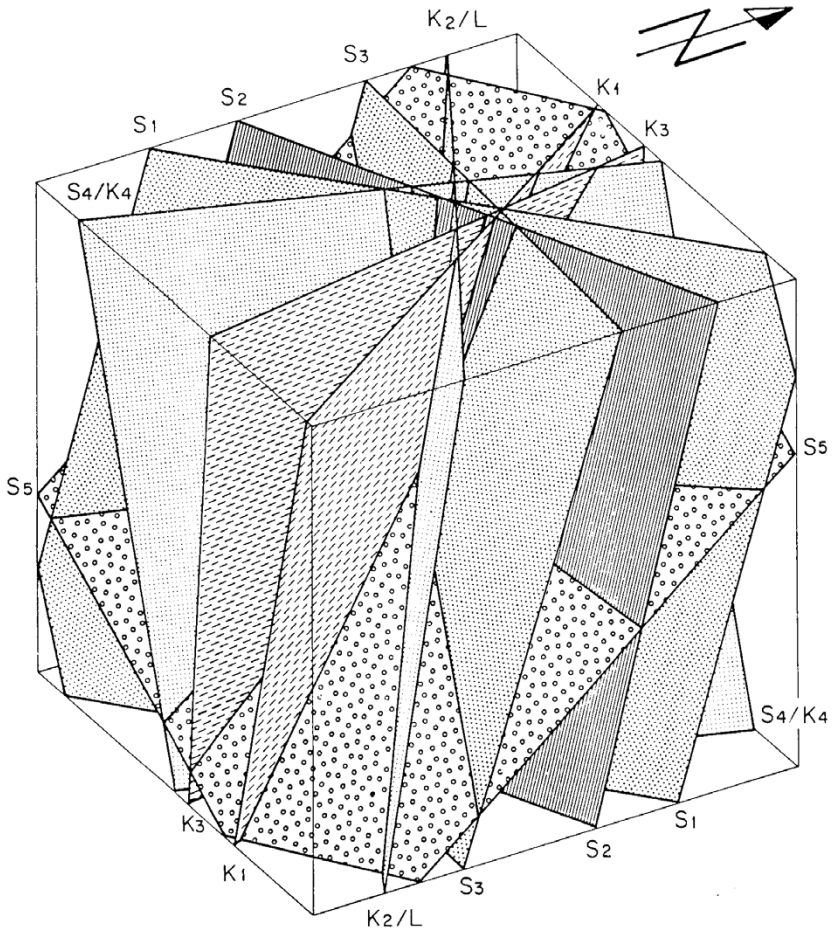

Figure A-7. *Block diagram of the dominant fracture systems (S: schistosity-related systems; K: joint systems; L: lamprophyre). For a better overview, the sub-horizontal system ZK and the hypothetical system S6 were left out (Keusen et al. 1989).*

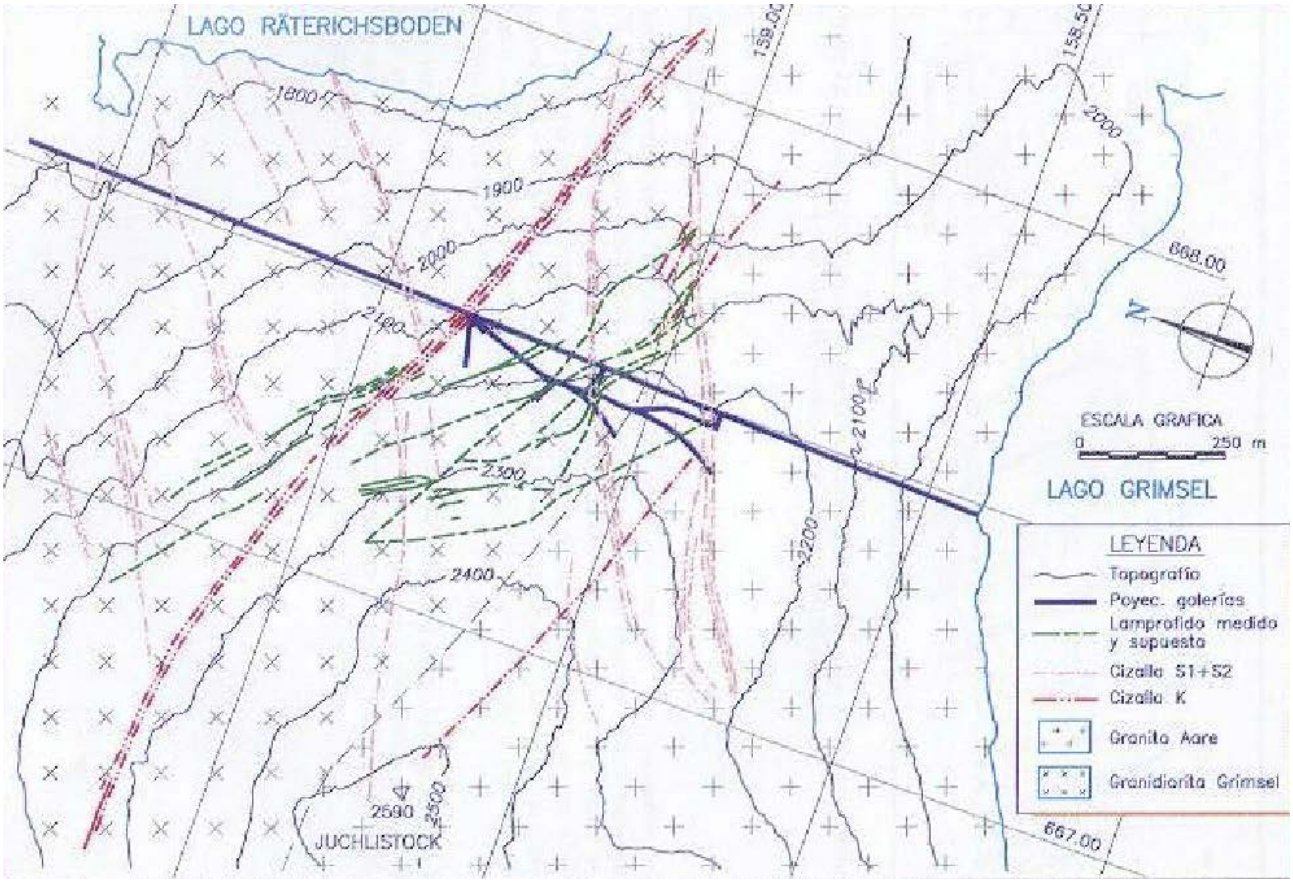

Figure A-8. *Geological map of the Grimsel area (Guimerà et al. 1998).*

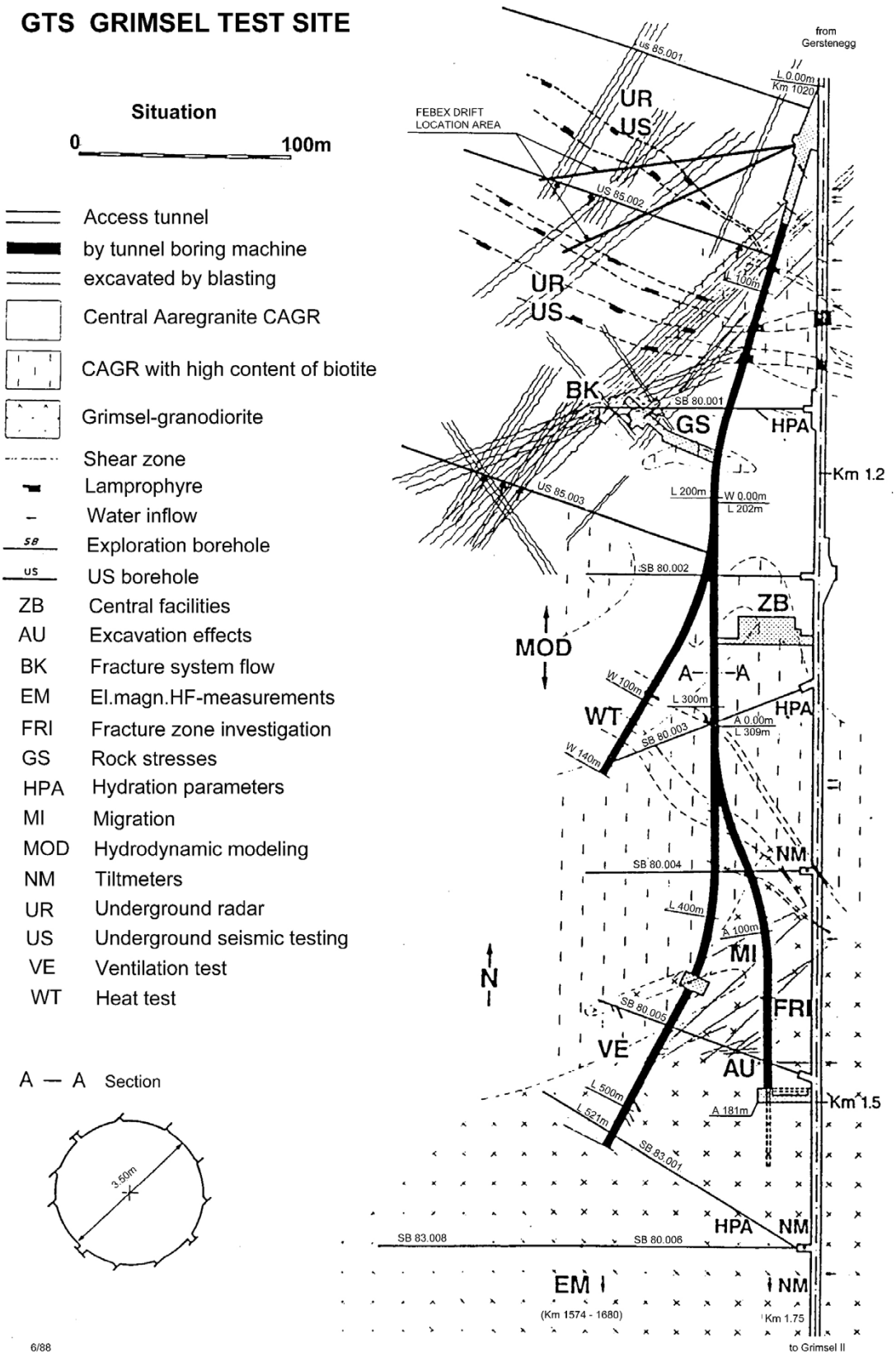

Figure A-9. *Geological model of the Grimsel Test Site (NAGRA).*

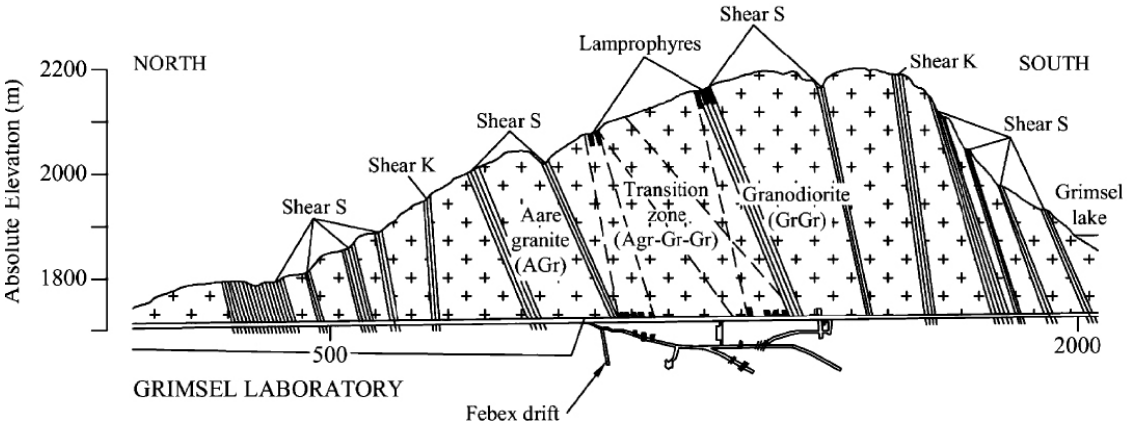

Figure A-10. *Geological cross section of the Grimsel area showing the major geological structures and their relative position at the KWO and GTS tunnels. (simplified from Guimerà et al. 1998).*

The GTS is excavated in a fractured rock mass of low permeability. Thus, parameter values will display high variability due to the heterogeneity of the medium. When measurable, outflows are small (in the order of ml/min). The numerical model produced by Voborny et al. (1991) described the hydrogeology at two scales: an area of several kilometres around the GTS and the area in the vicinity of the GTS in more detail. The regional model evidenced the importance of the topography as the main driving force of groundwater flow. The boundary conditions were of prescribed head on surface, discharge at valleys and tunnels (when present) and nil flow across the lateral and bottom boundaries. Groundwater discharges towards the Aare river valley. Therefore, calculated heads of the model points to a regional direction N–NW, according to the main direction of this valley. The presence of underground excavations disturbs such head distribution. Figure A-11 shows a head distribution at the GTS plane of this model, where the contribution of the most transmissive features is not so evident due to the strong hydraulic gradients imposed by the tunnels.

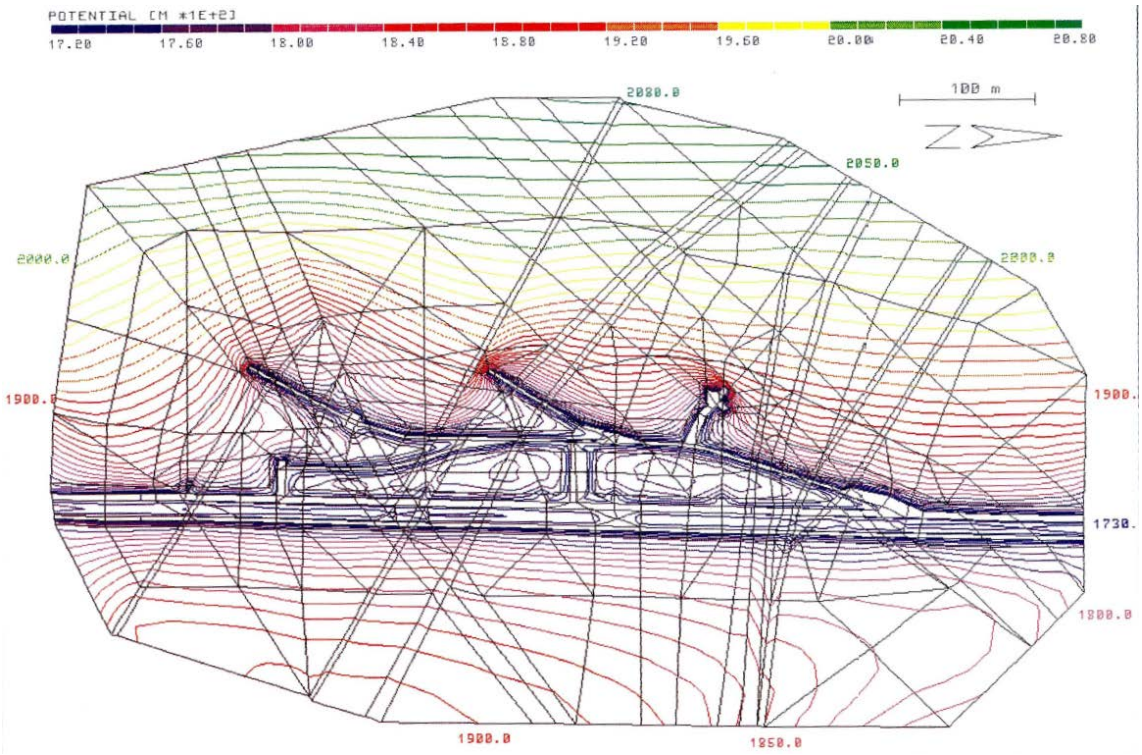

Figure A-11. *Computed head distribution at the GTS plane (Voborny et al. 1991). Note that in this plan view, heads at the FEBEX vicinity are mainly controlled by the tunnel presence and by the shear zone which is the target of the BK area.*

A2.1.2 Key data of the main rocks at Grimsel URL

Values of important mechanical properties of granitic rocks may be found in Amiguet (1985). This report is a summary from a literature review, including tests carried out in the Grimsel Test Site. The report contains (1) tables with characteristic values of various granitic rocks; (2) a summary table with typical values of intact granite and (3) diagrams showing the behaviour of various characteristic parameters under various mechanical and thermal conditions. For instance, Table A-3 shows a summary with the mean and possible values of intact granite properties. The ranges include most results of investigations, but they do not contain all the possible values nor correspond to a statistical standard deviation.

Keusen et al. (1989) (see Table A-4) gives rock mechanical parameters, together with a few geophysical parameters, and makes two important remarks: (1) the majority of measurements were carried out on drill cores in the laboratory and, because the in situ stresses are higher, do not correspond to true in situ values; (2) parameters refer to the intact rock on a small scale and not to the whole rock body on a large scale, where fractures and changes in rock type will have an influence.

Unconfined compression tests using two specimens of granite and two specimens of lamprophyre recovered from in-drift boreholes SF22 and SF13 were carried out in the Structural Technology Laboratory of the Construction Department of UPC (Pintado and Lloret 1997). The procedure adopted was based on the ASTM standard test method D3148-86. Three 60 mm long strain gauges were mounted centrally on each specimen, equally spaced around the circumference and parallel to the longitudinal axis. The stress versus axial strain recorded in the pre-failure regime of each test is shown in Figure A-12. A straight line was fitted through the linear part of each curve and its slope was used to calculate the elastic modulus. The location and type of rock of the specimens tested with the results obtained are summarised in Table A-5.

Table A-3. Properties of intact granite (Amiguet 1985). (* means in situ stress condition).

Property	Versus	Mean value	Range	Units
bulk density		2640	2600–2680	kg/m^3
grain density		2680	2650–2700	kg/m^3
porosity		1.6	0.5–2.5	%
uniaxial compression strength		185	150–220	MPa
Young's modulus		60	45–75	GPa
Poisson's ratio		0.25	0.20–0.30	-
tensile strength		10	5–15	MPa
triaxial strength	conf. pressure			
	5 MPa	35	25–40	MPa
	10 MPa	45	35–55	MPa
	20 MPa	65	55–75	MPa
	50 MPa	105	95–120	MPa
	100 MPa	160	140–180	MPa
	200 MPa	240	200–280	MPa
angle of friction (natural joint)		32	25–40	°
p-wave velocity		*5600	5000–6200	m/s
s-wave velocity		*3400	3000–3600	m/s
coef. linear thermal expansion		8.0×10^{-6}	$(5–12) \times 10^{-6}$	K^{-1}
coef. vol. thermal expansion		25×10^{-6}	$(20–30) \times 10^{-6}$	K^{-1}
thermal conductivity		3.3	2.7–3.8	W/mK
specific heat		920	800–1250	J/kgK
permeability		10^{-12}	$(0.1–5) \times 10^{-12}$	m/s

Table A-4. Rock mechanical parameters of the main rocks at the Grimsel Test Site (Keusen et al. 1989). (* refers to fractures).

Parameter	Granite (Central Aare)	Granodiorite (Grimsel)	Aplite	Lamprohyre	Units
density	2660 ± 23.8	2706 ± 13.6	2599 ± 17.4	2909 ± 31.0	kg/m^3
porosity	0.4–1.0				vol%
uniaxial comp. strength	169.1 ± 37.1	116.9 ± 47.9	225.6 ± 45.4	127.0 ± 31.8	MPa
Young's modulus E_{50}	53.3 ± 11.0	47.3 ± 15.4	60.2 ± 8.9	42.4 ± 8.5	GPa
Poisson's ratio	0.37 ± 0.12 0.33 ± 0.03	0.33 ± 0.15	0.40 ± 0.12	0.33 ± 0.17	-
tensile strength	9.06 ± 1.48	9.54 ± 2.17	9.27 ± 0.95	12.55 ± 3.59	MPa
triaxial comp. strength (σ_3 ; σ_1)	5.0 ; 263.0 ± 29.9 10.0 ; 333.0 ± 20.6 20.0 ; 410.0 ± 63.8	5.0 ; 230.0 ± 70.7 10.0 ; 287.0 ± 24.7 20.0 ; 355.0 ± 28.3	5.0 ; 297.0 10.0 ; 395.0 20.0 ; 455.0	5.0 ; 240.0 20.0 ; 226.0 ± 44	MPa
friction angle	(*) 33	(*) 30 ± 2 29	(*) 34 36	32.5 ± 3.5	°
p-wave vel. (specimen)	3111 ± 278	3351 ± 388	2948 ± 428	2120 ± 480	m/s
p-wave vel. (whole rock)	5600 ± 100	5600 ± 100	5400–5700	5700–6100	m/s
therm. conductivity (wet)	2.58 ± 0.19	2.66 ± 0.19	3.31 ± 0.35	2.21 ± 0.45	W/m·K
therm. conductivity (dry)	3.34 ± 0.35	3.22 ± 0.29	5.32 ± 0.49	2.71 ± 0.60	W/m·K
permeability	5×10^{-17} (10 MPa) $3.5–4.5 \times 10^{-12}$ (5–15 MPa) 5×10^{-12} (5–30 MPa)				m/s

Table A-5. Results of unconfined compression tests performed in specimens recovered from in-drift boreholes (Pintado and Lloret 1997). (1. depth = distance to FEBEX drift wall; 2. mean Ø = mean diameter; 3. E_{50} = Young's modulus; 4. comp = compressive strength) (Pintado and Lloret 1997).

Borehole	Depth (m)	Rock type	Mean Ø (mm)	E_{50} (GPa)	Comp (MPa)
SF22	0.17–0.27	granite	51.73	61.6	193.5
SF22	0.85–0.95	granite	51.64	50.8	110.0
SF22	12.16–12.26	lamprophyre	51.64	49.8	142.0
SF13	0.70–0.80	lamprophyre	51.78	35.7	85.4

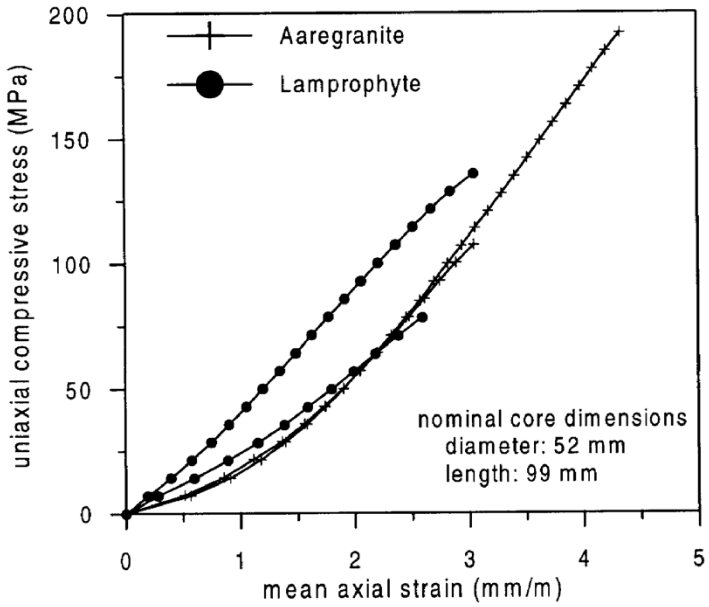

Figure A-12. *Unconfined compression tests performed in specimens recovered from in-drift boreholes (Pintado and Lloret 1997).*

Table A-6. Specimens recovered from in-drift boreholes to determine the water retention curve (Pintado and Lloret 1997) (depth = distance to FEBEX drift wall).

Specimen	Borehole	Depth (m)	Rock type
L1	SF13	0.05–0.07	lamprophyre
L2	SF22	12.14–12.16	lamprophyre
G1	SF22	0.04–0.06	granite
G2	SF22	0.06–0.08	granite
G3	SF13	0.95–0.97	granite

Water retention curves were determined at UPC (Pintado and Lloret 1997) for 2 lamprophyre and 3 granite specimens recovered from in-drift boreholes. Table A-6 shows the location and type of rock of each specimen. Suctions ranging from 2 to 200 kPa were applied using a pressure plate extractor with a porous ceramic plate. In order to apply higher suctions (0.6, 1.0 and 2.0 MPa) a pressure membrane extractor was used. For low suctions (2 and 5 kPa), suction was applied by means of a water column and for higher suctions positive air pressure was applied in the extractors. Figure A-13 shows the water retention curves obtained.

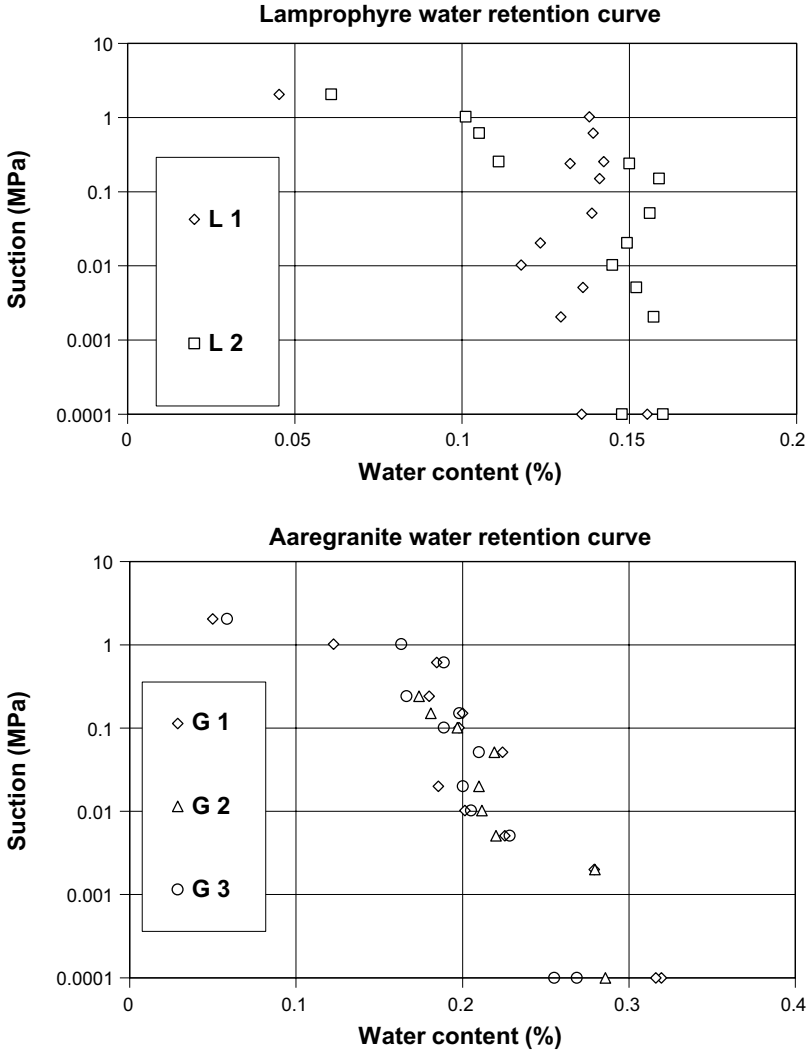

Figure A-13. *Water retention curves of lamprophyre and granite specimens (Pintado and Lloret 1997).*

These curves are coherent with the curves obtained by Schneebeli et al. (1995) performing similar tests but using samples of the ventilation test instead. On this ventilation test, Finsterle et al. (1995) obtained by backanalysis the following expressions for the retention curve and the relative permeability of the Grimsel granite:

$$s = 1.74\,(S_r^{-1.68} - 1)^{0.405} \quad \text{(A-1)}$$

$$k_r = S_r^{0.5}\,[1 - (1 - S_r^{1.68})^{0.595}]^2 \quad \text{(A-2)}$$

where s is the suction (in MPa), S_r is the degree of saturation and k_r is the relative permeability.

Values of properties of the rock around the FEBEX area may also be inferred from the geophysical investigations carried out in boreholes FEBEX 95.001 and FEBEX 95.002, and reported in Häring (1996).

In the Grimsel Test Site, investigations have been carried out to determine rock stresses. Information may be found in Bräuer et al. (1989) and Pahl et al. (1989). General remarks concerning stress measurements carried out by BGR, Hannover (Germany) are provided in Keusen et al. (1989): "(1) there is a difference of more than 10 MPa between the minimum and maximum horizontal stress; (2) the maximum horizontal stress lies between 18 and 45 MPa and the minimum principal stress between 15 and 32 MPa; (3) the maximum horizontal stresses are generally directed towards the SE, i.e. perpendicular to the main alpine schistosty S_2". It is concluded that "the stress, which is 4–5 times higher than the lithostatic pressure of around 9–12 MPa, indicates the presence of significant horizontal forces in the main compression direction NW–SE".

In the context of the project Rock Stresses carried out in the Grimsel Test Site (GS in Figure A-9) several rock stress investigations were carried out by BGR, Hannover (Germany). In these investigations several overcoring methods, borehole dilation tests and hydrofracture tests were used. Details may be consulted in Pahl et al. (1989). For instance, Figure A-14 shows the results of horizontal stress measurements using and overcoring method. Referring to this figure, Pahl et al. (1989) remark that "It can clearly be seen that the maximum stresses are approximately 25 to 40 MPa and the minimum horizontal stresses are between 15 and 30 MPa. We have then that the horizontal stresses (are) substantially higher than the depth-related overburden pressure".

Additional information may be found in Bräuer et al. (1989), where engineering geological investigations were carried out for the Rock Stresses and Fracture System Flow tests performed in the Grimsel Test Site (GS and BK in Figure A-9). The evaluation of the geological data showed structural tectonic and hence rock mechanical and rock hydraulic differences between closely neighbouring rock sections. The analysis of both test areas enables the transferability of rock stresses and rock hydraulic properties to other areas.

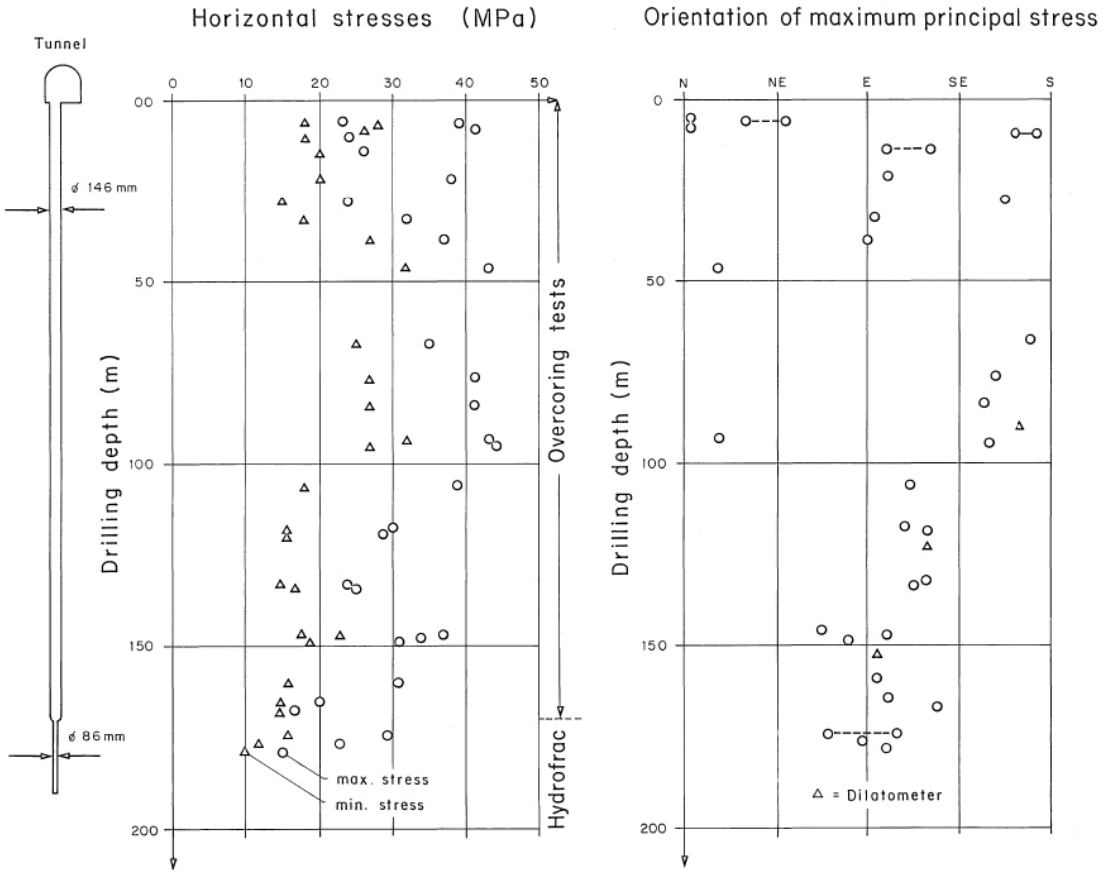

Figure A-14. *Size and direction of horizontal stresses obtained from BGR overcoring tests assuming isotropic rock mass behaviour (E = 40 GPa, v = 0.25) (adapted from Pahl et al. 1989).*

A2.1.3 Geology and hydrogeology of the FEBEX drift area

In order to perform the FEBEX in situ test, it was decided to excavate a new drift in the Underground Seismic (US) test area located in the northern part of the Grimsel Test Site. Prior to the FEBEX drift excavation, two pilot boreholes (FEBEX 95.001 and FEBEX 95.002) were drilled in the area between boreholes BOUS 85.001 and BOUS 85.002. Afterwards, the FEBEX drift was excavated between these pilot boreholes. It was parallel to FEBEX 95.002. Figure A-6 shows the location of the FEBEX drift and of the aforementioned boreholes in the GTS. From the end of the FEBEX drift, in the in situ test zone, 19 in-drift boreholes were drilled. Initially, the borehole layout was planned to be strictly radial. However, the boreholes were re-oriented in order to intersect the most relevant geological features. Figure A-15 shows a perspective of the FEBEX drift and associated boreholes. These 23 boreholes of depths ranging from 7 to 151 m (a total of about 750 m) were used to explore site of the FEBEX experiment. Geological and hydrological information, including the borehole logs may be found in Pardillo et al. (1997). All boreholes were equipped with multipacker systems by Solexperts AG and water pressures were monitored automatically. Details on the instrumentation can be found in Fierz (1996).

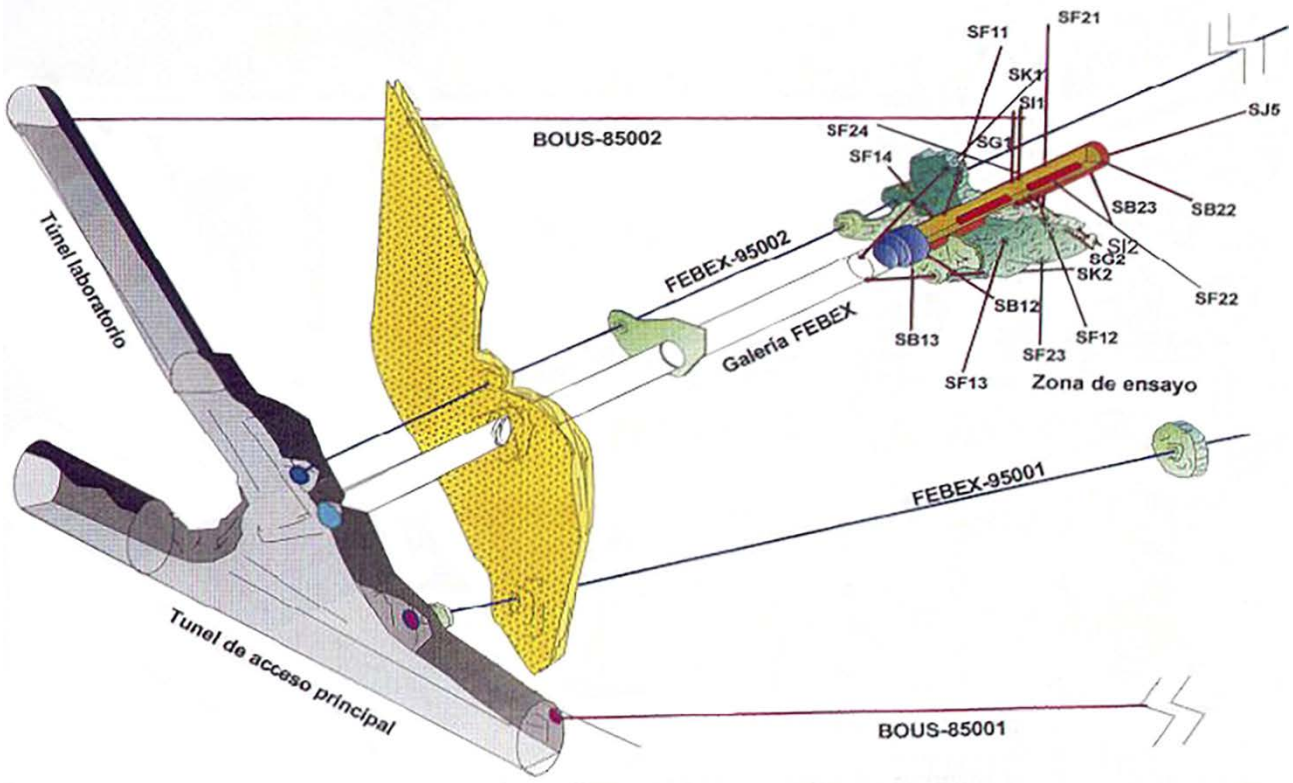

Figure A-15. *Perspective of the FEBEX drift and associated boreholes (Pardillo et al. 1997).*

The FEBEX drift is located at the Northern bound of the GTS. The most important geological features at this environment are two shear zones (K and S, see Figure A-8 and Figure A-10). Such shear zones constraint regional groundwater flow due to their 'high' transmissivity and therefore, they constitute boundaries of the FEBEX environment. Measured inflows of these shear zones towards the tunnels are on the order of 60 ml/min and 23 ml/min (K and S respectively). Such a difference in flow rate measurements may be attributed to the influence that the BK area, the GTS and the KWO exerts over the S shear zone, while the N one is only intersected by the KWO tunnel. Topography, the most pervious geological features and the tunnel presence control the hydraulic gradient at the FEBEX environment.

Available data consist of a geological map of the tunnel wall, the borehole configuration, core descriptions and head monitoring in borehole intervals. The main reference to the geology of the FEBEX area is Pardillo et al. (1997). Since this reference is only available in Spanish, a previous report (Pardillo and Campos 1996) in English, may be also of some help.

Within this domain, some other geological features are worth mentioning: a shear zone, which actually crosses the FEBEX drift at a depth of about 20 m, and a lamprophyre dyke, related to a major set of dykes. It intersects the GTS tunnel in the vicinity of the borehole BOUS 85.002, that is, close to the intersection of the S boundary. Figure A-16 and Figure A-17 display the geological map of the drift. The last 17.4 m are of immediate concern for the FEBEX experiments because the heater and the bentonite block are installed in this section. Relevant geological features at the tunnel scale include:

- Lamprophyre dykes
- 'en echelon' fractures
- Normal fractures

At about 20 m depth, the drift intersects a series of fractures with the same azimuth as shear zones. We consider this series of fractures as a shear zone because it is highly conductive (measured inflows in the order of ~30 ml/min, which can be considered high for the GTS and comparable to other shear zones).

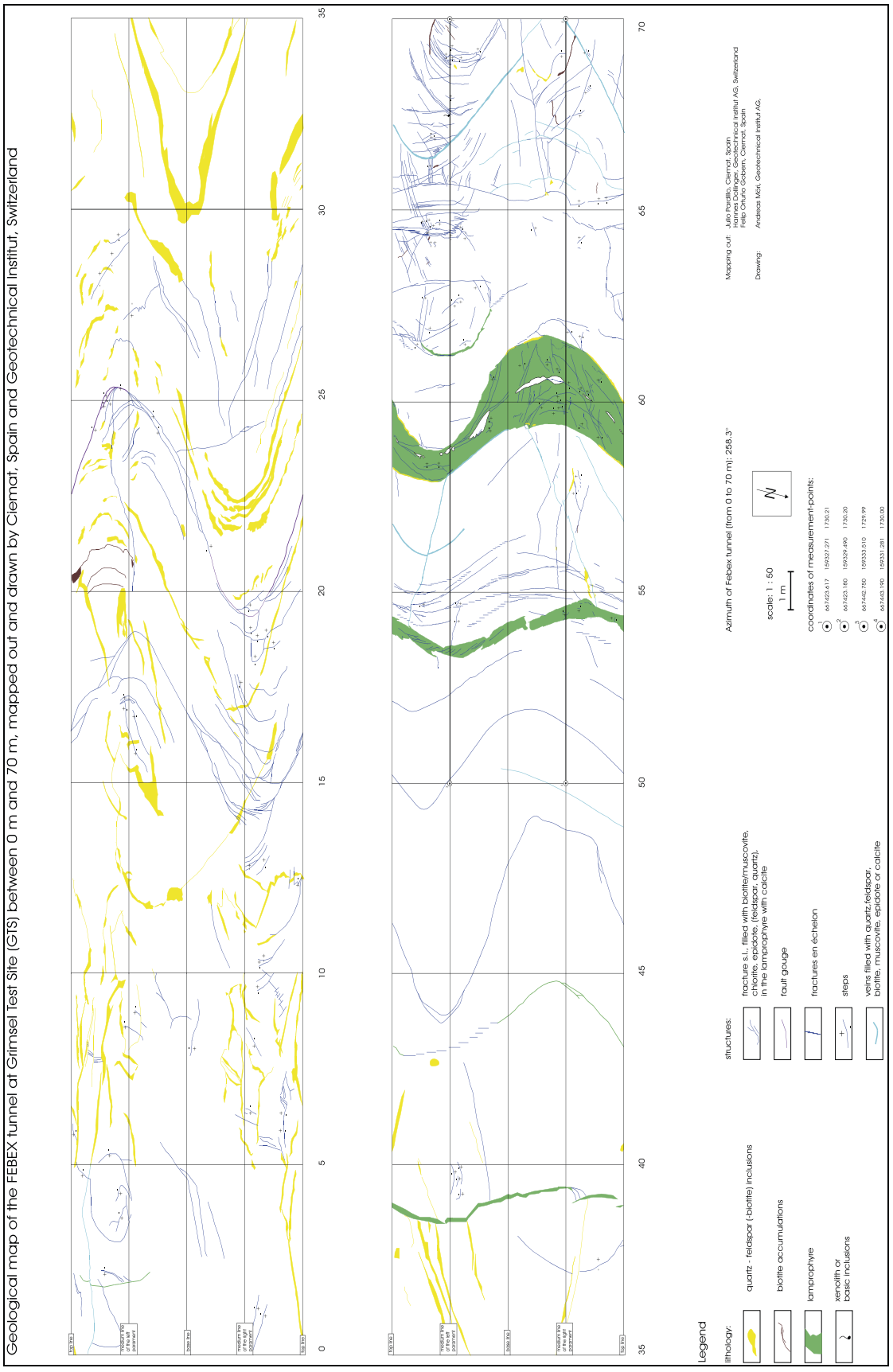

Figure A-16. *Geological map of the FEBEX drift between 0.0 m and 70.0 m (Pardillo et al. 1997). Note: zoom in to see the details of the figure.*

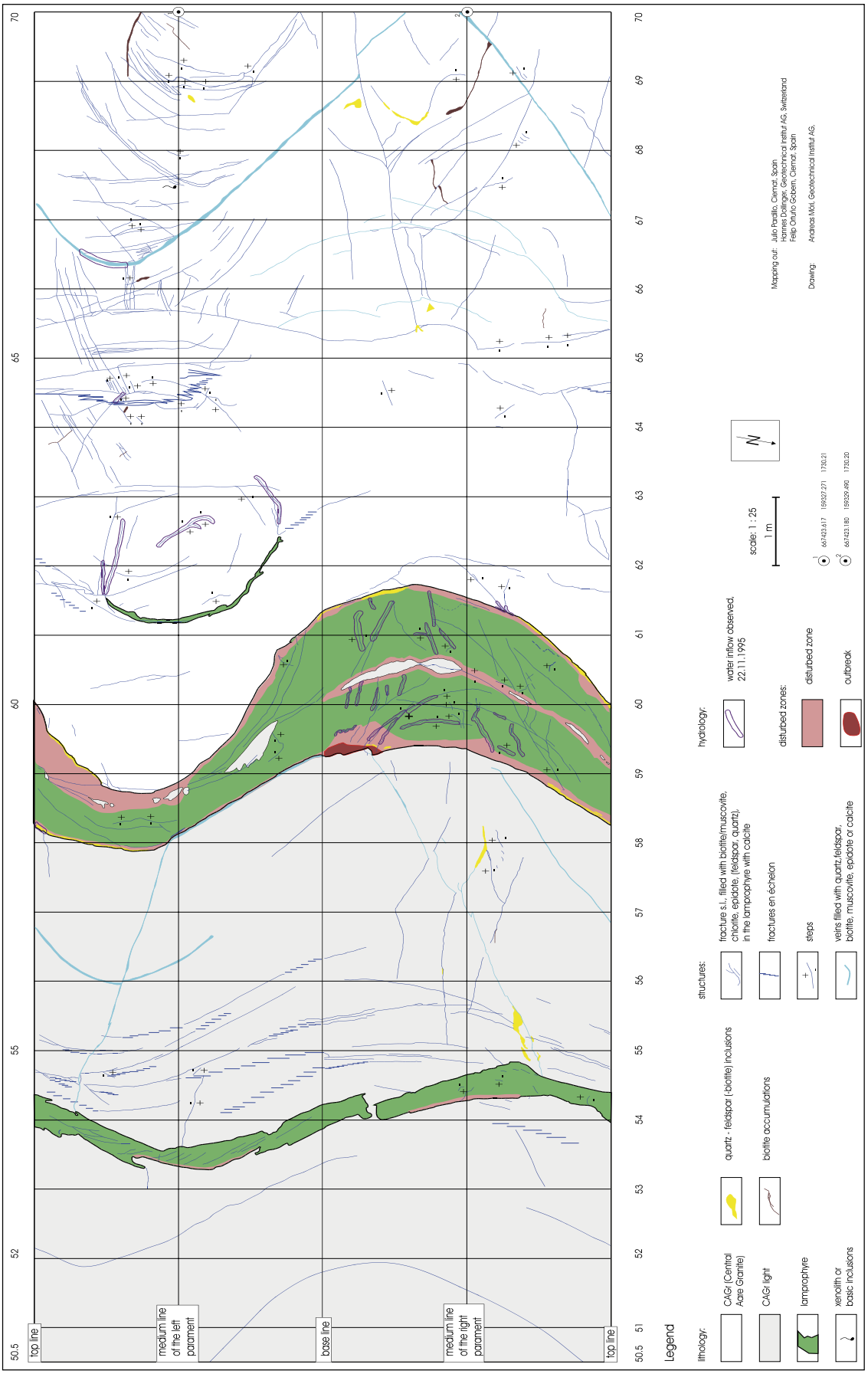

Figure A-17. *Geological map of the FEBEX drift between 50.5 and 70.0 m (Pardillo et al. 1997). Note: zoom in to see the details of the figure.*

Extensive hydraulic testing at existing and newly drilled boreholes was carried out. Tests are documented in Meier et al. (1995), Guimerà et al. (1996) and Guimerà et al. (1998). Testing progressed from static pressure recovery after a flowing period, pulse test and longer time production or injection period. The instrumentation used allowed both injection and extraction. The hydraulic tests performed allowed to determine the hydraulic conductivity and hydraulic head for each borehole interval, as well as the hydraulic parameters of the geologic features involved in the cross-hole tests. This information completed the information of the available geologic map.

After the hydraulic characterization campaign, the packer systems were removed, equipped with thermocouples and reinstalled by Solexeperts AG. The packer locations were not changed. The packer systems of in-drift boreholes SI-1 and SI-2 were removed and not reinstalled. Details may be found in Fierz (1996).

Finally, passive head monitoring was carried out from 07.96 on. Details and test results may be found in Guimerà et al. (1998).

The total water flow into the test area (the last 17.4 m of the FEBEX drift) was estimated before the tunnel excavation using borehole hydrogeological tests and steady state radial flow formula. It was also measured after the tunnel excavation using two techniques: (1) discrete flow measurements using absorbing pads on selected points on the tunnel wall and (2) bulk flow measurements of using a small gauge. In the first technique, absorbing pads were weighted before and after their emplacement to determine the volume of leaked water. Table A-7 shows the corresponding results, with values in the range between 4.5 and 8.5 ml/min.

Table A-7. Estimation and measurements of the total water flow into the test area (Guimerà et al. 1998).

Technique employed	Q (ml/min)
Estimation before tunnel excavation	8.0
Discrete flow measurement during tunnel excavation	8.5
Bulk flow measurement in January 1996	4.5
Discrete flow measurement in April 1996	7.5
Bulk flow measurement in May 1996	6.7

In the discrete flow measurement technique (F. Ortuño, personal communication), depending on the amount of water present after stopping several days the ventilation of the tunnel, various zones of water inflow were quantitatively identified on the tunnel surface of the test area, and a rank ranging from 0 to 6 was assigned to each of them. It was verified that the tunnel ventilation evaporated nearly all the incoming water. Ranks 0 and 1 were assigned to the granite matrix (surface zones), ranks 2, 3 and 4 were assigned to fractured zones (line zones) and ranks 5 and 6 were assigned to well-defined water inflow points (point zones). Using cellulose pads, that were weighted before and after their emplacement to determine the volume of leaked water, a water inflow was semi-quantitatively assigned to each of these ranks. Combination of these water inflows with the extensions (surface, length or number) of the water inflow zones yields the water inflows shown in Table A-8. The estimated total water inflow is 7.8 ml/min (27 % from matrix, 22 % from fractures, 51 % from well-defined points).

Table A-8. Assignment of water inflows to ranks, and computation of the various components of the total water inflow (F. Ortuño, personal communication).

Rank	Specific water inflow	Reference used	Area, length or points	Total water inflow
0	3.0×10^{-10} m^3/s/m^2	Point B FEBEX tunnel	75 m^2	2.25×10^{-8} m^3/s
1	7.0×10^{-10} m^3/s/m^2	L490 ventilation tunnel	18 m^2	1.26×10^{-8} m^3/s
2	1.5×10^{-9} m^3/s/m	Average of ranks 1 and 3	6.21 m	9.31×10^{-9} m^3/s
3	3.0×10^{-9} m^3/s/m	Point A FEBEX tunnel	3.62 m	1.09×10^{-8} m^3/s
4	5.0×10^{-9} m^3/s/m	Points C, D FEBEX tunnel	1.54 m	7.69×10^{-9} m^3/s
5	1.0×10^{-8} m^3/s	Measured	5 points	5.00×10^{-8} m^3/s
6	1.7×10^{-8} m^3/s	Measured	1 point	1.67×10^{-8} m^3/s
				1.30×10^{-7} m^3/s

With this information, the distribution of water input flow on the tunnel wall shown in Figure A-18 was obtained.

A2.1.4 Geometry of the FEBEX drift and associated boreholes

The co-ordinate system used in the Grimsel Test Site is the Swiss co-ordinate system. In order to define a point, use is made of east, north and height above the sea level. In order to define the direction of a line, use is made of the azimuth (angle formed by the projection of the line onto the horizontal plane with the north, measured clockwise using 0–360 degrees) and the inclination (angle formed by the line with the vertical plane, measured using 0–360 degrees). Figure A-19 below helps to clarify the aforementioned concepts.

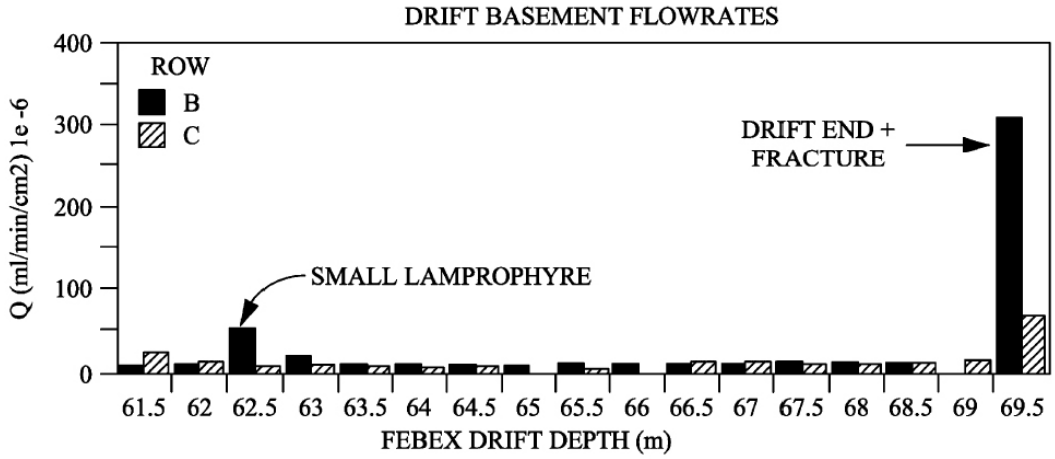

Figure A-18. *Results of inflow measurements in parts of the FEBEX area arranged in rows and their relationships to geological structures (Pardillo et al. 1997).*

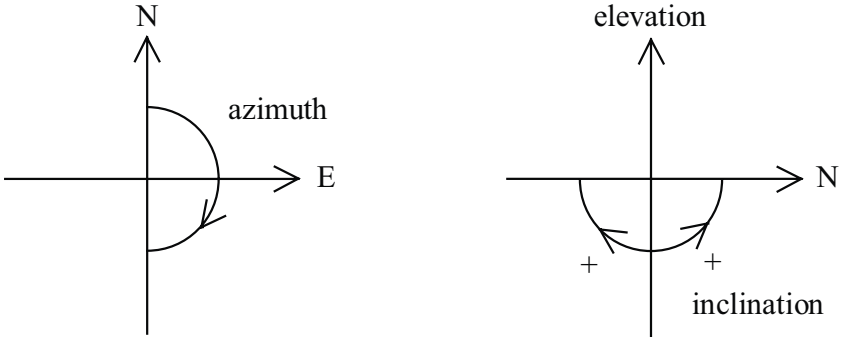

Figure A-19. *The co-ordinate system used in the Grimsel Test Site.*

Figure A-15 gives an overview the location of the FEBEX drift and associated boreholes, including the 19 short in-drift boreholes (7–15 m) which were drilled from test area of the FEBEX drift. Table A-9 and Table A-10 define the geometry of these boreholes and of the FEBEX drift. All boreholes were equipped with multipacker systems (Solexperts AG) and water pressures were monitored automatically. Details on the instrumentation can be found in Fierz (1996).

Table A-9. Co-ordinates (borehole mouth centre) and specifications of US and FEBEX boreholes, using GTS co-ordinates (US 1 = BOUS 85.001, US 2 = BOUS 85.002, FEX 1 = FEBEX 95.001, FEX 2 = FEBEX 95.002) (ENRESA).

Code	East (m)	North (m)	Height (m)	Azim (°)	Inclin (°)	Length (m)	Diam (mm)
US 1	667 500.46	159 357.13	1 728.11	290.00	75.00	149.83	101
US 2	667 481.95	159 287.77	1 729.34	290.00	75.00	150.27	101
FEX 1	667 496.71	159 347.56	1 730.04	275.40	89.43	76.00	101
FEX 2	667 493.49	159 338.67	1 730.24	258.47	89.43	132.36	86
Tunnel	667 491.92	159 342.52	1 729.34	258.30	90.69	71.41	2 280

Table A-10. Co-ordinates (borehole-mouth centre) and specifications of in-drift boreholes, using GTS co-ordinates (tunnel = FEBEX tunnel meter at which borehole starts) (ENRESA).

Code	East (m)	North (m)	Height (m)	Azim (°)	Inclin (°)	Length (m)	Diam (mm)	Tunnel (m)
SK1	667 444.86	159 333.22	1 731.10	259.10	110.00	22.00	66	48.00
SK2	667 445.00	159 332.45	1 728.96	260.90	70.00	20.00	66	48.00
SB12	667 439.41	159 332.84	1 729.83	349.00	79.20	7.00	66	53.40
SB13	667 439.59	159 331.93	1 728.91	348.40	10.10	7.00	66	53.40
SF11	667 436.86	159 331.16	1 731.17	259.00	159.80	15.00	66	56.25
SF12	667 429.04	159 330.68	1 729.73	10.00	75.00	15.00	66	64.00
SF13	667 429.95	159 329.94	1 728.91	53.40	22.50	15.00	66	63.30
SF14	667 436.97	159 330.06	1 729.74	191.80	72.00	15.00	66	56.40
SG1	667 431.11	159 329.98	1 731.17	209.00	179.40	7.00	146	62.10
SG2	667 430.87	159 331.07	1 729.83	348.00	79.20	7.00	146	62.10
SI1	667 430.13	159 329.77	1 731.17	165.20	179.40	7.00	66	63.10
SI2	667 429.89	159 330.87	1 729.83	348.00	80.00	7.00	66	63.10
SF21	667 427.66	159 329.26	1 731.17	15.10	179.30	15.00	66	65.70
SF22	667 427.42	159 330.36	1 729.83	350.00	76.90	15.00	66	65.70
SF23	667 427.68	159 329.06	1 728.91	168.20	10.00	15.00	66	65.70
SF24	667 428.51	159 328.29	1 729.83	170.00	80.00	15.00	66	65.00
SB22	667 423.16	159 329.48	1 729.83	328.60	80.20	7.00	66	70.00
SB23	667 423.38	159 328.38	1 728.89	258.20	19.90	7.00	66	70.00
SJ5	667 423.00	159 328.30	1 729.93	268.20	80.20	15.00	66	70.40

A2.1.5 Excavation of the FEBEX drift

The FEBEX drift was excavated using a TBM. The boring head had a diameter of 2.27 m. The drift was excavated from 25.09.95 to 30.10.95. The position of the FEBEX drift is given in the previous subsection. Geological and hydrogeological information may be found in Pardillo et al. (1997). Table A-11 shows the excavation status as a function of time.

Table A-11. Excavated length (in m) of the FEBEX drift as a function of time (when the TBM started (27.09.95), the length of the tunnel was 3.50 m) (Note: the excavated lengths marked with * were measured 30 min earlier than the time indicated in the table) (ENRESA).

	25 sep	26 sep	27 sep	28 sep	29 sep	02 oct	03 oct	04 oct	05 oct	06 oct
07:00			3.50	6.00	6.00	6.50	7.50	8.50	9.50	12.50
08:00			3.50				8.00		9.50	
09:00			3.50				8.50		10.00	
10:00			4.00		6.00		8.50		10.50	
11:00			4.40		6.50			8.50	11.00	12.50
12:00			4.90						11.50	13.00
13:00			4.90			6.50			11.50	13.00
14:00			5.30			6.50		8.50	12.00	13.50
15:00			5.70			7.00		8.50	12.50	
16:00			6.00			7.00		9.00	12.50	
17:00			6.00			7.50		9.00	12.50	
18:00	1.50	3.50	6.00	6.00	6.50	7.50	8.50	9.50	12.50	13.50

	09 oct	10 oct	11 oct	12 oct	13 oct	16 oct	17 oct	18 oct	19 oct	20 oct
07:00	13.50	16.50	16.50	20.90	26.50	26.50	31.70	36.00	40.50	43.65
08:00	14.00		16.90	21.30		26.90	31.70	36.00		43.65
09:00	15.00		17.30	22.10		27.30	31.70	36.00		44.55
10:00	15.00		17.70	22.50		27.70	32.50	36.90		45.00
11:00	15.00		18.10	23.30		28.50	32.90	37.35	40.50	45.45
12:00	16.00		18.50	24.10		29.30	33.30	37.80	40.95	45.90
13:00	16.00		18.50	24.10		29.30	33.30	37.80	41.40	45.90
14:00	16.50		18.90	24.10		29.30	33.75	38.25	41.40	46.35
15:00	16.50		19.70	24.50		30.10	34.20	38.70	41.85	46.35
16:00			20.10	25.30		30.50	34.65	39.60	42.30	46.35
17:00			20.50	25.70		31.30	35.55	40.05	42.75	
18:00	16.50	16.50	20.90	26.50	26.50	31.70	36.00	40.50	43.65	46.35

	23 oct	24 oct	25 oct	26 oct	27 oct	30 oct
07:00	46.35	50.00	55.70	60.95	61.90	66.65
08:00	46.35	50.00	55.70	60.95	62.40	66.65
09:00	46.35	50.95	56.65		62.85	67.15
10:00	46.35	51.45	57.15		63.80	67.60
11:00	46.85	51.90	57.60		64.30	68.55
12:00	47.35	52.40	58.10		64.75	69.05
13:00	47.35	52.40	58.10		64.75	69.50
14:00	47.80	52.85	58.55		65.25	70.00
15:00	48.30	53.80	59.05		66.20	70.45
16:00	48.75	54.30	59.50	60.95	*66.65	70.95
17:00	49.25	54.75	60.45	61.45		*71.40
18:00	50.00	55.70	60.95	*61.90		

A2.2 Components and installation of the FEBEX in situ test

The “in situ” test consisted of a full-scale simulation of a HLW disposal facility, based on ENRESA’s AGP Granito (Deep Geological Disposal, Granite) reference concept. Performance of this test implied the placing of two electrical heaters, of dimensions and weight equivalent to those of the canisters in the concept, in a 2.28 m diameter drift excavated in granite, the entire space surrounding the heaters being filled with blocks of compacted bentonite to complete the 17.4 m of barrier for the test section. This test zone was closed with a concrete plug. The test was installed in the underground laboratory managed located in Grimsel (Switzerland) and managed by NAGRA, because of the similarity between the Spanish and Swiss reference concepts. Figure A-20 shows the general scheme of the FEBEX in situ test.

In addition to the clay barrier, made up of 5 331 bentonite blocks with a total mass of 115.7 t, and the heaters, 632 sensors of very diverse types were installed. The sensors were installed to monitor the different thermo-hydro-mechanical processes that occur in both the clay barrier and the surrounding rock throughout the entire life of the test. A series of artificial chemical tracers, specimens of different metals, and gas collectors were installed in the test zone for the study of corrosion and transport phenomena.

A drift was specifically excavated for this test, in an area previously selected in accordance with the existing Grimsel laboratory database. To provide additional information, two exploratory boreholes were drilled in the area, practically parallel to the planned trace of the drift. Following excavation of the drift, a detailed reconnaissance of its geometry and geology was performed and 19 boreholes were drilled from its interior, to monitor the rock mass. A detailed hydrogeological study of the rock mass surrounding the drift was performed, using data taken from the existing boreholes in the area, the two boreholes made for the study, the walls of the drift, and the 19 boreholes drilled from the interior of the drift. The test was designed to function in an autonomous mode. Supervision, monitoring, and control were accomplished remotely from Madrid.

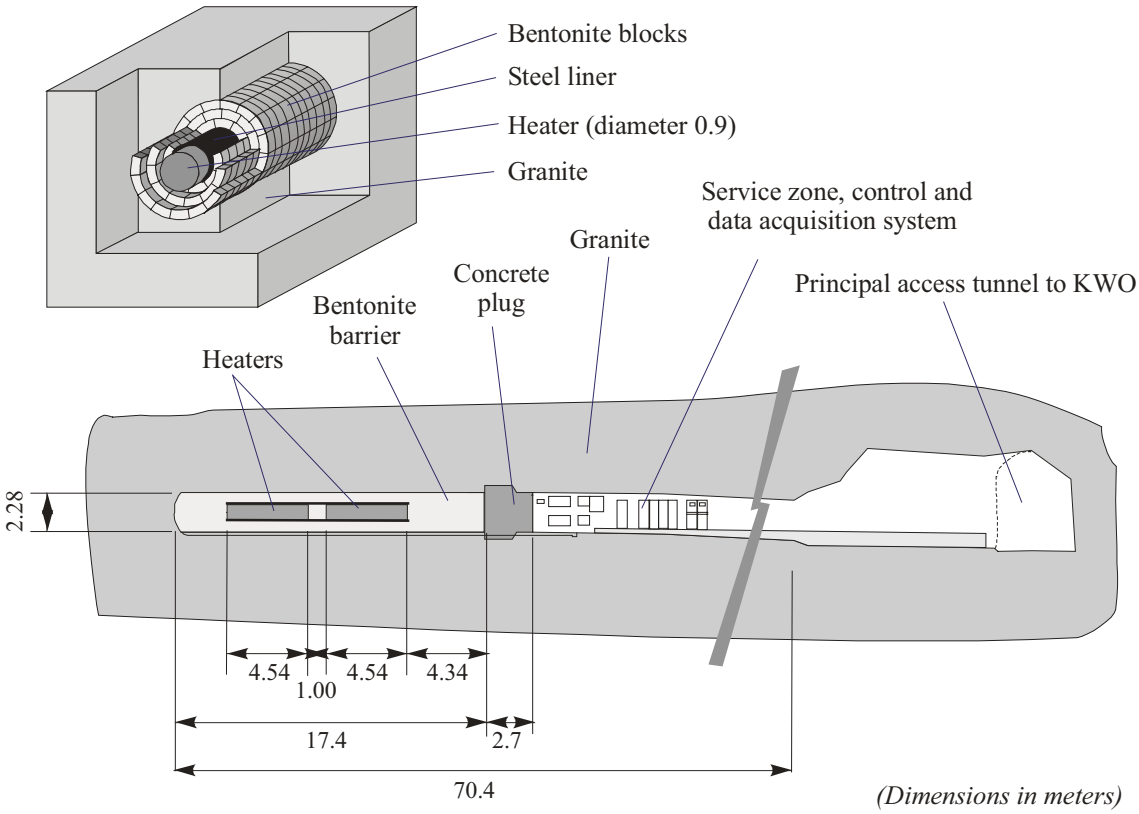

Figure A-20. *General scheme of the FEBEX in situ test.*

A2.2.1 Bentonite Blocks for the clay barrier

This section includes a summary of the most important aspects of the processes of designing, fabricating, quality control, packing, handling, transporting, and storing of the compacted bentonite blocks used to construct the clay barrier. The construction of the bentonite barrier is also described.

Design

Figure A-21 shows the geometry of the barrier in the heater and non-heater areas. In both areas, the three exterior crowns of the blocks are equal; in the heater area the interior crown of this group is in contact with the steel liner, while, in the non-heater area, the interior crown is in contact with a core of blocks. Five types of blocks form this barrier geometry: BB-G-01, BB-G-02, BB-G-03, BB-G-04, and BB-G-05. Figure A-22 and Table A-12 show the shapes and dimensions of the block types.

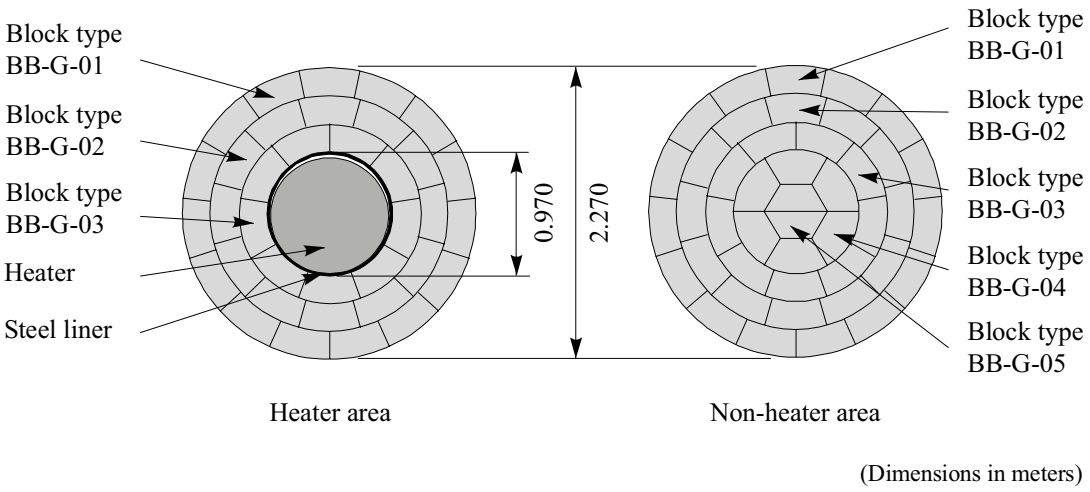

Figure A-21. *Geometry of the clay barrier.*

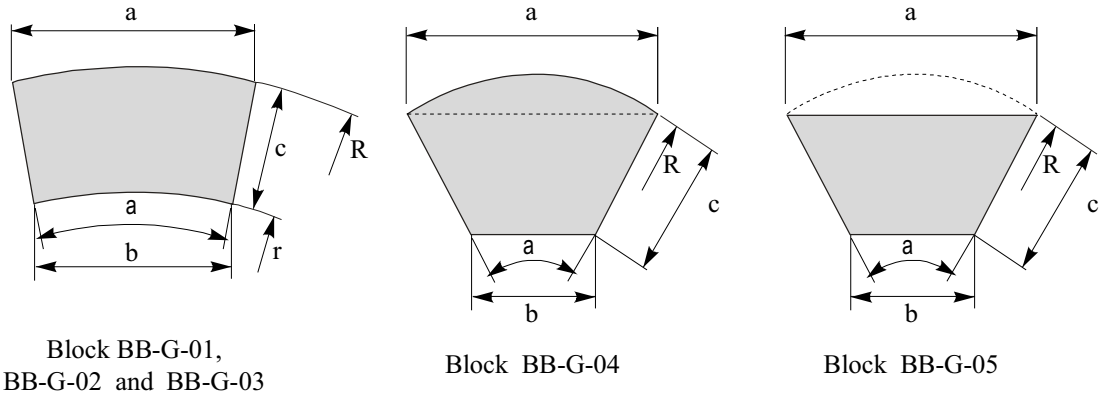

Figure A-22. *Shapes and dimensions of the blocks.*

Table A-12. Dimensions for block fabrication.

Type	a mm	b mm	c mm	thickness mm	R mm	r mm	α °
BB-G-01	470.0 (+2.0 –5.0)	380.0 (+2.0 –4.0)	214.0 (+2.0 –3.0)	125.0 (+2.0 –2.0)	1 133	919	24
BB-G-02	473.0 (+2.0 –5.0)	361.0 (+2.0 –4.0)	214.0 (+2.0 –3.0)	125.0 (+2.0 –4.0)	917	703	30
BB-G-03	478.0 (+2.0 –5.0)	330.0 (+2.0 –4.0)	214.0 (+2.0 –3.0)	125.0 (+2.0 –4.0)	701	487	40
BB-G-04	483.0 (+2.0 –5.0)	240.0 (+2.0 –4.0)	240.0 (+2.0 –3.0)	125.0 (+2.0 –4.0)	485	-	60
BB-G-05	483.0 (+2.0 –5.0)	240.0 (+2.0 –4.0)	240.0 (+2.0 –3.0)	125.0 (+2.0 –4.0)	-	-	60

The blocks were fabricated from FEBEX bentonite, the properties of which will be described in Section A3. The dry density specified in the design of the blocks was 1.70 g/cm^3. This density was determined by taking into account the probable volume of the construction gaps and the need to have a barrier with an average dry density of 1.60 g/cm^3. For a dry density of 1.60 g/cm^3, the swelling pressure is of the order of 5 MPa, which is the value proposed in the AGP Granito. The water content of the blocks is that specified for the raw bentonite, 12.5 % to 15.5 % (see Section A3).

Fabrication

For the fabrication of blocks BB-G-01, BB-G-02, BB-G-03, and BB-G-04 it was necessary to design and manufacture moulds, whereas block BB-G-05 was obtained from BB-G-04 by machining the curved face with a saw. The blocks were fabricated in the REFRACTA, S. A. plant at Quart de Poblet (Province of Valencia, Spain), by compaction in a uniaxial hydraulic press under a pressure of 40 MPa to 45 MPa. A quality assurance program was applied in fabrication of the blocks: external appearance, dimensions, water content, and dry density were controlled. Table A-13 shows the average values for the characteristics and the number of blocks fabricated for each type.

Table A-13. Average values of the physical properties and number of blocks fabricated.

	BB-G-01	BB-G-02	BB-G-03	BB-G-04	BB-G-05
Weight per block (kg)	22.1	21.8	21.3	23.1	18.0
Average water content (%)	14.49	14.07	14.87	13.69	13.07
Average dry density (g/cm^3)	1.69	1.69	1.69	1.70	1.70
Number of units fabricated	2 898	2 310	1 614	562	184
Total weight (kg)	64 046	50 358	34 378	12 982	3 312

Taking into account the dimensions of the blocks of each type, the average values of water content and dry density are 14.4 % and 1.69 g/cm^3, respectively. A total of 7 568 blocks were fabricated, with a total weight of 165 076 kg.

Packing, handling, transporting and storage

Laboratory tests and the study of some blocks placed in the tunnels of the GTS showed that the blocks deteriorate quite rapidly when exposed to an environment of high humidity. For this reason, the blocks were packed in boxes appropriately protected by sheets of plastic. Although the blocks have a high, unconfined compressive strength (of the order of 2.5 MPa), they were packed in boxes inside quilted plastic wrapping to avoid impact damage during their handling and transport.

The appropriately packed blocks were stored away from the GTS, in a warehouse with controlled temperature and humidity. During the construction of the barrier, the FEBEX drift was dried, heated, and ventilated to keep relative humidity low. Also the work was scheduled such that in the work area at the portal of the drift, where relative humidity is high, the time of exposure was compatible with the stability of the blocks.

Since no block was observed to have deteriorated as a result of the aforementioned causes, these precautions were confirmed to be effective.

A2.2.2 Heating system

General characteristics

The test uses two electrical heaters inserted within a steel liner. The heaters reproduce the mechanical characteristics of the AGP Granito canister, simulating the thermal effects.

The external dimensions of the heater are identical to those of the canister anticipated in the AGP Granito concept (a cylinder measuring 4.54 m in length with a diameter of 0.90 m) and the weight is of the same order (11 t). Both the material and the shape of the exterior body of the heaters are similar to those anticipated for the canister: carbon steel plate measuring 100 mm in thickness.

As regards the thermal aspect, the aim of the test is to subject the bentonite, at the point of contact with the steel liner, to a maximum constant temperature of 100ºC, which is the maximum value anticipated in the reference concept. Nevertheless, in order to reach this value in a period of time compatible with the duration of the test, and maintain it in an isolated drift, it was necessary to increase the power of the heaters beyond the value anticipated in the AGP Granito concept for the maximum residual thermal power of the canisters, that is 1 200 W. Following different analyses and modelling exercises, performed during the design phase of the experiment, the nominal power was fixed at 4 300 W per heater. This power will be the maximum required in the most unfavorable case of the clay barrier being totally saturated, with a certain margin of safety.

Mechanical characteristics

Figure A-23 shows a general view of the final design of the heater. The exterior casing consists of a forged tube with a wall thickness of 100 mm, and two welded end covers of metal plate, each measuring 150 mm in thickness. The casing is of carbon steel without any treatment or covering, except shot-peening of the exterior surface.

Inside the casing, the heating elements (resistances) are wound around a tube or reel measuring 660.4 mm in diameter and 12.7 mm in thickness. The assembly – reel and resistances – is covered with a copper sheet measuring 3 mm in thickness. This covering serves to distribute the temperatures more uniformly along the heater and to provide mechanical protection for the heating elements during heater assembly.

The thickness and shape of the end covers are based simply on convenience during assembly of the interior elements of the heater and do not correspond to the reference concept. The front end cover has a total of 24 perforations to allow for the exit of cables (6 for the heating elements and 18 for the control thermocouples) and is fitted with a cylindrical, screw-on box on the exterior for mechanical protection of the cable exits. On its outer face there are two key notches located at 36°, to allow for coupling with the pushing mechanism of the insertion system. The other end cover is solid, and its outer edge is chamfered to facilitate insertion into the liner.

The exterior casing is hermetically sealed. The cable exits were sealed with Viton gaskets and filled with epoxy resin, as shown in Figure A-24.

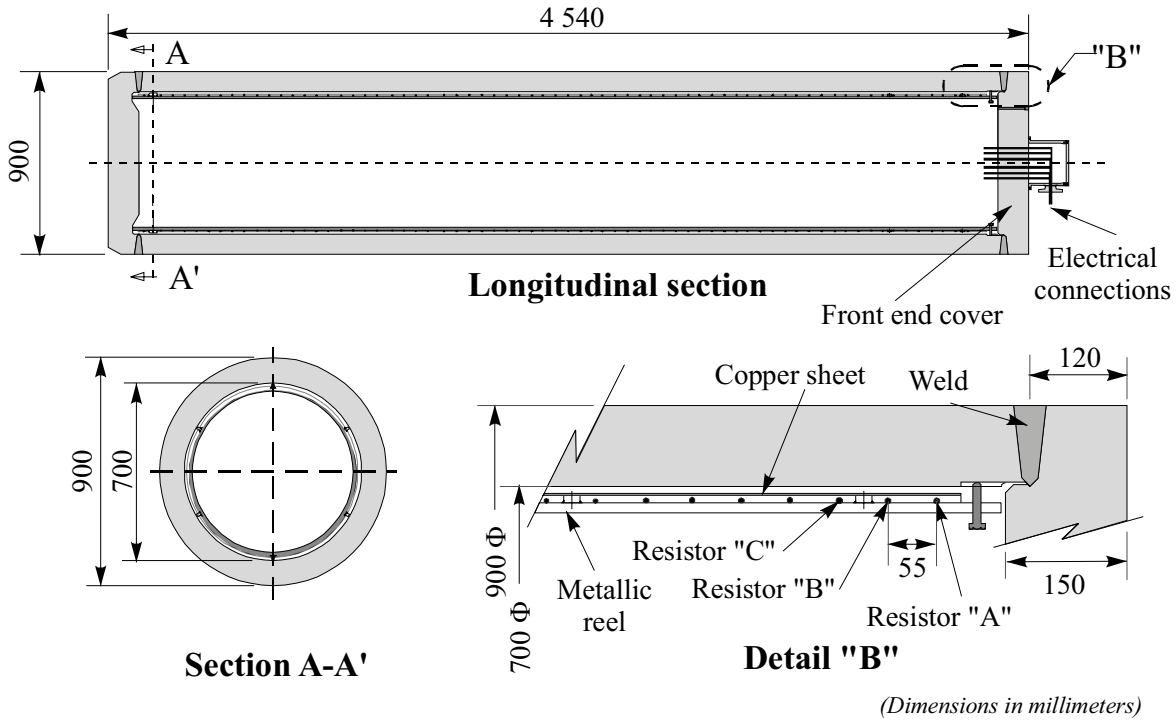

(Dimensions in millimeters)

Figure A-23. *Dimensions and construction details of the heaters.*

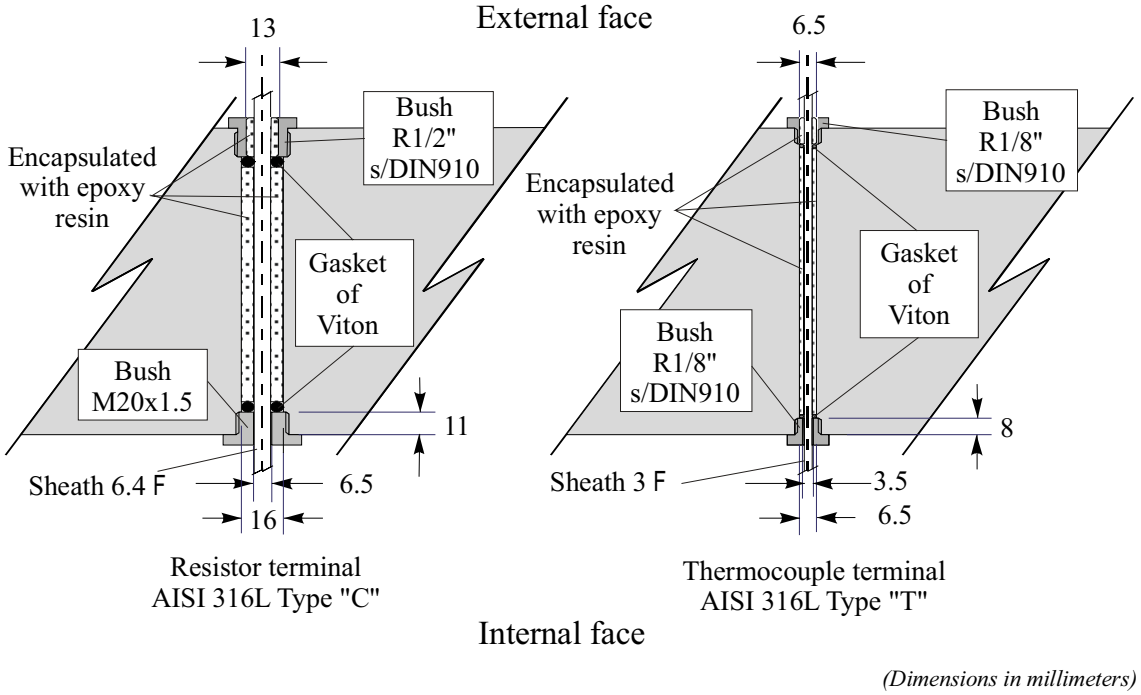

(Dimensions in millimeters)

Figure A-24. *Cable run sealing system.*

Electrical characteristics

In order to increase reliability, the system is redundant. Each heater has three independent heating elements, each of which is capable of supplying individually the nominal required power of 4 300 W. The elements are of the shielded resistor type and their main characteristics are summarized in Table A-14.

Table A-14. Characteristics of the heating elements.

Active conductor	material of the conductor core	Ni-Cr 80/20
	length	52 ± 3 %m
	supply voltage	400 V AC
	nominal power	4 300 ± 10 %W
	insulation	MgO
	sheath material	Inconel 600
	external diameter	4.6 mm
Cold terminals	conductor section	6 mm^2
	sheath material	AISI 304 L
	external diameter	6.4 mm

Each heating element is helicoidally wound on the internal reel of the heater, with a total of 25 windings per element and a separation between coils of the same element of 165 mm.

Since temperature is key to the expected life of the elements, 18 thermocouples were installed on the internal reel of the heater to measure the surface temperature of the heating element.

For reliability reasons, all types of electrical connections were avoided in the interior of the heater. The cold terminals of the heating elements are sufficiently long to exit the body of the heater, pass through the concrete plug, and reach the service zone without any electrical connection being made. These terminals, together with the shielded cables of the thermocouples, were placed in a continuous, seamless tube of corrugated Teflon, which extends from the front end cover to the service zone. This tube protects the set of cables against mechanical and corrosive action; it has sufficient flexibility to allow for a certain magnitude of heater movement produced by differential settlement or swelling of the bentonite.

Steel liner

The “in situ” test faithfully reproduces the AGP Granito reference concept, which considers the existence of a continuous steel liner, common to all the canisters emplaced in the same drift. This steel liner consists of a perforated steel tube measuring 15 mm in thickness, providing the space into which the canister is inserted. Given that in the actual design of the AGP Granito concept no consideration is given to the retrievability of the canisters, the function of the steel liner terminates when the canister is introduced; therefore, the deformation of the liner due to swelling of the bentonite is not important.

The steel liner required for the test has a length of 10 m, corresponding to the length of the two heaters plus the 1-m separation between them. Thus, 11 segments of 1 m each were made, designed to be coupled by means of a male/female conical coupling measuring 100 mm in length, machined in the ends of each segment Figure A-25. The material of the steel liner is conventional alloyed steel for boilers and pressure vessels.

The inner diameter of the liner is 940 mm; thus there is a gap of 40 mm with respect to the outer diameter of the heaters, a value that was considered sufficient for correct insertion of the heaters, taking into account the normal errors of alignment in an installation operation of this type.

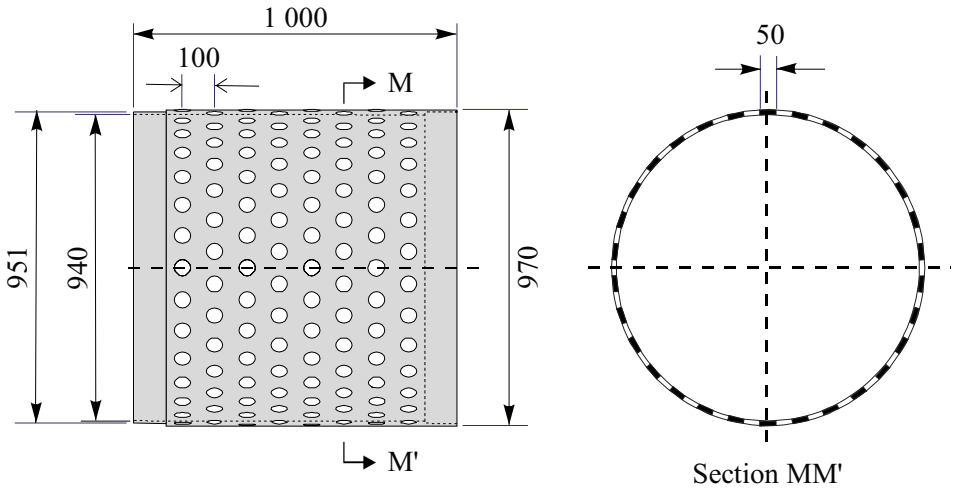

Figure A-25. *Steel liner.*

A2.2.3 Instrumentation

A total of 632 sensors were installed. Table A-15 indicates the variables measured, the types of sensors used and the locations of the sensors, by areas.

Table A-15. Installed sensors (G: granite; B: bentonite; C: heater; S: service zone).

Variable (or instrument)	Type of sensor	Area G	B	C	S	Total
Temperature	Thermocouple	62	91	36		189
Total pressure in borehole in rock (3-D)	Vibrating wire	4				4
Total pressure on rock surface	Vibrating wire	30				30
Total pressure on heater	Vibrating wire		6			6
Hydraulic pressure in borehole in rock	Piezoresistive	62				62
Packer pressure in borehole	Piezoresistive	62				62
Pore pressure in bentonite	Vibrating wire		52			52
Water content	Capacitive		58		1	59
Water content	Psychrometer	28	48			76
Water content	TDR	4	20			24
Extensometer in rock	Vibrating wire	2 × 3				6
Heater displacement	Vibrating wire		9			9
Expansion of bentonite block	Vibrating wire		8			8
Displacement within the bentonite barrier	Potentiometer		2 × 3			6
Clinometer	LVDT		6 × 2			12
Crack meter	LVDT	1 × 3				3
Gas pressure in the bentonite barrier	Magnetic		4			4
Gas flow	Manual measure		6			6
Atmospheric pressure	Piezoresistive				1	1
Velocity of ventilation air	Hot wire				1	1
Resistor intensity	Electric converter				6	6
Resistor voltage	Electric converter				6	6
TOTAL		**261**	**320**	**36**	**15**	**632**

The sensors in the clay barrier were grouped in a series of cross-sections, as indicated in Figure A-26: sections A, B1, B2, C, D1, D2, E1, E2, F1, F2, G, H, I, K, L, M1, M2 and N. The sections with an identical letter have similar sensor configurations.

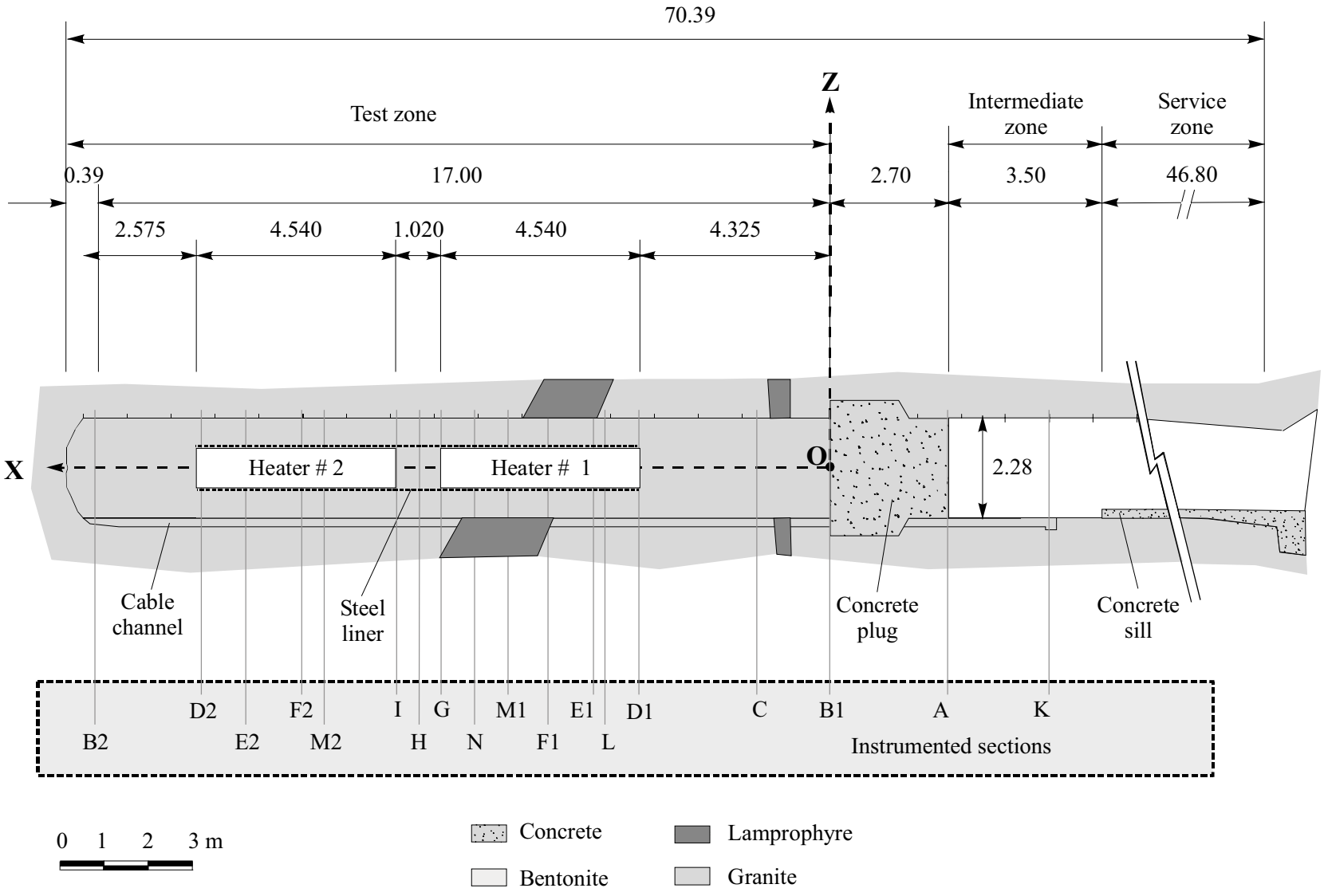

Figure A-26. *Arrangement of the instrumented sections.*

The boreholes BOUS-1, BOUS-2, FBX-1, and FBX-2 were used, along with the 19 boreholes drilled from the interior of the drift, for instrumentation the rock, in particular for hydrogeological and mechanical variations. Other sensors, such as psychrometers and TDR probes were installed in smaller boreholes, drilled from the drift in areas closer to the wall (up to 2.5 m).

Two examples of the location of sensors in the clay barrier and in the surrounding rock are shown in Figure A-27 and Figure A-28, respectively. Each sensor is identified by a code of the type:

AA-BBn-CC

where AA is the code of sensor type (see Table A-16), BB is the designation of location type (borehole, instrumented section, etc), n is the order number of section or borehole (where applicable) and CC is the order number within the corresponding section or borehole.

The final location of all the sensors is identified by their coordinates, in the local reference system XYZ indicated in Figure A-28.

Table A-16. Identification of sensor codes.

Code	Sensor
T	Temperature
P	Total pressure
Q	Pore pressure
SH	Heater displacement
SB	Bentonite block displacement
S	Displacement (general)
3S	Crack meter
PP	Hydraulic pressure of packer in borehole
IT	Clinometer
GP	Gas pressure
GF	Gas flow
WC	Water content (capacitive type)
WP	Water content (psychrometer type)
WT	Water content (TDR type)
AP	Atmospheric pressure (in service zone)
A	Anemometer
V	Voltage meter
C	Electric current meter
Ω	Insulation meter

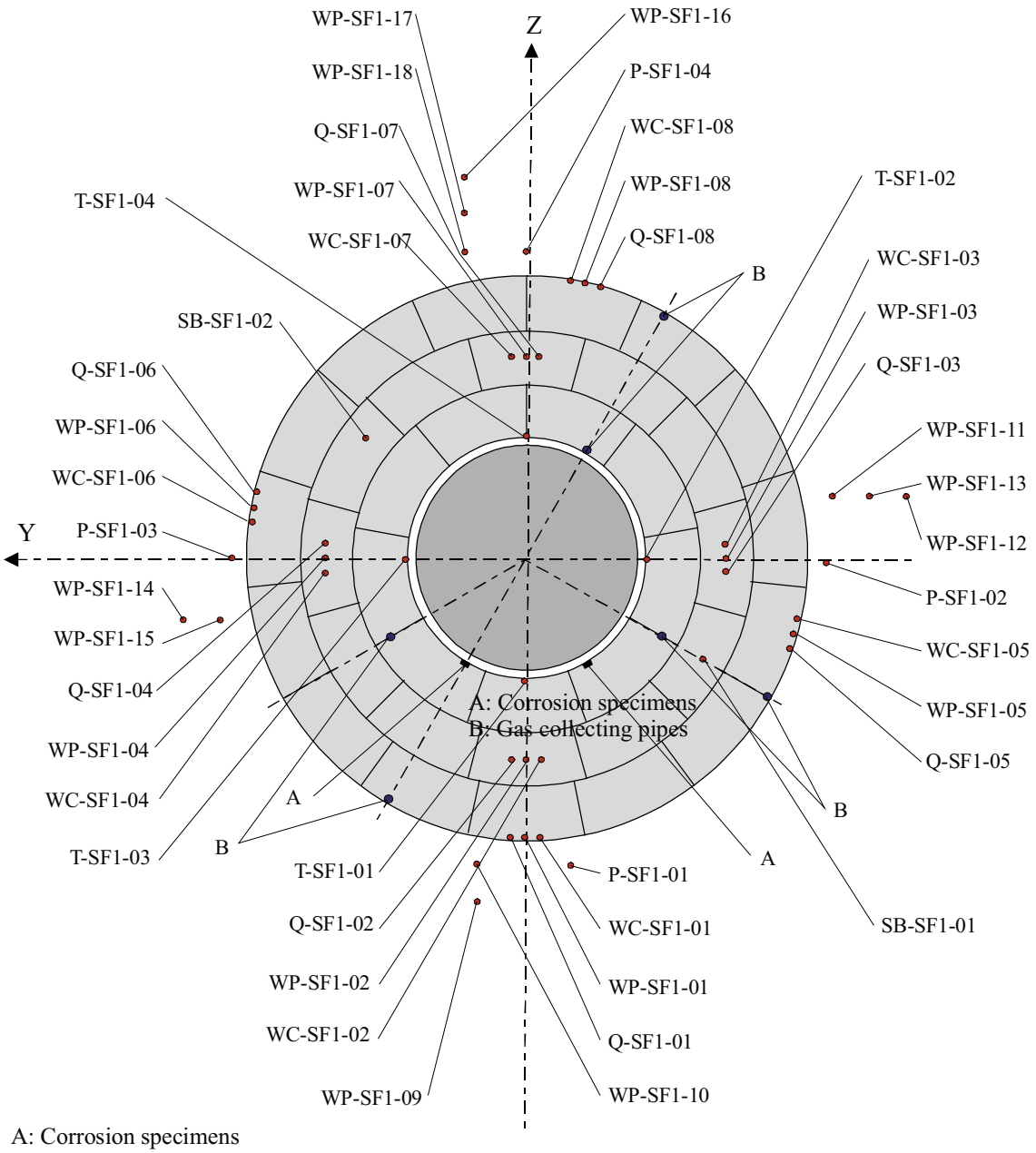

Figure A-27. *Final location of sensors in instrumented cross-section F1.*

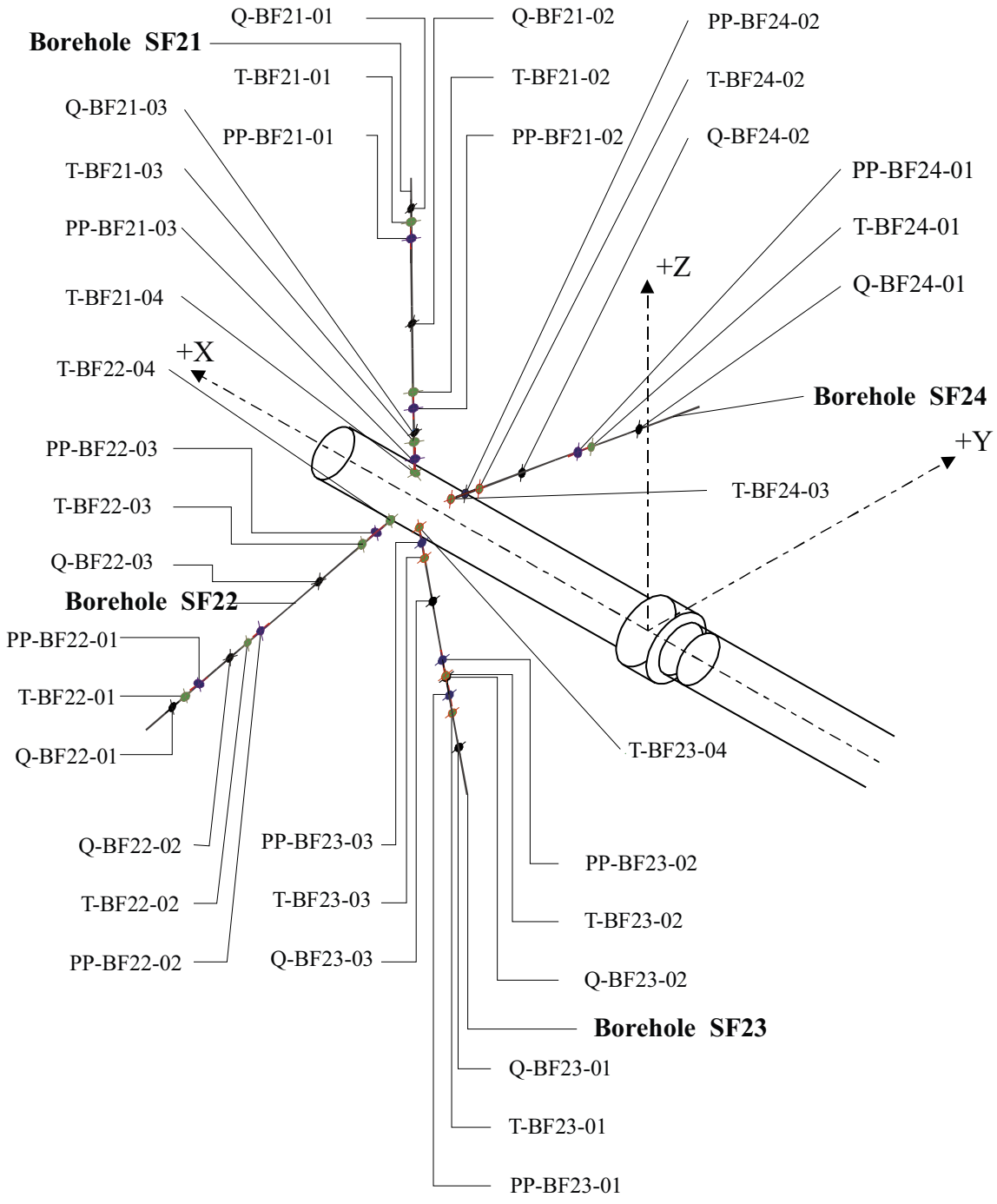

Figure A-28. *Location of sensors in boreholes SF21, SF22, SF23 and SF24.*

A2.2.4 Clay barrier construction

Preliminary tests

Due to the lack of previous experience in an installation of this type, especially in placing the engineered barriers in a horizontal position, a test installation was set up in a simulated drift of concrete (see Figure A-29) at the AITEMIN facilities in Toledo (Spain). This test was very useful, and served to detect certain important aspects associated with the installation. In particular, these aspects were the stability of the bentonite slices and the accumulative effects of the gap between the blocks themselves and the blocks and the drift.

The effects of mechanical degradation of the bentonite blocks due to the humidity of the environment and/or a film of water at the rock surface were studied by laboratory tests and in a tunnel at the GTS. As a result of these experiences, the decision was taken to protect the packages of blocks against humidity; to dry the working area within the drift to the extent possible and to minimize the time the blocks were exposed to the GTS environment, where the relative humidity is practically 100 %.

Installation procedure

The barrier was constructed manually, in accordance with the scheduled procedure. The sequence of installation is shown on Figure A-30. First the steel liner was placed on a provisional support; second, the alignment with the axis of the drift was checked and adjusted; and finally the barrier was constructed around the steel liner, in complete vertical slices, until the space for the heater was enclosed.

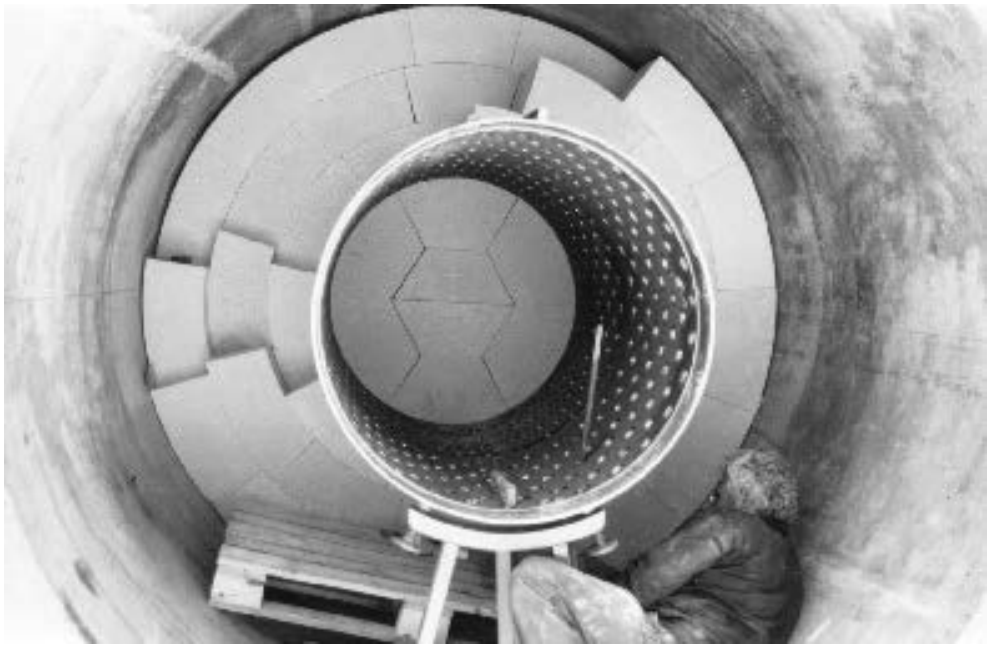

Figure A-29. *Toledo test installation.*

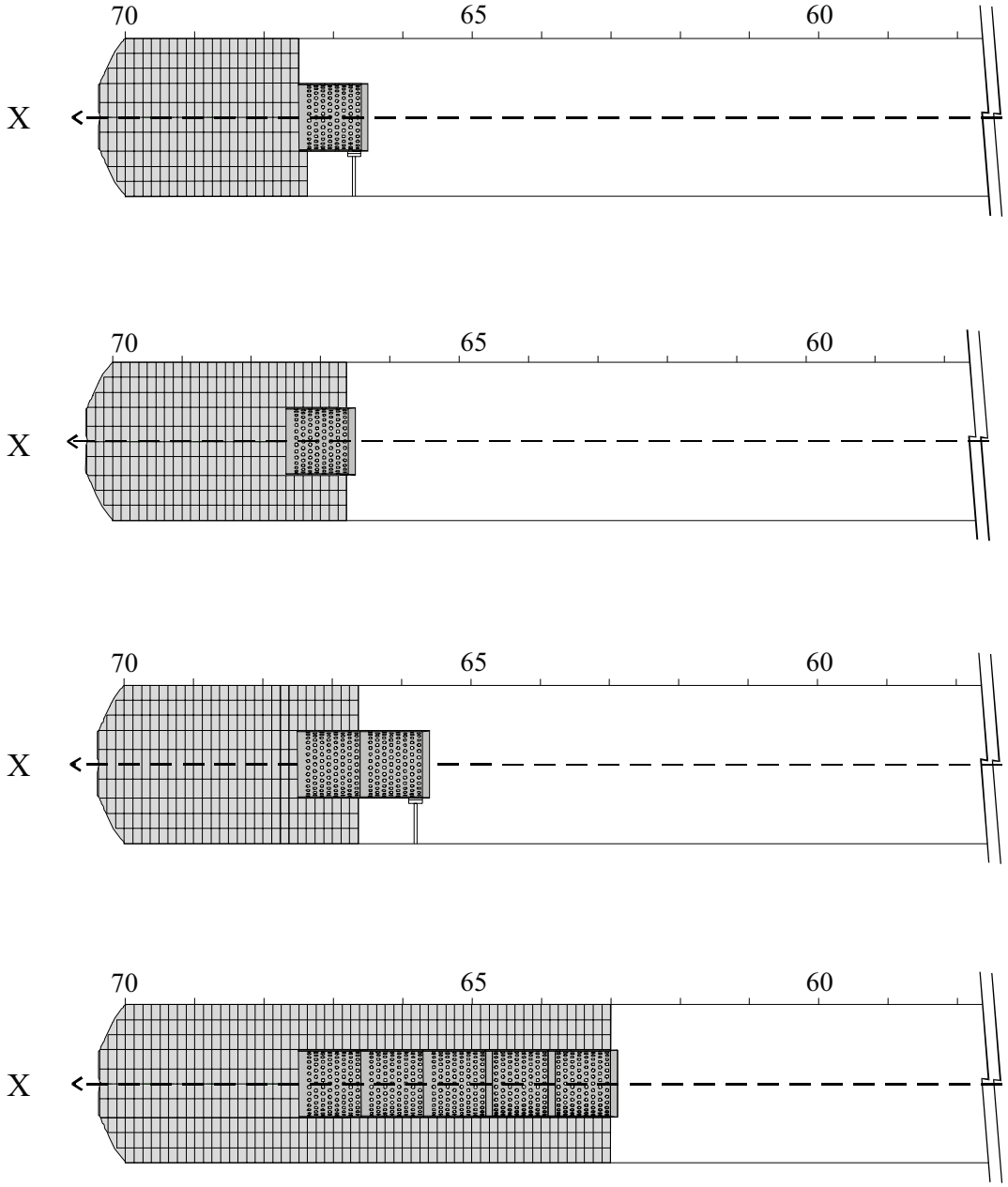

Figure A-30. *Sequence of clay barrier construction.*

The correct alignment of all the segments of the steel liner, with respect to one another and to the drift, is critical in order to avoid difficulties in inserting the heaters. Initially, once aligned, some points were welded in the joint between the liner segments, to ensure and maintain their correct position until the heater was inserted. Later it was decided that it was easier to ensure this alignment by introducing the steel liner into the drift already joined; as a result, up to three joined segments were installed. Figure A-31 shows the space for the heater, after being enclosed by the construction of the barrier around the steel liner.

In some cases, and especially for the first slices of the installation, it was necessary to wedge the top blocks against the rock to ensure the stability of the slices. The wedges used were of Grimsel granite.

On the other hand, all the gaps existing between the blocks, both by design and as a result of manufacturing tolerances, accumulate at the top part of each slice, resulting in a total gap of approximately 2 to 3 cm. Figure A-32 represents a typical cross-section of the drift. It may be seen that, for these reasons, the axis of the steel liner is off-center, displaced some 15 mm. Consequently, the heater is off-center by some 35 mm, the exact deviation depending on the actual diameter of the drift at each point.

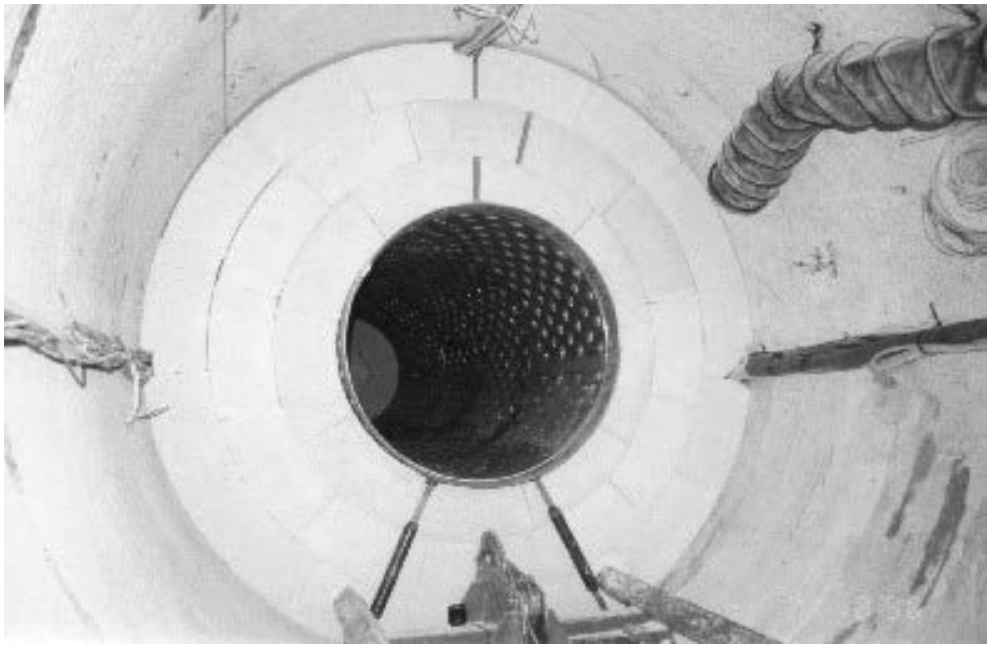

Figure A-31. *Enclosed space for the heater, after construction of the clay barrier.*

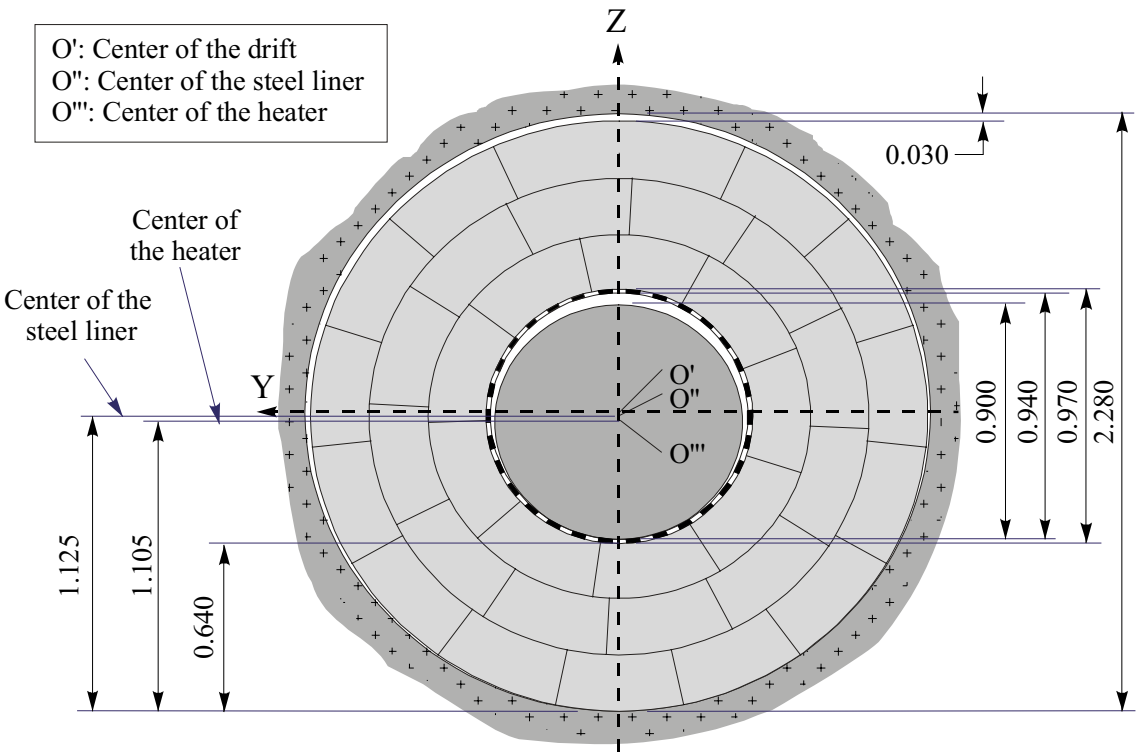

(Dimensions in meters)

Figure A-32. *Typical cross section of the clay barrier.*

Sensor installation and cabling

The sensors in granite were emplaced before the clay barrier was installed, whereas the sensors in bentonite were installed in mechanically made holes at their pre-assigned positions within the blocks on completion of each slice.

The cables were carried radially from each sensor to the rock surface in a machined groove or channel in the bentonite. All the cables, including those from the sensors in the granite, were grouped into four bundles. The bundles were carried along the rock face at the crown, the invert, and both springlines of the drift. To carry each bundle along the rock face and through the bentonite blocks, a channel equal to the size of the bundle was made in each slice (Figure A-33). At the crown and the two springlines, the bundles were fastened to the granite with spikes and loops. In the invert, a channel previously made along the entire length of the test zone was used to carry the heater power cables (which are quite rigid and fragile); this arrangement also avoids high initial compression on the cables from the weight of the bentonite barrier. Once all the cables were placed in the invert channel, it was filled with bentonite powder (Figure A-34).

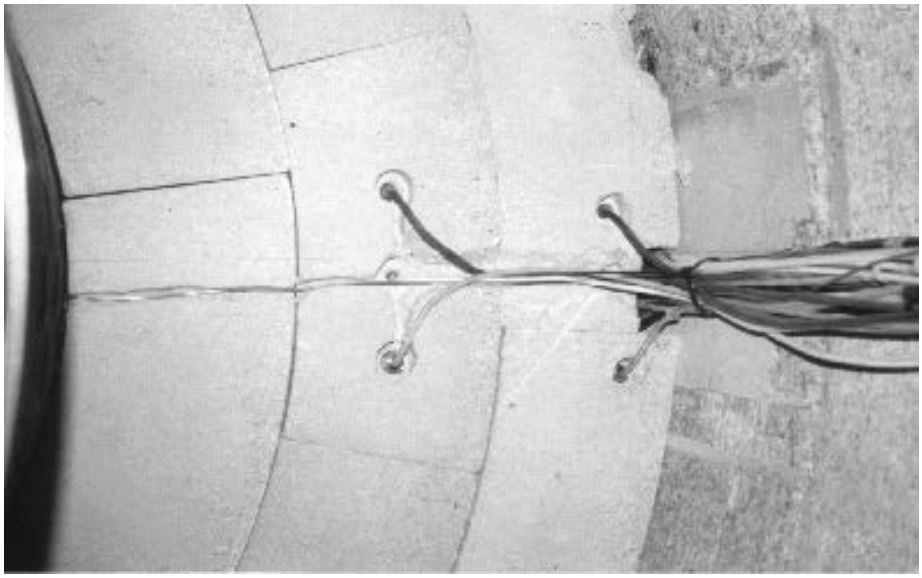

Figure A-33. *Sensor installation and cabling.*

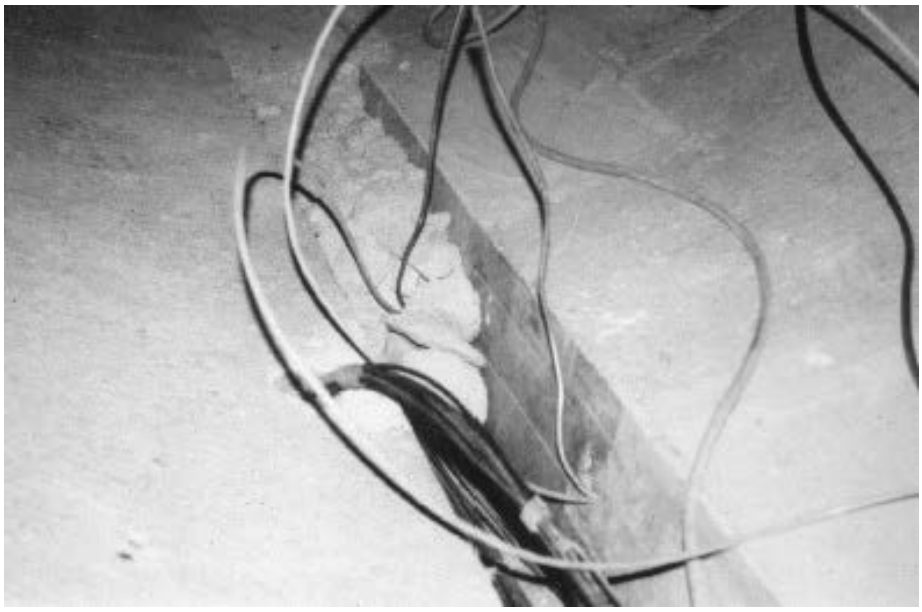

Figure A-34. *Cable channel in the invert of the drift.*

A2.2.5 Concrete plug

The test zone was closed with a concrete plug, the geometry of which is shown in Figure A-35. The plug was designed to resist the swelling pressure of the bentonite. No specification was included for the water tightness or gas tightness of the concrete plug.

The plug was constructed with mass concrete, without any reinforcement, to facilitate the planned future dismantling. It was designed to withstand a total force of 2 000 t, which corresponds to a swelling pressure of the bentonite of 5 MPa. The concrete used had a low value of hydration heat and minimum shrinkage. Table A-17 shows the proportions used for the concrete mix.

Table A-17. Concrete mix proportions used in plug construction.

Component	Type	Proportions kg/m³
cement	PCO “Sulfacem” (CEM I 32.5 HS)	160
silica fume	Sikafume HR	60
fine aggregate	Grimsel granite, 4 to 8 mm	660
coarse aggregate	Grimsel granite, 8 to 16 mm	430
sand	Quartz 0.1 to 5.6 mm	800
filler	limestone	170
water	city network	155
superplasticizer	Sikament-12+	13

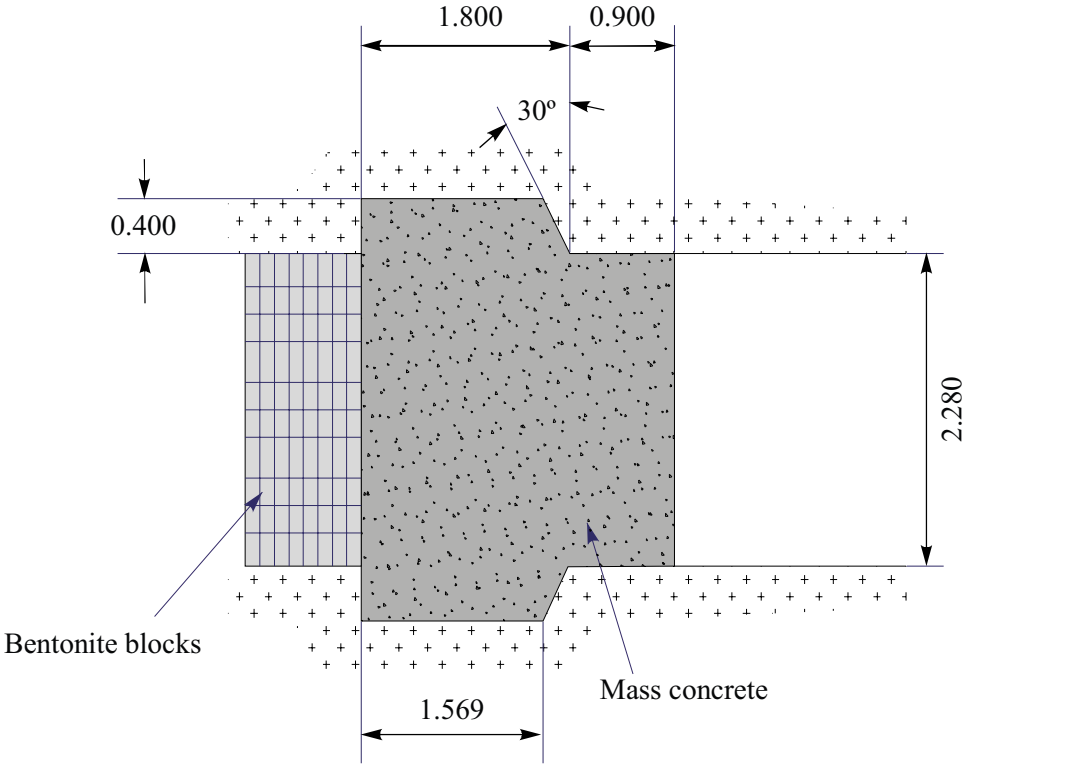

Figure A-35. *Longitudinal section of the concrete plug.*

The plug was concreted in three sections perpendicular to the axis of the drift, such that the filling of the upper part could be checked, at least for a part of the plug. The concrete was pumped from outside the drift and was compacted by vibration. This method did not allow for good concreting of the key, where a void remained, this subsequently being filled by means of injection. Table A-18 shows the results obtained from the concrete control tests.

Table A-18. Results of concrete control tests.

water/cement ratio	0.99
water/total hydraulic materials ratio	0.72
slump (Abrams cone) (mm)	44
density (before setting) (kg/m^3)	2394
air content (%)	0.4
28-day strength (MPa)	47.1

The four bundles of cables pass through the concrete plug inside 200 mm-diameter plastic pipes (Figure A-36). The pipes were later filled with fine mortar.

Figure A-36. *Pipes for concrete plug cable penetrations.*

A2.2.6 Quality assurance and quality control

Control of the dry density of the clay barrier was fundamental to its construction. The average dry density was to be no more than 1.60 t/m^3, in order not to exceed the maximum swelling pressure of 5 MPa used in the calculations for the test components. On the other hand, it was required not to be less than the minimum considered tolerable, 1.4 t/m^3. Furthermore, knowledge of the actual dry density obtained is necessary for modelling, as well as for the interpretation of the test results. For this reason, during the construction of the clay barrier, the real mass of bentonite placed and the volume of the drift occupied by each vertical slice of blocks was determined. From these values, the global dry density as well as the percentage of construction gaps for each slice were calculated. The profiles of dry density and construction gaps were drawn from each slice, these being shown in Figure A-37.

A total of 136 slices were installed, made up of 5 331 blocks and having an overall mass of 115 716 kg of bentonite. The average values of the barrier are a dry density of 1.60 t/m^3 and a volume of construction gaps of 5.53 %. It has been assumed that the barrier maintains the water content (an average of 14.4 %) from the fabrication of the blocks.

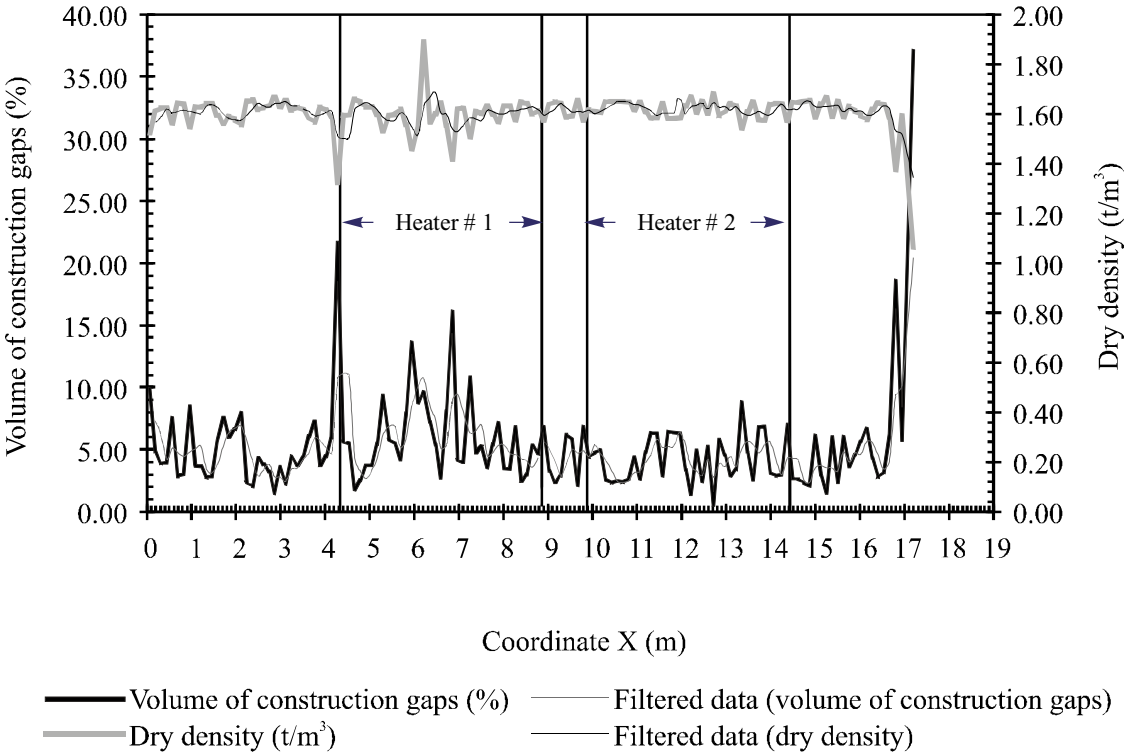

Figure A-37. *Profiles of dry density and volume of construction gaps in the clay barrier.*

A2.3 Test operation

A2.3.1 Initial tests and start-up

The mechanical installation tasks were completed in 16 weeks between 1 July 1996 and 15 October 1996, two weeks ahead of schedule. The assembly and setting up of the data acquisition and control systems were prolonged more than anticipated, until 27 February 1997.

Apart from some short duration tests, the heating (operational) stage began on 27 February 1997, the date identified as "day 0" on the time scale. The sequence of initiation was as follows:

- Throughout an initial period of 20 days a constant power of 1 200 W per heater was applied, with the aim of identifying the thermal response of the system and adjusting the control algorithms.
- Over the next 33 days the power was increased to 2 000 W per heater and maintained constant to approximate the temperature of 100 °C desired at the surface of the steel liner, but with a limitation on the rate of power increase to reduce thermally-induced stresses.
- Finally, on 21 April 1997 (day 53) the system was switched to the constant temperature control mode, allowing the power to fluctuate freely. Over a period of 8 days, three subsequent steps were performed to adjust the parameters of the control algorithm, the setpoints of the system being established successively at 95 °C, 99 °C, and 100 °C.

A2.3.2 Heating control and operation

Beginning in day 61, the power control system has been automatically regulating the power in the two heaters independently, so as to maintain a constant temperature of 100 °C at the hottest point of the steel liner/bentonite interface, as originally planned.

The reference used by the power control algorithm is the highest temperature value in the sensors located at the surface of the steel liner, which has always been at the center of the bottom line of the heater. Due to the shape of the heater casings, temperatures over 100 °C have been observed at the lids, but these have been discarded, as they are considered to be unique points.

With a view to increasing reliability, the heating system is redundant, and each heater has three independent heating elements, each having the rated nominal power of 4 300 W. During the test, only one of these elements, identified as Resistor A, has been used on each heater on a permanent basis, the other two being kept in reserve. The underlying reason for this was to check the operational life of these elements, which is inversely proportional to their external temperature. In any case, there has not been any failure of the elements after 1 000 days (2 years and 9 months, in 27th of November, 2000) of continuous operation.

A2.3.3 First dismantling

After 5 years of operation, heater #1 was switched off, marking the beginning of the operations of the first dismantling. After cooling down of heater #1, the concrete plug was demolished, the bentonite blocks and the corresponding part of the steel liner were removed up to 1 m before the front of heater #2. Heater #1 was extracted and the void left by it in the remaining steel liner was filled with a 1 m long dummy steel canister. During the dismantling process, samples of rock, concrete and bentonite were taken for analysis and additional sensors were also installed. Finally, a shotcrete plug was put in place. During all these operations, heater #2 was active, and care was taken to cause minimal disturbances to the remaining part of the FEBEX in situ test. The dismantling process is described in detail in Bárcena et al. (2003), on which the following summary is based.

The dismantling operation was made according to the following sequence:

1. Switching off of heater #1, one month in advance of plug demolition.
2. Rock sampling in the service area.
3. Demolition of the concrete plug (sampling).
4. Removal of bentonite up to the front of the first heater (sampling).
5. Extraction of heater #1.
6. Removal of liner and bentonite buffer up to the target point (sampling).
7. Insertion of a 1 m dummy steel cylinder in the central hole.
8. Installation of part of the new instruments.
9. Construction of the first section of the shotcrete plug.
10. Installation of additional instruments in the buffer.
11. Completion of the shotcrete plug to a total length of 3 m.

Table A-19 shows dates of relevant dates of the first dismantling operations.

Table A-19. Summary of important dates during the first dismantling.

Date	Event
28.02.2002	Heater #1 switch off
02.04.2002	Start of dismantling works
08.04.2002	Start demolition of concrete plug
28.05.2002	End demolition concrete plug
19.06.2002	Heater #1 extraction
17.07.2002	End dismantling bentonite
23.07.2002	End sampling
25.07.2002	End shotcrete stage #1
27.06.2003	End shotcrete stage #2

Heater #1 was switched off on the 28th of February 2002. As a result, the temperature on heater #1 started decreasing from the initial temperature of 100 °C and, about one month later, it reached the target range of 25–30 °C. Samples were taken from the rock.

Between the 8th of April 2002 and the 28th of May 2002, the demolition of the concrete plug took place. The demolition was carried out in 15 phases. In the first phase, a borehole was drilled in order to release the potential hydraulic or gas pressure behind the plug. In phase 2 three boreholes were drilled in order to get an initial free surface for concrete breaking, which was achieved with a hydraulic splitter. The operations of creating a free surface and subsequent breaking (see Figure A-38) were repeated several times until a final 30 cm thick concrete layer was left, in order to achieve a more controlled way to expose the bentonite. In phase 15, the final concrete layer was demolished, exposing the bentonite front. During the demolition, samples of concrete were taken.

The dismantling and sampling of bentonite layers (see Figure A-39) were made as fast as possible, to reduce the potential changes in the sampled materials, and with limited ventilation in the working area, to avoid excessive evaporation of the water contained in the clay. The first 4.3 m of clay buffer, between the inner part of the concrete plug and the front of heater #1, were first removed, which comprised 34 layers of bentonite blocks, whereby first the central blocks were removed, then some of the blocks of each ring were broken, and finally the rest of the blocks were easily removed. During this process, samples were taken.

Figure A-38. *Breaking pattern concentric to free surface. Hydraulic splitter in operation (Bárcena et al. 2003).*

Figure A-39. *Dismantling of bentonite layers (Bárcena et al. 2003).*

On the 19th of June 2002, heater #1 was extracted and transported (see Figure A-40) using the hauling system and a transport car that were used in the emplacement of heaters, but with important modifications. After fixing the return pulley to the heater, a peak pulling force of about 2 t was recorded at the moment of mobilisation, that decreased to about 1 t during the rest of the extraction.

The next 3.5 m of clay buffer, between the head of heater #1 and 1 m before the end of heater #1, were next removed (see Figure A-41), which comprised 28 layers of bentonite blocks, whereby the same procedure as in the previous section was used and samples were also taken. Additionally, the corresponding part of the steel liner was removed.

Figure A-40. *Heater extraction (Bárcena et al. 2003).*

Figure A-41. *Dismantling works in the heater section (Bárcena et al. 2003).*

In order to fill up the void left inside the remaining steel liner by the extraction of heater #1, a 1 m long dummy steel cylinder was emplaced (see Figure A-42). A thin steel lid was welded to the liner to prevent the intrusion of shotcrete during the construction of the new plug.

From the 23rd to the 24th of July 2002 the first section of the shotcrete was constructed (see Figure A-43) in 4 layers of 2, 39, 25 and 30 cm. From the 23rd to the 27th of June 2003, the second section of the shotcrete plug was constructed in 5 layers of first 43 and 67 cm, and then of about 30 cm.

Figure A-42. *Insertion of the dummy steel cylinder (Bárcena et al. 2003).*

Figure A-43. *Shotcreting of the first layer onto the bentonite front (Bárcena et al. 2003).*

During the dismantling operations, 71 additional sensors were installed. Table A-20 indicates the variables measured, the types of sensors used and the locations of the sensors, by areas.

Table A-20. Installed sensors (G: granite; B: bentonite; C: heater; P: plug).

Variable (or instrument)	Type of sensor	Area				Total
		G	B	C	P	
Temperature	Thermocouple	1	8			9
Total pressure	Vibrating wire	4	9			13
Relative humidity	Capacitive		21			21
Plug displacement	LVDT				4	4
Gas flow	Manual		6			6
Water	Fibre		18			18
TOTAL		**5**	**62**		**4**	**71**

A3 The FEBEX bentonite

The T-H-M behaviour of the FEBEX bentonite has been summarized in the report ENRESA (2000), which is the source of the summary that follows. More information can be found in ENRESA (2004).

In order to characterize the T-H-M behaviour of the FEBEX bentonite, besides the determination of identification properties, two types of tests have been carried out, namely: tests for direct parameter determination and tests for calibration of models. The first type of tests yields values of standard parameters or functions generally required by a mathematical T-H-M model. The second type of tests may be used with backanalysis techniques in order to infer the values of the parameters or functions required by particular mathematical models and to improve the accuracy of parameter determination. The design of these tests, especially the tests for calibration of models, has been guided by the FEBEX "mock-up" and the FEBEX "in situ" tests. The tests have been carried out mainly by CIEMAT and UPC.

In the tests carried out by CIEMAT, two types of samples of FEBEX bentonite have been used: unmixed and homogenized. The first type refers to samples taken from one of the bags into which the bentonite was packed. The second type refers to samples taken from the homogeneous mixture of all samples of the first type made by CIEMAT. Results obtained using any of these samples are considered to be representative of the characteristics of the FEBEX bentonite. In the tests that require addition of water, three types of water have been used: distilled water (used by convention and as a reference), granitic water (commercial water representative of the water that will saturate an engineered bentonite barrier) and saline water (water prepared with a chemical composition representative of the pore water inside the bentonite barrier). The chemical composition of the granitic water and of the saline water is given in Table A-21.

Table A-21. Chemical composition of the water used in the tests (in mg/l), and pH.

Dissolved ions and pH	Granitic	Saline
Cl^-	13.1	3550.0
SO_4^{2-}	14.4	1440.0
Br^-	0.1	-
NO_3^-	4.8	-
HCO_3^-	144.0	-
SiO2 (aq)	22.2	-
Mg^{2+}	9.4	360.0
Ca^{2+}	44.9	400.8
Na^+	11.0	253.9
K^+	1.0	-
Sr^{2+}	0.09	-
pH	8.3	7.0

In the tests carried out by UPC, the FEBEX bentonite taken from the homogenized sample was always used. Samples were prepared at the water content in equilibrium with the laboratory, which is of w = 13.3 ± 1.3 %. Distilled water was used in infiltration tests and for preparing samples with a water content higher than the hygroscopic.

NOTE: It should be noted that empirical relationships are provide for some parameters. There is NO OBLIGATION that they are used in the numerical analyses. The modelling teams are free to use any parameters that they think appropriate.

A3.1 Origin and general properties

A3.1.1 Origin and general aspects

The FEBEX bentonite (also called "Serrata" clay in some FEBEX reports) has been extracted from the Cortijo de Archidona deposit, exploited by Minas de Gádor, S. A., in the zone of Serrata de Níjar (Almería, Spain). This deposit was selected in the ENRESA R&D plans previous to the FEBEX project as the most suitable material for the backfilling and sealing of a HLW repository. Reasons for this selection were its very high content of montmorillonite, large swelling pressure, low permeability, acceptable thermal conductivity, good retention properties and ease of compaction for the fabrication of blocks.

Over several years prior to FEBEX, and following the selection of this deposit as the reference bentonite (called bentonite S-2 in reports and publications), numerous characterization and behavior (thermal, hydraulic, mechanical, and geochemical) studies were performed. As a result, there is an extensive database on the properties of this bentonite. These data were used in the preliminary modelling for the design of the two large-scale tests of the FEBEX project.

Approximately 300 tons of suitably homogenized and conditioned bentonite were stocked for FEBEX. Based on the experience acquired in the aforementioned studies, the selected raw bentonite was required to meet the following specifications:

- Fraction of particles of more than 5 mm, less than 5 %, and fraction of particles smaller than 74 μm, greater than 85 %.
- Liquid limit greater than 90 %.
- Swelling pressure ranging between 3 MPa and 7 MPa, for a dry density of 1.60 g/cm^3.
- Water content, after conditioning, between 12.5 % and 15.5 %.

The conditioning of the bentonite in the quarry, and later in the factory, was strictly mechanical (homogenization, rock fragment removal, drying, crumbling of clods, and sieving) to obtain a granulated material with the specified characteristics of grain-size distribution and water content. A quality assurance (QA) program was applied to the conditioning process. The conditioned material was packaged in large waterproof bags (about 1 300 kg each). During the packaging, a sample of 8 to 10 kg was taken every 2.5 tons of bentonite, for laboratory testing.

However homogeneous it might be, a bentonite deposit has both horizontal and vertical spatial variations. For a research project such as FEBEX, a material as homogeneous as possible must be used and, furthermore, its properties must be determined by specific tests on samples of the same material. Homogenization reduces the uncertainties in modelling, in laboratory results and in the final interpretation of the entire test. For performance assessment (PA) purposes, however, knowledge of the range of variations in the relevant properties of a massive source of bentonite supply is needed. Thus, it is important to compare the properties of clays (known as S-2 bentonite in the earlier studies and FEBEX bentonite in this test) obtained from the same deposit but in two study phases separated by more than five years.

Comparison of the results of the two sets of characterization tests – S-2 bentonite and FEBEX bentonite – indicates that the deposit is very homogeneous. Consequently, it was possible to use certain parameters from the tests on S-2 bentonite for the purposes of the FEBEX test.

In the following sections, several general conclusions on the properties of the bentonite from this deposit are summarized.

A3.1.2 Identification properties

The data presented in Table A-22 are the so-called identification properties (according to the terminology of geotechnical engineering). They provide an initial idea of the type of physico-chemical behavior to be expected in the clay buffers.

It is interesting to notice that the values of the liquid limit for the S-2 and FEBEX bentonites are very similar in the tests performed by CIEMAT, in contrast to those obtained by UPC-DIT for the FEBEX bentonite, which are somewhat lower. In any case, whichever laboratory is considered, the measured values seem to be low for a bentonite with such a high content of montmorillonite and which also has a relatively high concentration of sodium as exchangeable cation.

Regarding differences in the grain-size distributions between the S-2 and FEBEX bentonites, it should be noted that the results obtained from CIEMAT and UPC-DIT differ considerably as regards the content of the < 2 μm fraction (clay size). The proportion of the clay size fraction obtained depends on the previous treatment of the bentonite for the determination of its grain-size distribution. The differences may be explained by the fact that a very strong dispersion procedure, including ultrasounds, was used by CIEMAT, while UPC-DIT employed standard geotechnical techniques.

Table A-22. Identification properties (ENRESA 2000).

Property	Bentonite S-2		FEBEX Bentonite		
	CSIC-Zaidín	CIEMAT	CSIC-Zaidín	CIEMAT	UPC-DIT
Water content in equilibrium with the air in the laboratory, in %	-	10 to 13	-	13.7 ± 1.3	13.3 ± 1.3
Liquid limit, in %	-	105 ± 10	-	102 ± 4	93 ± 1
Plastic limit, in %	-	-	-	53 ± 3	47 ± 2
Plasticity index	-	-	-	49 ± 4	46 ± 2
Specific weight	-	2.78	-	2.70 ± 0.04	-
Grain-size distribution, in %					
Fraction less than 74 μm	93 ± 3	86	-	92 ± 1	87
Fraction less than 2 μm	82 ± 6	65 ± 1		68 ± 2	45
Specific surface, in m^2/g					
Total	614 ± 74[(1)]	516 ± 37[(2)]	649 ± 5[(1)]	725 ± 47[(1)]	-
External, BET	-	37	-	32 ± 3	-

[(1)] Determined by the Keeling hygroscopicity method.

[(2)] Determined by the methylene blue method.

The value obtained for the external specific surface (BET) is somewhat lower than the average values for smectites (as found in the scientific literature).

The low content of the < 2 μm fraction had already been noticed in the first studies performed on the S-2 bentonite. It was proposed at that time that the smaller particles were agglutinated or cemented with colloidal silica (during alteration of the original volcanic material). This would make dispersion of the clay, and consequently separation of the < 2 μm fraction, more difficult. This argument is supported since the most of the silt-sized material, and some of the sand-sized, is formed by "pseudomorphs" of volcanic grains transformed into smectite. The "pseudomorphs" are relatively stable and would moderate the physical behavior of the bentonite: they are identified as smectite from a chemical point of view, but do not have the physical effects of the bentonite. This interpretation may also explain the relatively low values of liquid limit found in tests.

A3.1.3 Porosity

The pore size distribution has been measured using a mercury injection porosimeter with a range of injection pressure from 7 kPa to 210 MPa that allows to measure pore diameters between 200 µm and 0.006 µm. Before placing the samples in the porosimeter, water was eliminated by liophilization, in order to minimize microstructural changes. 45 samples were taken from 15 of the bentonite blocks fabricated for the FEBEX "mock-up" test. These blocks were made using bentonite with a water content of 14.1 ± 1.0 % and uniaxially compacted at pressures of 40–45 MPa which produced a dry density ρ_d = 1.78 ± 0.03 g/cm^3. The samples tested had a dry density of ρ_d = 1.58–1.80 g/cm^3. The result of these porosimetric tests (see Figure A-44) did not show any significant difference between different positions in a given bentonite block nor between different block types.

A3.2 Parameter determination tests

A3.2.1 Mechanical properties

In order to characterize the mechanical behaviour of the bentonite, strength tests, compressibility tests, swelling pressure tests, swelling under load tests and resonant column tests were made.

Strength-unconfined compression and triaxial tests

In the years previous to FEBEX, strength had been determined only on samples of the bentonite S-2. Some of these data are presented herein for informative purposes.

The unconfined compressive strength is 2.5 MPa for samples prepared with a water content at equilibrium with the air in the laboratory (laboratory conditions) and at a density of 1.70 g/cm^3. It was found that unconfined compressive strength increases exponentially with dry density.

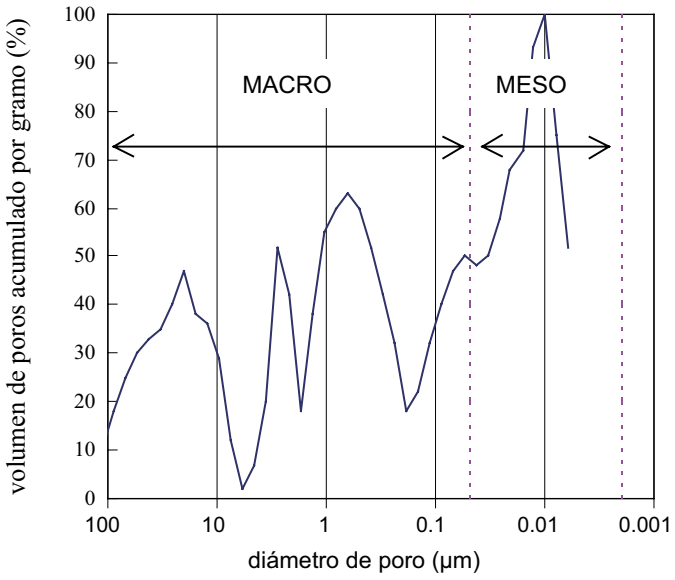

Figure A-44. *Typical pore size distribution of a sample of compacted FEBEX bentonite (cumulative pore volume per gram in % as a function of pore diameter in %).*

Various types of triaxial tests were performed, with saturated and unsaturated samples. The results from the unsaturated samples, prepared at different dry densities with the water content at equilibrium with the laboratory conditions, are presented in Table A-23.

Table A-23. Strength parameters obtained in triaxial tests on unsaturated specimens of bentonite S-2 prepared with a water content in equilibrium with the laboratory conditions and at different initial dry densities (ENRESA 2000).

ρ_d g/cm^3	Initial Sr %	Range of σ_3 MPa	Cohesion MPa	Friction angle degrees
1.6	41–47	0.5–3.0	0.7	25
1.6	41–47	3.0–10.0	2.8	14
1.6	41–47	10.0–30.0	4.4	14
1.7	49–60	0.5–3.0	0.8	30
1.7	49–60	3.0–10.0	1.0	26
1.7	49–60	10.0–30.0	3.5	16
1.8	53–59	3.0–10.0	4.3	16
1.8	53–59	10.0–30.0	3.6	18
1.9	65–79	3.0–10.0	4.5	19

Compressibility-oedometric tests

Oedometric tests have been performed on samples of the bentonite S-2 for initial dry densities of 1.40 g/cm^3 and 1.60 g/cm^3. Table A-24 shows the parameters resulting from these tests.

Table A-24. Oedometer parameters (C_c = compression index of the virgin compression line, with stress in decimal log scale; C_s = unloading-reloading compression index, with stress in decimal log scale; a_v = virgin confined compression index, with stress in natural scale; $m_v = a_v/(1 + e_0)$, where e_0 is the initial void ratio; and k = saturated permeability) (ENRESA 2000).

ρ_d g/cm^3	C_c	C_s	a_v m^2/kN	m_v m^2/kN	k m/s
1.4	0.38	0.20	2.5×10^{-5}	1.7×10^{-5}	4.7×10^{-12}
1.6	0.38	0.33	2.3×10^{-5}	1.4×10^{-5}	1.3×10^{-13}

Swelling pressure

Swelling pressure tests were performed using conventional oedometers on samples saturated with distilled water. A regression curve was developed as a function of dry density for the swelling pressure of the FEBEX bentonite, as shown on Figure A-45, and expressed by the equation

$$P_s = \exp(6.0\rho_d - 9.07) \qquad \text{(A-3)}$$

where P_s is the swelling pressure in MPa and ρ_d is the dry density in g/cm^3. The deviation of the experimental values with respect to this fitting may be as high as 25 %. The dispersion observed in the values is larger for higher dry densities, this probably being due to technical limitations, as the load capacity of the oedometers is almost exceeded by the swelling pressure. The swelling pressure values and the regression curve for the bentonite S-2 are also shown in Figure A-45. The difference in the swelling pressures of the S-2 and the FEBEX bentonites, may be considered negligible for practical purposes.

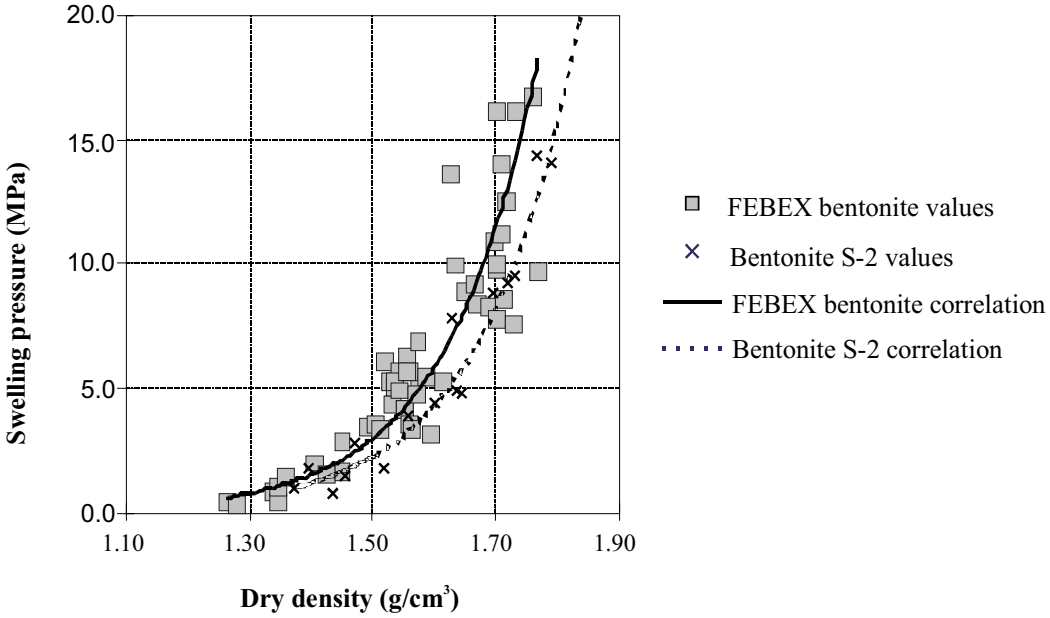

Figure A-45. *Swelling pressure as a function of dry density (ENRESA 2000).*

Swelling under load

These tests were performed using conventional oedometers on samples of the FEBEX bentonite.

During the pre-operational stage, CIEMAT carried out tests with distilled water on specimens with a nominal dry density of 1.60 g/cm^3. Four of these tests were performed under a load of 0.5 MPa and the other three under a load of 0.9 MPa. Subsequently, several series of swelling under load tests were performed, in which samples having a nominal dry density of 1.60 g/cm^3 were subjected to different loads ranging between 0.1 and 3.0 MPa. Both granitic and saline water were used to saturate the sample. A commercial granitic water was used. The saline water is a synthetic product having a chemical composition similar to that of the bentonite interstitial water, but simplified to include only the major elements. The chemical composition of both waters is shown in Table A-25.

Table A-25. Chemical composition of the water used in the tests (in mg/l), and pH.

dissolved ions and pH	granitic	saline
Cl^-	13.1	3550.0
SO_4^{2-}	14.4	1440.0
Br^-	0.1	-
NO_3^-	4.8	-
HCO_3^-	144.0	-
SiO2 (aq)	22.2	-
Mg^{2+}	9.4	360.0
Ca^{2+}	44.9	400.8
Na^+	11.0	253.9
K^+	1.0	-
Sr^{2+}	0.09	-
pH	8.3	7.0

In addition, some tests have been performed with specimens compacted to nominal dry densities of 1.70 and 1.50 g/cm^3 saturated with granitic water, and some others with specimens compacted to nominal dry densities of 1.70 g/cm^3 and saturated with saline water.

As expected, the specimens compacted to a dry density of 1.50 g/cm^3 undergo strain, on saturation with granitic water, somewhat lower than in the case of specimens compacted to a dry density of 1.60 g/cm^3. Specimens compacted to a dry density of 1.70 g/cm^3 experienced higher swelling strains under the same load, in tests with both saline and granitic water.

Figure A-46 shows the final swelling strain of the clay in the tests performed with samples compacted to nominal dry densities of 1.60 g/cm^3 and saturated with different kinds of water, along with the fitting for the tests performed with both granitic and saline water. The final values of strain do not seem to be particularly dependent on the kind of water, although in the tests performed with saline water they are somewhat higher than in those performed with granitic water, the values for distilled water being the highest.

Strain (ε, %) as a function of vertical load (σ, MPa) may be approximately expressed by the following equations:

$$\varepsilon = \begin{cases} -9.4 + 15.9 \log \sigma & \text{for granitic water} \\ -11.4 + 14.4 \log \sigma & \text{for saline water} \end{cases} \quad \text{(A-4)}$$

UPC performed 21 flooding-under-load tests on specimens prepared at various dry densities varying between 1.57 g/cm^3 and 1.87 g/cm^3, with an initial water content of 11.7 % (water content at equilibrium with laboratory conditions). The specimens were saturated with distilled water while being subjected to a constant load ranging between 0.01 MPa and 10.00 MPa.

The strain (ε, %) induced after saturation is shown in Figure A-47 and may be approximately expressed by the equation

$$\varepsilon = -46.9 - 19.4 \log \sigma + 36.6 \rho_d \quad \text{(A-5)}$$

where σ is the vertical load in MPa and ρ_d is the initial dry density in g/cm^3.

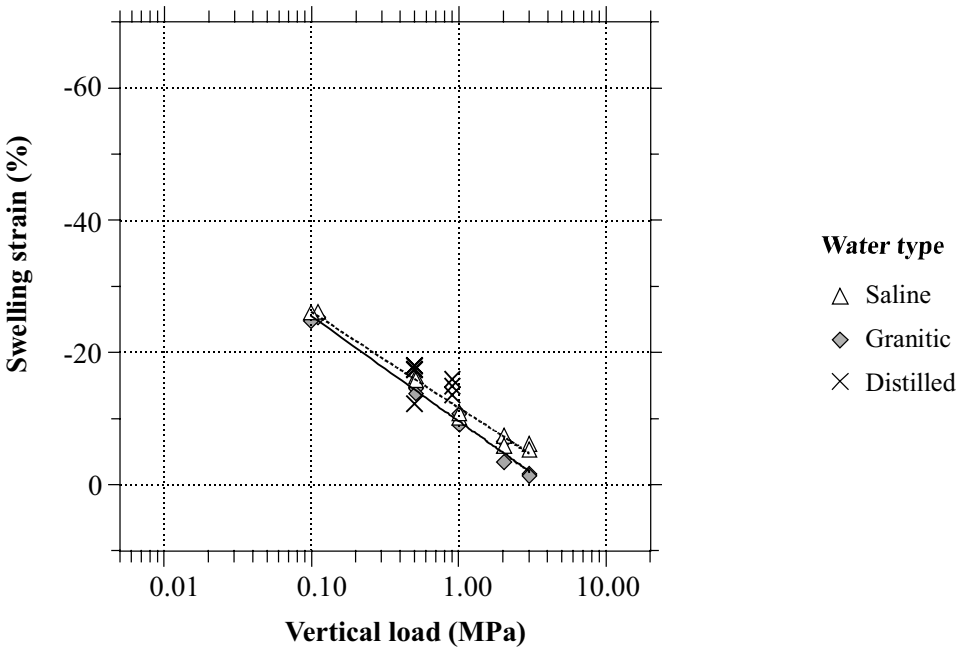

Figure A-46. *Swelling strain of specimens compacted to dry density 1.60 g/cm^3 on saturation under vertical load with different kinds of water (ENRESA 2000).*

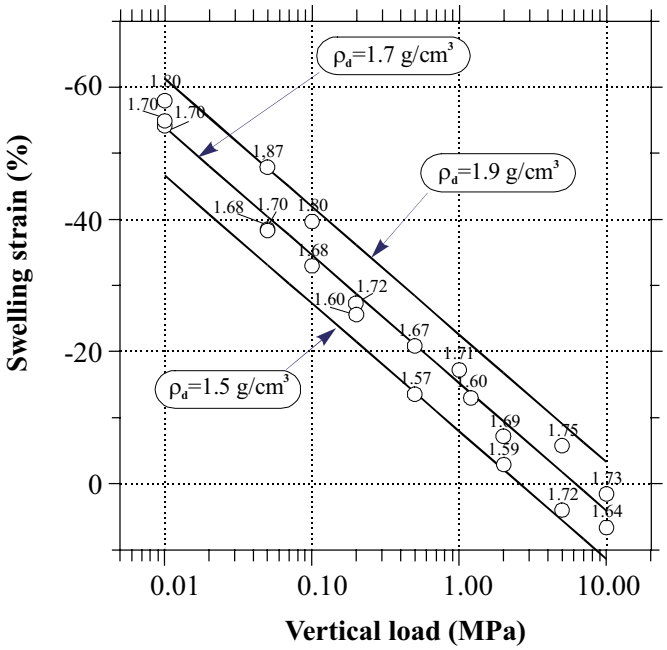

Figure A-47. *Swelling strain for different applied vertical loads with the value of initial dry density, in g/cm³, indicated for each point (ENRESA 2000).*

The strain values obtained with this equation for a dry density of 1.60 g/cm³ are slightly higher than those obtained with the fitting used by CIEMAT for tests performed with granitic water. The discrepancy is more marked for low loads, with a maximum difference of 5 percentage points. This would confirm that swelling under saturation with distilled water is somewhat higher than the swelling expected when saturation takes place with granitic water.

Elastic shear modulus, G

UPC-DIT determined the elastic shear modulus, G, at small deformations ($10^{-6} \leq \gamma \leq 10^{-4}$) for the FEBEX bentonite. The tests were performed in a resonant column on 10 specimens compacted at various dry densities and degrees of saturation. The results are shown in Table A-26 and in Figure A-48.

Table A-26. Elastic shear modulus obtained in resonant column tests (ENRESA 2000).

Dry density g/cm³	Water content %	Degree of saturation %	Void ratio	Elastic shear modulus, G, in MPa				
				s_3 = 0.01	s_3 = 0.1	s_3 = 0.2	s_3 = 0.4	s_3 = 0.8
1.58	14.7	54	0.757	140	207	245	300	370
1.66	13.6	57	0.668	211	223	270	-	-
1.54	3.4	12	0.802	78	106	174	208	326
1.56	2.8	10	0.777	89	106	138	-	-
1.62	24.6	95	0.717	240	270	-	331	336
1.66	21.3	87	0.677	252	296	370	429	502
1.65	4.7	19	0.685	74	90	137	190	310
1.72	10.4	47	0.615	200	219	293	381	429
1.68	3.7	16	0.652	61	89	141	200	290
1.62	12.7	50	0.713	122	180	240	299	387

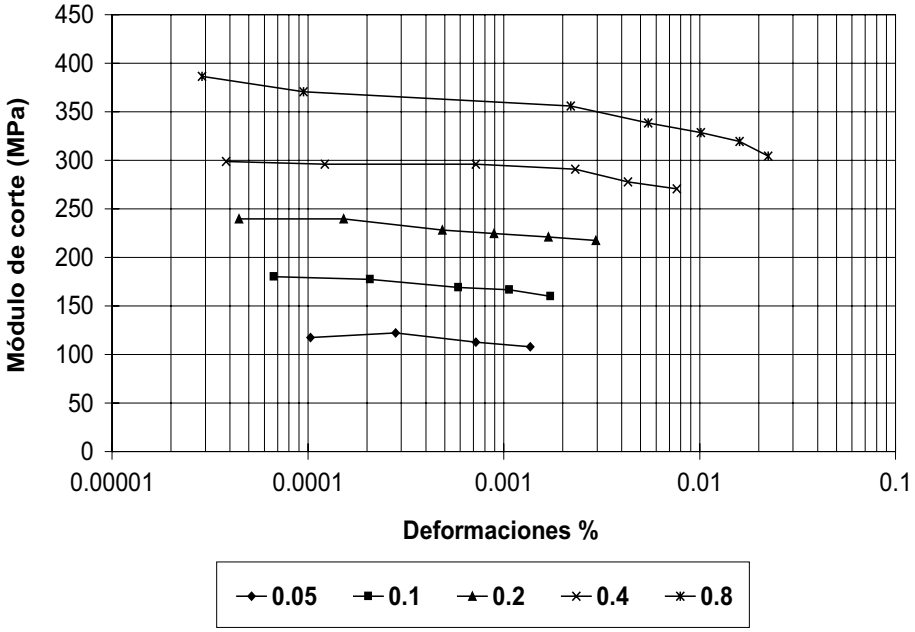

Figure A-48. *Shear modulus G as a function of the deformation at a degree of saturation of 0.5 and various confining pressures.*

Compressibility of joints

UPC-DIT performed unconfined compression tests on specimens of the FEBEX bentonite to obtain the relationship between normal stress and displacement in the joints between blocks. The joint displacements were calculated by comparing the average deformations in two specimens for the same level of load: one was a continuous specimen with a height of 7.8 cm and the other was formed by two pieces, each 3.9 cm in height, placed one on top of the other. Each specimen was tested with three different degrees of initial saturation. Figure A-49 shows the value of the decrease in distance between the joint surfaces of two blocks as a function of the normal load applied, for different degrees of saturation.

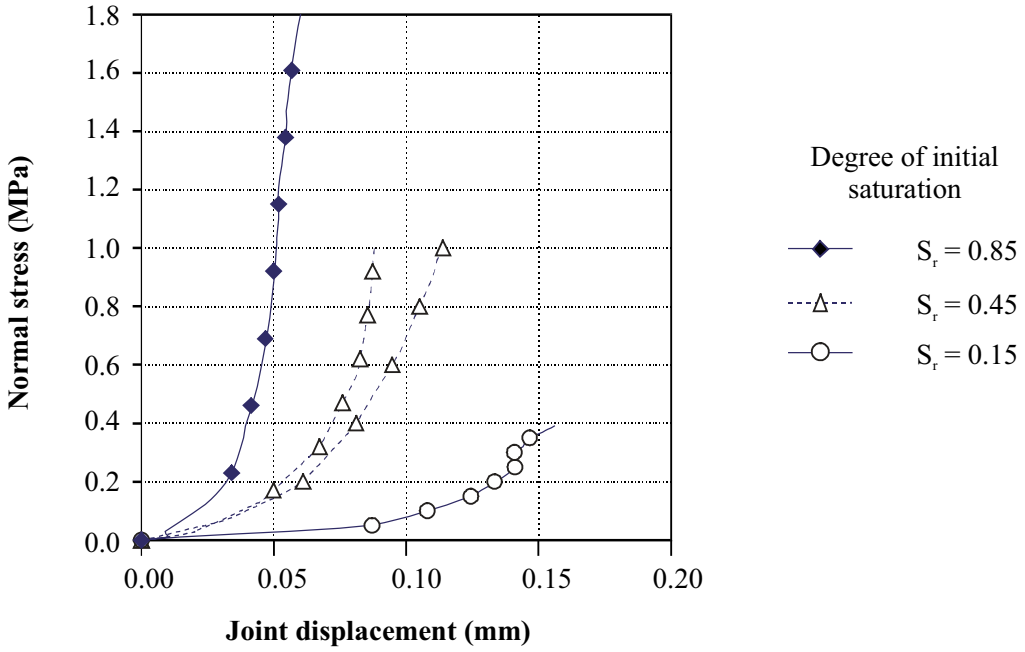

Figure A-49. *Displacement between joint surfaces for different degrees of saturation (ENRESA 2000).*

A3.2.2 Hydraulic properties

Saturated hydraulic conductivity

An empirical relationship has been obtained, using saturated specimens, for the coefficient of permeability of the FEBEX bentonite as a function of dry density. It was expressed by the following equations

$$\log k = \begin{cases} -6.00\rho_d - 4.09 & 1.30 \le \rho_d \le 1.47 \quad (r^2 = 0.97,\ 8 \text{ points}) \\ -2.96\rho_d - 8.57 & 1.47 \le \rho_d \le 1.84 \quad (r^2 = 0.70,\ 26 \text{ points}) \end{cases} \tag{A-6}$$

where k is the coefficient of permeability for distilled water, in m/s, and ρ_d is the dry density, in g/cm^3. The variation of the values actually obtained with respect to these fittings is of the order of 30 %.

Figure A-50 shows the regression lines for the coefficient of permeability of FEBEX bentonite shown above and the points obtained in different determinations. The influence of the water used as permeant has been tested, as well as the influence of the direction of the measurement, parallel or perpendicular to the compaction effort, in the value of the coefficient of permeability. None of these aspects seems to be relevant, with the exception of the use of saline water, that yields a higher hydraulic conductivity. The data indicate that the FEBEX bentonite is less permeable than the bentonite S-2. However, differences are small: in some cases it is even less than the scattering shown in the same set of tests.

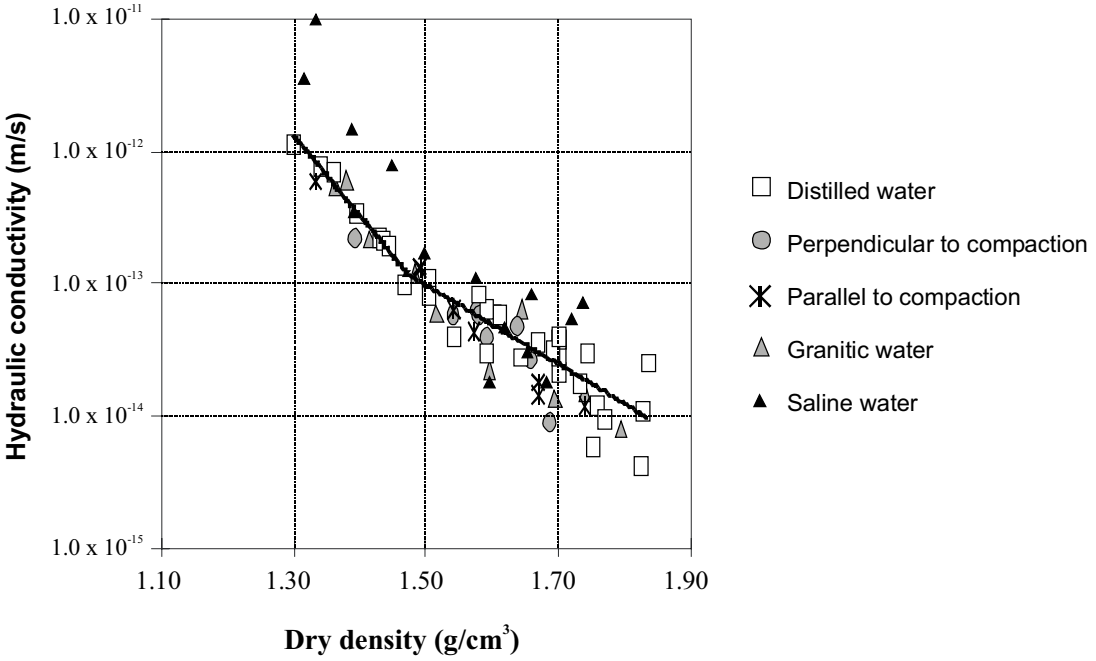

Figure A-50. *Saturated hydraulic conductivity as a function of dry density (ENRESA 2000).*

Relative permeability

Unsaturated hydraulic conductivity is highly dependent on the degree of saturation S_r and may be expressed as the product of relative permeability k_r times the saturated hydraulic conductivity. The dependence on the degree of saturation is usually expressed by means of a potential law for the relative permeability:

$$k_r = S_r^{\,n} \tag{A-7}$$

The water infiltration tests carried out by CIEMAT in small teflon cells (see Figure A-51) provide data allowing unsaturated hydraulic conductivity and its dependence on the degree of saturation to be obtained. In the tests, water content throughout the specimen was measured at different times after initiation of the infiltration process. By means of parameter identification techniques similar to those used in groundwater engineering and geophysics, intrinsic permeability and the exponent of the law used to obtain the relative permeability may be estimated. The values obtained were $K = 2.95 \times 10^{-21}$ m^2 (for a porosity of 0.4) and $n = 4.64$ respectively, in the case of samples with an initial dry density of 1.75 g/cm^3.

Similar infiltration tests have been carried out at UPC-DIT. In this case, in order to study the possibility of desaturation of the surrounding rock at the interface between the bentonite and the granite, a hydraulic gradient was prescribed across a specimen of granite in contact with another specimen of bentonite. The test was carried out in a triaxial cell with a confinement pressure of 0.8 MPa (see Figure A-52). Specimens were initially compacted at a dry density of 1.76 g/cm^3 and a water content of 13 %. No change in the water content of the granite was detected during the test. However, the measurements of water content in the bentonite allow a new value to be estimated for the exponent in the relative permeability law. Figure A-53 shows how good agreement is achieved between the measurements and numerical model computations, with the parameters derived from the identification process.

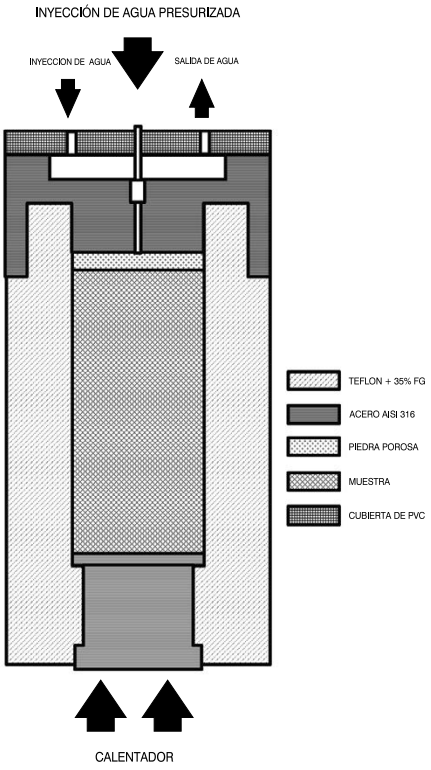

Figure A-51. *Scheme of the Teflon cell. The lateral walls of the cell are made of Teflon. Water may be enter or leave the cylindrical sample through a porous stone placed on the top of the sample. The openings in the upper steel cap allow the flow of water to or from the porous stone. The lower steel cap allows the heating of the bottom of the sample.*

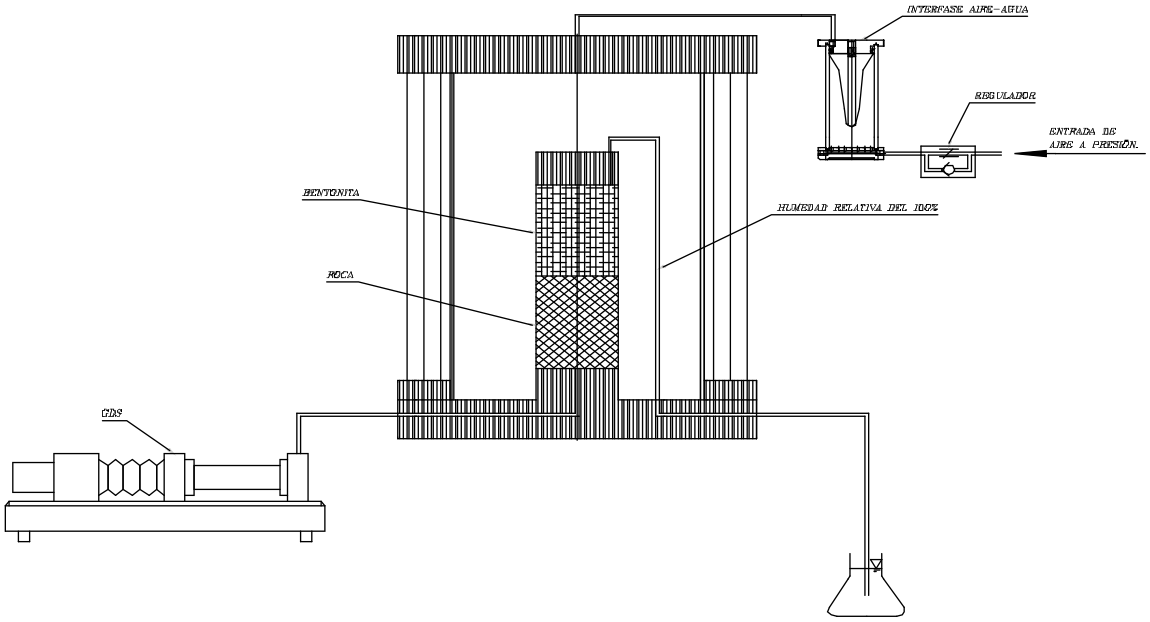

Figure A-52. *Scheme of the set up used in the infiltration tests.*

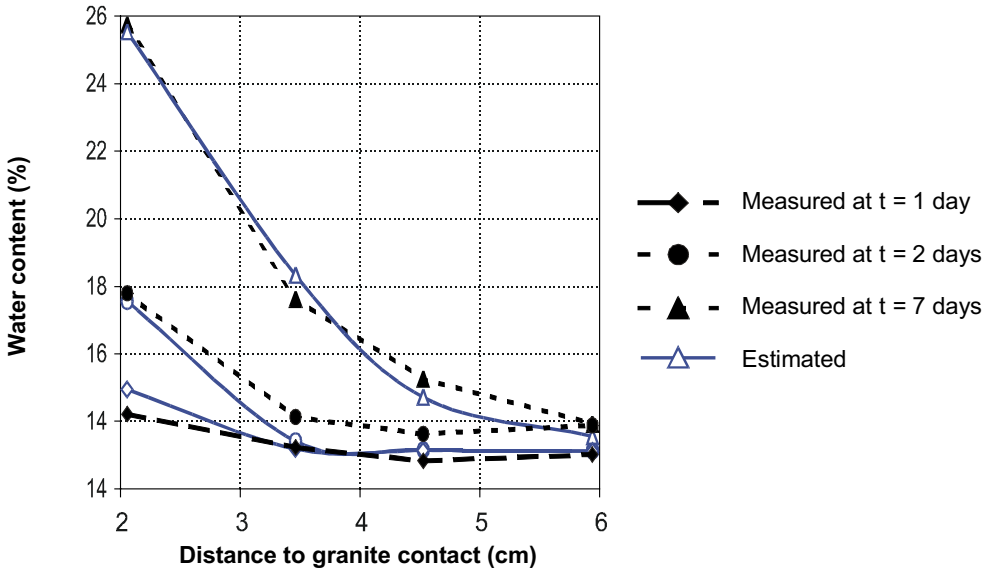

Figure A-53. *Measured and computed water content in infiltration tests (ENRESA 2000).*

In addition, the unsaturated water conductivity may be estimated in thermo-hydraulic experiments with prescribed heat and water flows. The summary of values obtained for the parameter *n* in the relative permeability law in Table A-27.

Table A-27. Exponent *n* in relative permeability law (3.5) from different test types (ENRESA 2000).

Test	*n*
Water infiltration in small teflon cells	4.64
Water infiltration in bentonite in contact with granite	3.50
Heat and water flow experiment 1	3.06
Heat and water flow experiment 2	1.10
Heat and water flow experiment 3	1.68

Suction–water content relationship at 20 °C

Tests on unconfined samples

CIEMAT has carried out suction–water content tests for the FEBEX bentonite, both in compacted samples and in samples trimmed from blocks. The relationship between suction and water content was initially determined in compacted samples for three different suction values and, subsequently following wetting and drying-wetting paths. UPC tested specimens at various temperatures and suctions between 3 MPa and 700 MPa following similar wetting and drying paths. Figure A-54 shows the tests results grouped according to initial dry density (ρ_{d0}). Tests with a dry density of 1.67 and 1.75 g/cm^3 were performed by CIEMAT and tests with a dry density of 1.64 g/cm^3 were performed by UPC. The relationship between suction s in MPa and the water content w in %, may be fitted by means of the following equation:

$$w = (45.1\rho_{d0} - 39.2) - (18.8\rho_{d0} - 20.34)\log s \quad \text{(A-8)}$$

where ρ_{d0} is the initial density in g/cm^3.

The volume variations observed with changing suction are important. Figure A-55 shows the relationship between the dry density and the change in suction for the different samples tested, grouped according to their initial dry densities. The dry density for values of suction ranging from 400 to 0.1 MPa may be obtained through the following expression:

$$\rho_d = 1.15\, s^{0.13\rho_{d0} - 0.15} \quad \text{(A-9)}$$

where ρ_{d0} is the initial dry density in g/cm^3 and s is the suction in MPa.

For suctions varying between 2.0 MPa and 385.0 MPa, an empirical equation relating water content and suction was determined for the bentonite S-2

$$w = 36.1 - 12.0\log s \quad (r^2 = 0.94,\ 191 \text{ points}) \quad \text{(A-10)}$$

which does not depend on initial dry density. In this equation, w is the water content in %, and s the suction in MPa. Figure A-56 shows the regression curves for the bentonites (S-2 and FEBEX) and the points obtained by CIEMAT and UPC for each bentonite.

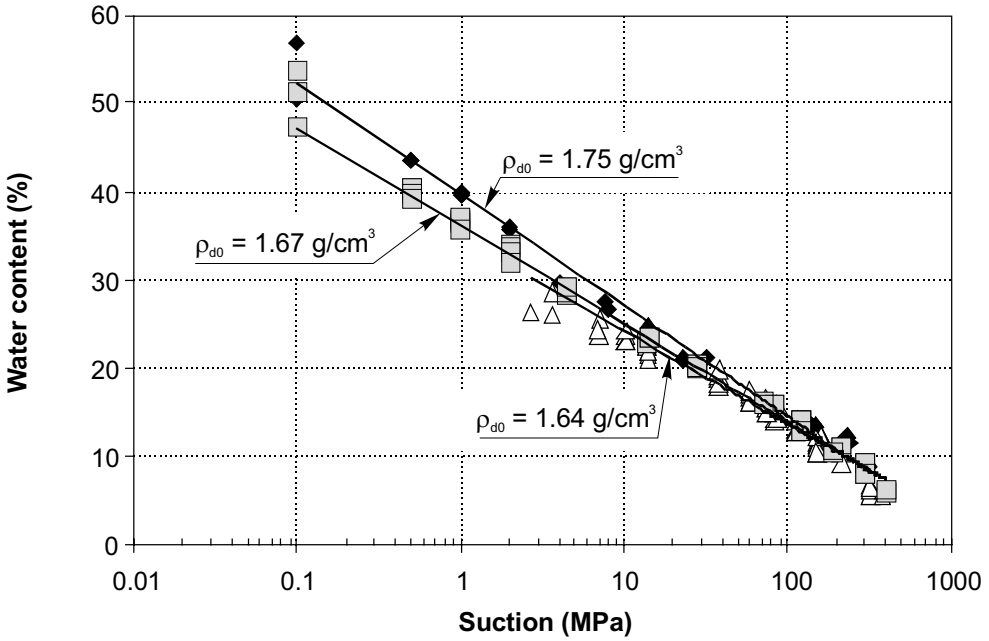

Figure A-54. *Suction/water content relationship in tests on unconfined samples, for FEBEX bentonite (ENRESA 2000).*

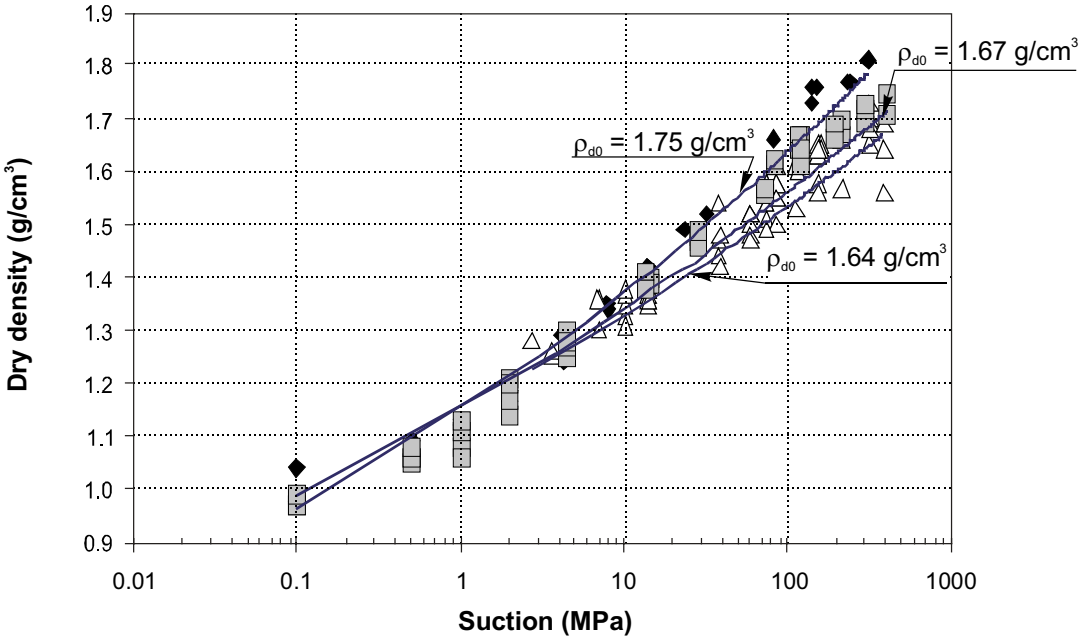

Figure A-55. *Relationship between dry density and suction in tests on unconfined samples, for FEBEX bentonite (ENRESA 2000).*

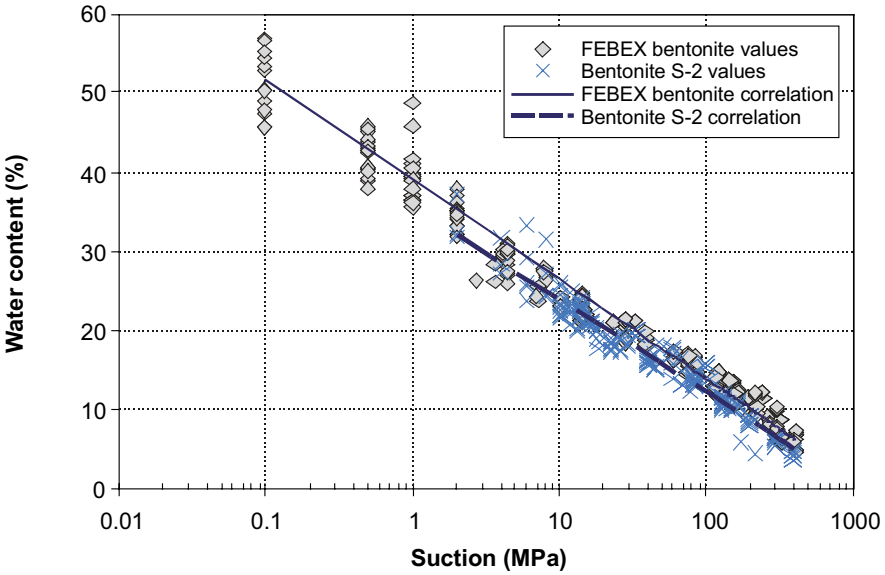

Figure A-56. *Suction/water content relationship in tests on unconfined samples, for S-2 and FEBEX bentonites (ENRESA 2000).*

As may be seen, the differences between the two curves are very small, one or two percentage points in the water content, depending on the suction value. Nevertheless, it may be said that there exists a difference that is reflected in the water content in equilibrium with the laboratory conditions, as was indicated in Table A-22. For all practical purposes, the differences between the two bentonites are very small.

In the low range of suction, water contents determined at a temperature of 72 °C are higher than those determined at 20 °C. However, the results are limited and more tests are required to quantify the effect of temperature on suction/water content relationship.

Tests on confined samples

In unconfined tests, the dry density and structure of the bentonite undergo important changes during the hydration process. However, volume changes are small in a bentonite barrier, and knowledge of the relationship between suction/water content at constant dry density (characteristic or water retention curve) is essential.

To determine the retention curve, two kinds of tests have been performed. CIEMAT used suction controlled oedometers to hinder swelling of the clay, by adding the appropriate loads. UPC designed containers made from sintered metal to fix the volume of the sample, while the water vapor in the clay changes with the atmosphere in which the capsule is placed. In both cases, minor volume changes have occurred.

The retention curves determined may be fitted by means of the Van Genuchten expression:

$$S_r = S_{r_0} + (S_{r_{max}} - S_{r_0}) \left[1 + \left(s/P_0\right)^{1/(1-\lambda)}\right]^{-\lambda} \quad \text{(A-11)}$$

or to a modification of this expression that is more suitable for higher values of suction:

$$S_r = S_{r_0} + (S_{r_{max}} - S_{r_0}) \left[1 + \left(s/P_0\right)^{1/(1-\lambda)}\right]^{-\lambda} \left[1 - s/P_s\right]^{\lambda_s} \quad \text{(A-12)}$$

where S_{r0} and $S_{r\max}$ are the residual and maximum degree of saturation and P_0 is the air entry value and λ, P_s and λ_s are material parameters. Table A-28 shows the parameters fitted for the wetting paths, that are plotted together with the experimental points in Figure A-57. Table A-29 shows the parameters fitted for the wetting paths, that are plotted together with the experimental points in Figure A-58.

Table A-28. Parameters of the retention curves (ENRESA 2000).

ρ_d range g/cm^3	Type of equation (no. in Figure A-57)	P_0 MPa	λ	$S_{r\,0}$	$S_{r\,max}$	P_s MPa	λ_s
1.70 – 1.75	Van Genuchten (1)	90	0.45	0.00	1.00	-	-
1.70 – 1.75	modified van Genuchten (2)	100	0.45	0.01	1.00	1 500	0.05
1.60 – 1.65	Van Genuchten (3)	30	0.32	0.10	1.00	-	-
1.60 – 1.65	modified van Genuchten (4)	35	0.30	0.01	1.00	4 000	1.5
1.58 – 1.59	Van Genuchten (5)	4.5	0.17	0.00	1.00	-	-
1.58 – 1.59	modified van Genuchten (6)	2.0	0.10	0.01	0.99	1 000	1.3

Table A-29. Parameters for fitting of the drying paths after saturation (ENRESA 2000).

ρ_d range g/cm^3	Type of equation (no. in Figure A-58)	P_0 MPa	λ	$S_{r\,0}$	$S_{r\,max}$	P_s MPa	λ_s
1.70 – 1.75 drying	Van Genuchten (1)	180	0.62	0.0	1.0	-	-
1.70 – 1.75 wetting	modified van Genuchten (2)	100	0.45	0.01	1.0	1 500	0.05
1.58 – 1.59 drying	Van Genuchten (3)	30.0	0.15	0.0	1.0	-	-
1.58 – 1.59 wetting	modified van Genuchten (4)	2.0	0.10	0.01	0.99	1 000	1.3

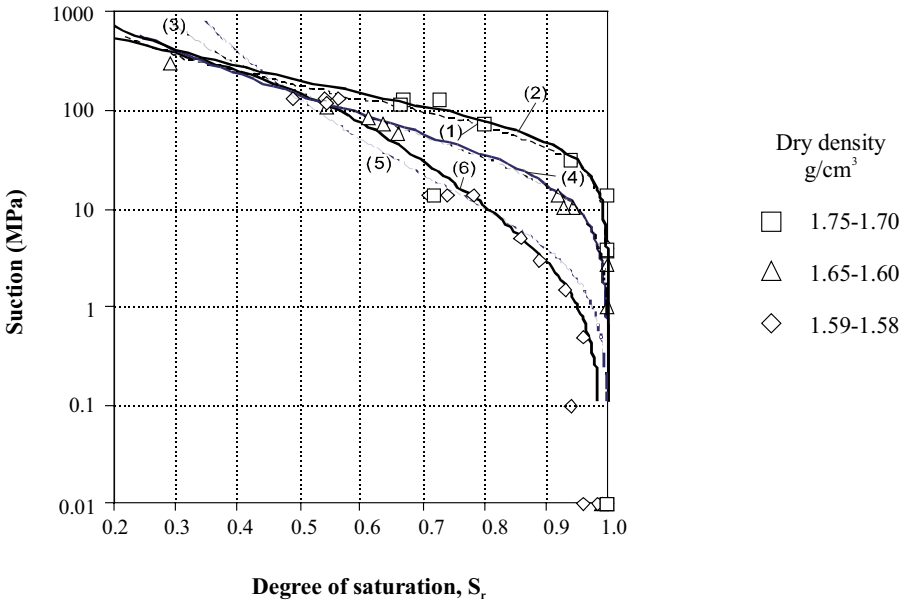

Figure A-57. *Measured and fitted retention curves in wetting paths performed on confined samples. In parentheses, the number of the equation used in Table A-28 is shown (ENRESA 2000).*

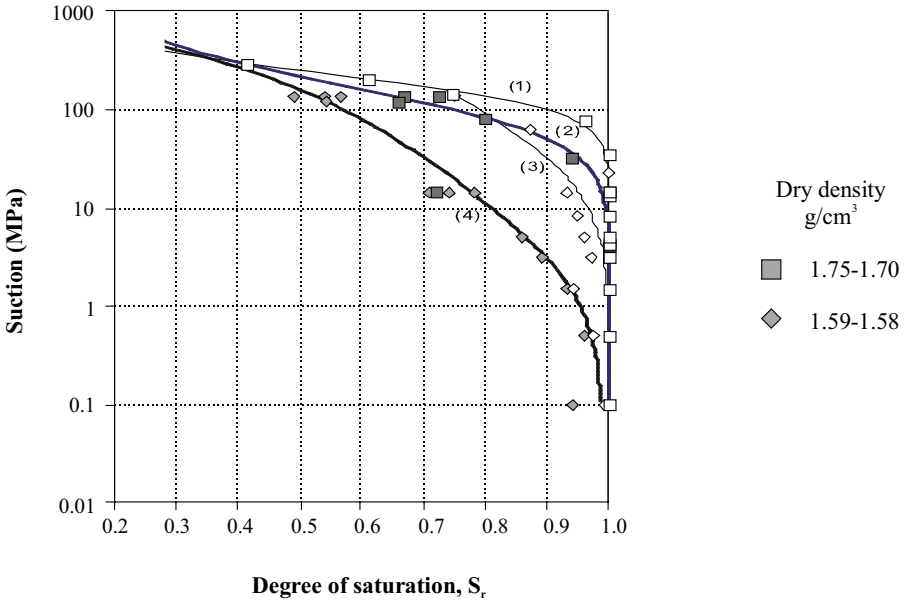

Figure A-58. *Hysteresis effect on the wetting-drying paths under confined conditions. Bold symbols correspond to wetting paths. In parentheses the numbers of the curves indicated in Table A-29 (ENRESA 2000).*

Gas permeability

The gas permeability of the compacted clay has been determined using nitrogen gas as a fluid, injected at a low pressure. Specimens of nominal dry densities ranging from 1.50 to 1.70 g/cm^3 and with different water contents have been tested. The values obtained are plotted in Figure A-59, together with the fitting obtained (valid only for the degree of saturation between 25 and 80 %):

$$K_g = 3.164 \cdot 10^{-6} [e(1 - S_r)]^{4.3} \quad (r^2 = 0.82, 39 \text{ points}) \qquad \text{(A-13)}$$

where K_g (m/s) is the gas permeability, e the void ratio and S_r the degree of saturation.

The gas permeability for the same degree of saturation is a function of dry density and decreases with the degree of saturation, for the same dry density. In tests performed with the bentonite equilibrium water content compacted to different dry densities it was observed that gas permeability decreases logarithmically with increasing dry density.

In all of the tests performed, the values of intrinsic permeability obtained (which ranges between 10^{-16} and 10^{-12} m/s) are higher than those obtained when intrinsic permeability is calculated from hydraulic conductivity tests conducted with the clay under saturated conditions (Figure A-60). This is due to the different structural disposition of the saturated and unsaturated specimens, caused by swelling of the clay as it hydrates. In water flow tests performed under saturated and confined conditions, the bentonite tries to swell and fill the interaggregate pores. Under these conditions, mean pore diameter is close to intra-aggregate pore size (about 0.01 µm). In the case of gas flow under dry conditions, this flow takes place through interaggregate pores with a diameter of more than 1 µm. This difference in accessible pore size may explain the different values of intrinsic permeability that have been derived from water and gas flow.

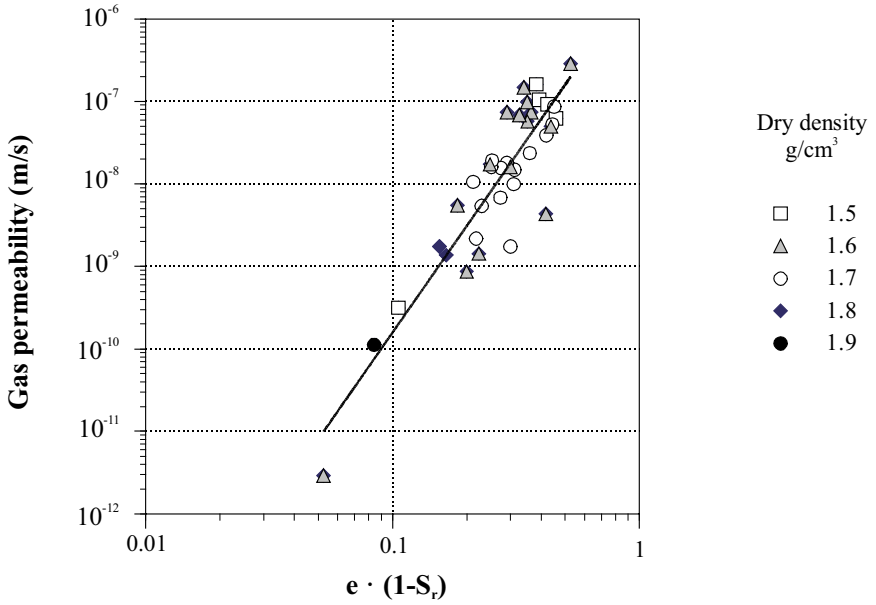

Figure A-59. *Gas permeability measured in specimens of FEBEX bentonite compacted to different dry densities and with varying water content (ENRESA 2000).*

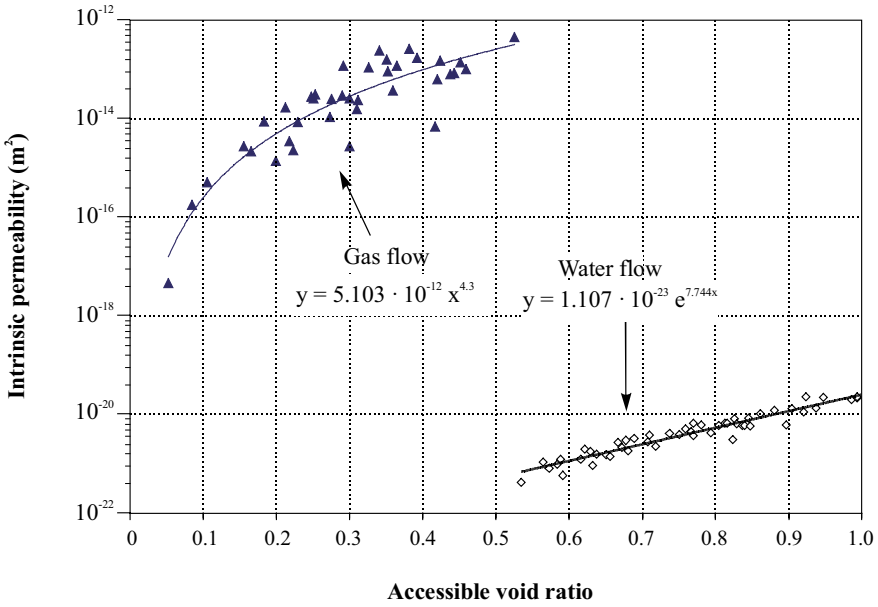

Figure A-60. *Intrinsic permeability of the compacted clay obtained from saturated water flow and from unsaturated gas flow tests. In gas flow tests, the accessible void ratio indicates the ratio between gas accessible pore volume and particle volume (e(1-Sr)) (ENRESA 2000).*

A3.2.3 Thermal properties

Specific heat

Specific heat has been determined only for bentonite S-2. The relationship between specific heat and temperature fit the following equation, in a range of temperatures of between 45 °C and 150 °C:

$$c_s = 1.38T + 732.5 \qquad \text{(A-14)}$$

where c_s is the specific heat, in J/kg°C, and T is the temperature, in °C.

Thermal conductivity

The superficial thermal conductivity of the FEBEX bentonite has been determined in compacted specimens at various nominal dry densities and with different water contents.

Figure A-61 shows the regression curves of the values of superficial thermal conductivity as a function of the degree of saturation, for bentonites S-2 and FEBEX. A good correlation of the sigmoidal type (Boltzmann) was obtained for the two bentonites by means of the following equation:

$$\lambda = A_2 + \frac{A_1 - A_2}{1 + e^{(S_r - x_0)/d_x}} \qquad \text{(A-15)}$$

where λ is the thermal conductivity, in W/m·°K, S_r is the degree of saturation, A_1 is the value of λ for $S_r = 0$, A_2 is the value of λ for $S_r = 1$, x_0 is the degree of saturation for which the thermal conductivity is the average value between the extreme values, and d_x is a parameter. Table A-30 shows the parameters obtained in the fitting of the curves.

There is a difference between the values measured for FEBEX and S-2 bentonite (see Figure A-61). This difference is more noticeable for lower values of the degree of saturation. No clear evaluation of the differences is possible, because thermal conductivity increases not only with the water content but also with dry density. In addition, for the bentonite S-2, there are only two points for the lower degrees of saturation. However, taking into account all the experimented points, differences between the two bentonites seem to be small.

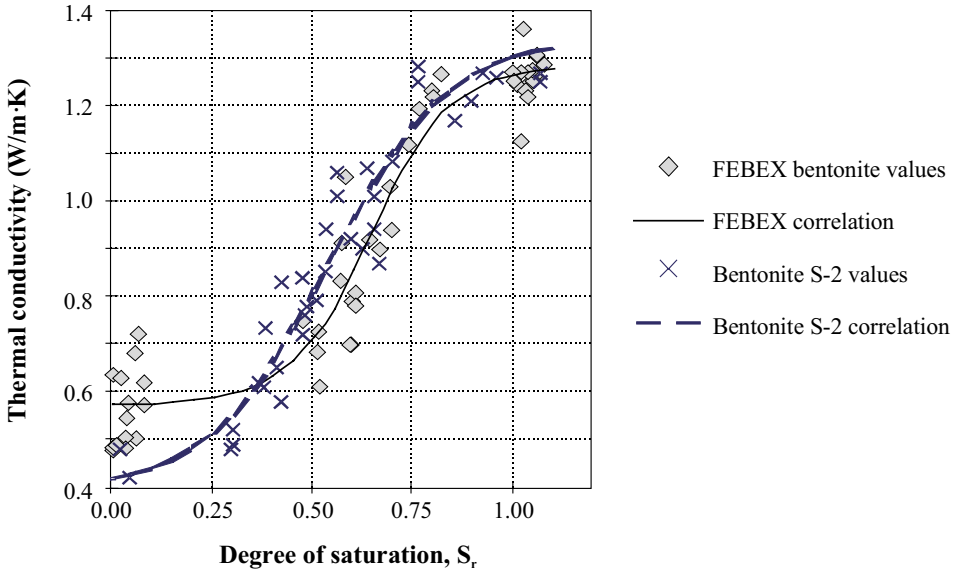

Figure A-61. *Thermal conductivity as a function of degree of saturation (ENRESA 2000).*

Table A-30. Parameters for fitting of the drying paths after saturation (ENRESA 2000).

Parameter	Bentonite S-2	FEBEX bentonite
A_1	0.39 ± 0.08	0.57 ± 0.02
A_2	1.34 ± 0.06	1.28 ± 0.03
x_0	0.54 ± 0.03	0.65 ± 0.01
d_x	0.15 ± 0.03	0.10 ± 0.02

Coefficient of linear thermal expansion

Measurements of thermal expansion have been carried out on 12 samples of compacted bentonite for initial dry densities ranging between 1.57 and 1.72 g/cm^3 and a water content varying between 12.5 and 25.1 %. The specimens (38 mm in diameter, 76 mm in height) were placed in an isothermal bath with controlled temperature. A latex membrane keeps the overall water content of the soil constant throughout the heating and cooling processes. Temperature varies between 25 and 70 ºC. In each test, several cycles of heating and cooling are applied to the sample.

The vertical strains in the first heating path are higher than the strains measured during the second and subsequent cycles. In addition, in each cycle the strains measured during the heating process are higher than those observed throughout the cooling path and, as a result, an accumulation of irreversible strains is observed. The slope of the relationship between temperature and strain is shown in Figure A-62. This slope increases slightly with temperature. The following correlations for the linear thermal expansion coefficient have been obtained from this figure:

$$\Delta\varepsilon_z/\Delta T = \begin{cases} -0.118\times10^{-4} + 6.5\times10^{-6}T & \text{(first heating paths)} \\ -1.265\times10^{-4} + 6.5\times10^{-6}T & \text{(subsequent heating paths)} \\ -1.538\times10^{-4} + 6.5\times10^{-6}T & \text{(cooling paths)} \end{cases} \quad \text{(A-16)}$$

where ε_z is the linear strain and T the temperature in °C. At temperatures higher than 55 °C, an increase in the dispersion of the results is observed. This dispersion is due to experimental difficulties, such as equipment calibration and specimen sealing.

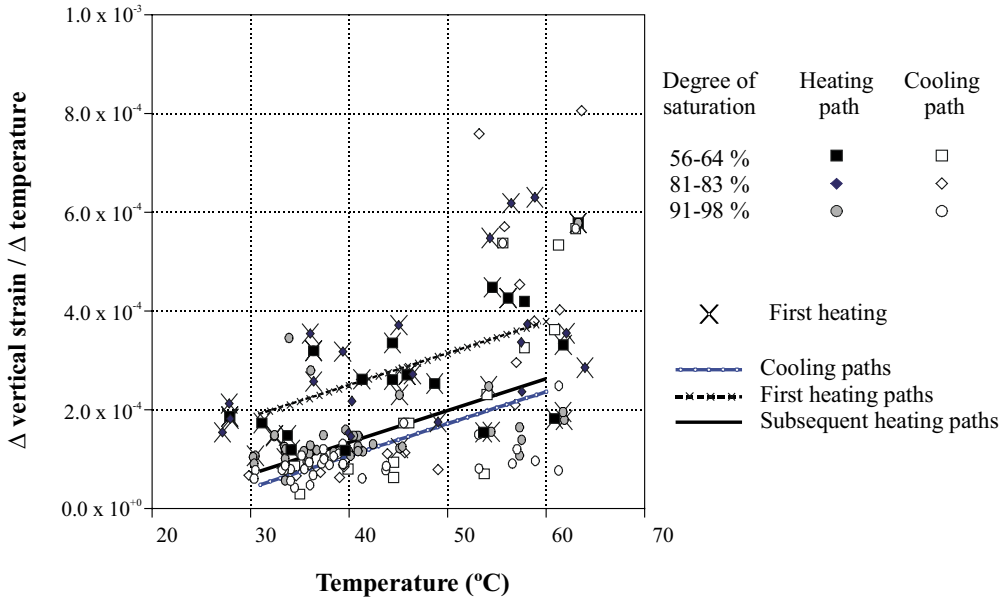

Figure A-62. *Linear thermal expansion as a function of temperature (ENRESA 2000).*

A3.3 Thermo-hydro-mechanical tests

A3.3.1 Tests for calibration of models by backanalyses. Thermohydraulic cell

A general methodology has been developed for the performance of systematic backanalysis of laboratory tests involving the thermohydraulic behaviour of bentonite. The procedure is based on a maximum likelihood approach, which defines a probabilistic framework in which error measurements and the reliability of the parameters identified can be estimated. With a view to identifying the model parameters, an objective function incorporating the differences between measured data and model computations is minimized. The method is applied to the identification of certain thermal and hydraulic properties of a bentonite specimen, using temperature and water content measurements as input data. The finite element code "CODE BRIGHT" (V2.0) has been used to model the thermohydraulic behaviour of clay. Although the code allows the mechanical behaviour of soils to be studied in a coupled manner, only the thermal and water flow capacities of the code have been used.

A new testing device has been developed to obtain the data required for the identification of certain thermohydraulic parameters. A controlled heat flux is applied at one end of a cylindrical specimen (38 mm in diameter, 76 mm long) and the other end is maintained at constant temperature. A latex membrane, that allows deformation and keeps overall water content constant, and a 5.5 cm thick heat insulating deformable foam surrounds the specimen. In order to ensure knowledge of the heat flux crossing the sample, two specimens symmetrically placed with respect to the heater are used in the tests. The heater is a copper cylinder (38 mm diameter, 50 mm long) with five small electrical resistances inside. A constant power of 2.6 W has been used in the tests, allowing steady temperatures in the range of 70–80 °C to be reached at the hotter end of the specimen. At the cold end, a constant temperature of 30 °C is maintained by flowing water in a stainless steel head in contact with the soil. Figure A-63 shows a scheme of the thermohydraulic cell.

Axisymmetric analyses performed with CODE BRIGHT allowed the effect of lateral loss of heat to be evaluated. It was estimated as 60 % of total heater power. This indicates the importance of performing a 2D analysis of the experiment.

During the tests, the temperatures at both ends of the specimen, and at three internal points located at regular intervals, are monitored. At the end of the tests, changes in diameter were measured at some points of the specimen, with an accuracy of up to 0.01 mm. Finally, the soil samples were cut in six small cylinders and the water content of each slice was determined.

Three specimens of bentonite compacted at a dry density of 1.68 g/cm^3 and with water contents of 15.3, 16.9 and 17.1 % were tested. The temperatures measured during the heating period for one of the specimens are shown in Figure A-64. Temperature reaches a quasi-steady regime 10 hours after the start of the test.

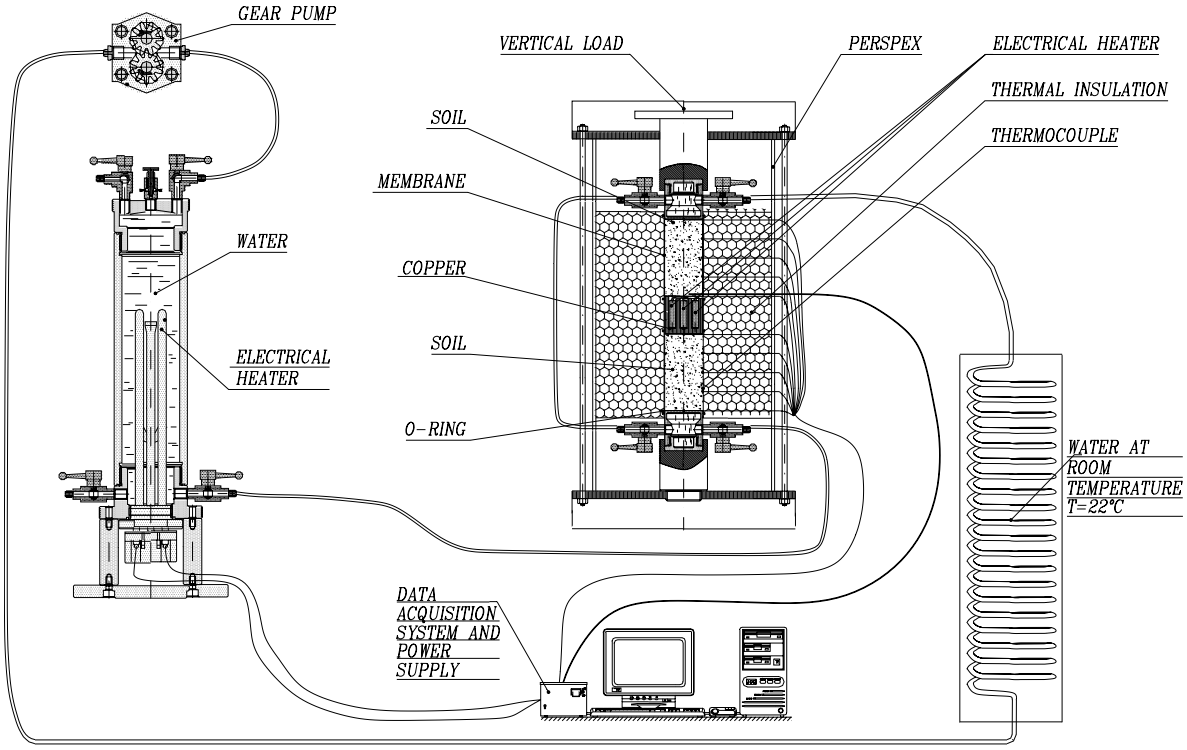

Figure A-63. *Scheme of the thermohydraulic cell.*

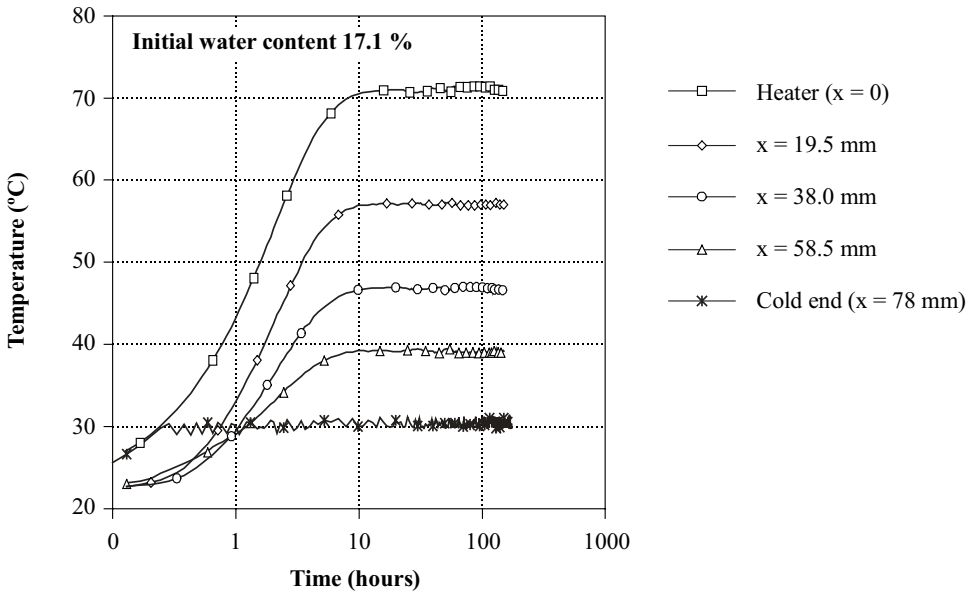

Figure A-64. *Evolution of temperature in a prescribed heat flow test (ENRESA 2000).*

A fully coupled thermo-hydraulic model has been used to simulate the experiment. The temperatures obtained under steady-state conditions and the water content measured at the end of the test have been considered as input data. In each test, three parameters have been identified: the conductivity of bentonite under saturated conditions, λ_{sat}, needed to obtain unsaturated thermal conductivity ($\lambda = (\lambda_{sat})^{Sr} (\lambda_{dry})^{(1-Sr)}$); the tortuosity, τ (a parameter of the diffusion constant) and the exponent "*n*" for the unsaturated (relative) permeability law ($k_r = S_r^n$). The thermal conductivity under dry conditions (λ_{dry}) is fixed at 0.47 W/m°C. The parameters obtained during the identification process are similar but not identical in the three tests, as shown in Table A-31. The values are within the normal range of these parameters. In addition, the identification technique provides a systematic and consistent procedure allowing the parameters that best reproduce the measurements for the selected model to be found. The method also gives an insight into the model structure, and allows the dependence and coupling between parameters to be detected. In the present type of test, analysis of the model structure shows that the values of the parameter "n" that has been obtained entail a higher degree of uncertainty than the values of the other parameters. This is in accordance with the relative influence of water flow in liquid and vapour phases.

Table A-31. Exponent n in relative permeability law, tortuosity factor t and saturated thermal conductivity l_{sat} obtained from different thermal flow tests (ENRESA 2000).

Test	Water content	n	τ	λ_{sat} W/m°C
1	15.5	3.06	0.56	1.19
2	16.9	1.10	0.74	1.31
3	17.1	1.08	0.90	1.18

The optimization procedure showed that there are a few combinations of parameters that give similar result in terms of the objective function. This is reasonable, as measured water content is a global quantity, and it is difficult to distinguish between water transported by liquid flow (controlled by "n") and by vapour diffusion (controlled by τ).

Figure A-65 shows the objective function in terms of the tortuosity factor t and the exponent "n" for the relative permeability law, for one of the controlled heat flow tests. In order to give the same importance to the sets of measurements for temperature and water content, a weighting procedure has been used to define the objective function. Contours are isolines of the objective function with different combinations of the parameters. The parameter values obtained by backanalysis are located at the minimum of the objective function. The same figure includes points representing the values of the parameters obtained in the other backanalyzed tests. In the case of the hydraulic tests described in Section A3.3.2 only the exponent "n" is known. In all cases, the representative points are located in the same area of the objective function, with similar values of error. A set of optimum parameters and laws (see Table A-32) may be selected taking all the tests into account.

Table A-32. Values for the saturated hydraulic conductivity k_{sat}, the relative permeability k_r, the tortuosity factor τ and the thermal conductivity λ (ENRESA 2000).

Parameter	Value
k_{sat}(porosity = 0.4)	2×10^{-21} m^2
k_r	S_r^3
τ	0.8
λ(W/m°C)	0.47^{1-Sr} 1.15^{Sr}

This set of parameters has been used to solve the direct problem and to simulate some water infiltration and heat flow tests. Figure A-66 to Figure A-69 show that the agreement between the measurements and the model computations is satisfactory.

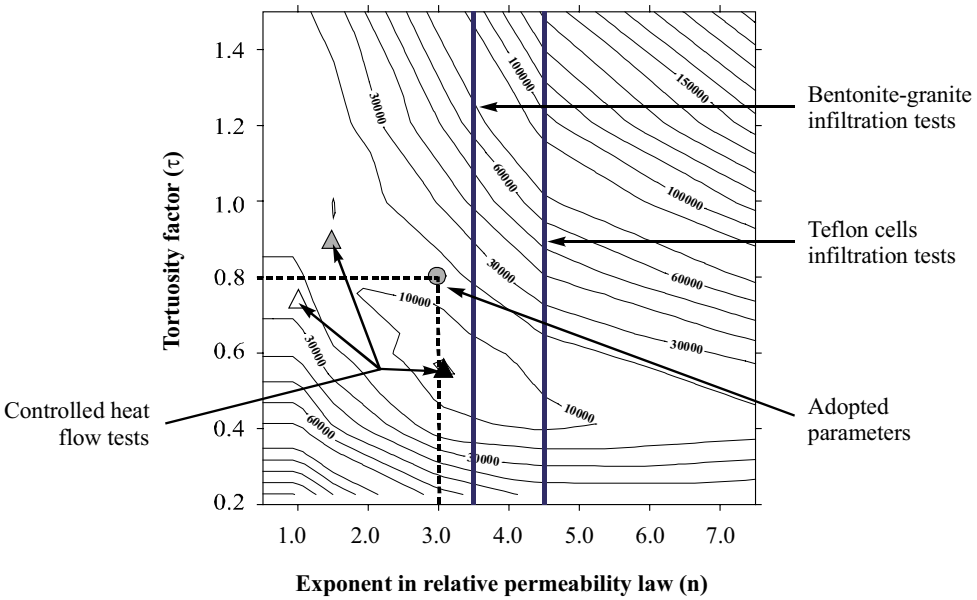

Figure A-65. *Contour map of objective function in the case of thermal flow test 1 (see details in Table A-31). The same graph shows the parameter values obtained by backanalyzing different tests (ENRESA 2000).*

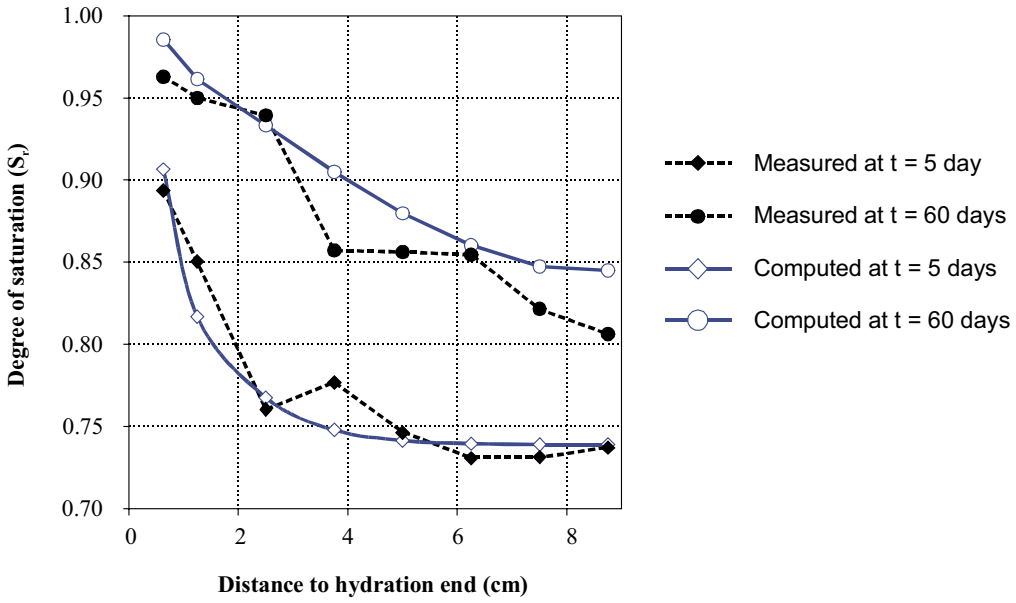

Figure A-66. *Measured and computed degree of saturation in small cell infiltration tests carried out in CIEMAT, using the final selected parameters (ENRESA 2000).*

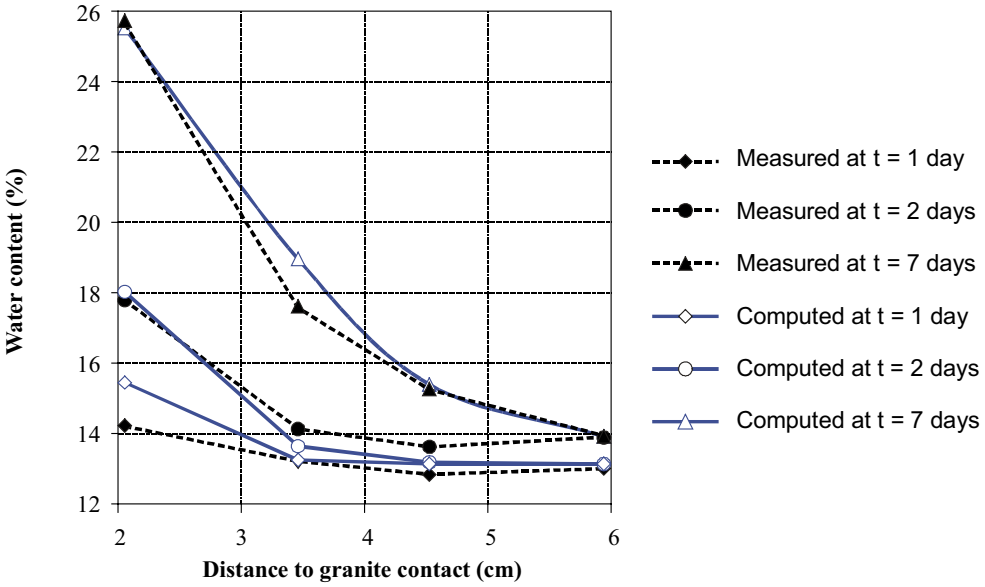

Figure A-67. *Measured and computed water content in bentonite-granite infiltration tests carried out at UPC, using the final selected parameters (ENRESA 2000).*

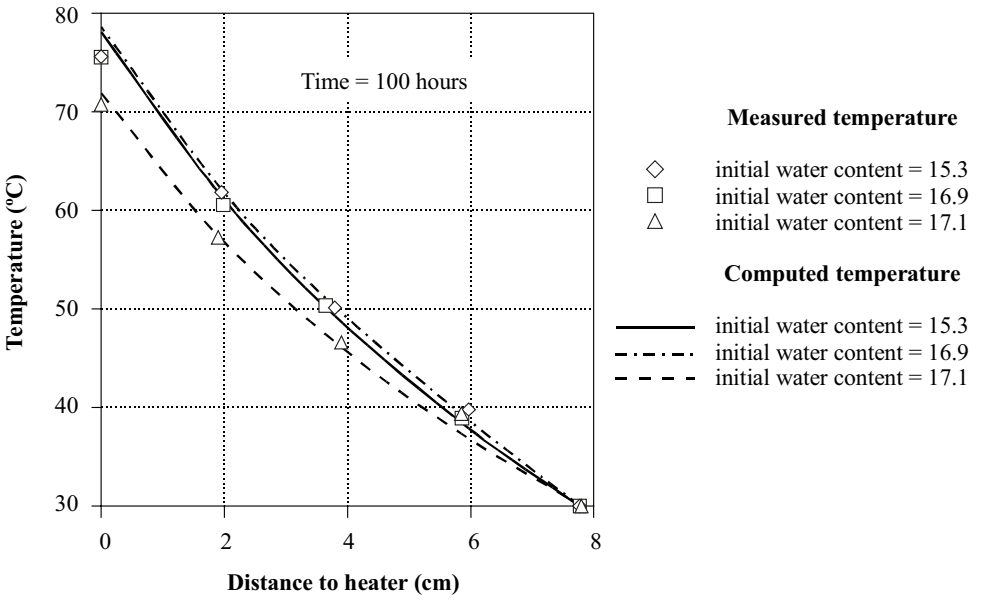

Figure A-68. *Measured and computed temperature in prescribed heat flow tests, using the final selected parameters (ENRESA 2000).*

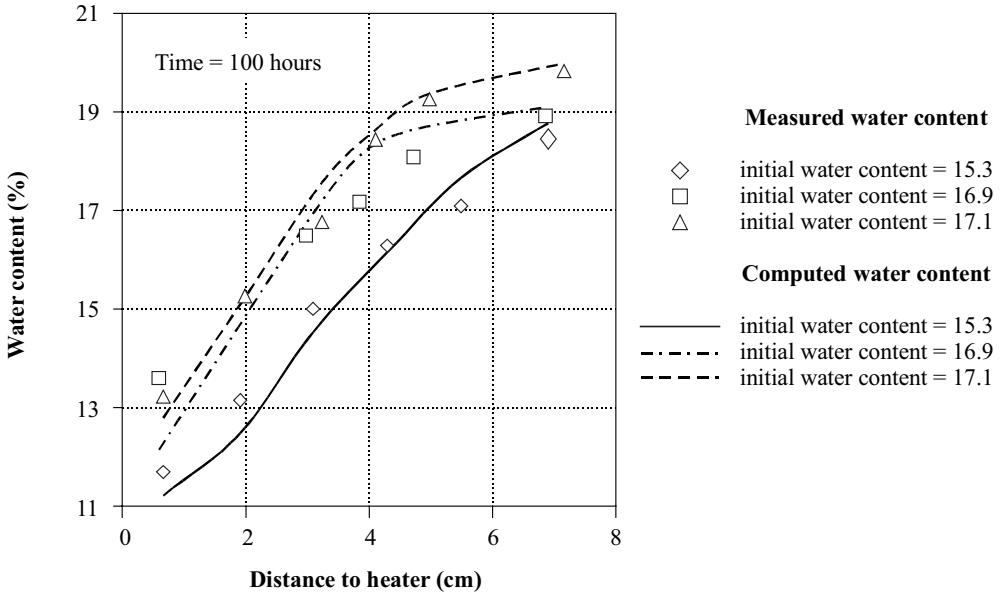

Figure A-69. *Measured and computed water content in prescribed heat flow tests, using the final selected parameters (ENRESA 2000).*

A3.3.2 Mechanical properties: oedometer tests with controlled suction

Suction controlled oedometer tests have been performed at CIEMAT (24 tests) and UPC (5 tests) on compacted bentonite with a water content in equilibrium with the laboratory conditions, and at dry densities of 1.7 and 1.65 g/cm^3 respectively. Three types of paths have been followed. In the first type, simulating the behaviour of a point near the heater, an initial drying process is followed by a loading path, and finally the bentonite is saturated. In the second type, simulating a point near the external boundary, an initial path of suction decrease is followed by an increase in load. In the third case, aimed at reproducing a swelling pressure test, an attempt was made to maintain the height of the sample constant during a suction reduction path by applying increments of vertical load. Suction is applied, with the relative humidity of the air on the sample being controlled by means of sulphuric acid or salt solutions in the high suction range, and by the axis translation technique in the case of suctions ranging from 0 to 14 MPa.

Figure A-70, reproduces the results of two of the tests carried out at CIEMAT (EDS3_9 and EDS5_5). The volume changes measured reflect the typical behaviour of compacted clay. It may be observed that for a small value of vertical load the vertical strains on saturation are higher than when a high load is applied. At the same time, the strain under the loading path is higher when the soil is in saturated conditions after reaching important swelling strains. Figure A-71 and Figure A-72 show the experimental results in the case of suction decrease paths with different values of applied vertical load and load increase paths with different values of applied suction.

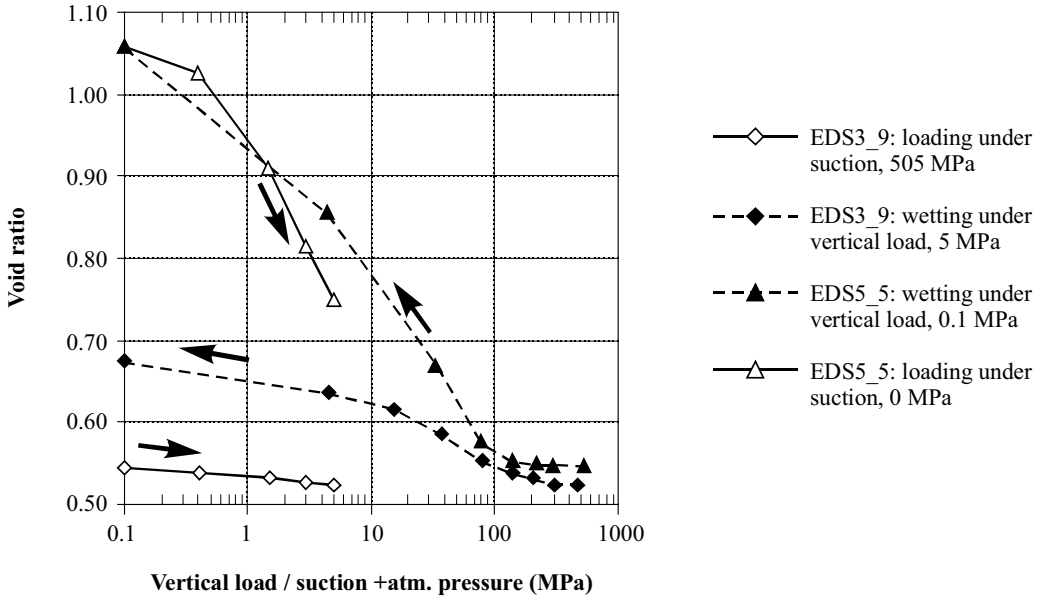

Figure A-70. *Typical results in two suction controlled oedometer tests on compacted bentonite with an initial density of 1.7 g/cm³ (ENRESA 2000).*

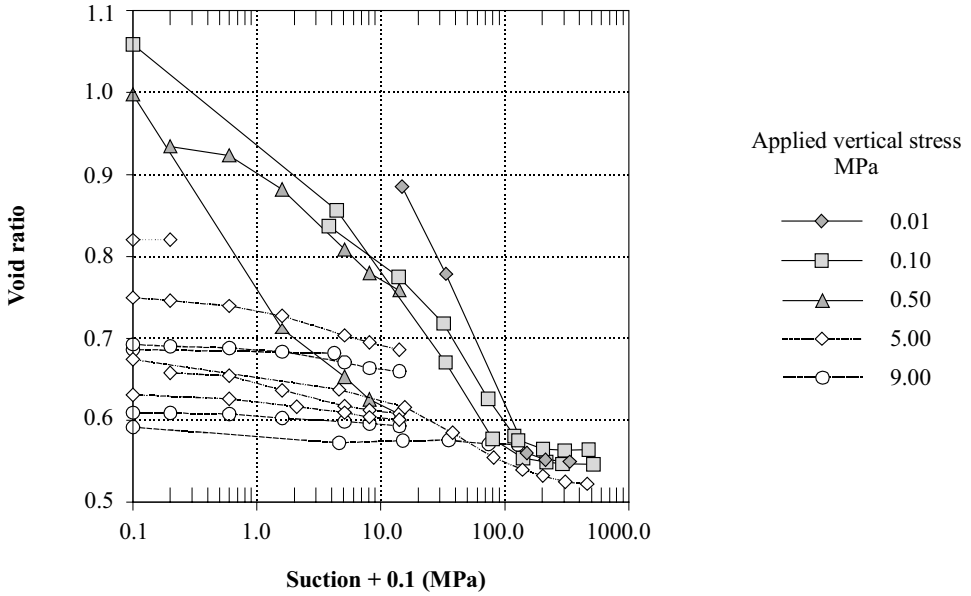

Figure A-71. *Volume changes measured in suction controlled oedometer tests, in wetting paths under different loads. Initial dry density 1.7 g/cm³ (ENRESA 2000).*

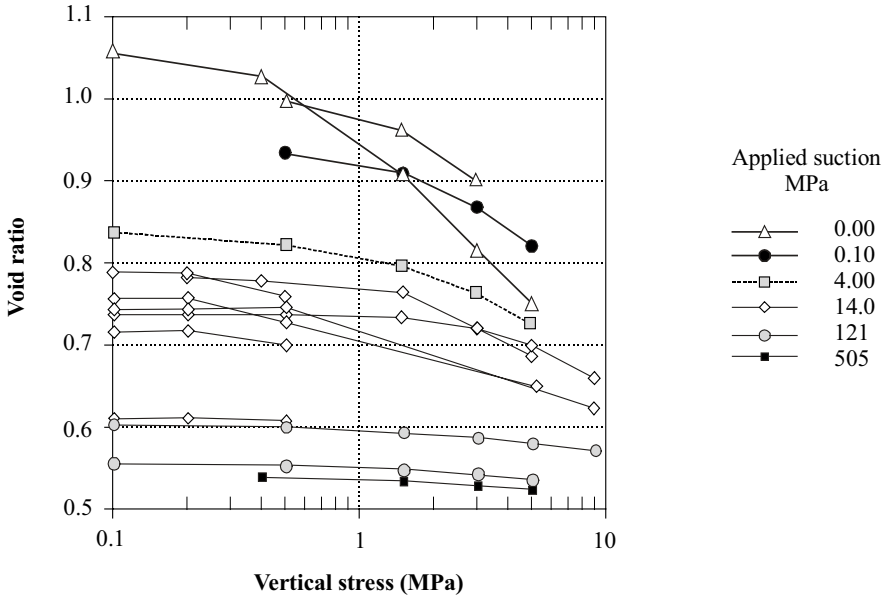

Figure A-72. *Volume changes measured in suction controlled oedometer tests, in loading paths under different suctions. Initial dry density 1.7 g/cm^3 (ENRESA 2000).*

In order to find the hydromechanical parameters of the constitutive model of the bentonite, tests were simulated by means of a numerical tool (CODE BRIGHT). A trial and error technique was used to reproduce the results of both the swelling pressure and swelling under load tests described in Sections A3.2.4 and A3.2.5. Figure A-73 shows a comparison between the numerical model output and the swelling strains measured at the CIEMAT and UPC laboratories.

Using the parameters obtained from the swelling tests, the suction controlled oedometer tests may be modelled as a boundary value problem, using CODE BRIGHT. Figure A-74 shows the results of both experimental and numerical model results in the case of wetting paths under different values of applied vertical stresses.

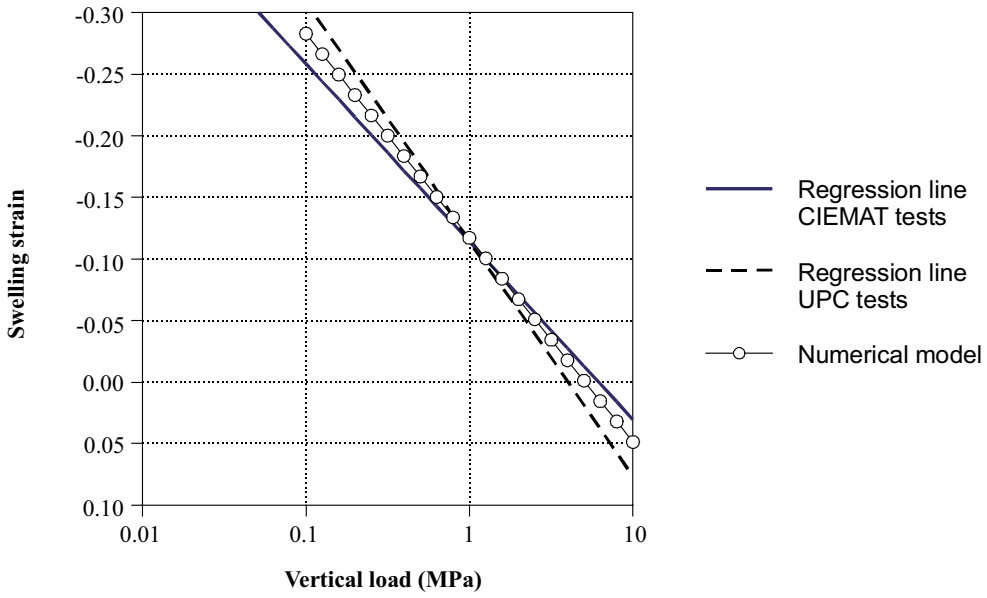

Figure A-73. *Comparison between swelling strains measured at the CIEMAT and UPC laboratories and computed strains obtained from constitutive equations used in numerical modelling (initial dry density 1.60 g/cm^3) (ENRESA 2000).*

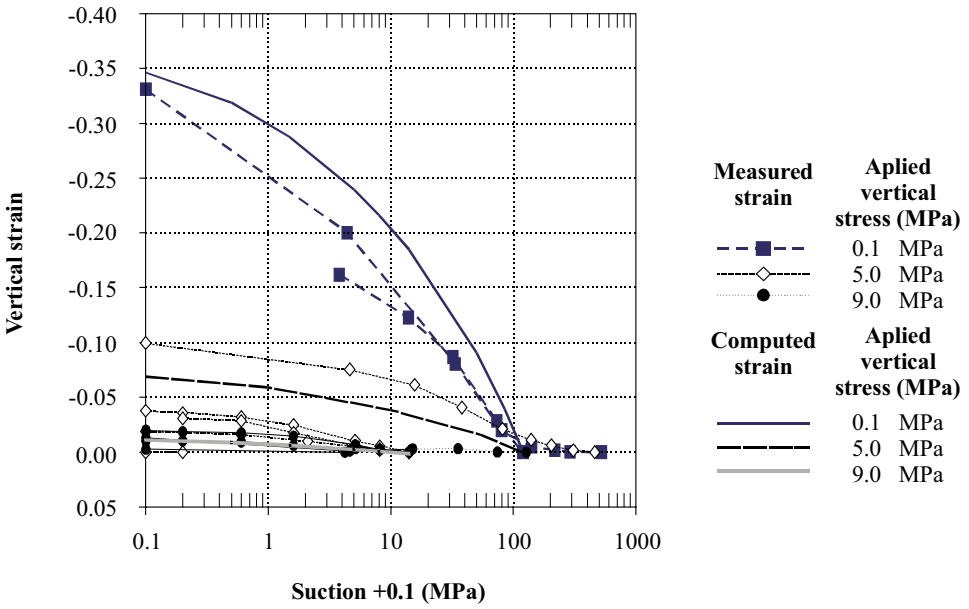

Figure A-74. *Comparison between swelling strains measured in suction controlled oedometer tests performed by CIEMAT and computed strains obtained from constitutive equations used in numerical modelling (ENRESA 2000).*

Some general comments may be made concerning the behaviour of the clay when subjected to different stress paths:

- As a result of equipment limitations, the compaction load of the specimens (about 20 MPa) has been higher than the highest external load applied in the oedometers (9 MPa). Furthermore, the samples have shown minor collapse (with suction decreasing to values of between 15 and 5 MPa) only when a high vertical load (9 MPa) is applied.
- High swelling strains have been measured in suction reduction paths in response to minor vertical stresses. The hydration process opens the bentonite structure (pore volume increases) developing irreversible swelling strains, and subsequently an important decrease in stiffness is measured when a vertical load is applied. In these cases, a yield point in the loading paths may be observed at relatively small vertical loads (Figure A-72).
- Drying of the sample beyond suctions of 120 MPa, does not imply a significant decrease in volume. Furthermore, under suctions higher than this value the external load does not produce any important consolidation of the sample, which remains very stiff. After a drying/wetting cycle the swelling pressure of the clay remains almost unchanged, in keeping with the fact that plastic strains are small in suction increase paths.

A3.3.3 Tests to advance knowledge of the THM behaviour of expansive clays

Hydraulic tests on joints

Hydraulic tests were performed on specimens in which joints were present, to gain insight into the influence of the joints of the clay barrier on its hydraulic behaviour. The analysis included mainly the influence of joints on hydration rate, their sealing capacity (see Figure A-75) and the modification that they induce on hydraulic conductivity. Different cylindrical cells with water inlet/outlet were used. The specimens were made from four compacted bentonite slices (with final dry densities ranging between 1.61 and 1.23 g/cm^3 and initial water content ranging between 15.0 and 11.7 %), some with vertical joints.

Figure A-75. *Perspex cell used in joint sealing tests.*

The main conclusions of this study are as follows:

- When hydration occurs under a given injection pressure, even if it is low, the volume of water taken up and its distribution inside the clay is controlled by the existence of joints (fissures), their volume and their configuration.
- The clay of the specimens takes the water both from the direct hydration surface and from the block joints. Figure A-76 shows the final distribution of water content in two hydrated tests, in which four half-sectioned specimens were piled and hydrated from the top, illustrating this observation.
- The volume of water initially taken up depends on hydration pressure.
- Once the joints have been filled with water, the rate of water intake appears not to depend on injection pressure but on the dry density of the clay.
- The sealing of a joint, attained after hydration for 24 hours, is effective against hydraulic pressures of up to 5 MPa.
- Before sealing of the joints is attained, the strain experienced by every slice on saturation is the strain which corresponds to its initial dry density.

Suction and temperature controlled oedometer tests

Four oedometer tests including suction decrease and increasing vertical load paths have been performed by CIEMAT at temperatures of 40 and 60 °C on bentonite compacted at a water content in equilibrium with laboratory conditions and at dry densities of 1.7 and 1.6 g/cm^3. Figure A-77 shows the evolution of the void ratio during wetting paths starting at a low range of suction (14 MPa), under a vertical stress of 5 MPa, and at a high range of suction (120–450 MPa), under a vertical load of 0.1 MPa. Figure A-78 shows the comparison curves measured at different combinations of suction and temperature, which were maintained constant during the test.

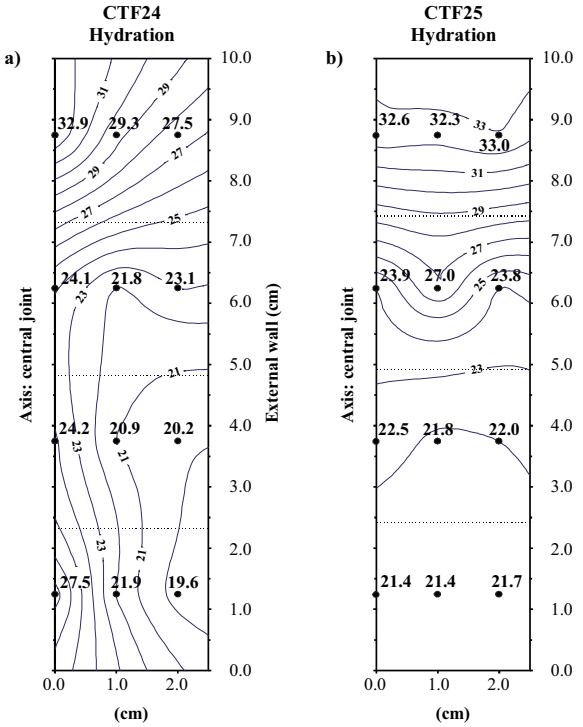

Figure A-76. *Water content distribution of the clay after two sealing tests (piling of four slices) performed under a hydration pressure of 0.5 MPa and lasting a) 1 day, b) 7 days (half section) (ENRESA 2000).*

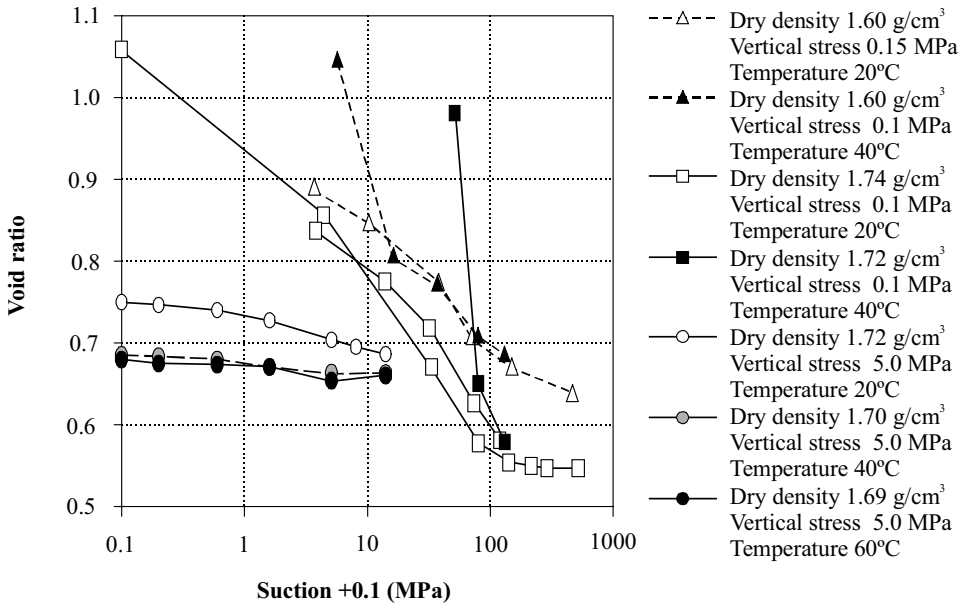

Figure A-77. *Wetting paths in suction controlled oedometer tests carried out at different temperatures (ENRESA 2000).*

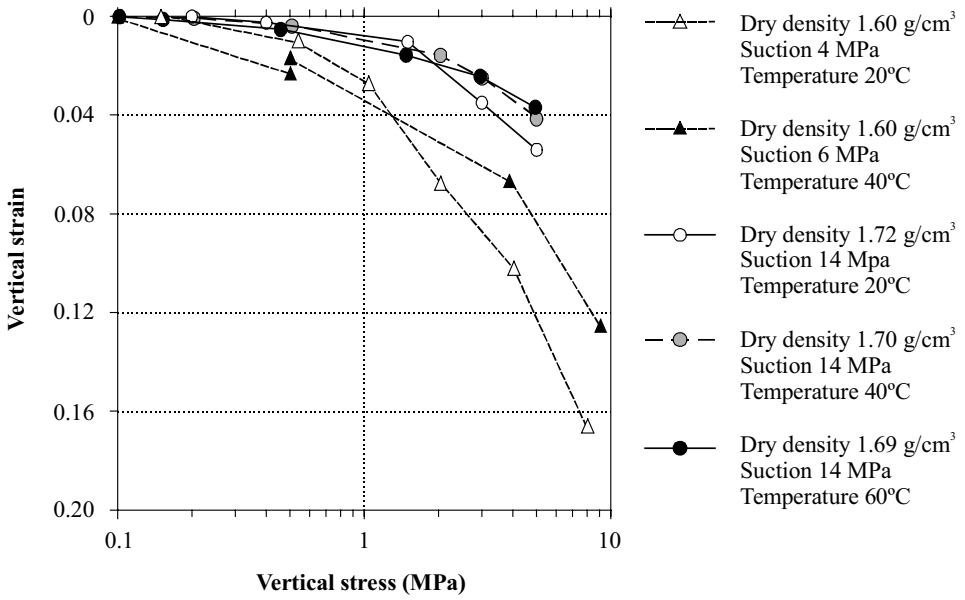

Figure A-78. *Loading paths in suction controlled oedometer tests carried out at different temperatures (ENRESA 2000).*

A3.3.4 Tests in thermo-hydraulic cells

The objective of these tests is to analyse the properties of the bentonite and its behaviour under conditions similar to those that will be found in a repository; that is, to subject the material simultaneously to heating and hydration, in opposite directions, for different periods of time.

The tests have been performed in cylindrical hermetic cells of different dimensions:

- Large cells, in which the thickness of the bentonite and the thermal gradient are similar to those of the real case, and the time length of tests are 0.5, 1 and 2 years. No results are yet available.
- Intermediate cells. As saturation will probably not be reached in the large cells, cells of intermediate dimensions have also been used. In these cells, a single bentonite block measuring 13 cm in height and 15 cm in diameter is heated at the top at 100 °C, while being simultaneously hydrated with distilled or granitic water at the bottom, with an injection pressure of 1 MPa (Figure A-79). The initial dry density and water content of the bentonite are 1.65 g/cm^3 and approximately 14 %, respectively. The quantity of sample is sufficient to allow the bentonite to be sliced into five sections at the end of the test (Figure A-80). Then, the bentonite porewater is extracted by squeezing techniques. In this way, physical and geochemical characterisation of the solid phase (dry density, water content, soluble salts, exchangeable cations) could be carried out. The test program is devised for study of the phenomena induced separately by the thermal front and the hydration front, and by the coupling of both fronts, in tests of equal duration. Some results are given in the next section. The data obtained in these cells have been used to calibrate THG modelling.
- Small cells. In this case, the bentonite specimen measure only 2.5 cm in thickness and 5.0 cm in diameter (Figure A-81). Saturation is reached after a few days, under an injection pressure of 1 MPa. This has allowed a large number of tests of different duration and conditions to be performed. The initial dry density of the bentonite was 1.65 g/cm^3 and the water content was at equilibrium value under the laboratory relative humidity conditions (around 14 %). Two sets of temperatures (60–35 ºC and 100–60 ºC) applied at the heating and hydration ends have been examined, in order to ascertain the effect of temperature on the observed processes. The influence of the chemistry of the hydration water on the processes observed has been verified by using two types of water: granitic and saline (Table A-25). The saline water has a chemical composition similar to that of the bentonite porewater under saturated conditions, but it is simplified to include only the major elements. The duration of the tests has been related to saturation time. The time needed for saturation has been verified previously, and amounts to 16 days for the tests performed at low temperature and to 10 days for the tests at high temperature.

On completion of the tests, physical, mineralogical and geochemical characterisation of the bentonite in different sections parallel to the heating front was performed. The influence of heating and/or hydration on the physico-chemical and hydro-mechanical properties of the bentonite (hydraulic conductivity and the swelling capacity) and the fabric modifications were also tested. Results are given subsequently.

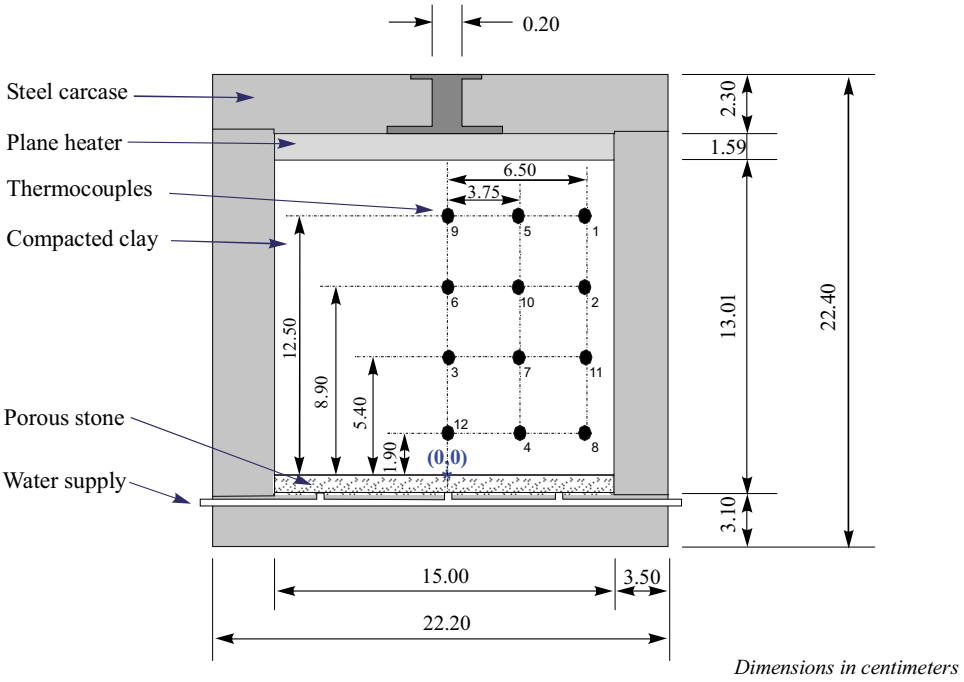

Figure A-79. *Schematic design of the intermediate cells for THG tests (ENRESA 2000).*

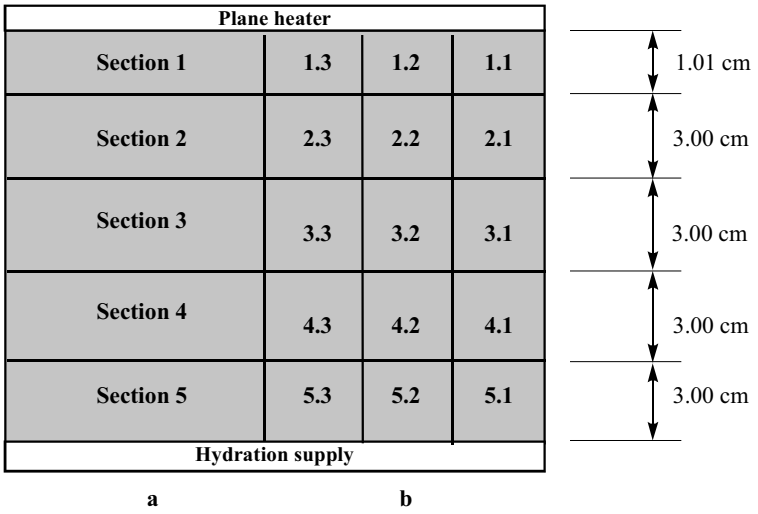

Figure A-80. *Sampling of the intermediate cells after T-H treatment for: a) porewater analysis by squeezing, b) physical and geochemical characterization of the solid phase (ENRESA 2000).*

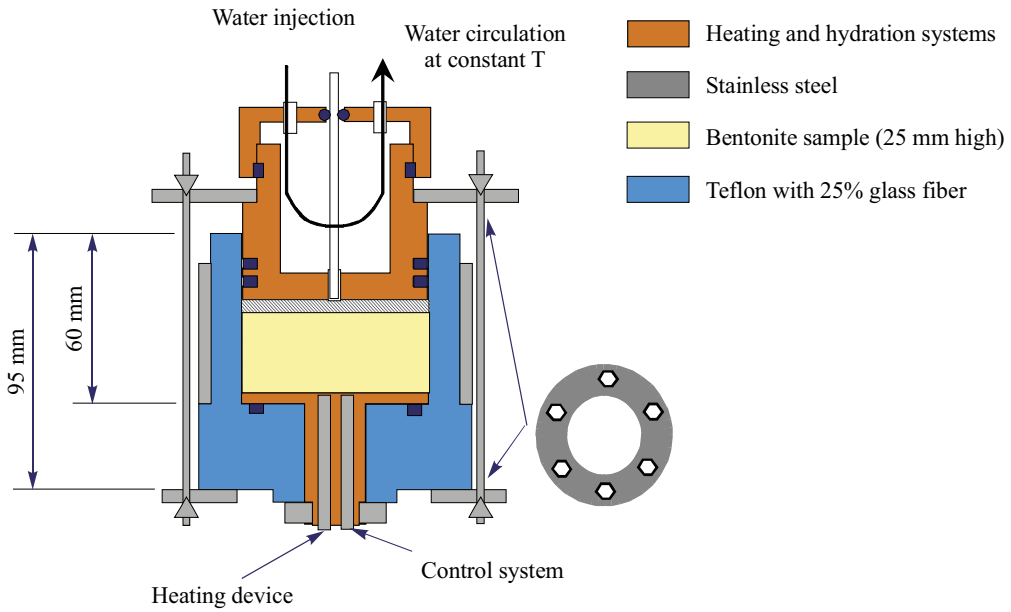

Figure A-81. *Schematic design of the small cells for THG tests (ENRESA 2000).*

Intermediate cells

The main objective of these tests is to understand the fundamental mechanisms of water flow and solute transport occurring in a compacted bentonite subjected to simultaneous heating and hydration. Also, the chemical evolution of the bentonite porewater and the hydrogeochemical processes involved in the system (dissolution/precipitation and cation exchange reactions) are studied. Different tests have been performed, and some are still in progress (Table A-33). The results presented belong to the transitory state, since saturated conditions have not been reached at the end of the thermohydraulic tests performed.

Table A-33. Tests performed with the intermediate cells.

Test number	Test type	Test time (days)	Initial conditions				Water uptake (cm^3)
			Mass (g)	ρ_d (gcm^3)	Water content (%)	Saturation degree (%)	
CT-22	heating + hydration	26	4 298	1.65	13.4	56.7	275
CT-23	heating + hydration	183	4 294	1.65	13.3	56.4	486
CT-24	heating	168	4 690	1.62	26.5	100	-
CT-26	heating	147	4 285	1.65	13.1	55.4	-
CT-27	hydration	148	4 247	1.65	13.1	55.4	390
CT-28	heating + hydration	302	4 315	1.65	13.9	58.8	
CT-30	hydration	302	4 278	1.65	13.9	58.8	

Figure A-82 and Figure A-83 show the distribution of temperature and water content in each section analysed, for various tests. The heating source is at the top of the cell (at the right of the following figures) and the hydration supply is at the bottom (to the left of the figures).

Significant changes in dry density, and therefore in porosity, are observed as hydration is induced in these experiments, probably due to the swelling of the bentonite (a slight deformation of the cell, with an increase of volume of the compacted bentonite block, was observed). Consequently, water contents (Figure A-83) above the saturation water content of the bentonite block initially compacted to a dry density of 1.65 g/cm^3 (23.6 % of water content) were measured.

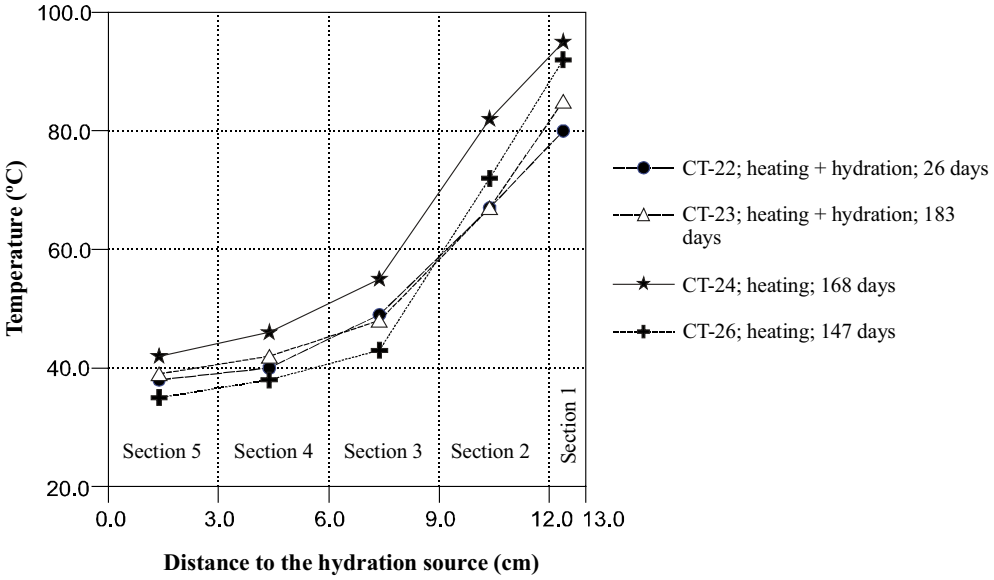

Figure A-82. *Final temperature distribution in the intermediate cells tests (ENRESA 2000).*

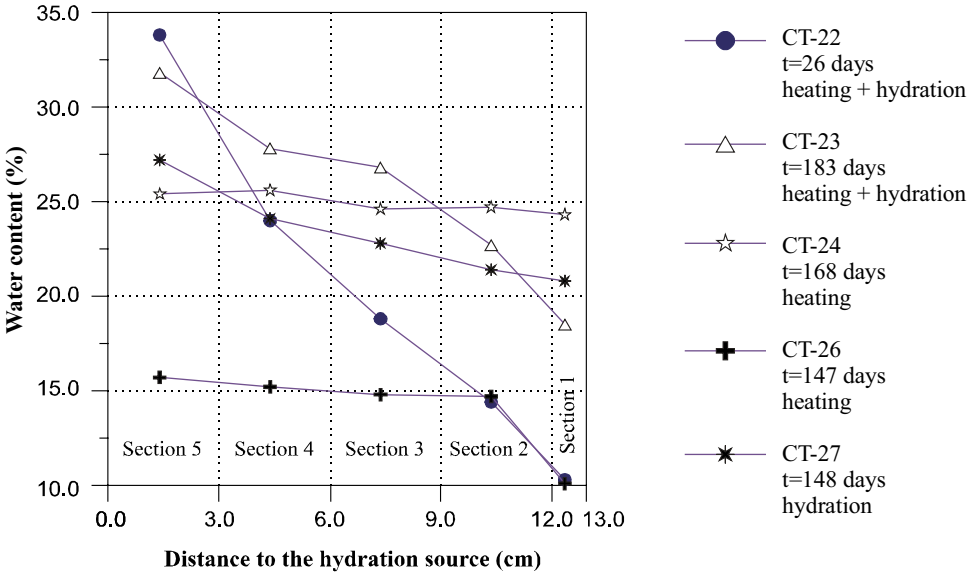

Figure A-83. *Final water content distribution in the intermediate cells tests (ENRESA 2000).*

A4 Requested results

Modelling teams should provide: (1) the numerical data for the computed requested results; and (2) a modelling report explaining the main features of the corresponding modelling work. Note that plots with the evolutions with time of all variables monitored by the sensors installed in the FEBEX in situ Experiment in the period from the 20th of February 1997 to the 31st of August 2003 may be found in the report (AITEMIN 2003). Furthermore, the corresponding numerical values will also be made available to the modelling teams. Consequently, the requested results are not blind predictions.

A4.1 General specifications

In what follows, the Cartesian co-ordinate system defined in Figure A-26, Figure A-27 and Figure A-28 will be used for space point references, and the 27th of February 1997 (heaters switch on) will be used for time references (day 0). Furthermore, a 3-character code has been assigned to each modelling team and to the co-ordinator (see Table A-34), that will be used in the project reports, particularly in comparison plots.

Table A-34. 3-character codes assigned to the modelling teams and to the co-ordinator.

Modelling team / co-ordinator	Code
Central Research Institute of Electric Power Industry (CRIEPI), Japan	CRP
Svensk Kärnbränslehantering AB (SKB), Sweden	SK1
Gesellschaft für Anlagen- und Reaktorsicherheit (GRS), Germany	GRS
Universitat Politècnica de Catalunya (UPC), Spain	UPC
Nationale Gesellschaft für die Lagerung radioaktiver Abfälle (NAGRA), Switzerland	NAG
Bundesanstalt für Geowissenschaften und Rohstoffe (BGR), Germany	BGR
Imperial College London (ICL), United Kingdom	ICL
Svensk Kärnbränslehantering AB (SKB), Sweden	SK2
Centre Internacional de Mètodes Numèrics en Enginyeria (CIMNE), Spain	CIM

A4.1.1 Numerical data

The required output results should be placed in a Microsoft Office Excel Workbook compatible with Microsoft Office Excel 2007 (with a maximum of 1 048 576 rows and 16 384 columns) named XXX_FBXs_Ri.xlsx (XXX is the team's code, s = 1 or 2 is the stage of the Task, i is the revision number, starting at 0). The Workbook should contain a Sheet labelled XXX (the team's code). In this Sheet, output results should be placed in named ranges, with names of the form XXX_* (XXX is the team's code and * denotes the variable part of the name), as indicated in the corresponding output specifications. Since the requested output data will be accessed through the named ranges, their locations in the Sheet may be freely decided by the modelling team. Though not required, it may be convenient to place a header above each named range with information on the data contained. Note that this additional information should not be included in the named range.

Note. To define a named range in Microsoft Office Excel 2007, perhaps the easiest way is to first select the range, then click the Name box at the left end of the formula bar (just above cell A1), type the desired name and press ENTER. The Name Manager dialog box on the Formulas tab, in the Defined Names group, allows to create, edit and delete named ranges. For more information on named ranges, reference is made to the article "Define and use names in formulas" at https://support.office.com/en-us/article/Define-and-use-names-in-formulas-4D0F13AC-53B7-422E-AFD2-ABD7FF379C64.

Both evolutions with time and spatial distributions of selected variables will be requested. Modelling teams should get the computed values of the requested variables as close as possible to the time instants or to the spatial points where they are requested. In fact, these values will be compared against the experimental data and to the values provided by the other modelling teams, without any interpolation.

On the other hand, modelling teams are free to provide values at additional time instants or points to properly define the required curve. In principle, all the provided points will be plotted and joined by straight-line segments. It should be emphasised that predictions are given at the points, whereas the straight-line segments merely join those points together. Note that, in order that the plotted symbols of points lying too close in the plotted curve do not result in a "thick line", the number of points provided should be limited.

A4.1.2 Modelling reports

The goal of the modelling reports is to explain in a concise way what has been done to get the results, by addressing the following issues: (1) justification and definition of the mathematical model used; (2) justification of the values adopted for the parameters defining the mathematical model; and (3) numerical solution of the mathematical model.

Modelling reports should be self-contained and written in a scientific paper-like form. This will ease their eventual publication. After being reviewed by the co-ordinator, modelling reports will be compiled within the project reports. To ease the reading of the ensemble and to ensure a minimum of coherence of the whole project report, the following points should be covered, albeit in a concise way (about 10–15 pages + graphics should suffice):

- Mathematical formulation
- Constitutive equations
- Code and main numerical features
- Parameters adopted and source/calibration procedure
- Initial and boundary conditions
- Additional comments
  - sensitivity analysis performed
  - difficulties encountered
- References

Modelling reports should be placed in a Microsoft Office Word file compatible with Microsoft Office 2007 named XXX_FBX_Ri.docx (XXX is the team's code, i is the revision number, starting at 0). To ease the compilation of the modelling reports, the format to be used should be the same as the format used to prepare the present document (e.g., Times New Roman, 12 point, single space, all margins set to 2.5 cm, ...).

A4.2 Requested results

Five types of results are requested: (1) evolutions of heating power; (2) distributions and evolutions of relative humidity; (3) distributions and evolutions of temperature; (4) evolutions of total stresses; and (5) distributions after the first dismantling of dry density, water content and degree of saturation.

A4.2.1 Evolutions of heating power

The unit to be used for heating power Q is W (Watt). As described in Section A2.3 (Test operation), a constant power of 1 200 W was applied to the heaters during the first 20 days of operation. Power was then increased to 2 000 W and maintained constant for an additional period of 33 days. Then, at day 53 the heating system was switched to an automatic constant temperature control mode to achieve a constant maximum temperature of 100 °C in the bentonite.

The computed evolutions of power input (in W) to both heaters from t = 53 days to t = 1 855 days are requested. The computed evolutions of heating power at heater H1 and heater H2 should be placed on the named range XXX_Q_H. The structure of this named range is shown in Figure A-84.

t_1	Q(H1, t_1)	Q(H2, t_1)
t_r	Q(H1, t_r)	Q(H2, t_r)
t_n	Q(H1, t_n)	Q(H2, t_n)

Figure A-84. *Structure of the named range XXX_Q_H. The range has 3 columns and a convenient number n of rows (to be decided by the modelling team). In row r (r = 1, …, n), column 1 contains a time t_r (in days) in the considered time interval, and column j + 1 (j = 1, 2) contains the heating power input Q(Hj, t_r) (in W) at heater Hj and time t_r (in days). Times t_r (r = 1, …, n) should increase with the row number r.*

A4.2.2 Distributions and evolutions of relative humidity

The unit to be used for relative humidity RH is % (water vapour density over water vapour density at full saturation, in per cent). Figure A-85 shows the locations of sections C, E1, H and F2, where distributions (along radial segments) and evolutions of relative humidity are requested.

Distributions of relative humidity (radial segments)

The computed distributions of relative humidity along 4 radial segments (RS1, RS2, RS3 and RS4) on 4 sections (C, E1, H and F2) at 3 times (t1, t2 and t3) are requested.

- **Section C**: x = 1.81 m (between concrete plug and heater H1). The computed distributions of relative humidity should be along the radial segments RS1, RS2, RS3 and RS4 on section C (see Table A-35) at times t1 = 90 days, t2 = 300 days and t3 = 1 800 days.

Table A-35. Definition of the radial segments on section C along which the distributions of relative humidity are requested.

Segment	Origin (x, y, z)	End (x, y, z)	Remarks
SCRS1	(1.81, 0.00, 0.00)	(1.81, 0.00, 1.13)	Parallel to the pos. z-axis
SCRS2	(1.81, 0.00, 0.00)	(1.81, 0.00, −1.13)	Parallel to the neg. z-axis
SCRS3	(1.81, 0.00, 0.00)	(1.81, 1.13, 0.00)	Parallel to the pos. y-axis
SCRS4	(1.81, 0.00, 0.00)	(1.81, −1.13, 0.00)	Parallel to the neg. y-axis

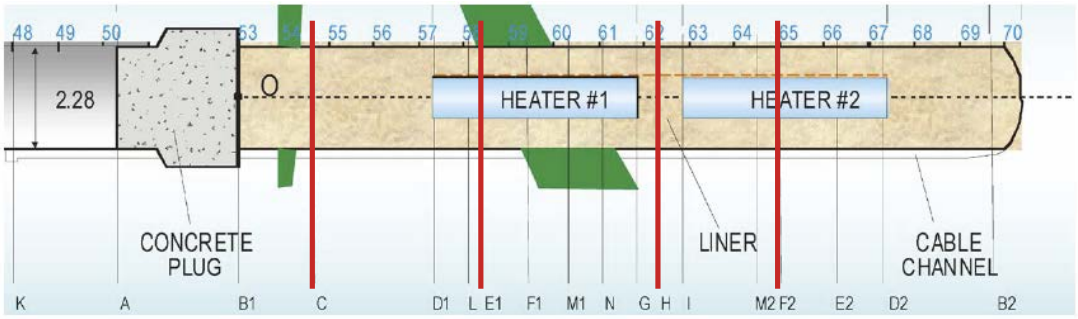

Figure A-85. *Required results: distributions and evolutions of relative humidity.*

- **Section E1**: x = 5.53 m (at heater H1). The computed distributions of relative humidity should be along the radial segments RS1, RS2, RS3 and RS4 on section E1 (see Table A-36) at times t1 = 90 days, t2 = 300 days and t3 = 1 800 days.

Table A-36. Definition of the radial segments on section E1 along which the distributions of relative humidity are requested.

Segment	Origin (x, y, z)	End (x, y, z)	Remarks
SE1RS1	(5.53, 0.00, 0.49)	(5.53, 0.00, 1.13)	Parallel to the pos. z-axis
SE1RS2	(5.53, 0.00, −0.49)	(5.53, 0.00, −1.13)	Parallel to the neg. z-axis
SE1RS3	(5.53, 0.49, 0.00)	(5.53, 1.13, 0.00)	Parallel to the pos. y-axis
SE1RS4	(5.53, −0.49, 0.00)	(5.53, −1.13, 0.00)	Parallel to the neg. y-axis

- **Section H**: x = 9.50 m (centred between the two heaters). The computed distributions of relative humidity should be along the radial segments RS1, RS2, RS3 and RS4 on section H (see Table A-37) at times t1 = 90 days, t2 = 300 days and t3 = 1 800 days.

Table A-37. Definition of the radial segments on section H along which the distributions of relative humidity are requested.

Segment	Origin (x, y, z)	End (x, y, z)	Remarks
SHRS1	(9.50, 0.00, 0.00)	(9.50, 0.00, 1.13)	Parallel to the pos. z-axis
SHRS2	(9.50, 0.00, 0.00)	(9.50, 0.00, −1.13)	Parallel to the neg. z-axis
SHRS3	(9.50, 0.00, 0.00)	(9.50, 1.13, 0.00)	Parallel to the pos. y-axis
SHRS4	(9.50, 0.00, 0.00)	(9.50, −1.13, 0.00)	Parallel to the neg. y-axis

- **Section F2**: x = 12.30 m (at heater 2). The computed distributions of relative humidity should be along the radial segments RS1, RS2, RS3 and RS4 on section F2 (see Table A-38) at times t1 = 90 days, t2 = 300 days and t3 = 1 800 days.

Table A-38. Definition of the radial segments on section F2 along which the distributions of relative humidity are requested.

Segment	Origin (x, y, z)	End (x, y, z)	Remarks
SF2RS1	(12.30, 0.00, 0.49)	(13.44, 0.00, 1.13)	Parallel to the pos. z-axis
SF2RS2	(12.30, 0.00, −0.49)	(13.44, 0.00, −1.13)	Parallel to the neg. z-axis
SF2RS3	(12.30, 0.49, 0.00)	(13.44, 1.13, 0.00)	Parallel to the pos. y-axis
SF2RS4	(12.30, −0.49, 0.00)	(13.44, −1.13, 0.00)	Parallel to the neg. y-axis

If the model used is 3D, the computed distributions of relative humidity along radial segment RSi (i = 1, 2, 3, 4) on section Sk (k = C, E1, H, F2) at times tj (j = 1, 2, 3) should be placed on the named range XXX_RH_SkRSi (a total of 4 × 4 = 16 named ranges). If the model used is 2D axisymmetric, the computed distributions of relative humidity along the radial segment RD on section Sk (k = C, E1, H, F2) at times tj (j = 1, 2, 3) should be placed on the named range XXX_RH_SkRS (a total of 4 named ranges). In both cases, the structure of the named ranges is shown in Figure A-86.

$r(P_1)$	$RH(P_1, t1)$	$RH(P_1, t2)$	$RH(P_1, t3)$
$r(P_r)$	$RH(P_r, t1)$	$RH(P_r, t2)$	$RH(P_r, t3)$
$r(P_n)$	$RH(P_n, t1)$	$RH(P_n, t2)$	$RH(P_n, t3)$

Figure A-86. *Structure of the named ranges XXX_RH_SkRSi (k = C, E1, H, F2; i = 1, 2, 3, 4) or XXX_RH_SkRS (k = C, E1, H, F2). Each named range has 4 columns and a convenient number n of rows (to be decided by the modelling team and may be different for each named range). In row r (r = 1, ..., n), column 1 contains the radial distance r(P_r) (in m) of a point P_r on the considered radial segment, and column j + 1 (j = 1, 2, 3) contains the relative humidity RH(P_r, tj) (in %) at point P_r and time tj (in days). Radial distances r(P_r) (r = 1, ..., n) should increase with the row number r.*

Evolutions of relative humidity

The computed evolutions of relative humidity should be given at 3 points (P1, P2 and P3) on 3 sections (C, E1 and H) and at 2 points (P1 and P2) on 1 section (F2) from t = 0 days to t = 1 855 days are requested.

- **Section C**: x = 1.81 m (between concrete plug and heater H1). The computed evolutions of relative humidity at points P1, P2 and P3 on section C (see Table A-39) should be from t = 0 days to t = 1 855 days.

Table A-39. Definition of the points on section C at which the evolutions of relative humidity are requested.

Point	(x, y, z)	Remarks
SCP1	(1.81, 0.00, 0.00)	At the centre
SCP2	(1.81, −0.60, 0.07)	Neg. y-axis, near mid- bentonite
SCP3	(1.81, −1.10, 0.07)	Neg. y-axis, near granite

- **Section E1**: x = 5.53 m (at heater H1). The computed evolutions of relative humidity should be at points P1, P2 and P3 on section E1 (see Table A-40) from t = 0 days to t = 1 855 days.

Table A-40. Definition of the points on section E1 at which the evolutions of relative humidity are requested.

Point	(x, y, z)	Remarks
SE1P1	(5.53, −0.52, 0.00)	Neg. y-axis, near steel liner
SE1P2	(5.53, −0.81, 0.07)	Neg. y-axis, near mid. bentonite
SE1P3	(5.53, −1.10, −0.17)	Neg. y-axis, near granite

- **Section H**: x = 9.50 m (centred between the two heaters). The computed evolutions of relative humidity should be at points P1, P2 and P3 on section H (see Table A-41) from t = 0 days to t = 1 855 days.

Table A-41. Definition of the points on section H at which the evolutions of relative humidity are requested.

Point	(x, y, z)	Remarks
SHP1	(9.50, −0.52, 0.05)	Neg. y-axis, near steel liner
SHP2	(9.50, −0.81, 0.05)	Neg. y-axis, near mid. bentonite
SHP3	(9.50, −1.07, −0.16)	Neg. y-axis, near granite

- **Section F2**: x = 12.30 m (at heater 2). The computed evolutions of relative humidity should be at points P1 and P3 on section F2 (see Table A-42) from t = 0 days to t = 1 855 days.

Table A-42. Definition of the points on section F2 at which the evolutions of relative humidity are requested.

Point	(x, y, z)	Remarks
SF2P1	(12.30, −0.81, 0.09)	Neg. y-axis, near mid. bentonite
SF2P2	(12.30, −1.05, 0.08)	Neg. y-axis, near granite

The computed evolutions of relative humidity at point Pi (i = 1, 2, 3) on section Sk (k = C, E1, H) should be placed on the named range XXX_RH_SkP (a total of 3 named ranges). The structure of the named ranges is shown in Figure A-87.

The computed evolutions of relative humidity at point Pi (i = 1, 2) on section F2 should be placed on the named range XXX_RH_F2P. The structure of this named range is shown in Figure A-88.

t_1	RH(P1, t_1)	RH(P2, t_1)	RH(P3, t_1)
t_r	RH(P1, t_r)	RH(P2, t_r)	RH(P3, t_r)
t_n	RH(P1, t_n)	RH(P2, t_n)	RH(P3, t_n)

Figure A-87. *Structure of the named ranges XXX_RH_SkP (k = C, E1, H). Each named range has 4 columns and a convenient number n of rows (to be decided by the modelling team and which may be different for each named range). In row r (r = 1, ..., n), column 1 contains a time t_r (in days) in the considered time interval, and column j + 1 (j = 1, 2, 3) contains the relative humidity RH(Pj, t_r) (in %) at point Pj and time t_r (in days). Times t_r (r = 1, ..., n) should increase with the row number r.*

t_1	RH(P1, t_1)	RH(P2, t_1)
t_r	RH(P1, t_r)	RH(P2, t_r)
t_n	RH(P1, t_n)	RH(P2, t_n)

Figure A-88. *Structure of the named range XXX_RH_F2P. This named range has 3 columns and a convenient number n of rows (to be decided by the modelling team). In row r (r = 1, ..., n), column 1 contains a time t_r (in days) in the considered time interval, and column j + 1 (j = 1, 2) contains the relative humidity RH(Pj, t_r) (in %) at point Pj and time t_r (in days). Times t_r (r = 1, ..., n) should increase with the row number r.*

A4.2.3 Distributions and evolutions of temperature

The unit to be used for temperature T is °C (degree Celsius). Figure A-89 shows the locations of sections D1, I and and D2, where distributions (along radial segments) and evolutions (at selected points) of temperature are requested. It also shows the location of the axial segments along which distributions of temperature are requested.

Distributions of temperature (radial segments)

The computed distributions of temperature along 2 radial segments (RS1 and RS2) on 3 sections (D1, I and G) at 2 times (t1 and t2) are requested.

- **Section D1**: x = 4.42 m (end of heater H1, closest to concrete plug). The computed distributions of temperature should be along the radial segments RS1 and RS2 on section D1 (see Table A-43) at times t1 = 90 days and t2 = 1 800 days.

Table A-43. Definition of the radial segments on section D1 along which the distributions of temperature are requested.

Segment	Origin (x, y, z)	End (x, y, z)	Remarks
SD1RS1	(4.42, 0.00, 0.49)	(4.42, 0.00, 1.13)	Parallel to the pos. z-axis
SD1RS2	(4.42, −0.49, 0.00)	(4.42, −1.13, 0.00)	Parallel to the neg. z-axis

- **Section I**: x = 9.93 m (end of heater H2, closest to concrete plug). The computed distributions of temperature should be along the radial segments RS1 and RS2 on section I (see Table A-44) at times t1 = 90 days and t2 = 1 800 days.

Table A-44. Definition of the radial segments on section I along which the distributions of temperature are requested.

Segment	Origin (x, y, z)	End (x, y, z)	Remarks
SIRS1	(9.93, 0.00, 0.49)	(9.93, 0.00, 1.13)	Parallel to the pos. z-axis
SIRS2	(9.93, −0.49, 0.00)	(9.93, −1.13, 0.00)	Parallel to the neg. z-axis

- **Section D2**: x = 14.38 m (end of heater H2, closest to tunnel end). The computed distributions of temperature should be along the radial segments RS1 and RS2 on section D2 (see Table A-45) at times t1 = 90 days and t2 = 1 800 days.

Table A-45. Definition of the radial segments on section D2 along which the distributions of temperature are requested.

Segment	Origin (x, y, z)	End (x, y, z)	Remarks
SD2RS1	(14.38, 0.00, 0.49)	(14.38, 0.00, 1.13)	Parallel to the pos. z-axis
SD2RS2	(14.38, −0.49, 0.00)	(14.38, −1.13, 0.00)	Parallel to the neg. z-axis

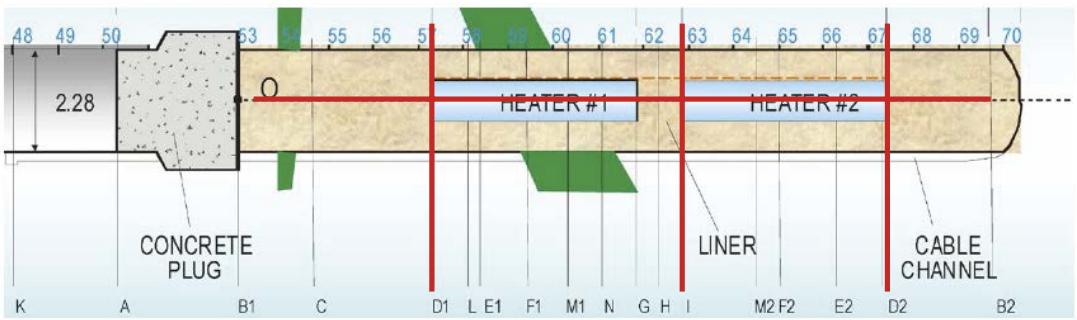

Figure A-89. *Required results: distributions and evolutions of temperature.*

If the model used is 3D, the computed distributions of temperature along radial segment RSi (i = 1, 2, 3, 4) on section Sk (k = D1, I, D2) at times tj (j = 1, 2) should be placed on the named range XXX_T_SkRSi (a total of 2 × 3 = 6 named ranges). If the model used is 2D axisymmetric, the computed distributions of relative humidity along the radial segment RS on section Sk (k = D1, I, D2) at times tj (j = 1, 2) should be placed on the named range XXX_T_SkRS (a total of 3 named ranges). In both cases, the structure of the named ranges is indicated in Figure A-90.

Distributions of temperature (axial segments)

The computed distributions of temperature should be along the axial segments AS1 and AS2 (see Table A-46) at times t1 = 90 days and t2 = 1 800 days.

Table A-46. Definition of the axial segments along which the distributions of temperature are requested.

Segment	Origin (x, y, z)	End (x, y, z)	Remarks
AS1	(0.00, −0.81, 0.00)	(17.00, −0.81, 0.00)	Paral. pos. x-axis, mid. bentonite
AS2	(0.00, −1.14, 0.00)	(17.00, −1.14, 0.00)	Paral. pos. x-axis, near granite

The computed distributions of temperature along axial segment ASi (i = 1, 2) at times tj (j = 1, 2) should be placed on the named range XXX_T_ASi (a total of 2 × 2 = 4 named ranges). The structure of the named ranges is indicated in Figure A-91.

$r(P_1)$	$T(P_1, t1)$	$T(P_1, t2)$
$r(P_r)$	$T(P_r, t1)$	$T(P_r, t2)$
$r(P_n)$	$T(P_n, t1)$	$T(P_n, t2)$

Figure A-90. *Structure of the named ranges XXX_T_SkRSi (k = D1, I, D2; i = 1, 2) or XXX_T_SkRS (k = D1, I, D2). Each named range has 3 columns and a convenient number n of rows (to be decided by the modelling team and may be different for each named range). In row r (r = 1, ..., n), column 1 contains the radial distance $r(P_r)$ (in m) of a point P_r on the considered radial segment, and column j + 1 (c = 1, 2) contains the temperature $T(P_r, tj)$ (in °C) at point P_r and time tj (in days). Radial distances $r(P_r)$ (r = 1, ..., n) should increase with the row number r.*

$x(P_1)$	$T(P_1, t1)$	$T(P_1, t2)$
$x(P_r)$	$T(P_r, t1)$	$T(P_r, t2)$
$x(P_n)$	$T(P_n, t1)$	$T(P_n, t2)$

Figure A-91. *Structure of the named ranges XXX_T_ASi (i = 1, 2). Each named range has 3 columns and a convenient number n of rows (to be decided by the modelling team and may be different for each named range). In row r (r = 1, ..., n), column 1 contains the x co-ordinate $x(P_r)$ (in m) of a point P_r on the considered longitudinal segment, and column j + 1 (j = 1, 2) contains the temperature $T(P_r, tj)$ (in °C) at point P_r and time tj (in days). x-co-ordinates $x(P_r)$ (r = 1, ..., n) should increase with the row number r.*

Evolutions of temperature

The computed evolutions of temperature at 1 point (P1) on 2 sections (D1 and G) from t = 0 days to t = 1 855 days are requested.

- **Section D1**: x = 4.42 m (end of heater 1, closest to concrete plug). The computed evolutions of temperature should be at point P1 on section D1 (see Table A-47) from t = 0 days to t = 1 855 days.

Table A-47. Definition of the point on section D1 at which the evolution of temperature is requested.

Point	(x, y, z)	Remarks
SD1P1	(4.42, −1.14, 0.00)	Neg. y-axis, near granite

- **Section I**: x = 9.93 m (end of heater H2, closest to concrete plug). The computed evolutions of temperature should be at point P1 on section I (see Table A-48) from t = 0 days to t = 1 855 days.

Table A-48. Definition of the point on section I at which the evolution of temperature is requested.

Point	(x, y, z)	Remarks
SIP1	(9.93, −1.12, −0.17)	Neg. y-axis, near granite

- **Section D2**: x = 14.38 m (end of heater H2, closest to tunnel end). The computed evolutions of temperature should be at point P1 on section D2 (see Table A-49) from t = 0 days to t = 1 855 days.

Table A-49. Definition of the point on section D2 at which the evolution of temperature is requested.

Point	(x, y, z)	Remarks
SD2P1	(14.38, −1.14, 0.00)	Neg. y-axis, near granite

The computed evolutions of temperature at point P1 on section Sk (k = D1, I, D2) should be placed on the named range XXX_T_SkP (a total of 3 named ranges). The structure of the named ranges is shown in Figure A-92.

t_1	$T(P1, t_1)$
t_r	$T(P1, t_r)$
t_n	$T(P1, t_n)$

Figure A-92. *Structure of the named ranges XXX_T_SkP (k = D1, I, D2). Each named range has 2 columns and a convenient number n of rows (to be decided by the modelling team and which may be different for each named range). In row r (r = 1, ..., n), column 1 contains a time t_r (in days) in the considered time interval, and column 2 contains the temperature $T(P1, t_r)$ (in °C) at point P1 and time t_r (in days). Times t_r (r = 1, ..., n) should increase with the row number r.*

A4.2.4 Evolutions of total stresses

The unit to be used for total stresses TS is MPa (megapascal), with the convention that compressions are positive. Figure A-93 shows the locations of sections E2 and B2, where evolutions (at selected points) of total stresses are requested.

The computed evolutions of radial total stresses at 3 points (P1, P2 and P3) on 1 section (E2) and the computed evolution of axial total stress at 1 point (P1) on 1 section (B2) from t = 0 days to t = 1 855 days are requested.

- **Section E2**: x = 13.44 m (at heater 2). The computed evolutions of radial total stresses should be at points Pi (i = 1, 2, 3) on section E2 (see Table A-50) from t = 0 days to t = 1 855 days.

Table A-50. Definition of the points on section E2 at which the evolutions of radial total stresses are requested.

Point	(x, y, z)	Remarks
SE2P1	(13.28, 0.00, −0.48)	Neg. z-axis, near heater
SE2P2	(13.45, −0.28, −1.19)	Neg. z-axis, near granite
SE2P3	(13.46, −1.19, 0.00)	Neg. y-axis, near granite

- **Section B2**: x = 17.32 m (near the end of the test area). The computed evolution of axial total stress should be at point P1 on section B2 (see Table A-51) from t = 0 days to t = 1 855 days.

Table A-51. Definition of the point on section B2 at which the evolution of temperature is requested.

Point	(x, y, z)	Remarks
SB2P1	(17.32, 0.26, 0.76)	Pos. z-axis, mid. bentonite

The computed evolutions of the radial total stress at points Pi (i = 1, 2, 3) on section E2 should be placed on the named range XXX_RTS_SE2P. The structure of this named range is shown in Figure A-94.

The computed evolution of the axial total stress at point P1 on section B2 should be placed on the named range XXX_ATS_SB2P. The structure of this named range is shown in Figure A-95.

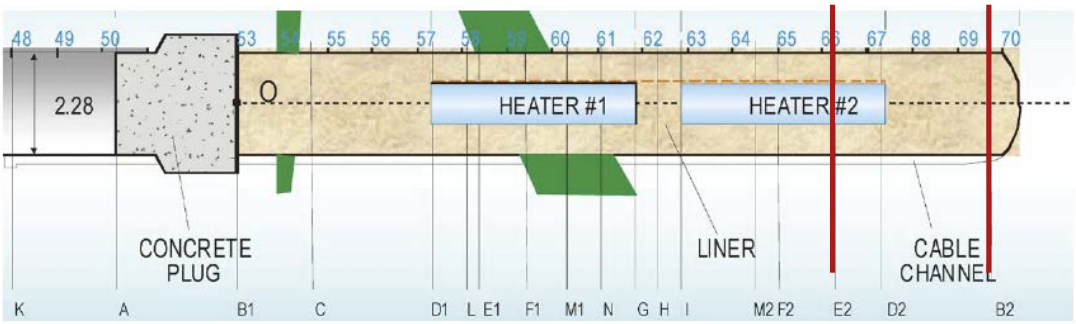

Figure A-93. *Required results: evolutions of total stresses.*

t_1	RTS(P1, t_1)	RTS(P2, t_1)	RTS(P3, t_1)
t_r	RTS(P1, t_r)	RTS(P2, t_r)	RTS(P3, t_r)
t_n	RTS(P1, t_n)	RTS(P2, t_n)	RTS(P3, t_n)

Figure A-94. *Structure of the named range XXX_RTS_E2P. This named range has 3 columns and a convenient number n of rows (to be decided by the modelling team). In row r (r = 1, ..., n), column 1 contains a time t_r (in days) in the considered time interval, and column j + 1 (j = 1, 2, 3) contains the radial total stress RTS(Pj, t_r) (in MPa) at point Pj and time t_r (in days). Times t_r (r = 1, ..., n) should increase with the row number r.*

t_1	ATS(P1, t_1)
t_r	ATS(P1, t_r)
t_n	ATS(P1, t_n)

Figure A-95. *Structure of the named range XXX_ATS_SB2P. This named range has 2 columns and a convenient number n of rows (to be decided by the modelling team). In row r (r = 1, ..., n), column 1 contains a time t_r (in days) in the considered time interval, and column 2 contains the axial total stress ATS(P1, t_r) (in MPa) at point P1 and time t_r (in days). Times t_r (r = 1, ..., n) should increase with the row number r.*

A4.2.5 Distributions of dry density, water content and degree of saturation after the first dismantling

The unit to be used for dry density DD is g/cm^3, the unit to be used for water content WC is % (ratio between the masses of water and of dry soil particles in a volume of soil, in per cent) and the unit to be used for degree of saturation SR is % (proportion of the volume of the void occupied by water, in per cent). Figure A-96 shows the locations of the dismantling sections 15, 27 and 31, where distributions (at selected points) of dry density, water content and degree of saturation are requested.

Distributions of dry density after the first dismantling (radial segments)

The computed distributions of dry density after the first dismantling along 3 radial segments (RS1, RS2 and RS3) on 3 dismantling sections (15, 27 and 31) are requested.

- **Section 15**: x = 3.27 m (between concrete plug and heater H1). The computed distributions of dry density after the first dismantling should be along the radial segments RS1, RS2 and RS3 on dismantling section 15 (see Table A-52).

Table A-52. Definition of the radial segments on dismantling section 15 along which the distributions of dry density after the first dismantling are requested.

Segment	Origin (x, y, z)	End (x, y, z)	Remarks
S15RS1	(3.27, 0.00, 0.00)	(3.27, 0.87, 0.73)	Angle with pos. y-axis = 40°
S15RS2	(3.27, 0.00, 0.00)	(3.27, −0.48, 1.03)	Angle with pos. y-axis = 115°
S15RS3	(3.27, 0.00, 0.00)	(3.27, 0.00, −1.13)	Angle with pos. y-axis = 270°

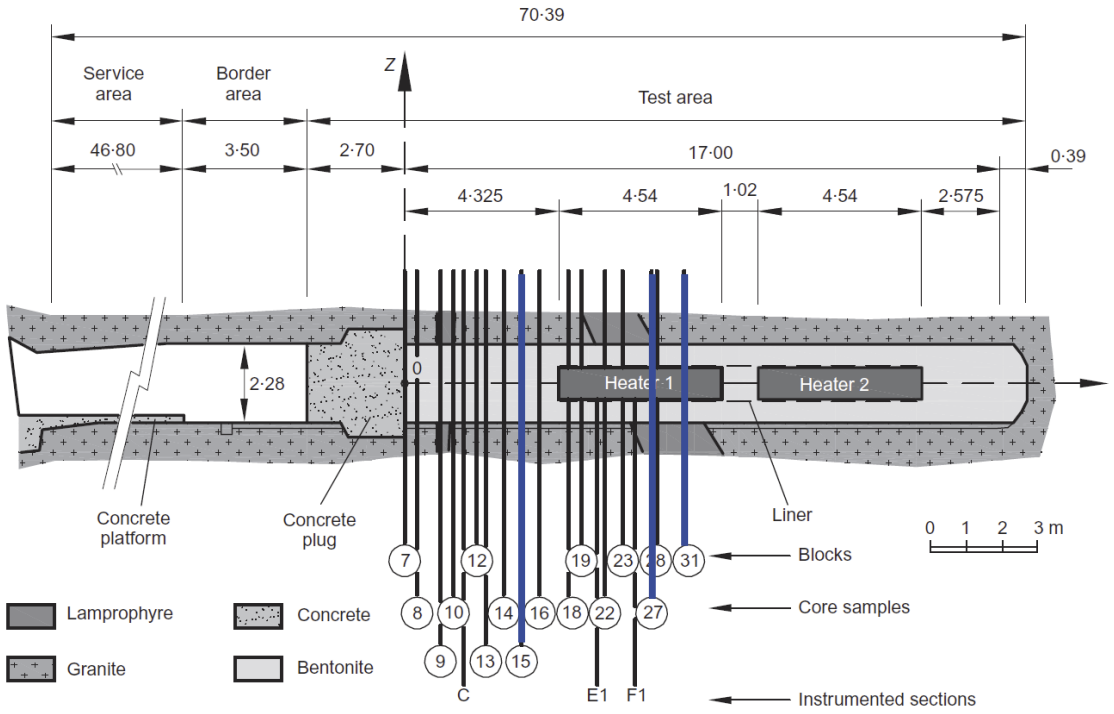

Figure A-96. *Required results: distributions of dry density, water content and degree of saturation after dismantling.*

- **Section 27**: x = 6.85 m (on heater H1). The computed distributions of dry density after the first dismantling should be along the radial segments RS1, RS2 and RS3 on dismantling section 27 (see Table A-53).

Table A-53. Definition of the radial segments on dismantling section 27 along which the distributions of dry density after the first dismantling are requested.

Segment	Origin (x, y, z)	End (x, y, z)	Remarks
S27RS1	(6.85, 0.37, 0.31)	(6.85, 0.87, 0.73)	Angle with pos. y-axis = 40°
S27RS2	(6.85, −0.17, 0.46)	(6.85, −0.39, 1.07)	Angle with pos. y-axis = 110°
S27RS3	(6.85, 0.00, −0.49)	(6.85, 0.00, 1.13)	Angle with pos. y-axis = 270°

- **Section 31**: x = 7.74 m (on heater H1). The computed distributions of dry density after the first dismantling should be along the radial segments RS1, RS2 and RS3 on dismantling section 31 (see Table A-54).

Table A-54. Definition of the radial segments on dismantling section 31 along which the distributions of dry density after the first dismantling are requested.

Segment	Origin (x, y, z)	End (x, y, z)	Remarks
S31RS1	(7.74, 0.47, −0.17)	(7.74, 1.10, −0.29)	Angle with pos. y-axis = −15°
S31RS2	(7.74, −0.17, 0.46)	(7.74, −0.39, 1.07)	Angle with pos. y-axis = 110°
S31RS3	(7.74, −0.32, −0.37)	(7.74, −0.73, −0.87)	Angle with pos. y-axis = 270°

If the model used is 3D, the computed distributions of dry density after the first dismantling along radial segment RSi (i = 1, 2, 3) on dismantling section Sk (k = 15, 27, 31) should be placed on the named range XXX_DD_SkRSi (a total of 3 × 3 = 9 named ranges). If the model used is 2D axisymmetric, the computed distributions of dry density after the first dismantling along the radial segment RS on dismantling section Sk (k = 15, 17, 31) should be placed on the named range XXX_DD_SkRS (a total of 3 named ranges). In both cases, the structure of the named ranges is indicated Figure A-97.

$r(P_1)$	$DD(P_1)$
$r(P_r)$	$DD(P_r)$
$r(P_n)$	$DD(P_{n,})$

Figure A-97. *Structure of the named ranges XXX_DD_SkRSi (k = 15, 27, 31; i = 1, 2, 3) or XXX_DD_SkRS (k = 15, 27, 31). Each named range has 2 columns and a convenient number n of rows (to be decided by the modelling team and may be different for each named range). In row r (r = 1, ..., n), column 1 contains the radial distance r_r (in m) of a point P_r on the considered radial segment, and column 2 contains the dry density after the first dismantling $DD(P_r)$ (in g/cm^3) at point P_r. Radial distances $r(P_r)$ (r = 1, ..., n) should increase with the row number r.*

Distributions of water content after the first dismantling (radial segments)

The computed distributions of water content after the first dismantling along 3 radial segments (RS1, RS2 and RS3) on 3 dismantling sections (15, 27 and 31) are requested.

- **Section 15**: x = 3.27 m (between concrete plug and heater H1). The computed distributions of water content after the first dismantling should be along the radial segments RS1, RS2 and RS3 on dismantling section 15 (see Table A-55).

Table A-55. Definition of the radial segments on dismantling section 15 along which the distributions of water content after the first dismantling are requested.

Segment	Origin (x, y, z)	End (x, y, z)	Remarks
S15RS1	(3.27, 0.00, 0.00)	(3.27, 0.87, 0.73)	Angle with pos. y-axis = 40°
S15RS2	(3.27, 0.00, 0.00)	(3.27, −0.48, 1.03)	Angle with pos. y-axis = 115°
S15RS3	(3.27, 0.00, 0.00)	(3.27, 0.00, −1.13)	Angle with pos. y-axis = 270°

- **Section 27**: x = 6.85 m (on heater H1). The computed distributions of water content after the first dismantling should be along the radial segments RS1, RS2 and RS3 on dismantling section 27 (see Table A-56).

Table A-56. Definition of the radial segments on dismantling section 27 along which the distributions of water content after the first dismantling are requested.

Segment	Origin (x, y, z)	End (x, y, z)	Remarks
S27RS1	(6.85, 0.37, 0.31)	(6.85, 0.87, 0.73)	Angle with pos. y-axis = 40°
S27RS2	(6.85, −0.17, 0.46)	(6.85, −0.39, 1.07)	Angle with pos. y-axis = 110°
S27RS3	(6.85, 0.00, −0.49)	(6.85, 0.00, 1.13)	Angle with pos. y-axis = 270°

- **Section 31**: x = 7.74 m (on heater H1). The computed distributions of water content after the first dismantling should be along the radial segments RS1, RS2 and RS3 on dismantling section 31 (see Table A-57).

Table A-57. Definition of the radial segments on dismantling section 31 along which the distributions of water content after the first dismantling are requested.

Segment	Origin (x, y, z)	End (x, y, z)	Remarks
S31RS1	(7.74, 0.47, −0.17)	(7.74, 1.10, −0.29)	Angle with pos. y-axis = −15°
S31RS2	(7.74, −0.17, 0.46)	(7.74, −0.39, 1.07)	Angle with pos. y-axis = 110°
S31RS3	(7.74, −0.32, −0.37)	(7.74, −0.73, −0.87)	Angle with pos. y-axis = 270°

If the model used is 3D, the computed distributions of water content after the first dismantling along radial segment RSi (i = 1, 2, 3) on dismantling section Sk (k = 15, 27, 31) should be placed on the named range XXX_WC_SkRSi (a total of 3 × 3 = 9 named ranges). If the model used is 2D axisymmetric, the computed distributions of water content after the first dismantling along the radial segment RS on dismantling section Sk (k = 15, 17, 31) should be placed on the named range XXX_WC_SkRS (a total of 3 named ranges). In both cases, the structure of the named ranges is indicated Figure A-98.

Distributions of degree of saturation after the first dismantling (radial segments)

The computed distributions of degree of saturation after the first dismantling along 3 radial segments (RS1, RS2 and RS3) on 3 dismantling sections (15, 27 and 31) are requested.

- **Section 15**: x = 3.27 m (between concrete plug and heater H1). The computed distributions of degree of saturation after the first dismantling should be along the radial segments RS1, RS2 and RS3 on dismantling section 15 (see Table A-58).

Table A-58. Definition of the radial segments on dismantling section 15 along which the distributions of degree of saturation after the first dismantling are requested.

Segment	Origin (x, y, z)	End (x, y, z)	Remarks
S15RS1	(3.27, 0.00, 0.00)	(3.27, 0.87, 0.73)	Angle with pos. y-axis = 40°
S15RS2	(3.27, 0.00, 0.00)	(3.27, −0.48, 1.03)	Angle with pos. y-axis = 115°
S15RS3	(3.27, 0.00, 0.00)	(3.27, 0.00, −1.13)	Angle with pos. y-axis = 270°

- **Section 27**: x = 6.85 m (on heater H1). The computed distributions of degree of saturation after the first dismantling should be along the radial segments RS1, RS2 and RS3 on dismantling section 27 (see Table A-59).

Table A-59. Definition of the radial segments on dismantling section 27 along which the distributions of degree of saturation after the first dismantling are requested.

Segment	Origin (x, y, z)	End (x, y, z)	Remarks
S27RS1	(6.85, 0.37, 0.31)	(6.85, 0.87, 0.73)	Angle with pos. y-axis = 40°
S27RS2	(6.85, −0.17, 0.46)	(6.85, −0.39, 1.07)	Angle with pos. y-axis = 110°
S27RS3	(6.85, 0.00, −0.49)	(6.85, 0.00, 1.13)	Angle with pos. y-axis = 270°

$r(P_1)$	$WC(P_1)$
$r(P_r)$	$WC(P_r)$
$r(P_n)$	$WC(P_{n,})$

Figure A-98. *Structure of the named ranges XXX_WC_SkRSi (k = 15, 27, 31; i = 1, 2, 3) or XXX_WC_SkRS (k = 15, 27, 31). Each named range has 2 columns and a convenient number n of rows (to be decided by the modelling team and may be different for each named range). In row r (r = 1, ..., n), column 1 contains the radial distance r_r (in m) of a point P_r on the considered radial segment, and column 2 contains the water content after the first dismantling $WC(P_r)$ (in %) at point P_r. Radial distances $r(P_r)$ (r = 1, ..., n) should increase with the row number r.*

- **Section 31**: x = 7.74 m (on heater H1). The computed distributions of degree of saturation after the first dismantling should be along the radial segments RS1, RS2 and RS3 on dismantling section 31 (see Table A-60).

Table A-60. Definition of the radial segments on dismantling section 31 along which the distributions of degree of saturation after the first dismantling are requested.

Segment	Origin (x, y, z)	End (x, y, z)	Remarks
S31RS1	(7.74, 0.47, −0.17)	(7.74, 1.10, −0.29)	Angle with pos. y-axis = −15°
S31RS2	(7.74, −0.17, 0.46)	(7.74, −0.39, 1.07)	Angle with pos. y-axis = 110°
S31RS3	(7.74, −0.32, −0.37)	(7.74, −0.73, −0.87)	Angle with pos. y-axis = 270°

If the model used is 3D, the computed distributions of degree of saturation after the first dismantling along radial segment RSi (i = 1, 2, 3) on dismantling section Sk (k = 15, 27, 31) should be placed on the named range XXX_SR_SkRSi (a total of 3 × 3 = 9 named ranges). If the model used is 2D axisymmetric, the computed distributions of degree of saturation after the first dismantling along the radial segment RS on dismantling section Sk (k = 15, 17, 31) should be placed on the named range XXX_SR_SkRS (a total of 3 named ranges). In both cases, the structure of the named ranges is indicated Figure A-99.

$r(P_1)$	$SR(P_1)$
$r(P_r)$	$SR(P_r)$
$r(P_n)$	$SR(P_{n,})$

Figure A-99. *Structure of the named ranges XXX_WC_SkRSi (k = 15, 27, 31; i = 1, 2, 3) or XXX_WC_SkRS (k = 15, 27, 31). Each named range has 2 columns and a convenient number n of rows (to be decided by the modelling team and may be different for each named range). In row r (r = 1, ..., n), column 1 contains the radial distance $r(P_r)$ (in m) of a point P_r on the considered radial segment, and column 2 contains the degree of saturation after the first dismantling $SR(P_r)$ (in %) at point P^r. Radial distances $r(P_r)$ (r = 1, ..., n) should increase with the row number r.*

Appendix B

Specifications Stage 2 – Operational period after first dismantling until final dismantling

B1 Introduction

The Febex in situ test Task will be developed within the framework of the Engineered Barrier System (EBS) Task Force. The envisaged objectives of the task are:

- Enhance understanding of the THM EBS behaviour during the transient phase.
- Study the state of the engineered barrier at two different stages of its evolution. Observation of degree of homogenization.
- Improve the computational capabilities and validate the performance of coupled THM formulations and associated codes.
- Develop (or enhance) constitutive relationships of the bentonite: thermal, hydraulic and mechanical.
- Compare the performance of different formulations, numerical codes and constitutive laws.
- Examine other issues of potential interest such as: gap between dummy heater and bentonite, gap between rock and bentonite, swelling through liner grids, closure of joints between bentonite blocks.

B1.1 Test to be modelled

The FEBEX (Full-scale Engineered Barriers Experiment in Crystalline Host Rock) “in situ” test was a full-scale test conducted during 18.4 years in the Grimsel URL (Switzerland) managed by NAGRA. It was based on the ENRESA AGP Granito (Deep Geological Disposal, Granite) reference concept. A 70.4 m long drift with a circular section 2.28 m in diameter was excavated in the Grimsel granite. In the last 17.4 m of the gallery, two electrical heaters of dimensions and weight equivalent to those considered in the ENRESA and NAGRA concepts were emplaced and in the remaining space compacted bentonite blocks were emplaced. The test zone was closed with a concrete plug (see Figure B-1).

The experiment was instrumented with sensors monitoring the thermo-hydro-mechanical processes taking place in the clay barrier and in the surrounding Grimsel granite. The experiment was in operation during 5.0 years. Thereafter, the outer heater was switched off and the outer half of the experiment was dismantled, whereby samples were taken from various points of the rock, the concrete and the bentonite buffer. During this first dismantling, the remaining half of the experiment, including the second heater, continued in operation. This remaining half of the experiment was in operation during 13.2 years more. Thereafter, the experiment was completely dismantled and, as before, samples from various points were taken. Table B-1 summarizes the dates of important events in the FEBEX in situ experiment.

Table B-1. Summary of important dates in the FEBEX in situ experiment.

Date	Event
25.09.1995	Start of tunnel excavation
30.10.1995	End of tunnel excavation
01.07.1996	Start of installation
15.10.1996	End of installation
27.02.1997	Heaters switch on (day 0)
28.02.2002	Heater #1 switch off
19.07.2002	End of first dismantling
24.04.2015	Heater #2 switch off
30.08.2015	End of dismantling

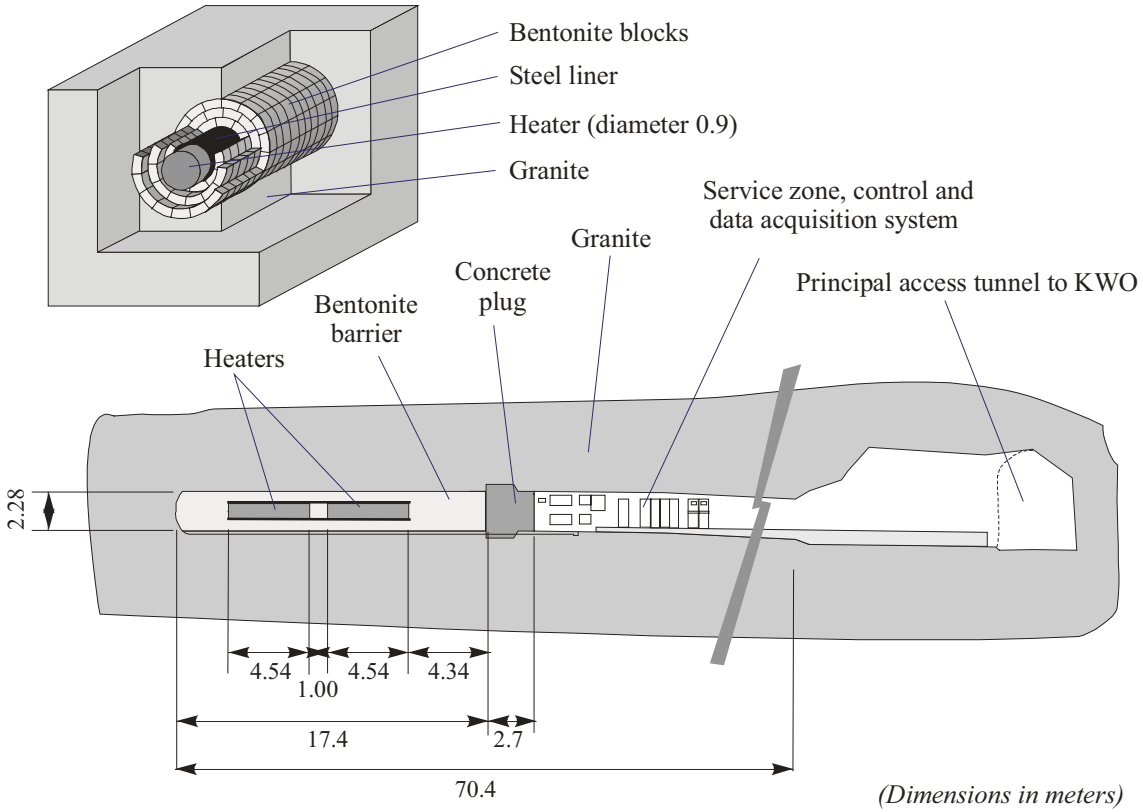

Figure B-1. *FEBEX "in situ" test layout (ENRESA 2000).*

B1.2 Stages of the Task

The work to be performed in the Task has been divided into 2 stages:

- Stage 1: Operational period of the FEBEX experiment up to and including the dismantling of the first heater (5.0 years). The duration time should allow teams to become familiar with the problem and to develop/tune their formulations and codes for the FEBEX case.
- Stage 2: Operational period of the FEBEX experiment after the dismantling of the first heater up to and including the final dismantling of the test (13.2 years).

B2 The FEBEX in situ test after the first dismantling

The FEBEX in situ experiment up to and including its first dismantling was described in the specifications of stage 1 of the Task 9 of the EBS Task Force (Annex A) in its Section A2: The FEBEX in situ test, which contained subsections 2.1: The FEBEX experiment at the Grimsel Test Site, 2.2: Components and installation of the FEBEX in situ test and 2.3: Test operation. The following descriptions of the FEBEX in situ test after the first dismantling and the final dismantling complete the description of the FEBEX in situ test.

B2.1 FEBEX "in situ" test configuration after dismantling of heater #1

After the demolition of the concrete plug, the extraction of heater #1, the partial dismantling of the bentonite buffer and the construction of a new shotcrete plug, about the half of the FEBEX "in situ" test remained in operation until its final dismantling. During the first dismantling operations, 71 additional sensors were also installed. Figure B-2 shows the test configuration after the first dismantling.

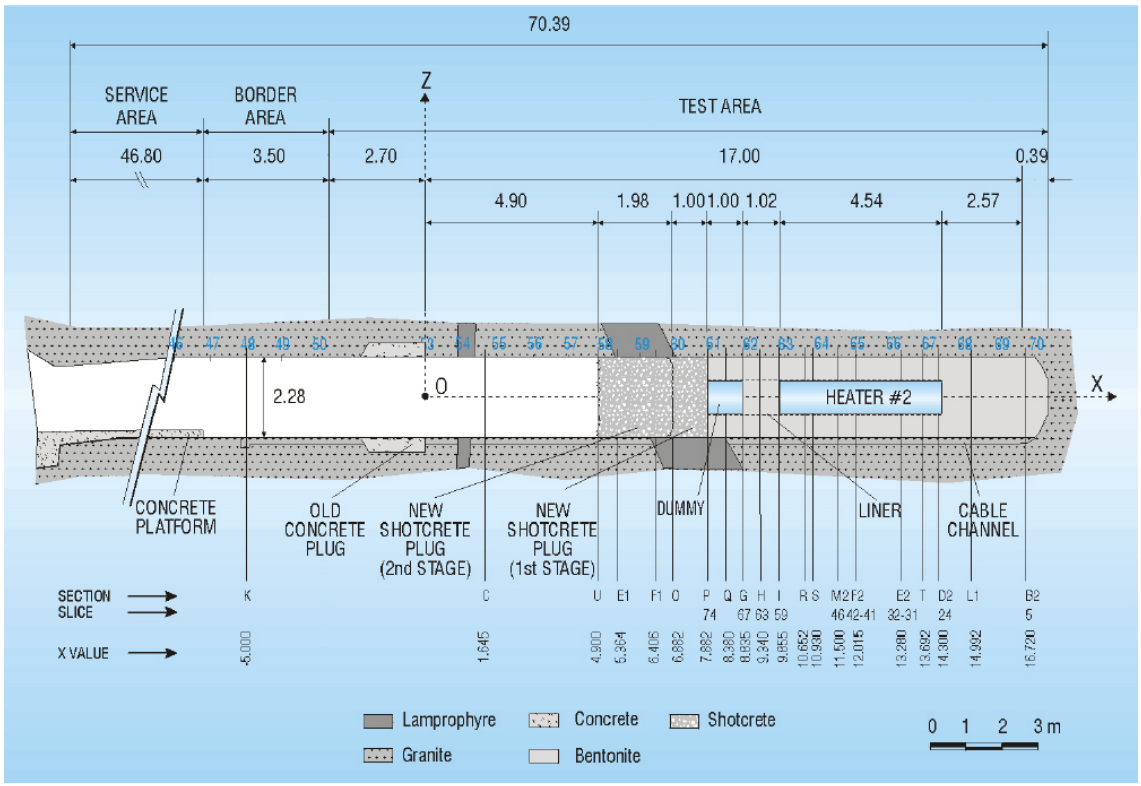

Figure B-2. *FEBEX "in situ" test configuration after dismantling of heater #1 (Bárcena et al. 2003).*

B2.2 Test operation after the first dismantling

The heater #2 remained in operation since the start of the FEBEX "in situ" and was switched off one month before its extraction during the final dismantling. In total, the heater #2 was in operation during more than 18 years.

B2.2.1 Heating control and operation

The regulation of the electrical power to heater #2 used so far was maintained, namely a constant temperature of 100 °C at the hottest point of the steel liner/bentonite interface.

B2.2.2 Final dismantling

About 13 years after the first partial dismantling, heater #2 was switched off. After cooling down of heater #2, the concrete plug was demolished, the steel liner and the heater #2 were removed, and the bentonite blocks were completely excavated. During the dismantling process, samples of rock, concrete and bentonite were taken for analysis. The dismantling process is described in detail in García-Siñeriz et al. (2016) on which the following summary is based.

The dismantling operation was made according to the following sequence:

1. Long coring and overcoring through the shotcrete plug and sampling.
2. Demolition of the first section (2 m long) of the shotcrete plug and sampling.
3. Switching off of heater #2, one month in advance of its extraction.
4. Coring through the remaining section (1 m long) of the shotcrete plug and sampling.
5. Demolition of the remaining section (1 m long) of the shotcrete plug and sampling.
6. Removal of bentonite buffer up to the front of heater #2 and sampling.
7. Extraction of heater #2.
8. Removal of the remaining bentonite buffer and the liner and sampling.

Relevant events and dates of the final dismantling process are shown in Table B-2.

Table B-2. Summary of important dates during the final dismantling.

Date	Event
17.02.2015	Start long coring and overcoring through the plug
07.04.2015	Start demolition of the 1st section of the plug
17.04.2015	End demolition of the 1st section of the plug
24.04.2015	Heater #2 switch off
27.04.2015	Start demolition of the 2nd section of the plug
08.05.2015	End demolition of the 2nd section of the plug
18.05.2015	Start dismantling of buffer until heater #2
04.06.2015	Extraction of heater #2
30.08.2015	End of dismantling

From the 17th and the 19th of February 2015, three long cores of concrete were extracted from the shotcrete plug, in order to get shotcrete samples. Additionally, from 24th and 26th of February 2015, three long cores obtained using an overcoring technique were extracted from the shotcrete plug and bentonite buffer, in order to get shotcrete/bentonite interface samples. The locations of these boreholes are shown in Figure B-3.

From the 7th to the 17th of April 2015, the first section (2 m long) of the shotcrete plug was demolished. This section of the plug was separated from the next one by an impermeable mat. For the demolition of the first shotcrete plug section, an autonomous arm-sized little robot was used, instead of the manual hydraulic drilling machines used for the demolition of the concrete plug during the first dismantling. Figure B-4 shows the partially excavated first section of the shotcrete plug and a partial view of the robot.

From the 17th to the 23rd of April 2015, coring took place to get interface concrete/rock and concrete samples. A decrease of pressure at the at the bentonite/plug interface during this process was observed.

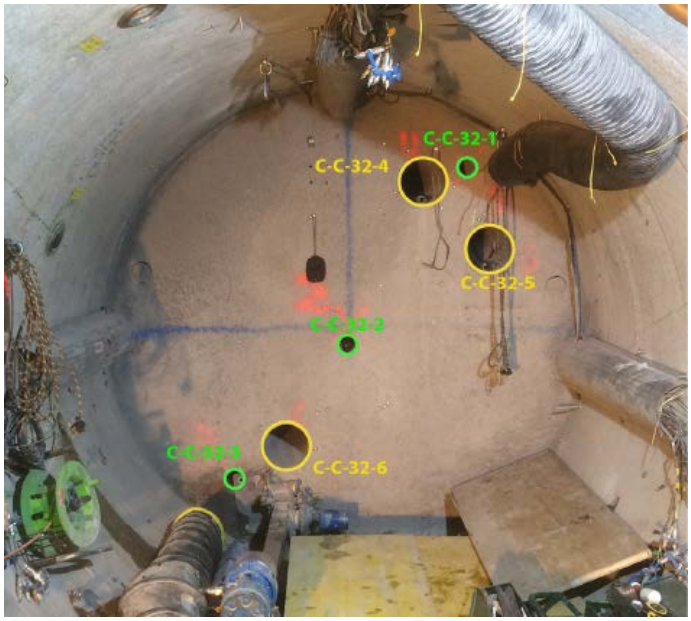

Figure B-3. *Locations of the 3 long core boreholes (green) for sampling of shotcrete and the 3 long core boreholes with overcoring (yellow) for sampling of the shotcrete/bentonite interface (García-Siñeriz et al. 2016).*

Figure B-4. *Marking of plug face on the gallery (red) and partial view of the autonomous robot. Some debris were left on the bottom of the tunnel to facilitate the robot movement (García-Siñeriz et al. 2016).*

On the 24th of April 2015, after 6 630 days of heating, the heater #2 was switched off in a single step, as it was done with heater #1 during the first dismantling. The goal was to reduce the designed control temperature of 100 °C at the heater/bentonite interface to 25–30 °C at the start of the excavation of the zone. This range of temperatures was reached in 20 days, whereas in the first dismantling it was reached 30 days after the switching off of heater #1.

From the 27th of April to the 8th of May 2015, the remaining section (1 m long) of the shotcrete plug was demolished using the same procedure as in the demolition of the first section of the shotcrete plug. Just after the start of this demolition, a drop of the total pressure in the shotcrete/bentonite interface was observed. Figure B-5 shows the gallery after the dismantling of the shotcrete plug.

Figure B-5. *View of the gallery after the dismantling of the shotcrete plug. The front of the 1 m long dummy steel cylinder that was placed during the first dismantling to fill the void left by heater #1 is visible. (García-Siñeriz et al. 2016).*

The shotcrete/bentonite interface was sampled using a manual drilling tool provided with a suitable crown. Additionally, bulky pieces of bentonite were also taken. Due to the pressure generated in the bentonite buffer and the intrusion of bentonite through the holes of the steel liner, the dummy 1 m steel cylinder that filled the void left by heater #1 was stuck to the steel liner. Because of this, the part of the bentonite buffer surrounding this portion of the steel liner (bentonite layers 74 to 66) was removed and sampled first, and then the dummy steel cylinder and the surrounding liner section were extracted. Afterwards, the bentonite buffer up to heater # 2 (bentonite layers 65 to 60) was dismantled and sampled following the same procedure as before. Figure B-6 shows the uncovered heater front.

On the 4th of June 2015, the heater #2 was extracted with the same equipment that was used to emplace the heaters, which had already been modified to extract the heater #1. It consisted of a vehicle whose basic structure was a chassis having a bed of rollers and rolling balls, a pulling system with a hydraulic winch installed on board of the vehicle that pulled the heater using a steel rope, and a return pulley fixed to the heater front. The hydraulic power group, that was mounted on the vehicle, allowed a continuous regulation of the pulling force, which could be measured by a tensile load sensor. Figure B-7 shows the heater #2 on the extraction vehicle.

Figure B-6. *View of the heater #2 before its extraction. Part of the steel lining is also visible (García-Siñeriz et al. 2016).*

Figure B-7. *Extraction of heater #2. View of the extracted heater, part of the extraction vehicle and the return pulley (García-Siñeriz et al. 2016).*

After the extraction of heater #2, the remaining bentonite buffer (bentonite layers 59 to 1) was extracted and sampled. The bentonite layers were dismantled one by one and sampling was carried out at the same time. The procedure and tools used were the same as before (see Figure B-8 and Figure B-9), but blocks in the ring around the liner were broken first. During the extraction of the bentonite buffer, the remaining liner was removed.

Figure B-8. *Samples extraction with core drill (García-Siñeriz et al. 2016).*

Figure B-9. *Partial dismantling of a section (García-Siñeriz et al. 2016).*

B3 Requested results

Plots with the evolutions with time of all variables monitored by the sensors installed in the FEBEX in situ Experiment in the period from the 20th of February 1997 to the 30th of August 2015 may be found in the report Martínez et al. (2016). The corresponding numerical values have also been made available to the modelling teams. Consequently, the requested results are not blind predictions.

B3.1 General specifications

The general specifications for the requested results are presented in Section A4.1 of the specifications of stage 1 of the Task 9 of the EBS Task Force (Annex A). Most aspects of these specifications will be recalled below. The Cartesian co-ordinate system defined there will be used for space references, and the 27th of February 1997 (heaters switch on) will be used for time references (day 0). Similarly, the 3-character codes that were assigned to each modelling team and to the co-ordinator (see Table B-3), will be used in the project reports, particularly in comparison plots.

Table B-3. 3-character codes assigned to the modelling teams and to the co-ordinator.

Modelling team / co-ordinator	Code
Central Research Institute of Electric Power Industry (CRIEPI), Japan	CRP
Svensk Kärnbränslehantering AB (SKB), Sweden	SK1
Gesellschaft für Anlagen- und Reaktorsicherheit (GRS), Germany	GRS
Universitat Politècnica de Catalunya (UPC), Spain	UPC
Nationale Gesellschaft für die Lagerung radioaktiver Abfälle (NAGRA), Switzerland	NAG
Bundesanstalt für Geowissenschaften und Rohstoffe (BGR), Germany	BGR
Imperial College London (ICL), United Kingdom	ICL
Svensk Kärnbränslehantering AB (SKB), Sweden	SK2
Centre Internacional de Mètodes Numèrics en Enginyeria (CIMNE), Spain	CIM

B3.1.1 Numerical data

The required output results should be placed in a Microsoft Office Excel Workbook compatible with Microsoft Office Excel 2007 (with a maximum of 1 048 576 rows and 16 384 columns) named XXX_ FBXs_Ri.xlsx (XXX is the team's code, s = 1 or 2 is the stage of the task, i is the revision number, starting at 0). The Workbook should contain a Sheet labelled XXX (the team's code). In this Sheet, output results should be placed in named ranges, with names of the form XXX_* (XXX is the team's code and * denotes the variable part of the name), as indicated in the corresponding output specifications. Since the requested output data will be accessed through the named ranges, their locations in the Sheet may be freely decided by the modelling team. Though not required, it may be convenient to place a header above each named range with information on the data contained. Note that this additional information should not be included in the named range.

Note. To define a named range in Microsoft Office Excel 2007, perhaps the easiest way is to first select the range, then click the Name box at the left end of the formula bar (just above cell A1), type the desired name and press ENTER. The Name Manager dialog box on the Formulas tab, in the Defined Names group, allows to create, edit and delete named ranges. For more information on named ranges, reference is made to the article "Define and use names in formulas" at https://support.office.com/en-us/article/Define-and-use-names-in-formulas-4D0F13AC-53B7-422E-AFD2-ABD7FF379C64.

Both evolutions with time and spatial distributions of selected variables will be requested. Modelling teams should get the computed values of the requested variables as close as possible to the time instants or to the spatial points where they are requested. In fact, these values will be compared against the experimental data and to the values provided by the other modelling teams, without any interpolation. On the other hand, modelling teams are free to provide values at additional time instants or points to properly define the required curve. In principle, all the provided points will be plotted and joined by straight-line segments. It should be emphasised that predictions are given at the points, whereas the straight-line segments merely join those points together. Note that, in order that the plotted symbols of points lying too close in the plotted curve do not result in a "thick line", the number of points provided should be limited.

B3.1.2 Modelling reports

Updated modelling reports should be submitted if the numerical model has been modified in any way for this stage of the Task. The specifications for compiling the report are presented in Section A4.1.2 of the specifications of stage 1 of the Task 9 of the EBS Task Force (Annex A). As requested in that document, modelling reports should be placed in a Microsoft Office Word file compatible with Microsoft Office 2007 named XXX_FBX_Ri.docx (XXX is the team's code, i is the revision number, starting at 0). To ease the compilation of the modelling reports, the format to be used should be the same as the format used to prepare the present document (e.g., Times New Roman, 12 point, single space, all margins set to 2.5 cm).

B3.2 Requested results

Five types of results are requested: (1) evolutions of heating power; (2) distributions and evolutions of relative humidity; (3) distributions and evolutions of temperature; (4) evolutions of total stresses; and (5) distributions after final dismantling of dry density, water content and degree of saturation.

B3.2.1 Evolution after first dismantling of heating power

The unit to be used for heating power Q is W (Watt). The computed evolution of power input (in W) to heater 2 from t = 2 325 days to t = 6 600 days is requested. The computed evolution of heating power at heater H2 should be placed on the named range XXX_Q_H. The structure of this named range is shown in Figure B-10.

B3.2.2 Distributions and evolutions after first dismantling of relative humidity

The unit to be used for relative humidity RH is % (water vapour density over water vapour density at full saturation, in per cent). Figure B-11 shows the location of section F2, where distributions (along radial segments) and evolutions (at selected points) of relative humidity are requested.

t_1	$Q(H2, t_1)$
t_r	$Q(H2, t_r)$
t_n	$Q(H2, t_n)$

Figure B-10. *Structure of the named range XXX_Q_H. This named range has 2 columns and a convenient number n of rows (to be decided by the modelling team). In row r (r = 1, ..., n), column 1 contains a time t_r (in days) in the considered time interval, and column 2 contains the heating power input $Q(H2, t_r)$ (in W) at heater H2 and time t_r (in days). Times t_r (r = 1, ..., n) should increase with the row number r.*

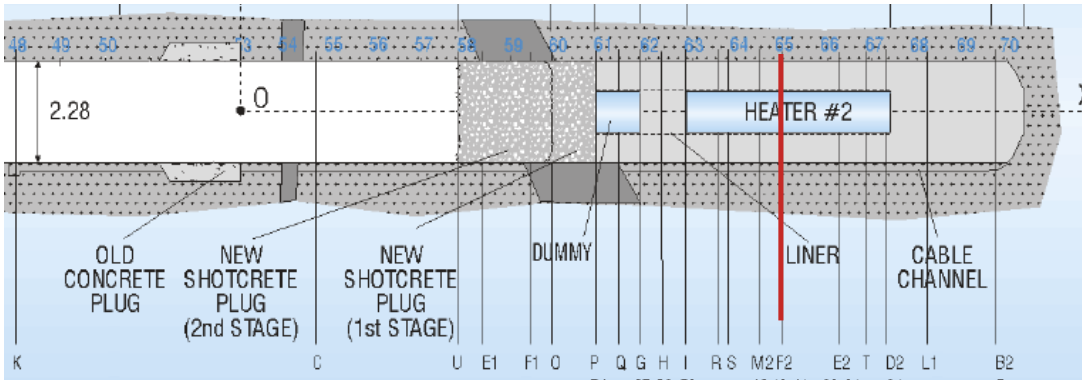

Figure B-11. *Required results: distributions and evolutions of relative humidity.*

Distributions of relative humidity (radial segments)

The computed distributions of relative humidity along 4 radial segments (RS1, RS2, RS3 and RS4) on 1 section (F2) at 1 time (t1) are requested.

- **Section F2**: x = 12.30 m (near the middle of heater 2). The computed distributions of relative humidity should be along the radial segments RS1, RS2, RS3 and RS4 on section F2 (see Table B-4) at time t1 = 4 000 days.

Table B-4. Definition of the radial segments on section F2 along which the distributions of relative humidity are requested.

Segment	Origin (x, y, z)	End (x, y, z)	Remarks
SF2RS1	(12.30, 0.00, 0.49)	(12.30, 0.00, 1.13)	Parallel to the pos. z-axis
SF2RS2	(12.30, 0.00, −0.49)	(12.30, 0.00, −1.13)	Parallel to the neg. z-axis
SF2RS3	(12.30, 0.49, 0.00)	(12.30, 1.13, 0.00)	Parallel to the pos. y-axis
SF2RS4	(12.30, −0.49, 0.00)	(12.30, −1.13, 0.00)	Parallel to the neg. y-axis

If the model used is 3D, the computed distributions of relative humidity along radial segment RSi (i = 1, 2, 3, 4) on section SF2 at time t1 should be placed on the named range XXX_RH_SF2RSi (a total of 4 named ranges). If the model used is 2D axisymmetric, the computed distributions of relative humidity along the radial segment RD on section SF2 at time t1 should be placed on the named range XXX_RH_SF2RS. In both cases, the structure of the named ranges is shown in Figure B-12.

Evolutions of relative humidity

The computed evolutions of relative humidity should be given at 5 points (P1, P2, P3, P4 and P5) on 1 section (F2) from t = 2 325 days to t = 6 600 days are requested.

- **Section F2**: x = 12.30 m (near the middle of heater 2). The computed evolutions of relative humidity should be at points P1, P2, P3 P4 and P5 on section F2 (see Table B-5) from t = 2 325 days to t = 6 600 days.

Table B-5. Definition of the points on section F2 at which the evolutions of relative humidity are requested.

Point	(x, y, z)	Remarks
SF2P1	(12.30, −0.81, 0.09)	Neg. y-axis, near mid. bentonite
SF2P2	(12.30, −1.05, 0.08)	Neg. y-axis, near granite
SF2P3	(12.30, −0.27, −0.52)	Near heater
SF2P4	(12.30, 0.72, 0.36)	Near mid, bentonite
SF2P5	(12.30, 0.53, 0.24)	Near heater

$r(P_1)$	$RH(P_1, t1)$
$r(P_r)$	$RH(P_r, t1)$
$r(P_n)$	$RH(P_n, t1)$

Figure B-12. *Structure of the named ranges XXX_RH_SF2RSi (i = 1, 2, 3, 4) or XXX_RH_SF2RS. Each named range has 2 columns and a convenient number n of rows (to be decided by the modelling team and may be different for each named range). In row r (r = 1, ..., n), column 1 contains the radial distance $r(P_r)$ (in m) of a point P_r on the considered radial segment, and column 2 contains the relative humidity $RH(P_r, t1)$ (in %) at point P_r and time t1 (in days). Radial distances $r(P_r)$ (r = 1, ..., n) should increase with the row number r.*

The computed evolutions of relative humidity at point Pi (i = 1, 2, 3, 4, 5) on section F2 should be placed on the named range XXX_RH_F2P. The structure of this named range is shown in Figure B-13.

B3.2.3 Distributions and evolutions after first dismantling of temperature

The unit to be used for temperature T is °C (degree Celsius). Figure B-14 shows the locations of section D2, where distributions (along radial segments) and evolutions (at selected points) of temperature are requested. It also shows the location of the axial segments along which distributions of temperature are requested.

Distributions of temperature (radial segments)

The computed distributions of temperature along 2 radial segments (RS1 and RS2) on 1 section (D2) at 1 time (t1) are requested.

- **Section D2**: x = 14.38 m (end of heater H2, closest to tunnel end). The computed distributions of temperature should be along the radial segments RS1 and RS2 on section D2 (see Table B-6) at time t1 = 5 600 days.

Table B-6. Definition of the radial segments on section D2 along which the distributions of temperature are requested.

Segment	Origin (x, y, z)	End (x, y, z)	Remarks
SD2RS1	(14.38, 0.00, 0.49)	(14.38, 0.00, 1.13)	Parallel to the pos. z-axis
SD2RS2	(14.38, −0.49, 0.00)	(14.38, −1.13, 0.00)	Parallel to the neg. z-axis

t_1	RH(P1, t_1)	RH(P2, t_1)	RH(P3, t_1)	RH(P4, t_1)	RH(P5, t_1)
t_r	RH(P1, t_r)	RH(P2, t_r)	RH(P3, t_r)	RH(P4, t_r)	RH(P5, t_r)
t_n	RH(P1, t_n)	RH(P2, t_n)	RH(P3, t_n)	RH(P4, t_n)	RH(P5, t_n)

Figure B-13. *Structure of the named range XXX_RH_F2P. This named range has 6 columns and a convenient number n of rows (to be decided by the modelling team). In row r (r = 1, ..., n), column 1 contains a time t_r (in days) in the considered time interval, and column j + 1 (j = 1, ..., 5) contains the relative humidity RH(Pj, t_r) (in %) at point Pj and time t_r (in days). Times t_r (r = 1, ..., n) should increase with the row number r.*

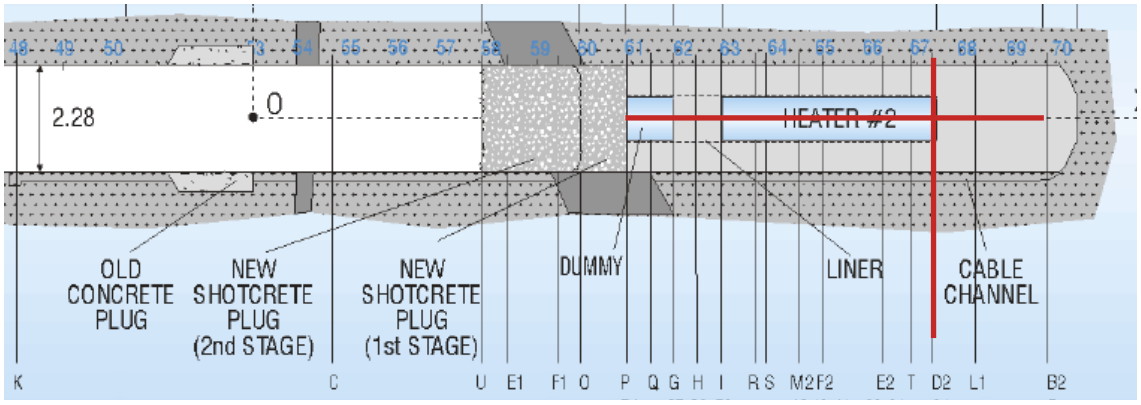

Figure B-14. *Required results: distributions and evolutions of temperature.*

If the model used is 3D, the computed distributions of temperature along radial segment RSi (i = 1, 2) on section D2 at time t1 should be placed on the named ranges XXX_T_SD2RSi (a total of 2 named ranges). If the model used is 2D axisymmetric, the computed distributions of relative humidity along the radial segment RS on section SD2 at time t1 should be placed on the named range XXX_T_SD2RS. In both cases, the structure of the named ranges is indicated in Figure B-15.

Distributions of temperature (axial segments)

The computed distributions of temperature should be along the axial segments AS1 and AS2 (see Table B-7) at time t1 = 5 600 days.

Table B-7. Definition of the axial segments along which the distributions of temperature are requested.

Segment	Origin (x, y, z)	End (x, y, z)	Remarks
AS1	(7.88, −0.81, 0.00)	(17.00, −0.81, 0.00)	Paral. pos. x-axis, mid. bentonite
AS2	(7.88, −1.14, 0.00)	(17.00, −1.14, 0.00)	Paral. pos. x-axis, near granite

The computed distributions of temperature along axial segment ASi (i = 1, 2) at time t1 should be placed on the named range XXX_T_ASi (a total of 2 named ranges). The structure of the named ranges is indicated in Figure B-16.

$r(P_1)$	$T(P_1, t1)$
$r(P_r)$	$T(P_r, t1)$
$r(P_n)$	$T(P_n, t1)$

Figure B-15. *Structure of the named ranges XXX_T_D2RSi (i = 1, 2) or XXX_T_SD2RS. Each named range has 2 columns and a convenient number n of rows (to be decided by the modelling team and may be different for each named range). In row r (r = 1, ..., n), column 1 contains the radial distance $r(P_r)$ (in m) of a point P_r on the considered radial segment, and column 2 contains the temperature $T(P_r, t1)$ (in °C) at point P_r and time t1(in days). Radial distances $r(P_r)$ (r = 1, …, n) should increase with the row number r.*

$x(P_1)$	$T(P_1, t1)$
$x(P_r)$	$T(P_r, t1)$
$x(P_n)$	$T(P_n, t1)$

Figure B-16. *Structure of the named ranges XXX_T_ASi (i = 1, 2). Each named range has 2 columns and a convenient number n of rows (to be decided by the modelling team and may be different for each named range). In row r (r = 1, ..., n), column 1 contains the x co-ordinate $x(P_r)$ (in m) of a point P_r on the considered longitudinal segment, and column 2 contains the temperature $T(P_r, t1)$ (in °C) at point P_r and time t1 (in days). x-co-ordinates $x(P_r)$ (r = 1, …, n) should increase with the row number r.*

Evolutions of temperature

The computed evolution of temperature at 1 point (P1) on 1 section (D2) from t = 2 325 days to t = 6 600 days is requested.

- **Section D2**: x = 14.38 m (end of heater H2, closest to tunnel end). The computed evolution of temperature should be at point P1 on section D2 (see Table B-8) from t = 2 325 days to t = 6 600 days.

Table B-8. Definition of the point on section D2 at which the evolution of temperature is requested.

Point	(x, y, z)	Remarks
SD2P1	(14.38, −1.14, 0.00)	Neg. y-axis, near granite

The computed evolution of temperature at point P1 on section SD2 should be placed on the named range XXX_T_SD2P. The structure of this named range is shown in Figure B-17.

B3.2.4 Evolutions after first dismantling of total stress

The unit to be used for total stresses TS is MPa (megapascal), with the convention that compressions are positive. Figure B-18 shows the locations of sections E2 and B2, where evolutions (at selected points) of total stresses are requested.

t_1	$T(P1, t_1)$
t_r	$T(P1, t_r)$
t_n	$T(P1, t_n)$

Figure B-17. *Structure of the named range XXX_T_SD2P. This named range has 2 columns and a convenient number n of rows (to be decided by the modelling team). In row r (r = 1, ..., n), column 1 contains a time t_r (in days) in the considered time interval, and column 2 contains the temperature $T(P1, t_r)$ (in °C) at point P1 and time t_r (in days). Times t_r (r = 1, ..., n) should increase with the row number r.*

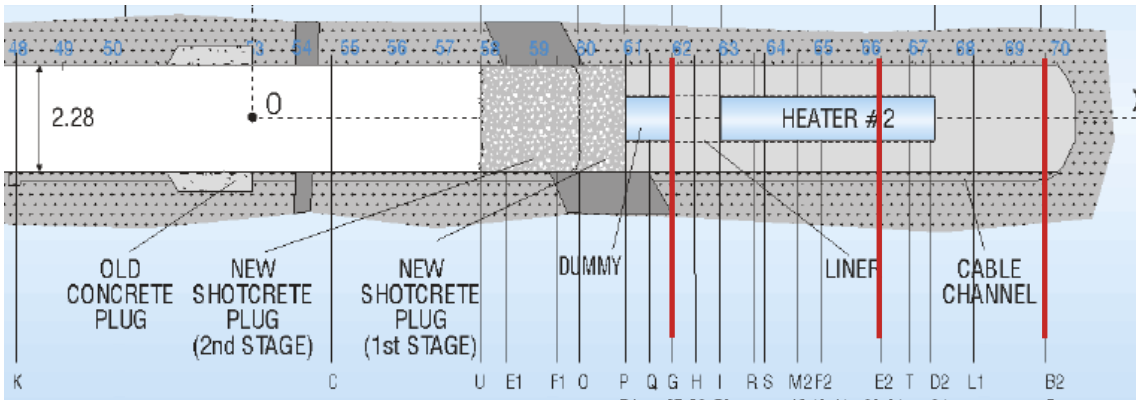

Figure B-18. *Required results: evolutions of total stresses.*

The computed evolutions of radial total stresses at 3 points (P1, P2 and P3) on 1 section (E2) and the computed evolution of axial total stress at 1 point (P1) on 2 sections (G and B2) from t = 2 325 days to t = 6 600 days are requested.

- **Section E2**: x = 13.44 m (at heater 2). The computed evolutions of radial total stresses should be at points Pi (i = 1, 2, 3) on section E2 (see Table B-9) from t = 2 325 days to t = 6 600 days.

Table B-9. Definition of the points on section E2 at which the evolutions of radial total stresses are requested.

Point	(x, y, z)	Remarks
SE2P1	(13.28, 0.00, −0.48)	Neg. z-axis, near heater
SE2P2	(13.45, −0.28, −1.19)	Neg. z-axis, near granite
SE2P3	(13.46, −1.19, 0.00)	Neg. y-axis, near granite

- **Section G**: x = 8.84 m (at the end of the 1 m dummy canister closest to heater 2). The computed evolution of axial total stress should be at point P1 on section G (see Table B-10) from t = 2 325 days to t = 6 600 days.

Table B-10. Definition of the point on section G at which the evolution of axial total stress is requested.

Point	(x, y, z)	Remarks
SGP1	(8.84, 0.00, 0.00)	Center of section

- **Section B2**: x = 17.32 m (near the end of the test area). The computed evolution of axial total stress should be at point P1 on section B2 (see Table B-11) from t = 2 325 days to t = 6 600 days.

Table B-11. Definition of the point on section B2 at which the evolution of axial total stress is requested.

Point	(x, y, z)	Remarks
SB2P1	(17.32, 0.26, 0.76)	Pos. z-axis, mid. bentonite

The computed evolutions of the radial total stress at points Pi (i = 1, 2, 3) on section E2 should be placed on the named range XXX_RTS_SE2P. The structure of this named range is shown in Figure B-19.

t_1	RTS(P1, t_1)	RTS(P2, t_1)	RTS(P3, t_1)
t_r	RTS(P1, t_r)	RTS(P2, t_r)	RTS(P3, t_r)
t_n	RTS(P1, t_n)	RTS(P2, t_n)	RTS(P3, t_n)

Figure B-19. *Structure of the named range XXX_RTS_E2P. This named range has 4 columns and a convenient number n of rows (to be decided by the modelling team). In row r (r = 1, ..., n), column 1 contains a time t_r (in days) in the considered time interval, and column j + 1 (j = 1, 2, 3) contains the radial total stress RTS(Pj, t_r) (in MPa) at point Pj and time t_r (in days). Times t_r (r = 1, ..., n) should increase with the row number r.*

The computed evolution of the axial total stress at point P1 on section Sk (k = G, B2) should be placed on the named range XXX_ATS_SkP (a total of 2 named ranges). The structure of this named ranges is shown in Figure B-20.

B3.2.5 Distributions of dry density, water content and degree of saturation after dismantling

The unit to be used for dry density DD is g/cm^3, the unit to be used for water content WC is % (ratio of the masses of water and of dry soil particles in a volume of soil, in per cent) and the unit to be used for degree of saturation SR is % (proportion of the volume of the void occupied by water, in per cent). Figure B-21 shows the locations of the dismantling sections 43, 49, 56 and 61, where distributions (along radial segments) of dry density, water content and degree of saturation are requested.

t_1	ATS(P1, t_1)
t_r	ATS(P1, t_r)
t_n	ATS(P1, t_n)

Figure B-20. *Structure of the named ranges XXX_ATS_SkP (k = G, B2). Each named range has 2 columns and a convenient number n of rows (to be decided by the modelling team and which may be different for each named range). In row r (r = 1, ..., n), column 1 contains a time t_r (in days) in the considered time interval, and column 2 contains the axial total stress ATS(P1, t_r) (in MPa) at point P1 and time t_r (in days). Times t_r (r = 1, ..., n) should increase with the row number r.*

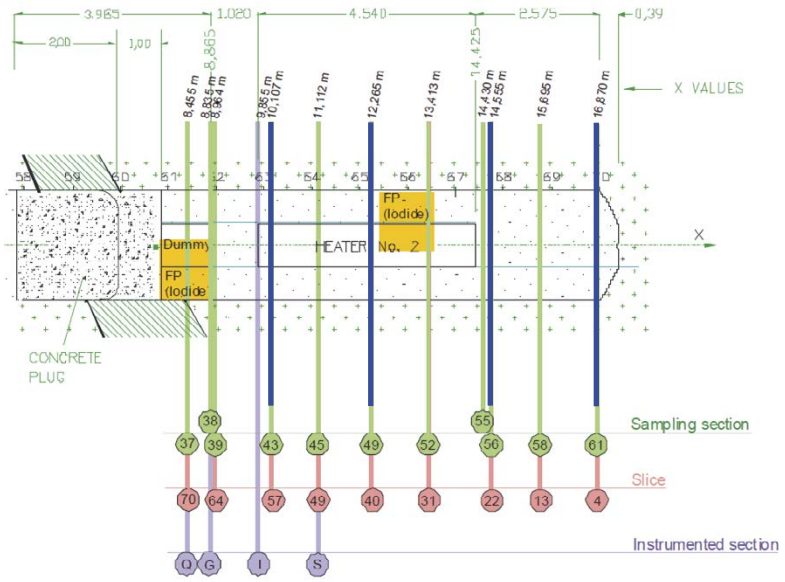

Figure B-21. *Required results: distributions of dry density, water content and degree of saturation after dismantling.*

Distributions of dry density after final dismantling (radial segments)

The computed distributions of dry density after dismantling along 3 radial segments (RS1, RS2 and RS3) on 4 dismantling sections (43, 49, 56 and 61) are requested.

- **Section 43**: x = 10.12 m (on heater H2, near its end closest to concrete plug). The computed distributions of dry density after dismantling should be along the radial segments RS1, RS2 and RS3 on dismantling section 43 (see Table B-12).

Table B-12. Definition of the radial segments on dismantling section 43 along which the distributions of dry density after dismantling are requested.

Segment	Origin (x, y, z)	End (x, y, z)	Remarks
S43RS1	(10.12, 0.00, 0.49)	(10.12, 0.00, 1.14)	Angle with pos. y-axis = 90°
S43RS2	(10.12, −0.37, −0.31)	(10.12, −0.87, −0.73)	Angle with pos. y-axis = 220°
S43RS3	(10.12, 0.42, −0.24)	(10.12, 0.98, −0.57)	Angle with pos. y-axis = 330°

- **Section 49**: x = 12.27 m (on heater H2, near its centre). The computed distributions of dry density after dismantling should be along the radial segments RS1, RS2 and RS3 on dismantling section 49 (see Table B-13).

Table B-13. Definition of the radial segments on dismantling section 49 along which the distributions of dry density after dismantling are requested.

Segment	Origin (x, y, z)	End (x, y, z)	Remarks
S49RS1	(12.27, 0.42, 0.24)	(12.27, 0.98, 0.57)	Angle with pos. y-axis = 30°
S49RS2	(12.27, −0.42, 0.24)	(12.27, −0.98, 0.57)	Angle with pos. y-axis = 150°
S49RS3	(12.27, 0.00, −0.49)	(12.27, 0.00, −1.14)	Angle with pos. y-axis = 270°

- **Section 56**: x = 14.56 m (on bentonite buffer, near end of heater H2 closest to tunnel end). The computed distributions of dry density after dismantling should be along the radial segments RS1, RS2 and RS3 on dismantling section 31 (see Table B-14).

Table B-14. Definition of the radial segments on dismantling section 56 along which the distributions of dry density after dismantling are requested.

Segment	Origin (x, y, z)	End (x, y, z)	Remarks
S56RS1	(14.56, 0.00, 0.00)	(14.56, 0.98, 0.57)	Angle with pos. y-axis = 30°
S56RS2	(14.56, 0.00, 0.00)	(14.56, −1.03, 0.48)	Angle with pos. y-axis = 155°
S56RS3	(14.46, 0.00, 0.00)	(14.56, 0.00, −1.14)	Angle with pos. y-axis = 270°

- **Section 61**: x = 16.87 m (on bentonite buffer, near to tunnel end). The computed distributions of dry density after dismantling should be along the radial segments RS1, RS2 and RS3 on dismantling section 61 (see Table B-15).

Table B-15. Definition of the radial segments on dismantling section 61 along which the distributions of dry density after dismantling are requested.

Segment	Origin (x, y, z)	End (x, y, z)	Remarks
S61RS1	(16.87, 0.00, 0.00)	(16.87, 0.00, 1.14)	Angle with pos. y-axis = 90°
S61RS2	(16.87, 0.00, 0.00)	(16.87, −0.93, −0.65)	Angle with pos. y-axis = 215°
S61RS3	(16.87, 0.00, 0.00)	(16.87, 0.98, −0.57)	Angle with pos. y-axis = 330°

If the model used is 3D, the computed distributions of dry density after dismantling along radial segment RSi (i = 1, 2, 3) on dismantling section Sk (k = 43, 49, 56, 61) should be placed on the named range XXX_DD_SkRSi (a total of 3 × 4 = 12 named ranges). If the model used is 2D axisymmetric, the computed distributions of dry density after dismantling along the radial segment RS on dismantling section Sk (k = 43, 49, 56, 61) should be placed on the named range XXX_DD_SkRS (a total of 4 named ranges). In both cases, the structure of the named ranges is indicated Figure B-22.

Distributions of water content after final dismantling (radial segments)

The computed distributions of water content after dismantling along 3 radial segments (RS1, RS2 and RS3) on 4 dismantling sections (43, 49, 56 and 61) are requested.

- **Section 43**: x = 10.12 m (on heater H2, near its end closest to concrete plug). The computed distributions of water content after dismantling should be along the radial segments RS1, RS2 and RS3 on dismantling section 43 (see Table B-16).

Table B-16. Definition of the radial segments on dismantling section 43 along which the distributions of water content after dismantling are requested.

Segment	Origin (x, y, z)	End (x, y, z)	Remarks
S43RS1	(10.12, 0.00, 0.49)	(10.12, 0.00, 1.14)	Angle with pos. y-axis = 90°
S43RS2	(10.12, −0.37, −0.31)	(10.12, −0.87, −0.73)	Angle with pos. y-axis = 220°
S43RS3	(10.12, 0.42, −0.24)	(10.12, 0.98, −0.57)	Angle with pos. y-axis = 330°

- **Section 49**: x = 12.27 m (on heater H2, near its centre). The computed distributions of water content after dismantling should be along the radial segments RS1, RS2 and RS3 on dismantling section 49 (see Table B-17).

Table B-17. Definition of the radial segments on dismantling section 49 along which the distributions of water content after dismantling are requested.

Segment	Origin (x, y, z)	End (x, y, z)	Remarks
S49RS1	(12.27, 0.42, 0.24)	(12.27, 0.98, 0.57)	Angle with pos. y-axis = 30°
S49RS2	(12.27, −0.42, 0.24)	(12.27, −0.98, 0.57)	Angle with pos. y-axis = 150°
S49RS3	(12.27, 0.00, −0.49)	(12.27, 0.00, −1.14)	Angle with pos. y-axis = 270°

$r(P_1)$	$DD(P_1)$
$r(P_r)$	$DD(P_r)$
$r(P_n)$	$DD(P_{n,})$

Figure B-22. *Structure of the named ranges XXX_DD_SkRSi (k = 43, 49, 56, 61; i = 1, 2, 3) or XXX_DD_SkRS (k = 43, 49, 56, 61). Each named range has 2 columns and a convenient number n of rows (to be decided by the modelling team and may be different for each named range). In row r (r = 1, ..., n), column 1 contains the radial distance r_r (in m) of a point P_r on the considered radial segment, and column 2 contains the dry density after dismantling $DD(P_r)$ (in g/cm^3) at point P_r. Radial distances $r(P_r)$ (r = 1, ..., n) should increase with the row number r.*

- **Section 56**: x = 14.56 m (on bentonite buffer, near end of heater H2 closest to tunnel end). The computed distributions of water content after dismantling should be along the radial segments RS1, RS2 and RS3 on dismantling section 56 (see Table B-18).

Table B-18. Definition of the radial segments on dismantling section 56 along which the distributions of water content after dismantling are requested.

Segment	Origin (x, y, z)	End (x, y, z)	Remarks
S56RS1	(14.56, 0.00, 0.00)	(14.56, 0.98, 0.57)	Angle with pos. y-axis = 30°
S56RS2	(14.56, 0.00, 0.00)	(14.56, −1.03, 0.48)	Angle with pos. y-axis = 155°
S56RS3	(14.46, 0.00, 0.00)	(14.56, 0.00, −1.14)	Angle with pos. y-axis = 270°

- **Section 61**: x = 16.87 m (on bentonite buffer, near to tunnel end). The computed distributions of water content after dismantling should be along the radial segments RS1, RS2 and RS3 on dismantling section 61 (see Table B-19).

Table B-19. Definition of the radial segments on dismantling section 61 along which the distributions of water content after dismantling are requested.

Segment	Origin (x, y, z)	End (x, y, z)	Remarks
S61RS1	(16.87, 0.00, 0.00)	(16.87, 0.00, 1.14)	Angle with pos. y-axis = 90°
S61RS2	(16.87, 0.00, 0.00)	(16.87, −0.93, −0.65)	Angle with pos. y-axis = 215°
S61RS3	(16.87, 0.00, 0.00)	(16.87, 0.98, −0.57)	Angle with pos. y-axis = 330°

If the model used is 3D, the computed distributions of water content after dismantling along radial segment RSi (i = 1, 2, 3) on dismantling section Sk (k = 43, 49, 56, 61) should be placed on the named range XXX_WC_SkRSi (a total of 3 × 4 = 12 named ranges). If the model used is 2D axisymmetric, the computed distributions of water content after dismantling along the radial segment RS on dismantling section Sk (k = 43, 49, 56, 61) should be placed on the named range XXX_WC_SkRS (a total of 4 named ranges). In both cases, the structure of the named ranges is indicated Figure B-23.

$r(P_1)$	$WC(P_1)$
$r(P_r)$	$WC(P_r)$
$r(P_n)$	$WC(P_{n,})$

Figure B-23. *Structure of the named ranges XXX_WC_SkRSi (k = 43, 49, 56, 61; i = 1, 2, 3) or XXX_WC_SkRS (k = 43, 49, 56, 61). Each named range has 2 columns and a convenient number n of rows (to be decided by the modelling team and may be different for each named range). In row r (r = 1, ..., n), column 1 contains the radial distance r_r (in m) of a point P_r on the considered radial segment, and column 2 contains the water content after dismantling $WC(P_r)$ (in %) at point P_r. Radial distances $r(P_r)$ (r = 1, ..., n) should increase with the row number r.*

Distributions of degree of saturation after final dismantling (radial segments)

The computed distributions of degree of saturation after dismantling along 3 radial segments (RS1, RS2 and RS3) on 4 dismantling sections (43, 49, 56 and 61) are requested.

- **Section 43**: x = 10.12 m (on heater H2, near its end closest to concrete plug). The computed distributions of degree of saturation after dismantling should be along the radial segments RS1, RS2 and RS3 on dismantling section 43 (see Table B-20).

Table B-20. Definition of the radial segments on dismantling section 43 along which the distributions of degree of saturation after dismantling are requested.

Segment	Origin (x, y, z)	End (x, y, z)	Remarks
S43RS1	(10.12, 0.00, 0.49)	(10.12, 0.00, 1.14)	Angle with pos. y-axis = 90°
S43RS2	(10.12, −0.37, −0.31)	(10.12, −0.87, −0.73)	Angle with pos. y-axis = 220°
S43RS3	(10.12, 0.42, −0.24)	(10.12, 0.98, −0.57)	Angle with pos. y-axis = 330°

- **Section 49**: x = 12.27 m (on heater H2, near its centre). The computed distributions of degree of saturation after dismantling should be along the radial segments RS1, RS2 and RS3 on dismantling section 49 (see Table B-21).

Table B-21. Definition of the radial segments on dismantling section 49 along which the distributions of degree of saturation after dismantling are requested.

Segment	Origin (x, y, z)	End (x, y, z)	Remarks
S49RS1	(12.27, 0.42, 0.24)	(12.27, 0.98, 0.57)	Angle with pos. y-axis = 30°
S49RS2	(12.27, −0.42, 0.24)	(12.27, −0.98, 0.57)	Angle with pos. y-axis = 150°
S49RS3	(12.27, 0.00, −0.49)	(12.27, 0.00, −1.14)	Angle with pos. y-axis = 270°

- **Section 56**: x = 14.56 m (on bentonite buffer, near end of heater H2 closest to tunnel end). The computed distributions of degree of saturation after dismantling should be along the radial segments RS1, RS2 and RS3 on dismantling section 56 (see Table B-22).

Table B-22. Definition of the radial segments on dismantling section 56 along which the distributions of degree of saturation after dismantling are requested.

Segment	Origin (x, y, z)	End (x, y, z)	Remarks
S56RS1	(14.56, 0.00, 0.00)	(14.56, 0.98, 0.57)	Angle with pos. y-axis = 30°
S56RS2	(14.56, 0.00, 0.00)	(14.56, −1.03, 0.48)	Angle with pos. y-axis = 155°
S56RS3	(14.46, 0.00, 0.00)	(14.56, 0.00, −1.14)	Angle with pos. y-axis = 270°

- **Section 61**: x = 16.87 m (on bentonite buffer, near to tunnel end). The computed distributions of degree of saturation after dismantling should be along the radial segments RS1, RS2 and RS3 on dismantling section 61 (see Table B-23).

Table B-23. Definition of the radial segments on dismantling section 61 along which the distributions of degree of saturation after dismantling are requested.

Segment	Origin (x, y, z)	End (x, y, z)	Remarks
S61RS1	(16.87, 0.00, 0.00)	(16.87, 0.00, 1.14)	Angle with pos. y-axis = 90°
S61RS2	(16.87, 0.00, 0.00)	(16.87, −0.93, −0.65)	Angle with pos. y-axis = 215°
S61RS3	(16.87, 0.00, 0.00)	(16.87, 0.98, −0.57)	Angle with pos. y-axis = 330°

If the model used is 3D, the computed distributions of degree of saturation after dismantling along radial segment RSi (i = 1, 2, 3) on dismantling section Sk (k = 43, 49, 56, 61) should be placed on the named range XXX_SR_SkRSi (a total of 3 × 4 = 12 named ranges). If the model used is 2D axisymmetric, the computed distributions of degree of saturation after dismantling along the radial segment RS on dismantling section Sk (k = 43, 49, 56, 61) should be placed on the named range XXX_SR_SkRS (a total of 4 named ranges). In both cases, the structure of the named ranges is indicated Figure B-24.

$r(P_1)$	$SR(P_1)$
$r(P_r)$	$SR(P_r)$
$r(P_n)$	$SR(P_{n,})$

Figure B-24. *Structure of the named ranges XXX_SR_SkRSi (k = 43, 49, 56, 61; i = 1, 2, 3) or XXX_SR_SkRS (k = 43, 49, 56, 61). Each named range has 2 columns and a convenient number n of rows (to be decided by the modelling team and may be different for each named range). In row r (r = 1, ..., n), column 1 contains the radial distance $r(P_r)$ (in m) of a point P_r on the considered radial segment, and column 2 contains the degree of saturation after dismantling $SR(P_r)$ (in %) at point P_r. Radial distances $r(P_r)$ (r = 1, ..., n) should increase with the row number r.*

Appendix C

CRIEPI Report

Central Research Institute of Electric Power Industry, Japan (CRIEPI)
Masataka Sawada

C1 Introduction

The FEBEX in situ test was adopted as Task 9 in Engineered Barrier System (EBS) Task Force. The objectives of the task are:

- Enhance understanding of the THM EBS behaviour during the transient phase.
- Study the state of the engineered barrier at two different stages of its evolution. Observation of degree of homogenization.
- Improve the computational capabilities and validate the performance of coupled THM formulations and associated codes.
- Develop (or enhance) constitutive relationships of the bentonite: thermal, hydraulic and mechanical.
- Compare the performance of different formulations, numerical codes and constitutive laws.
- Examine other issues of potential interest such as: gap between dummy heater and bentonite, gap between rock and bentonite, swelling through liner grids, closure of joints between bentonite blocks.

C1.1 Test to be modelled

The FEBEX (Full-scale Engineered Barriers Experiment in Crystalline Host Rock) “in situ” test was a full-scale test conducted during 18.4 years in the Grimsel URL (Switzerland) managed by NAGRA. It was based on the ENRESA AGP Granito (Deep Geological Disposal, Granite) reference concept. A 70.4 m long drift with a circular section 2.28 m in diameter was excavated in the Grimsel granite. In the last 17.4 m of the gallery, two electrical heaters of dimensions and weight equivalent to those considered in the ENRESA and NAGRA concepts were emplaced and in the remaining space compacted bentonite blocks were emplaced. The test zone was closed with a concrete plug.

The experiment was instrumented with sensors monitoring the thermo-hydro-mechanical processes taking place in the clay barrier and in the surrounding Grimsel granite. The experiment was in operation during 5.0 years. Thereafter, the outer heater was switched off and the outer half of the experiment was dismantled, whereby samples were taken from various points of the rock, the concrete and the bentonite buffer. During this first dismantling, the remaining half of the experiment, including the second heater, continued in operation. This remaining half of the experiment was in operation during 13.2 years more. Thereafter, the experiment was completely dismantled and, as before, samples from various points were taken.

C1.2 Stages of the task

The work to be performed in the Task has been divided into 2 stages:

- Stage 1: Operational period of the FEBEX experiment up to and including the dismantling of the first heater (5.0 years). The duration time should allow teams to become familiar with the problem and to develop/tune their formulations and codes for the FEBEX case.
- Stage 2: Operational period of the FEBEX experiment after the dismantling of the first heater up to and including the final dismantling of the test (13.2 years).

C1.3 Contents of the document

This documents contains features of the numerical program “LOSTUF” which CRIEPI has developed, a description of CRIEPI’s modelling and results in the simulation of base case for Stage 1b and 2 of the Task.

C2 Governing equations and formulation in LOSTUF

C2.1 T-H-M-coupled formulation

CRIEPI developed an in-house T-H-M-coupled analysis program, LOSTUF. The original formulation of coupled hydroelasticity was extended to a partially saturated thermohydroelastic medium. In this formulation, three phases were considered, namely solid, liquid, and gas. However, the gas pressure is assumed to be constant and equal to the atmospheric pressure throughout the porous medium. Vapour transport occurs only through the molecular diffusion driven by a gradient in the vapour concentration (Fick's law), while the advection of vapour with the bulk gas flow is neglected.

CRIEPI established the balance equations for the porous medium as a whole. CRIEPI adopted the compositional approach in order to establish the mass-balance equations. This approach involves balancing the species rather than the phases. We considered balance equations for the energy, mass of water, and momentum.

The final governing equations were obtained in terms of the displacement vector **u**, pore liquid pressure P_l, and absolute temperature T by substituting constitutive laws including Darcy's law, Fick's law, and Fourier's law, into the balance equations. The governing equation for water flow is obtained as

$$\begin{aligned} &\rho_l S_l \frac{\partial(\nabla\cdot\mathbf{u})}{\partial t} + \{\rho_{l0}\phi S_l\beta_{Pl} + (\rho_l-\rho_v)C_{lP} + \rho_l C_{vP}\}\frac{\partial P_l}{\partial t} \\ &\quad - (\rho_{l0}\phi S_l\beta_{Tl} - \rho_l C_{vT})\frac{\partial T}{\partial t} \\ &+\nabla\cdot\left\{\left(-\rho_l\frac{\mathbf{k}k_{rl}}{\mu_l} - \rho_l D_{Pv}\mathbf{I}\right)\nabla P_l\right\} + \nabla\cdot\{(-\rho_l D_{Tv}\mathbf{I})\nabla T\} = Q_B + \nabla\cdot\left(\rho_l\frac{\mathbf{k}k_{rl}}{\mu_l}\mathbf{g}\right) \end{aligned} \quad \text{(C-1)}$$

where ρ_l is the liquid water density, ρ_{l0} is the reference liquid water density, ρ_v is the vapor water density, S_l is the liquid water saturation, ε_v is the volumetric strain, and ϕ is the porosity. β_{Pl} is the compressibility of water, β_{Tl} is the linear thermal expansion coefficient of water, **k** is the intrinsic permeability tensor, k_{rl} is the relative permeability function, μ_l is the fluid viscosity, **I** is the identity tensor, Q_B is a source term of the water flow, and **g** is the gravity acceleration vector. The total strain tensor **ε** and volumetric strain ε_v are defined by **u** as $\boldsymbol{\varepsilon} = 0.5(\nabla\mathbf{u} + (\nabla\mathbf{u})^{tr})$, $\varepsilon_v = \nabla\cdot\mathbf{u}$, where tr denotes the transpose of the tensor. In the unsaturated state, the suction s is defined by the pore liquid pressure P_l and the pore gas pressure P_g as $s = P_g - P_l$, and $s = -P_l$ in LOSTUF because the pore gas pressure is assumed to be atmospheric pressure. C_{lP} is the liquid water capacity obtained from a water retention curve. C_{vP} and C_{vT} are defined as

$$C_{vP} = \frac{\phi S_g \rho_v}{\rho_l^2 R_v T} \quad \text{and} \quad \text{(C-2)}$$

$$C_{vT} = \frac{\phi S_g}{\rho_l}\frac{\partial\rho_{vS}}{\partial T}RH - \frac{\phi S_g P_l}{\rho_l^2 R_v T^2}, \quad \text{(C-3)}$$

respectively, where S_g is the gas saturation (= $1-S_l$), R_v is the specific gas constant of the water vapor (= 461.5 J/(kg K)), ρ_{vS} is the saturated vapor density which is dependent on the temperature, and RH is the relative humidity. D_{Pv} and D_{Tv} are the isothermal vapor-diffusion coefficient and thermal vapor-diffusion coefficient, respectively, and they are obtained by expanding the equation of Fick's law for vapor diffusion. We obtain the vapor flux $\mathbf{q}_{rv}$ from the following equation with the assumption of atmospheric gas pressure:

$$\mathbf{q}_{rv} = -D_v I\nabla\rho_v \quad \text{(C-4)}$$

where D_v is an effective molecular diffusion coefficient of water vapor, and it is defined as

$$D_v = \phi S_g \tau D_m \quad \text{(C-5)}$$

where D_m is the molecular diffusion coefficient for the vapor flow in air, and τ is the tortuosity factor. D_m can be evaluated as

$$D_m(\mathrm{m^2/s}) = 2.16\times10^{-5}(T/273)^{1.8} \quad \text{(C-6)}$$

The vapor density is given by the following equation:

$$\rho_v = \rho_{vS}(T)RH = \rho_{vS}\exp\left(\frac{P_l}{\rho_l R_v T}\right) \tag{C-7}$$

where ρ_{vS} is the temperature-dependent saturated vapor density. The vapor gradient in Equation (C-4) is further expanded using Equation (C-7), leading to the following expression for the vapor flux:

$$\mathbf{q}_{rv} = -\rho_l(D_{Pv}\mathbf{I}\nabla P_l + D_{Tv}\mathbf{I}\nabla T) \tag{C-8}$$

where

$$D_{Pv} = \frac{D_v\rho_v}{\rho_l^2 R_v T} \tag{C-9}$$

$$D_{Tv} = D_v\left(\frac{RH}{\rho_l}\frac{\partial\rho_{vS}}{\partial T} - \frac{\rho_v P_l}{\rho_l^2 R_v T^2}\right) \tag{C-10}$$

The governing equation for the heat transfer is obtained as

$$\begin{aligned}(1-\phi)3K_D\beta_{TD}T\frac{\partial(\nabla\cdot\mathbf{u})}{\partial t} + (\rho c)_m\frac{\partial T}{\partial t} - \nabla\cdot\left\{T\left(\frac{\beta_{Tl}}{\beta_{Pl}}\right)\frac{\mathbf{k}k_{rl}}{\mu_l} + \rho_l L D_{Pv}\mathbf{I}\right\}\nabla P_l \\ -\nabla\cdot(\lambda_m\mathbf{I}\nabla T) + (c_l\mathbf{q}_l)\cdot\nabla T = Q_{TB}\end{aligned} \tag{C-11}$$

where K_D is the bulk modulus of the solid phase, β_{TD} is the drained linear thermal-expansion coefficient of the medium, L is the latent heat of vaporization of water, and Q_{TB} is a heat-source term. The apparent macroscopic thermal conductivity of the medium λ_m and the heat capacity of the unit volume $(\rho c)_m$ are defined as

$$\lambda_m = S_l\lambda_{sat} + (1-S_l)\lambda_{dry} \quad \text{and} \tag{C-12}$$

$$(\rho c)_m = \phi S_l\rho_l c_l + (1-\phi)\rho_s c_s\,, \tag{C-13}$$

respectively, where λ_{sat} is the thermal conductivity of the saturated medium, λ_{dry} is the thermal conductivity of the dried medium, c_l is the specific heat of the liquid water, c_s is the specific heat of the solid phase, and ρ_s is the density of the solid phase. In Equation (C-11), the term for the heat convection caused by water flow is neglected.

For the stress equilibrium, the governing equation is as follows:

$$\begin{aligned}\nabla\cdot\left\{\mathbf{D}:\frac{\partial(\nabla\mathbf{u} + (\nabla\mathbf{u})^{tr})}{\partial t}\right\} + \nabla\cdot\left(-\mathbf{I}\chi\frac{\partial P_l}{\partial t}\right) + \nabla\cdot\left\{(-\mathbf{D}:\mathbf{I}\beta_{TD})\frac{\partial T}{\partial t}\right\} \\ = \frac{\partial}{\partial t}(\rho_m\mathbf{g}) + \mathbf{F}_B\end{aligned} \tag{C-14}$$

where **D** is the tangential stiffness tensor for the solid phase, and it can be defined by Young's modulus E and Poisson's ratio v for a linear isotropic elastic body. χ is Bishop's parameter for effective stress, and it is generally defined as a function of water saturation. However, in this formulation, $\chi = 1$ for saturated media and $\chi = 0$ for unsaturated media. The swelling of the bentonite is modeled not by a stress-strain relationship but by the equivalent nodal force, as mentioned in Sawada et al. (2017). ρ_m is the density of the mixture and $\mathbf{F}_B$ is an external force vector.

The governing equations (C-1), (C-11), and (C-14) were discretized using a standard Galerkin finite-element solution approach, and the time integration was carried out using a finite-difference scheme.

C2.2 Bentonite swelling model

The swelling of bentonite is modeled not by stress-strain relationship but by the nodal force equivalent to the maximum swelling strain in LOSTUF. Figure C-1(a) shows the calculation flow employed to model bentonite swelling in LOSTUF. In the swelling calculation we use a relationship between mean stress and maximum swelling strain. The maximum swelling pressure (constant volume swelling pressure) of bentonite is expressed as a function of the dry density, effective clay density, or porosity. We can obtain the relationship between the applied mean stress σ_m and the maximum swelling strain at saturation ε_{smax} from the function as follows.

$$\sigma_m = f(\varepsilon_{smax}) \tag{C-15}$$

Figure C-1(b) shows this relationship. It was assumed that swelling occurs with degrease of suction (increase of pore pressure) during the water infiltration process. The maximum swelling strain at an unsaturated state ω_{smax} is calculated by the following equation.

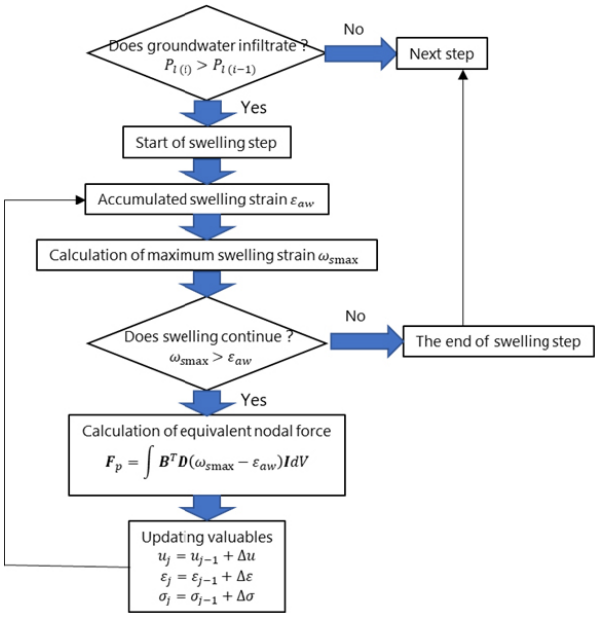

(a) Flow of swelling calculation

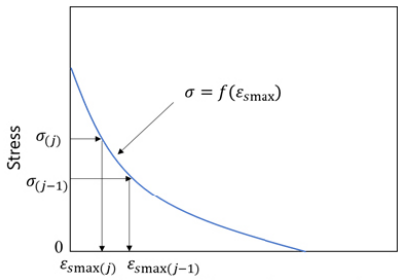

Maximum swelling strain in unsaturated state ω_{smax}

$$\omega_{smax}(P_l) = \varepsilon_{smax}\left(\frac{|P_l - P_{l0}|}{|P_{l0}|}\right)^l$$

($l = 1$ in the following calculation)

(b) Calculation of maximum swelling strain

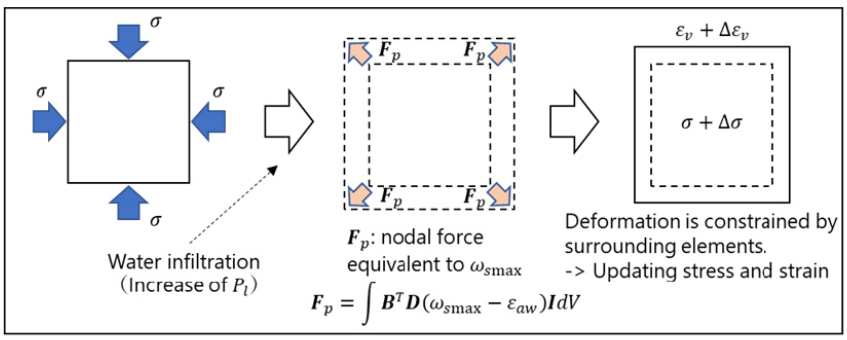

This process is repeated until the accumulated swelling strain ε_{aw} reaches the maximum swelling strain $\omega_{smax}(P_l)$.

(c) Schematic of element behavior during swelling calculation

Figure C-1. *Swelling-calculation method.*

$$\omega_{\mathrm{smax}} = \varepsilon_{\mathrm{smax}} \left(\frac{|P_l - P_{l0}|}{|P_{l0}|} \right)^l \tag{C-16}$$

where P_l is the pore pressure, P_{l0} is the initial pore pressure and l is a parameter (l = 1 in the following calculation). When pore pressure increases in an element, calculation enter the swelling step and a nodal force that is equivalent to the maximum swelling strain, with the exception of the accumulated swelling strain, is applied (see Figure C-1 (a)). The nodal force vector $\mathbf{F}_p$ is obtained from the following equation.

$$\mathbf{F}_p = \int \mathbf{B}^T \mathbf{D}(\omega_{smax} - \varepsilon_{aw})\mathbf{I} dV \tag{C-17}$$

where **B** is the strain-displacement operator matrix and ε_{aw} is the accumulated swelling strain.

Since the swelling deformation is constrained by the surrounding elements, both of displacements and stresses are updated (see Figure C-1(c)). Then, the maximum swelling strain is re-calculated under the updated mean stress (see Figure C-1(b)). The new evaluation generally produces smaller values. This loop is repeated until the updated maximum swelling strain is smaller than the accumulated swelling strain.

C3 Modelling

C3.1 Basic assumptions, geometry, and boundary conditions

C3.1.1 Basic assumptions and geometry

A 2-D axisymmetric longitudinal section has been analysed, in which most geometrical features of the in situ test are represented. The geometry also takes into account the presence of the access drift and the concrete plug. No gap between liner and buffer has been considered. The outer boundary of the model is placed at a distance of 50 m from the tunnel axis, the drift end and the concrete plug (see Figure C-2). The size of analysis domain is 120 m in the axial direction and 50 m in the radial direction.

Figure C-3 shows finite element mesh. It consists of 7 017 nodes and 6 940 linear quadrilateral elements. Figure C-4 focuses on the test area. Lamprophyre and fracture zone are considered as high-permeability zone in host rock. The number of elements across the bentonite barrier is 6 in the heater section, and 10 in the no-heater section.

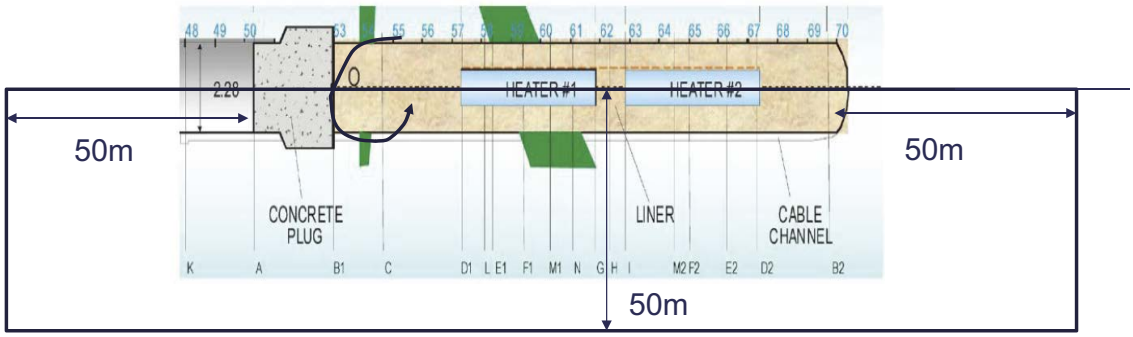

Figure C-2. *Analysis domain.*

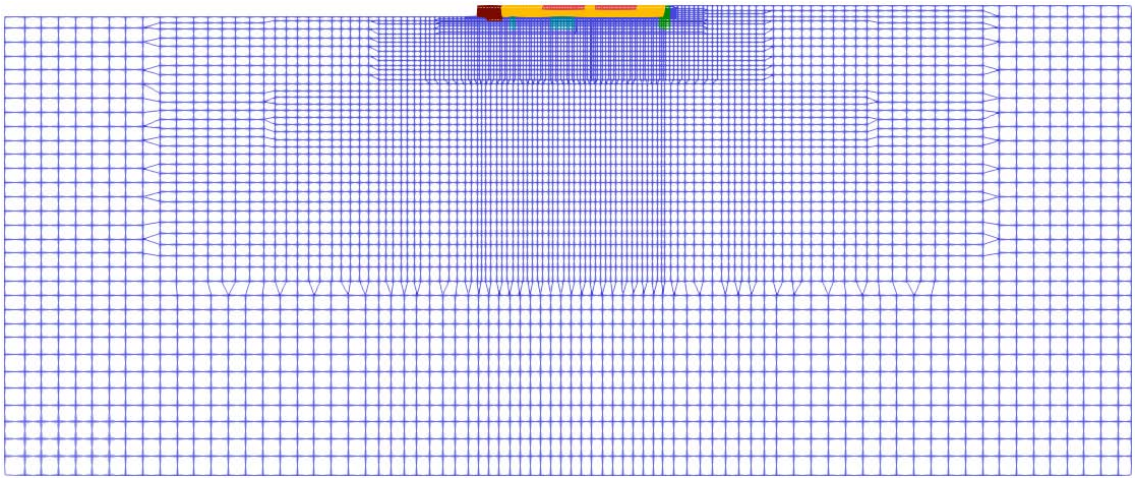

Figure C-3. *Finite element mesh.*

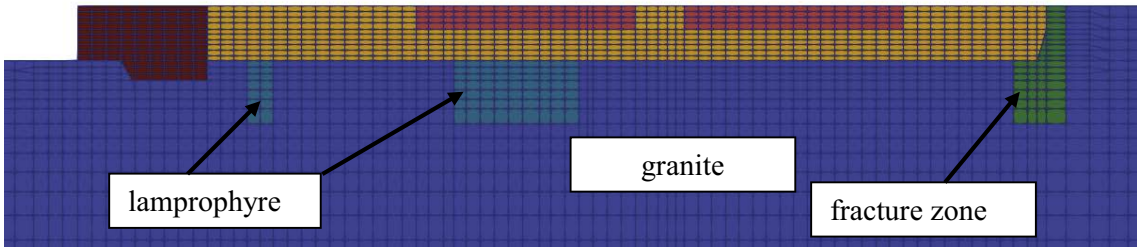

Figure C-4. *Finite element mesh around the test area.*

C3.1.2 Boundary conditions and initial conditions for host rock

The thermal, hydraulic and mechanical boundary conditions prescribed at outer boundaries are:

- Temperature, T = 12 °C
- Water pressure, P = 1.3 MPa
- Displacement, Roller constraint

Water pressure on outer boundaries was determined in reference with Börgesson et al. (2004). Water pressure of 0 MPa and temperature of 12 °C were prescribed at drift surface.

The initial thermal, hydraulic and mechanical conditions are shown in Table C-1. We are not focusing on rock stress because the value does not affect the numerical results. We considered that average initial stress of the bentonite was 20 kPa, and applied it to the entire analysis domain. Initial conditions are also summarized in Section C5.

Table C-1. Initial conditions of host rock.

	Units	Values
Temperature	°C	12
Water pressure	MPa	1.3
Rock stress	kPa	20

C3.2 Material properties

Material properties were mainly determined by the average values written in the specification (Annex A). Key parameters are also summarized in Appendix.

C3.2.3 Host rock

Table C-2 shows the parameter values for host rock. They were determined mainly in reference with the specification. Some parameter values of lamprophyre were assumed to be equal to those of granite. The permeability of lamprophyre and fracture zone was assumed to be one and two order larger than that of granite, respectively. Fracture zone was assumed to have one order larger porosity than granite.

Table C-2. Parameters of host rock.

Parameter	Units	Granite	Lamprophyre	Fracture zone
Density	kg/m^3	2660	2909	2909
Porosity	vol%	1.6	1.6	16
Young´s modulus	GPa	53.3	42.4	42.4
Poisson´s ratio	-	0.37	0.37	0.37
Coef. linear thermal expansion	K^{-1}	8.0×10^{-6}	8.0×10^{-6}	8.0×10^{-6}
Therm. conductivity (dry)	W/mK	2.58	2.21	2.21
Therm. conductivity (wet)	W/mK	3.34	2.71	2.71
Specific heat	J/kgK	920	920	920
Permeability	m/s	4.0×10^{-12}	4.0×10^{-11}	4.0×10^{-10}

For retention curve and relative permeability, the following equations are used (specification). Figure C-5 shows the retention curve and the relative permeability of host rock.

$$s = 1.74(S_r^{-1.68} - 1)^{0.405} \quad \text{(C-18)}$$

$$k_r = S_r^{0.5}[1 - (1 - S_r^{1.68})^{0.595}]^2 \quad \text{(C-19)}$$

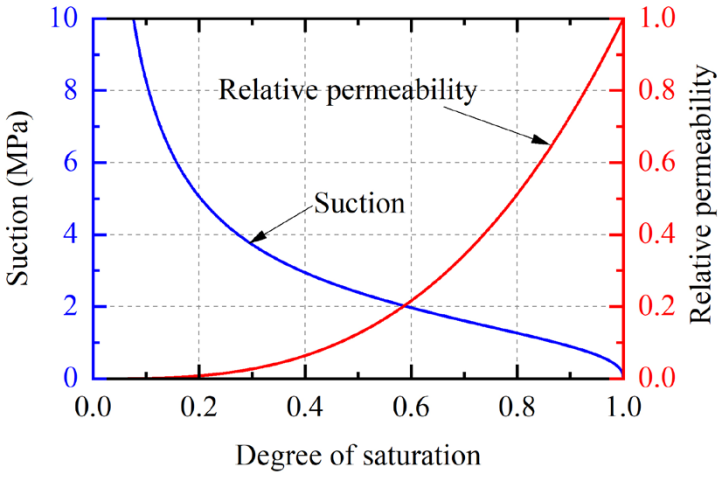

Figure C-5. *Retention curve and relative permeability for host rock.*

C3.2.2 Bentonite

Table C-3 shows the material parameters and initial valuables of bentonite. The values of Young's modulus and Poisson's ratio were guessed for saturated bentonite. The other values were determined from the specification. The density of solid phase was 2 630 kg/m^3 which is derived from the porosity and the dry density.

Table C-3. Material parameters and initial valuables of bentonite.

Parameter	Units	Bentonite
Density	kg/m^3	1 600
Porosity	-	0.39
Suction	MPa	135
Relative humidity	%	35.8
Degree of saturation	%	47.7
Intrinsic permeability	m/s	2.0×10^{-21}
Hydrolic conductivity	m/s	1.59×10^{-14}
Relative permeability	-	S_r^3
Thermal conductivity	W/mK	0.677
Swelling pressure	MPa	7.82
Young´s modulus	MPa	20
Poisson´s ratio	-	0.2
Initial stress	kPa	20
Tortuosity	-	0.8

For retention curve, van Genuchten formulation is used.

$$S_r = S_{r0} + (S_{rmax} - S_{r0})\left[1 + \left(\frac{s}{P_0}\right)^{\frac{1}{1-\lambda}}\right]^{-\lambda} \quad \text{(C-20)}$$

where P_0 = 30 MPa, λ = 0.32, S_{r0} = 0.10, and S_{rmax} = 1.00 were used in reference with ENRESA (2000). Figure C-6 shows the retention curve and the relative permeability of the bentonite. Initial suction was 135 MPa.

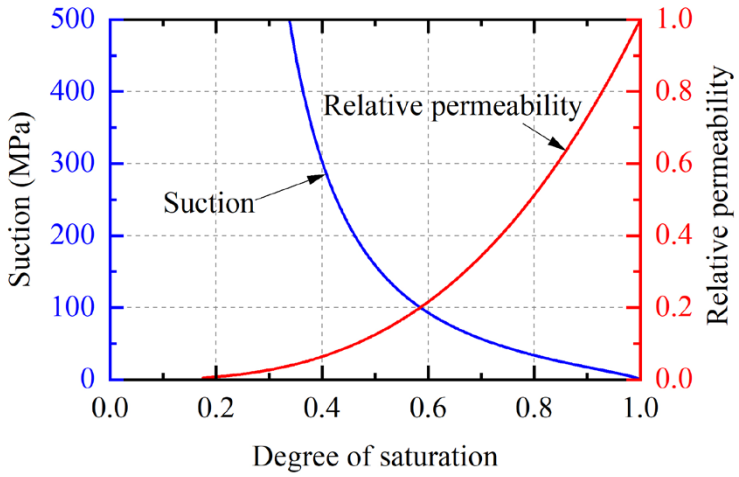

Figure C-6. *Retention curve and relative permeability for bentonite.*

Specific heat of solid phase was defined as a function of temperature (specification).

$$c_s = 1.38T + 732.5 \tag{C-21}$$

Thermal conductivity was set by the following equation.

$$\lambda = A_2 + \frac{A_1 - A_2}{1 + e^{(S_r - x_0)/d_x}} \tag{C-22}$$

where A_1 = 0.57, A_2 = 1.28, x_0 = 0.65, and d_x = 0.10 were used in reference with ENRESA (2000). Figure C-7 shows the thermal conductivity of the bentonite.

Coefficient of linear thermal expansion was determined from the first heating paths as the following function of temperature (specification).

$$\frac{\Delta\varepsilon_z}{\Delta T} = -0.118 \times 10^{-4} + 6.5 \times 10^{-6} T \tag{C-23}$$

Effective molecular diffusion coefficient of water vapour was defined as a function of void ratio and degree of saturation (specification).

$$K_s = 3.164 \times 10^{-6} [e(1 - S_r)]^{4.3} \tag{C-24}$$

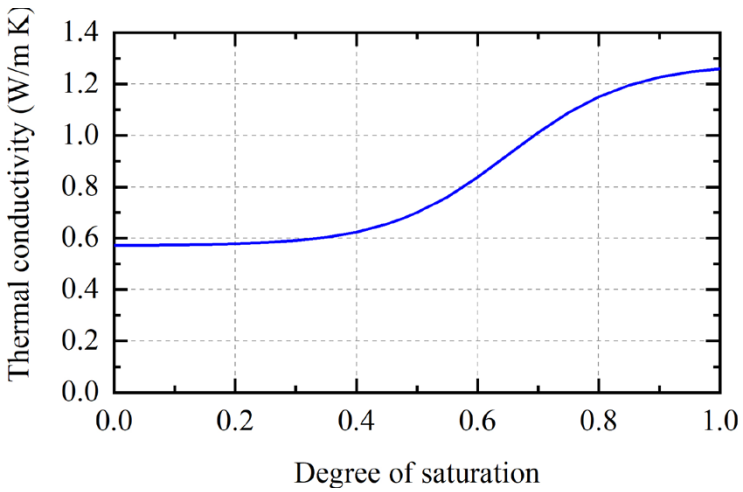

Figure C-7. *Thermal conductivity of the bentonite.*

Finally, the relationship between applied stress and maximum swelling strain in Figure C-2 and Equation (C-15) was derived from the following laboratory-test-based equation (Alonso et al. 2005).

$$P_s = \exp\left(6.77\rho_d - 9.07\right) \quad \text{(C-25)}$$

where P_s is the swelling pressure. Figure C-8 shows the derived swelling pressure – strain relationship. When the maximum swelling pressure in Figure C-8 was derived from Equation (C-25), the dry density of 1 643 kg/m^3 was used. This dry density was obtained from void ratio of 0.6429 and the density of solid phase of 2 700 kg/m^3, and different from the value 1 600 kg/m^3 used in other part.

C3.2.3 Concrete

Table C-4 shows the parameters of the concrete plug. The density of the concrete plug was determined in reference with the specification. The other parameter values are generally used for concrete. The concrete plug was assumed to be impermeable in the simulation.

Table C-4. Parameters of the concrete plug.

Parameter	Units	Concrete
Density	kg/m^3	2 394
Young´s modulus	GPa	30
Poisson´s ratio	-	0.2
Coef. linear thermal expansion	-	1.0×10^{-5}
Specific heat	J/kgK	880
Thermal conductivity	W/mK	1.6

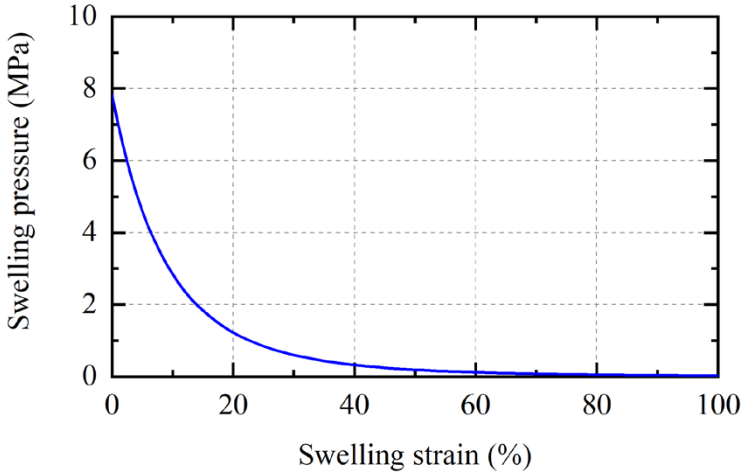

Figure C-8. *Swelling pressure – strain relationship.*

C3.2.4 Canister

Table C-5 shows parameters of the canister. These parameters are determined in reference with Börgesson et al. (2004).

Table C-5. Parameters of the canister.

Parameter	Units	Concrete
Density	kg/m^3	7 850
Young´s modulus	GPa	200
Poisson´s ratio	-	0.3
Coef. linear thermal expansion	-	1.15×10^{-5}
Specific heat	J/kgK	460
Thermal conductivity	W/mK	450

C3.3 Modelling of the dismantling

In the FEBEX in situ test, the first heater was switched off after 5 years of operation, the concrete plug was demolished and the first 7.865 m of the test area were dismantled. The corresponding bentonite blocks and the first heater were extracted, a 1 m long dummy steel cylinder was emplaced to fill the void left by the extracted heater and a new 2.98 m thick shotcrete plug was emplaced in two stages.

About 13 years after the first partial dismantling, heater #2 was switched off. After cooling down of heater #2, the concrete plug was demolished, the steel liner and the heater #2 were removed, and the bentonite blocks were completely excavated.

Table C-6 shows the important dates during the first dismantling of the FEBEX in situ test. Figure C-9 shows the modelling of the first dismantling. Figure C-10 shows the process of the second dismantling. Only excavation of the shotcrete plug was modelled for the second dismantling.

Table C-6. Important dates during the first dismantling.

Date	Event
28.02.2002	Heater #1 switch off
02.04.2002	Start of dismantling works
08.04.2002	Start demolition of concrete plug
28.05.2002	End demolition of concrete plug
19.06.2002	Heater #1 extraction
17.07.2002	End dismantling bentonite
23.07.2002	End sampling
25.07.2002	End shotcrete stage #1
27.06.2003	End shotcrete stage #2

Time = 1867 days

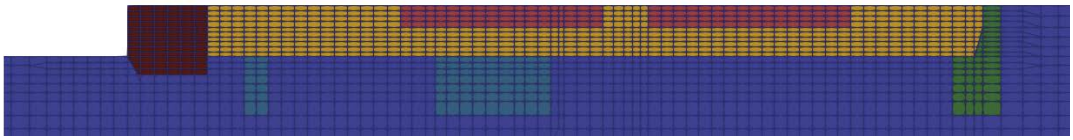

(1) Excavation of the concrete plug #1 (in the step after 1866 days)

Time = 1887 days

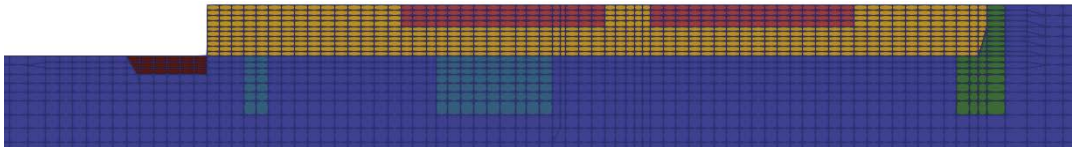

(2) Excavation of the concrete plug #2 (in the step after 1886 days)

Time = 1917 days

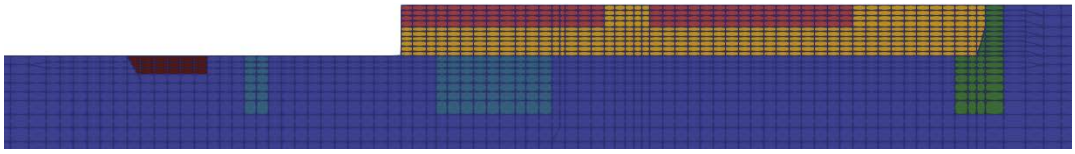

(3) Excavation of bentonite (in the step after 1916 days)

Time = 1928 days

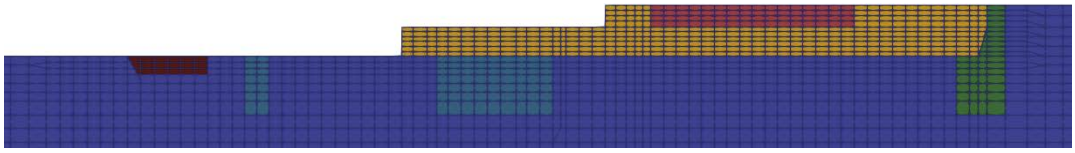

(4) Extraction of the first heater (in the step after 1927 days)

Time = 1940 days

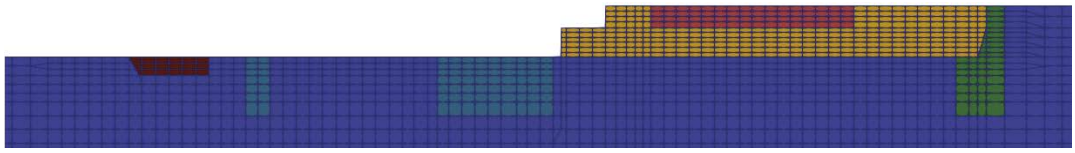

(5) Excavation of the bentonite (in the step after 1938 days)

Time = 1968 days

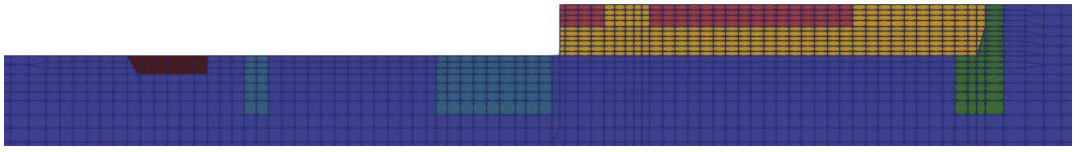

(6) Emplacement of the dummy heater (in the step after 1966 days)

Time = 1974 days

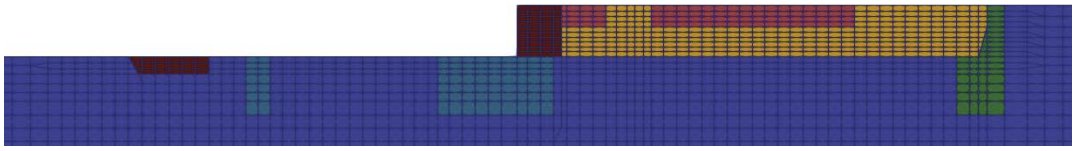

(7) Emplacement of shotcrete #1 (in the step after 1972 days)

Time = 1976 days

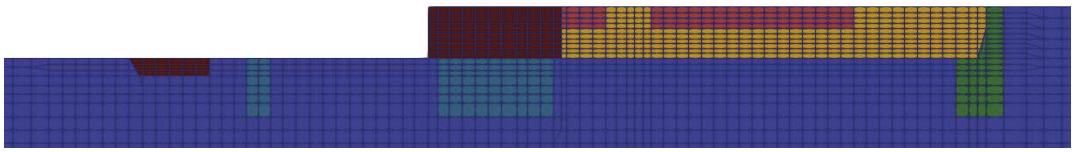

(8) Emplacement of shotcrete #2 (in the step after 1974 days)

Figure C-9. *Modelling of the first dismantling.*

Time = 6613 days

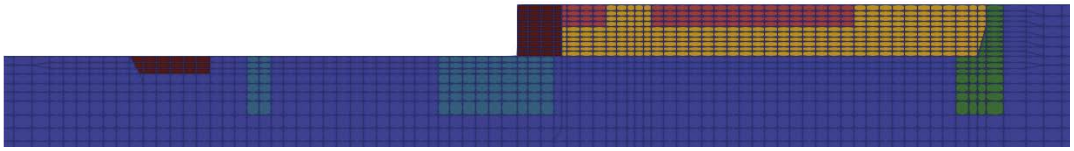

(1) Excavation of shotcrete plug #2 (in thestep after 6613 days)

Time = 6633 days

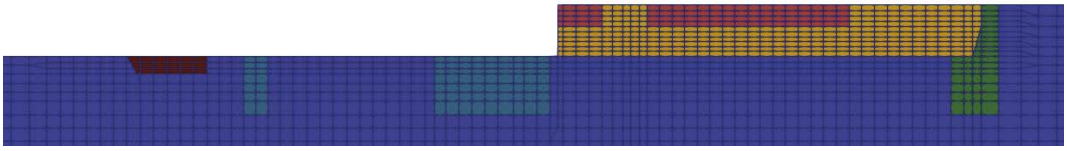

(2) Excavation of shotcrete plug #1 (in the step after 6633 days)

Figure C-10. *Modelling of the second dismantling.*

At newly emplaced elements, the initial temperature was 12 °C, the initial suction is 135 MPa, and the initial stress is zero. The front end of the test body was kept at 12 °C, atmospheric pressure, and traction free.

C4 Results

C4.1 Groundwater analysis

At first, groundwater analysis was conducted in order to determine initial water pressure distribution of T-H-M simulation. The drift was open from the start of calculation, that is, excavation process was not considered. Initial and boundary water pressure was 1.3 MPa. It took almost one year from the start of drift excavation to the end of installation. Figure C-11 shows the distribution of water pressure around the test area after one year. It was used as initial water pressure in the following T-H-M simulation.

Figure C-12 shows the calculated and measured water inflow to the drift. Calculated water inflow is less than measured inflow at lamprophyre and drift end fracture, but is in good agreement with inflow at other granite sections.

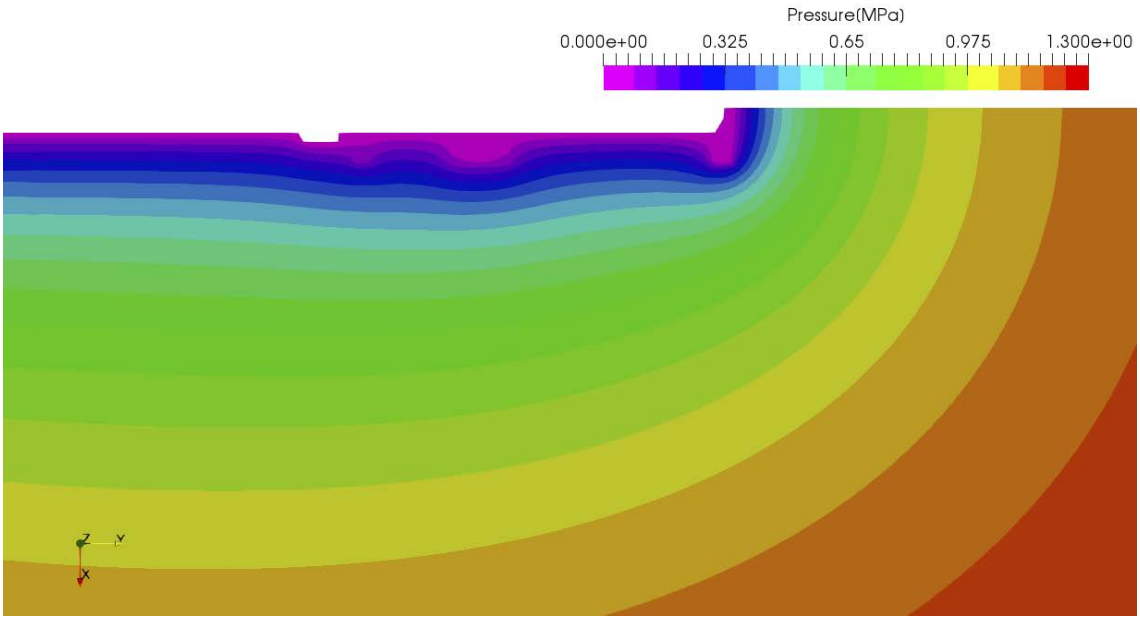

Figure C-11. *Water pressure distribution after one year.*

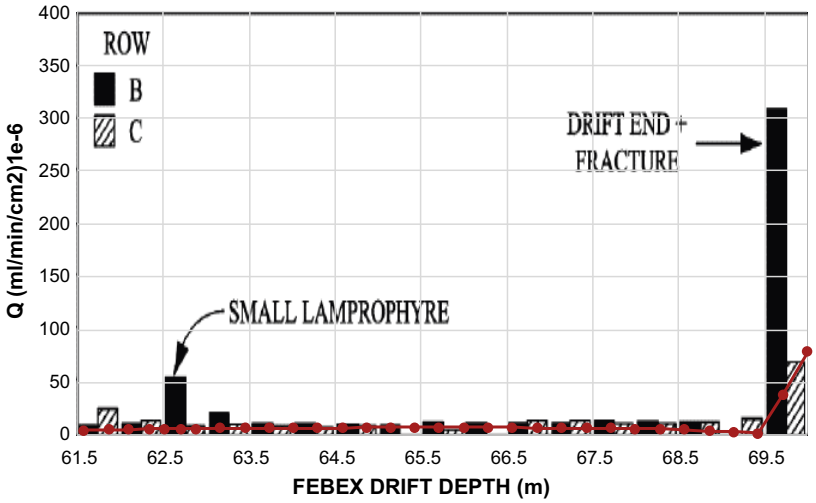

Figure C-12. *Calculated and measured water inflow to the drift: red plot is calculated inflow, bar graphs are measured inflow.*

C4.2 T-H-M simulation – results for Stage 1b

In this subsection, graphs of required results are shown. A stage before the start of heating (135 days) was included in the analysis.

Evolution of heating power

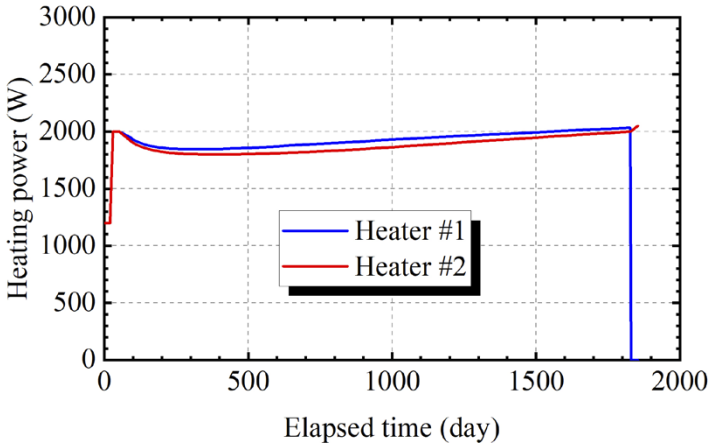

Figure C-13. *Evolution of power of heaters 1 and 2.*

Distributions and evolutions of relative humidity

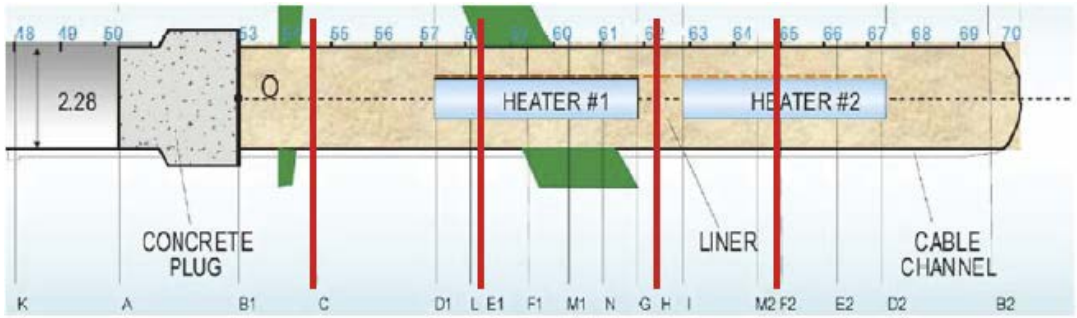

Figure C-14. *Required results: distributions and evolutions of relative humidity.*

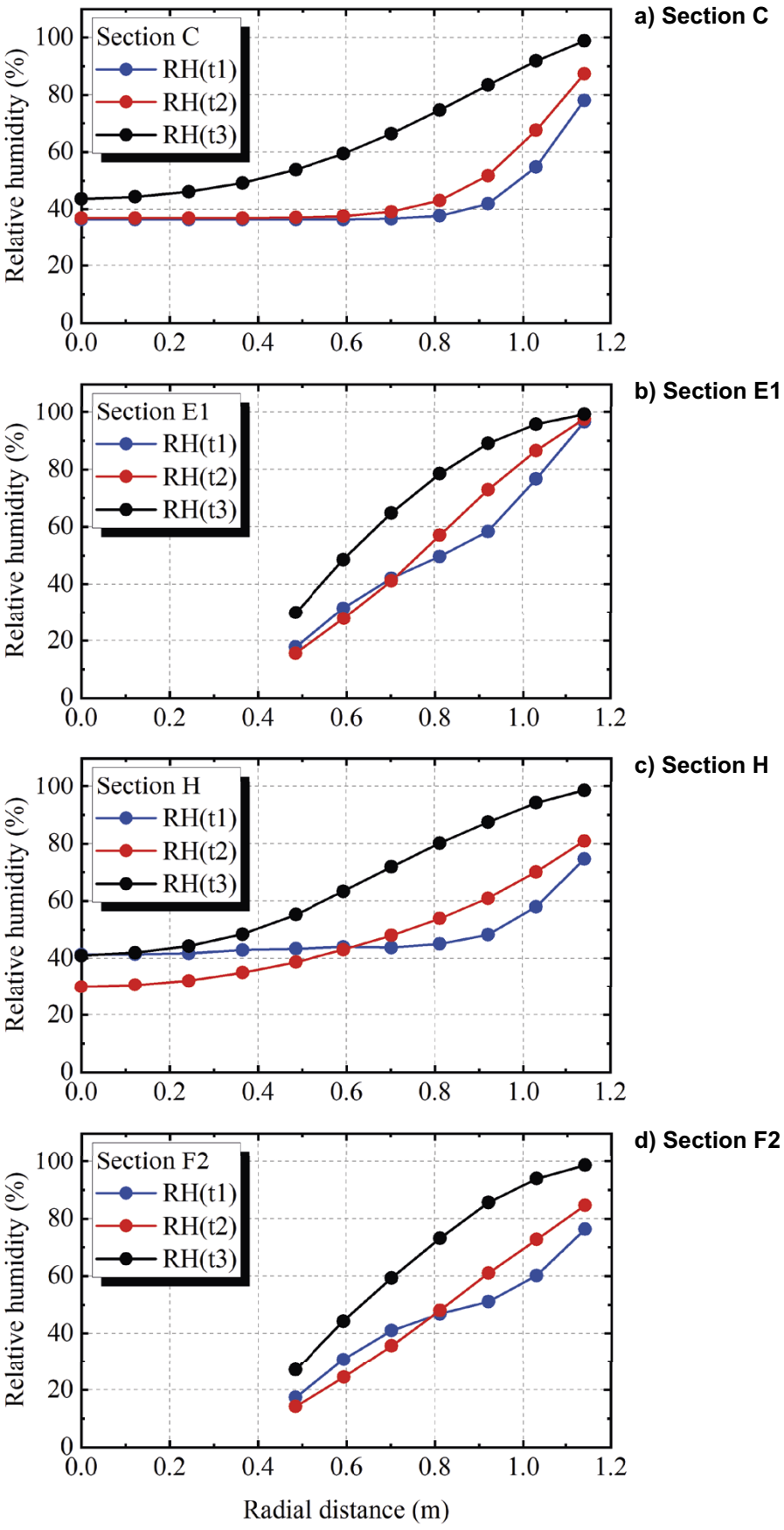

Figure C-15. *Distributions of relative humidity on section C, E1, H, F2 at times t1 = 90 days, t2 = 300 days and t3 = 1 800 days.*

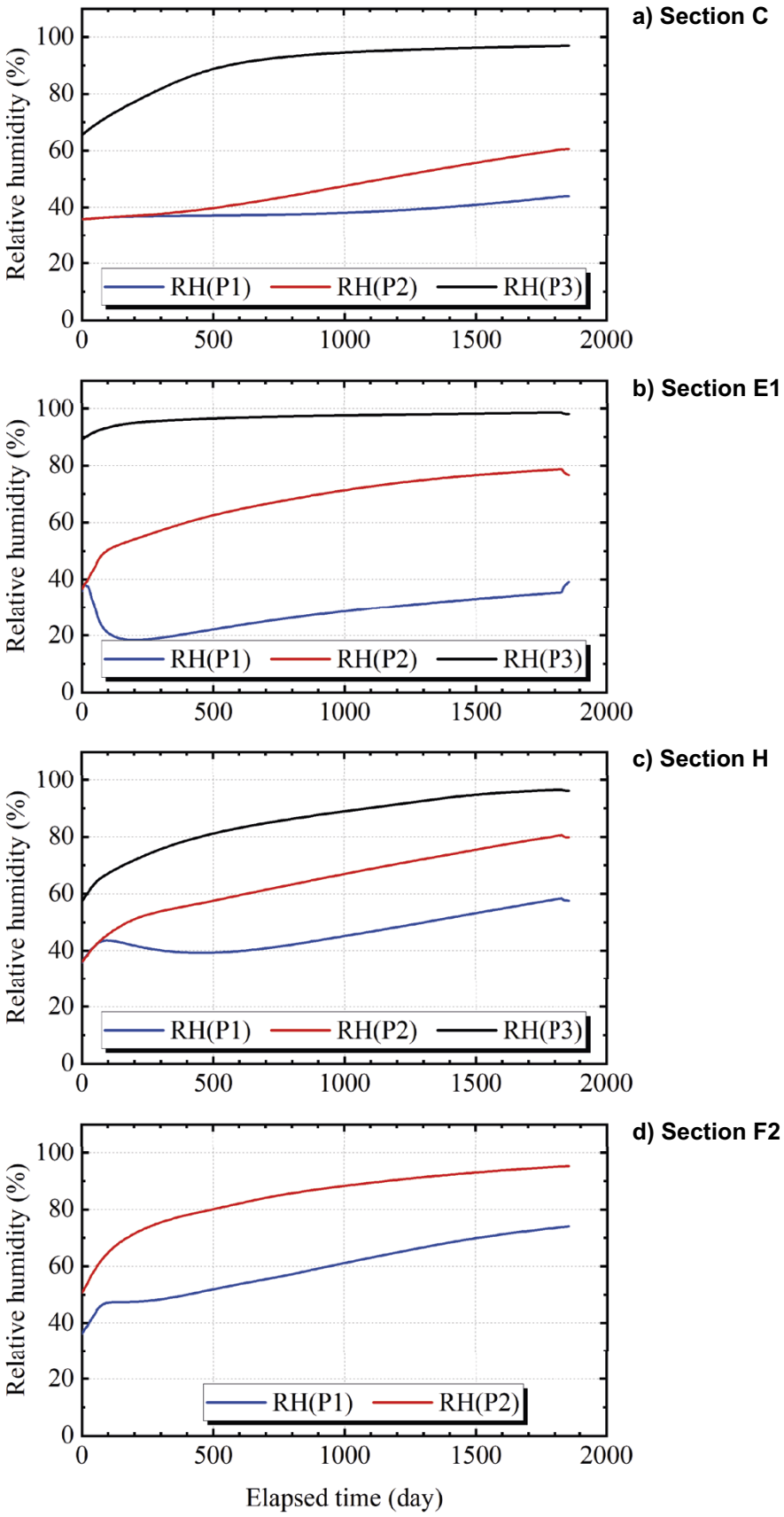

Figure C-16. *Evolutions of relative humidity on sections C, E1, H, and F2.*

Distributions and evolutions of temperature

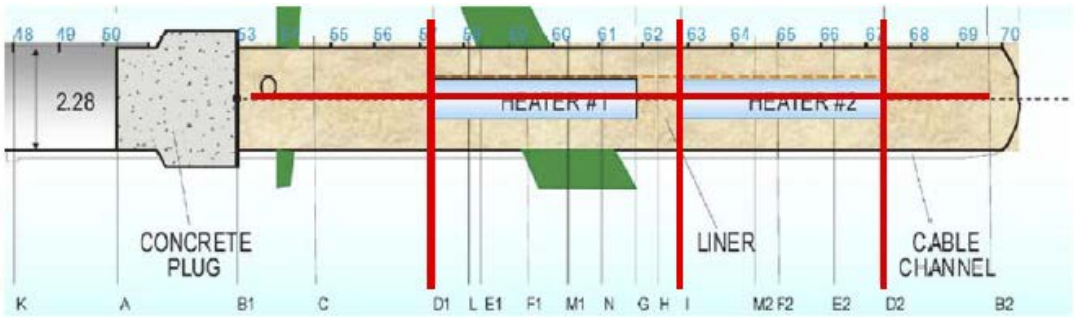

Figure C-17. *Required results: distributions and evolutions of temperature.*

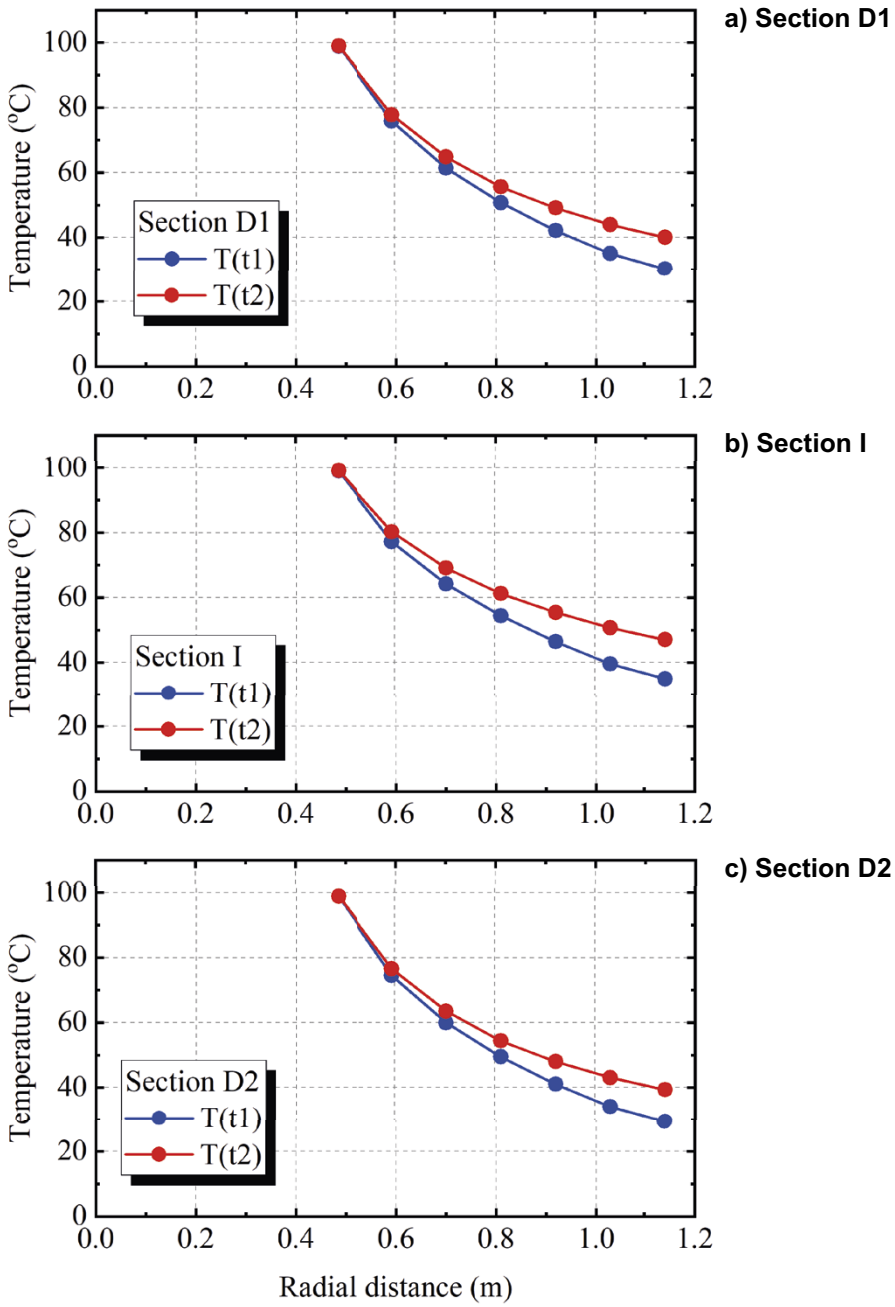

Figure C-18. *Distribution of temperature on sections D1, I, and D2 on times t1 = 90 days and t2 = 1 800 days.*

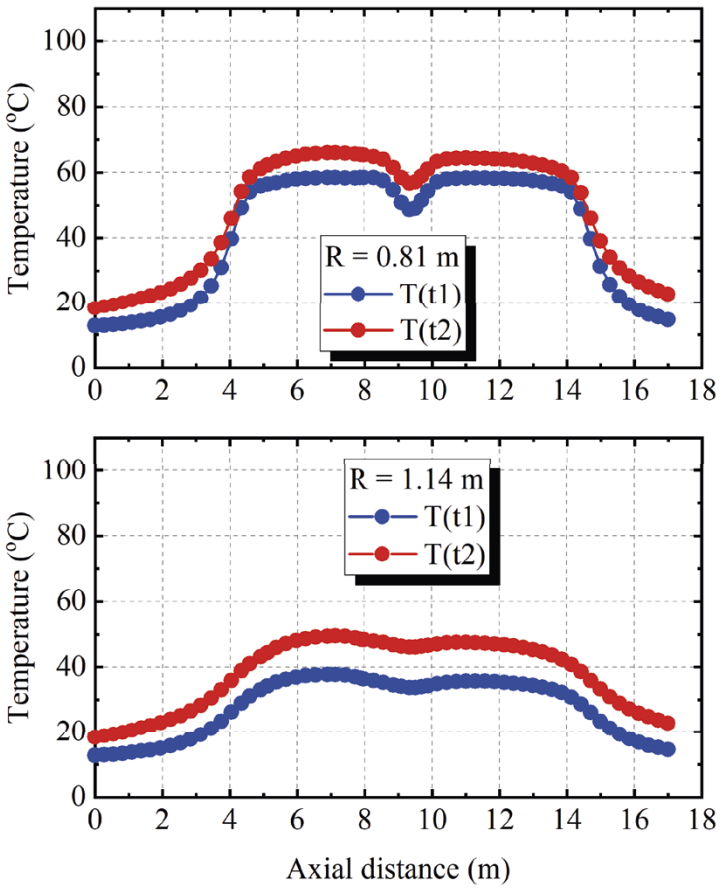

Figure C-19. *Distribution of temperature on axial section 1 and 2 on times t1 = 90 days and t2 = 1 800 days.*

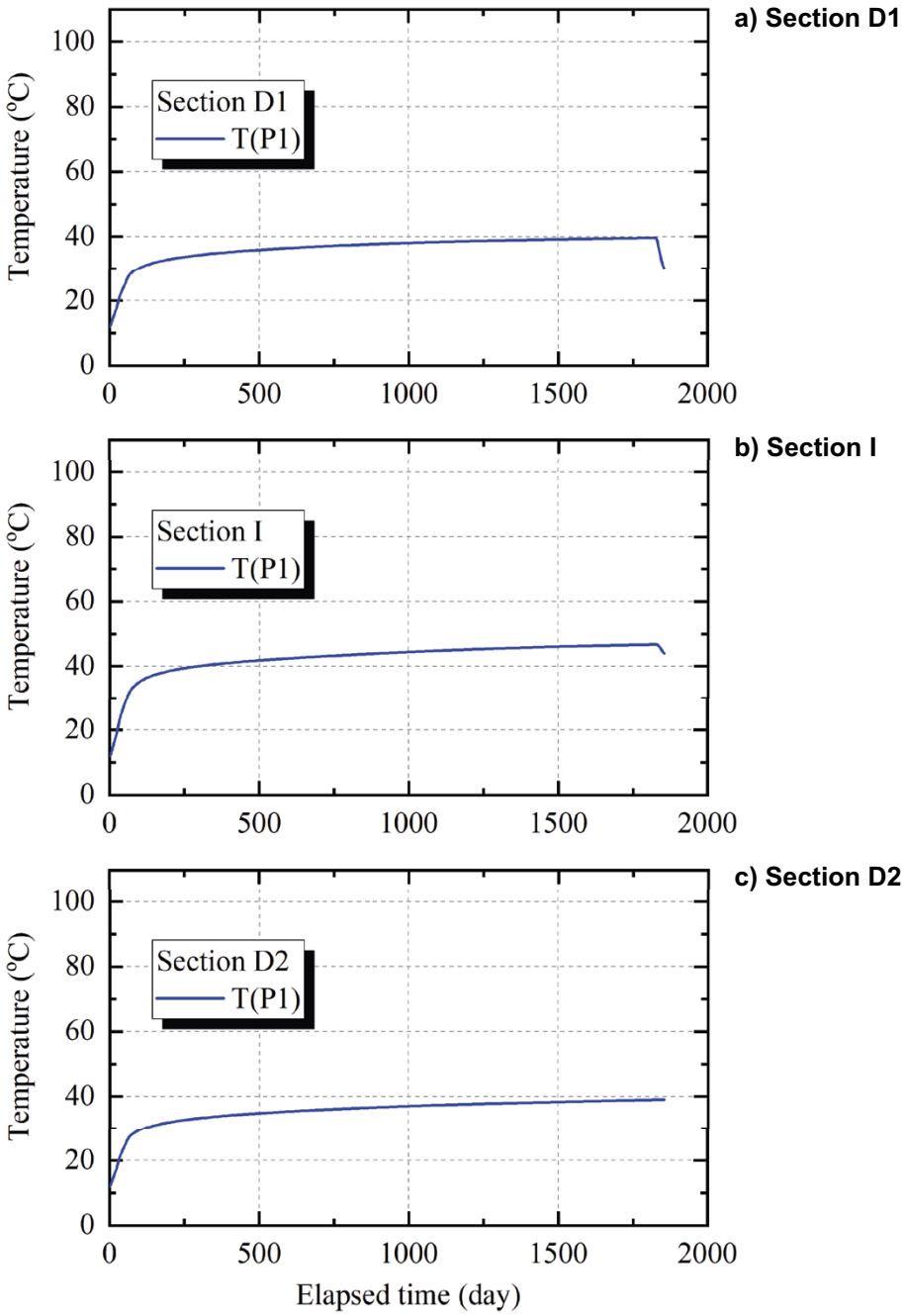

Figure C-20. *Evolution of temperature on sections D1, I, and D2.*

Evolutions of total stresses

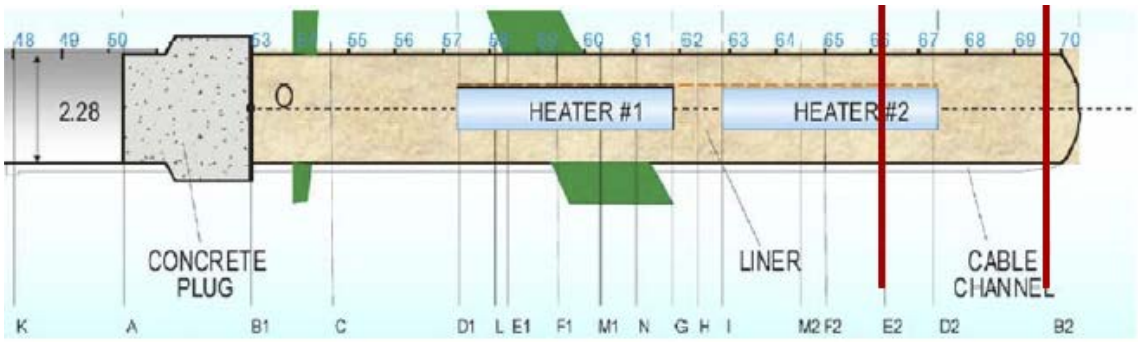

Figure C-21. *Required results: evolutions of total stresses.*

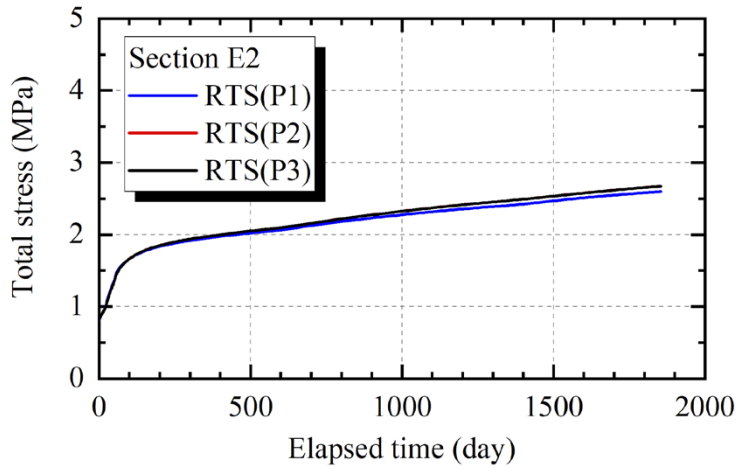

Figure C-22. *Evolution of total stresses on section E2.*

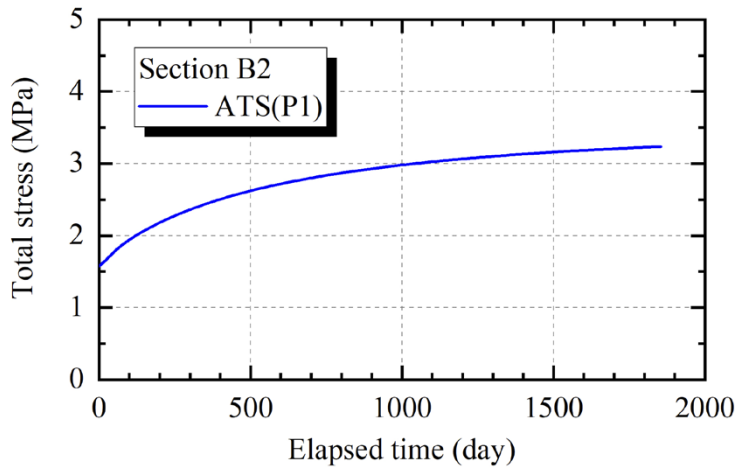

Figure C-23. *Evolution of total stress on section B2 (axial stress).*

Distributions of dry density, water content and degree of saturation after the dismantling

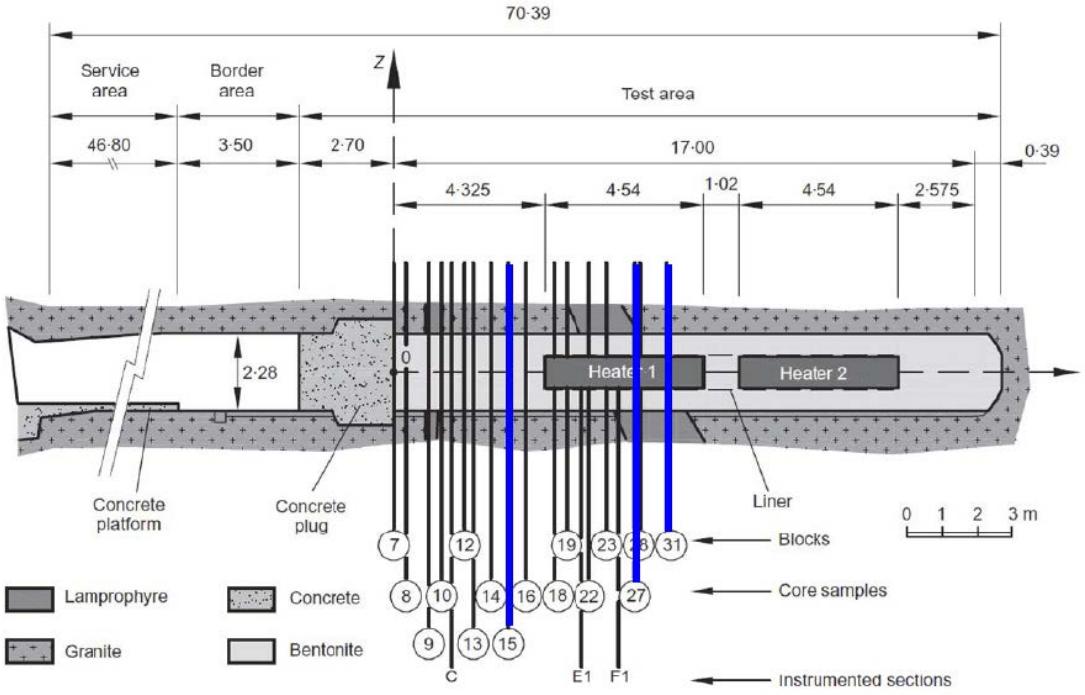

Figure C-24. *Required results: distributions of dry density, water content and degree of saturation.*

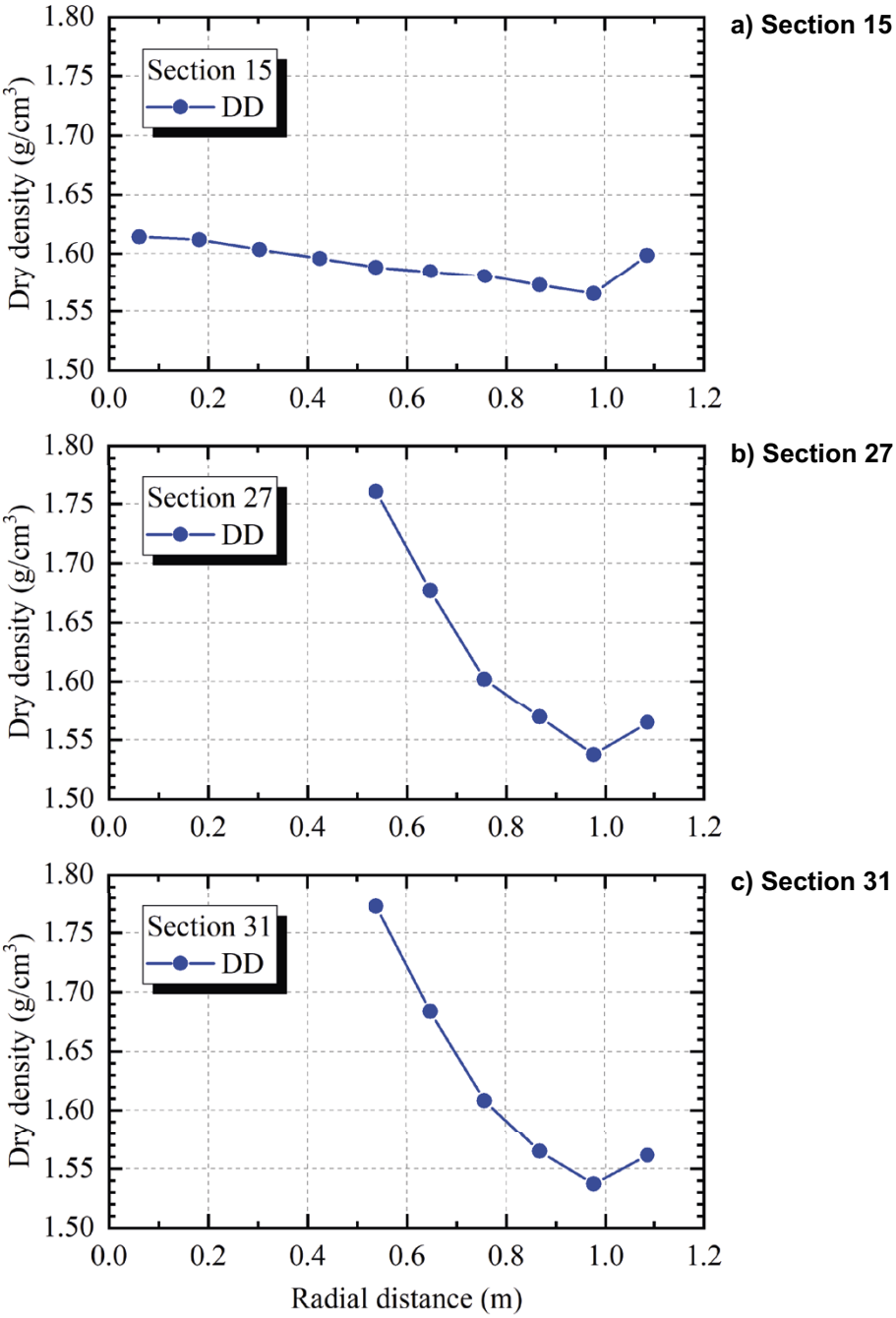

Figure C-25. *Distributions of dry density on sections 15, 27 and 31.*

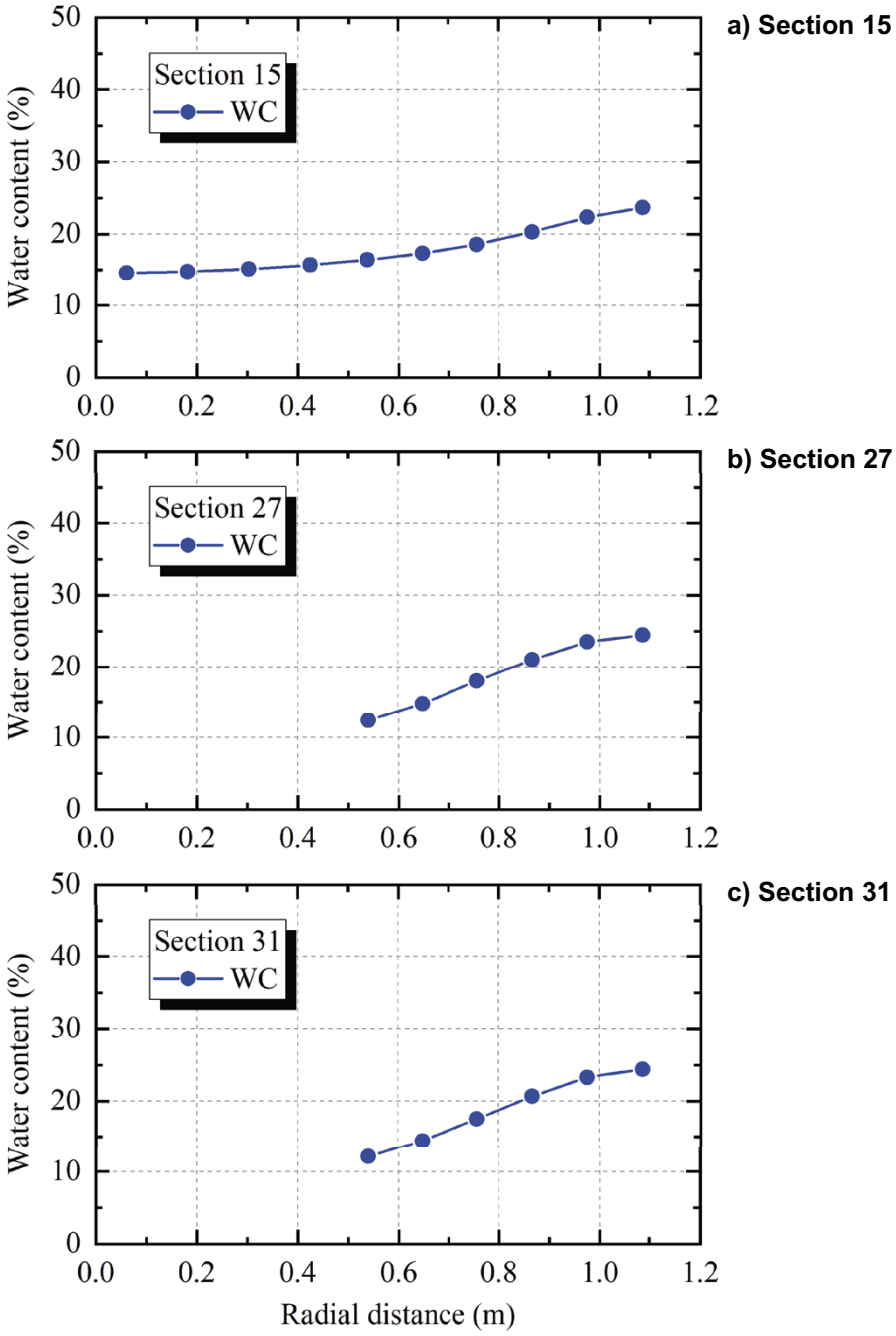

Figure C-26. *Distributions of water content on sections 15, 27 and 31.*

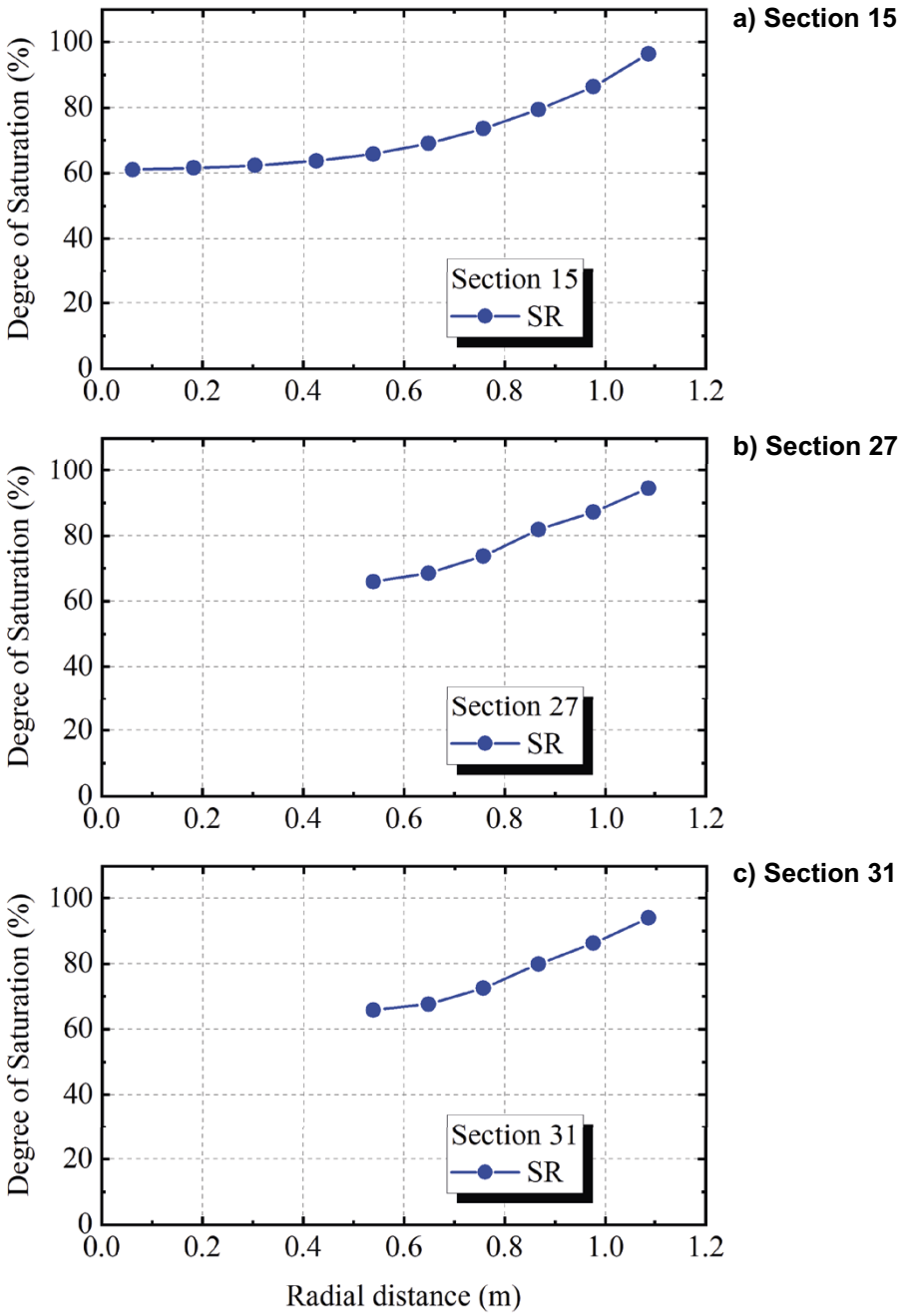

Figure C-27. *Distributions of saturation rate on sections 15, 27 and 31.*

C4.3 T-H-M simulation – results for Stage 2

In this subsection, graphs of required results are shown.

Evolution after first dismantling of heating power

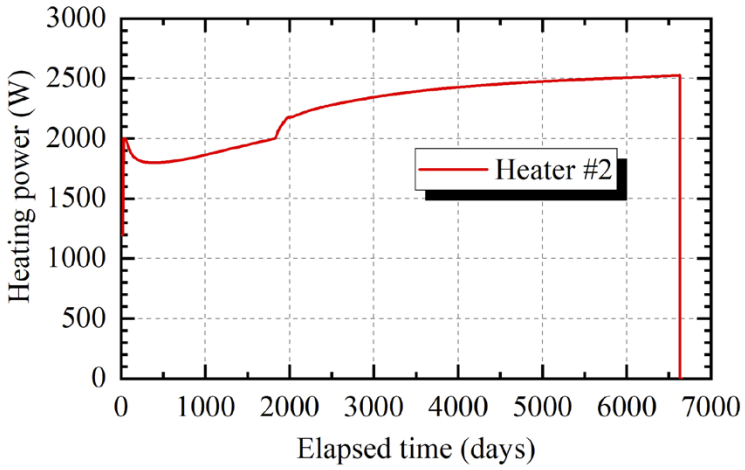

Figure C-28. *Evolution of power of heater 2.*

Distributions and evolutions after first dismantling of relative humidity

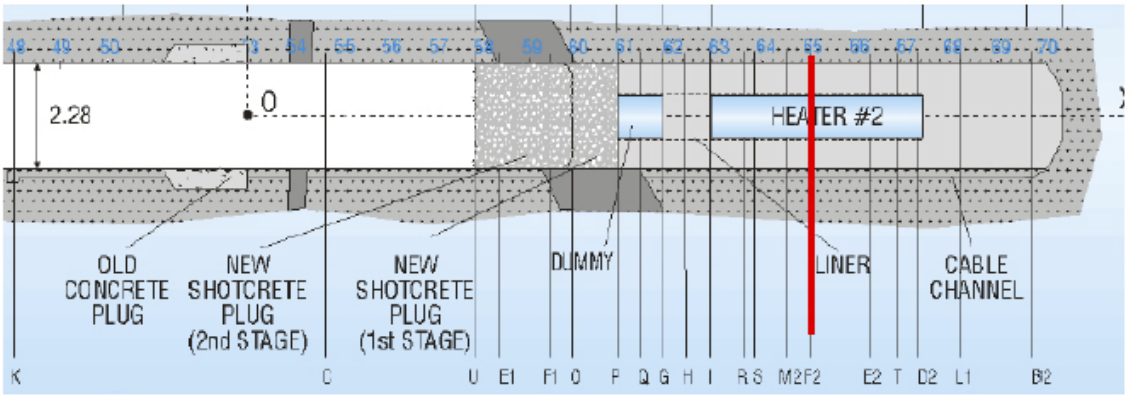

Figure C-29. *Requested results distributions and evolutions of relative humidity.*

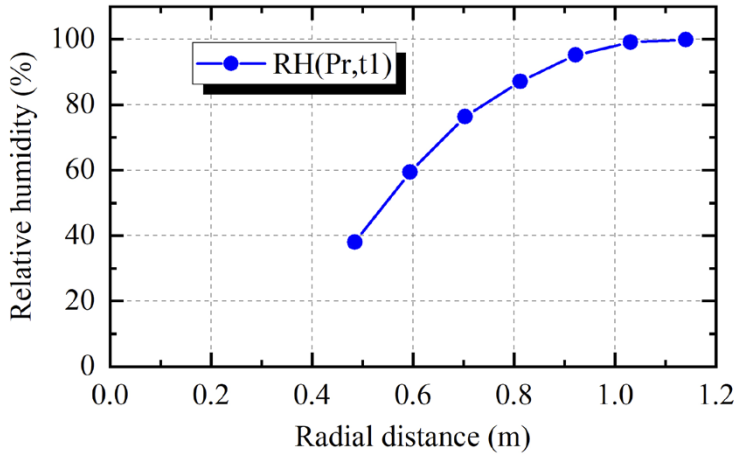

Figure C-30. *Distribution of relative humidity on section F2 at the time t1 = 4 000 days.*

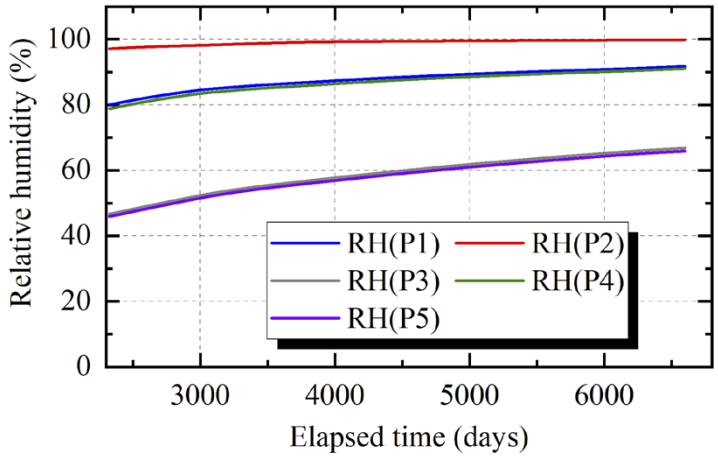

Figure C-31. *Evolution of relative humidity on section F2 from t = 2 325 days to t = 6 600 days.*

Distributions and evolutions after first dismantling of temperature

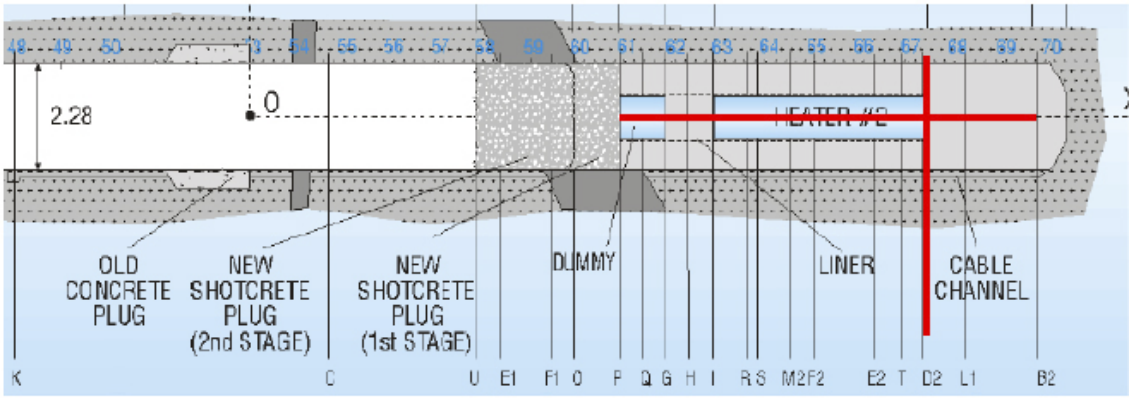

Figure C-32. *Required results: distributions and evolutions of temperature.*

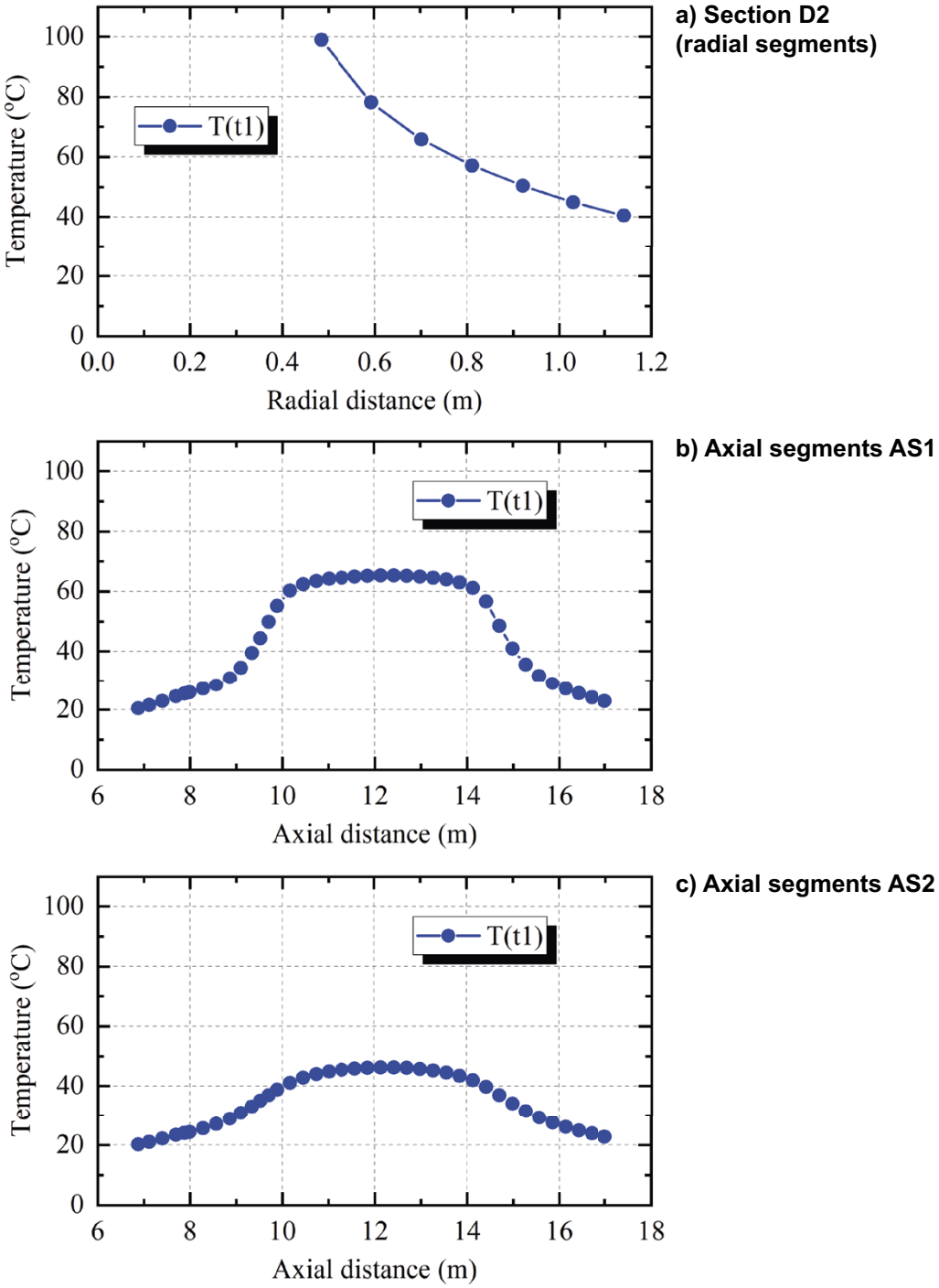

Figure C-33. *Distribution of temperature on segments D2, AS1, AS2 on time t1 = 5 600 days.*

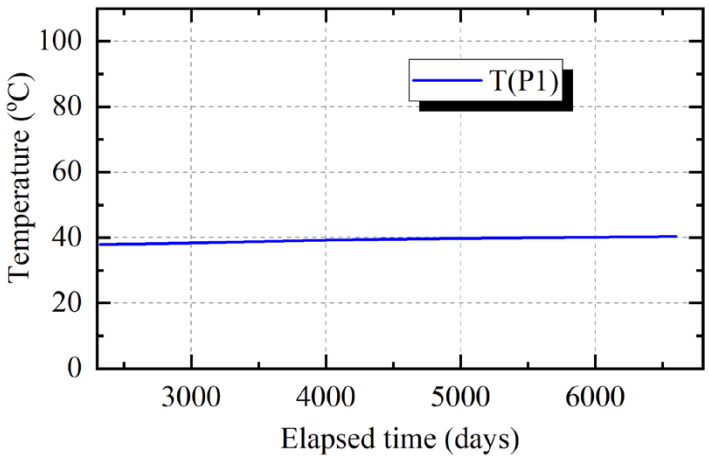

Figure C-34. *Evolution of temperature on section D2 from t = 2 325 days to t = 6 600 days.*

Evolutions after first dismantling of total stress

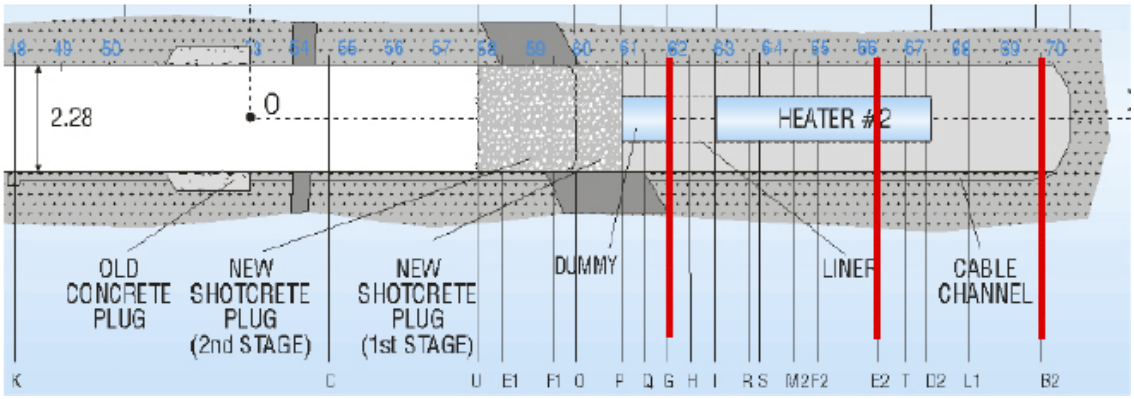

Figure C-35. *Required results: evolutions of total stresses.*

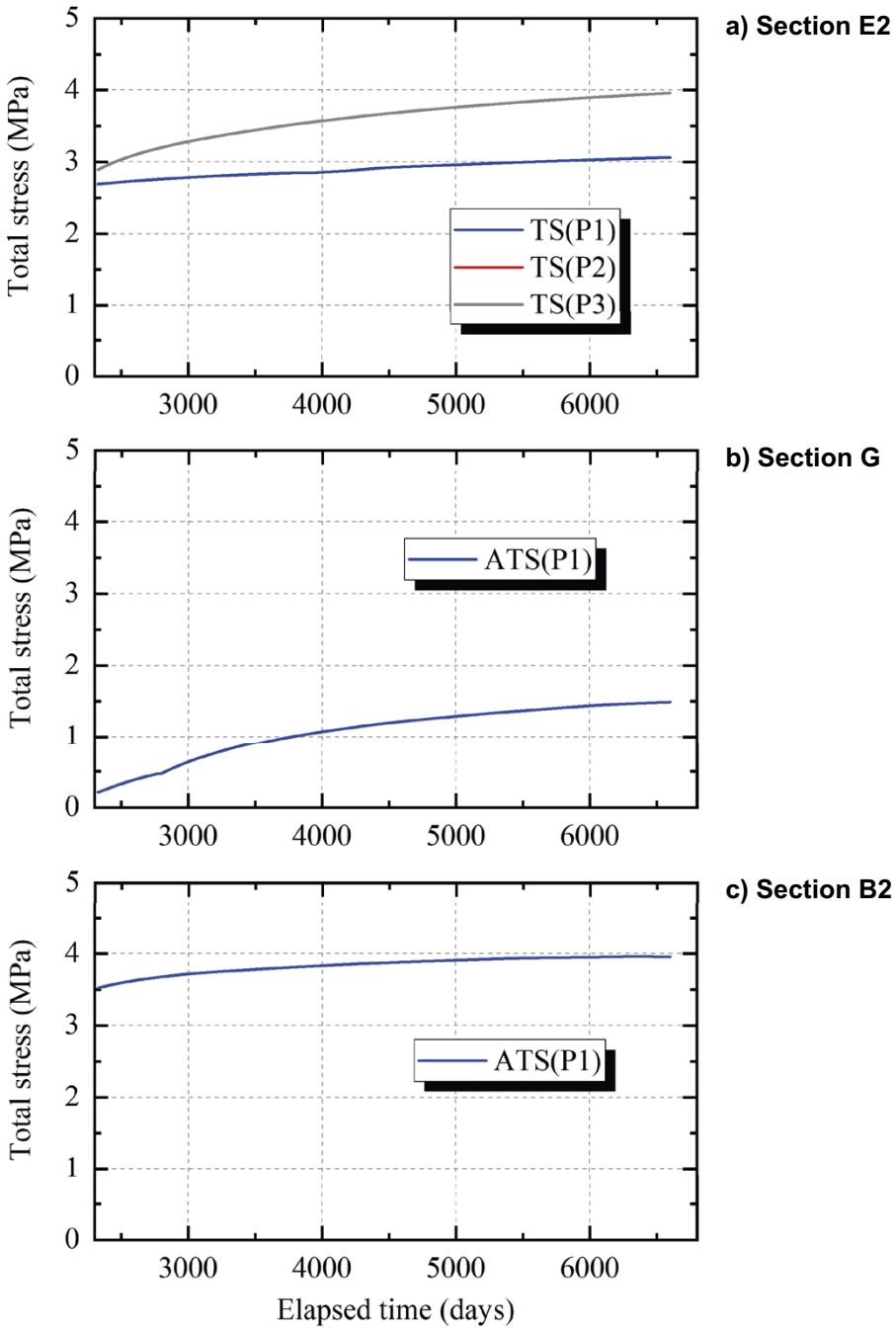

Figure C-36. *Evolution of total stress on sections E2, G and B2 from t = 2 325 days to t = 6 600 days.*

Distributions of dry density after dismantling

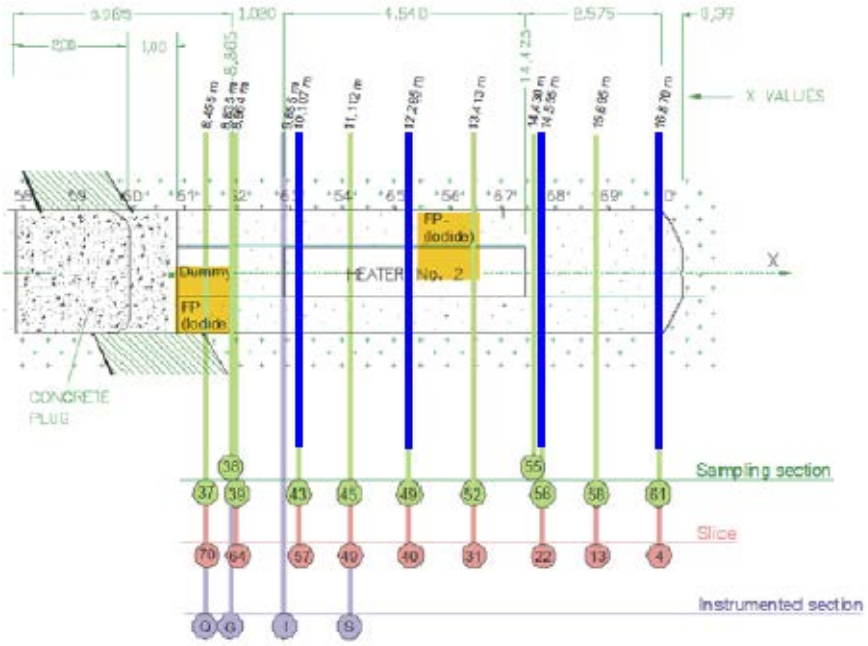

Figure C-37. *Required results: distributions of dry density, water content and degree of saturation after dismantling.*

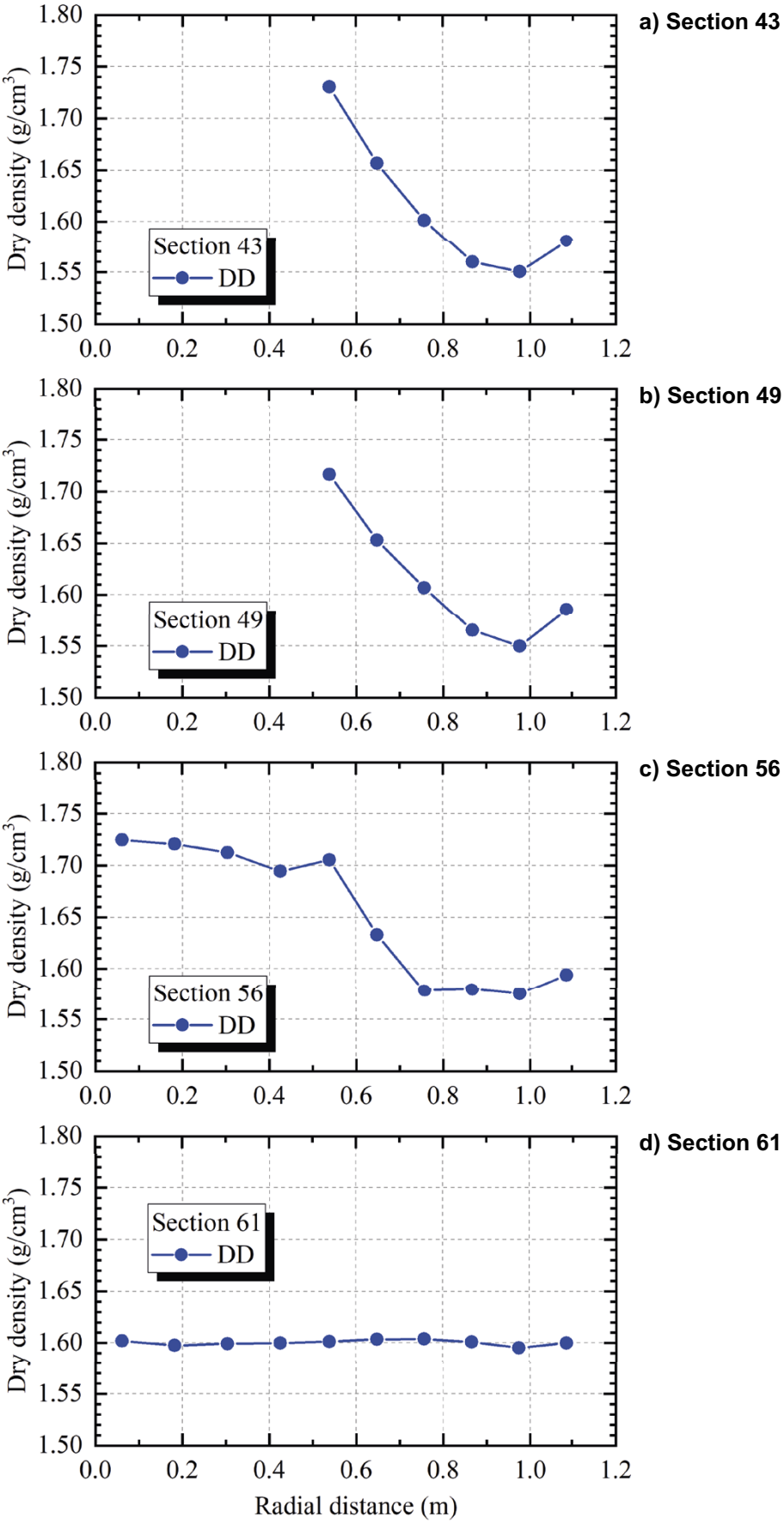

Figure C-38. *Distributions of dry density on sections 43, 49, 56 and 61.*

Distributions of water content after dismantling

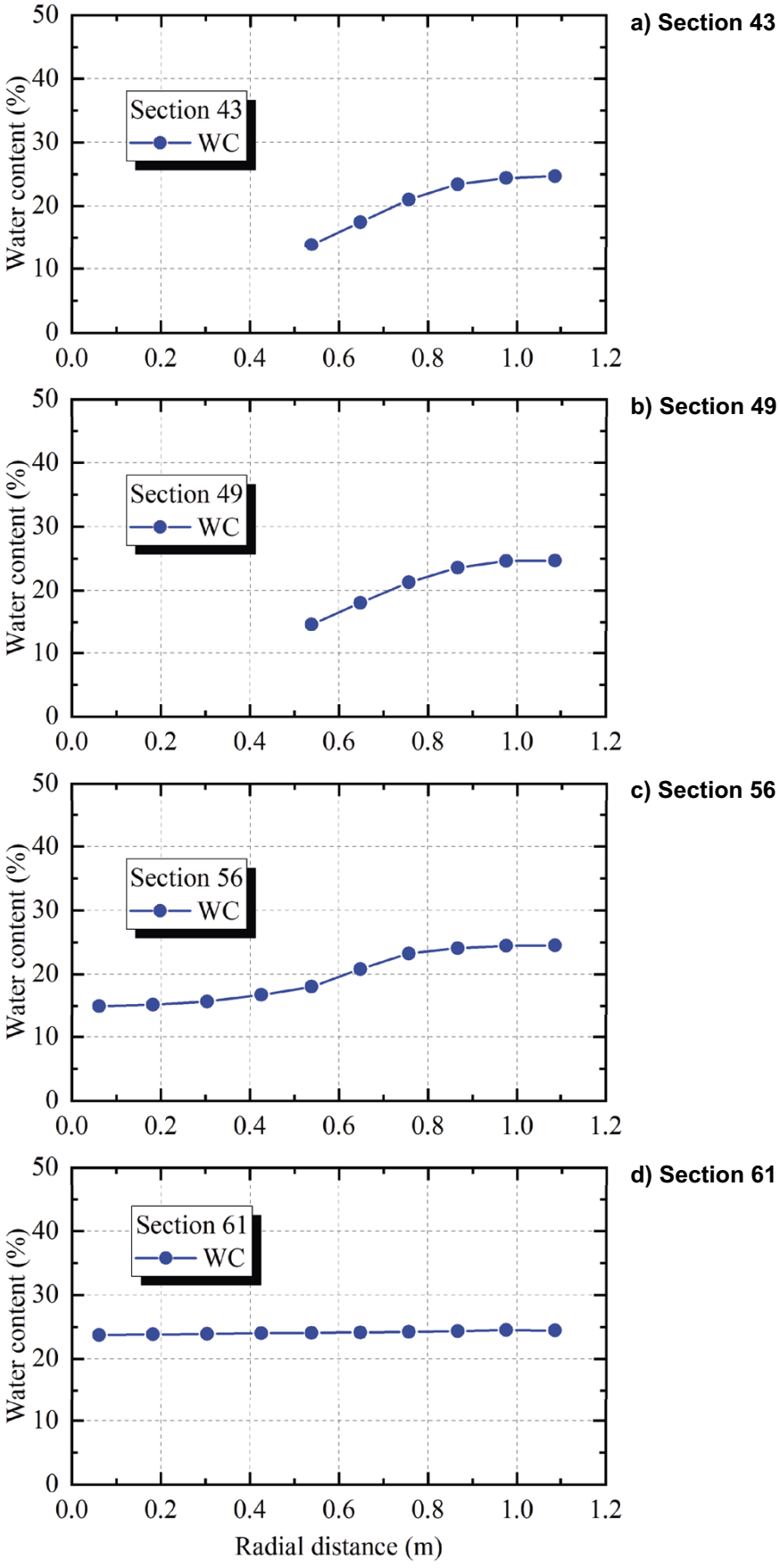

Figure C-39. *Distributions of water content on sections 43, 49, 56 and 61.*

Distributions of degree of saturation after dismantling

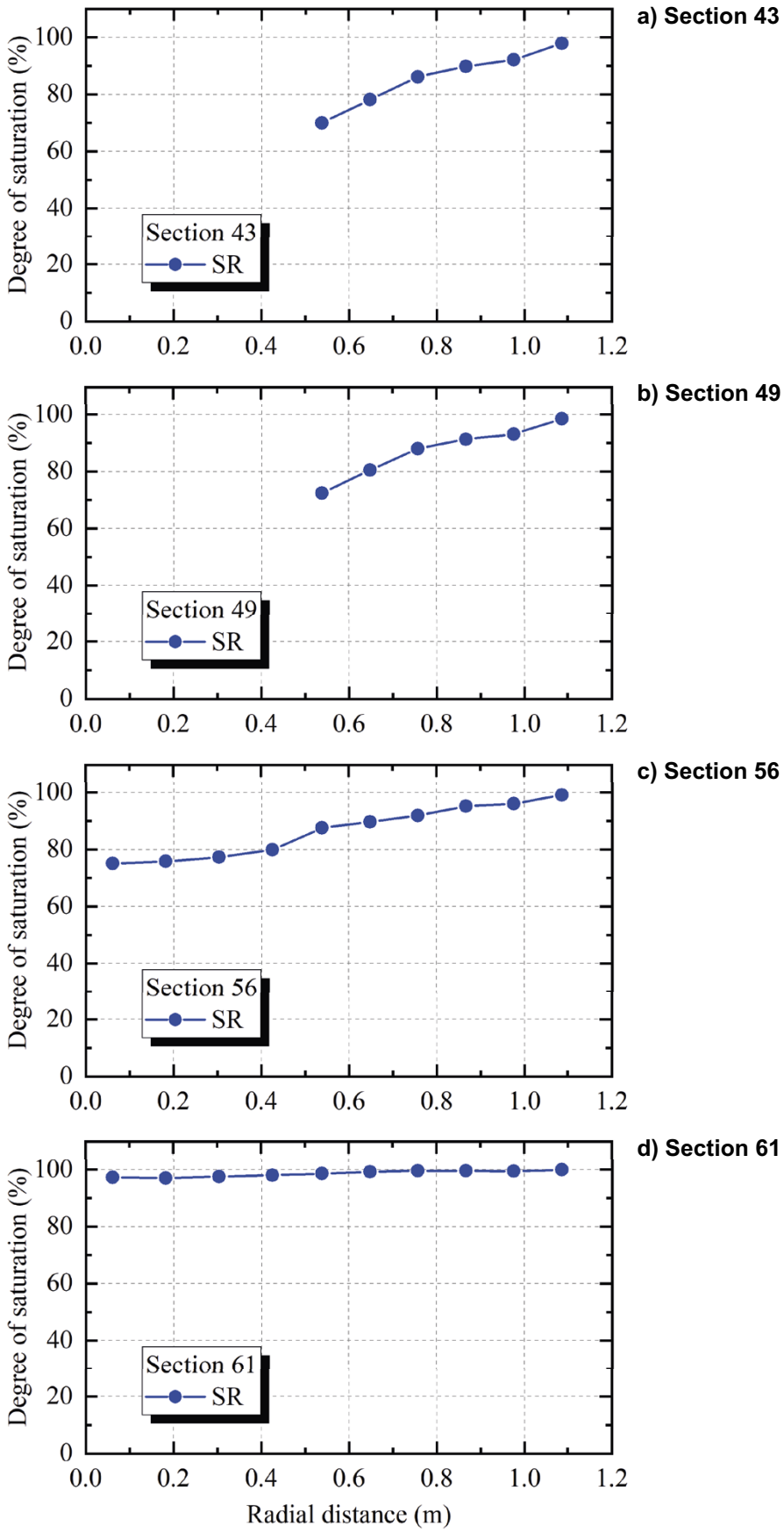

Figure C-40. *Distributions of degree of saturation on sections 43, 49, 56 and 61.*

C5 Initial conditions

C5.1 General features of numerical analysis

- Type of analysis: axisymmetric
- Type of analysis: THM
- Coupled
- Size of the analysis domain: 50 m (radial size), 120 m (axial size)
- Type and number of elements: 6 940 linear quadrilateral elements
- Number of elements across the bentonite barrier: 6 in the heater section and 10 in the no-heater section
- Number of nodes: 7 017

C5.2 Stages of the analysis domain

Stage number	Brief description	Start time (day)	Duration (days)
1	Tunnel excavation	−500	0
2	Tunnel ventilation	−500	365
3	Hydration without heating	−135	135
4	Heating Power 1 200 W	0	20

C5.3 Initial valuables and key parameters

C5.3.1 Rock

Initial conditions of the rock at the start of the analysis (1)

Initial temperature at tunnel axis level (°C)	Initial stresses at tunnel axis level (MPa)	Initial pore water pressure at tunnel axis level (MPa)
12	1.3	0.020

Initial conditions of the rock at the start of the analysis (2)

	Initial density (g/cm^3)	Initial porosity	Initial water content (%)
Granite	2.660	0.016	0.6
Lamprophyre	2.909	0.016	0.6
Fracture zone	2.909	0.160	9.1

Main rock properties (1)

	Initial thermal conductivity (W/mK)	Specific heat capacity (J/kgK)	Initial intrinsic permeability (m^2)	Initial hydraulic permeability (m/s)
Granite	3.34	920	5.0×10^{-19}	4.0×10^{-12}
Lamprophyre	2.71	920	5.0×10^{-18}	4.0×10^{-11}
Fracture zone	2.71	920	5.0×10^{-17}	4.0×10^{-10}

Main rock properties (2)

	Volumetric thermal expansion coefficient (K^{-1})	Young's modulus (MPa)	Poisson's ratio
Granite	8.0×10^{-6}	5.33×10^{4}	0.37
Lamprophyre	8.0×10^{-6}	4.24×10^{4}	0.37
Fracture zone	8.0×10^{-6}	4.24×10^{4}	0.37

Main rock properties: retention curve (3)

Equation used

$$s = 1.74(S_r^{-1.68} - 1)^{0.405}$$

s: MPa

Main rock properties: retention curve (4)

Equation used

$$k_r = S_r^{0.5}[1 - (1 - S_r^{1.68})^{0.595}]^2$$

C5.3.2 Bentonite

Initial conditions of the bentonite at installation (1)

Initial temperature (°C)	Initial stresses (MPa)	Initial suction (MPa)	Initial relative humidity (%)
12	0.020	135	35.8

Initial conditions of the bentonite at installation (2)

Initial dry density (g/cm^3)	Initial density of the solid phase (g/cm^3)	Initial porosity	Initial water content (%)	Initial degree of saturation
1.60	2.63	0.39	11.3	47.7

Main bentonite properties (1)

Initial thermal conductivity (W/mK)	Initial thermal conductivity dry bentonite (W/mK)	Initial thermal conductivity saturated bentonite (W/mK)	Initial specific heat capacity of the solid phase (J/kgK)	Thermal expansion coefficient (K^{-1})
0.677	0.571	1.259	749.1	$-0.118 \times 10^{-4} + 6.5 \times 10^{-6} T$

Main bentonite properties (2)

Initial intrinsic permeability (m^2)	Initial hydraulic permeability (m/s)	Initial intrinsic permeability (saturated) (m^2)	Initial hydraulic permeability (saturated) (m/s)	Swelling pressure under initial conditions (MPa)
2.2×10^{-22}	1.7×10^{-15}	2.0×10^{-21}	1.59×10^{-14}	7.82

Main bentonite properties: permeability dependence on dry density (or porosity) (3)

The bentonite permeability is constant.

Main bentonite properties: retention curve (4)

Equation used	P_0 (MPa)	λ	S_{r0}	S_{rmax}
$S_r = S_{r0} + (S_{rmax} - S_{r0})\left[1 + \left(\frac{s}{P_0}\right)^{\frac{1}{1-\lambda}}\right]^{-\lambda}$	30	0.32	0.10	1.00

Main bentonite properties: relative permeability (5)

Equation used

$k_r = S_r^3$

Main bentonite properties: thermal conductivity (6)

Equation used	A_1	A_2	x_0	d_x
$\lambda = A_2 + \frac{A_1 - A_2}{1 + e^{(S_r - x_0)/d_x}}$	0.57	1.28	0.65	0.10

Main bentonite properties: vapour transport (7)

Molecular diffusion coefficient of vapour in free air (m²/s)	Tortuosity
$K_s = 3.164 \times 10^{-6}[e(1 - S_r)]^{4.3}$	0.8

C5.3.3 Constitutive functions

- Permeability vs dry density

  Permeability of bentonite is constant, and saturated hydraulic conductivity of rock is constant.

- Retention curve and relative permeability of bentonite

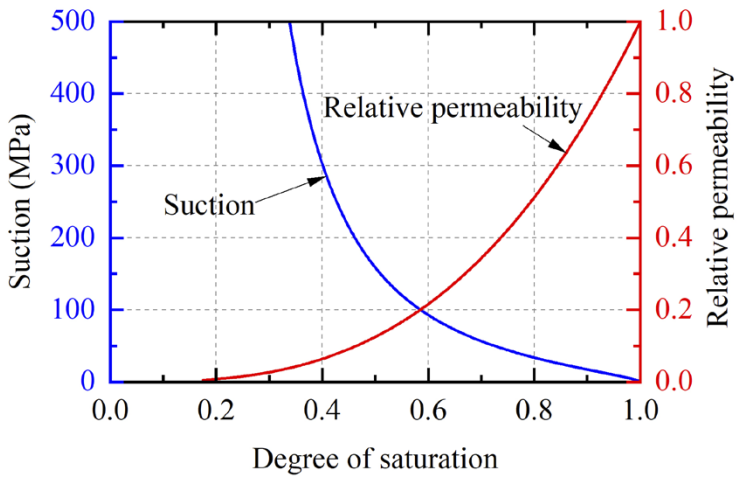

- Retention curve and relative permeability of rock

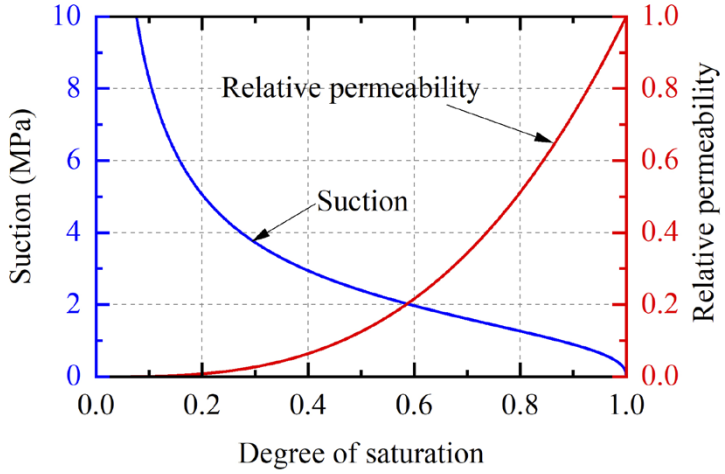

- Thermal conductivity of the bentonite vs degree of saturation

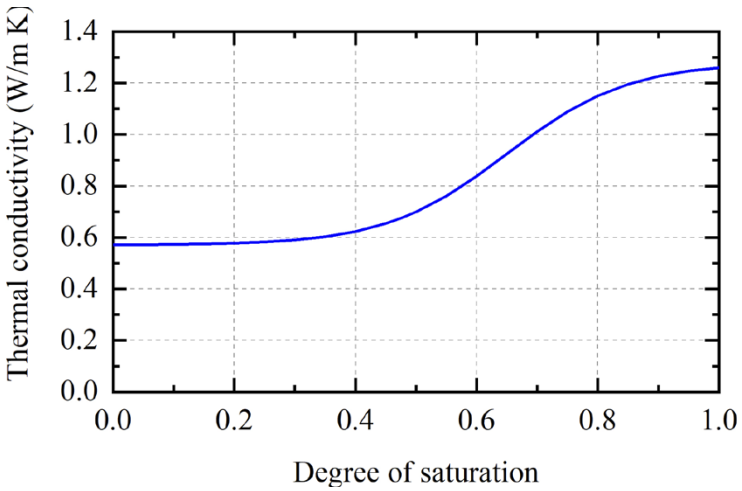

C5.4 Sensitivity analyses

CRIEPI conducted sensitivity analyses on some material parameters that are considered to affect the numerical results or to have large uncertainty. The parameters are rock permeability, bentonite permeability, bentonite Young's modulus, bentonite Poisson's ratio and bentonite swelling parameter l in Equation (C-16).

C5.4.1 Rock permeability

In the base case, the granite permeability was 4.0×10^{-12} m/s in reference with the specification document. For a sensitivity analysis, 4.0×10^{-11} m/s was used. The permeability of lamprophyre and fracture zone were not changed.

Figure C-41 shows the calculated and measured water inflow to the test drift in the case of higher granite permeability. Calculated inflow got slightly closer to the measured in this case than in the base case shown in Figure C-12.

Figure C-42 shows the calculated evolution of power of heater 2 in the base case and the case of higher permeability of granite. In the case of higher granite permeability, calculated heating power got higher because of the fast water infiltration resulting in higher thermal conductivity. Figures C-43 and C-44 show that water infiltration got faster in the case of higher granite permeability.

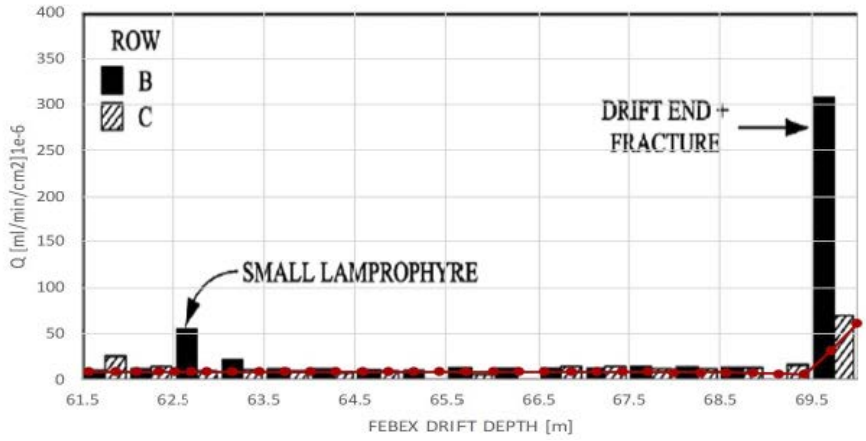

Figure C-41. *Calculated and measured water inflow to the drift: red plot is calculated inflow with the rock permeability of 4.0×10^{-11} m/s, bar graphs are measured inflow.*

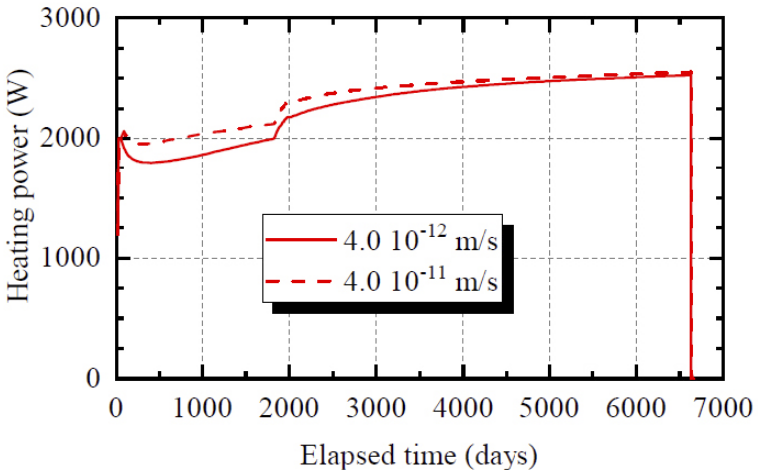

Figure C-42. *Evolution of power of heater 2.*

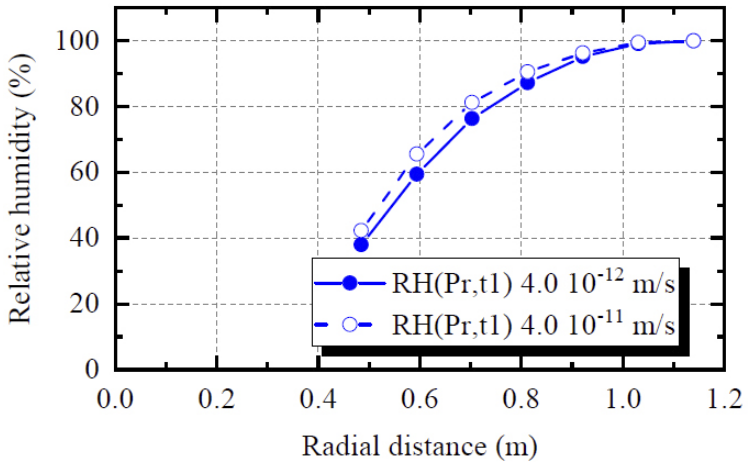

Figure C-43. *Distributions of relative humidity on section F2 at the time t1 = 4000 days.*

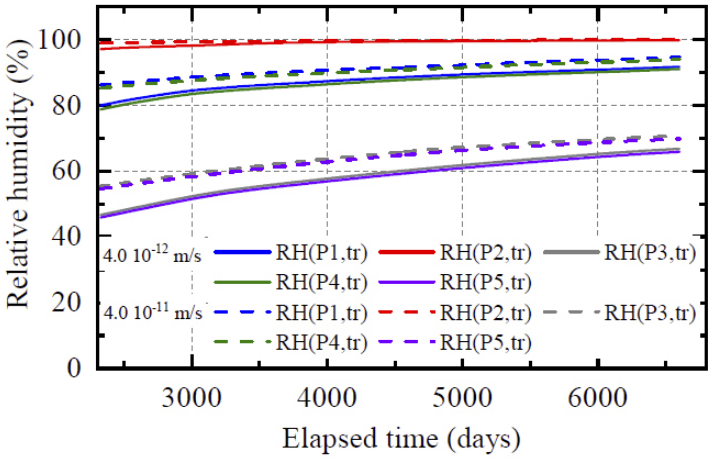

Figure C-44. *Evolution of relative humidity on section F2 from t = 2 325 days to t = 6 600 days.*

C5.4.2 Bentonite permeability

In the base case, bentonite permeability of 2.0×10^{-21} m^2 was used. For a sensitivity analysis, 1.3×10^{-20} m^2 was used. This is another value found in the specification document.

Figure C-45 shows the heating power evolution. In the case of higher bentonite permeability, calculated heating power got higher because of fast water infiltration resulting in higher thermal conductivity.

Figures C-46 and C-47 show radial distribution and evolution of relative humidity in the section F2, respectively. Water infiltration was faster and bentonite was saturated after 3 200 days in the case of higher bentonite permeability.

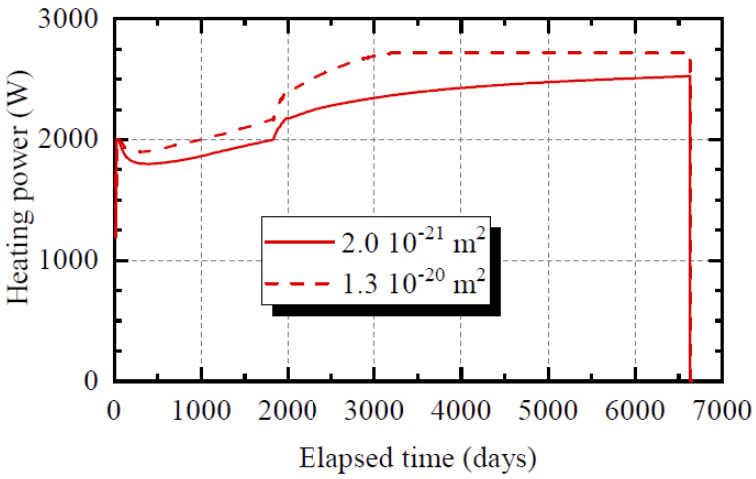

Figure C-45. *Evolution of power of heater 2.*

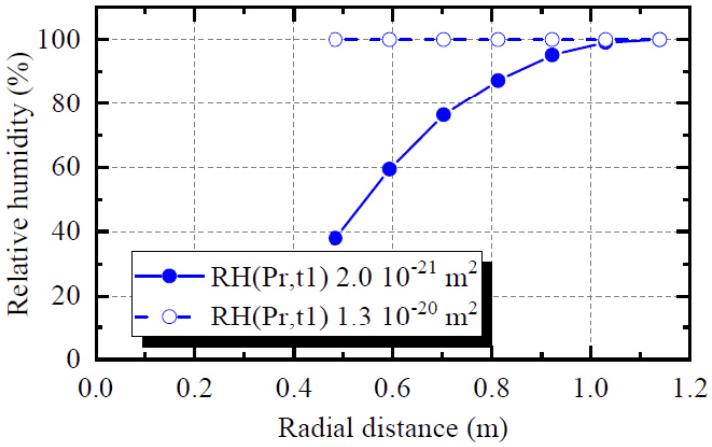

Figure C-46. *Distributions of relative humidity on section F2 at the time t1 = 4 000 days.*

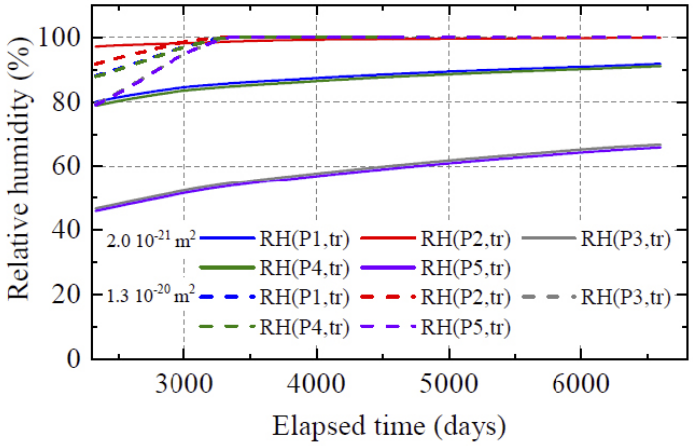

Figure C-47. *Evolution of relative humidity on section F2 from t = 2 325 days to t = 6 600 days.*

C5.4.3 Bentonite Young's modulus

In the base case, bentonite Young's modulus of 20 MPa was used. This value was determined for saturated bentonite. Young's modulus of unsaturated bentonite is considered larger. Here, 50 MPa was used in the comparative case.

In the case of larger Young's modulus, total stress got larger and bentonite deformation got smaller shown in Figures C-48 and C-49, respectively.

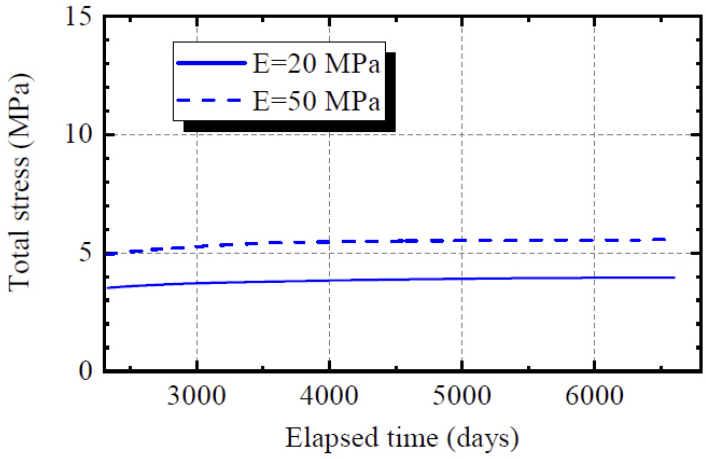

Figure C-48. *Evolution of total stress on section B2 from t = 2 325 days to t = 6 600 days.*

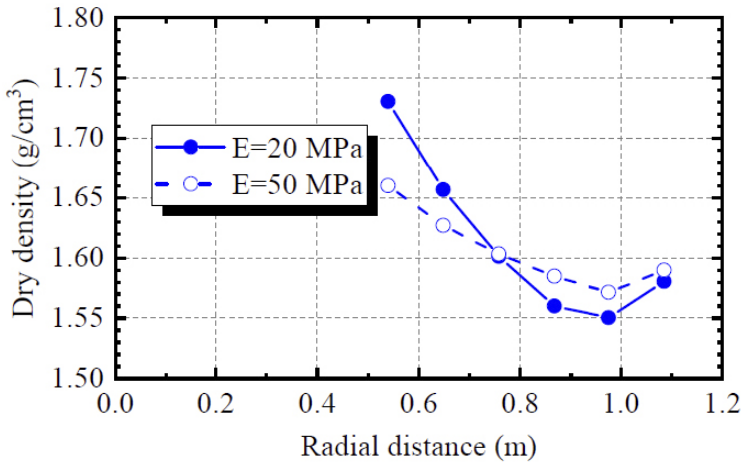

Figure C-49. *Distributions of dry density on section 49.*

C5.4.4 Bentonite Poisson's ratio

In the base case, Poisson's ratio of 0.2 was used for bentonite. As Bishop's parameter χ for effective stress is zero for unsaturated bentonite in LOSTUF, the value close to 0.5 should be used for bentonite of high saturation rate. As a sensitivity analysis, Poisson's ratio of 0.45 was used. Calculated bentonite swelling is expected to get more isotropic in the case of $\nu = 0.45$.

In the case of $\nu = 0.45$, total stress got larger, and dry density distribution got more monotonic shown in Figures C-50 and C-51, respectively.

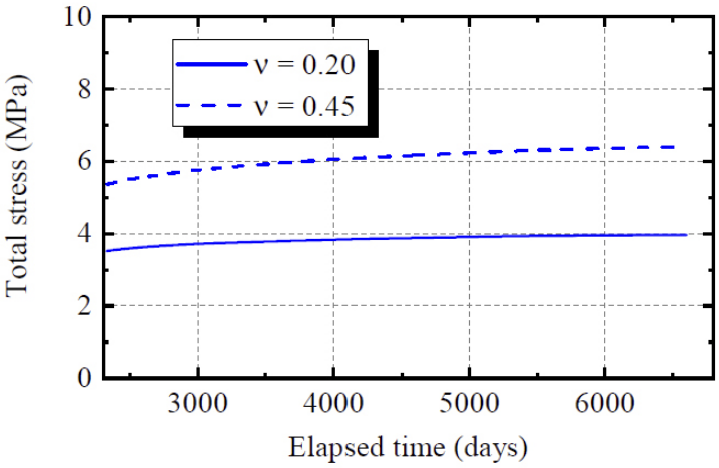

Figure C-50. *Evolution of total stress on section B2 from t = 2 325 days to t = 6 600 days.*

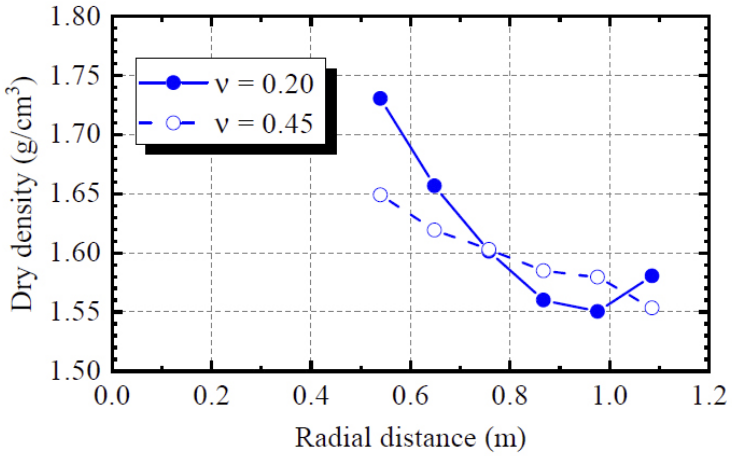

Figure C-51. *Distributions of dry density on section 49.*

C5.4.5 Bentonite swelling parameter l

Bentonite swelling parameter l in Equation (C-16) controls the progress of swelling with water infiltration. While $l = 1$ was used in the base case, $l = 3$ was used in the comparative case.

Figures C-52 and C-53 show the evolution of total stress on sections E2 and B2 in Stage 1, respectively. In the case of larger l, total stresses increased more slowly. However, final values were not so different.

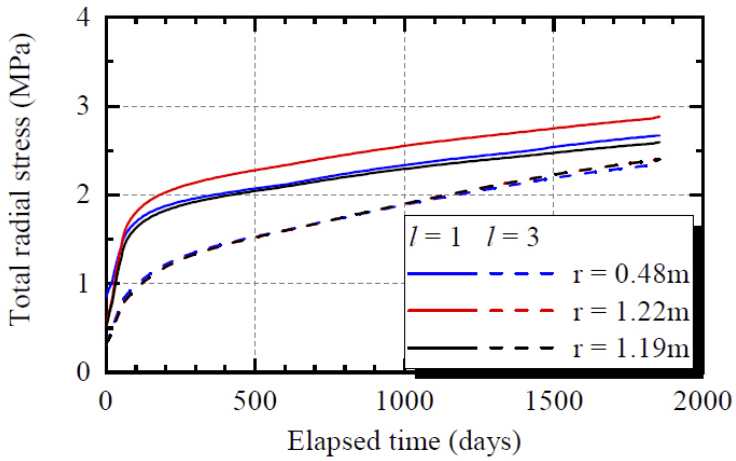

Figure C-52. *Evolution of total stress on section E2 in Stage 1.*

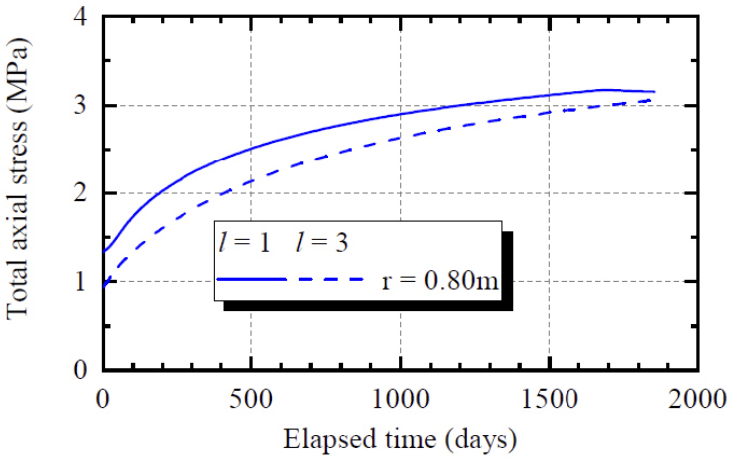

Figure C-53. *Evolution of total stress on section B2 in Stage 1.*

C5.5 Simulation of Stage 1 with 100-year extension

CRIEPI conducted a simulation of Stage 1 with 100-year extension in order to estimate when the bentonite would be fully saturated. It was assumed that the heaters were not switched off but their surfaces were kept 100 °C in the extended 100 years. The other analytical conditions were the same as the base case.

C5.5.1 Relative humidity

Figure C-54 shows the evolution of relative humidity on sections C, E1, H, and F2. The bentonite is fully saturated in 16 000 days, roughly 44 years.

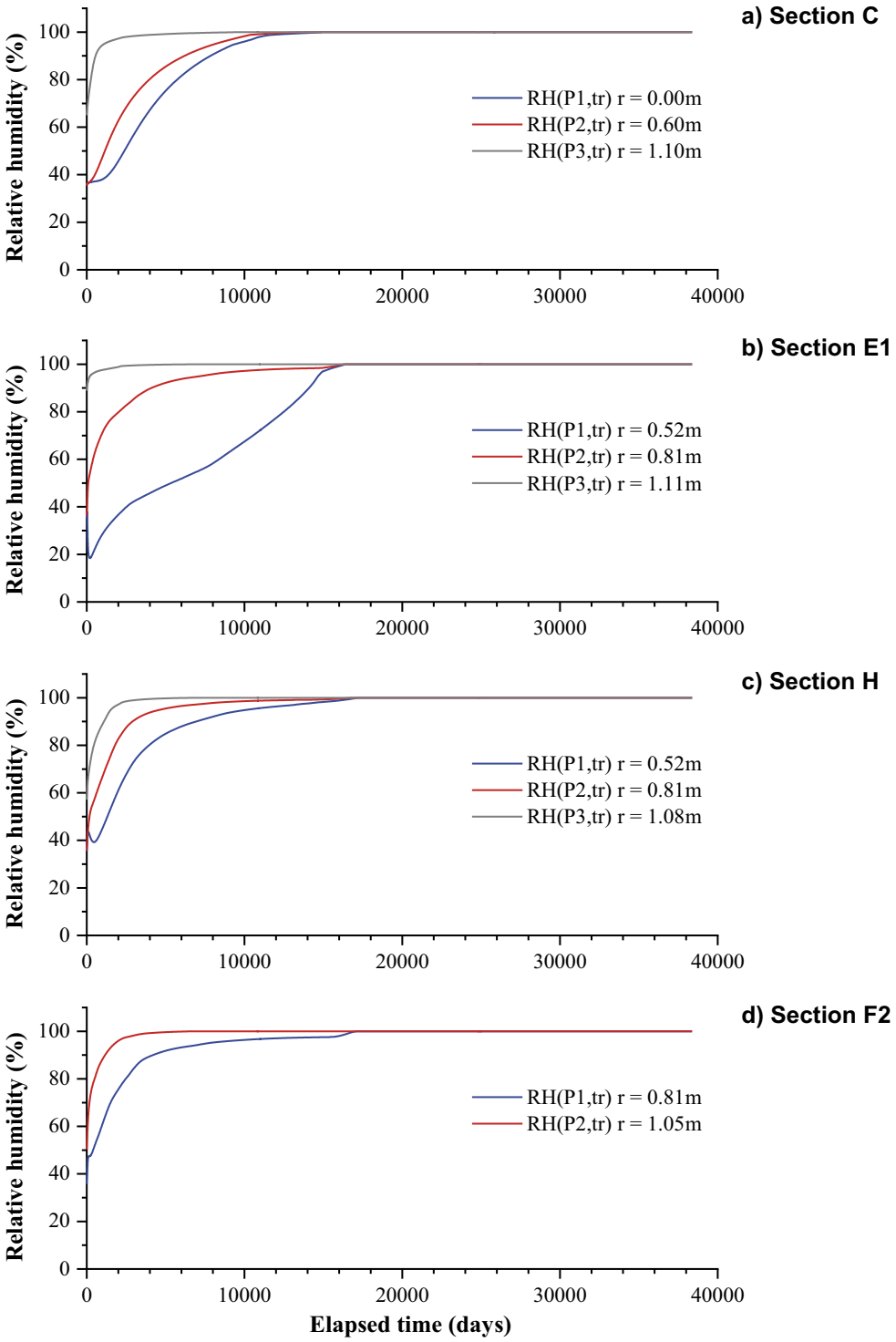

Figure C-54. *Evolutions of relative humidity on sections C, E1, H, and F2.*

C5.5.2 Temperature

Figure C-55 shows evolution of temperature on sections D1, I, and D2. Temperature are constant after fully saturation of bentonite.

C5.5.3 Total stress

Figure C-56 shows evolution of total stresses on sections E2 and B2. Total stresses increased by 0.5 to 1.0 MPa in the extended 100 years.

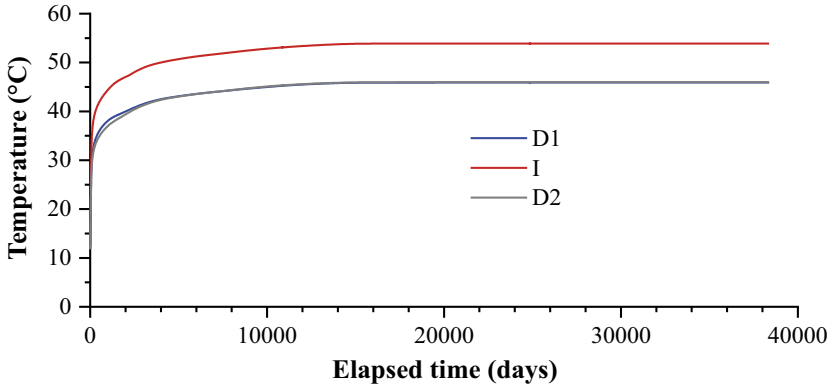

Figure C-55. *Evolution of temperature on sections D1, I, and D2.*

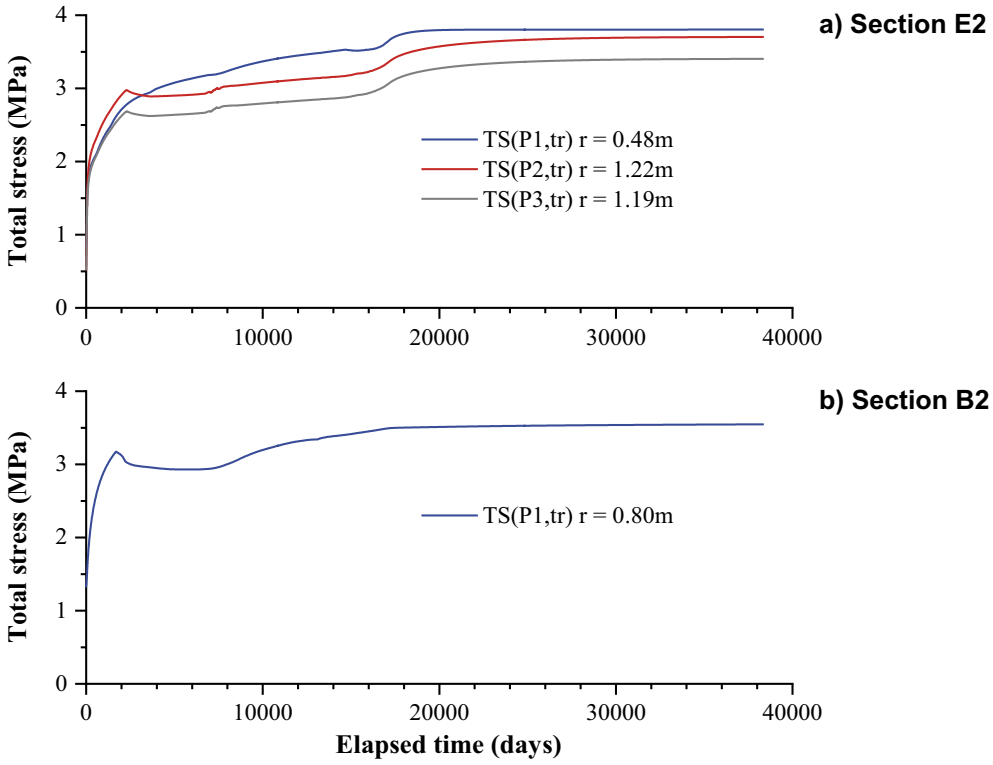

Figure C-56. *Evolution of total stresses on sections E2 and B2.*

C5.5.4 Dry density

Figure C-57 shows the distribution of dry density of bentonite on sections 15, 27, and 31 at the end of Stage 1 and the extended 100 years. Inner part was compressed by swelling in outer part in Stage 1. During the extended 100 years, bentonite was saturated. Inner part swelled after pushed back the outer part. Dry density of bentonite was not perfectly homogeneous after full saturation in this simulation because of linear elasticity of bentonite.

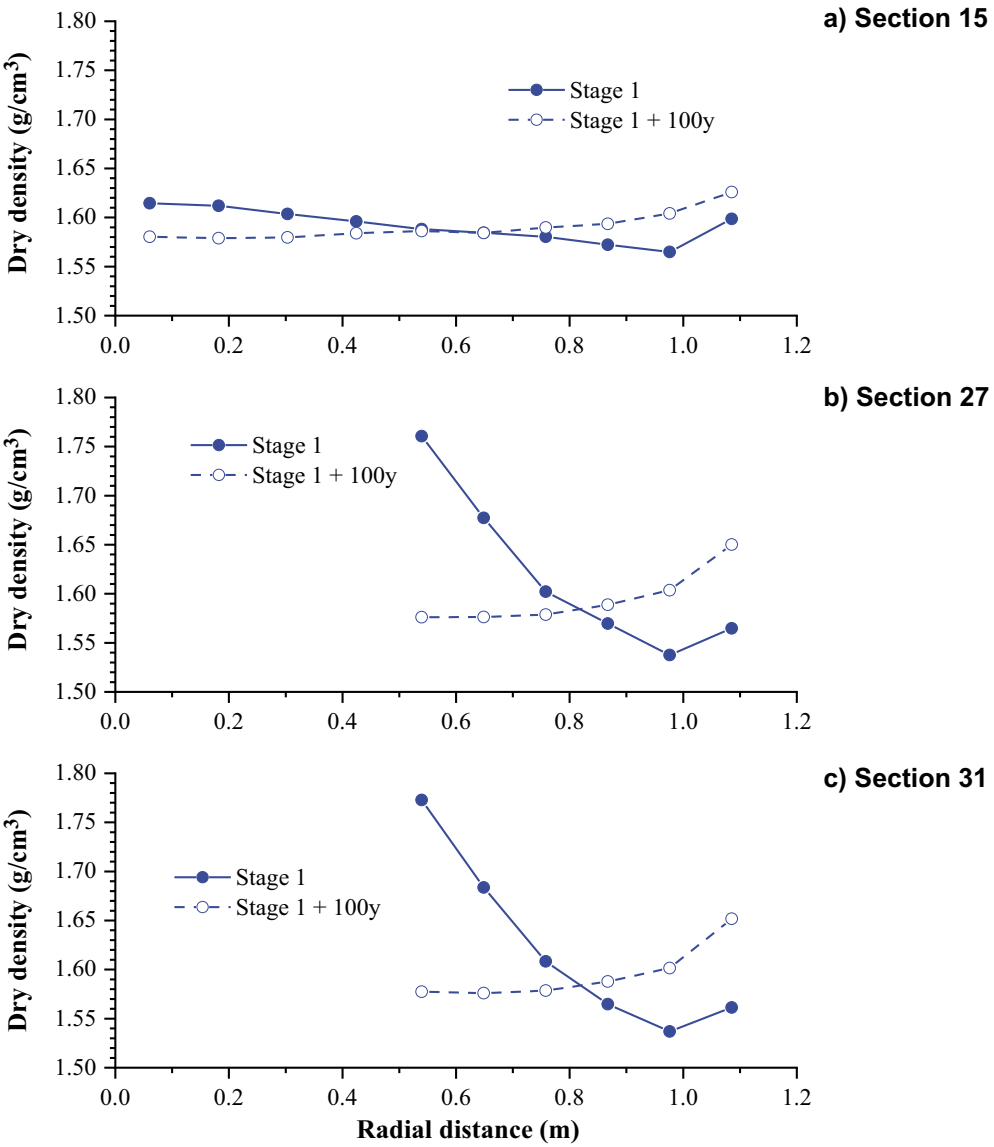

Figure C-57. *Distributions of dry density on sections 15, 27 and 31.*

Appendix D

GRS Report

Gesellschaft für Anlagen- und Reaktorsicherheit, Germany (GRS) gGmbH
Klaus-Peter Kröhn

D1 Task[1]

The FEBEX (Full-scale Engineered Barriers Experiment in Crystalline Host Rock) "in situ" test was a full-scale test conducted during 18.4 years in the Grimsel URL (Switzerland) managed by NAGRA. It was based on the ENRESA AGP Granito (Deep Geological Disposal, Granite) reference concept. A 70.4 m long drift with a circular section 2.28 m in diameter was excavated in the Grimsel granite. In the last 17.4 m of the gallery, two electrical heaters of dimensions and weight equivalent to those considered in the ENRESA and NAGRA concepts were emplaced and in the remaining space compacted bentonite blocks were emplaced. The test zone was closed with a concrete plug (see Figure D-1).

The experiment was instrumented with sensors monitoring the thermo-hydro-mechanical processes taking place in the clay barrier and in the surrounding Grimsel granite. The experiment was in operation for 5.0 years. Thereafter, the outer heater was switched off and the outer half of the experiment was dismantled, whereby samples were taken from various points of the rock, the concrete and the bentonite buffer. During this first dismantling, the remaining half of the experiment, including the second heater, continued in operation. This remaining half of the experiment was in operation for 13.2 years more. Thereafter, the experiment was completely dismantled and, as before, samples from various points were taken.

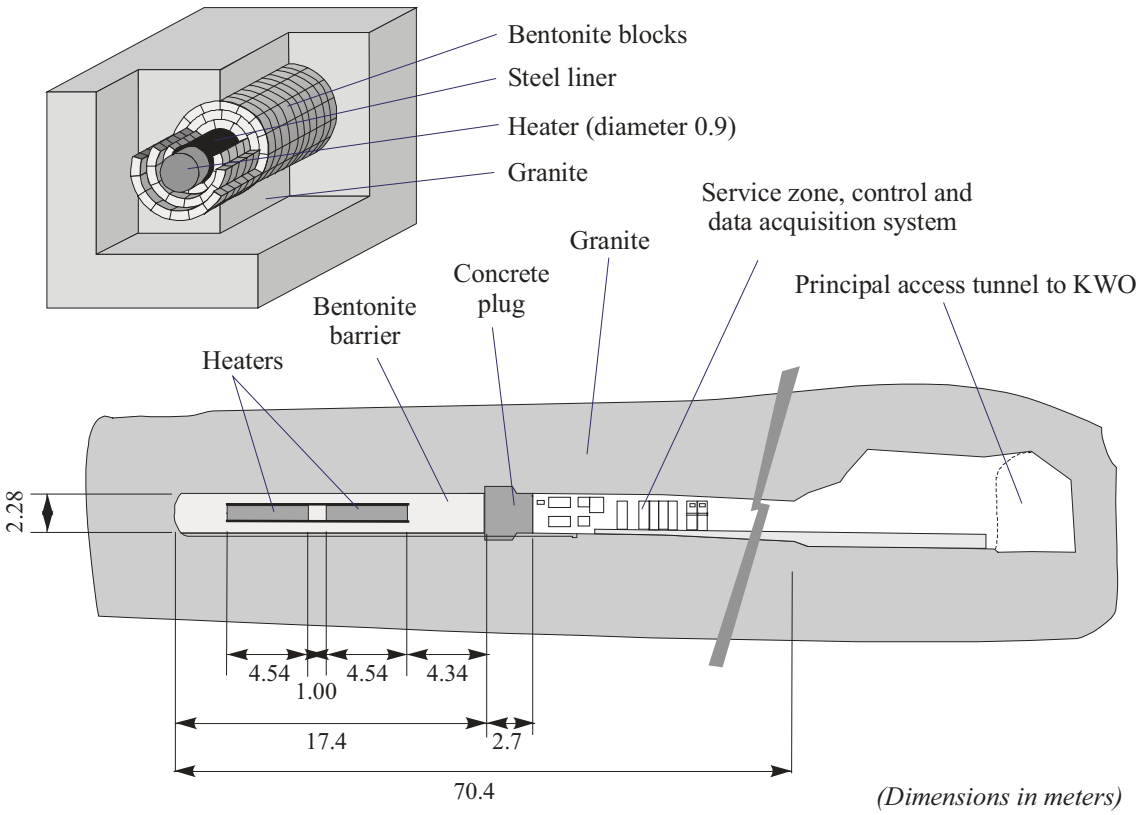

Figure D-1. *FEBEX "in situ" test layout; from ENRESA (2000).*

[1] Most of the text in this section is copied from the Task Description.

Of interest for the task at hand are several cross-sections along the FEBEX-tunnel. They are depicted in Figure D-2. For reasons discussed in the following section only cross-sections C and F2 were considered, though. Characteristic periods of the experiment are listed in Table D-1. The work described in the following refers to stages 1 and 2 which are defined as the period until dismantling heater 1 and the subsequent period until dismantling heater 2.

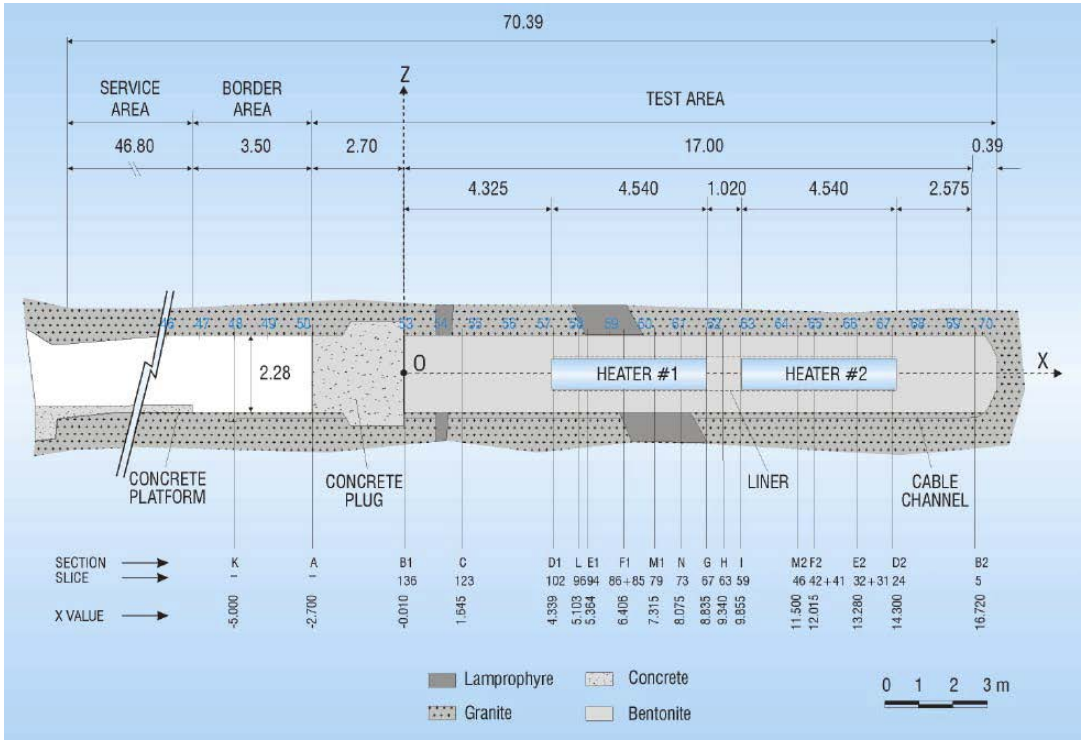

Figure D-2. *General layout for stage 1 of the FEBEX in situ test; from Bárcena et al. (2003).*

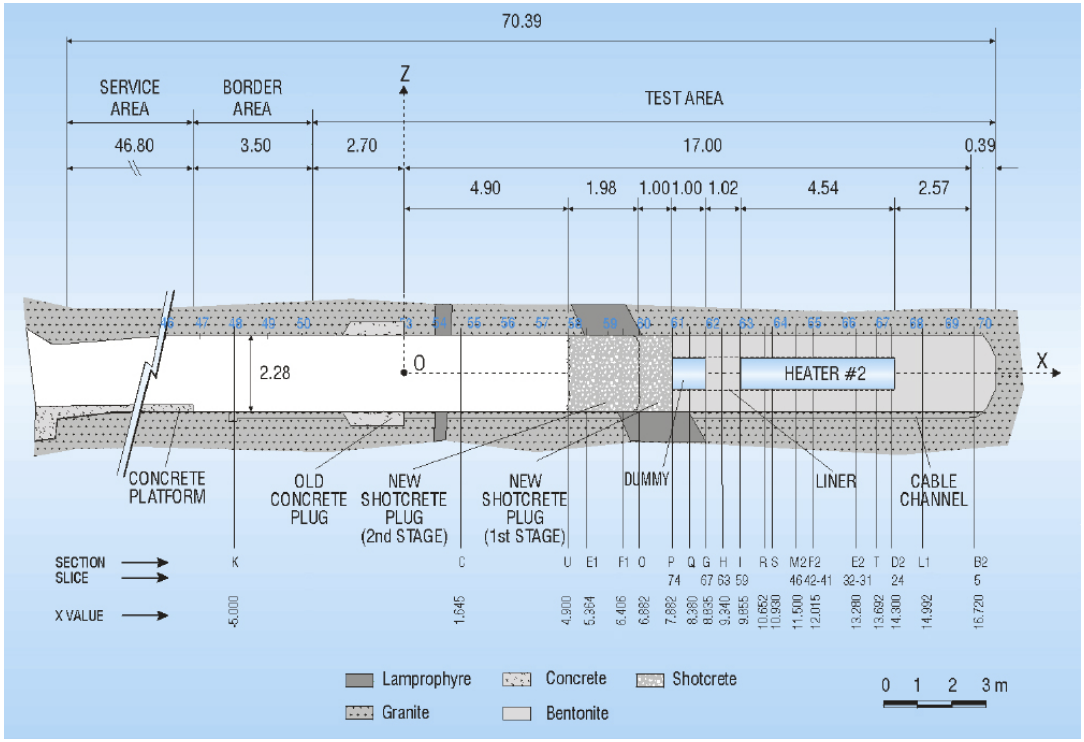

Figure D-3. *General layout for stage 2 of the FEBEX in situ test; from Bárcena et al. (2003).*

Table D-1. Characteristic periods of the experiment.

Event	Date	Day relative to the start of the heaters
Start of tunnel excavation	25.09.1995	−521
End of tunnel excavation	30.10.1995	−486
Start of installation	01.07.1996	−241
End of installation	15.10.1996	−135
Heaters switch on (day 0)	27.02.1997	0
Heater #1 switch off	28.02.2002	1827
End of first dismantling	19.07.2002	1968
Start demolition of the 1st section of the plug	07.04.2015	6613
End demolition of the 1st section of the plug	17.04.2015	6623
Heater #2 switch off	24.04.2015	6630
Start demolition of the 2nd section of the plug	27.04.2015	6633
End demolition of the 2nd section of the plug	08.05.2015	6644
Start dismantling of buffer until heater #2	18.05.2015	6654
Extraction of heater #2	04.06.2015	6671
End of dismantling	20.07.2015	6717

Table D-2. Characteristic periods for the models.

Event	Day relative to the start of the heaters
Begin of wetting	−135
Begin of power-controlled heating	0
Begin of temperature-controlled heating[2]	51
Heater #1 switch off	1827
Time of post-dismantling data aquisition	1968
Heater #2 switch off	6630
Time of post-dismantling data aquisition	6717

D2 Model concept

No fully coupled THM-approach is used. The influence of water flow on the temperature field is neglected. Instead, the thermal calculations are done first with an axisymmetric 2D-Model using the resulting temperature fields as input for the calculation of the non-isothermal water uptake.

For stage 2 the changes in the system due to excavation and renewed plugging are neglected. Heater 1 is just switched off at the end of stage 1.

The water uptake code allows only for 1D- and axisymmetric 1D-model domains. Possible re-saturation effects along the system axis can therefore not be covered by this model. Unfortunately, this excludes most of the envisioned cross-sections. Best met by these restrictions are thus cross-sections that are orthogonal to the system axis and either cutting through the barycentre of the heaters or being located at a certain distance to the heaters as well as to the tunnel ends. This leaves sections C, F1, and F2 for modelling. Section F1, however, crossing the slanted lamprophyre layer which might have disturbed axisymmetry for the thermal model is eventually also skipped for this investigation.

135 days of isothermal wetting preceding heating are simulated. The resulting humidity distribution is used as initial condition for simulation of the non-isothermal water uptake. This allows for keeping the model time in sync with the beginning of heating.

[2] See Section D3.4 for details.

D3 Thermal model

D3.1 Geometry and numerical grid

Heaters as well as the tunnel have a circular cross-section and there are no relevant anisotropies in the granitic host rock. The model for stage 1 is therefore chosen to be 2d-axisymmetric with a length of 50 m and a radius of 45 m. The radius has been chosen according to a numerical pre-test where the maximum temperature increases at the outer boundary at 45 m did not increase above 1.5 °C after 6 717 days. This condition is important to ensure that the error induced by closing the outer boundaries to heat flow remains minimal. A 3D-view of the full model as well as a cut-out in 2D is depicted in Figure D-4.

The mesh is chosen in such a way that the highest spatial resolution can be found where the highest temperature gradients are expected. In total there are 3 793 triangular elements that are expanded into 3D-space by axial symmetry and 13 484 nodes. The highest grid density can therefore be found at the heaters with about 5 elements per meter with slightly varying size in the radial direction. An impression of the mesh is given in Figure D-5.

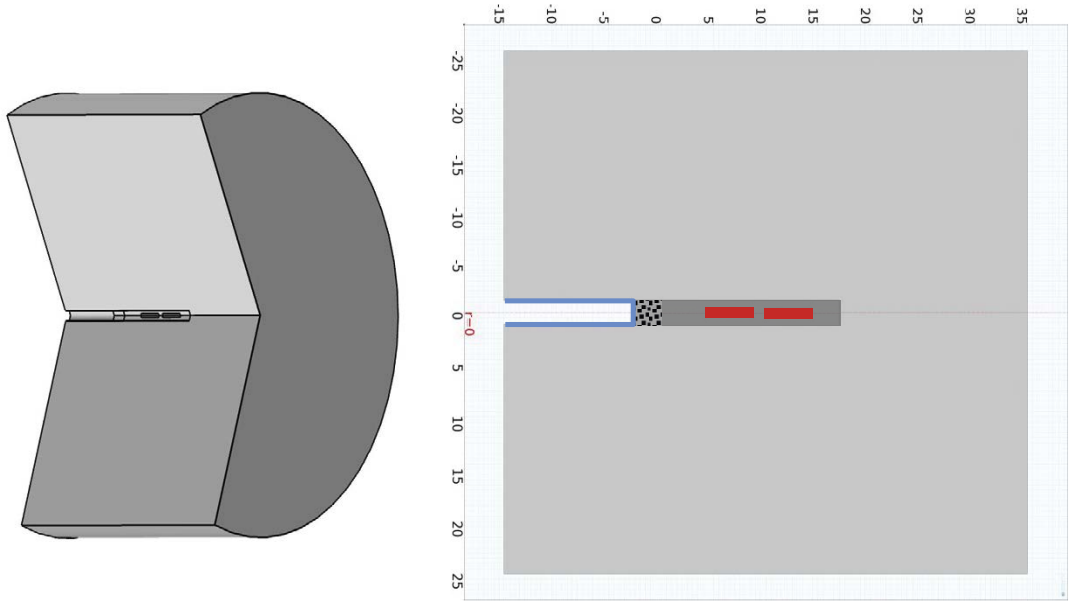

Figure D-4. *Domain of the thermal model; left: full model in 3D, right: Cut-out in 2D.*

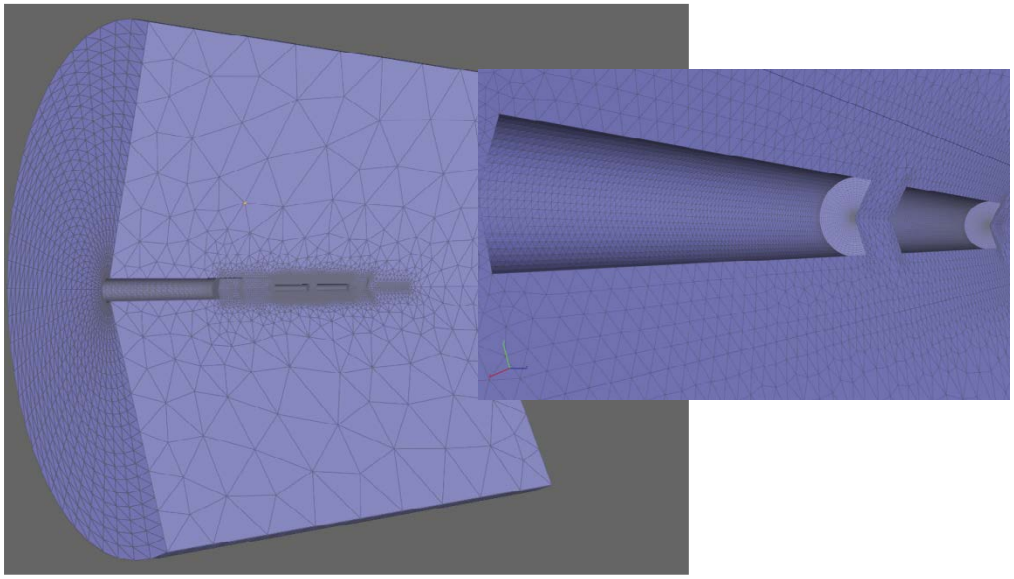

Figure D-5. *Numerical grid; left: opened whole domain, right: close-up.*

D3.2 Mathematical model

The heat flow problem is solved with the help of code COMSOL. In the heat transport module the following equation is numerically solved:

$$\rho C_p \frac{\partial T}{\partial t} + \rho C_p \boldsymbol{u} \cdot \nabla T = \nabla \cdot (k \nabla T) + Q \qquad \text{(D-1)}$$

ρ: density [kg/m³]

C_p: specific heat capacity [J/(kg K)]

T: temperature [K]

t: time [s]

$\boldsymbol{u}$: velocity vector [m/s]

k: thermal conductivity [W/(m K)]

Q: heat source/sink [W/(m³ s)]

However, the advective term is not considered here.

D3.3 Material data

The model comprises four materials which are granite, the bentonite buffer, steel heaters and concrete for the tunnel plug. The parameters for granite and concrete could be taken from the COMSOL material data library. The heater materials are approximated by steel AISI 4340, for which the parameters are also available from the COMSOL-library. The material has also been envisioned for the steel dummy that replaced heater 1 partly after the first dismantling. Buffer data are taken from Gens (2018) and Kristensson and Börgesson (2007). The data are compiled in Table D-3.

Table D-3. Material parameters for the thermal model.

	Granite	Concrete	Buffer	Heaters
Thermal conductivity [W/(m K)]	3.3	1.8	1[3]	44.5
Specific heat capacity [J/(kg K)]	850	880	800[4]	475
Density [kg/m³]	2600	2300	2780	7850

D3.4 Initial and boundary conditions

An initial temperature of 12 °C is assumed throughout the system. The same temperature is assigned to the surfaces of tunnel and of the plug at all times. The faces and the lateral surface of the cylindrical piece of granite are assumed to be thermally insulated, also for the whole modelling time.

Most complex are of course the boundary conditions for the heaters. From day 1 to day 21 a constant power of 1 200 W is fed into each of the heaters. Between days 21 to 53 the power is increased to 2 000 W. After that period, the temperature of the canister surface is controlled by varying the heater power and successively switched up to 95 °C, 99 °C, and 100 °C from day 53 to day 61. The surface temperature of 100 °C is ascribed further on for the respective running time of the heaters. Heater 1 is switched off on day 1827 in the model, heater 2 on day 6630. Excavation is assumed to be represented by the results for day 6717.

[3] Relates to a degree of saturation of S = 0.85 according to Annex 2 in Gens (2018).

[4] Chosen erroneously after Kristensson and Börgesson (2007); better fitting would have been using 750 J/(kg K) according to the Task Description.

D3.5 Model performance

Thermal simulations are performed on a grid with 3 793 triangular 2D-axisymmetric elements and 13 484 nodes. Five elements are assigned to the distance across the buffer. Running time of the model is 24 s including stage 1 and stage 2. Note again, that stage 2 is approximated by simply switching off heater 1.

D3.6 Results

D3.6.1 Temperature

As mentioned above, the temperature increase at the boundary of the granitic block was checked. According to the results, the temperature increases at the observation point indicated in Figure D-6 after 6 717 days by 1.53 °C.

With respect to temperature, the following data are either requested by the task description or required for the subsequent re-saturation model:

- Evolution of temperature at P1 of sections D1, I, and D2 (see Figure D-7).
- Radial temperature profiles in cross-sections D1, I, and D2 (see Figure D-8).
- Axial temperature profiles along segments AS 1 and AS 2 (see Figure D-9).
- Radial temperature profiles in sections C and F2 (for water uptake calculations) (see Figure D-10 and Figure D-11).

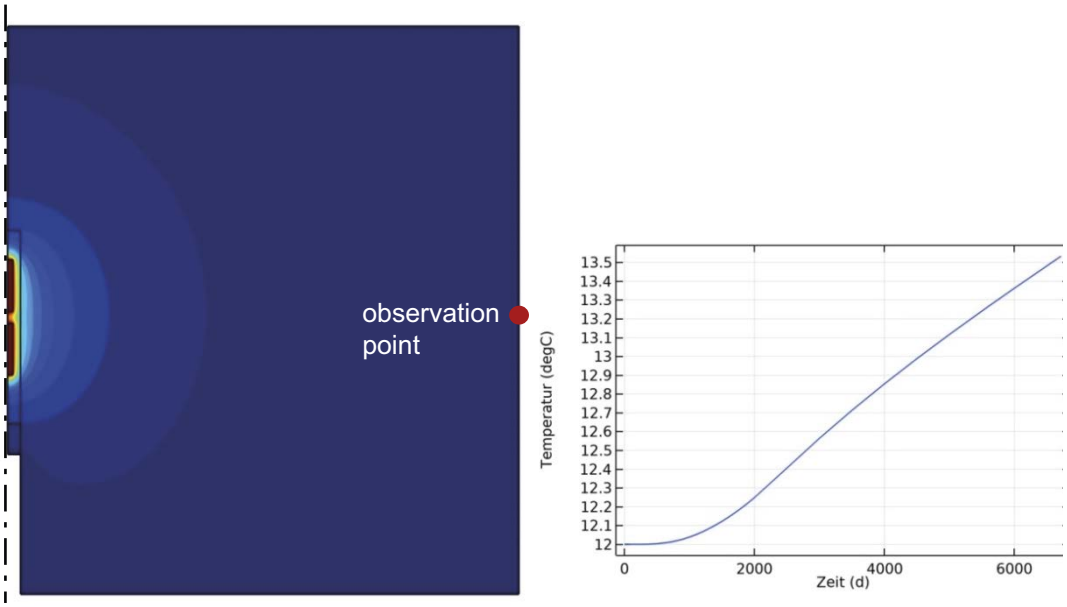

Figure D-6. *Temperature field after 18 years of heating; left: isolines and temperature observation point (red dot) right: breakthrough temperature at observation point.*

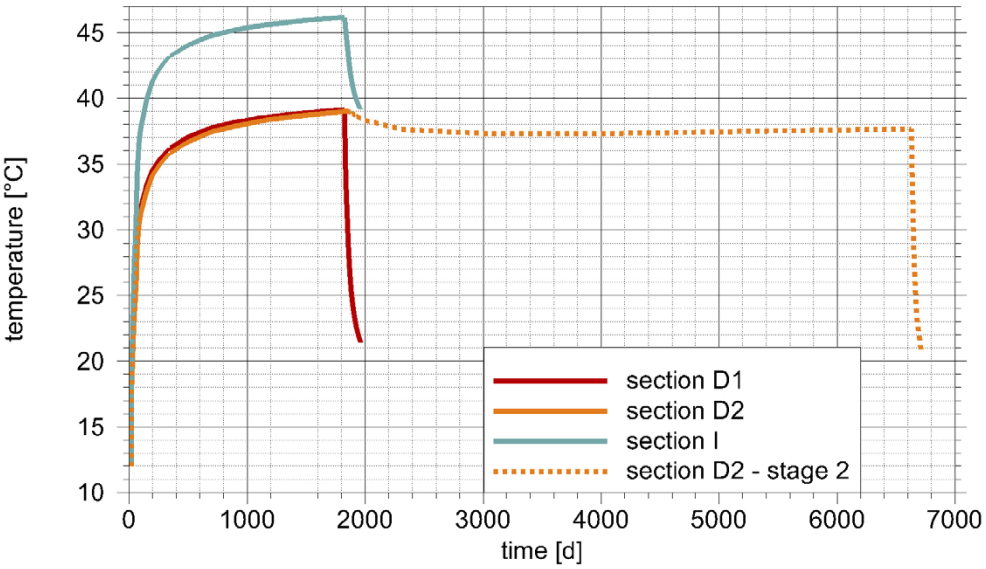

Figure D-7. *Temperature evolution at point P1 on sections D1, D2, and I.*

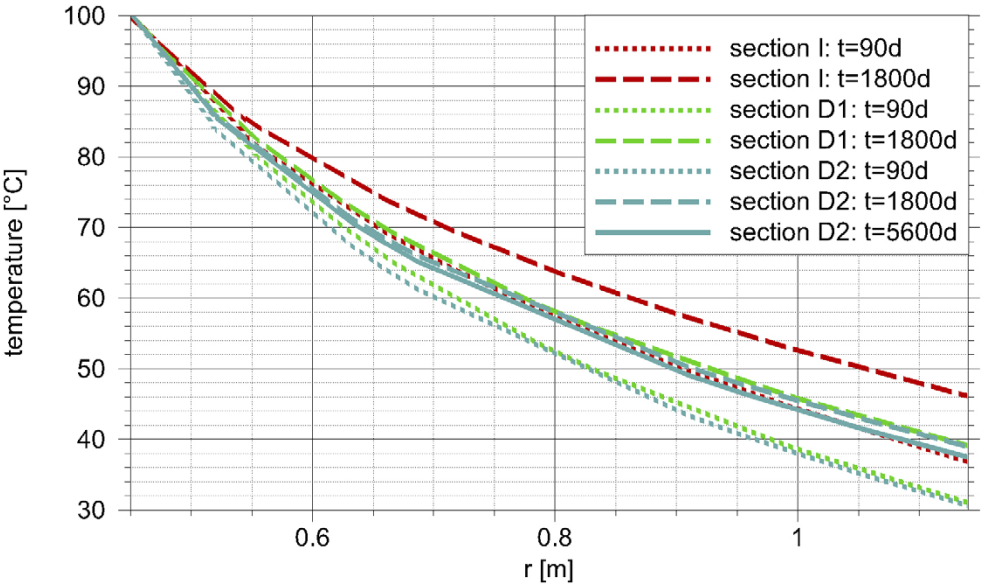

Figure D-8. *Temperature profiles for sections I, D1 and D2 at 90, 1 800, and 5 600 days.*

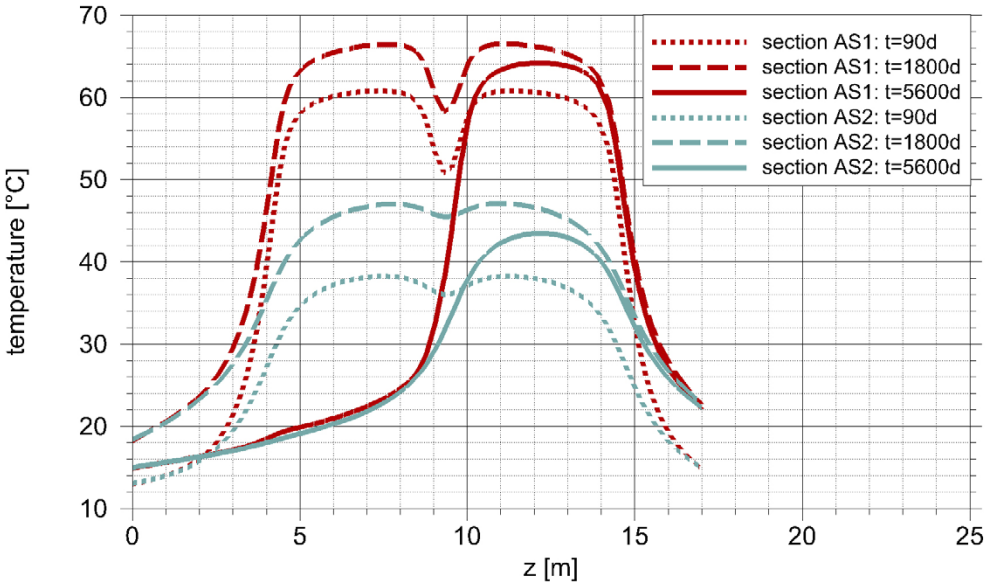

Figure D-9. *Temperature profiles for axial sections AS1 and AS2 at 90, 1 800, and 5 600 days.*

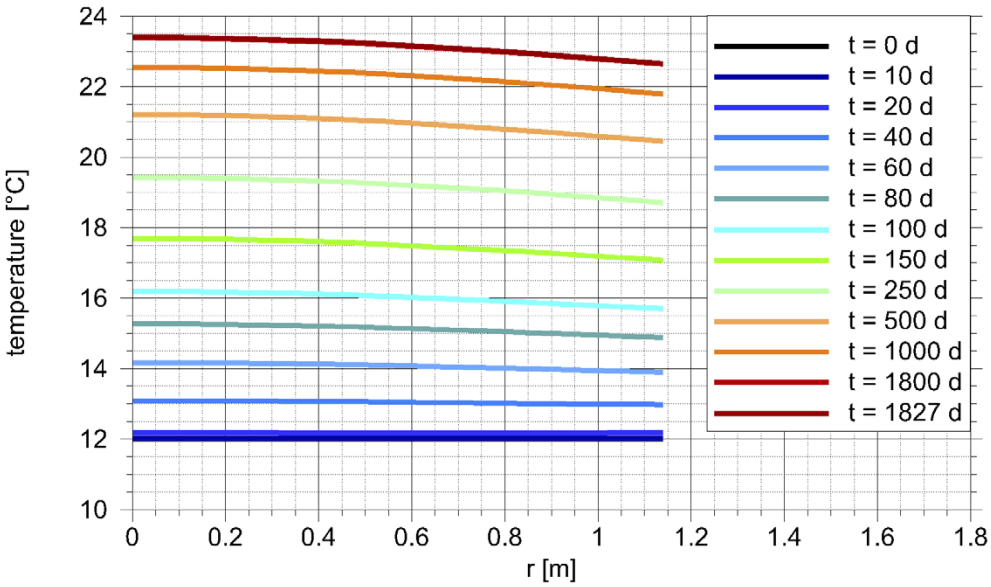

Figure D-10. *Transient radial temperature profiles in cross-section C.*

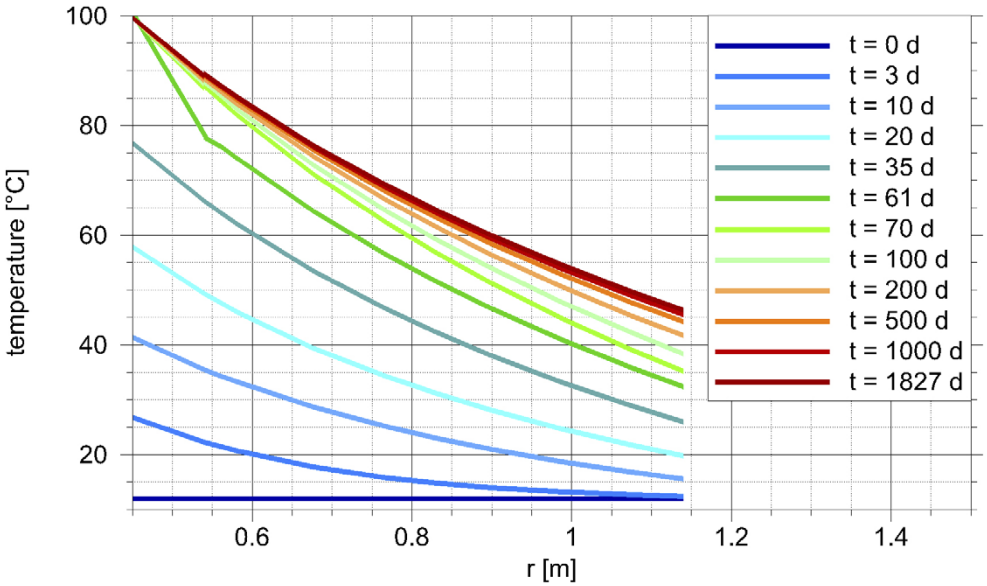

Figure D-11. *Transient radial temperature profiles in cross-section F2.*

D3.6.2 Evolutions of heating power

Back calculated from the temperature gradient at the respective heater surface is the power consumption over time. It is shown for stage 1 in Figure D-12 and for stages 1 and 2 in Figure D-13.

As has to be expected the calculations show similar curves for heaters 1 and 2 during stage 1 (see Figure D-12). After switching off heater 1 there is a slight increase of power consumption in heater 2 to compensate the loss of heat from neighbouring heater 1 (see Figure D-13). Contrary to the measurements the simulations do not reproduce the increase of power consumption that results from the increase of thermal conductivity due to increasing water content because this coupling has been neglected.

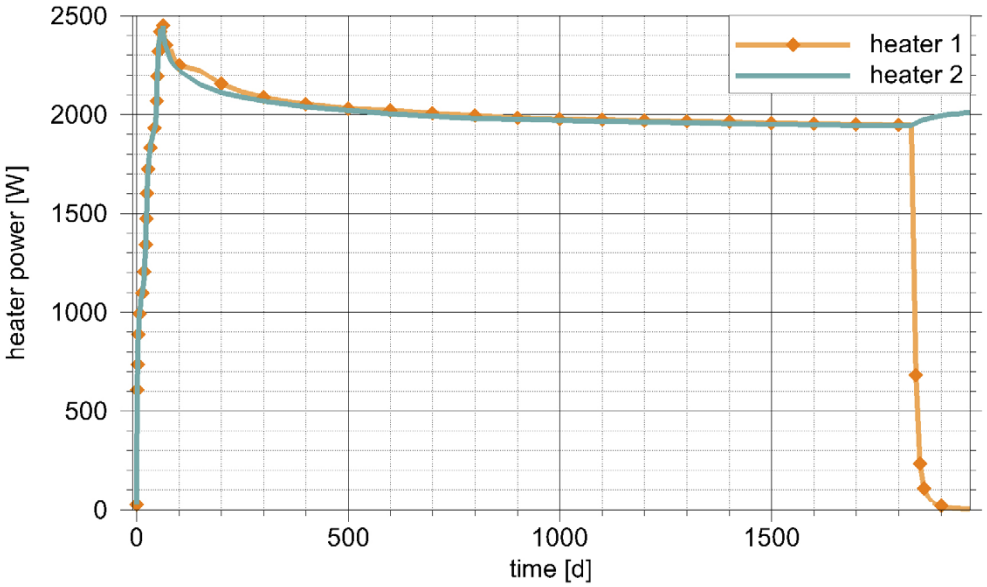

Figure D-12. *Evolution of power for heaters 1 and 2 during stage 1 at z = 6.60 m.*

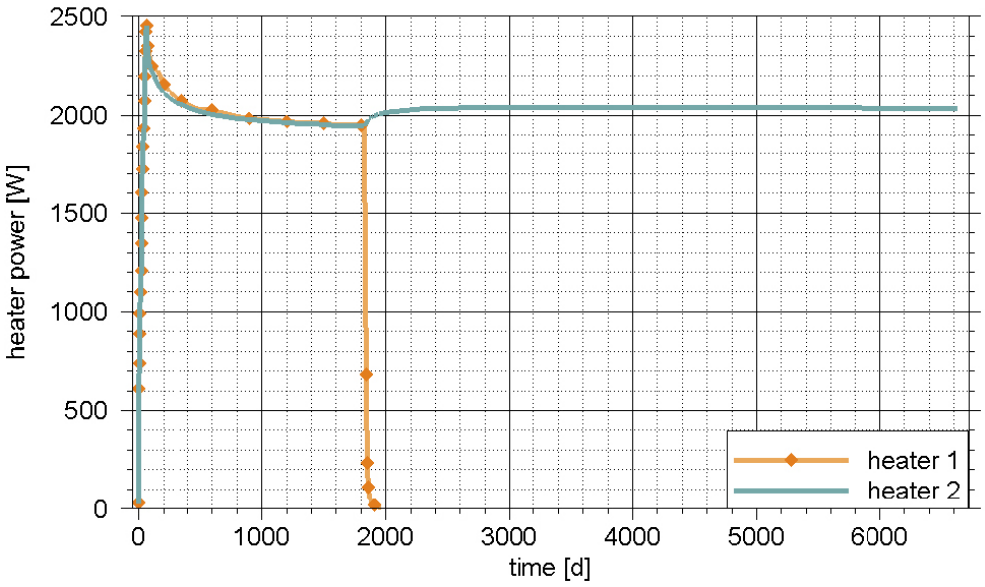

Figure D-13. *Evolution of power for heaters 1 and 2 during both stages at z = 6.60 m.*

D4 Water uptake Model

D4.1 Geometry

The restriction of the re-saturation simulating code VIPER to 1d-axial symmetry requires avoiding cross-sections with axial heat flow for modelling. What has been looked for are thus sections where the temperature gradient is orthogonal to the tunnel axis. As a basis for the choice of appropriate cutting planes Figure D-14 shows exemplarily the isolines of the temperature field around the heaters after 1 800 days. Apparently, the condition of no axial heat flux is met in the middle of the heaters, in the middle between the heaters and in close to the tunnel plug.

Illustrated in Figure D-15 are the cross-sections of interest in the task description in relation to tunnel and heaters. Sections E1 and H do not meet the requirement of no axial heat flow but sections C and F2 do so and are thus investigated further on. Figure D-16 shows the geometry of the re-saturation models.

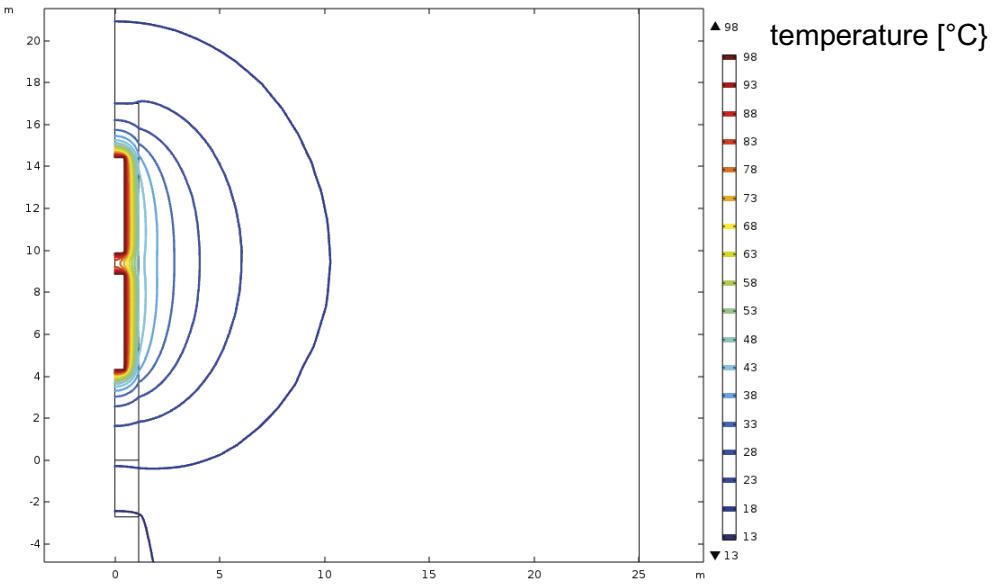

Figure D-14. *Temperature isolines around the heaters after 1 800 days.*

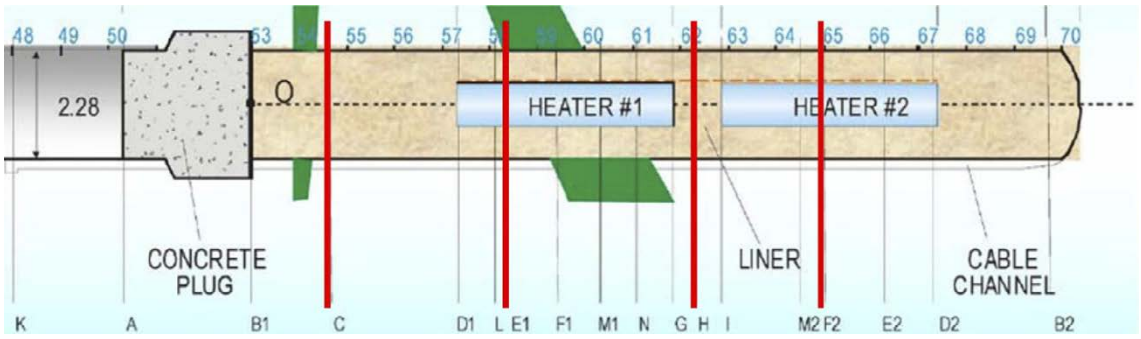

Figure D-15. *Experimental setup with the cross-sections of interest marked in red.*

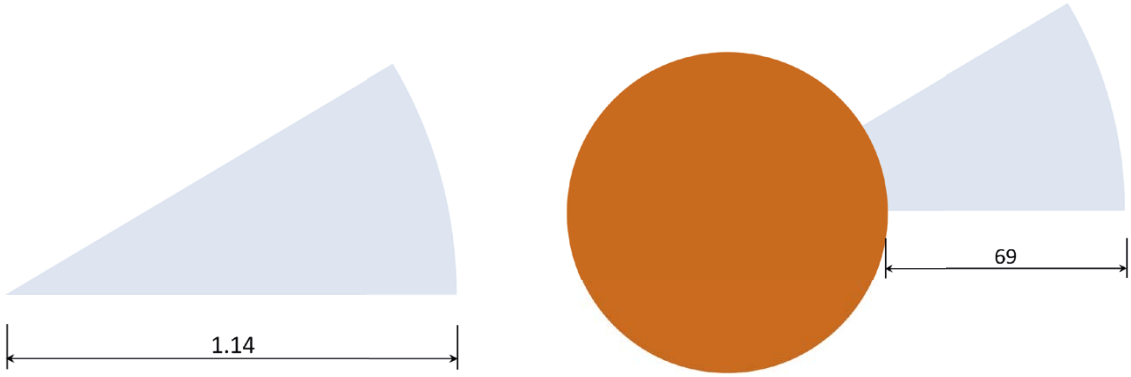

Figure D-16. *Model domain for the buffer in cross-sections C and F2.*

D4.2 Code and equations

The code VIPER (Kröhn 2011, Kröhn 2017) is used to simulate water-uptake and re-saturation of the bentonite. VIPER considers one-dimensional, axisymmetric wetting under unrestricted or restricted access to water, and includes vapour diffusion in the pore space, water diffusion in interlamellar space, and instantaneous exchange of water between these two spaces using an adsorption isotherm. Non-isothermal problems can be solved by using pre-determined transient temperature fields as input.

The conceptual background is therefore basically a double-continuum model which is composed of the intergranular pore space and the interlamellar space of the clay grains. Balance equations were set up for water vapour in the pore space as well as for hydrated water in the interlamellar space. In each balance equation, just one migration process is considered; vapour diffusion in the pore space and diffusion of hydrated water in the interlamellar space:

$$\frac{\partial\left(\Phi\rho_v\right)}{\partial t}-\nabla\left(\Phi\,\tau\,D_m\cdot\nabla\rho_v\right)=\tilde{r} \tag{D-2}$$

$$\rho_d\frac{\partial w}{\partial t}-\rho_d\,\nabla\left(\tau_{hyd}\,D'\cdot\nabla w\right)=\bar{r} \tag{D-3}$$

Symbols

Φ: porosity [-]

ρ: density [kg m^{-3}]

t: time [s]

τ: tortuosity of the pore space [-]

D_m: coefficient of binary vapour diffusion in air [m^2 s^{-1}]

w: gravimetric water content of the bentonite [kg_{water} kg_{solids}^{-1}]

τ_{hyd}: tortuosity of the interlamellar space [-]
D': coefficient of diffusion of the interlamellar water [m² s^{-1}]
$\overline{r}$: source of interlamellar water [kg m^{-3} s^{-1}]
$\tilde{r}$: source of vapour [kg m^{-3} s^{-1}]

Indices
d: dry state of the bentonite
v: vapour

The equations are linked by the process of hydration that is idealised as an instantaneous water exchange according to an isotherm[5], an equivalent to the more commonly used retention curve. Note that the isotherm changes shape with temperature, which is appropriately accounted for in the model. The model concept is schematically depicted for a horizontal two-dimensional domain in Figure D-17.

Possible boundary conditions are

- Full saturation in terms of vapour saturation density and maximum water content,
- Vapour saturation density but initial water content,
- Water inflow rate, or
- Closed boundary.

Initial conditions are given as a water content distribution.

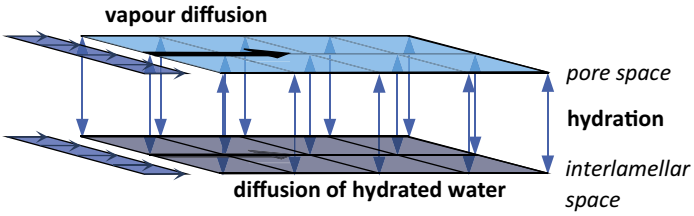

Figure D-17. *Processes acting according to the extended vapour diffusion model.*

[5] In the context of this report, the expression "isotherm" denotes the relationship between water content and relative humidity at a constant temperature.

D4.3 Material data

Crucial for the model is the temperature-dependent isotherm. The approach realised in VIPER starts with an established isotherm which is – as the name says – valid for a specific temperature. Such an isotherm for FEBEX-bentonite has been provided for Task 1 with the non-isothermal laboratory test by CIEMAT (Villar et al. 2005). In order to provide a continuous formulation for VIPER a polynomial of degree 5 has been fitted to the discrete data points (see Figure D-18).

Dependence on temperature is then introduced by a factor depending on temperature and relative humidity that has been based on data for MX-80 bentonite (Kröhn 2017). The family of curves resulting from applying such a deviation function is depicted in Figure D-19. Note that the maximum influence of temperature lies in the range of 70 % relative humidity.

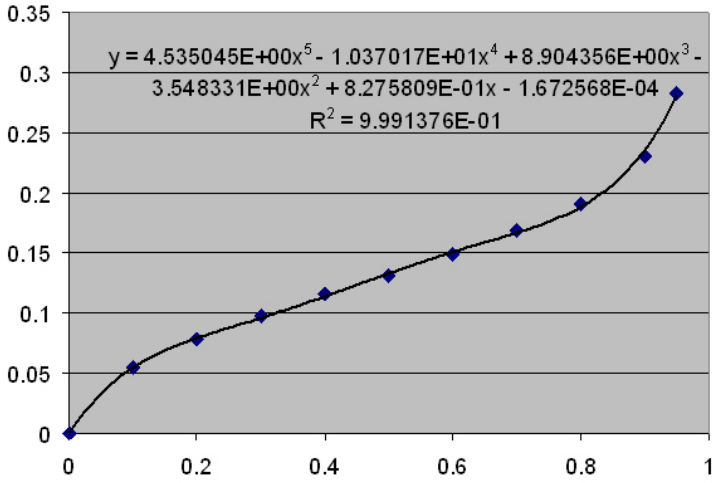

Figure D-18. *Mathematical approach for the isotherm for unconfined FEBEX-bentonite (Kröhn 2010).*

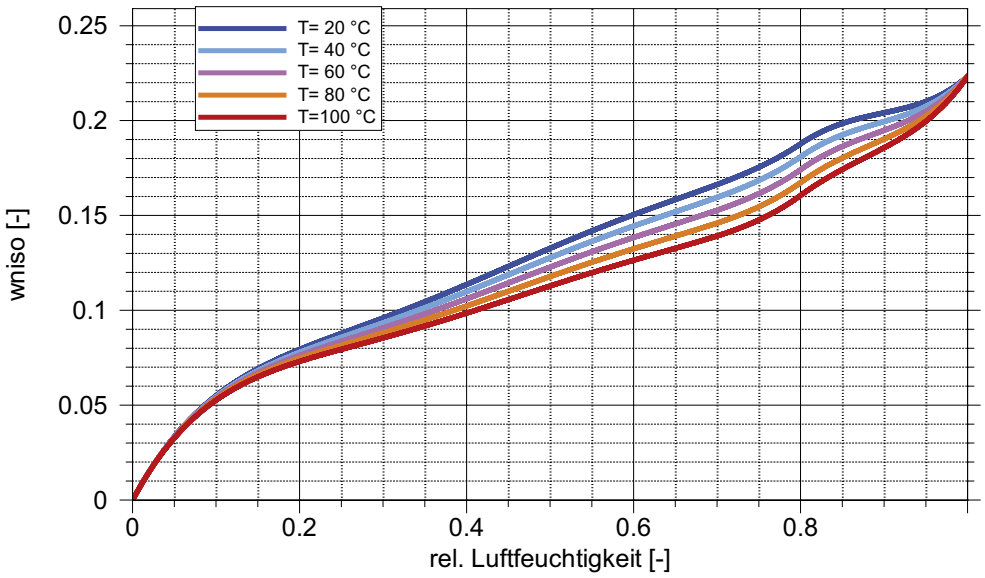

Figure D-19. *Temperature-dependent isotherm for confined FEBEX-bentonite (Kröhn 2010).*

The remaining parameters required by the model including their source are listed in Table D-4.

Table D-4. Material parameters for the re-saturation model.

Parameter	Value	Unit	Remarks
Tortuosity τ	0.65	[-]	general experience
End porosity Φ_e	0.05	[-]	guess based on Pusch et al. (1990)
Density of the solids	2700	[kg/m³]	Villar (2005)
Density of the interlamellar water	1000	[kg/m³]	(Assumption)

D4.4 Initial and boundary conditions

The following boundary conditions hold for the entire modelling time:

- Maximum water content at the granite contact (1.14 m): 22.3 %.
- Closed boundary at the axis (0 m) and at the heater surface (0.45 m), respectively.

The parameters for the initial state of the re-saturation model are compiled in Table D-5.

Table D-5. Parameters for the initial state of the re-saturation model.

Parameter	Value	Unit	Remarks
Bentonite dry density r_b[6]	1600	[kg/m³]	Task description
Relative humidity r_h	37.9	[%]	guessed from AITEMIN (2003)
Water content	11.0	[%]	From r_h and isotherm
Porosity Φ_i	23.1	[%]	geometric considerations

D4.5 Model performance

Re-saturation simulations are performed on a grid of 100 1D-axisymmetric elements with 101 nodes. A characteristic running time has been 186 s which includes the pre-heating stage of 135 days, stage 1 and stage 2.

D4.6 Results

The results of the re-saturation modelling are given in terms of either relative humidity or water content as distributions at a specific point in time or as breakthrough curves:

- Distributions of relative humidity (subsection D4.6.1)
  - Section C at the end of the pre-heating stage (Figure D-20)
  - Section C at 90, 300, and 1800 days (Figure D-21)
  - Section C at 90, 300, 1800, and 4000 days (Figure D-22)
- Evolutions of relative humidity (subsection D4.6.2)
  - Section C at 0, 60.4, and 112.2 cm from the tunnel axis (Figure D-23)
  - Section F2 at 58.4, 81.5, and 105.3 cm from the tunnel axis (Figure D-24)
- Water content and saturation after dismantling (subsections D4.6.3 and D4.6.4)
  - section F2 as a proxy to section 27 at 1968 days (Figure D-25)
  - section F2 as a proxy to section 49 at 6717 days (Figure D-26)

[6] The dry density of the bentonite is approximated by a constant, i.e. it does not change with water content.

D4.6.1 Distributions of relative humidity

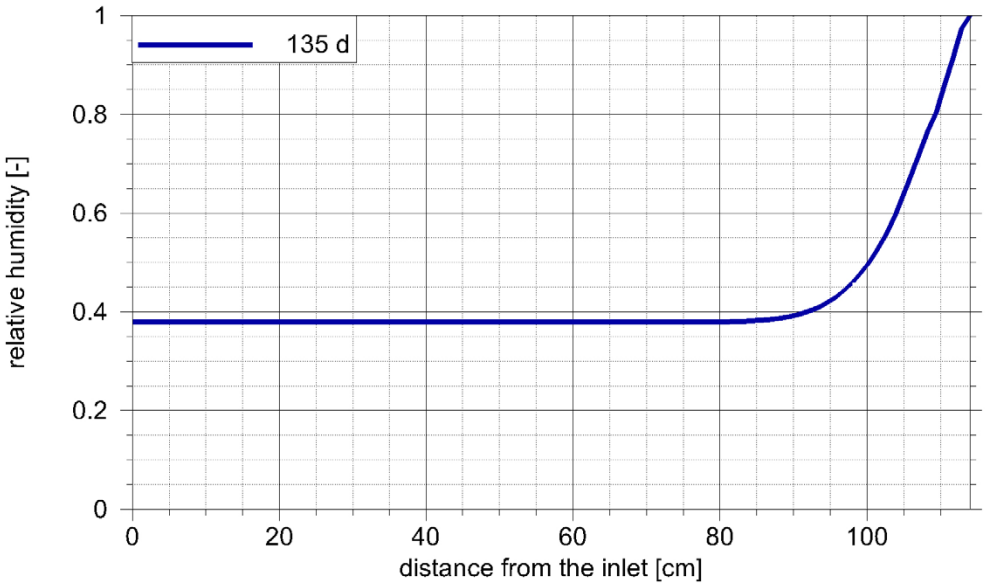

Figure D-20. *Isothermal water uptake after 135 days of isothermal uptake in section C.*

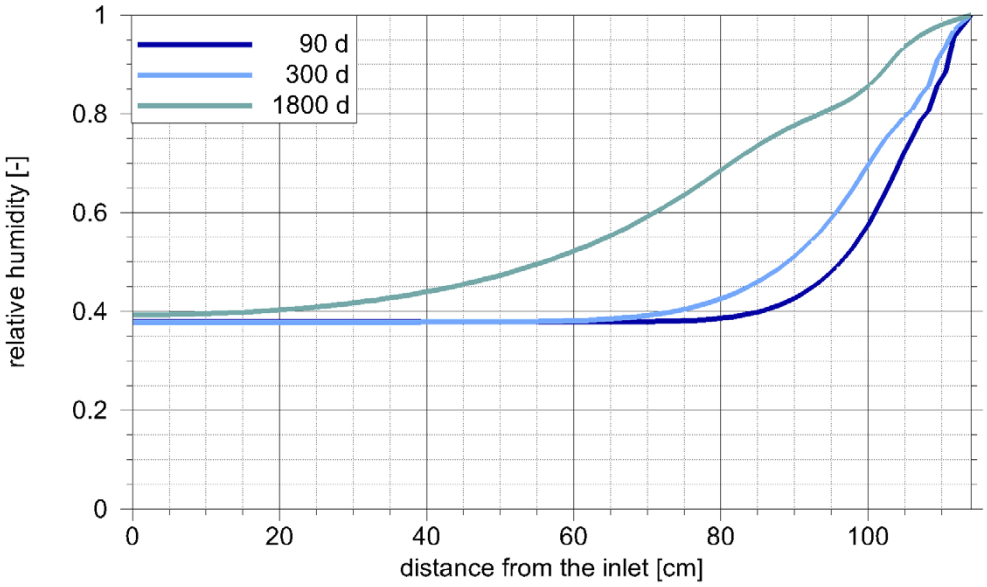

Figure D-21. *Distributions of relative humidity at appointed times in section C.*

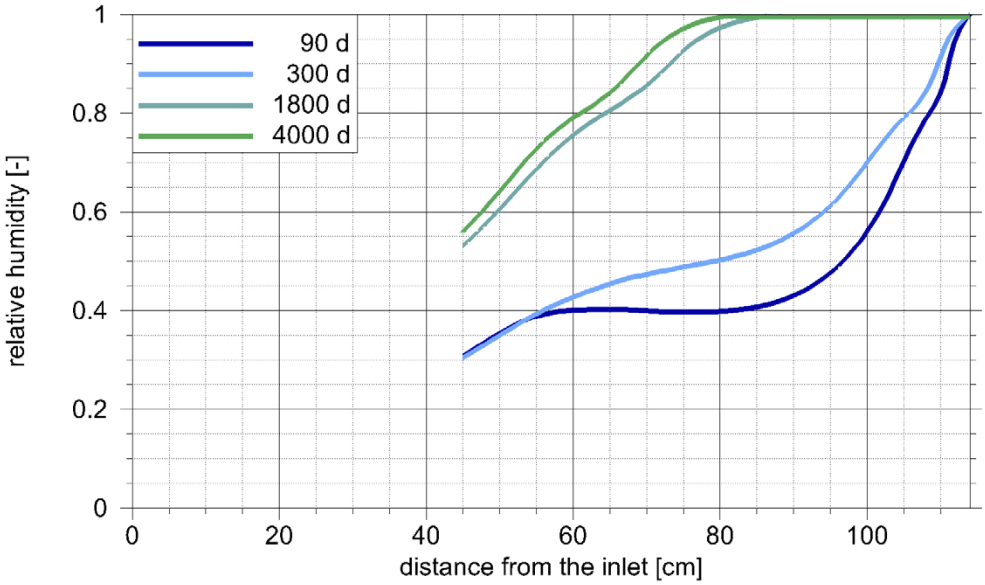

Figure D-22. *Distributions of relative humidity at appointed times in section F2.*

D4.6.2 Evolutions of relative humidity

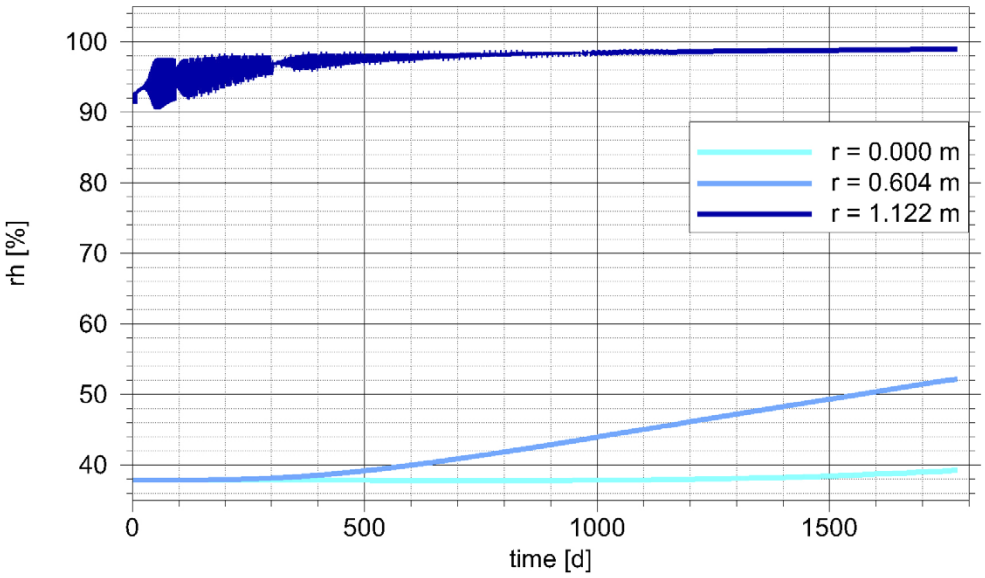

Figure D-23. *Evolutions of relative humidity at appointed locations in section C.*

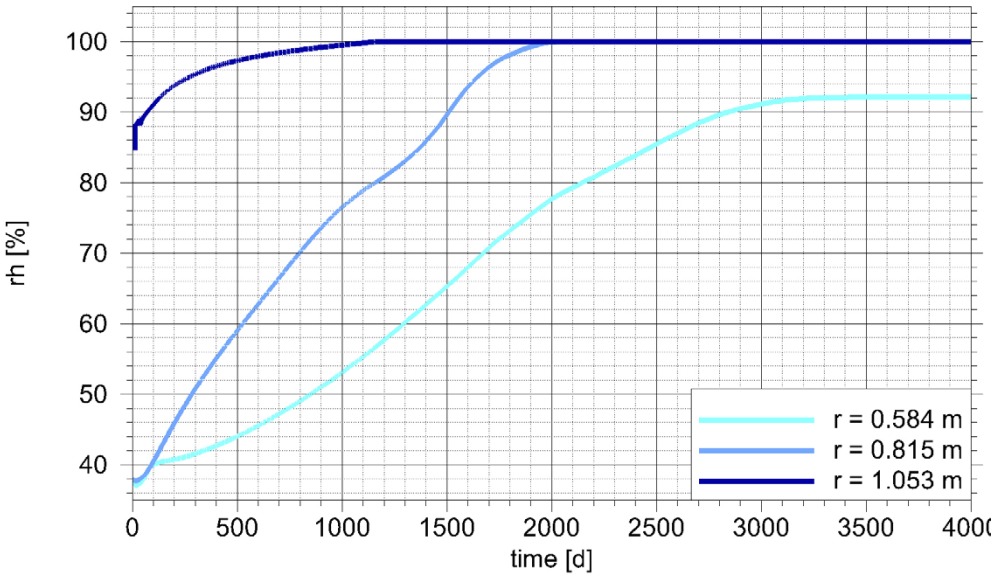

Figure D-24. *Evolutions of relative humidity at appointed locations in section F2.*

D4.6.3 Water content and saturation after dismantling of heater 1

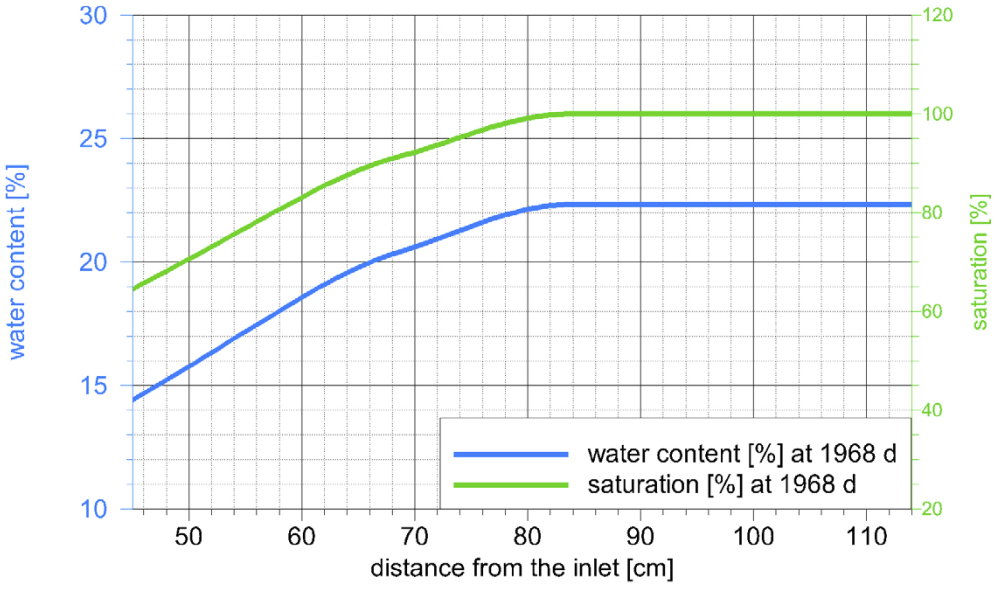

Figure D-25. *Water content and saturation in section F2 as a proxy to section 27.*

D4.6.4 Water content and saturation after dismantling of heater 2

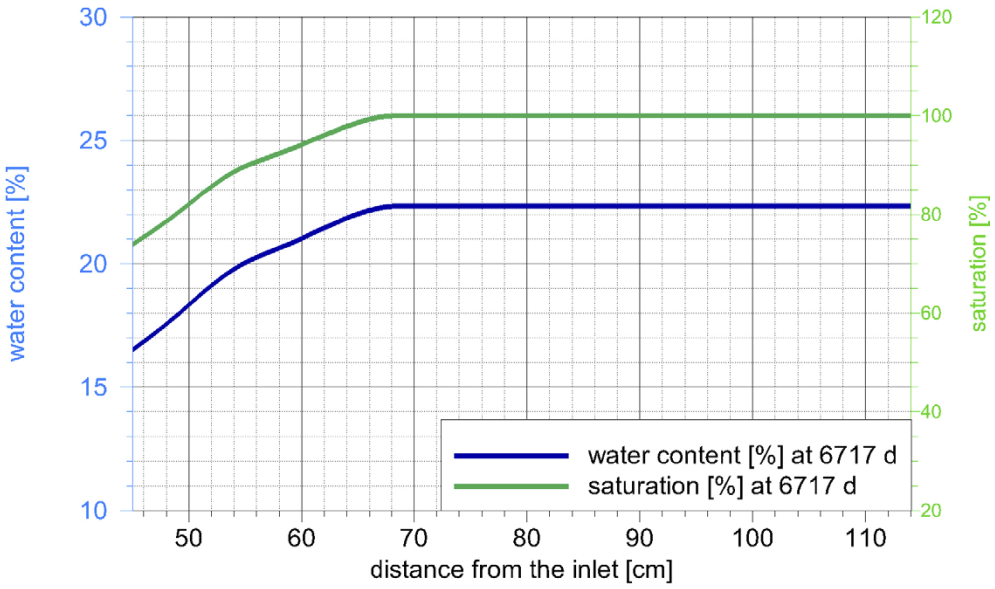

Figure D-26. *Water content and saturation in section F2 as a proxy to section 49.*

D5 Summary and conclusions

D5.1 Summary

The model used here for simulating the non-isothermal water uptake in the FEBEX in situ test is based on the following assumptions:

- Rock permeability is high enough to provide as much water as the bentonite can take up.
- Buffer and heater are thus considered to be 2d-axisymmetric.
- Re-saturation of the buffer has negligible impact on heat flow.

This set of assumptions allows for dropping flow modelling for the rock and for decoupling of heat flow from bentonite re-saturation. Therefore, heat flow is modelled first using COMSOL. Since the outer boundaries were treated as closed boundaries the size was chosen in such a way that the increase of temperature at these boundaries did not exceed roughly 1.5 °C. Unfortunately, decoupling prevented getting model results on the slow increase of power uptake over time, as this should be caused by the increase of thermal conductivity with the water content.

Using the experimental code VIPER for modelling bentonite re-saturation requires restriction to 1D-axisymmetric domains. Prerequisite for the hydraulic modelling is therefore that heat flow occurs orthogonal to the tunnel axis. Only cross-sections C and F2 thus qualify for the simulation of the relative humidity evolution. Based on symmetry considerations in the temperature field, section F2 is also taken as a proxy for sections 27 and/or 31. A pre-heating isothermal period of 135 days has been added to the calculations in the course of work on the FEBEX. Data for the bentonite have been chosen according to the non-isothermal CIEMAT test from Task 1 of the Task Force on EBS.

The following data are acquired from the thermal model:

- (1) Power uptake of heaters 1 and 2 after day 61
- (2) Radial temperature profiles in cross-sections
  - D1, I, and D2 as requested
  - C and F2 for water uptake calculations
- (3) Axial temperature profiles along segments AS 1 and AS 2

From the hydraulic model the following data are derived:

- (4) Evolution of temperature at P1 of sections D1, I, and D2
- (5) Distribution of relative humidity in sections C and F2
- (6) Evolution of relative humidity at three/two points in sections C and F2
- (7) Distributions of water content and degree of saturation at day 1968

Not calculated because of the model simplifications are

- evolutions of total stress and
- distributions of dry density at days 1968 and 6717.

The results have not been compared in detail with the measurements. A comparison of the resulting curves by eye confirms a reasonable fit, though.

D5.2 Conclusions

Decoupling of the thermal calculations from the hydraulic part seems to have rather little influence on the overall temperature field as well as on the relative humidity evolution in the bentonite buffer. The same observation has been made already with the two previous non-isothermal models that have been set up by GRS within the Task Force on EBS. The decoupling accelerates modelling considerably. A drawback is, however, that calculation the increase of power uptake of the heaters due to changes in the thermal conductivity is excluded by this measure.

D6 Data compilated for review

D6.1 Numerical data

General features of the numerical analysis

- Type of analysis; dimensionality
  - Thermal model: 2D-axisymmetric
  - Re-saturation model: 1D-axisymmetric
- Type of analysis; coupling
  - TH
  - Thermal calculations coupled to hydraulic calculations but not vice versa
- Size of the analysis domain
  - Thermal: length of 50 m, radius of 45 m
  - Hydraulic: length 69 and 114 cm, respectively, depending on presence of heater
- Type and number of elements
  - Thermal: 3 793 triangular elements that are expanded into 3D-space by axial symmetry and 13 484 nodes
  - Hydraulic: 100 linear 1D-axisymmetric elements
- Number of elements across the bentonite barrier: 100
- Number of nodes
  - Thermal: 13 484 nodes
  - Hydraulic: 101 nodes

Stages of the analysis and boundary conditions

Stage number	Brief description	Start time (day)	Duration (days)
1	End of installation (pre-heating)	−135	135
2	Heaters 1 200 W	0	20
3	Heaters 2 000 W	20	32
4	Approaching 100 °C	52	8
5	Both heaters at 100 °C	60	1 767
6	Switching off heater 1 and dismantling	1827	41
7	Undisturbed test with heater 2 only	1968	4 749
8	Switching off heater 2	6717	

Initial variables and key parameters

- Thermal model
  An initial temperature of 12 °C is assumed throughout the system. The same temperature is assigned to the surfaces of the tunnel and of the plug at all times. The faces and the lateral surface of the cylindrical piece of granite are assumed to be thermally insulated, also for the whole modelling time.

  Material data are taken from the parameter library of COMSOL except for the buffer where the data is based on Kristensson and Börgesson (2007) and Gens (2018).

	Granite	Concrete	Buffer	Heaters
Thermal conductivity [W/(m K)]	3.3	1.8	1[7]	44.5
Specific heat capacity [J/(kg K)]	850	880	800[8]	475
Density [kg/m³]	2 600	2 300	2 780	7 850

[7] Relates to a degree of saturation of S = 0.85 according to Annex 2 in Gens (2018).

[8] Chosen erroneously after Kristensson and Börgesson (2007); better fitting would have been using 750 J/(kg K) according to the Task Description.

- Hydraulic model

Parameters for the initial state of the re-saturation model

Parameter	Value	Unit	Remarks
Bentonite dry density r_b	1600	[kg/m³]	Task description
Relative humidity r_h	37.9	[%]	guessed from AITEMIN (2003)
Water content	11.0	[%]	From r_h and isotherm
Porosity Φ_i	23.1	[%]	geometric considerations

Material parameters for the hydraulic model

Parameter	Value	Unit	Remarks
Tortuosity τ	0.65	[-]	general experience
End porosity Φ_e	0.05	[-]	guess based on Pusch et al. (1990)
Density of the solids	2700	[kg/m³]	Villar (2005)
Density of the interlamellar water	1000	[kg/m³]	(Assumption)

Data for the isotherm are taken from Kröhn (2010) which are based on Villar (2005).

D6.2 Rock

Just one rock material is considered in the analysis.

Initial conditions of the rock at the start of the analysis (1)

Initial temperature at tunnel axis level (°C)	Initial stresses at tunnel axis level (MPa)	Initial pore water pressure at tunnel axis level (MPa)
12	(not applicable; no mechanics)	(not applicable)

Initial conditions of the rock at the start of the analysis (2)

Initial density (g/cm³)	Initial porosity	Initial water content (%)
2.6	(not applicable; changes in the rock are not considered)	

Main rock properties (1)

Initial thermal conductivity (W/mK)	Specific heat capacity (J/kgK)	Initial intrinsic permeability (m^2)	Initial hydraulic conductivity (m/s)
3.3	850	(not applicable; flow not considered)	

Main rock properties (2)

Linear thermal expansion coefficient (K^{-1})	Young's modulus (MPa)	Poisson's ratio
(not applicable; no mechanics)		

Main rock properties: retention curve (3)

Equation used	Parameter 1 (units)	Parameter 2 (units)	Parameter 3 (units)	Parameter 4 (units)
(not applicable; flow not considered)				

Main rock properties: relative permeability (4)

Equation used	Parameter 1 (units)	Parameter 2 (units)	Parameter 3 (units)	Parameter 4 (units)
(not applicable; flow not considered)				

D6.3 Bentonite

Initial conditions of the bentonite at installation (1)

Initial temperature (°C)	Initial stresses (MPa)	Initial pore water pressure/suction (MPa)	Initial relative humidity (%)
12	(not applicable)	(not applicable)	37.9

Initial conditions of the bentonite at installation (2)

Initial dry density (g/cm^3)	Initial density of the solid phase (g/cm^3)	Initial porosity	Initial water content (%)	Initial degree of saturation (%)
1.600	2.700	0.231	11	(not calculated)

Note: It is recommended (but not compulsory) to use a density of the solid phase of 2.7 g/cm^3 to compute initial dry density (or porosity) and initial degree of saturation. Please, specify if a different value has been used.

Main bentonite properties (1)

Initial thermal conductivity (W/mK)	Initial thermal conductivity dry bentonite (W/mK)	Initial thermal conductivity saturated bentonite (W/mK)	Initial specific heat capacity of the solid phase (J/kgK)	Linear thermal expansion coefficient (K^{-1})
(not applicable, values constant over time)				

Main bentonite properties (2)

Initial intrinsic permeability (m^2)	Initial hydraulic conductivity (m/s)	Initial intrinsic permeability (saturated) (m^2)	Initial hydraulic conductivity (saturated) (m/s)	Swelling pressure under initial conditions (oedometric conditions) (MPa)
(not applicable; no liquid water flux considered)				

Note: A virtual swelling pressure test (oedometric conditions) may be required to determine the swelling pressure of the bentonite under initial conditions.

Main bentonite properties: permeability dependence on dry density (or porosity) (3)

Equation used	Parameter 1 (units)	Parameter 2 (units)	Parameter 3 (units)	Parameter 4 (units)
(not applicable; no liquid water flux considered)				

Notes: Please, replace “Parameter 1” etc... by the symbol used in your equation.

• If permeability is assumed not to depend on dry density or porosity, state so under “Equation used”.

Main bentonite properties: retention curve; actually, an isotherm was used (4)

Equation used	
$w(\mathrm{rh}) = a_0 + \sum_{n=1}^{5} (a_n\ \mathrm{rh}^n)$ water content *w* relative humidity r_h	a_0 [-] = −1.672568e−4 a_1 [-] = 8.275809e−1 a_2 [-] = 3.548331 a_3 [-] = 8.904356 a_4 [-] = −10.37017 a_5 [-] = 4.535045

Note: Please, replace “Parameter 1” etc... by the symbol used in your equation.

Main bentonite properties: relative permeability (5)

Equation used	Parameter 1 (units)	Parameter 2 (units)	Parameter 3 (units)	Parameter 4 (units)
(not applicable; no liquid water flux considered)				

Note: Please, replace “Parameter 1” etc... by the symbol used in your equation.

Main bentonite properties: thermal conductivity (6)

Equation used	Parameter 1 (units)	Parameter 2 (units)	Parameter 3 (units)	Parameter 4 (units)
(not applicable; no dependence on liquid water flux considered)				

Note: Please, replace “Parameter 1” etc... by the symbol used in your equation.

Main bentonite properties: vapour transport (7)

Molecular diffusion coefficient of vapour in free air (m^2/s)	Tortuosity
2.16e−5 at 0 °C	0.65

Main bentonite properties: vapour transport (8)

Diffusion coefficient of water in the interlayer (m^2/s)	Interlayer-tortuosity
1.0e−9 at 0 °C for w < 17 % 2.0e−9 at 0 °C for w > 17 %	0.40

Constitutive functions

- Permeability (or saturated hydraulic conductivity) vs dry density (or porosity)
  (not applicable; no liquid water flux considered)
- Retention curve of the bentonite → isotherm

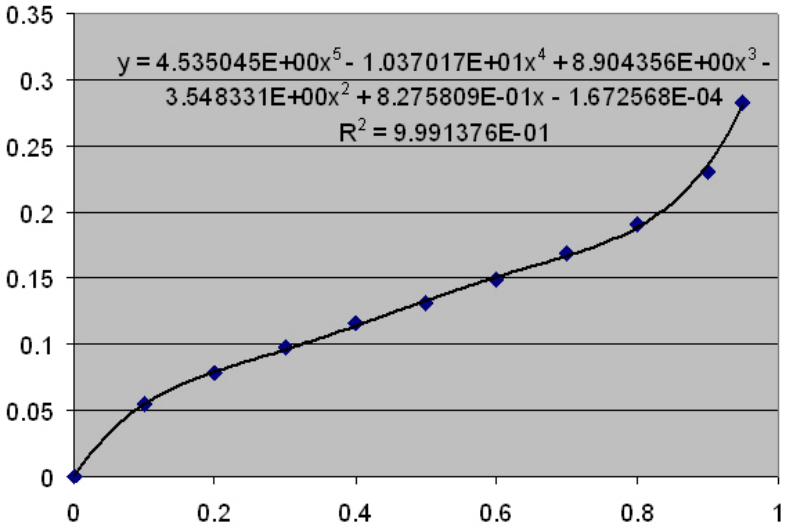

- Retention curve of the rock
  (not applicable; no liquid water flux considered)
- Relative permeability of the bentonite
  (not applicable; no liquid water flux considered)
- Relative permeability of the rock
  (not applicable; no liquid water flux considered)
- Thermal conductivity of the bentonite vs degree of saturation
  (not applicable; coupling of hydraulic to thermal model neglected)
- Molecular vapour diffusion vs temperature

$$D_m = D_{m\,0}\left(\frac{T}{T_0}\right)^{\theta}$$

Appendix E

ICL Report

Imperial College London, modelling team, UK (ICL)
Giulia M Ghiadistri, Lidija Zdravkovic, David M Potts, Aikaterini Tsiampousi

E1 Introduction

This report details the numerical study of stage 1A, 1B and stage 2 of the FEBEX in situ test.

E2 General features of the numerical model

An axi-symmetric THM coupled analysis of the FEBEX in situ experiment is performed in ICFEP. The discretised domain, shown in Figure E-1, has an axis of symmetry along the y-direction. It includes the entire FEBEX drift, comprising the concrete plug and the surrounding host rock, both behind the tunnel face and around the tunnel walls. The axis of the drift coincides with the axis of symmetry. The dimension of the domain, namely the extension of the rock to be included in the analysis, was chosen after preliminary, two-dimensional (2D) plane strain analyses were carried out on the drift's transverse section, providing an estimation of the area perturbed by the experiment. The mesh in Figure E-1 employs 2016 8-noded quadrilateral elements. In particular, there are 10 elements across the thickness of the bentonite buffer in sections of the drift where the heater is also present (for example, section F2 where the thickness of the bentonite is 1.14 m – 0.45 m = 0.69 m) and 16 elements where sections comprise bentonite only (for example, section G where the thickness of the bentonite is 1.14 m). The geometry of the FEBEX drift was divided into several sections, as are shown in Figure E-2.

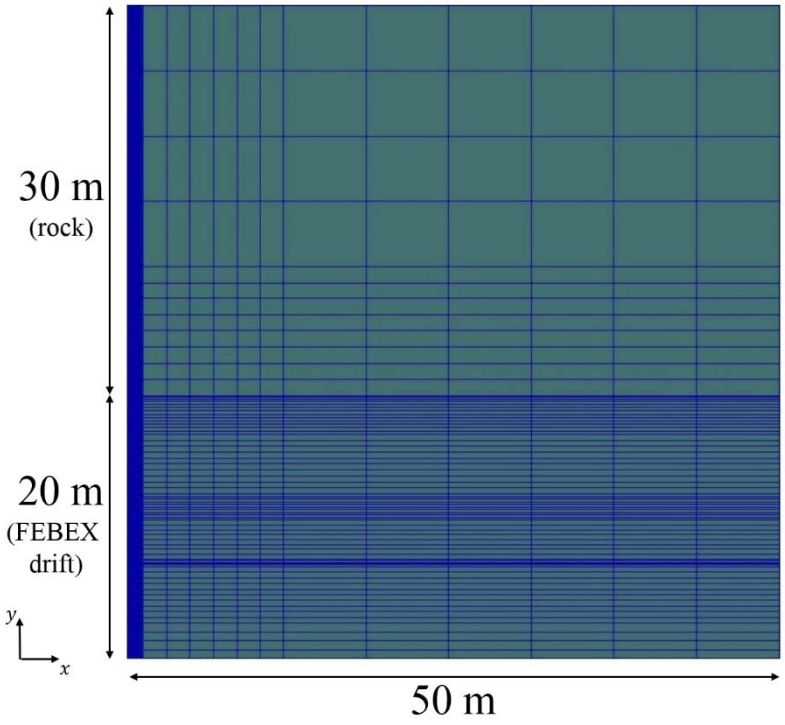

Figure E-1. *Finite element mesh for the analysis of the FEBEX in situ experiment.*

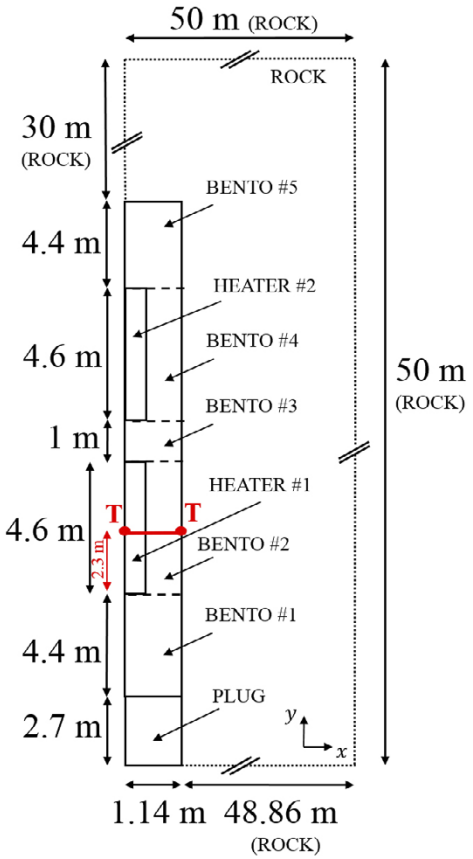

Figure E-2. *Geometry of the domain of the axi-symmetric analysis of the FEBEX in situ experiment.*

E3 Boundary conditions

Throughout the analysis, the mechanical boundary conditions impose zero horizontal (i.e. parallel to the x-axis) displacements on the vertical boundaries of the mesh, zero vertical displacements (i.e. parallel to the y-axis) on the base and top surfaces. In terms of hydraulic boundary conditions, the rock is assumed to be an infinite source of water, hence no change in pore water pressure is imposed on the right-hand side and top boundaries of the mesh. Equally, in terms of thermal conditions, no change in temperature is imposed on these boundaries. The remaining boundaries are assumed to have no hydraulic flow or temperature flux across them. The simulation reproduces the course of the experiment, from the installation to the end of stage 2, including: the excavation of the FEBEX drift, the construction and installation of the buffer and the two heaters, Stage 1 of operation, the first dismantlement and, finally, Stage 2 of operation. The installation was completed 135 days before heating was started, and this explains the delayed RH increase in the bentonite close to the rock. The phases are articulated as indicated in Table E-1, giving the duration of each phase, a brief description of the activity and the corresponding boundary conditions applied. It is specified that the start of the heating coincides with “Stage 1: temperature increase”.

Table E-1. phases of the FEBEX three-dimensional analysis.

	Time	Description	Action
Initial conditions	-	All mesh is rock	-
Set up and installation	24 days	Excavation of the FEBEX drift (all excavated parts are rock at this stage)	Deactivation 1st plug and bento #1 Deactivation bento #2 and heater #1 Deactivation bento #3 and #4 and heater #2 Deactivation bento #5
	42 days	Construction of buffer, heaters and plug	Construction of bento #5 Construction of bento #4 Construction of heater #2 Construction of bento #3 Construction of bento #2 Construction of heater #1 Construction of bento #1 Construction of 1st plug
Stage 1	60 days	Temperature increase	Thermal gradient of ΔT = 0.733 °C applied during 120 increments of the analysis in the heaters
	1665 days	Stage 1 operation	Imposed temperature T = 100 °C in both heaters
1st dismantling operations	30 days	Heater 1 switched off	Thermal gradient of ΔT = −2.5 °C applied during 30 increments of the analysis in heater #1
	81 days	Excavation for first dismantling	Deactivation of 1st plug Deactivation of bento #1 Deactivation of heater #1 Deactivation of part of bento #2
	16 days	Construction of dummy canister and new plug	Construction of the dummy canister Construction of the 2nd plug
Stage 2	4300 days	Stage 2 operation	Heater #2 is still functioning as before.

E4 Initial conditions

The initial conditions of the rock are reported in Table E-2, whereas those of the buffer are given in Table E-3. The initial total stress in the rock is set to the same value in both the vertical and horizontal direction in agreement with the assumed axi-symmetric conditions.

Table E-2. Initial conditions of the rock.

Parameter	Rock
Suction, s (MPa)	−4.5
Vertical stress, σ_v (MPa)	28
Horizontal stress, σ_h (MPa)	28
Temperature, T (°C)	10

Table E-3. Initial conditions of the bentonite.

Parameter	Bentonite
Suction, s (MPa)	120
Vertical stress, σ_v (MPa)	0
Horizontal stress, σ_h (MPa)	0
Temperature, T (°C)	12
Dry density, ρ_d (g/cm^3)	1.65
Degree of Saturation, S_r (%)	50
Hydraulic conductivity (at 120 MPa of suction), h (m/s)	0.8×10^{-14}
Thermal conductivity, (kW/mK)	0.55×10^{-3}

E5 Finite element Code

All analyses presented in this report have been carried out using the finite element code ICFEP, Potts and Zdravkovic (1999). A fully-coupled thermo-hydro-mechanical (THM) formulation is herein implemented and has been used to study the FEBEX experiment. The formulation of the governing finite element equations for THM analysis, as implemented in ICFEP, can be found in Cui et al. (2018).

E6 Materials and constitutive models

Three materials have been employed in the analyses:

1) *granite rock*, modelled using the unsaturated Mohr-Coulomb model (Smith 2003);
2) *FEBEX bentonite*, modelled using the Imperial College Double Structure Model (IC DSM, Ghiadistri et al. 2018, Ghiadistri 2019);
3) *steel canister and concrete plug*, assumed to be thermally inactive and non-consolidating.

A brief description of the IC DSM is given in the next subsections.

E6.1 IC DSM

The Imperial College Double Structure Model (IC DSM, Ghiadistri et al. 2018, Ghiadistri 2019) has been adopted to model bentonite. Comparisons with the performance of the Imperial College Single Structure Model (IC SSM, Georgiadis et al. 2003, 2005, Tsiampousi et al. 2013) have been drawn where relevant.

E6.1.1 Background to IC DSM model development

The IC DSM double-structure model for unsaturated highly expansive clays is developed in the framework of elasto-plasticity and critical state-based soil mechanics. The model is an extension of a single structure model, IC SSM, developed for unsaturated moderately expansive clays, and described in Georgiadis et al. (2003, 2005), Tsiampousi et al. (2013). The IC SSM is a modified and generalised version of the Barcelona Basic Model (BBM, Alonso et al. 1990), while IC DSM adopts the conceptual basis of the Barcelona Expansive Model (BExM, Gens and Alonso 1992, Sanchez et al. 2005). Both IC SSM and IC DSM are implemented in ICFEP, which is applied here to demonstrate the performance of the double-structure model.

E6.1.2 Scope and hypotheses

Double-porosity structure

The formulation of the IC DSM adopts the concept of double porosity in the structure of a compacted clay. One level of porosity is the void space between the clay aggregates, defined as macro- or inter-aggregate porosity (as sketched in Figure E-3). The second level of porosity is the void space within an aggregate, defined as micro- or intra-aggregate porosity (Figure E-3). Macro-porosity is associated with the evolution of negative pore water pressures (suctions) in the clay, while micro-porosity

governs the physico-chemical processes associated with the clay mineralogy. It is believed that the interaction between the two levels of structure upon saturation of compacted clays contributes to their swelling potential, which is the principal mechanism of developing a protection layer around nuclear waste canisters.

The existence of this structure is evidenced by the electro-scanning micrographs (ESEMs) of compacted clay and/or mercury intrusion porosimetry (MIP) tests performed on samples of compacted clay (e.g. Romero 1999, Sanchez et al. 2005, Monroy et al. 2010, Seiphoori et al. 2014). Example graphs in Figure E-4(a) show a clear dual concentration of pore sizes in compacted FEBEX bentonite, with the dominant intra-aggregate (micro) pore size of ~10 nm, and the inter-aggregate (macro) pore size greater than ≥ 10 µm. The figure also shows the dependency of the macro-porosity on the dry density, ρ_d, of the compacted clay, with a larger value of ρ_d (= 1.8 Mg/m^3) generating larger and a greater quantity of macro-pores, compared to the sample of lower ρ_d (= 1.5 Mg/m^3). Figure E-4(b) shows a very similar double porosity initial structure for compacted MX-80 bentonite ("as compacted" curve). Additionally, it also shows that, upon full hydration, the macro-pores seem to disappear, leaving a higher concentration of micro-pores ("fully saturated" curve). This interaction creates a low-permeability buffer, which should prevent the escape of radionuclides into the surrounding ground.

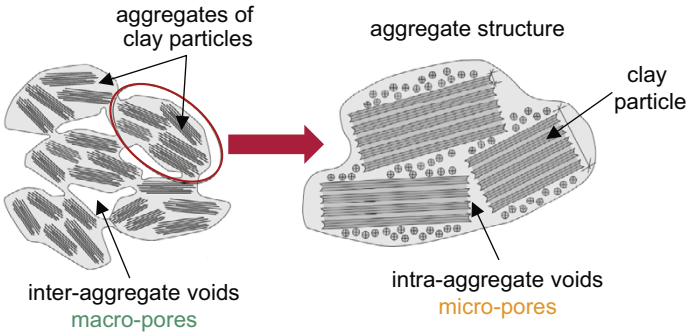

Figure E-3. *Conceptual illustration of a double-porosity structure in compacted clays.*

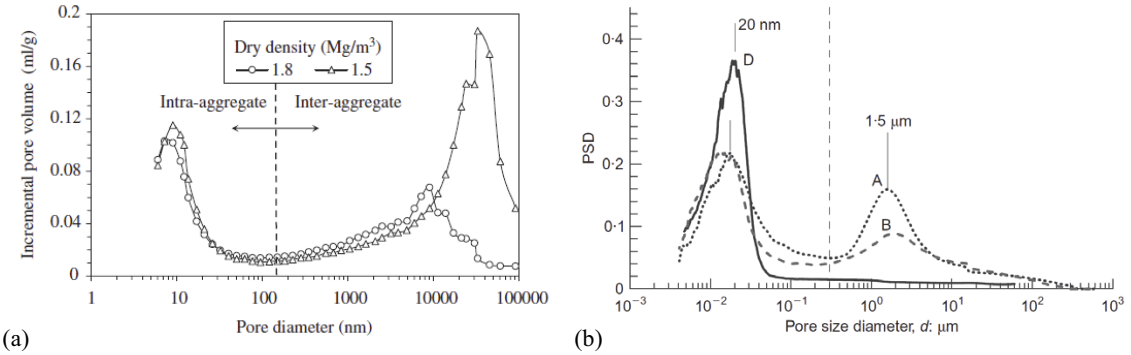

Figure E-4. *MIP evidence of a double-porosity structure in compacted clays: (a) compacted FEBEX bentonite (Sanchez et al. 2005); (b) compacted MX-80 bentonite (Seiphoori et al. 2014).*

Stress variables

The mathematical formulation of the IC DSM adopts two independent stress variables to describe the mechanical behaviour of unsaturated soils: the matric suction, $s = u_{air} - u_w$, defined as the difference between the air pressure, u_{air}, and water pressure, u_w, in the macro pores; and net stress, $\bar{\sigma} = \sigma_{tot} - u_{air}$, defined as the difference between the total stress, σ_{tot}, and the pore air pressure. Additionally, to enable a seamless transition from a saturated to an unsaturated state, and vice versa, the model introduces the equivalent suction, $s_{eq} = s - s_{air}$, where s_{air} is the air-entry value of suction. This necessarily leads to the introduction of equivalent stress, $\sigma = \bar{\sigma} + s_{air}$.

E6.1.3 IC DSM model formulation

The IC DSM model is generalised in the $J - p - \theta - s_{eq}$ space, as an extension of the IC SSM model, where p is the mean equivalent stress (Equation E-1), J is the generalised deviatoric stress (Equation E-2), and θ is the Lode's angle (Equation E-3).

$$p = \frac{\sigma_x + \sigma_y + \sigma_z}{3} \tag{E-1}$$

$$J = \left(\frac{1}{6}\left[\left(\sigma_x - \sigma_y\right)^2 + \left(\sigma_y - \sigma_z\right)^2 + (\sigma_x - \sigma_z)^2\right] + \tau_{xy}^2 + \tau_{xz}^2 + \tau_{yz}^2\right)^{1/2} \tag{E-2}$$

$$\theta = -\frac{1}{3} \cdot \sin^{-1}\left[\frac{3\sqrt{3}}{2} \cdot \frac{\det \boldsymbol{s}}{J^3}\right] \tag{E-3}$$

where

$$\det \boldsymbol{s} = \begin{vmatrix} \sigma_x - p & \tau_{xy} & \tau_{xz} \\ \tau_{xy} & \sigma_y - p & \tau_{yz} \\ \tau_{xz} & \tau_{yz} & \sigma_z - p \end{vmatrix} \tag{E-4}$$

Similarly, the strain invariants ε_{vol} (volumetric strain) and E_d (generalised deviatoric strain) are calculated as:

$$\varepsilon_{vol} = \varepsilon_x + \varepsilon_y + \varepsilon_z \tag{E-5}$$

$$\mathrm{E}_d = \left(\frac{1}{6}\left[\left(\varepsilon_x - \varepsilon_y\right)^2 + \left(\varepsilon_y - \varepsilon_z\right)^2 + (\varepsilon_x - \varepsilon_z)^2\right] + \gamma_{xy}^2 + \gamma_{xz}^2 + \gamma_{yz}^2\right)^{1/2} \tag{E-6}$$

Figure E-5 shows a three-dimensional view of the model's yield surface in the $p - s_{eq} - J$ space, distinguishing the load-collapse (LC) curve and the increase of cohesion with equivalent suction, $f(s_{eq})$, on the primary yield surface, as well as the secondary yield surface (SI). The following sections describe the formulation that is common to both the IC SSM and IC DSM.

Yield and plastic potential surfaces

Formulation in the p–J plane

The model adopts versatile primary yield (F_{LC}) and plastic potential (G_{LC}) surfaces, with projections in the p–J plane as shown in Figure E-6(a). The surface is defined originally in Georgiadis et al. (2005) for the single structure model and reproduced in Equation E-7. This function can reproduce some of the well-known shapes of yield surfaces, including Sinfonietta Classica (Nova 1988), Cam clay (Roscoe and Schofield 1963), or modified Cam clay (Roscoe and Burland 1968), the latter surface being adopted in the BBM model (Alonso et al. 1990). The yield and the plastic potential surfaces can be different and the model is therefore capable of reproducing both associated and non-associated plasticity. The advantage of this formulation is its ability to produce a more accurate simulation of the strength of overconsolidated clays on the 'dry side' of the critical state, which is otherwise significantly over-estimated by the modified Cam clay's elliptical shape. More recently, the nonlinear Hvorslev surface was added to the model's formulation on the dry side, with a non-associated plastic potential surface (Tsiampousi et al. 2013).

$$\frac{F_{LC}}{G_{LC}} = \frac{p + k \cdot s_{eq}}{p_0 + k \cdot s_{eq}} - \frac{\left(1 + \frac{\eta}{K_2(\alpha,\mu)}\right)^{K_2(\alpha,\mu)/\beta_f(\alpha,\mu)}}{\left(1 + \frac{\eta}{K_1(\alpha,\mu)}\right)^{K_1(\alpha,\mu)/\beta_f(\alpha,\mu)}} \quad \text{(E-7)}$$

where p_0 is the hardening parameter of the yield surface; η is the generalised normalised stress ratio; α_F and μ_F are the model parameters controlling the shape of the yield surface; and α_G and μ_G are the model parameters controlling the shape of the plastic potential surface.

Additionally, the critical state strength is defined by the maximum stress ratio $\eta = M_j = J/(p + f(s_{eq}))$, as shown in Figure E-6(b), which is a model parameter.

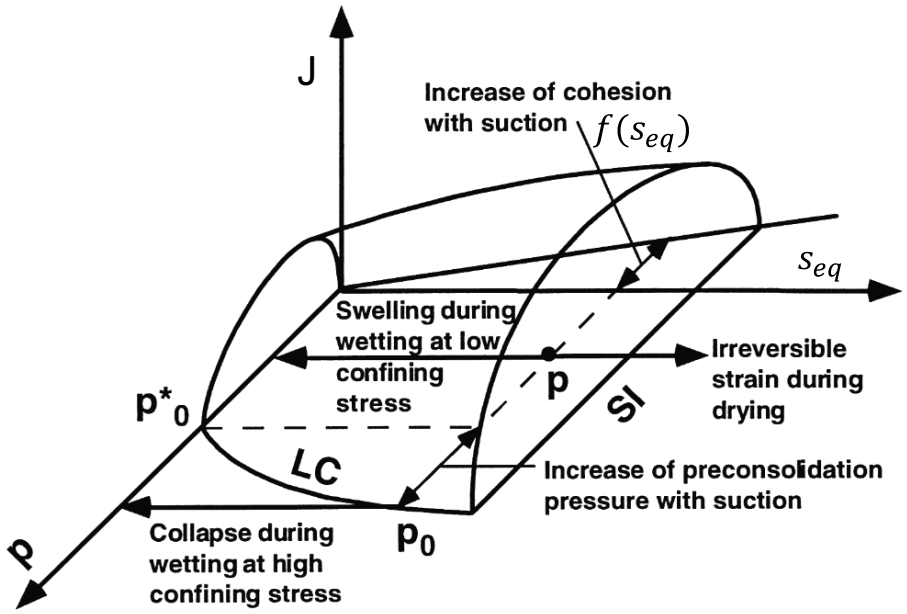

Figure E-5. *General shape of the yield surface in the $J - p - s_{eq}$ plane (adapted from Alonso et al. 1999).*

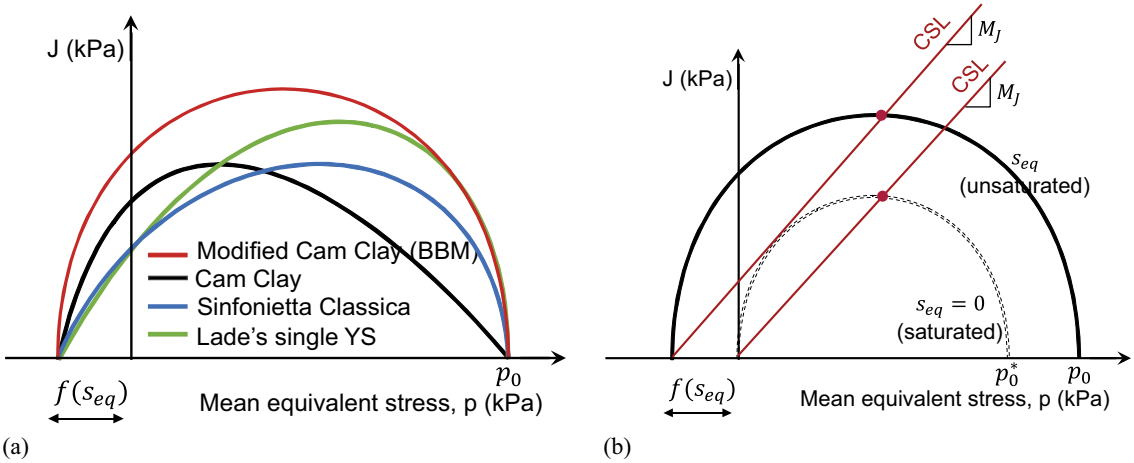

Figure E-6. *IC DSM yield and plastic potential surfaces in the p-J plane: (a) Yield surface shapes in p-J plane; (b) Critical state strength, M_j.*

Formulation in the isotropic plane

Figure E-7(a) shows the projection of the yield surface in the $p-s_{eq}$ plane, where p_0^* is the size of the yield surface in a saturated state. The expansion of the yield surface, $f(s_{eq}) = k \cdot s_{eq}$, into the tensile region of the mean equivalent stress, due to the increase of equivalent suction, s_{eq}, can be defined either by a constant gradient, k (the same as the BBM), or as a function of the degree of saturation, i.e. $k = s_r$. The latter option is more realistic as it limits the increase of the surface at very large suctions. Apart from k, the size of the secondary yield surface, $s_{eq,0}$, is also a model parameter.

There are three options to describe the isotropic compression of an unsaturated clay in the $\ln p-v$ plane (Figure E-7 (b), where v is the specific volume. Option 1 is that of a normal compression line with a constant slope, $\lambda(s_{eq})$, the magnitude of which depends on the value of equivalent suction, s_{eq}. This option is the same as in the BBM model and predicts an increasing magnitude of the potential collapse with increasing stress level, from a stress state on an unsaturated compression line to that on a fully saturated compression line with a slope $\lambda(0)$. Experimental evidence from (Josa et al. 1992) has shown this to be unrealistic and a nonlinear: Option 3 was introduced for the compression line to reflect those experiments. Finally, as a simplification of this option, Option 2 compression line follows initially the $\lambda(s_{eq})$ line, the same as Option 3, continuing subsequently with the $\lambda(0)$ slope upon reaching the stress level p_m. The magnitude of p_m is determined from the equations of the two curves.

Figure E-7(b) also indicates the parameters of the load-collapse (LC) curve on the primary yield surface, which is defined as:

$$p_0 = p_c \cdot \left(\frac{p_0^*}{p_c}\right)^{[\lambda(0)-\kappa]/[\lambda(s_{eq})-\kappa]} \tag{E-8}$$

where

$$\lambda(s_{eq}) = \lambda(0) \cdot \left[(1-r) \cdot \mathrm{e}^{-\beta \cdot s_{eq}} + r\right] \tag{E-9}$$

and p_c is a characteristic pressure, κ is the swelling coefficient, r is the soil stiffness parameter and β is the stiffness increase parameter. Together with $\lambda(0)$, the latter parameters are model input parameters that describe the behaviour in isotropic compression for Option 1. Details for Options 2 and 3 can be found in Georgiadis et al. (2005).

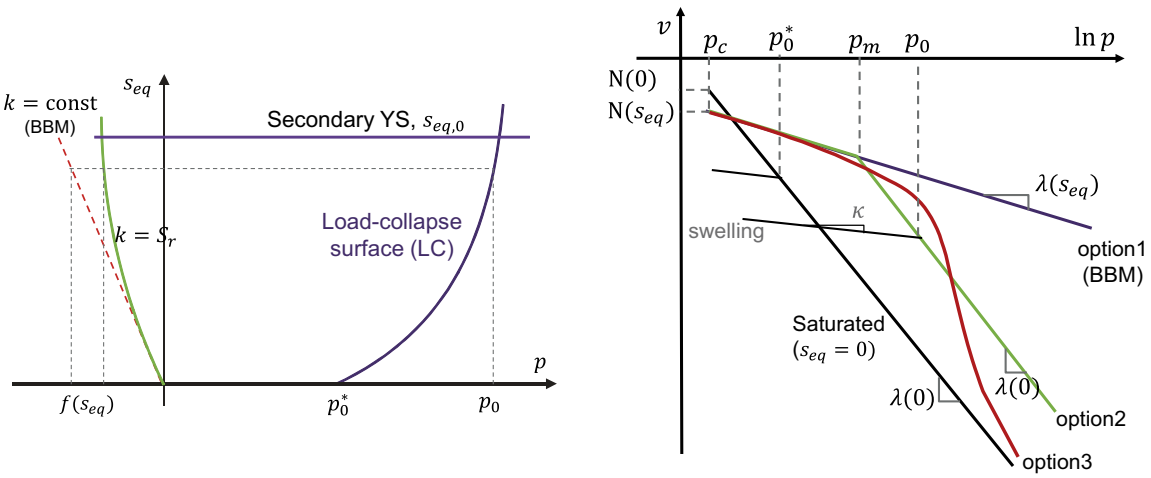

Figure E-7. *Parameters of the yield surface in the isotropic plane: (a) Yield surface in $p - s_{eq}$ plane; (b) Isotropic compression.*

Formulation in the deviatoric plane

The final aspect of the primary yield surface is its formulation in the deviatoric (or π) plane, which adopts the Matsuoka-Nakai shape (Matsuoka and Nakai 1974), as shown in Figure E-8. This differs from the BBM yield surface, which adopts a circular shape in the deviatoric plane, in line with the classical critical state approach. However, the circular shape implies a variable angle of shearing resistance, ϕ', for geomaterials, from triaxial compression ($\theta = -30°$) to triaxial extension ($\theta = +30°$). This variation is unrealistically high and unsupported by experimental data, and is therefore unconservative for the design of geotechnical problems. The Matsoka-Nakai surface also implies variable ϕ', but this variation resembles that experimentally measured. Potts and Zdravkovic (2001) further discuss this pitfall of the circular yield surface shape in deviatoric plane.

Elastic behaviour

The formulation of the yield and plastic potential surfaces previously described is common for both the single structure model (IC SSM, Georgiadis et al. 2003) and the double structure model (IC DSM, Ghiadistri et al. 2018). The IC SSM, like the BBM, assumes elastic behaviour inside the yield surface depicted in Figure 5. The elastic volumetric strain, $\Delta\varepsilon^e_{vol}$, has contributions from both the stress change, Δp, and the suction change, Δs_{eq}, as given by Equation E-10:

$$\Delta\varepsilon^e_{vol} = \frac{\kappa}{v \cdot p} \cdot \Delta p + \frac{\kappa_s}{v \cdot \left(s_{eq} + p_{atm}\right)} \cdot \Delta s_{eq} \qquad \text{(E-10)}$$

where κ_s is the elastic swelling coefficient for changes in suction and is a model parameter, while p_{atm} is the atmospheric pressure, equal to 101.3 kPa.

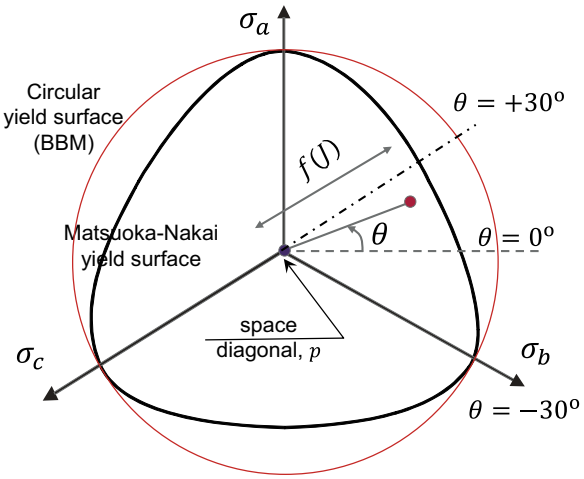

Figure E-8. *Yield surface in the deviatoric plane.*

Hardening rules

The magnitude of the plastic volumetric strains, ε_{vol}^{p}, when either of the two yield surfaces is activated is related to the change of the hardening / softening parameters p_0^* and $s_{eq,0}$, through the following equations:

– primary yield surface:

$$\frac{\mathrm{d}p_0^*}{p_0^*} = \frac{v}{\lambda(0) - \kappa} \cdot d\varepsilon_{vol}^{p} \tag{E-11}$$

– secondary yield surface:

$$\frac{\mathrm{d}s_{eq,0}}{s_{eq,0} + p_{atm}} = \frac{v}{\lambda(s_{eq}) - \kappa_s} \cdot d\varepsilon_{vol}^{p} \tag{E-12}$$

Extended formulation for the IC DSM

The model formulation presented above is valid for a single porosity structure, which is governed by the evolution of suction in the inter-aggregate (macro) pores. As previously described, a double porosity model introduces the second level of structure in terms of intra-aggregate (micro) pores. The formulation assumes that the micro-structure is saturated, elastic and volumetric, hence the associated changes are expressed in terms of effective stresses, $\{\sigma'\} = \{\sigma\} + \{s_{eq}\}$. The following assumptions are introduced into the IC SSM formulation to additionally take account of the micro-structure in the new IC DSM formulation.

Additional plastic strains

The first assumption is that the elastic volumetric deformations of the micro-structure, $\Delta\varepsilon_{vol,m}^{e}$, induce additional volumetric plastic deformations of the macro-structure, $\Delta\varepsilon_{vol,m,\beta}^{e}$, via the so-called β interaction mechanism, Equation E-13. The model formulation introduces a line of neutral loading in the $p-s_{eq}$ plane. The zero stress change, $\Delta p' = 0$, implies the stress state is on the neutral line, which does not generate micro-strains. If $\Delta p' > 0$, the suction increase promotes micro-structural compression, whereas $\Delta p' < 0$ triggers a reduction in suction and hence micro-structural swelling (Figure E-9). Consequently, the material behaviour below the primary yield surface is no longer elastic and the total volumetric plastic strain is the sum of the plastic strains from the primary yield surface (macro-mechanism) and those from the β mechanism, Equation E-14.

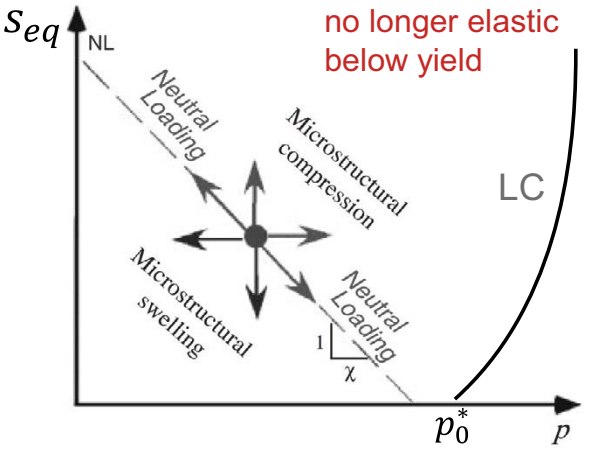

Figure E-9. *Introduction of micro-structural effects in the p – s_{eq} plane.*

$$\Delta\varepsilon^{p}_{vol,M,\beta} = f_{\beta} \cdot \Delta\varepsilon^{e}_{vol,m} \tag{E-13}$$

$$\Delta\varepsilon^{p}_{vol} = \Delta\varepsilon^{p}_{vol,M,LC} + \Delta\varepsilon^{p}_{vol,M,\beta} \tag{E-14}$$

The micro-structural elastic volumetric strain is calculated as:

$$\Delta\varepsilon^{e}_{vol,m} = \frac{\Delta p'}{K_m} \tag{E-15}$$

with the micro-structural bulk modulus being:

$$K_m = \frac{1 + e_m}{\kappa_m} \cdot p' \tag{E-16}$$

where e_m is the void ratio of the micro-pores and κ_m is the elastic compressibility of the micro-structure and is an additional model parameter (compared to the IC SSM model).

β interaction mechanism

The function f_β in Equation E-14 describes a nonlinear interaction between the two levels of structure, as shown in Figure E-10. This interaction depends on the current stress state with respect to the yield surface, which is represented by the stress ratio p_r/p_0, as shown in Figure E-11.

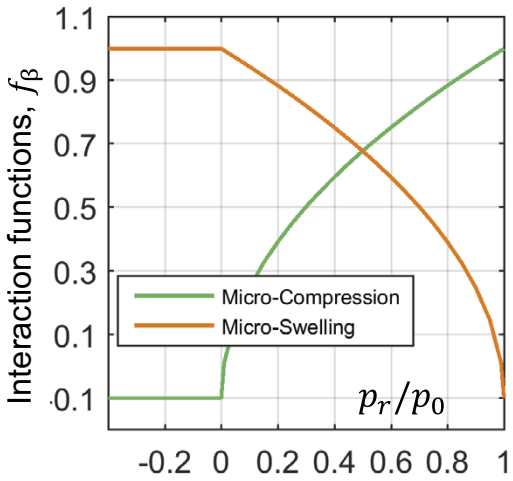

Figure E-10. *f_β interaction functions.*

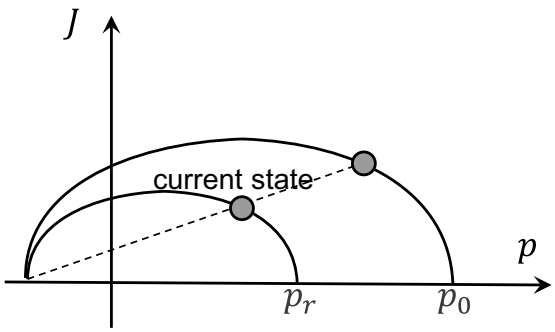

Figure E-11. *Stress state estimate for f_β functions.*

The empirical expressions for f_β take the following form:

– micro-compression

$$f_\beta = \begin{cases} c_{c1} + c_{c2} \cdot \left(\frac{p_r}{p_0}\right)^{c_{c3}} & if \ \frac{p_r}{p_0} \geq 0 \\ c_{c1} & if \ \frac{p_r}{p_0} < 0 \end{cases} \quad \text{(E-17)}$$

– micro-swelling

$$f_\beta = \begin{cases} c_{s1} + c_{s2} \cdot \left(\frac{p_r}{p_0}\right)^{c_{s3}} & if \ \frac{p_r}{p_0} \geq 0 \\ c_{s1} & if \ \frac{p_r}{p_0} < 0 \end{cases} \quad \text{(E-18)}$$

with c_{c1}, c_{c2}, c_{c3} being the shape coefficients for micro-compression and, similarly, c_{s1}, c_{s2}, c_{s3} being the shape coefficients for micro-swelling. These coefficients are also additional input parameters for the double-structure model, IC DSM.

Void factor

The final input to the double-structure model is the void factor, $VF = e_m/e$, defined as a ratio of the micro void ratio, e_m, to the total void ratio, $e = e_m + e_M$ (with e_M being the macro void ratio). Its role is to monitor the evolution of the micro void ratio and is therefore introduced as a new hardening parameter for the IC DSM, defined as:

$$\Delta VF = \frac{\Delta e}{e} \cdot \frac{\Delta p'}{K_m \cdot \Delta \varepsilon_{vol}} \quad \text{(E-19)}$$

E7 Material constitutive parameters

There are 4 different materials included in the analysis:

Granitic rock

The host rock is characterised using the unsaturated Mohr-Coulomb model. From a mechanical standpoint, the material is assumed to have a purely cohesive behaviour, therefore its angle of shearing resistance is set to $\phi' = 0$ °C and its cohesion is set to a large value ($c' = 10$ MPa).

From a hydraulic standpoint, the permeability is assumed to be isotropic, constant and equal to 10^{-12} m/s (Annex A). In terms of the retention behaviour, the data collected and elaborated by Pintado and Lloret (1997) and Finsterle and Pruess (1995) is shown in Figure E-12. It can be noted how the range of the degree of saturation spans over a very limited suction interval. This implies that any numerical retention curve fitting this data would yield a very steep gradient. Consequently, the host rock would saturate and desaturate almost instantaneously, which could potentially cause numerical issues in a boundary value problem. For this reason and in absence of further experimental evidence of the retention properties of the material, the host rock is always assumed to be saturated. This is achieved by imposing a large air entry value of suction ($s_{air} = 150$ MPa). From a physical point of view this seems reasonable, as the portion of the rock that de-saturates due to the presence of the FEBEX drift is expected to be very limited, given the small diameter of the drift and the large depth at which it is located.

From a thermal standpoint, thermal conductivity is assumed to be isotropic, constant and equal to 3.2×10^{-3} kW/mK, while the specific heat capacity is equal to 920 J/kg°C (Annex A).

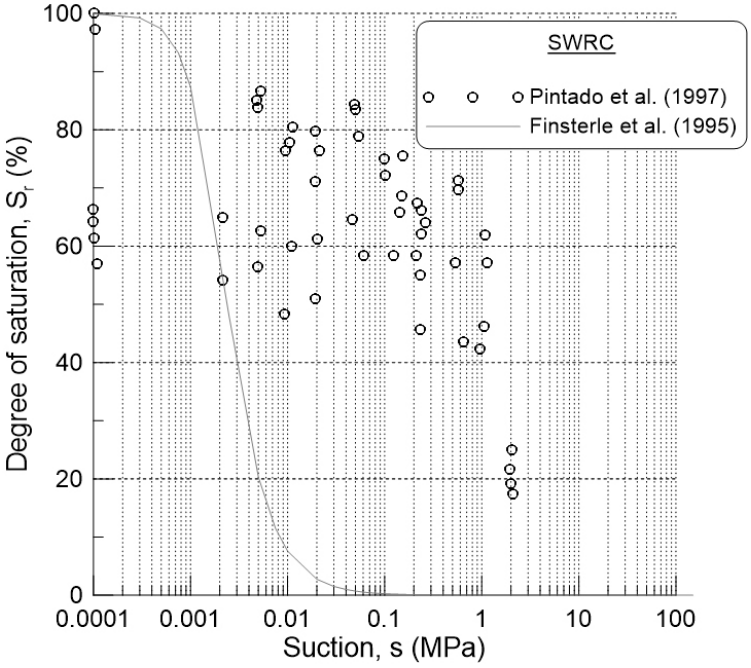

Figure E-12. *Data about the retention properties of the granitic rock.*

FEBEX bentonite

The buffer material is characterised with the IC DSM (Ghiadistri 2019). This framework accounts for the double porosity structure typical of compacted, expansive clays. The mechanical parameters employed in the analysis are reported in Table E-4. These parameters were obtain using data from Annex A according to the calibration process of the IC DSM discussed in Ghiadistri (2019).

Table E-4. IC DSM parameters for the FEBEX bentonite.

Parameter	Value
Parameters controlling the shape of the yield surface, α_F, μ_F	0.4, 0.9
Parameters controlling the shape of the plastic potential surface, α_G, μ_G	0.4, 0.9
Strength parameters, M_f, M_g	0.5
Characteristic pressure, p_c (kPa)	50
Fully saturated compressibility coefficient, $\lambda(0)$	0.3
Elastic compressibility coefficient, κ	0.07
Maximum soil stiffness parameter, r	0.9
Soil stiffness increase parameter, β (1/kPa)	0.00004
Elastic compressibility coefficient for changes in suction, κ_s (kPa)	0.05
Poisson ratio, ν	0.4
Plastic compressibility coefficient for changes in suction, λ_s	0.5
Air-entry value of suction, s_{air} (kPa)	1000
Yield value of equivalent suction, s_0 (kPa)	10^6
Microstructural compressibility parameter, κ_m	0.2
Void factor, VF	0.4
Coefficients for the micro swelling function, c_{s1}, c_{s2}, c_{s3}	0.001, 1.1, 2.0
Coefficients for the micro compression function, c_{c1}, c_{c2}, c_{c3}	0.001, 1.1, 2.0

In terms of hydraulic properties, permeability is assumed to vary with suction according to the de-saturation permeability model available in ICFEP (Potts and Zdravkovic 1999; Nyambao and Potts 2010), pictured in Figure E-13. For suctions below 1 MPa permeability is assumed at 10^{-13} m/s (Annex A). For suctions between 1 and 20 MPa, permeability reduces linearly until 0.8×10^{-14} m/s. For higher suctions, permeability remains constant. The parameters for the de-saturation permeability model are reported in Table E-5. The retention behaviour is modelled by fitting the Van Genughten et al. (1980) model to the available data (Annex A, Villar 2005), as shown in Figure E-14. All model parameters for the retention curve are reported in Table E-6.

In terms of thermal properties, thermal conductivity is assumed to be isotropic, constant and equal to 0.55×10^{-3} kW/mK, while the specific heat capacity is 870 J/kg°C (Annex A).

Table E-5. permeability parameters for the FEBEX bentonite buffer.

Parameter	Value	Unit	Description
k_{sat}	10^{-13}	[m/s]	Saturated permeability
k_{min}	0.8×10^{-14}	[m/s]	Minimum permeability
p_1	1 000	[kPa]	Suction
p_2	20 000	[kPa]	Suction

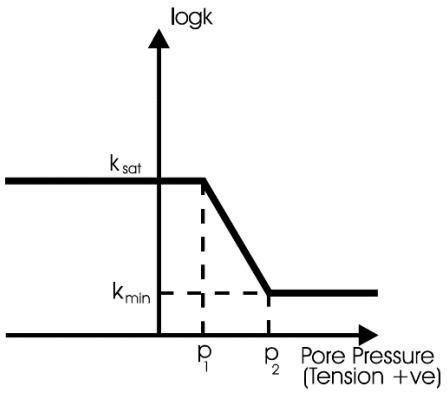

Figure E-13. *Variable permeability model (Potts and Zdravkovic, 1999, Nyambao and Potts 2010). Tension positive convention is adopted in ICFEP, therefore positive pore pressure is suction.*

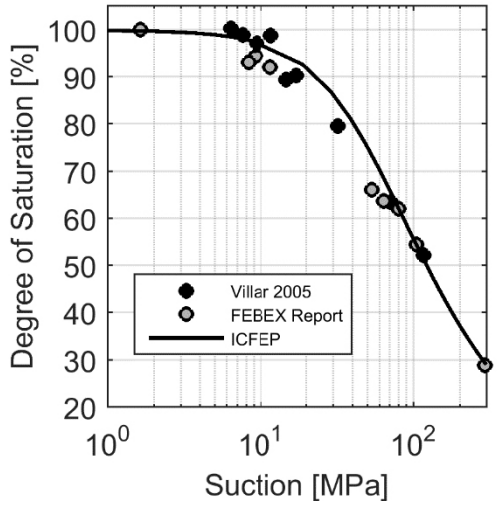

Figure 14. *Characteristic curve of the FEBEX bentonite.*

Table E-6. Retention properties of the FEBEX bentonite buffer.

Parameter	Value
Fitting parameter, α	0.00002
Fitting parameter, m	0.4
Fitting parameter, n	1.7
Residual degree of saturation, S_{r0}	0
Suction in the long term, S_0 (kPa)	10^5

Canister (i.e. steel) and concrete plug

Both materials have been assumed to be thermally inactive and non-consolidating. Their Young's modulus is set to a large value ($E = 2 \times 10^5$ MPa) to simulate rigidity and their Poisson's ratio is equal to 0.25.

E8 Stages of analysis, boundary conditions, initial variables and key parameters

Stages of analysis and boundary conditions

Stage number	Brief description	Start time (day)	Duration (days)
1	Tunnel excavation	−66	24
2	Buffer and heater construction	−42	42
3	Temperature increase in both heaters from T_{init} = 12 °C to T_{final} = 100 °C; ΔT = 0.733 °C	0	60
4	Stage 1 operation of the test at T = 100 °C	61	1 725
5	Heater #1 switched off; ΔT = −2.5 °C	1726	1 755
6	Excavation for first dismantling of plug, part of buffer and heater #1	1756	1 836
7	Construction of dummy canister and new plug	1837	1 852
8	Stage 2 operation – only heater #2	1853	6 152

E8.1 Rock

Initial conditions of the rock at the start of the analysis (1)

Initial temperature at tunnel axis level (°C)	Initial stresses at tunnel axis level (MPa)	Initial pore water pressure at tunnel axis level (MPa)
10	28	4.5

Notes: If the initial stresses are not isotropic, please indicate all component – "tunnel axis level" is specified in case initial conditions are not uniform.

Initial conditions of the rock at the start of the analysis (2)

Initial density (g/cm^3)	Initial porosity	Initial water content (%)
2.64	0.4	22

Main rock properties (1)

Initial thermal conductivity (W/mK)	Specific heat capacity (J/kgK)	Initial intrinsic permeability (m^2)	Initial hydraulic conductivity (m/s)
3.2	920	1.33E−19	1.0E−12

Main rock properties (2)

Linear thermal expansion coefficient (K^{-1})	Young's modulus (MPa)	Poisson's ratio
8E−6	20 000	0.2

Main rock properties: retention curve (3)

Equation used	α (-)	n (-)	m (-)	S_{r0} (-)
$S_r = \left[\frac{1}{1+(\alpha \cdot s_{eq})^n}\right]^m \cdot (1 - S_{r0}) + S_{r0}$	0.4	0.9	0.2	0.2

Note: $s_{eq} = s - s_{air}$, where s_{air} = 100 MPa to ensure the rock remains saturated and a constant soured of water.

Main rock properties: relative permeability (4)

Equation used	Parameter 1 (units)	Parameter 2 (units)	Parameter 3 (units)	Parameter 4 (units)
N/A				

E8.2 Bentonite

Initial conditions of the bentonite at installation (1)

Initial temperature (°C)	Initial stresses (MPa)	Initial pore water pressure/suction (MPa)	Initial relative humidity (%)
12	0	120	40

Note: If the initial stresses are not isotropic, please indicate all components.

Initial conditions of the bentonite at installation (2)

Initial dry density (g/cm^3)	Initial density of the solid phase (g/cm^3)	Initial porosity	Initial water content (%)	Initial degree of saturation (%)
1.65	2.7	0.66	12.2	50

Note: It is recommended (but not compulsory) to use a density of the solid phase of 2.7 g/cm^3 to compute initial dry density (or porosity) and initial degree of saturation. Please, specify if a different value has been used.

Main bentonite properties (1)

Initial thermal conductivity (W/mK)	Initial thermal conductivity dry bentonite (W/mK)	Initial thermal conductivity saturated bentonite (W/mK)	Initial specific heat capacity of the solid phase (J/kgK)	Linear thermal expansion coefficient (K^{-1})
0.55	N/A	N/A	870	6.5E−6

Main bentonite properties (2)

Initial intrinsic permeability (m^2)	Initial hydraulic conductivity (m/s)	Initial intrinsic permeability (saturated) (m^2)	Initial hydraulic conductivity (saturated) (m/s)	Swelling pressure under initial conditions (oedometric conditions) (MPa)
1.0E−21	0.8E−14	1.33E−20	1E−13	9

Note: A virtual swelling pressure test (oedometric conditions) may be required to determine the swelling pressure of the bentonite under initial conditions.

Main bentonite properties: permeability dependence on dry density (or porosity) (3)

Equation used *-dependence on suction-*	s_1 (MPa)	s_2 (MPa)	k_{sat}/k_{min} (-)	Parameter 4 (units)
$\log k = \log k_{sat} - \left(\frac{s - s_1}{s_2 - s_1}\right) \cdot \log(k_{sat}/k_{min})$	1	20	12	-

Notes: If permeability is assumed not to depend on dry density or porosity, sate so under “Equation used”.

Main bentonite properties: retention curve (4)

Equation used	α (-)	n (-)	m (-)	S_{r0} (-)
$S_r = \left[\frac{1}{1 + (\alpha \cdot s_{eq})^n}\right]^m \cdot (1 - S_{r0}) + S_{r0}$	0.00002	1.7	0.4	0.0

Note: $s_{eq} = s - s_{air}$, where s_{air} = 1 MPa.

Main bentonite properties: relative permeability (5)

Equation used	Parameter 1 (units)	Parameter 2 (units)	Parameter 3 (units)	Parameter 4 (units)
N/A				

Note: Please, replace “Parameter 1” etc... by the symbol used in your equation.

Main bentonite properties: thermal conductivity (6)

Equation used	Parameter 1 (units)	Parameter 2 (units)	Parameter 3 (units)	Parameter 4 (units)
N/A				

Note: Please, replace “Parameter 1” etc... by the symbol used in your equation.

Main bentonite properties: vapour transport (7)

Molecular diffusion coefficient of vapour in free air (m^2/s)	Tortuosity
N/A	

Appendix F

SNL Report

Sandia National Laboratories, US (SNL)
Teklu Hadgu, Thomas Dewers, Steven Gomez, Edward Matteo

F1 Introduction

This report outlines Sandia National Laboratories modeling studies applied to Stage 1 and Stage 2 of the Full-scale Engineered Barriers Experiment in Crystalline Host Rock (FEBEX) in situ test for the SKB EBS Task Force Task 9. The FEBEX test was a full-scale test conducted over ~18 years at the Grimsel, Switzerland Underground Research Laboratory (URL) managed by NAGRA. It involved emplacing simulated waste packages, in the form of welded cylindrical heaters, inside a tunnel in crystalline granitic rock and surrounded by a bentonite barrier and cement plug. Sensors emplaced within the bentonite monitored the wetting-up, heating, and drying out of the bentonite barrier, and the large resulting data set provides an excellent opportunity for validation of multiphysics Thermal-Hydrological (TH), Thermal-Hydrologic-Chemical (THC), and Thermal-Hydrological-Mechanical (THM) modeling approaches for underground nuclear waste storage and the performance of engineered bentonite barriers. The present status of the EBS Task Force is finalizing Task 9, which follows years of modeling studies of the FEBEX test, by many notable modeling teams (Gens et al. 2009, Sanchez et al. 2010, 2012, Samper et al. 2018). These modeling studies generally use two-dimensional axisymmetric meshes, ignoring three-dimensional effects, gravity and asymmetric wetting and dry out of the bentonite engineered barrier. This study investigates these effects with use of the PFLOTRAN THC code with massively parallel computational methods in modeling FEBEX Stage 1 and Stage 2 results. The PFLOTRAN numerical code is an open source, state-of-the-art, massively parallel subsurface flow and reactive transport code operating in a high-performance computing environment (Hammond et al. 2014).

Section F2 describes the applied partial differential equations describing mass, momentum and energy balance used in this study, considerations derived by assuming phase equilibrium between gas and liquid phases, constitutive equations for granite, cement plug, and bentonite domains, and specific approaches for use in the PFLOTRAN code. Section F3 describes the geometry, meshing, and model set-up. Section F4 describes modeling results, Section F5 compares modeling results to field testing data, and Section F6 gives conclusions.

F2 General Modeling Approach

F2.1 Balance equations

Fundamental first principles for TH modeling are expressions for mass and energy conservation. Here we outline partial differential equations commonly used in porous media compositional two-phase, two-component modeling for air and water components (denoted by "*a*" and "*w*" respectively) in gas and aqueous liquid phases (denoted by "*g*" and "*l*" respectively), where the solid phase is denoted by 's'. The benefits of the compositional approach in modeling multiphase problems is that terms representing mass transfer between phases cancel, simplifying the equations and reducing the "stiffness" associated with solving kinetic terms, which is equivalent to assuming local equilibrium between liquid water and water vapor. We assume that the solid phases (granite, cement, and bentonite) are inert, and ignore shrink-swell changes in the bentonite barrier associated with wetting and drying. This amounts to an assumption of constant porosity in all solid phases.

A general mass or energy density balance equation with density d of component α in phase β takes the form

$$\frac{\partial d_\beta^\alpha}{\partial t} + \boldsymbol{\nabla} \cdot \boldsymbol{q}_\beta^\alpha - Q_\beta^\alpha \tag{F-1}$$

where **q** is the total flux density with respect to a frame of reference and Q is a source/sink term. In multiphase problems, the total mass density is a function of porosity, phase saturation S_β, and component density (component α in phase β) ρ_β^α ($d_\beta^\alpha = \phi S_\beta \rho_\beta^\alpha$), where the relative phase flux includes

an advective term with relative phase velocity $\boldsymbol{v}_r$ relative to a fixed reference frame and diffusive/ dispersive flux $\boldsymbol{J}$ such that

$$\boldsymbol{q}_{r,\beta}^{\alpha} = \phi S_{\beta} \rho_{\beta}^{\alpha} \boldsymbol{v}_{r,\beta} + \boldsymbol{J}_{\beta}^{\alpha} \tag{F-2}$$

We denote the Darcy velocity as $\boldsymbol{V}_{\beta}$

$$\boldsymbol{V}_{\beta} = \phi S_{\beta} \boldsymbol{v}_{\beta} \tag{F-3}$$

Expressing the mass balance of air (a) and water (w) components in a non-deformable inert porous medium is expressed as (see, e.g. Martinez and Stone 2008)

$$\frac{\partial}{\partial t}\left(\rho_l^w S_l \phi + \rho_g^w S_g \phi\right) + \nabla \cdot \left(\boldsymbol{q}_{r,l}^w + \boldsymbol{q}_{r,g}^w\right) + Q^w = 0 \tag{F-4a}$$

$$\frac{\partial}{\partial t}\left(\rho_l^a S_l \phi + \rho_g^a S_g \phi\right) + \nabla \cdot \left(\boldsymbol{q}_{r,l}^a + \boldsymbol{q}_{r,g}^a\right) + Q^a = 0 \tag{F-4b}$$

where the Q are source/sink terms not including kinetic expressions or mass transfer between phases. Here ρ_l^w is the mass density of water component in the liquid phase, ρ_g^w is the mass density of the water component in the gas phase (water vapor), ρ_l^a is the mass density (or concentration) of air dissolved in the liquid phase, and ρ_g^a is the mass density of dry air in the gas phase such that, with mass fractions Y_{β}^{α} and ρ_l and ρ_g being the liquid and gas phase densities respectively,

$$\rho_l^w = Y_l^w \rho_l,\ \rho_g^w = w\rho_g,\ \rho_l^a = Y_l^a \rho_l,\ \rho_g^a = Y_g^a \rho_g \tag{F-5}$$

The saturations of both phases must sum to unity, so that

$$S_g = 1 - S_l \tag{F-6}$$

The total fluxes include both advective (with Darcy velocities V_{β} for each phase β) and diffusive fluxes (the latter denoted $\boldsymbol{J}$)

$$\begin{aligned} \boldsymbol{q}_{r,l}^w &= \rho_w \boldsymbol{V}_l \\ \boldsymbol{q}_{r,g}^w &= \rho_g^w \boldsymbol{V}_g + \boldsymbol{J}_g^w \\ \boldsymbol{q}_{r,l}^a &= \rho_l^a \boldsymbol{V}_l + \boldsymbol{J}_l^a \\ \boldsymbol{q}_{r,g}^a &= \rho_a \boldsymbol{V}_g + \boldsymbol{J}_g^a \end{aligned} \tag{F-7}$$

Darcy fluxes for phase β are given by

$$\begin{aligned} \boldsymbol{V}_l &= -K_w k_{rw}/\mu_l(\boldsymbol{\nabla} P_l - \rho_l g \boldsymbol{z}) \\ \boldsymbol{V}_g &= -K_g k_{rg}/\mu_g(\boldsymbol{\nabla} P_g - \rho_g g \boldsymbol{z}) \end{aligned} \tag{F-8}$$

Later we will give expressions for relative permeability and phase saturation in terms of a suction or capillary pressure given by

$$P_c = P_g - P_l \tag{F-9}$$

For binary diffusion of water and air components in the gas phase, we follow Gens et al. (2009) and use

$$\boldsymbol{J}_g^w = -J_g^a = -\phi(1 - S_l)\tau D_g^w \rho_g \boldsymbol{\nabla} Y_g^w$$

and (F-10)

$$\boldsymbol{J}_l^a = -\phi(S_l)\tau D_l^a \rho_w \boldsymbol{\nabla} Y_l^a$$

The internal energy balance equation for the solid plus pores with two fluid phases has been derived previously, and here we use the approach of Martinez and Stone (2008)

$$\frac{\partial}{\partial t}\left(e_s\rho_s(1-\phi)+e_l\rho_l S_l\phi+e_g\rho_g S_g\phi\right)+\boldsymbol{\nabla}\cdot\boldsymbol{q_e}=Q^e \tag{F-11}$$

where the total heat flux vector includes terms for heat conduction, convection relative to a deforming solid frame, and heat transport due to binary diffusion in the gas phase:

$$\boldsymbol{q}_e=-\lambda_T\boldsymbol{\nabla}T+\rho_l\boldsymbol{V}_l h_l+\rho_g\boldsymbol{V}_g h_g+h_g^w\boldsymbol{J}_g^w+h_g^{wa}\boldsymbol{J}_g^a \tag{F-12}$$

Here h_β is the enthalpy of phase β, and h_g^a is the enthalpy of component α in the gas phase. We explore phenomenology for the thermal conductivity λ in terms of saturations and other parameters later in subsection F2.3.

F2.2 Equilibrium considerations for Air-Water and Air-Water-Bentonite systems

With the assumption of phase equilibrium comes the application of the familiar expressions of Henry's, Dalton's Law, and Kelvin's Law, which permit the interrelationship between pressure and density variables. Henry's Law expresses the equilibrium between dissolved air in the liquid phase and dry air in the gas phase

$$\rho_l^a=H_a\rho_a \tag{F-13}$$

A further common assumption in air-water systems is that the gas phase is an ideal mixture of air and water vapor components, such that

$$P_g=P_a+P_v \tag{F-14}$$

where P_a is the partial pressure of dry air in the gas phase and P_v is the partial pressure of water vapor in the gas phase. It is convenient to introduce the relationships between the partial pressures and densities used in the conservation laws where (M_a and M_v are molecular weights of dry air and water vapor, respectively, and R is the gas constant)

$$\rho_g^a=\rho_a=\frac{M_a}{RT}P_a \text{ and } \rho_g^w=\rho_v=\frac{M_v}{RT}P_v \tag{F-15}$$

For water vapor in contact with bentonite, Kelvin's Law expresses the psychrometric relationship between state of suction, s (= $P_g - P_l$ or capillary pressure) in the bentonite and vapor pressure of water P_v in the gas phase (with M_w being the molecular weight of water component):

$$P_v=P_v^0 e^{-sM_w/RT\rho_w} \tag{F-16}$$

This expression is used to calculate the relative humidity (RH) within the bentonite, where,

$$RH=100\ \%\ {P_v}\Big/{P_v^0} \text{ and } P_v^0=136075\ e^{-5239.7/T} \tag{F-17}$$

P_v^0 is the saturated vapor pressure of water in MPa, and the expression we use here is from Gens et al. (2009).

For the two-phase flow portions of the above model, we have multiple variables – four ρ_β^a for the two components in the two phases, the liquid and gas pressures P_l and P_g, and the liquid and gas saturations S_l and S_g. The equilibrium conditions and the compatibility condition between saturations reduce the number of variables to two (so-called primary variables), with added algebraic calculations between the calculated primary variables and the secondary variables being necessary (in compositional modeling, these are sometimes called "flash" calculations associated with the appearance of gas phase, e.g. steam flashing). During numerical simulation, it is common to calculate one of the pressures and liquid saturation, for example. Problems arise when phases appear or disappear, leading to various approaches for multiphase flow. For the PFLOTRAN simulations, we use P_g and S_l as primary variables.

F2.3 Constitutive Equations for Granite, Bentonite, and Cement

Bentonite, Cement, and Granite Water Retention

Water retention properties for FEBEX bentonite have been studied by many authors, notably by Pintado et al. (2002) and Villar and Lloret (2004). We use a bentonite water retention curve following the familiar van Genuchten formulation

$$S_{el} = \left[1 + \left(\frac{s}{P_0}\right)^{\frac{1}{1-\lambda_0}}\right]^{-\lambda_0} \tag{F-18}$$

where $S_{el} = \frac{S_l - S_{lr}}{S_{ls} - S_{lr}}$, where S_{lr} is residual liquid saturation and S_{ls} is the maximum saturation, taken as unity. For relative permeability, PFLOTRAN has the option of the Mualem functions for liquid (k_{rl}) and gas-phase (k_{rg}) relative permeability, which are adopted here:

$$k_{rl} = \sqrt{S_{el}}\left\{1 - \left(1 - S_{el}^{\lambda}\right)^{1/\lambda}\right\}^2 \tag{F-19a}$$

$$k_{rg} = \sqrt{1 - S_{eg}}\left\{1 - S_{eg}^{1/\lambda}\right\}^{2\lambda} \tag{F-19b}$$

where $S_{eg} = 1 - \frac{S_l - S_{lr}}{1 - S_{lr} - S_{gr}}$, with S_{gr} being the residual gas saturation taken as zero.

Water Equation of State

We use a simple equation of state for liquid water,

$$\rho_l = \rho_l^0 e^{\{\beta(P_l - P_l^0) + \alpha_T(T - T^0)\}} \tag{F-20}$$

where β is the water compressibility at standard conditions and α_t is the volumetric expansion coefficient of water at standard conditions.

Vapor Diffusion

The gas phase binary diffusional fluxes of vapor and dry air are expressed in terms of the vapor mass fraction gradient and take the form

$$J_g^w = -J_g^a = -\varphi(1 - S_r)\tau D_g^w \rho_g \nabla Y_g^w \tag{F-21}$$

where the diffusion coefficient (m^2/s) is temperature and gas pressure dependent, in the form from Vargaftik (1975) and Walker et al. (1981):

$$D_g^w = D_g^0 \frac{P_g^0}{P_g}\left[\frac{T}{T^0}\right]^{1.8} \tag{F-22}$$

where P^0 and T^0 are pressure and temperature at standard conditions (i.e. 1 atm. And 0 □).

Effective Thermal Conductivity and Heat Capacity

Thermal conductivity was assumed to be a function of liquid saturation following the form of Somerton et al. (1974):

$$k_{th} = k_{dry} + \sqrt{S_l}\left(k_{sat} - k_{dry}\right) \tag{F-23}$$

where k_{th} = thermal conductivity, k_{dry} = dry thermal conductivity, and k_{sat} = fully saturated thermal conductivity.

F3 TH Modeling with PFLOTRAN

F3.1 Stage 1 Modeling

Thermal-hydrologic modeling was conducted for Task 9, Stage 1 FEBEX in situ test, up to first dismantlement (5 years). A 3-D modeling domain was developed based on project specifications (Figure F-1) with domain size 60 m × 20 m × 40 m in the x, y and z directions, respectively. To reduce mesh size an axisymmetric boundary condition was applied (Figure F-2).

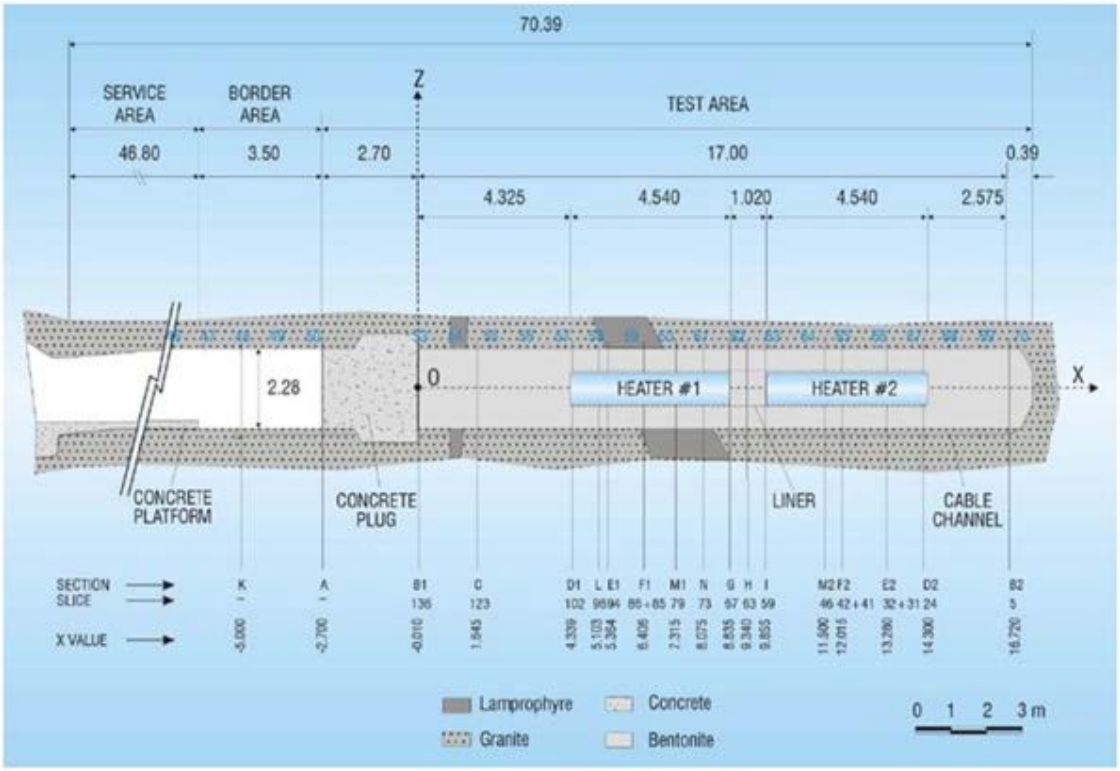

Figure F-1. *General layout of the FEBEX in situ test for Stage 1 (Bárcena et al. 2003).*

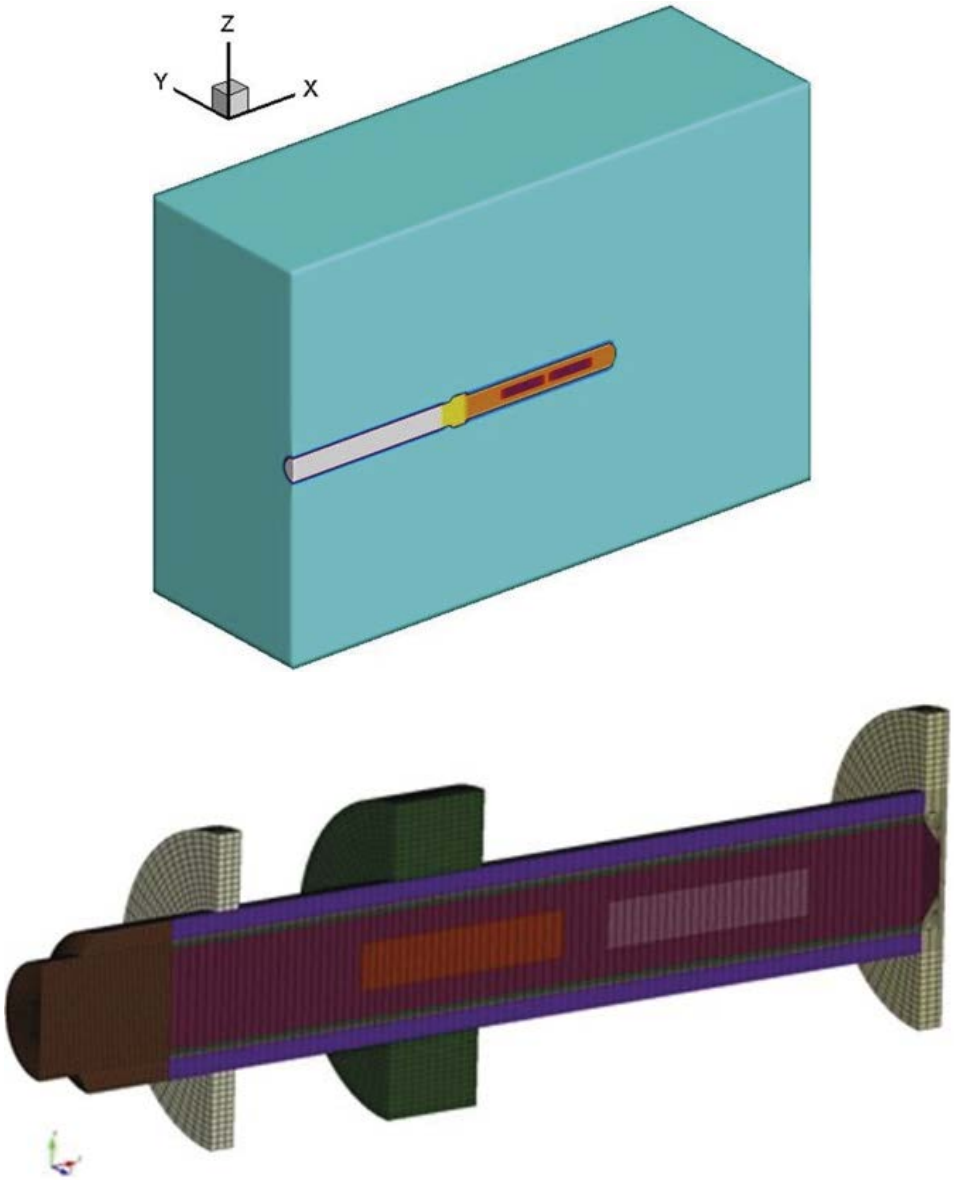

Figure F-2. *3D modeling domain with axisymmetric meshing for Stage 1.*

For TH simulations using PFLOTRAN numerical code the domain was discretized using an unstructured grid with fine discretization around the heaters and the buffer (Figure F-3). Figure F-4 shows discretization of the buffer. The mesh size for Stage 1 is 125 824 grid blocks. The buffer is represented by a total of 4 096 grid blocks (elements), with 46 grid blocks (elements) across the bentonite barrier. The simulation domain includes details of various regions representing different materials including granite, disturbed rock zone (DRZ), bentonite buffer, heaters, plug, liner, micro-annulus, lamprophyre and fracture at back of test area. For this report, we have assumed that the DRZ, lamprophyre dikes and fracture zones have the same properties as the granite domain.

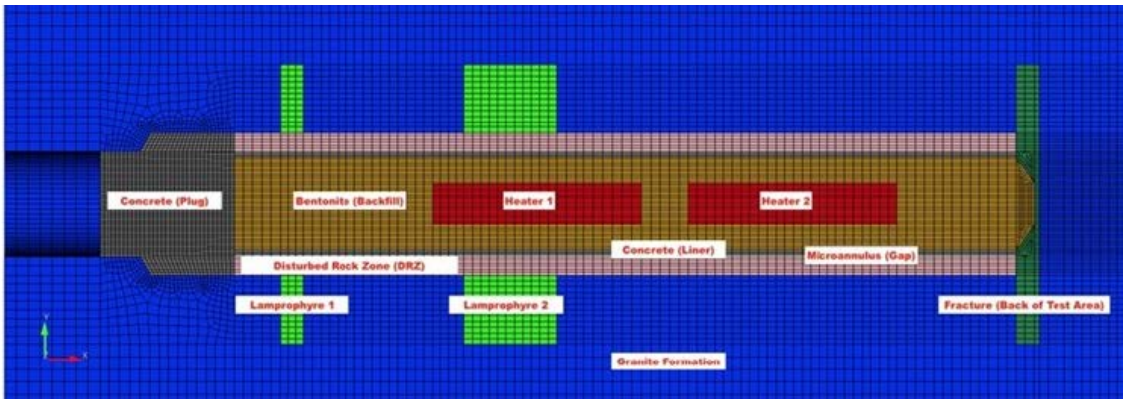

Figure F-3. *Meshing of the TH modeling domain for Stage 1.*

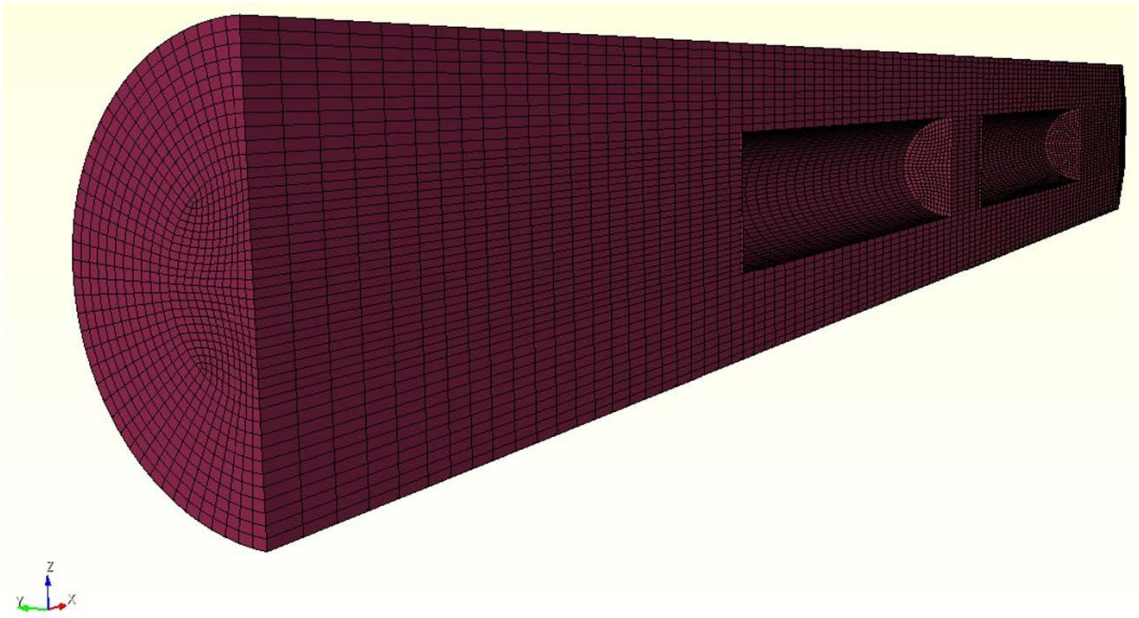

Figure F-4. *Meshing of the bentonite buffer for Stage 1.*

F3.1.1 TH Model Setup

Dates of important events in the FEBEX heater test that are examined in this report are given in Table F-1. A complete list of parameters used in the TH simulations are given in Section F8. The system is assumed to be at 12 °C at the beginning of the simulation. When the bentonite buffer is emplaced in the test area, a pressure of one atmosphere and a liquid saturation of 0.36 were applied. At the beginning of the heating phase the bentonite is assumed to be at a higher liquid saturation of 0.65 due to hydration from the formation. Hydrostatic pressure boundary condition was assigned on the sides of the modeling domain with a pressure of 0.7 MPa at the top of the domain. Based on the project specification, a 1 200 W heat was applied at the two heaters for the first 20 days of simulation time. The power was raised to 2 000 W per heater between Day 20 and Day 60. For the rest of the simulation time in Stage 1, time varying heat was applied at the two heaters to maintain a temperature of 100 °C.

Table F-1. Sequence of events in the FEBEX in situ test.

Event	Date (Month/Day/Year)	Interval/Days	Cumulative Days
Start of Tunnel Excavation	9/25/95	-	-
End of Tunnel Excavation	10/30/95	35	35
Start of Installation	7/1/96	245	280
End of Installation	10/15/96	106	351
Heaters switched on	2/27/97	135	241
Heater 1 switched off	2/28/02	1827	1962
End of 1st Dismantling	7/19/02	141	1968
Heater 2 switched off	4/20/05	1006	1147
End of 2nd dismantling	7/20/15	3743	4749

Material properties of main components selected for modeling are specified in Table F-2 and in Appendix A. Retention curve parameters are given in Table F-3 and in Appendix A. Molecular diffusion of vapor in free air of 2.0×10^{-5} m^2/s and diffusion coefficient in liquid of 2.0×10^{-9} m^2/s were used.

Table F-2. Material properties used in the TH simulations.

	Units	Granite	Buffer	Concrete Plug
Permeability	m^2	1.26×10^{-19}	1.60×10^{-20}	2.0×10^{-20}
Porosity	-	0.01	0.375	0.01
Density	Kg/m^3	2750	1600	2600
Thermal Conductivity dry/wet	W/m K	3.2/3.3	0.6/1.3	3.0/3.0
Specific Heat	kJ/kg	793	1091	1000.0

Table F-3. Retention curve parameters used in the TH simulations.

	Units	Granite	Buffer	Concrete Plug
P_0	MPa	0.0021	25.0	0.0021
I	-	0.7	0.2	0.7
S_{lr}	-	0.0	0.1	0.01
S_{gr}	-	0.0	0.1	0.01
S_{ls}	-	1.0	1.0	1.0

F3.2 Stage 2 Modeling

Thermal-hydrologic modeling was conducted for Task 9, Stage 2 FEBEX in situ test, between the first and second dismantlement as listed in Table F-1. Because of change in domain geometry, and the complexity of the mesh used in Stage 1 modeling, the same mesh could not be used for Stage 2. A different 3-D mesh was needed to include all the changes that occurred after the first dismantlement. This also meant that Stage 1 modeling output at the end of simulation time could not be transferred to the Stage 2 TH modeling. Thus, for Stage 2, modeling is performed for 18 years with heater 2 only operating to obtain reasonable initial conditions for the Stage 2 modeling. This neglects the contributions of heater 1 for Stage 2.

A 3-D modeling domain was developed based on project specifications (Figure F-5) with domain size 60 m × 20 m × 40 m in the x, y and z directions, respectively. To reduce mesh size an axisymmetric boundary condition was applied (Figure F-6). For TH simulations using PFLOTRAN numerical code the domain was discretized using an unstructured grid with fine discretization around the heaters and the buffer (Figure F-6). The mesh size for Stage 2 is 329828 grid blocks and includes a total of 1052 grid blocks (elements) across the bentonite barrier. The simulation domain includes details of various regions representing different materials including granite, disturbed rock zone (DRZ), bentonite buffer, heaters, old concrete plug, new shotcrete plug, liner, micro-annulus, lamprophyre and fracture at back of test area. For modeling purposes the new shotcrete plug was assigned the same material properties as the old concrete plug.

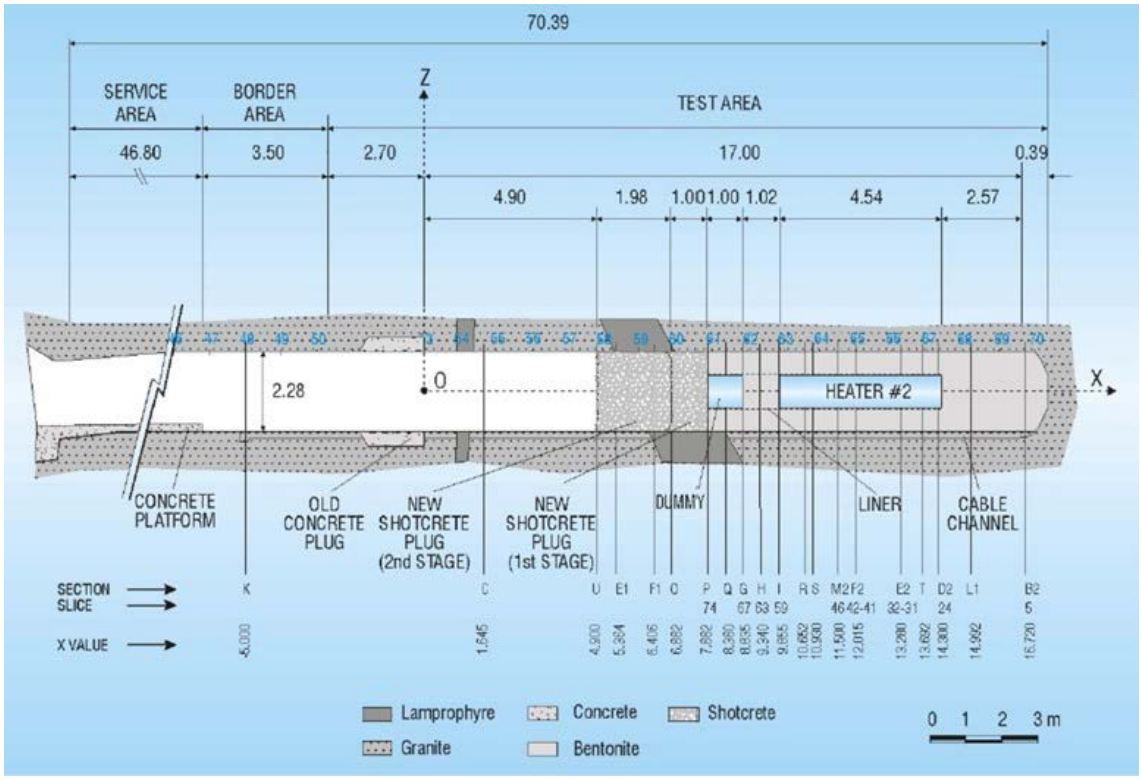

Figure F-5. *General layout of the FEBEX in situ test after first dismantlement.*

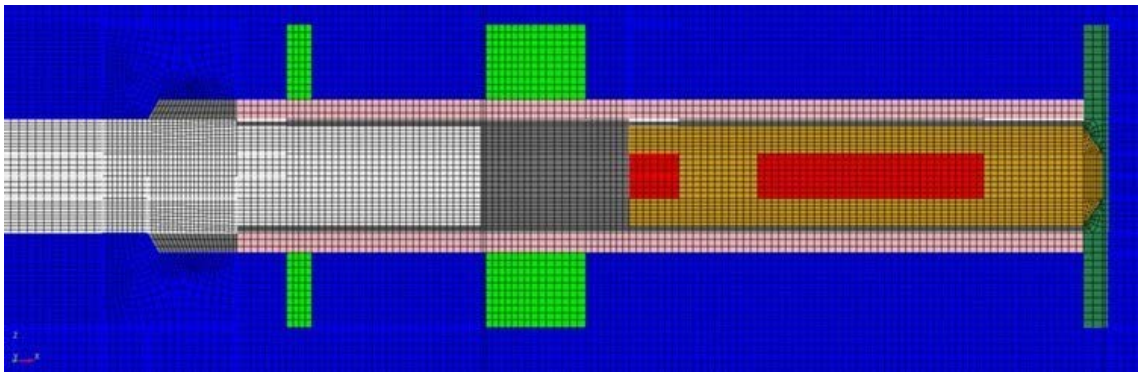

Figure F-6. *Meshing of the TH modeling domain for Stage 2.*

F3.2.1 TH Model Setup

As stated above, Stage 2 modeling starts at the beginning of heating. As for Stage 1 the system is assumed to be at 12 °C at the beginning of the simulation. At the beginning of heating the bentonite buffer is at pressure of one atmosphere and a liquid saturation of 0.65. Hydrostatic pressure boundary condition was assigned on the sides of the modeling domain with a pressure of 0.7 MPa at the top of the domain. Based on the project specification, a 1 200 W heat was applied at Heater 2 for the first 20 days of simulation time. The power was raised to 2 000 W between Day 20 and Day 60. For the rest of the simulation time, time varying heat was applied at Heater 2 to maintain a temperature of 100 °C. The PFLOTRAN numerical code was used for the simulation in a high-performance computing environment. The same material properties specified in Table F-1 and also in Appendix A were used for Stage 2 modeling.

F4 Modeling Results

PFLOTRAN runs were made using up to 160 processors per run using HPC facilities at Sandia National Laboratories. For Stage 1, simulations were run for a total of 1 800 days with both heaters operating and parameter values described in Section F3. In addition, simulations were conducted with a cooling period for 141 days. For Stage 2, simulations were run for a total of 6 700 days with heater 2 only operating and using the same parameter values as in Stage 1. In addition, simulations were conducted with a cooling period for 128 days. Simulation results and comparison with experimental data are described in Section F6.1.

Figure F-7 shows initial system pressure before heating is applied. The system is at hydrostatic pressure conditions except across the buffer barrier. The buffer is at a liquid saturation of 0.65 and gas pressure of one atmosphere. The corresponding suction is 167 MPa with relative humidity at 27 %.

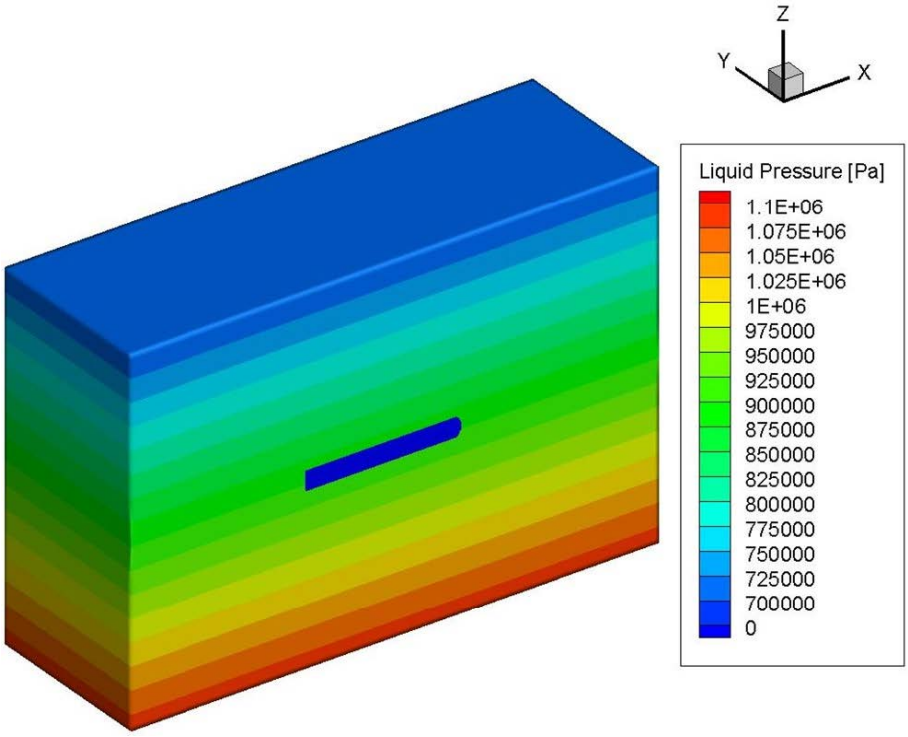

Figure F-7. *Initial condition for both Stage 1 and Stage 2 simulations. Note that negative liquid pressures in the buffer related to suction have not been included in the figure.*

TH modeling results at the end of the Stage 1 are shown in Figures F-8 and F-9. Figure F-8 shows distribution of temperature along the axis of the tunnel, a perpendicular cross-section at the location of heater 1 and a horizontal cross-section. The figure shows migration of heat into the buffer and host rock. Figure F-9 shows the corresponding distribution of liquid saturation.

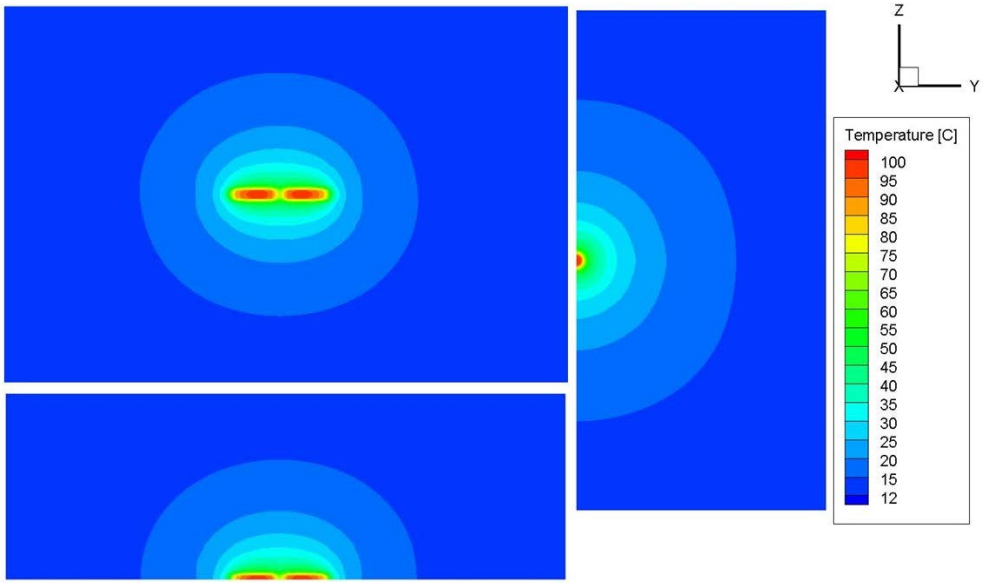

Figure F-8. *Predicted temperature distribution for Stage 1 at 1800 days.*

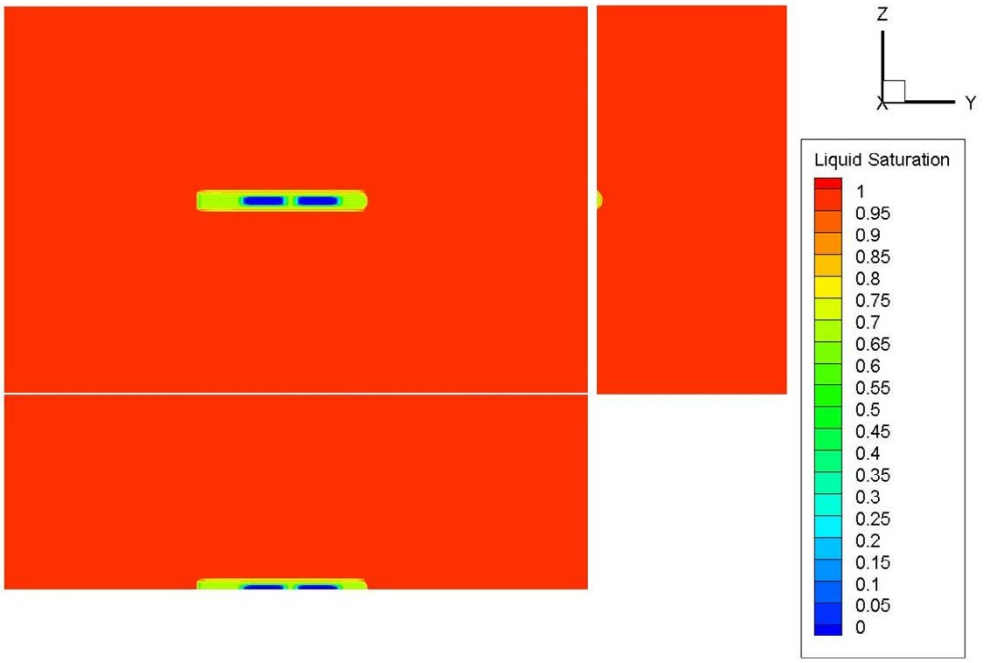

Figure F-9. *Predicted liquid saturation distribution for Stage 1 at 1800 days.*

F5 Comparison to Field Results

F5.1 Stage 1: Analysis of Results

F5.1.1 Evolution of Heating Power

For Stage 1 simulations to maintain 100 °C at the heaters the power applied to both heaters was kept at 2 000 W for the rest of the simulation time. Figures F-10 and F-11 show comparison of the measured and simulated results for heating power. The predicted power is close to experimental for heater 1. For heater 2 the predicted power is lower by up to 10 %.

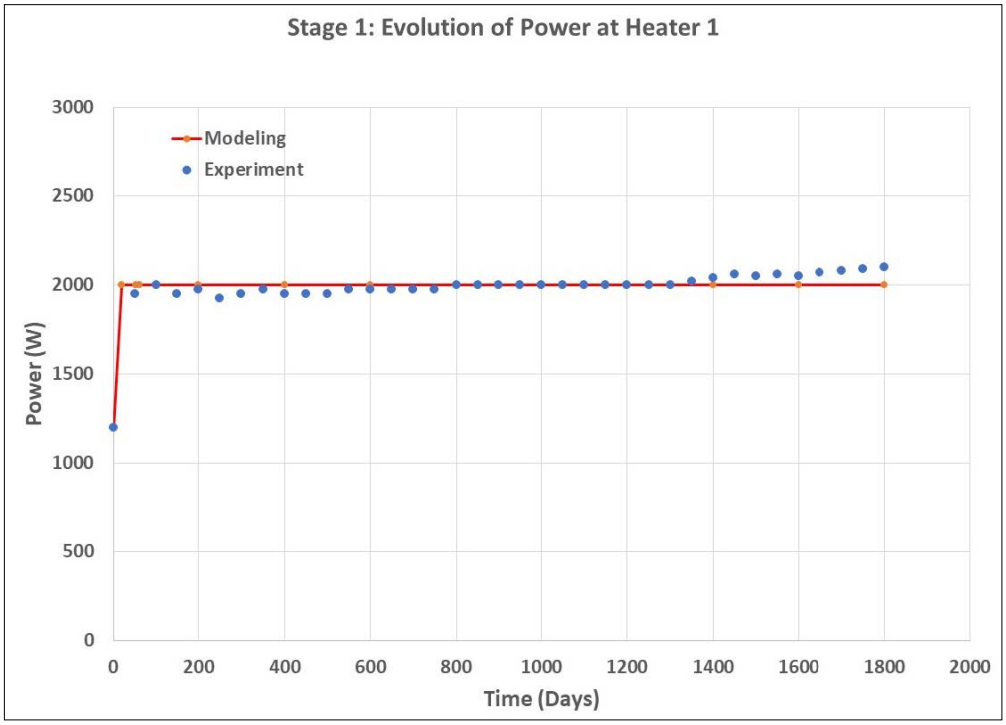

Figure F-10. *Predicted evolution of power at heater 1 for Stage 1.*

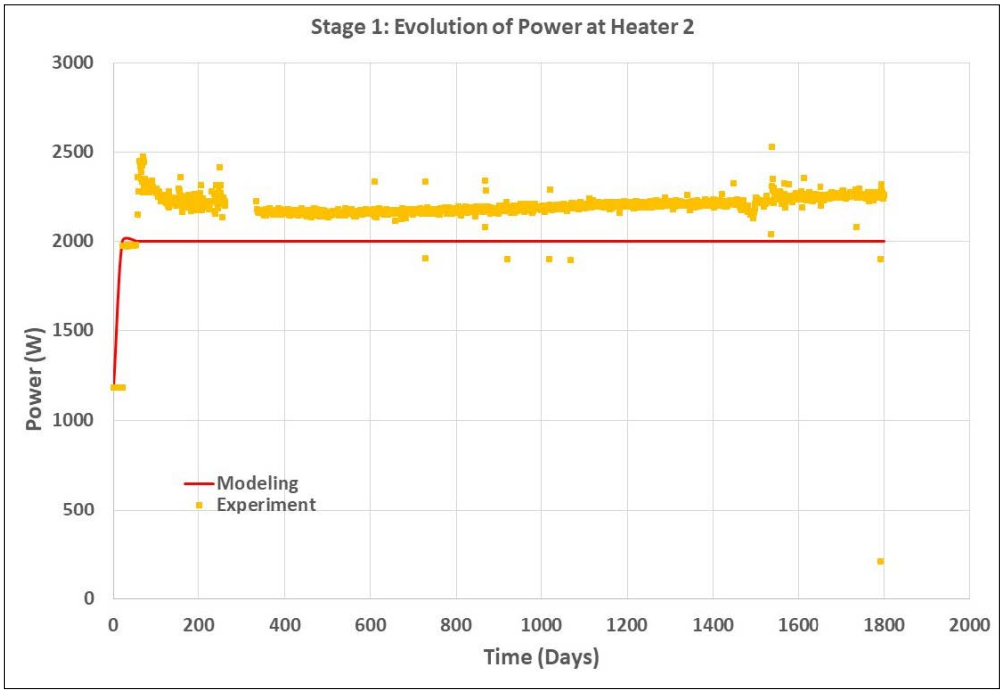

Figure F-11. *Predicted evolution of power at heater 2 for Stage 1.*

F5.1.2 Prediction of Temperature

Prediction of distribution of temperature along radial segments on Section D1 at 90 days and 1 800 days simulation times are shown in Figures F-12 and F-13, respectively, along with experimental data. Section D1 is close to Heater 1 and thus temperatures are higher at radial distances close to the heater. Temperatures are lower away from the heater. At 90 days simulation time predicted temperatures are lower than experimental close to the heater. For the rest of the radial locations the model results are close to experimental. Results at 1 800 days are similar to those at 90 days with slightly lower predicted temperatures near the heater but excellent matching at other radial locations.

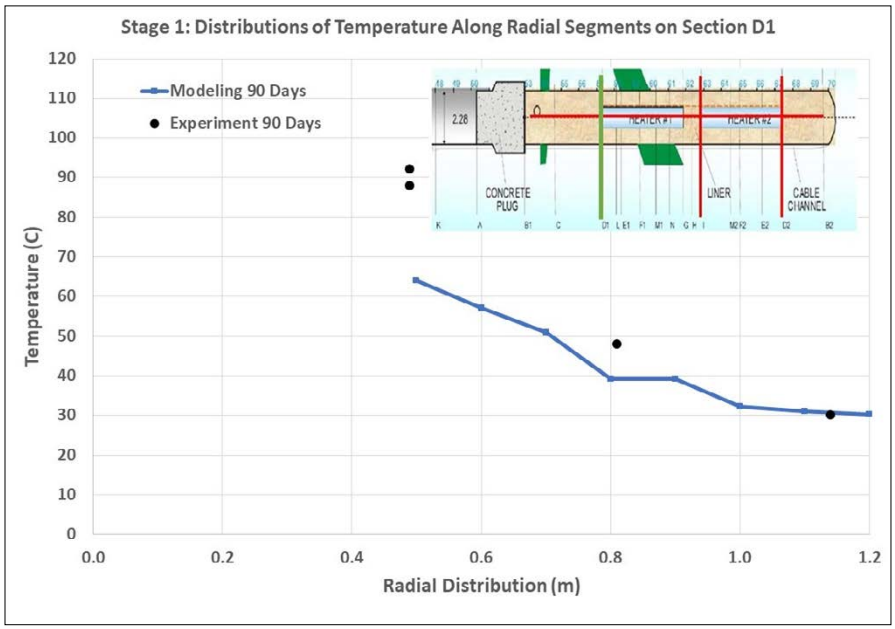

Figure F-12. *Stage 1: Predicted distributions of temperature along radial segments on section D1 at 90 days simulation time.*

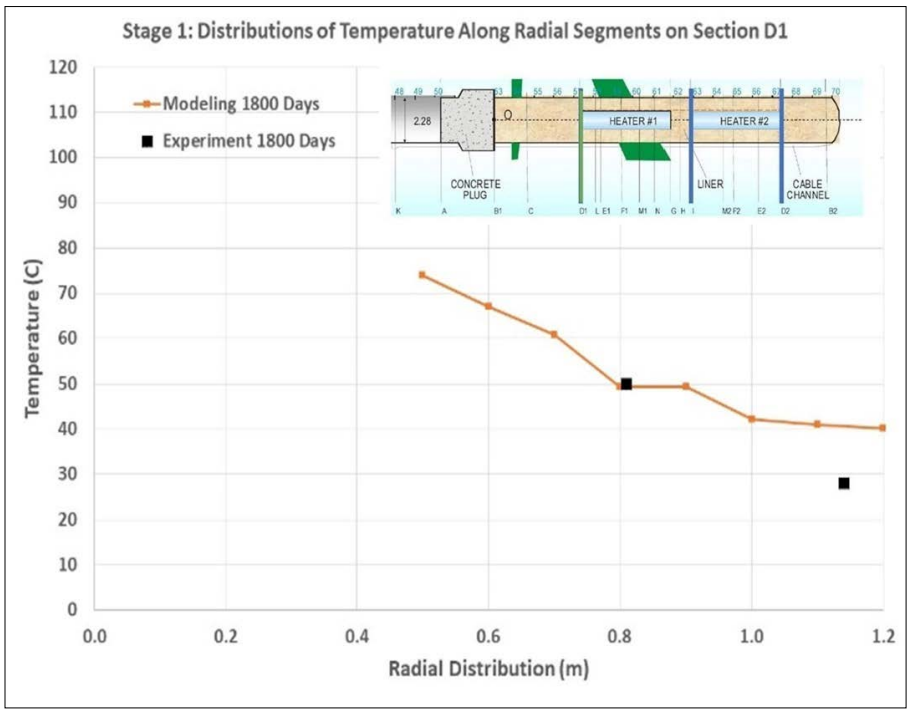

Figure F-13. *Stage 1: Predicted distributions of temperature along radial segments on section D1 at 1 800 days simulation time.*

Prediction of distribution of temperature along radial segments on Section D2 at 90 days and 1 800 days simulation times are shown in Figures F-14 and F-15, respectively, along with experimental data. Section D2 is close to heater 2 on the other end from Section D1. The simulation results are similar to those of Section D1. At both 90 days and 1 800 days predicted temperatures are slightly lower than experimental near the heater. Better matching is obtained at other radial locations.

Predictions of distribution of temperature along axial segments AS1 and AS2 (Table F-4) are shown in Figures F-16 to F-19 at 90 days and 1 800 days along with experimental data. The predictions are very close to the experimental data. As would be expected temperatures rise close to the heaters and decrease away from the heaters. Segment AS1 is closer to the heaters than AS2 and thus temperatures are higher at AS1.

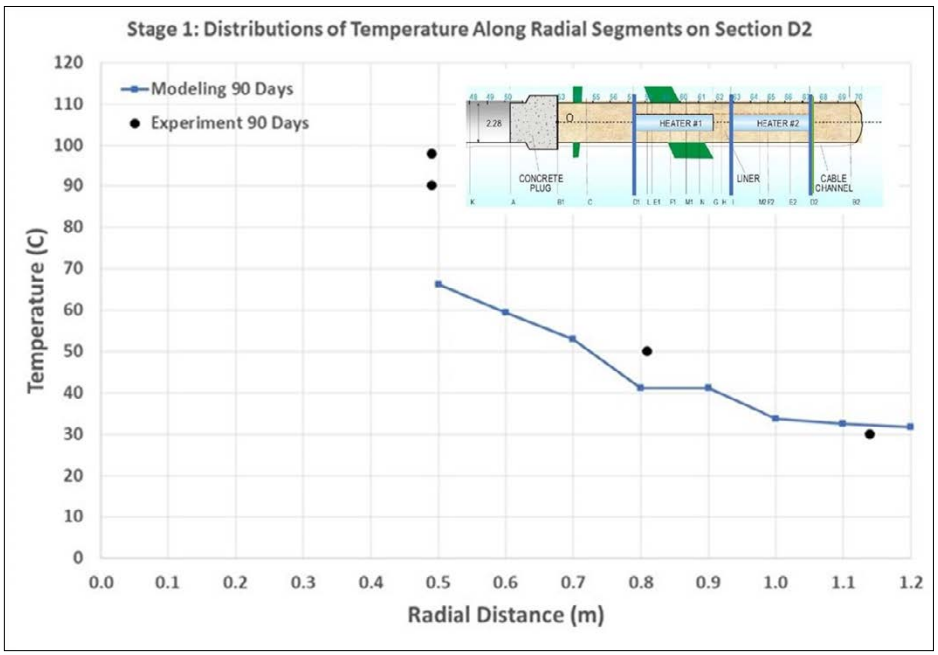

Figure F-14. *Stage 1: Predicted distributions of temperature along radial segments on section D2 at 90 days simulation time.*

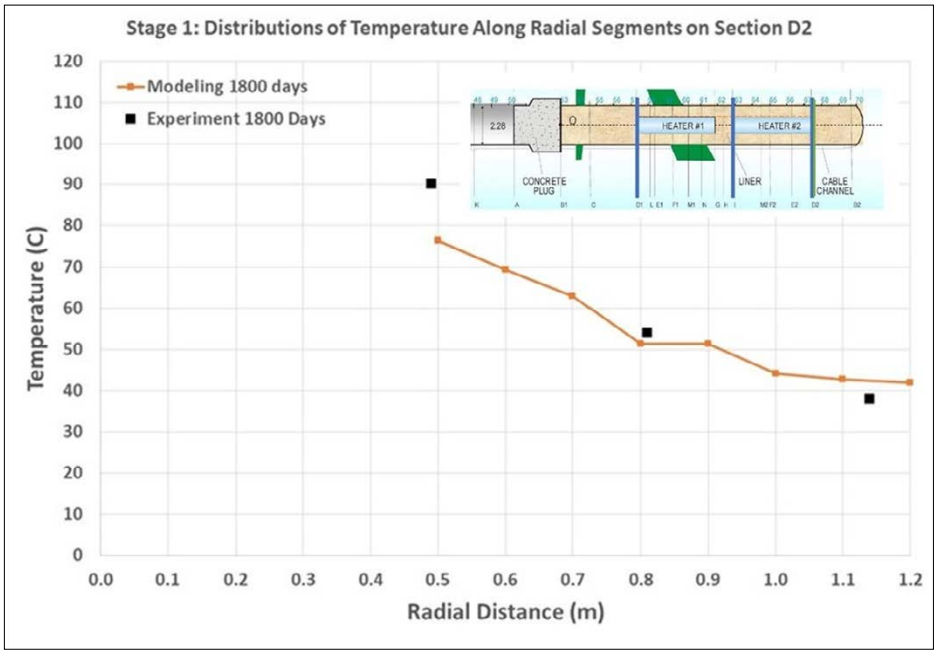

Figure F-15. *Stage 1: predicted distributions of temperature along radial segments on section D2 at 1 800 days simulation time.*

Table F-4. Locations of the axial segments AS1 and AS2.

Segment	Origin (x, y, z)	End (x, y, z)	Remarks
AS1	(0.00, −0.81, 0.00)	(17.00, −0.81, 0.00)	Parallel to x-axis, between heaters and granite
AS2	(0.00, −1.14, 0.00)	(17.00, −1.14, 0.00)	Parallel to x-axis, near granite

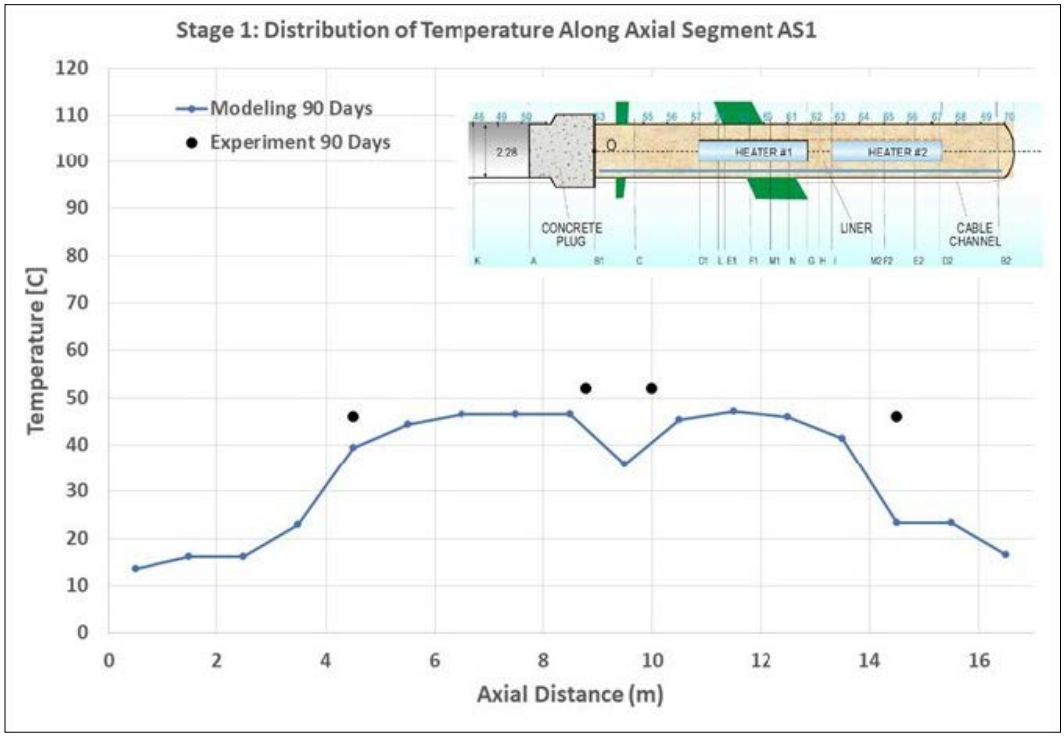

Figure F-16. *Stage 1: predicted distributions of temperature along axial segment AS1 at 90 days simulation time.*

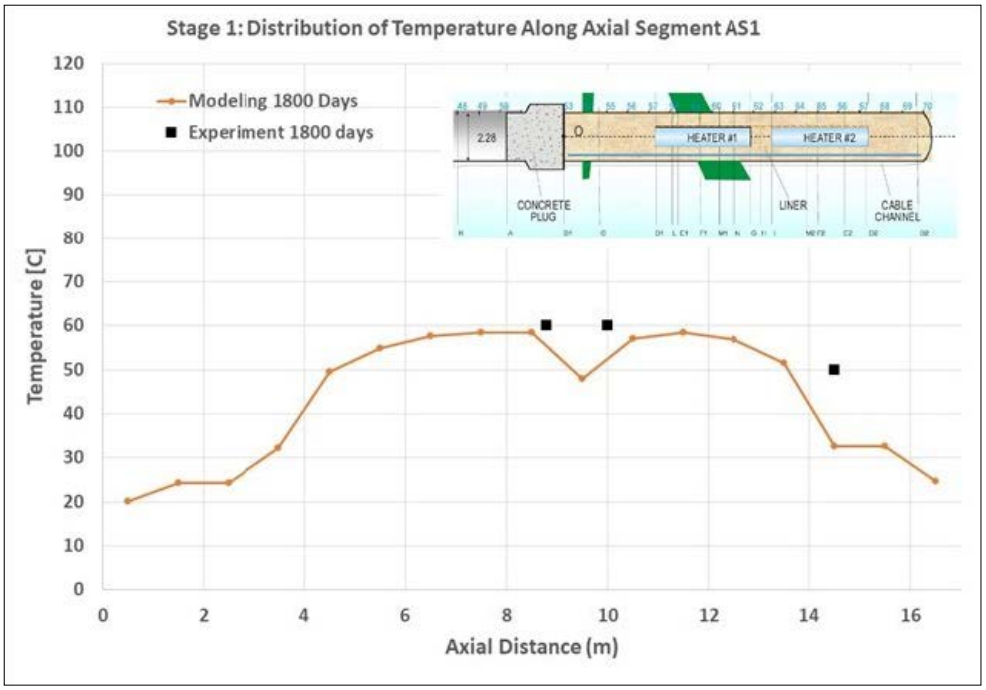

Figure F-17. *Stage 1: predicted distributions of temperature along axial segment AS1 at 1800 days simulation time.*

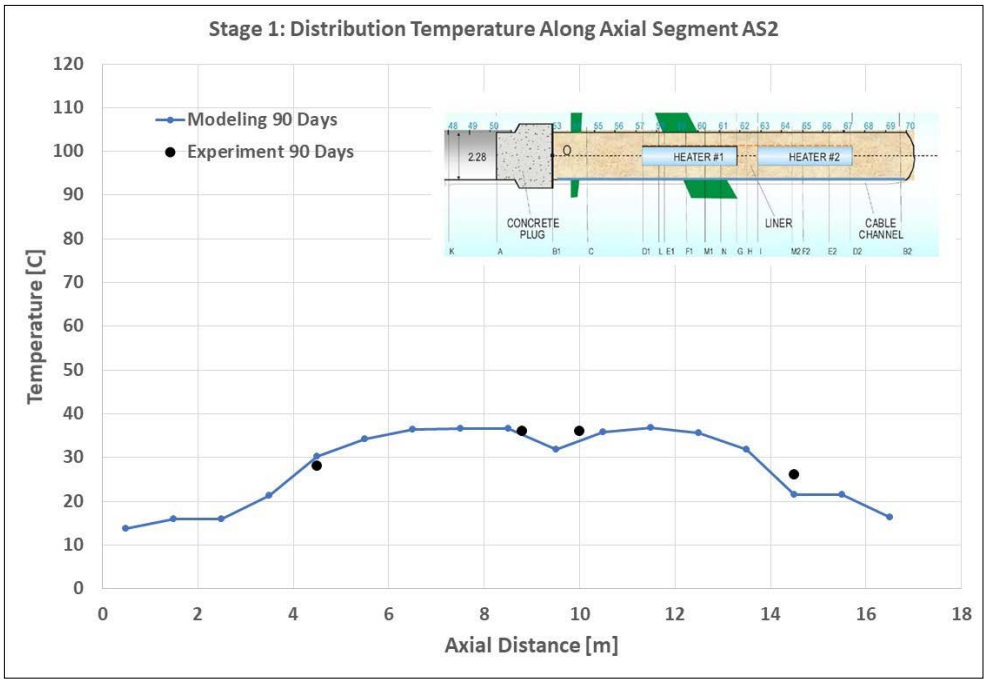

Figure F-18. *Stage 1: predicted distributions of temperature along axial segment AS2 at 90 days simulation time.*

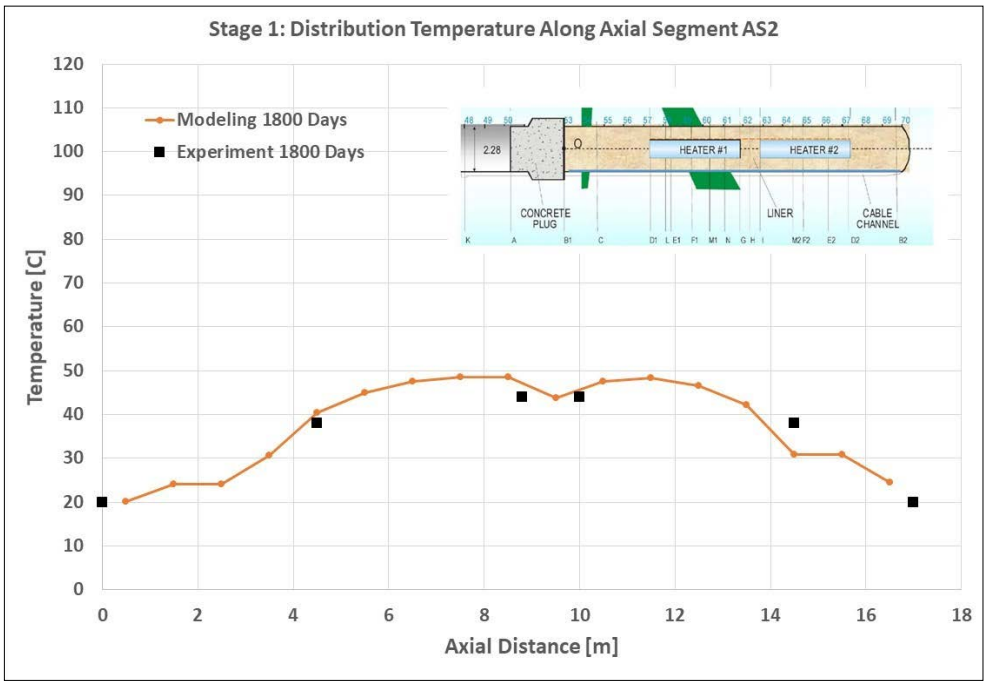

Figure F-19. *Stage 1: predicted distributions of temperature along axial segment AS2 at 1 800 days simulation time.*

Predicted evolution of temperature at Point P1 on Section D1 (Table F-5) is shown in Figure F-20 along with experimental data. Point P1 is away from heater 1, close to the wall. Thus, temperatures are lower. Predicted temperatures are close to the experimental everywhere, except at early time where predicted temperatures are slightly lower. Figure F-21 shows results for Point P1 on Section D2 (Table F-5). The results are similar to D1.

Table F-5. Locations of points on sections D1 and D2.

Segment	Origin (x, y, z)	Remarks
SD1P1	(4.42, −1.14, 0.00)	Negative y-axis, near granite
SD2P2	(14.38, −1.14, 0.00)	Negative y-axis, near granite

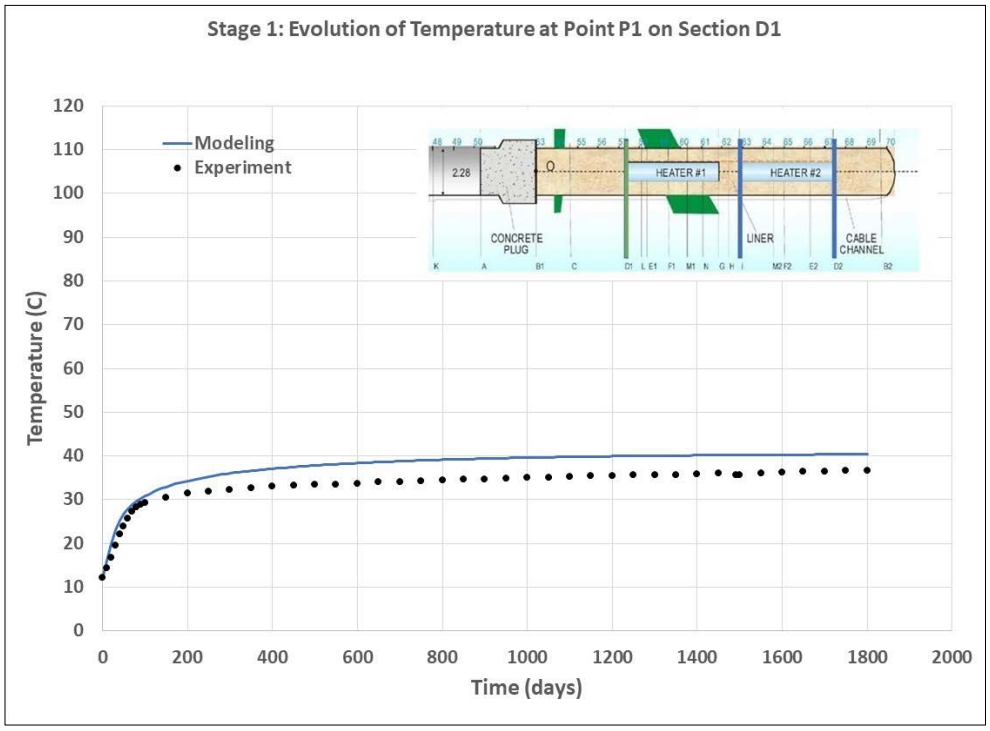

Figure F-20. *Stage 1: predicted evolution of temperature at point P1 on section D1.*

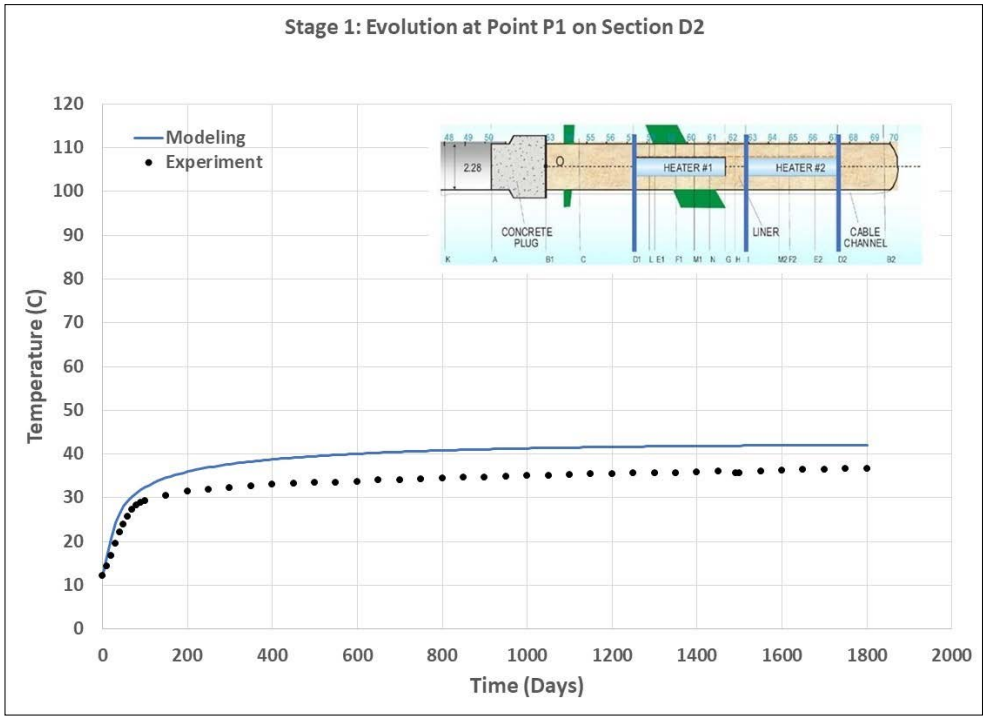

Figure F-21. *Stage 1: predicted evolution of temperature at point P1 on section D2.*

F5.1.3 Prediction of Relative Humidity

Predicted evolution of relative humidity at Points P1, P2 and P3 on Section E1 (Table F-6) are shown in Figure F-22. At early times predicted results at Point P1 are higher than the experimental. Predicted and experimental results are equivalent at later times. At Point P2 the predicted values are close to the experimental at early times but are lower at later times. The predicted results at Point P3 match the experimental data. A sensitivity analysis showed that predictions at Points P1 and P2 improve at higher granite permeability.

Table F-6. Locations of points on Section E1.

Segment	Origin (x, y, z)	Remarks
SE1P1	(5.53, −0.52, 0.00)	Negative y-axis, near steel liner
SE1P2	(5.53, −0.81, 0.07)	Negative y-axis, near middle of bentonite
SE1P3	(5.53, −1.10, −0.17)	Negative y-axis, near granite

Predicted evolution of relative humidity at Points P1, P2 and P3 on Section H (Table F-7), which is located between the two heaters, are shown in Figure F-23 together with experimental data. For Points P1 and P2 predicted results are lower than the experimental at later times. Predicted results for Point P3 match the experimental. Predicted evolution of relative humidity at Points P1, P2 and P3 on Section C (Table F-8), which is located close to the concrete plug, are shown in Figure F-24 together with experimental data. For Points P1 and P2 the predicted results are lower than the experimental. Predicted results for Point P3 are close to the experimental.

Table F-7. Locations of points on Section H.

Segment	Origin (x, y, z)	Remarks
SHP1	(9.50, −0.52, 0.05)	Negative y-axis, near steel liner
SHP2	(9.50, −0.81, 0.05)	Negative y-axis, near middle of bentonite
SHP3	(950, −1.17, −0.16)	Negative y-axis, near granite

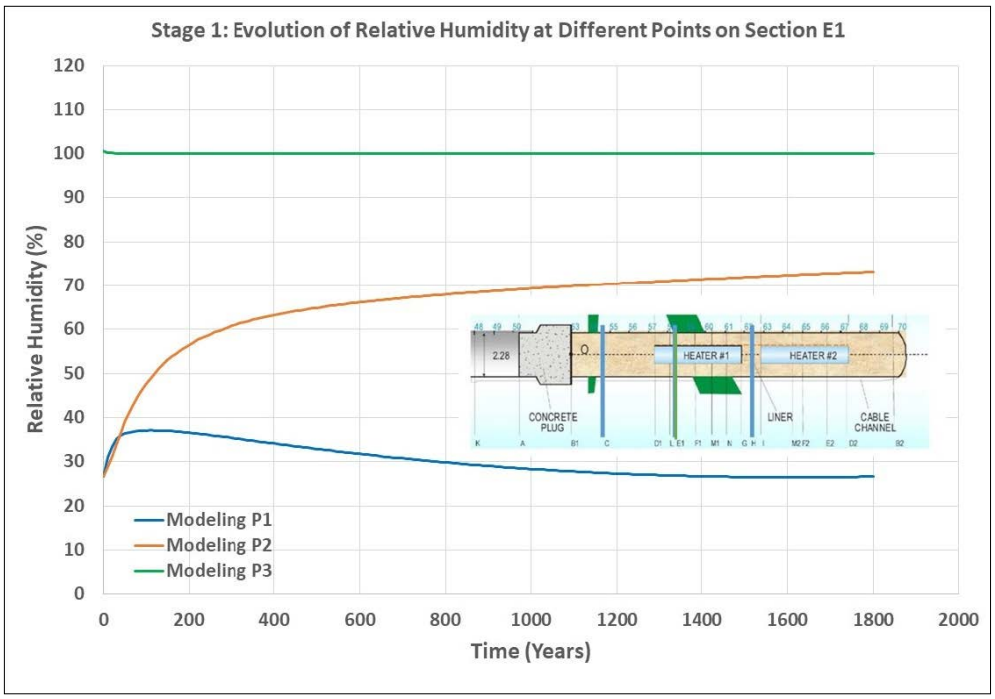

Figure F-22. *Stage 1: predicted evolution of relative humidity at points P1, P2 and P3 on section E1.*

Table F-8. Locations of points on Section C.

Segment	Origin (x, y, z)	Remarks
SCP1	(1.81, 0.0, 0.00)	Negative y-axis, near steel liner
SCP2	(1.81, −0.60, 0.07)	Negative y-axis, near middle of bentonite
SCP3	(1.81, −1.10, 0.07)	Negative y-axis, near granite

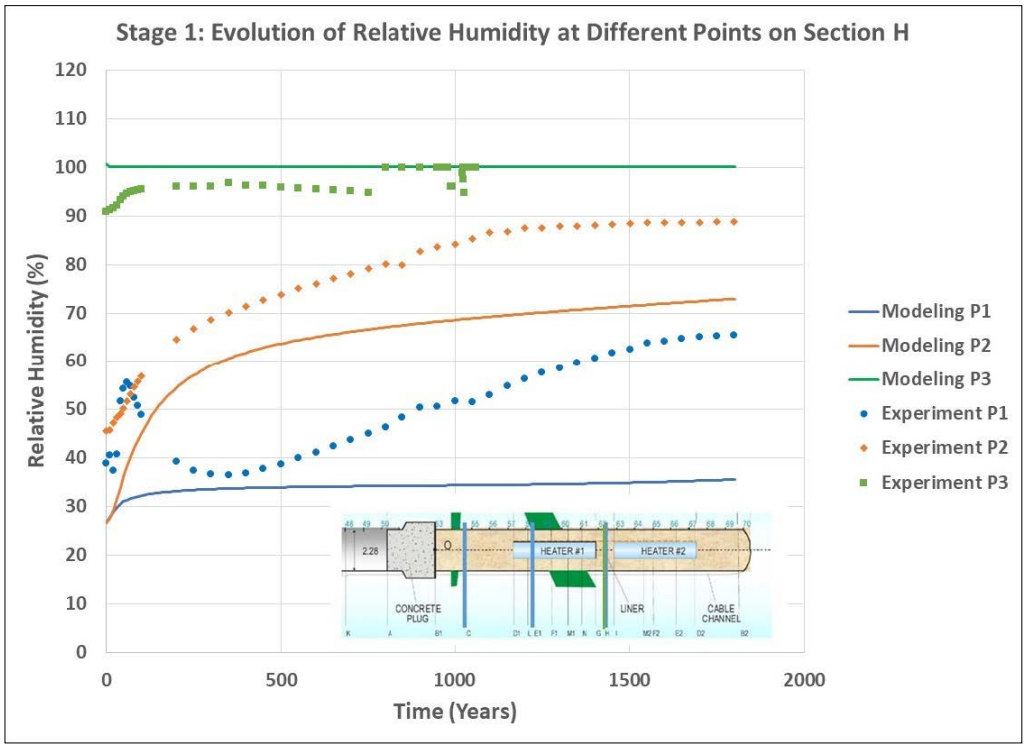

Figure F-23. *Stage 1:Predicted evolution of relative humidity at points P1, P2 and P3 on section H.*

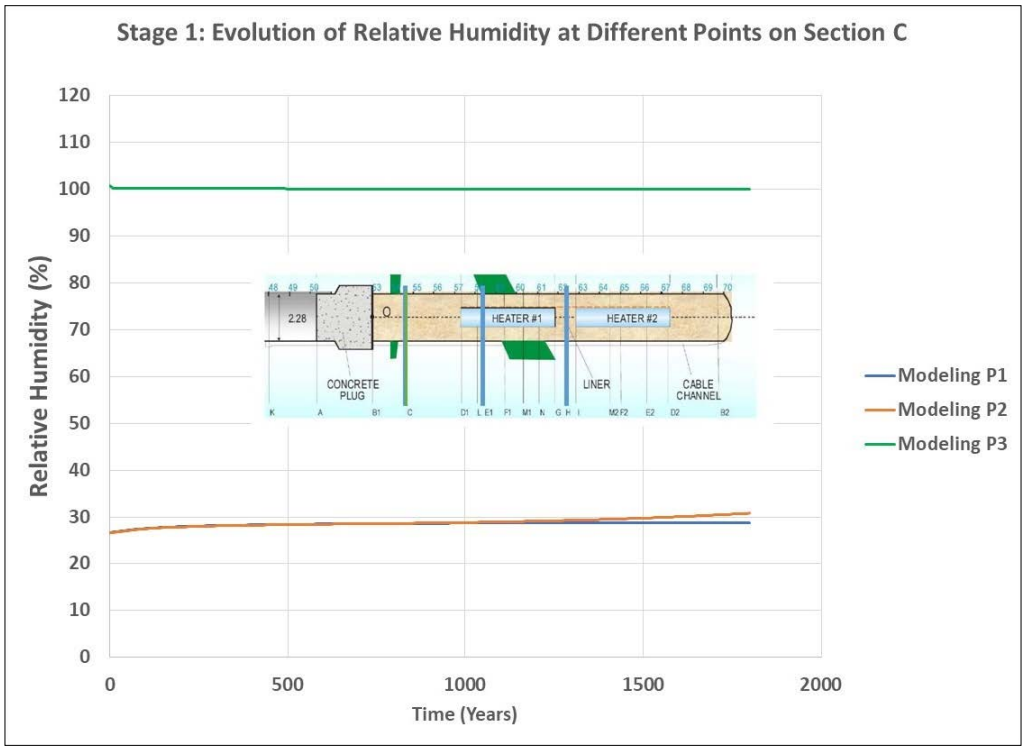

Figure F-24. *Stage 1: Predicted evolution of relative humidity at points P1, P2 and P3 on section C.*

Figure F-25 shows predicted distribution of relative humidity along radial segments on Section E1 at 90 days, 300 days and 1 800 days simulation times. For all specified times the results are close to experimental. Figure F-26 shows predicted distribution of relative humidity along radial segments on Section H at 90 days, 300 days and 1 800 days simulation times. For all specified times the predicted results are lower than the experimental data. Figure F-27 shows predicted distribution of relative humidity along radial segments on Section C at 90 days, 300 days and 1 800 days simulation times. For 90 days and 300 days results are close to experimental data. Results for 1 800 days are lower than experimental data. Some of the differences between simulation results and experimental data could be attributed to mislocation of observation points.

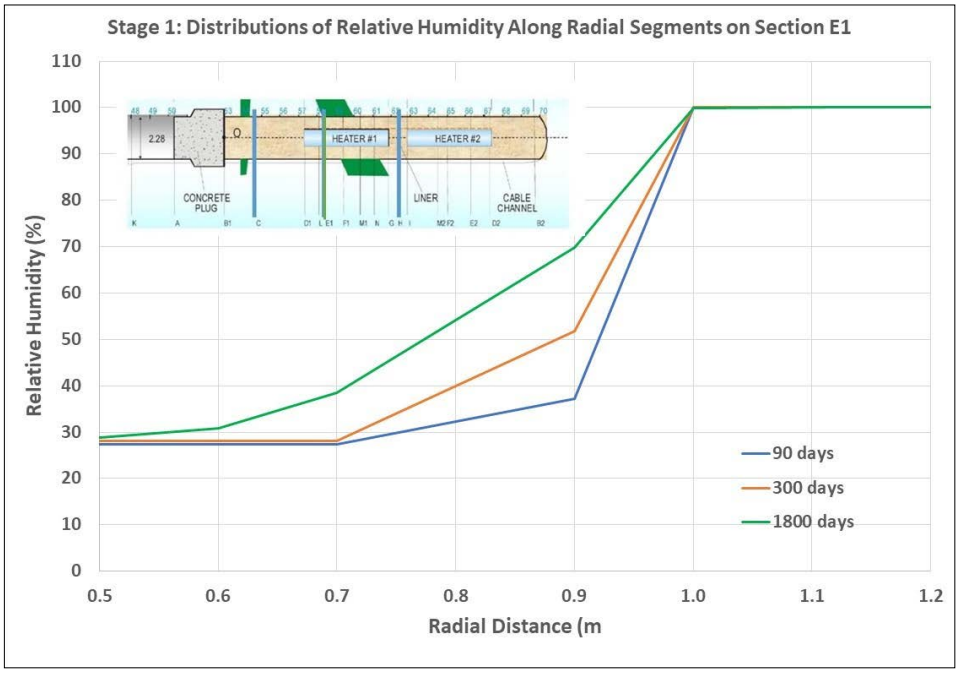

Figure F-25. *Stage 1: Predicted distribution of relative humidity along radial segments on section E1 at different times.*

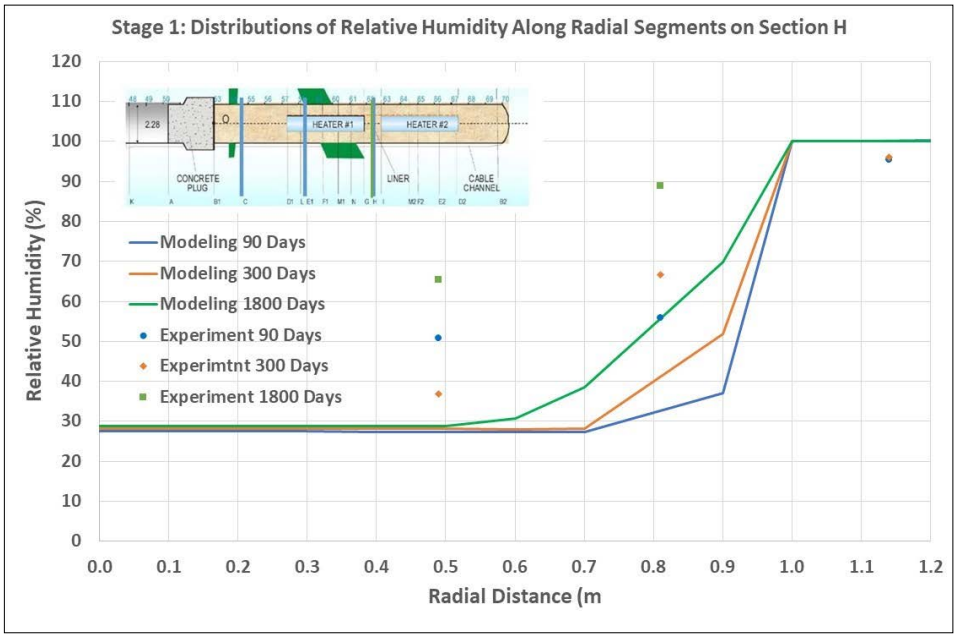

Figure F-26. *Stage 1: Predicted distribution of relative humidity along radial segments on section H at different times.*

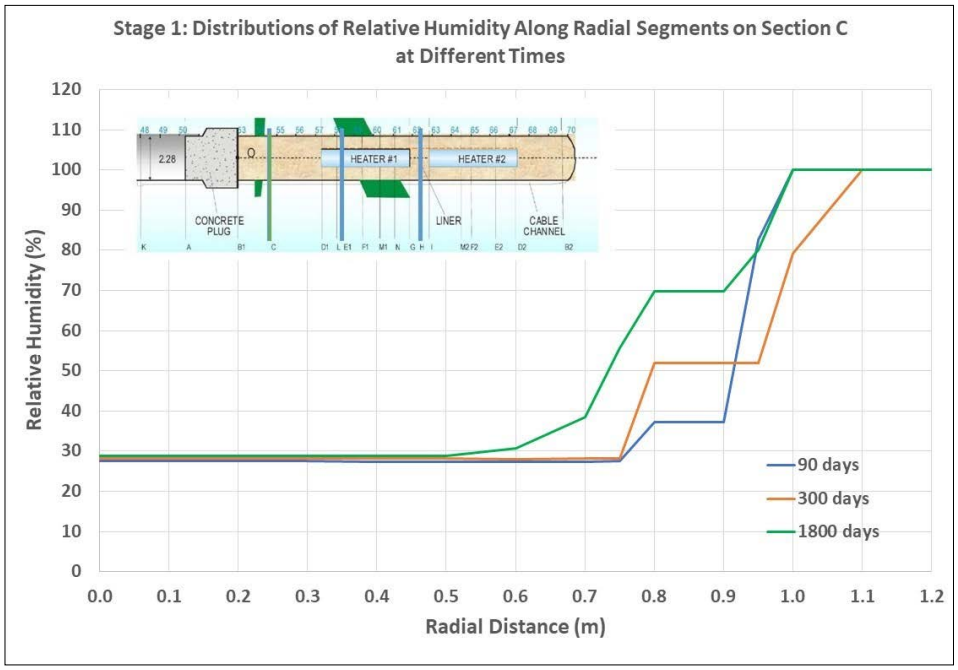

Figure F-27. *Stage 1: Predicted distribution of relative humidity along radial segments on section C at different times.*

F5.1.4 Stage 1 Dismantling Results

Simulations were conducted for 141 days for the period after heater 1 was shut off. Heat was applied at heater 2 only. For TH simulations with PFLOTRAN bentonite swelling was not modeled. Thus, only liquid saturation results at specified locations are reported. Figure F-28 shows locations of the three sections where results are provided (sections 15, 27 and 31). These locations are close to heater 1 and are described below.

- Section 15: x = 3.27 m (between concrete plug and heater H1).

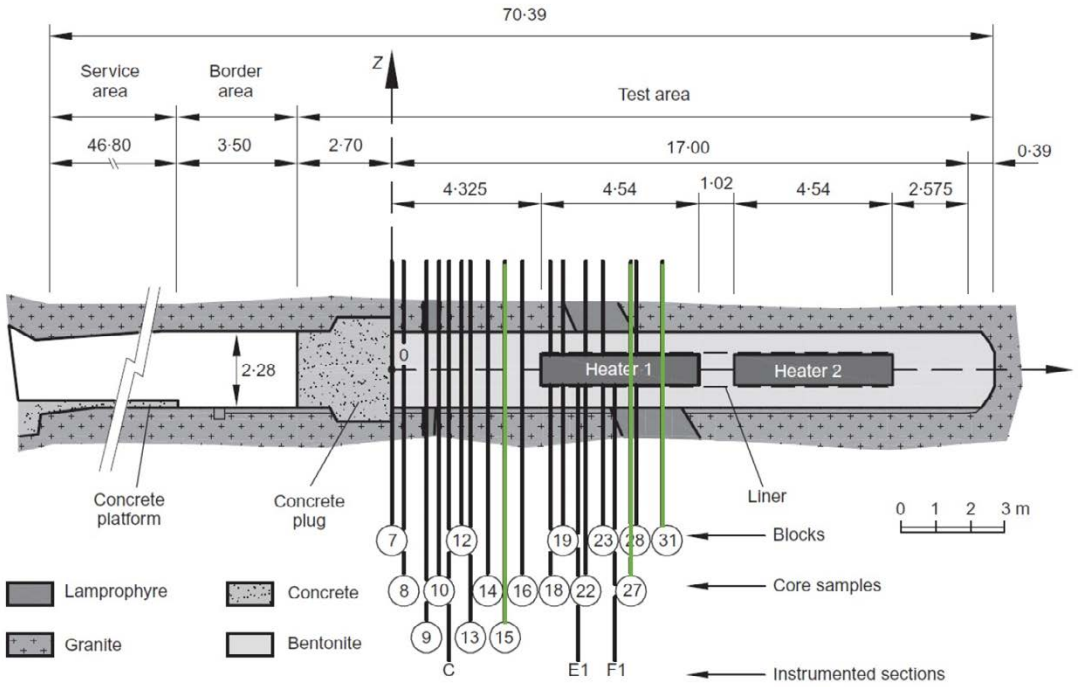

Figure F-28. *Stage 1: locations of three dismantling sections for requested results for distributions of liquid saturation after dismantling (sections 15, 27 and 31 are shown in green).*

Table F-9. Definition of the radial segments on dismantling section 15.

Segment	Origin (x, y, z)	End (x, y, z)	Remarks
S15RS1	(3.27, 0.00, 0.00)	(3.27, 0.87, 0.73)	Angle with pos. y-axis = 40°
S15RS2	(3.27, 0.00, 0.00)	(3.27, −0.48, 1.03)	Angle with pos. y-axis = 115°
S15RS3	(3.27, 0.00, 0.00)	(3.27, 0.00, −1.13)	Angle with pos. y-axis = 270°

- Section 27: x = 6.85 m (on heater H1).

Table F-10. Definition of the radial segments on dismantling section 27.

Segment	Origin (x, y, z)	End (x, y, z)	Remarks
S27RS1	(6.85, 0.37, 0.31)	(6.85, 0.87, 0.73)	Angle with pos. y-axis = 40°
S27RS2	(6.85, −0.17, 0.46)	(6.85, −0.39, 1.07)	Angle with pos. y-axis = 110°
S27RS3	(6.85, 0.00, −0.49)	(6.85, 0.00, 1.13)	Angle with pos. y-axis = 270°

- Section 31: x = 7.74 m (on heater H1).

Table F-11. Definition of the radial segments on dismantling section 31.

Segment	Origin (x, y, z)	End (x, y, z)	Remarks
S31RS1	(7.74, 0.47, −0.17)	(7.74, 1.10, −0.29)	Angle with pos. y-axis = −15°
S31RS2	(7.74, −0.17, 0.46)	(7.74, −0.39, 1.07)	Angle with pos. y-axis = 110°
S31RS3	(7.74, −0.32, −0.37)	(7.74, −0.73, −0.87)	Angle with pos. y-axis = 270°

Figure F-29 shows prediction of distributions of liquid saturation along radial segments on section 15 along with experimental data. Section 15 is in the buffer between the original concrete plug and heater 1. The predicted results are slightly lower at lower radial distances while better matching with experimental data is observed for the rest of the radial distances. Figures F-30 and F-31 show results at sections 27 and 31. Both the sections are close to heater 1. For both locations excellent matching of predicted and experimental data was obtained.

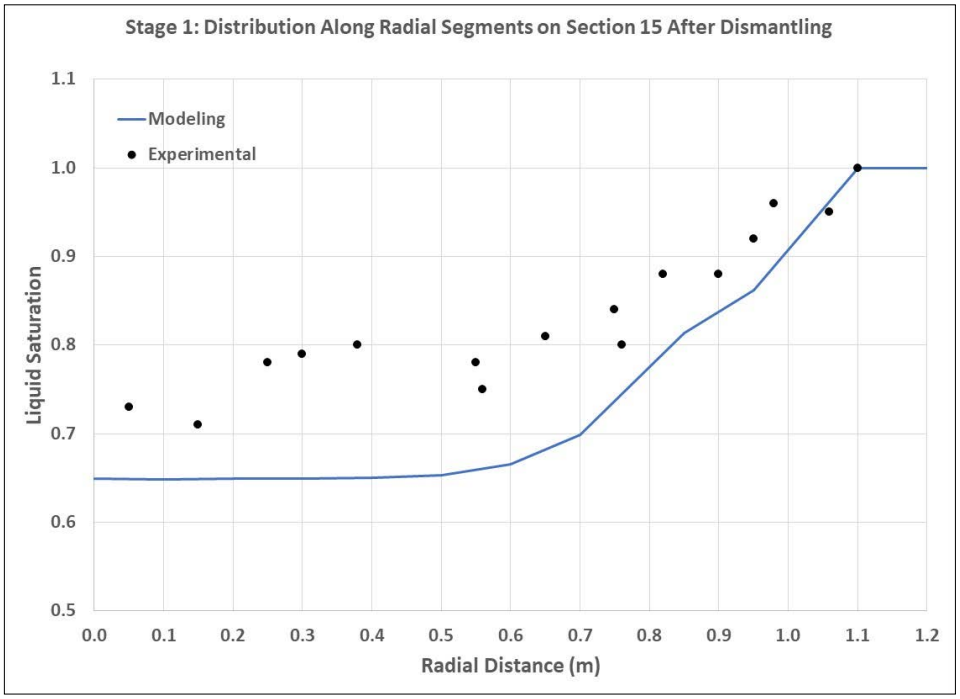

Figure F-29. *Stage 1: Predicted distribution of liquid saturation along radial segments on section 15 after dismantling.*

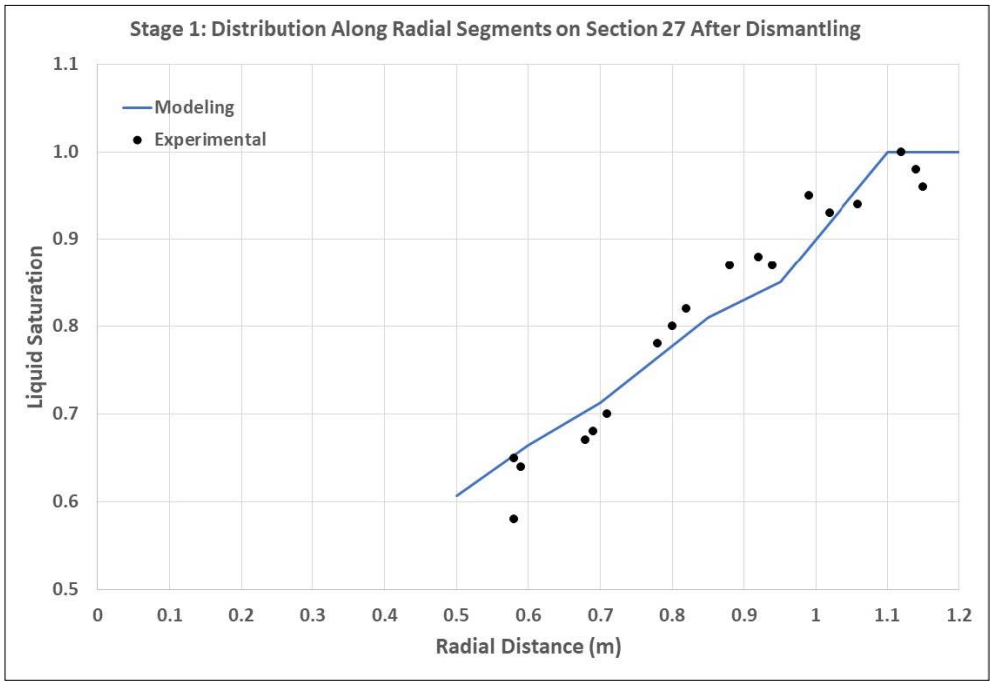

Figure F-30. *Stage 1: predicted distribution of liquid saturation along radial segments on section 27 after dismantling.*

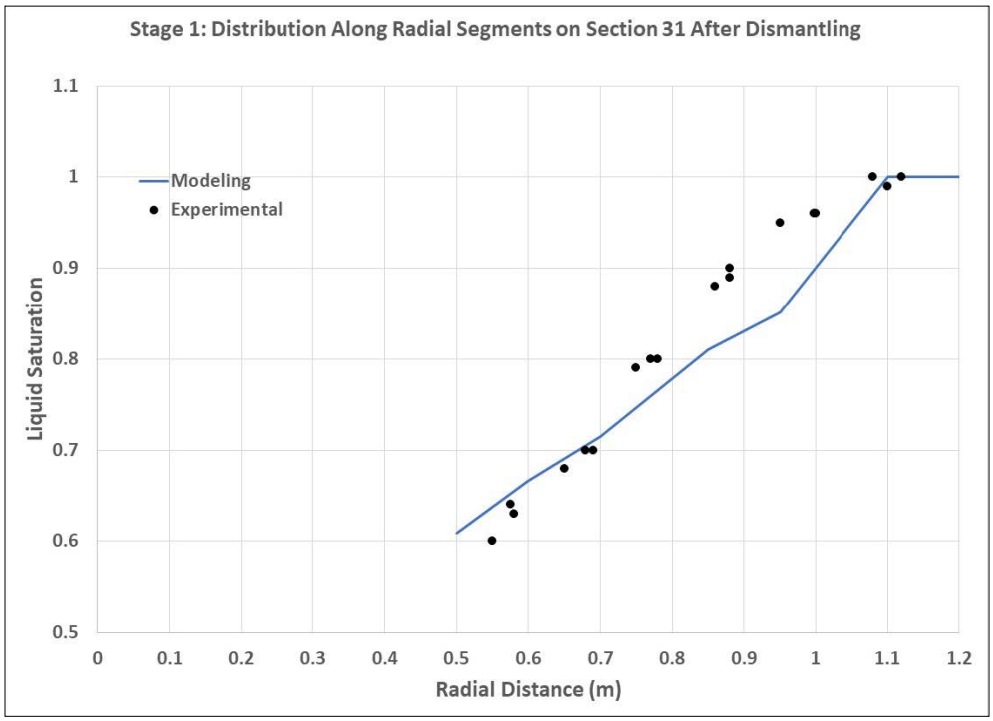

Figure F-31. *Stage 1: predicted distribution of liquid saturation along radial segments on section 31 after dismantling.*

F5.2 Stage 2: Analysis of Results

F5.2.1 Evolution of Heating Power

For Stage 2 simulations, power was kept at 2 200 W between the first dismantling and the final dismantling to maintain 100 °C at heater 2. Figure F-32 shows comparison of the measured and simulated results for heating power. As in the Stage 1 simulations the predicted power for heater 2 is underpredicted.

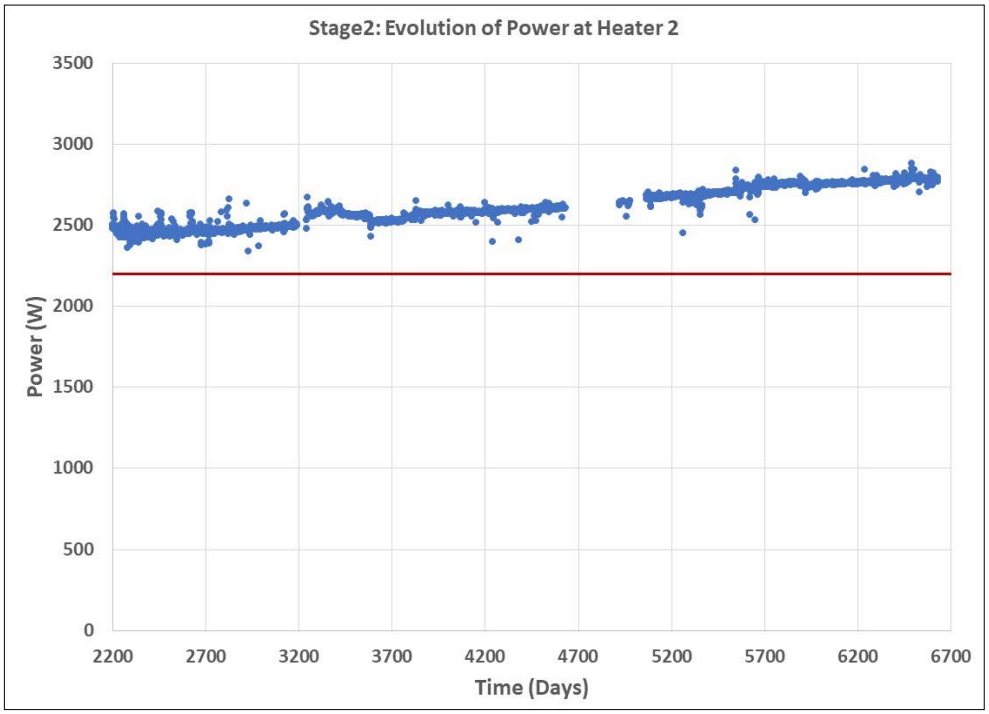

Figure F-32. *Predicted evolution of power at heater 2 for Stage 2.*

F5.2.2 Prediction of Temperature

Prediction of distribution of temperature along radial segments on section D2 at 5 600 days simulation time is shown in Figure F-33, along with experimental data. The predicted temperatures are very close to the measured. Predictions of distribution of temperature along axial segment AS1 are shown in Figure F-34 at 5 600 days along with experimental data. The predictions are very close to the experimental data. Differences at lower axial distances could be due to discrepancies in the location of observation points.

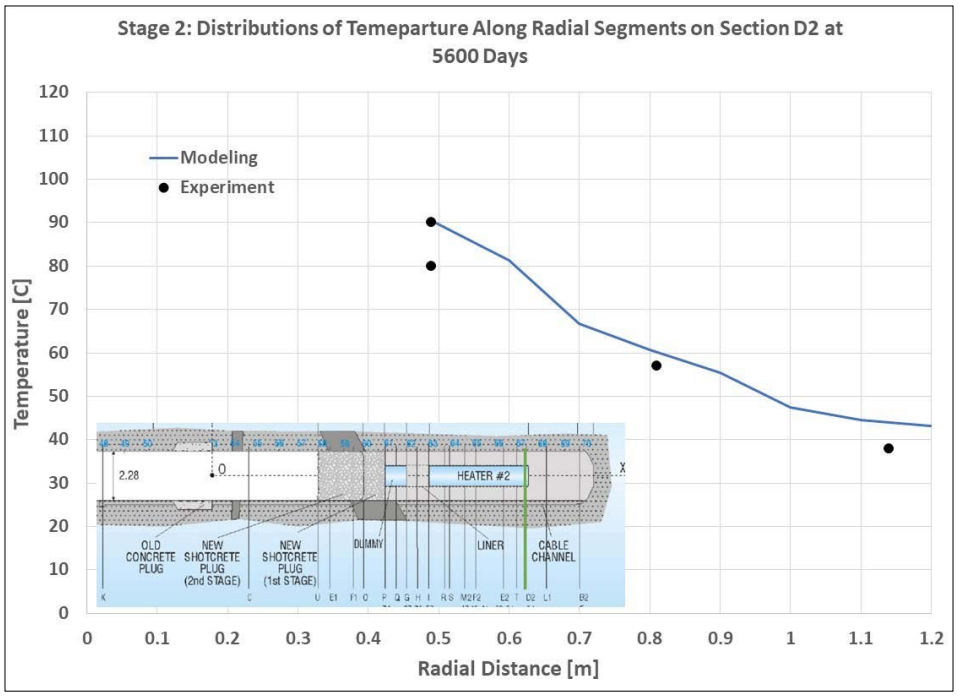

Figure F-33. *Stage 2: predicted distributions of temperature along radial segments on section D2 at 5 600 days simulation time.*

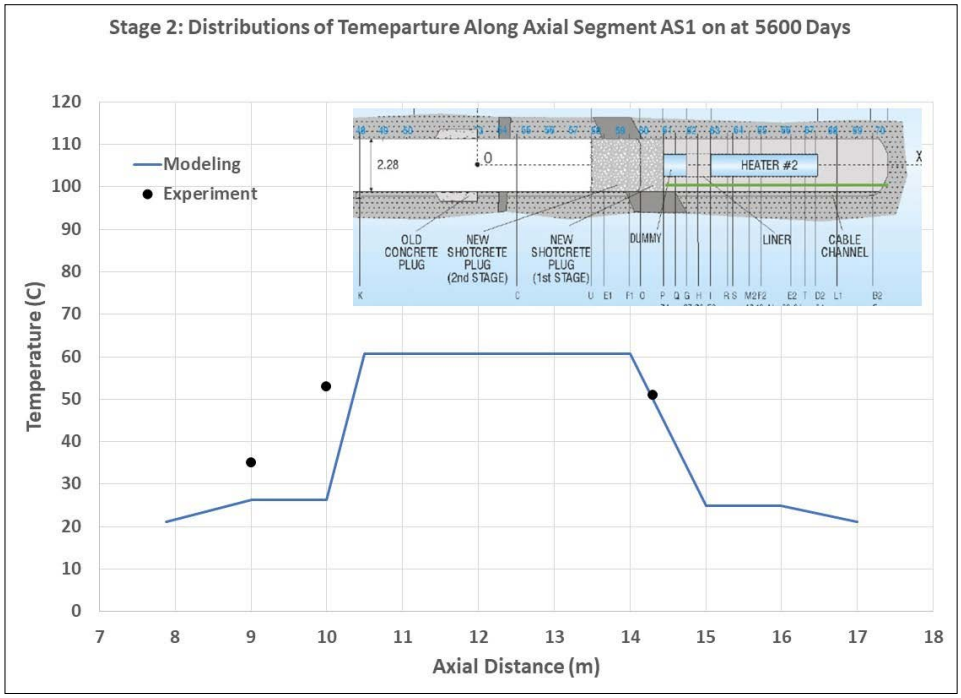

Figure F-34. *Stage 2: predicted distributions of temperature along axial segment AS1 at 5 600 days simulation time.*

Predicted evolution of temperature at Point P1 on section D2 is shown in Figure F-35 along with experimental data. Point P1 is away from heater 1, close to the wall. Thus, temperatures are lower. Predicted temperatures are slightly higher but close to experimental data.

F5.2.3 Prediction of Relative Humidity

Predicted evolution of relative humidity at Points P3 and P5 on section F2 (Table F-12) are shown in Figure F-36. The simulation results for P3 and p5 are similar. The predicted relative humidity for P3 is very close to the experimental. The predicted relative humidity for P5 is lower that the experimental. Further study will be needed to account for the difference.

Table F-12. Locations of points on section F2 (near the middle of heater 2).

Segment	Origin (x, y, z)	Remarks
SF2P3	(12.30, −0.27, −0.52)	Near heater 2
SF2P5	(12.30, 0.53, 0.24)	Near heater 2

F5.2.4 Stage 2 Dismantling Results

Simulations were conducted for 128 days for the period after heater 2 was shut off with no heat applied. For TH simulations with PFLOTRAN bentonite swelling was not modeled. Thus, only liquid saturation results at specified locations are reported. Figure F-37 shows locations of the four sections where results are provided (sections 43, 49, 56 and 61). These locations are close to heater 2 and are described below.

- Section 43: x = 10.12 m (on heater H2, near its end closest to concrete plug).

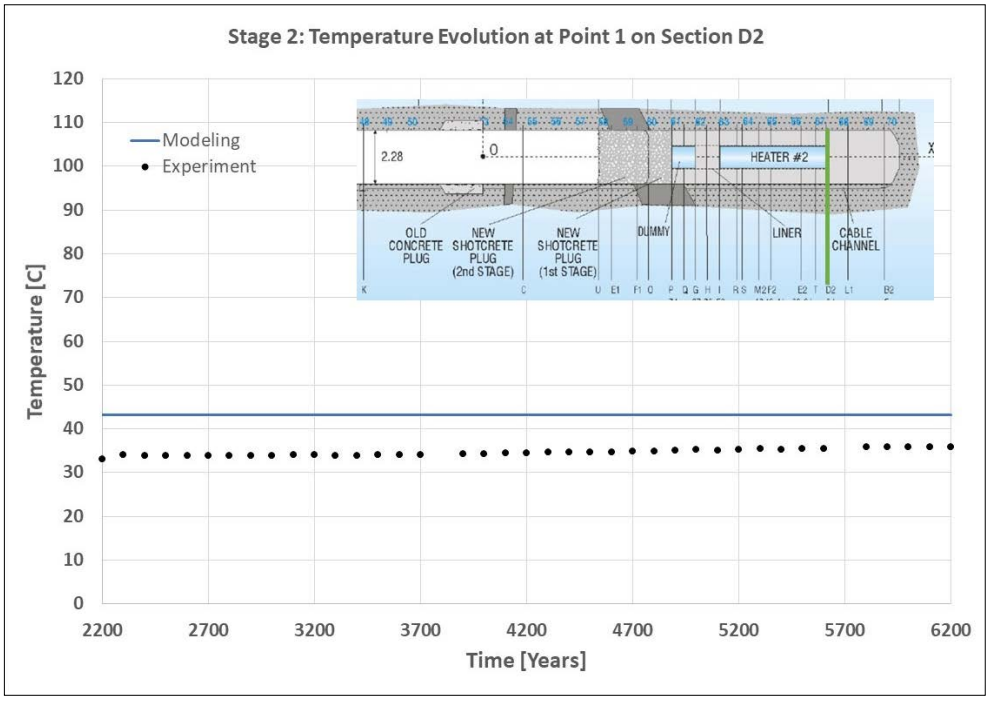

Figure F-35. *Stage 2: predicted evolution of temperature at Point P1 on section D2.*

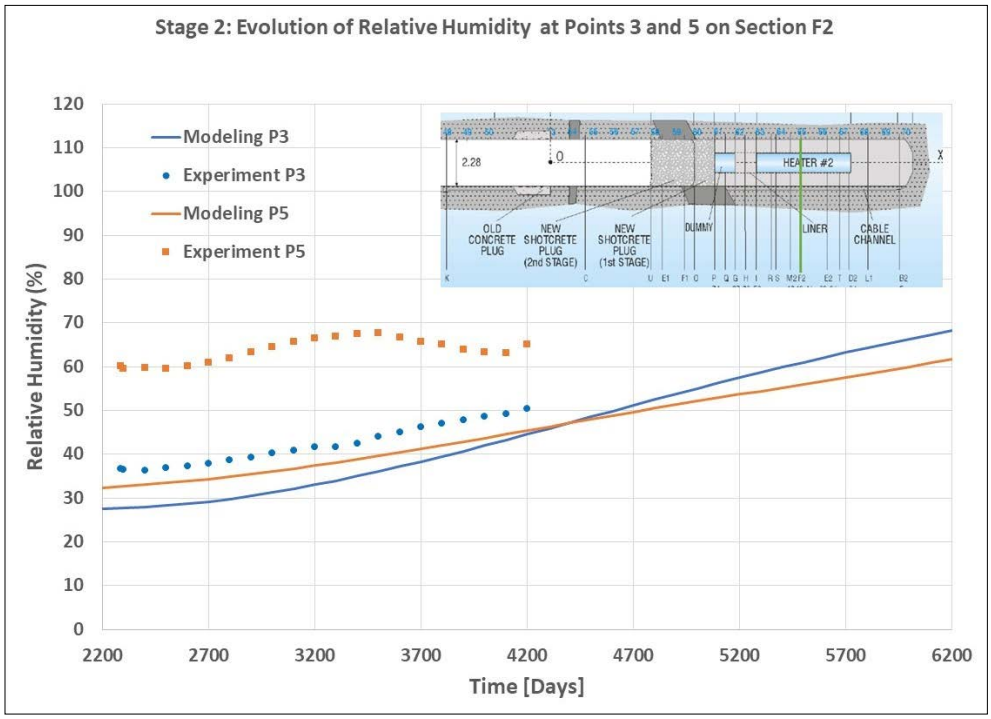

Figure F-36. *Stage 2: predicted evolution of relative humidity at Points P3 and P5 on section F2.*

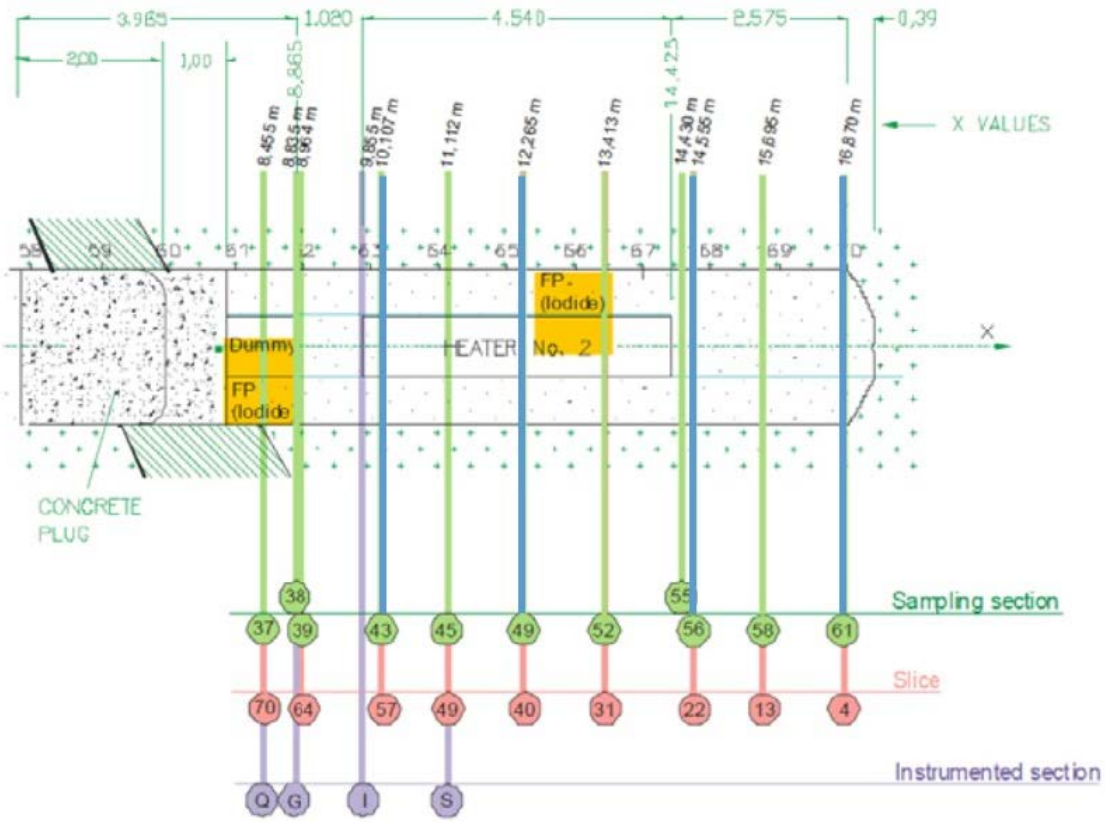

Figure F-37. *Stage 2: Locations of four dismantling sections for requested results for distributions of liquid saturation after final dismantling (sections 43, 49, 56 and 61 are shown in blue).*

Table F-13. Definition of the radial segments on dismantling section 43.

Segment	Origin (x, y, z)	End (x, y, z)	Remarks
S43RS1	(10.12, 0.00, 0.49)	(10.12, 0.00, 1.14)	Angle with pos. y-axis = 90°
S43RS2	(10.12, −0.37, −0.31)	(10.12, −0.87, −0.73)	Angle with pos. y-axis = 220°
S43RS3	(10.12, 0.42, −0.24)	(10.12, 0.98, −0.57)	Angle with pos. y-axis = 330°

- Section 49: x = 12.27 m (on heater H2, near its center).

Table F-14. Definition of the radial segments on dismantling section 49.

Segment	Origin (x, y, z)	End (x, y, z)	Remarks
S49RS1	(12.27, 0.42, 0.24)	(12.27, 0.98, 0.57)	Angle with pos. y-axis = 30°
S49RS2	(12.27, −0.42, 0.24)	(12.27, −0.98, 0.57)	Angle with pos. y-axis = 150°
S49RS3	(12.27, 0.00, −0.49)	(12.27, 0.00, −1.14)	Angle with pos. y-axis = 270°

- Section 56: x = 14.56 m (on bentonite buffer, near end of heater H2 closest to tunnel end).

Table F-15. Definition of the radial segments on dismantling section 56.

Segment	Origin (x, y, z)	End (x, y, z)	Remarks
S56RS1	(14.56, 0.00, 0.00)	(14.56, 0.98, 0.57)	Angle with pos. y-axis = 30°
S56RS2	(14.56, 0.00, 0.00)	(14.56, −1.03, 0.48)	Angle with pos. y-axis = 155°
S56RS3	(14.46, 0.00, 0.00)	(14.56, 0.00, −1.14)	Angle with pos. y-axis = 270°

- Section 61: x = 16.87 m (on bentonite buffer, near to tunnel end).

Table F-16. Definition of the radial segments on dismantling section 61.

Segment	Origin (x, y, z)	End (x, y, z)	Remarks
S61RS1	(16.87, 0.00, 0.00)	(16.87, 0.00, 1.14)	Angle with pos. y-axis = 90°
S61RS2	(16.87, 0.00, 0.00)	(16.87, −0.93, −0.65)	Angle with pos. y-axis = 215°
S61RS3	(16.87, 0.00, 0.00)	(16.87, 0.98, −0.57)	Angle with pos. y-axis = 330°

Figure F-38 shows prediction of distributions of liquid saturation along radial segments on section 43 along with experimental data. Section 43 is located near heater 2 but close to the dummy heater. The predicted results are lower than the experimental. Figure F-39 shows results for section 49, which is also close to the middle of heater 2. The predicted results are better for this location. Figure F-40 are the results for section 56, which is in the buffer close to the end of heater 2. The predicted results for this section are close to the experimental data. Results for section 61 are shown in Figure F-41. Section 61 is close to the wall. For this location excellent matching of predicted results and experimental data was obtained.

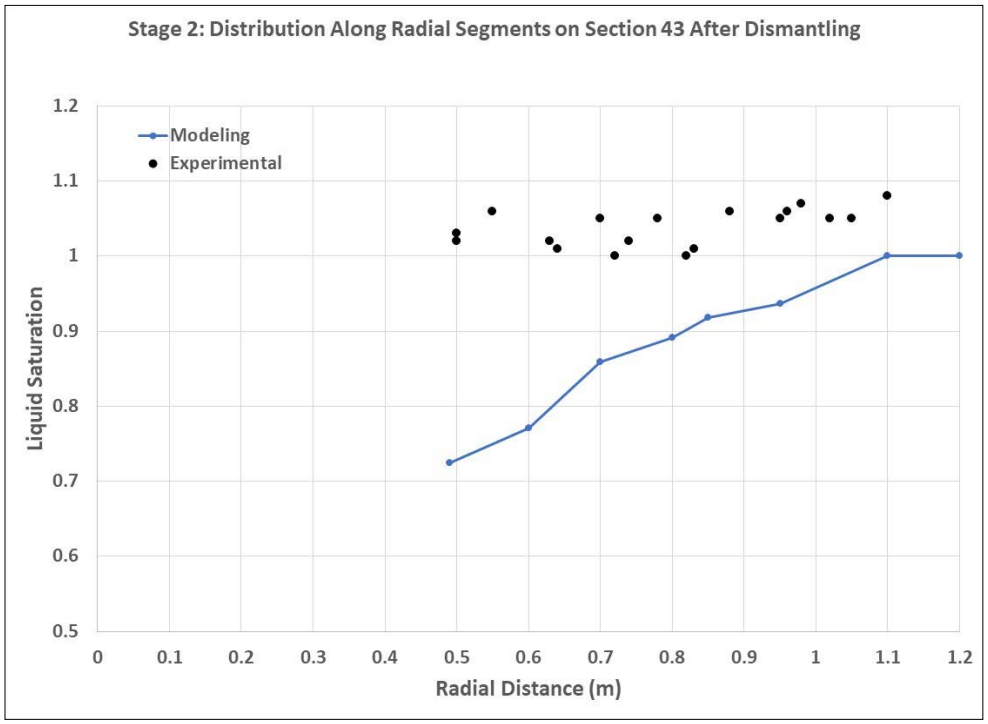

Figure F-38. *Stage 2: Predicted distribution of liquid saturation along radial segments on section 43 after final dismantling.*

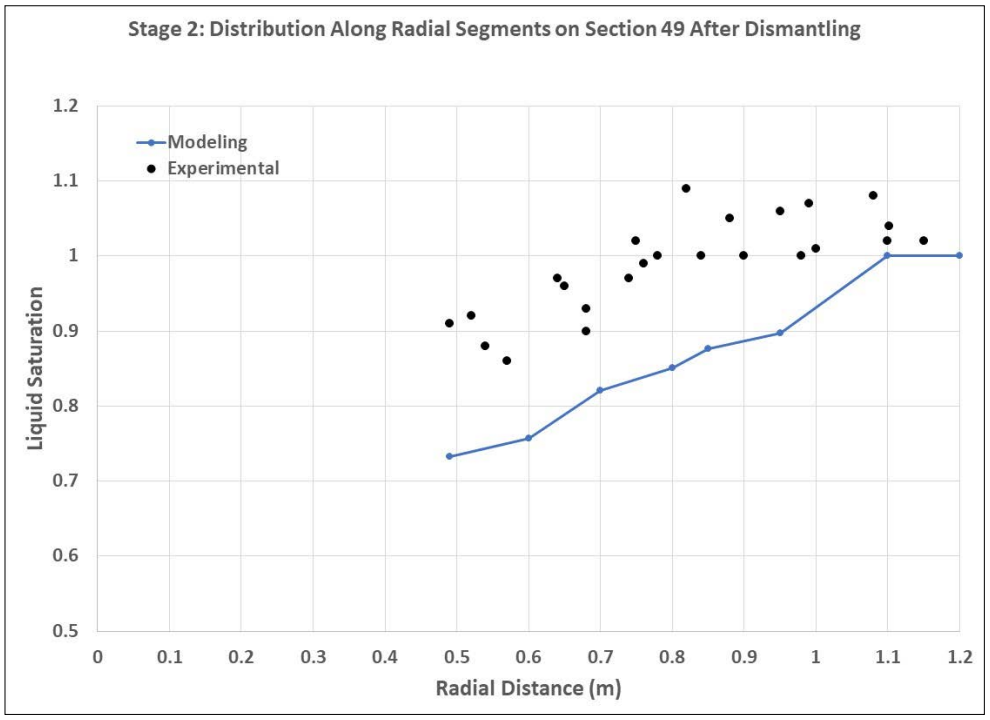

Figure F-39. *Stage 2: Predicted distribution of liquid saturation along radial segments on section 49 after final dismantling.*

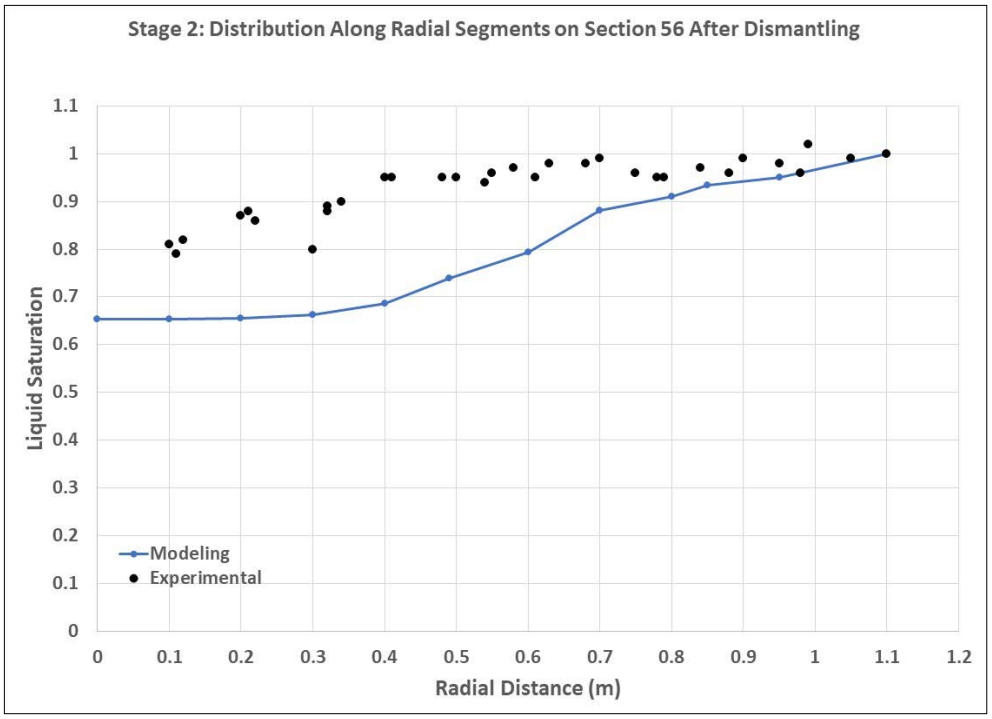

Figure F-40. *Stage 2: predicted distribution of liquid saturation along radial segments on section 56 after final dismantling.*

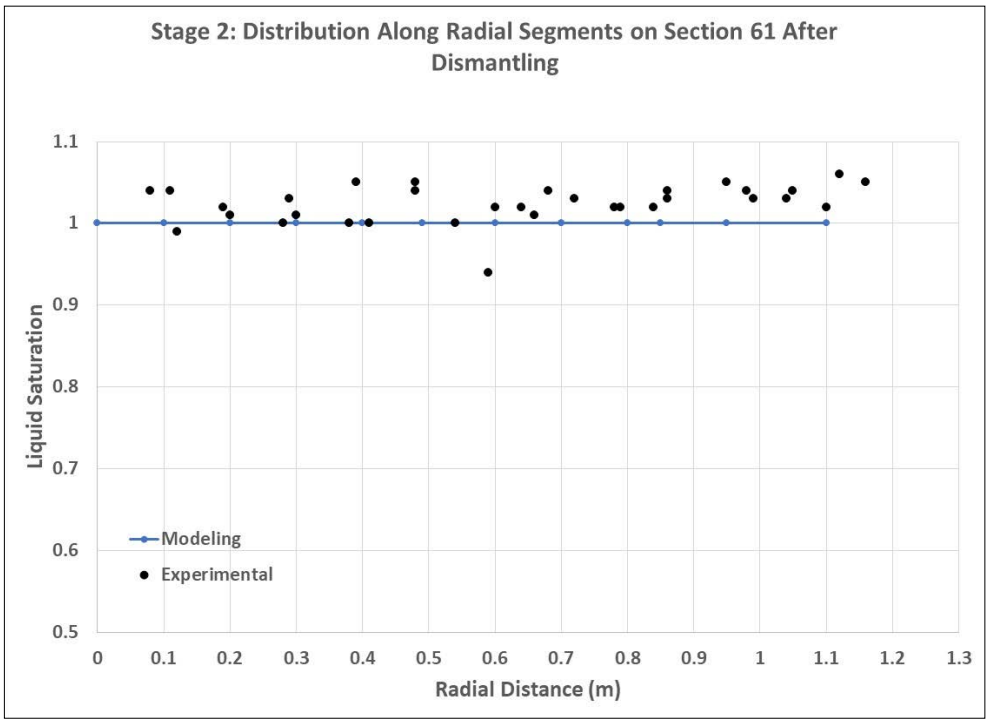

Figure F-41. *Stage 2: predicted distribution of liquid saturation along radial segments on section 61 after final dismantling.*

F6 Conclusions

TH modeling of the Stage 1 and Stage 2 FEBEX in situ experiment using the massively parallel reactive transport code PFLOTRAN was accomplished using HPC facilities at Sandia National Laboratories. Being TH modeling only, we neglected shrink/swell aspects and other structural deformational aspects of the bentonite barrier. Nonetheless the simulation results show good agreement with some FEBEX measurements, while some disagreement with some others. In general, the modeling results show:

- Good agreement with temperature measurements near heater 1, while slightly underpredicting temperatures measured near heater 2 for Stage 1.
- Good agreement with measured liquid saturations after the first dismantling.
- Good agreement with measured temperatures during Stage 2 (heater 2).
- Underprediction of liquid saturations at the end of Stage 2.

In general, the modeling under-calculated humidity measurements, which may have been a consequence of the spatially constant initial conditions for bentonite wetting assumed in the modeling.

F7 Acknowledgements

Sandia National Laboratories is a multimission laboratory managed and operated by National Technology and Engineering Solutions of Sandia, LLC., a wholly owned subsidiary of Honeywell International, Inc., for the U.S. Department of Energy's National Nuclear Security Administration under contract DE-NA-0003525. SAND2020-4195 R.

F8 Initial variables and key parameters

Stages of the analysis

Stage number	Brief description	Start time (day)	Duration (days)
1	Tunnel excavation	−120	30
2	Tunnel ventilation	−90	90
3	Heating Power 1200 W	0	20

F8.1 Rock

Initial conditions of the rock at the start of the analysis (1)

Initial temperature at tunnel axis level (°C)	Initial stresses at tunnel axis level (MPa)	Initial pore water pressure at tunnel axis level (MPa)
12	Not used in TH modeling	0.7

Notes: "tunnel axis level" is specified in case initial conditions are not uniform.

Initial conditions of the rock at the start of the analysis (2)

Initial density (g/cm^3)	Initial porosity	Initial water content (%)
2.75	0.01	saturated

Main rock properties (1)

Initial thermal conductivity (W/mK) dry/wet	Specific heat capacity (J/kgK)	Initial intrinsic permeability (m^2)	Initial hydraulic conductivity (m/s)
3.2/3.3	793.0	1.26×10^{-19}	1.24×10^{-12}

Main rock properties: retention curve (3)

Equation used	P_o (MPa)	λ (-)	Slr (-)	Sls (-)
Van Genuchten	0.0021	0.7	0.0	1.0

Main rock properties: relative permeability (4)

Equation used	P_o (MPa)	λ (-)	Slr (-)	Sls (-)
Van Genuchten	0.0021	0.7	0.0	1.0

F8.2 Bentonite

Initial conditions of the bentonite at installation (2)

Initial dry density (g/cm^3)	Initial density of the solid phase (g/cm^3)	Initial porosity	Initial water content (%)	Initial degree of saturation (%)
1.6	1.6	0.375	24.4	0.65

Main bentonite properties (1)

Initial thermal conductivity (W/mK)	Initial thermal conductivity dry bentonite (W/mK)	Initial thermal conductivity saturated bentonite (W/mK)	Initial specific heat capacity of the solid phase (J/kgK)	Linear thermal expansion coefficient (K^{-1})
1.16	0.6	1.3	1 091	

Main bentonite properties (2)

Initial intrinsic permeability (m^2)	Initial hydraulic conductivity (m/s)	Initial intrinsic permeability (saturated) (m^2)	Initial hydraulic conductivity (saturated) (m/s)	Swelling pressure under initial conditions (oedometric conditions) (MPa)
1.6×10^{-20}				

Main bentonite properties: retention curve (4)

Equation used	P_o (MPa)	λ (-)	Slr (-)	Sls (-)
Van Genuchten	25.0	0.2	0.1	1.0

Main bentonite properties: relative permeability (5)

Equation used	P_o (MPa)	λ (-)	Slr (-)	Sls (-)
Van Genuchten	25.0	0.2	0.1	1.0

Main bentonite properties: vapour transport (7)

Molecular diffusion coefficient of vapour in free air (m^2/s)	Tortuosity
2.0×10^{-5}	1.0

Constitutive functions

Constitutive functions are defined in the main text.

Appendix G

SKB-CT Report

Svensk Kärnbränslehantering AB – Clay Technology, Sweden (SKB-CT)
Ola Kristensson

G1 Introduction

This report concern information produced by modelling team SKB1 regarding Task 9: FEBEX in situ test within the EBS Task Force. THM simulations performed using the finite element solver Code_Bright are described. The objectives of the task were stated in the task description:

- Enhance understanding of the THM EBS behavior during the transient phase.
- Study the state of the engineered barrier at two different stages of its evolution. Observation of degree of homogenization.
- Improve the computational capabilities and validate the performance of coupled THM formulations and associated codes.
- Develop (or enhance) constitutive relationships of the bentonite: thermal, hydraulic and mechanical.
- Compare the performance of different formulations, numerical codes and constitutive laws.
- Examine other issues of potential interest such as: gap between dummy heater and bentonite, gap between rock and bentonite, swelling through liner grids, closure of joints between bentonite blocks.

Section G2 contains a description of the general theory on which Code_Bright is based. In Section G3 follows a full but brief description of the model. In Section G4 'Discussion of model setup' some details of the model are fleshed out for further clarification and motivation. The performance of the model is planned to be evaluated together with the other teams' models in a future compilation report, but in Section G5 'Comparison with experimental data' a brief evaluation is given where model responses are compared against experimental data. In 'Final comments', the last section, general conclusions and findings are given.

G2 Theory

The following description of the thermo-hydro-mechanical theory, on which Code_Bright is based, is a brief and less general version of what is given in Alcoverro and Alonso (2001). A constant gas pore pressure (p_g = 0.1 MPa) was used in the current simulations and no air was allowed to be dissolved into the liquid phase.

The theory used in Code_Bright has its roots in a traditional geomechanical porous formulation, based on considering the material as a mixture of the constituents:

- minerals,
- liquid water,
- dissolved air,
- water vapor, and
- dry air.

The constituents are divided in three **components** (i): minerals (m), water (w), and air (a) (the component belonging of entities is indicated by a superscript) and an assumption of three **immiscible phases** (α): solid (s), liquid (l), and gas (g) (the phase belonging of entities is indicated by a subscript) are made. The solid phase only consists of the mineral component, so the component superscript index (m) will not be written in the following.

From considering the structural assumptions of the mixture, following primitives may be defined:

- mixture volume element (dv),
- solid phase volume (dv_s),
- liquid phase volume (dv_l),
- gas phase volume ($dv_g = dv - dv_s - dv_l$), and
- pore volume ($dv_p = dv - dv_s$).

Further primitives, regarding mass and energy are introduced for the constituents:

- solid mass (dm_s),
- water mass in liquid (dm_l^w),
- water mass in gas (i.e. water vapor mass) (dm_g^w),
- dry air mass in gas (dm_g^a),
- specific internal energy for minerals in solid (e_s),
- specific internal energy for water in liquid (e_l^w),
- specific internal energy for water in gas (e_g^w), and
- specific internal energy for air in gas (e_g^a).

With use of the primitives above the definitions below may be formulated:

- porosity ($\phi = dv_p/dv$),
- solid density ($\rho_s = dm_s/dv_s$),
- liquid water mass per liquid phase volume ($\theta_l^w = dm_l^w/dv_l$),
- water vapor mass per gas phase volume ($\theta_g^w = dm_g^w/dv_g$),
- dry air mass per gas phase volume ($\theta_g^a = dm_g^a/dv_g$),
- degree of liquid saturation ($S_l = dv_l/dv_p$), and
- degree of gas saturation ($S_g = dv_g/dv_p$).

Below functions that give values of variables are indicated with ~ above the variable name.

G2.1 Balance equations

The solid mass per mixture volume element can be expressed,

$$\frac{dm_s}{dv} = \frac{dm_s}{dv_s}\frac{dv - dv_p}{dv} = \rho_s(1-\phi).$$

and by using this as a basis, the **solid mass balance equation**,

$$\frac{\partial}{\partial t}\left(\rho_s(1-\phi)\right) + \nabla \cdot \rho_s(1-\phi)\frac{d\boldsymbol{u}}{dt} = 0,$$

can be derived.

The water mass per mixture volume element can be expressed as,

$$\frac{dm^w}{dv} = \frac{dm_l^w + dm_g^w}{dv} = \theta_l^w S_l \phi + \theta_g^w S_g \phi.$$

If introducing a source term f^w and fluxes of water in the liquid and gas phase, $\boldsymbol{j}_l^w$ and $\boldsymbol{j}_g^w$, the **water mass balance equation**,

$$\frac{\partial}{\partial t}\left(\theta_l^w S_l \phi + \theta_g^w S_g \phi\right) + \nabla \cdot \left(\boldsymbol{j}_l^w + \boldsymbol{j}_g^w\right) = f^w,$$

can be derived.

The used **quasi-static** formulation of the **balance of momentum** for the porous media reads,

$$\nabla \cdot \boldsymbol{\sigma} + \boldsymbol{b} = \mathbf{0},$$

in terms of total stress, $\boldsymbol{\sigma}$, and body force, $\boldsymbol{b}$. As can be seen (from the absent inertia term), a mechanical equilibrium condition assuming an insignificant effect from inertia (i.e. quasi-static conditions), has been used. In the present formulation ordinary continuum mechanics sign conventions are used, i.e. stress components are positive for tensile conditions.

A continuity equation for energy can be formulated using the specific internal energies per volume element:

$$\frac{\sum e_p^e dm_p^e}{dv} = e_s \rho_s (1-\phi) + e_l^w \theta_l^w S_l \phi + e_g^w \theta_g^w S_g \phi + e_g^a \theta_g^a S_g \phi,$$

a source term f^e, and fluxes $\{\boldsymbol{h}, e_l^w \boldsymbol{j}_l^w, e_g^w \boldsymbol{j}_g^w, e_g^a \boldsymbol{j}_g^a\}$. The first element, $\boldsymbol{h}$, in the given set of fluxes, is the conductive heat flux of the mixture as a whole and the following energy fluxes are due to mass transport of the constituents with respect to the solid. The obtained **energy balance equation** reads:

$$\frac{\partial}{\partial t}\left(e_s \rho_s (1-\phi) + e_l^w \theta_l^w S_l \phi + e_g^w \theta_g^w S_g \phi + e_g^a \theta_g^a S_g \phi\right) + \nabla \cdot \left(\boldsymbol{h} + e_l^w \boldsymbol{j}_l^w + e_g^w \boldsymbol{j}_g^w + e_g^a \boldsymbol{j}_g^a\right) = f^e.$$

In addition to the balance equations, *three equilibrium restrictions* have been used. The thermal, mechanical and phase change equilibrium restriction are described in the next section.

In order to close the formulation, variables are selected as independent or dependent and **material specific constitutive relations** are specified where dependent variables are given by expressions of independent variables. The independent variables in Code_Bright are T, p_l and $\boldsymbol{u}$. The temperature, liquid pore pressure and displacement vector. **Initial and boundary conditions** are finally selected as completely specify the problem formulation.

It should here be mentioned that the liquid pore pressure loses its ordinary physical meaning for a bentonite type of material where the chemical potential governs the processes. For such materials the pore pressure could be considered an entity describing the material's water absorption potential.

G2.2 Equilibrium restrictions

As a basic assumption in the formulation, all constituents have a common temperature, T. This comes from the **thermal equilibrium condition**.

For the present systems accelerations are assumed insignificant. This **mechanical equilibrium condition** makes its appearance in the used quasi-static form of the balance of momentum.

The **phase change equilibrium** may be taken as manifested through the equality between chemical potentials of a constituent in different phases. Assuming phase change equilibrium for water and that the gas phase is a mixture of two ideal gases (air and water vapor) give the phase change equilibrium for water,

$$\tilde{\theta}_g^w(p_l, T) = \frac{\tilde{p}_g^w(T) M_w}{R(273.15+T)} \exp\left(\frac{-(p_g - p_l) M_w}{R(273.15+T)\tilde{\rho}_l(p_l, T)}\right).$$

In the expression above, the physical parameters molar mass of water, M_w, and the constant of gases, R, appear.

G2.3 Constitutive relations

As mentioned earlier, to close the formulation, variables are selected as independent or dependent and material specific constitutive relations are specified where dependent variables are given by expressions of independent variables; in Code_Bright temperature, liquid pore pressure and displacement. Thus, temperature, liquid pore pressure and displacement become the unknowns to be solved for.

The constitutive relations can be ordered into the following four categories:

1) **Porous medium relations** describing interactions between constituents in various phases:
   - Retention law
   - Advective mass flow
   - Diffusive (non-advective) mass flow
   - Conductive heat flow
2) **Solid phase relations:**
   - Solid phase density
   - Solid phase specific internal energy
   - Solid phase stress, expressed through the total stress and the fluid pressures
3) **Liquid phase relations:**
   - Liquid phase density
   - Liquid phase viscosity
   - Liquid phase specific internal energy
4) **Gas phase relations:**
   - Water gas pore pressure
   - Air gas pore pressure
   - Gas phase specific internal energy

G3 Model description

In this chapter an attempt has been made as to present a complete but brief description of the model. The description is structured into three sections regarding: (1) Geometry, (2) Initial conditions, boundary conditions and loads (sources), and (3) Material models. For some parts of the model more details can be found in the following chapter 'Discussion of model setup'.

G3.1 Geometry

An assumption of axisymmetry has been used. The components in the model are: Rock, Plug, Heaters, Blocks (made out of Febex bentonite), and Gap. The geometry of the model with the position of the components is given in Figure G-1. The outer gap width of 2.8 cm was calculated from knowing the initial dry density of the blocks (1 700 kg/m^3), the geometry of a canister-mid section, and assuming a fully homogenized dry density of (1 600 kg/m^3) of that section. More details about this can be found in Chapter G4 'Discussion of model setup'.

The finite element mesh shown in Figure G-1 and forthcoming pictures is not the one that was used when performing the calculations. The utilized finite element mesh was somewhat finer with 18 elements radially across the cylinder-shaped buffer blocks. The outer gap (and inner gap when present) was divided in 2 elements radially. The total number of elements was 8 064 and the total number of nodes was 7 244. Two different element types were used, linear quadrilateral elements with 4 integration points and selective integration by means of the "B-matrix" in the inner part of the model and linear triangular elements in the outer part consisting of the rock representation.

To facilitate the mechanical representation and solution, by allowing for radial displacement at the "buffer gables" without introducing an explicit friction representation, a volume of rock material was "removed" at the end of the buffer. This created artificial open disc-shaped volumes at the buffer gables which was not present in the real experiment. More information about this feature can be found in

Chapter G4 ‘Discussion of model setup’. All dimensions of the model are given in Figure G-2, except for the inner slot between the canister and the ring-shaped blocks, only present in the ‘Gap-model’, which was 0.035 m wide.

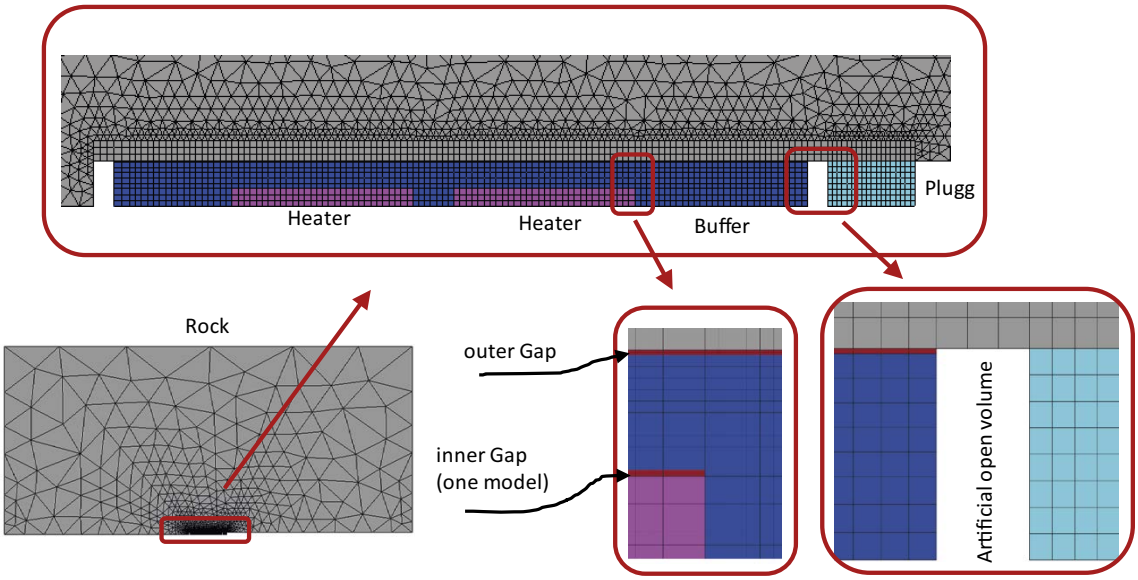

Figure G-1. *Geometry with components the artificial open volume and finite element discretization indicated.*

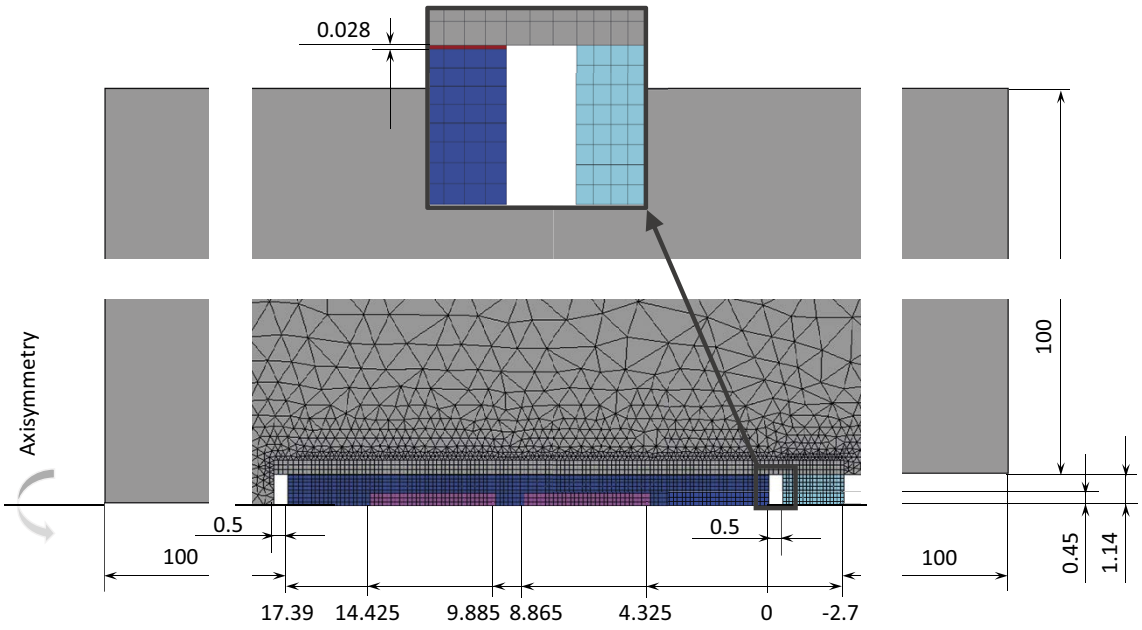

Figure G-2. *Geometry with dimensions. The 0.035 m inner gap, between the canister and ring-shaped blocks, is missing in the drawing.*

G3.2 Initial conditions, boundary conditions and loads (sources)

In Papafotiou et al. (2017), Mattias Åkesson reported the data shown in Table G-1 as the basis for the initial conditions of the bentonite in the Febex in situ experiment:

Table G-1. Basis for initial conditions used in the model.

Water content [a]	Dry density for blocks [a]	Particle density [b]	Initial temperature[c]
14.4 %	1 700 kg/m^3	2 735 kg/m^3	12 °C

[a] Lanyon et al. (2013); [b] Svensson et al. (2011); [c] Sensor data.

Taking this as the starting point the *initial conditions* of the model, i.e. those at the state representing the state at installation, the values as given by Table G-2 were chosen.

Table G-2. Initial conditions, porosity, temperature, liquid pore pressure and total stress (isotropic state).

Component	ϕ [-]	T_0 [°C]	p_{l0} [MPa]	σ [MPa]
Rock (R)	0.01	12	0.1	−0.11
Plug (P)	0.01 [a]	12	0.1	−0.11
Heaters (H)	0.01	12	−124.9	−0.11
Blocks (B)	0.378	12	−124.9 [b]	−0.11
Gap inner and outer (G)	0.9	12	−124.9	−0.11

[a] The Plug porosity is too low but will not affect parts of the solution we are interested in. [b] The liquid pore pressure for the buffer is identical to what Åkesson choose when considering retention data presented in Villar (2002) where 14.4 % corresponded to about 40 % in RH.

The initial conditions for the bentonite together with the used material representation, described in G3.3, give the values shown in Table G-3, as requested in the task description.

Table G-3. Values of variables for the initial condition in the bentonite block material.

ρ_d kg/m^3	ϕ -	$p_g - p_l$ MPa	RH %	S_l -	k m^2	K m/s	λ W/(mK)	p_s MPa	σ MPa
1 700	0.378	125	40	0.647	1.1×10^{-21}	1.1×10^{-14}	0.92	15–16	−0.11

The present model accounts for three phases of the experiment:

- Phase 0 (t = [−135 – 0] days): No heating, water uptake and redistribution.
- Phase 1 (t = [0 – 1 855] days): Heating from both canisters, water uptake and redistribution.
- Phase 2 (t = [1 855 – 6 758] days): Heating from the inner canister, water uptake and redistribution.

The only **boundary condition** that changes for the phases is the applied temperature at the outer surface of the plug, being 12 °C for phase 0 and 16 °C for phase 1 and 2. The dismantling operations have not been considered in the present representation.

The applied **thermal boundary conditions** (see Figure G-3) are:

- T = 12 °C at the outer rock boundary,
- T = 12 °C and γ = 10 W/°C at the tunnel boundary, and
- T = 12 °C (for phase 0) and 16 °C (for phase 1 and 2) at the plug boundary.

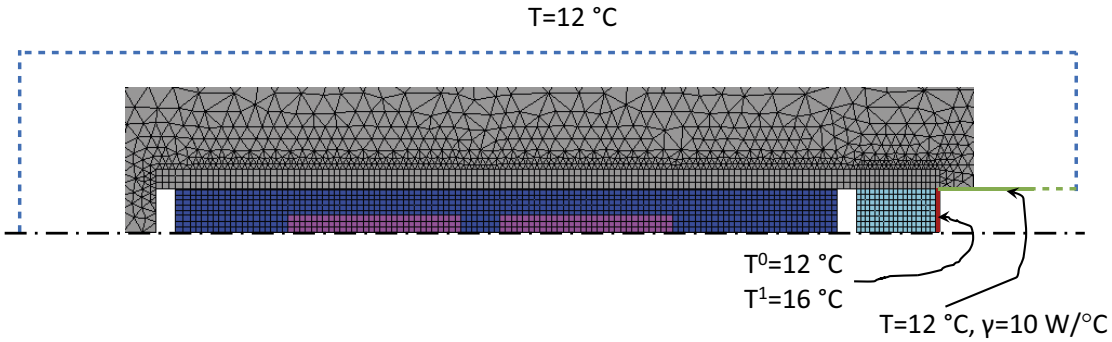

Figure G-3. *Thermal boundary conditions.*

The applied **hydraulic boundary conditions** (see Figure G-4) are:

- j_l^w = 0 kg/(m^2·s) at the outer rock boundary,
- p_{l0} = 0.1 MPa and inflow only at the plug and tunnel boundary

The applied **mechanical boundary conditions** (see Figure G-5) are:

- du_n = 0 m and dt_t = 0 MPa (i.e. roller conditions) along the entire boundary.

The **thermal load** applied along the center of the heater representations (see Figure G-6) was obtained by adapting a piecewise linear function, as defined by the protocol given in Table G-4, to the measured heater powers, see Figure G-7. More details can be found in Chapter G4 ‘Discussion of model setup’.

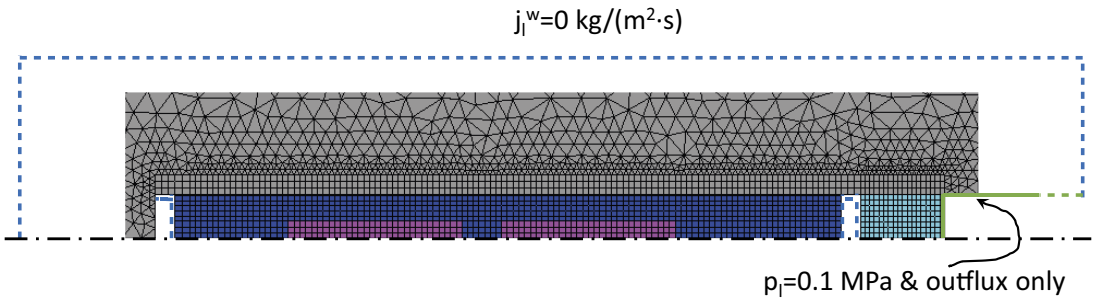

Figure G-4. *Hydraulic boundary conditions.*

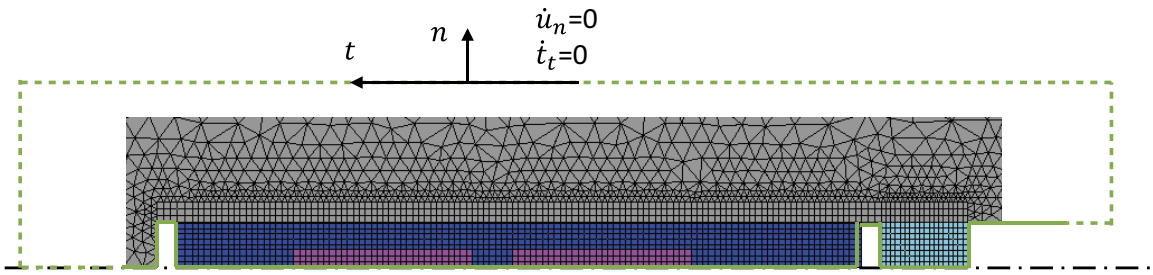

Figure G-5. *Mechanical boundary conditions.*

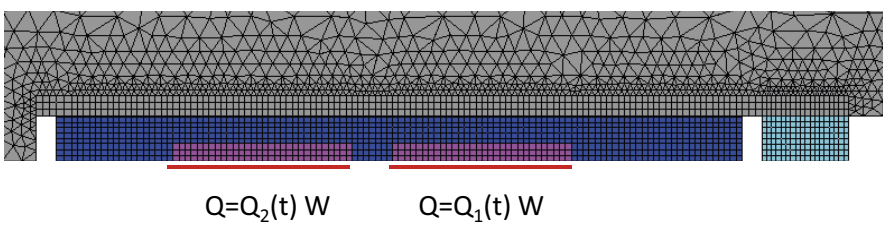

Figure G-6. *Thermal load application.*

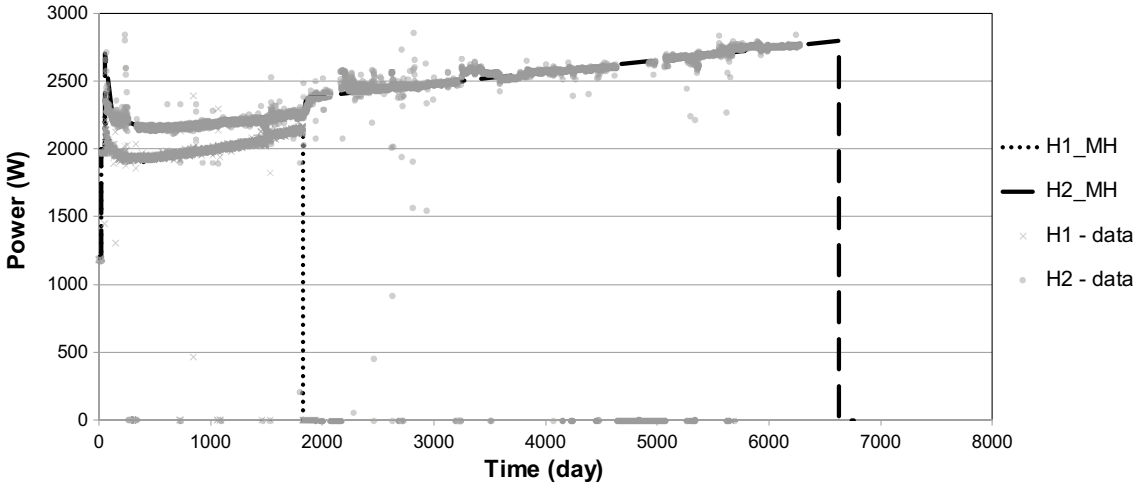

Figure G-7. *Measured heater power and the functions used for prescribing the heater power in the model.*

Table G-4. Applied thermal load protocol.

Time interval [days]	Heater 1 power [kW]	Heater 2 power [kW]
[0–20]	1.2	1.2
[20–53]	2	2
[53–120]	[2.2–2]	[2.7–2.25]
[120–400]	[2–1.9]	[2.25–2.15]
[400–1000]	[1.9–2]	[2.15–2.2]
[1000–1827]	[2–2.15]	[2.2–2.25]
[1827–1855]	0	[2.25–2.35]
[1855–1886]	0	[2.35–2.38]
[1886–3886]	0	[2.38–2.56]
[3886–5400]	0	[2.56–2.69]
[5400–6630]	0	[2.69–2.8]
[6630–6758]	0	0

A **liquid source** was introduced by prescribing the liquid pore pressure to 0.1 MPa at a line positioned 0.5 m outside of the outer boundary of the bentonite buffer, as shown in Figure G-8. More details can be found in Chapter G4 ‘Discussion of model setup’.

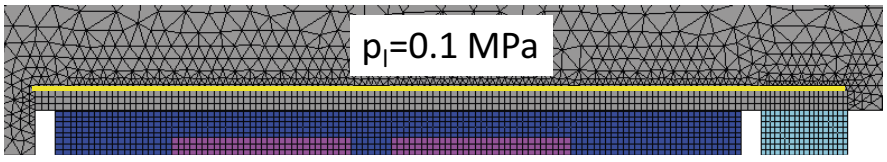

Figure G-8. *Hydraulic load (source) prescription.*

G3.3 Material models

A large part of the Febex bentonite representation is identical to that reported by Mattias Åkesson in Papafotiou et al. (2017). When this is the case it will be indicated by "In accordance with Åkesson" or similar.

G3.3.1 Porous media relations

In the present formulation the **water retention** relates the degree of liquid saturation of the porous medium to the negative of liquid pore pressure (or suction, when adding the gas pore pressure) by use of van Genuchten's ordinary or extended law,

$$S_l = f_d \left(1 + \left(\frac{p_g - p_l}{p_0}\right)^{\frac{1}{1-\lambda}}\right)^{-\lambda},$$

where $f_d = 1$ and $f_d = \left(1 - \frac{p_g - p_l}{p_d}\right)^{\lambda_d}$ give the ordinary and extended version, respectively. Figure G-9 shows the retention curves for the bentonite and rock.

Table G-5. Retention related variables.

Component	p_0 [MPa]	λ [-]	p_d [MPa]	λ_d [-]	Van Genuchten version
R [a]	1.74	0.6	-	-	Ordinary
P [a]	0.6	0.24	-	-	Ordinary
H [a]	1	0.6	-	-	Ordinary
B [b]	22.5	0.09	1 100	2.1	Extended
G [c]	1.74	0.6	-	-	Ordinary

[a] The impact of the retention properties of this component is not considered significant for this particular model. The rock properties, however, are similar to Equation A-1 in the task spec. [b] In accordance with Åkesson. [c] Here chosen equal to the Rock-value.

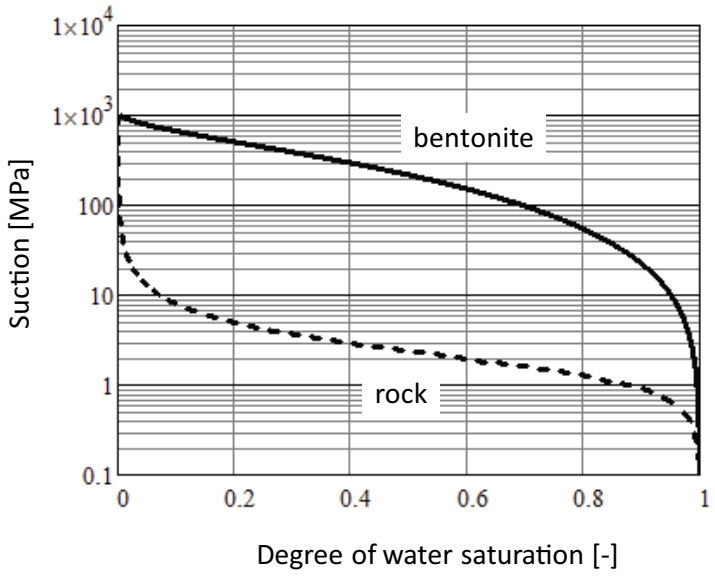

Figure G-9. *Retention curves for the bentonite and rock representations.*

Advective mass flow is given by Darcy's law,

$$\boldsymbol{q}_l|_{Darcy} = -\frac{\boldsymbol{k}k_{rl}}{\mu_l}(\nabla p_l - \rho_l \boldsymbol{g}),$$

which is obtained from a combination of balance of momentum of the fluid phases together with constitutive assumptions of momentum exchange with other phases. The intrinsic permeability is prescribed as isotropic, $\boldsymbol{k} = k\boldsymbol{I}$, and either constant, $k = k_0$ or dependent on porosity, $k = \tilde{k}(\phi)$.The relative permeability has been prescribed both as constant $k_{rl} = k_{rl0}$ or as dependent on degree of liquid saturation $k_{rl} = \tilde{k}_{rl}(S_l)$. Figure G-10 shows the relative permeability for block and rock materials.

Table G-6. Darcy's law, intrinsic and relative permeability.

Component	$\boldsymbol{k}$ [m²]	$\boldsymbol{k_{rl}}$ [-]
R P	10^{-10} [a] 10^{-17} [c]	$\sqrt{S_l}\left(1-\left(1-S_l^{\frac{1}{\lambda}}\right)^{\lambda}\right)^2$ [b]
H [d]	10^{-29}	1
B [e]	$1.1\times10^{-21}\frac{\phi^3}{(\phi-1)^2}\frac{(0.378-1)^2}{0.378^3}$	S_l^3
G	10^{-10} [a]	$\sqrt{S_l}\left(1-\left(1-S_l^{\frac{1}{\lambda}}\right)^{\lambda}\right)^2$ [b]

[a] The material is given a value significantly higher as compared to the Block. [b] The same value of λ as prescribed for the retention. For the Rock the choice is similar to Equation A-2 given in the task spec. [c] The impact of the permeability of the Plug is not considered significant for this particular model, it is given a value within a range to what was used in the Sr-Site analysis (Åkesson et al. 2010). [d] The Heater is given an impermeable representation as compared to the Block. [e] In accordance with Åkesson.

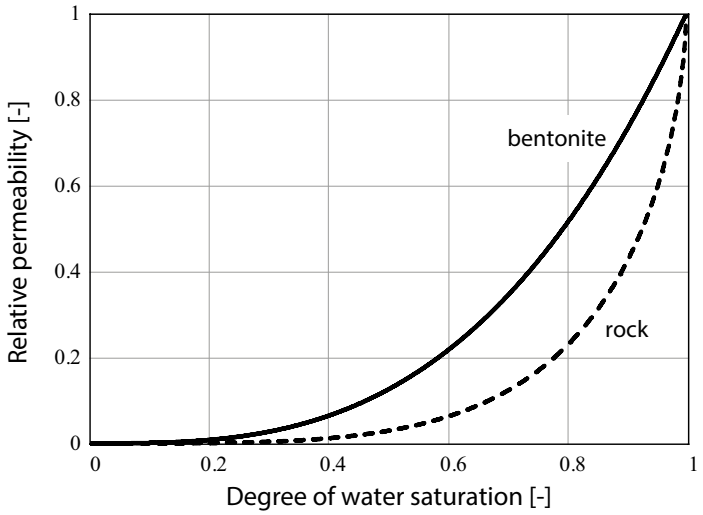

Figure G-10. *Relative permeability for the bentonite and rock representations.*

Diffusive mass flow is given by Fick's law,

$$\boldsymbol{i}_g^w\big|_{Fick} = -\tau\phi\rho_g(1-S_l)D_g^w \boldsymbol{I}\nabla(\theta_g^w/\rho_g)$$

is obtained by consideration of the constituent balance of momentum, the phase balance of momentum and the exchange of momentum with the other constituents. The diffusion of water in the gas phase is given by,

$$D_g^w = 5.9\cdot 10^{-6}(273.15+T)^{2.3}/p_g.$$

The tortuosity is assumed to be constant, i.e. $\tau = \tau_0$ where the values in the table below have been used.

Table G-7. Fick's law, tortuosity.

Component	τ_0 [-]
R [a]	1
P [a]	1
H [b]	0.001
B [c]	0.5
G [a]	1

[a] The component is set as to be permeable to vapor. [b] The component is set as to be impermeable to vapor. [c] The component is set as to meet the results from an inverse modeling reported in Pintado et al. (2002), see Figure G-11, which focused on MX-80 bentonite but is here assumed to be relevant also for Febex bentonite. The parameter choice also agrees well with what is given in Figure A-65 in the task spec.

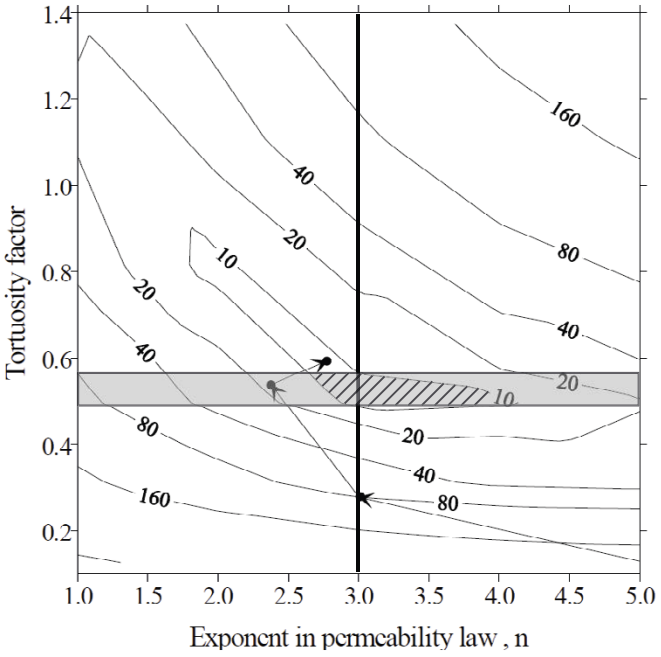

Figure G-11. *Iso-error plot in the Tortuosity/Permeability exponent – plane obtained from inverse modeling. The vertical line and shaded area are added to the original plot given in Pintado et al. 2002.*

The **conductive heat flux** is given by Fourier's law,

$$\boldsymbol{h} = -\lambda \nabla T,$$

where the **thermal conductivity** is taken as constant $\lambda = \lambda_0$ or dependent on the degree of liquid saturation $\lambda = \tilde{\lambda}(S_l)$. In Table G-8 the nonlinear function $\tilde{\lambda}(S_l)$ used for representing the bentonite is given together with values obtained from evaluating experimental data and a linear function. Information about the calibration of rock thermal conductivity is given in Chapter G4 'Discussion of model setup' and Section G7.

Table G-8. Fourier's law, thermal conductivity.

Component	λ [MPa]
R [(a)]	3.8
P [(b)]	1.7
H [(c)]	45
B [(d)]	$0.57 + \frac{1.28 - 0.57}{1 + \exp\left(\frac{S_l - 0.65}{-0.1}\right)}$
G [(e)]	1.3

[a)] Obtained from calibrating a thermal model against measured rock temperature, see Section G7. The value is within the range given in Table A-3 in the task specification. [b)] Handbook value for concrete. [c)] Handbook value for steel. [d)] In Figure G-12, from Papafotiou et al. (2017), experimental data and the fitted nonlinear model (red line) are shown. [e)] The Gap is given the thermal conductivity of about the fully saturated Block material.

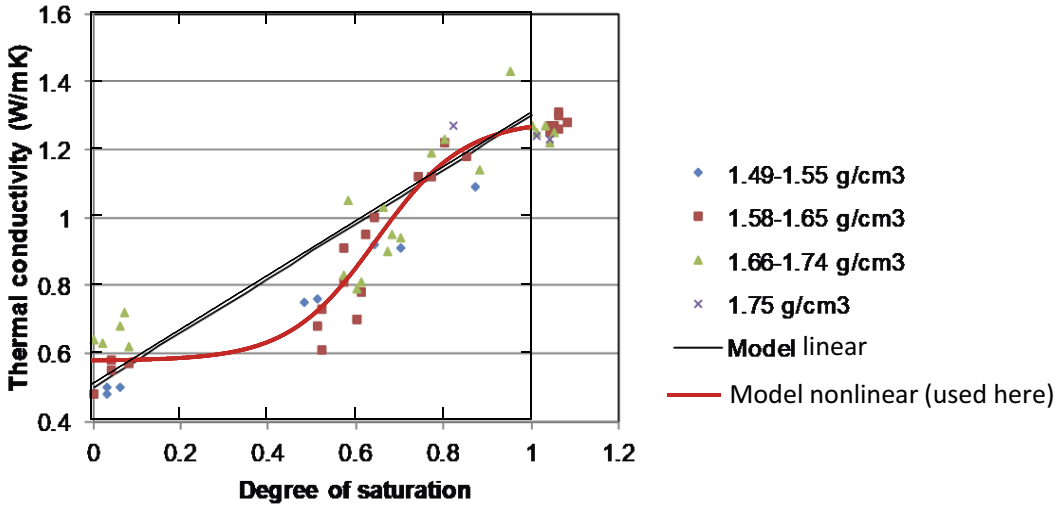

Figure G-12. *Thermal conductivity. Estimated from experimental data (symbols) and given by models (lines).*

G3.3.2 Solid phase relations

The **solid phase density** is constant, i.e. $\rho_s = \rho_{s0}$. The *solid phase specific internal energy* is given by the **solid phase specific heat capacity**, according to $e_s = c_s T$.

Table G-9. Solid phase parameters, mass density and specific heat capacity.

Component	ρ_{s0} [kg/m^3]	c_s [J/(kg·K)]
R	2660 [a]	920 [a]
P	2000 [b]	900 [b]
H	7800 [c]	460 [c]
B	2735 [d]	1091 [d]
G	2660 [e]	920 [e]

[a] In agreement with Table A-3 in task spec. [b] Handbook value for concrete. [c] Handbook value for steel. [d] In agreement with Åkesson. [e] Equal to Rock properties.

An overview of the utilized type of **mechanical material models**, which give expressions for the stress tensor, is given in Table G-10. In short, the linear elastic representations of the Rock, Plug and Heater are identical (Table G-11), a modified version of the Barcelona Basic Model (BBM) is used for representing the properties of the Block material (Table G-12) and a bilinear elastic model is used for representing the shifting properties of the Gap material (Table G-13). The base setup for the mechanical model of the block material was according to Åkesson. Some changes were, however, made and more information can be found in Chapter G4 'Discussion of model setup'.

Table G-10. Overview of the solid phase mechanical material models.

Component	Model
R	Linear elastic
P	Linear elastic
H	Linear elastic
B	Modified BBM
G	Bilinear elastic (gap model)

Table G-11. Linear elastic model and parameter values.

Total strain increment	$d\boldsymbol{\varepsilon} = d\boldsymbol{\varepsilon}^e$	Parameter	R, P, H [a]
Elastic strain increment	$d\boldsymbol{\varepsilon}^e = -\frac{1}{3} d\varepsilon_v^e \mathbf{1} + d\boldsymbol{e}^e$ $d\varepsilon_v^e = \frac{dp'}{K}, K = \frac{E}{3(1-2\upsilon)}$ $d\boldsymbol{e}^e = \frac{d\boldsymbol{s}}{2G}, 2G = \frac{E}{1+\upsilon}$	E [GPa]	100
		υ	0.2

[a] The Rock, Plug and Heater are given mechanical properties which results in a stiff material as compared to the block. The properties are however fairly reasonable on their own as well. For example, according to Table A-3 in task spec. E = 45–75 GPa and υ = 0.20 – 0.30 for the rock.

Table G-12. Modified BBM model and parameter values in agreement with Åkesson except K_{min} and p_{ref} where the "original" value is given within brackets.

Total strain increment	$d\varepsilon = d\varepsilon^e + d\varepsilon^p + d\varepsilon^h$	**Parameter**	**B**
	$e_0 = \phi_0/(1-\phi_0)$ [a]	e_0	0.609
Elastic strain increment	$d\boldsymbol{\varepsilon}^e = -\frac{1}{3}d\varepsilon_v^e\mathbf{1} + d\boldsymbol{e}^e$ $d\varepsilon_v^e = \frac{dp'}{K}, K = \max\left\{\frac{(1+e)p'}{\tilde{\kappa}_i(s)}, K_{min}\right\}$ $\tilde{\kappa}_i(s) = \kappa_i(1 + \alpha_{il}\ln(s/0.1 + 1))$ $d\boldsymbol{e}^e = \frac{d\boldsymbol{s}}{2G}, 2G = \frac{3(1-\upsilon 2)}{(1+\upsilon)}K$	κ_{i0} α_{il} υ K_{min} [MPa]	0.12 −0.12 0.2 200 (20)
Plastic strain increment	$d\boldsymbol{\varepsilon}^p = d\Lambda\frac{\partial g}{\partial \boldsymbol{\sigma}}$ $f = q^2 - M^2(p' + p_s)(p_0 - p')$ $g = \alpha q^2 - M^2(p' + p_s)(p_0 - p')$ $p_0 = p^c\left(\frac{p_0^*}{p^c}\right)^{\frac{\lambda_0-\kappa_{i0}}{\bar{\lambda}(s)-\kappa_{i0}}}$ $dp_0^* = \frac{1+e}{\lambda_0-\kappa_{i0}}p_0^* d\varepsilon_v^p$	α p_0^* [MPa] p_c [MPa] λ_0 p_s [MPa] M	0.5 19 1 0.2 2.6 0.234
Hydraulic strain increment	$d\boldsymbol{\varepsilon}^h = -\frac{1}{3}d\varepsilon_v^h\mathbf{1}$ $d\varepsilon_v^h = \frac{\kappa_s}{(1+e)(s+p_{atm})}ds$ $\kappa_s = \kappa_{s0}f^m(p', e)f^h(s)$ $^{(b)}f^m(p', e) = \begin{cases} 1 & \text{if } p' < p_{ref} \\ 10^{-20} & \text{if } p' > p_{swell}(e) \\ 1 - \frac{\ln p' - \ln p_{ref}}{\ln(\tilde{p}_{swell}(e)) - \ln p_{ref}} & \text{otherwise} \end{cases}$ $\log\left(\tilde{p}_{swell}(e)\right) = -4.741 + 4.117\cdot 10^{-3}\frac{\rho_s}{1+e} - 3.94\cdot 10^{-7}\left(\frac{\rho_s}{1+e}\right)^2$ $f^h(s) = \exp(\alpha_{ss}s)$	κ_{s0} p_{ref} [MPa] α_{ss} [MPa^{-1}]	0.3 0.5 (1) −0.02

[a] The initial void ratio is used as an input parameter to the modified BBM model. It should be set as to match the porosity given as the initial condition. [b] The function $f^m(p',e)$ is a feature developed at Clay Technology.

Table G-13. Bilinear elastic model (gap model) and parameter values.

Total strain increment	$d\varepsilon = d\varepsilon^e$	**Parameter**	**G** [a]
Elastic strain increment	$d\boldsymbol{\varepsilon}^e = -\frac{1}{3}d\varepsilon_v^e\mathbf{1} + d\boldsymbol{e}^e$ $d\varepsilon_v^e = \frac{dp'}{K}, K = \frac{E}{3(1-2\upsilon)}$ $d\boldsymbol{e}^e = \frac{d\boldsymbol{s}}{2G}, 2G = \frac{E}{1+\upsilon}$ $E = \begin{cases} E_0 \text{ if } \varepsilon_v \le \varepsilon_v^{limit} \\ E_C \text{ otherwise} \end{cases}$	E_0 [MPa] E_C [MPa] ε_v^{limit} υ	0.1 1×10^3 100 0.2

[a] The parameters are set as to obtain a soft material (as compared to the Block) when the Gap is open and stiff when the Gap is closed, defined as when the volumetric strain > ε_v^{limit}.

G3.3.3 Liquid phase relations

The liquid phase is here equal to liquid water. The **liquid phase density** and **liquid phase viscosity** are given by specified functions $\rho_l = \tilde{\rho}_l(p_l,T)$ and $\mu_l = \tilde{\mu}_l(T)$, respectively. The **specific internal energy of water** is given by, $e_l^w = c_l^w T$.

Table G-14. Liquid phase relations/parameters, mass density, viscosity and specific heat capacity as specified by default in Code_Bright.

	Unit
$\tilde{\rho}_l(p_l,T) = 1002.6\exp(4.5\cdot10^{-4}(p_l-0.1)+3.4\cdot10^{-4}T)$	kg/m³
$\tilde{\mu}_l(T) = 2.1\cdot10^{-12}\exp\left(\frac{1808.5}{273.15+T}\right)$	
c_l^w = 4 180	J/(kg·K)

G3.3.4 Gas phase relations

Regarding the gas phase it should be remembered that a constant gas pore pressure, p_g = 0.1 MPa, has been used in the present simulations. The gas phase is considered an ideal gas mixture, thus Dalton's law is adopted

$$p_g = p_g^a + p_g^w.$$

The **pore pressure of water in gas phase** (vapor pressure) is given by,

$$p_g^w = \tilde{p}_g^w(T),$$

and the **pore pressure of air in the gas phase** p_g^a is related to the density variable θ_g^a which, by using Dalton's law, makes it possible to write

$$\theta_g^a = \tilde{\theta}_g^a\left(T, p_g^a = p_g - p_g^w\right).$$

The **gas specific internal energies** are given by,

$$e_g^w = L_g^w + c_g^w T \text{ and } e_g^a = c_g^a T.$$

Table G-15. Gas phase relations/parameters, vapor pressure, air density, specific latent heat and specific heat capacity as specified by default in Code_Bright.

	Unit
$\tilde{p}_g^w(T) = 13607\exp\left(\frac{-5239.7}{273.15+T}\right)$	MPa
$\tilde{\theta}_g^a\left(T, p_g - p_g^w\right) = \frac{M_a}{R}\frac{1}{273.15+T}\left(p_g - p_g^w\right)$ [1]	kg/m³
L_g^w = 2.5 × 10⁶	J/kg
c_g^w = 1 900, c_g^a = 1 006	J/(kg·K)

[1] M_w: molar mass of water; R: constant of gases.

G4 Discussion of model setup

The artificial open disc-shaped volumes between the buffer and the tunnel end surface and plug surface were introduced as to reduce the complexity of the model. By doing this a mechanical boundary condition could be used as to let the buffer move radially relative to the neighboring surfaces without introducing special mechanical material models, see Figure G-13. This also prevented the introduction of artificial stiffness, and stress concentrations, at these interfaces and thereby facilitated the numerical solution. One obvious drawback with this is that thermal and hydraulic fields become cut at the interfaces as well. Small test models did, however, show that the effect was insignificant in the interior of the buffer some distance from the end surfaces. Another drawback was that it turned out to be difficult trying to describe why this was done. The thickness of the removed disc of material could of course been reduced but this would not change the solution, only mask what had been done.

In Figure G-14 averaged dry density measurements are given for positions along the tunnel axis. The averaged dry density obtained from the experimental measurements was about 1 600 kg/m^3 at the central part of the inner heater but at other positions a value of 1 575 kg/m^3 would be more in line with the measurements. At the tunnel end the averaged dry density was significantly lower due to difficulties at installation of the buffer blocks.

In the model the radially homogenized dry density for a section about the canister mid has been assumed to be 1 600 kg/m^3 which agrees with the intentions described in the design for the experiment. When looking back at the outcome of the experimental data given in Figure G-14 this is a bit on the high side. Using the initial dry density of the blocks (1 700 kg/m^3) and the known geometry of a canister-mid section, an outer slot width of 2.8 cm was calculated. This slot width was also used for sections without the canister which results in a radially homogenized dry density of 1 618 kg/m^3. The significantly lower density at the tunnel end was not considered in the models.

In the experiment the heater power was controlled by a circuit so that the maximum temperature monitored by temperature sensors at the canister surface should be 100 °C. It was decided that incorporation of such a logic in a model would be unnecessary complex. It was also decided not to prescribe the temperature to 100 °C along the entire surface of the canister since this was not the condition in the experiment. Instead, the thermal loads were prescribed by designing functions matching the recorded heater powers, see Figure G-3 and Table G-4. The rock thermal conductivity was then calibrated so that calculated temperatures for a purely thermal model agreed with experimental sensor data, see Section G7. A rock thermal conductivity of 3.8 W/(m·K) was found suitable.

The "conventional" setup for how water enters a model, using pressure boundary conditions, was not used. Instead, a hydraulic line source, with a liquid pore pressure of 0.1 MPa, was introduced close to (0.5 m) the tunnel surface. This allowed the buffer to always have full access to water and was motivated from considering the reports of a highly permeable and water bearing host rock in the experiment. One could even think of position this source of liquid at the very interface between the buffer and rock.

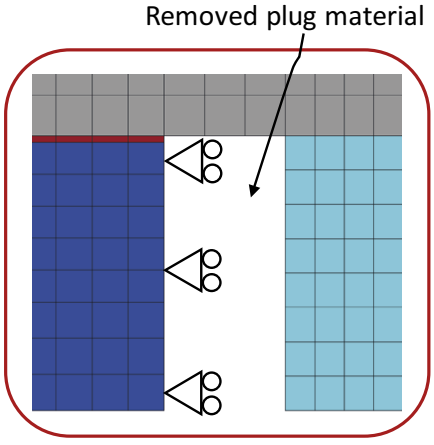

Figure G-13. *Artificial open volume and the introduced roller boundary conditions.*

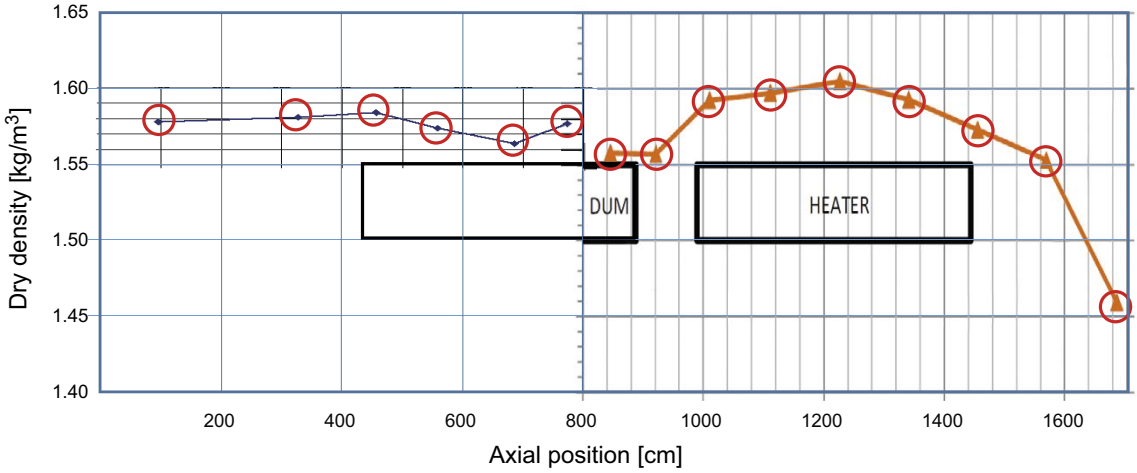

Figure G-14. *Average dry density distribution determined from excavated samples along the tunnel axis.*

The removal of material during the dismantling of the experiment was not included in order to simplify and keep down the complexity of the model.

The parameter set for the buffer material origins from the model previously undertaken by Mattias Åkesson as described in Papafotiou et al. (2017). During the development of the model it was found out that some alterations of the original material model setup would give improvements. The main reason for changing the representation was that the model solution agreed poorly with excavation data regarding dry density profiles. Two different changes were made:

1. Increasing the minimum elastic bulk modulus K_{min}, from 20 to 200 MPa.
2. Decreasing the incremental swelling during water uptake by decreasing p_{ref}, from 1 to 0.5 MPa.

More details about the changes will follow in subsequent Chapters G4.1 to G4.3.

The poor agreement with dry density data also induced scrutiny of the assumption made regarding the effect of the steel liner present between the canister and buffer, see Figure G-15.

In the model the steel liner was not included directly, but the effect from its presence was indirectly considered. To see that the presence of the steel liner had an effect in the experiment, dry density profiles at comparable positions but with/without steel liner can be compared, see Figure G-16.

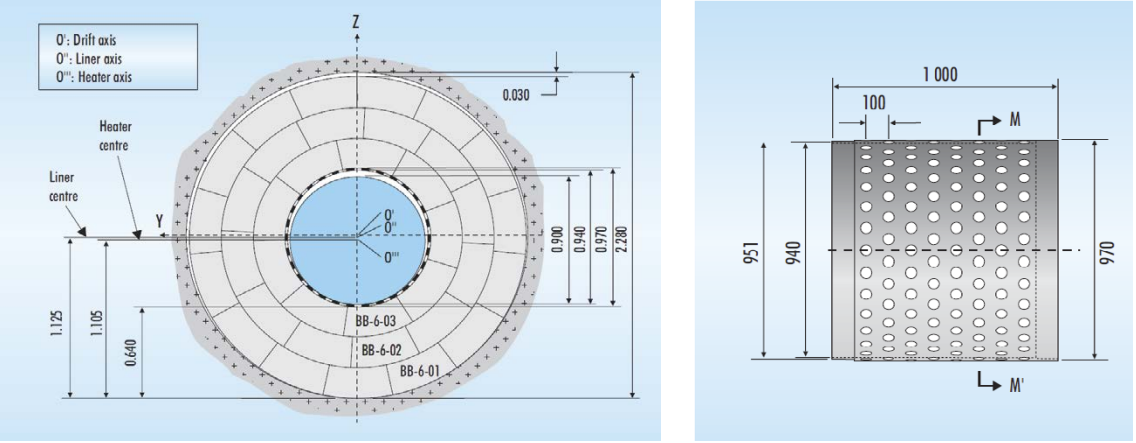

Figure G-15. *Drawing of the Febex experimental design where a steel liner is present between the heater and buffer.*

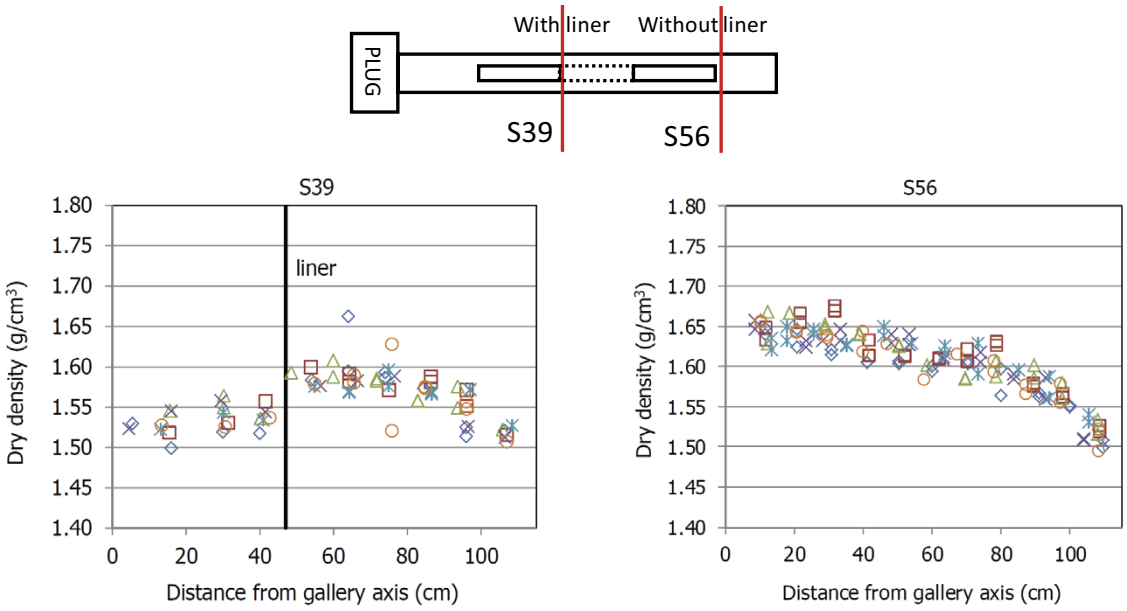

Figure G-16. *Dry density distribution determined from excavated samples in different cross sections along the tunnel axis.*

Two extreme assumptions can be made when setting up the model as to evaluate the effect from the steel liner:

1. The steel liner is a perfect barrier for the clay.
2. The steel liner is not a barrier for the clay.

These assumptions will generate two different final states, see Figure G-17:

1. No penetration trough the liner = the buffer inner surface is located at the steel liner outer surface.
2. Resistant-free penetration through the liner = the buffer inner surface is located at the canister surface.

When designing models using the assumptions above, designs sketched in Figure G-18 can be utilized. The difference between them is the material type allotted to the volume between the buffer and heater. A steel liner material (for which the canister material can be used) and an inner gap material (for which the outer gap material can be used), respectively. In the original (base case) model the first assumption was used.

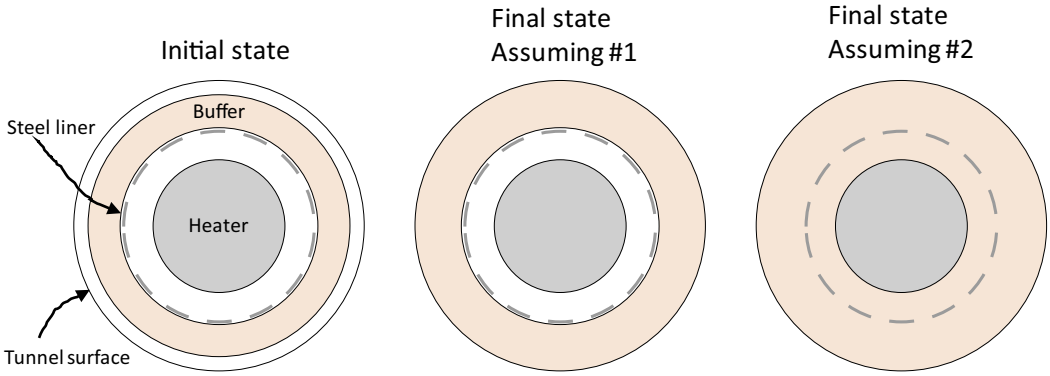

Figure G-17. *Initial state and the final states following from the different assumptions of the effect from the steel liner.*

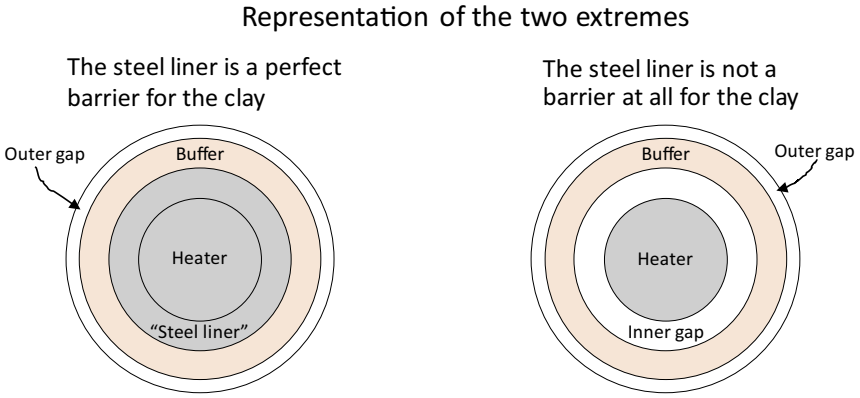

Figure G-18. *Initial states used for representing the different assumptions of the effect from the steel liner.*

G4.1 Buffer material alteration: Increased K_{min}

The first buffer material alteration was to increase the minimum bulk modulus K_{min}. By increasing K_{min} the significant initial compression close to the canister, at small stresses, was trying to be avoided.

This parameter is part of the expression for the elastic strain increment, $d\boldsymbol{\varepsilon}^e$. K_{min} determines the minimum value of the bulk modulus K, relating an increment in net pressure dp' to an increment in volumetric elastic strain $d\boldsymbol{\varepsilon}_v^e$.

The equations below show the formulation,

$$d\boldsymbol{\varepsilon}^e = -\frac{1}{3} d\varepsilon_v^e \mathbf{1} + d\boldsymbol{e}^e \,,$$

$$d\varepsilon_v^e = \frac{dp'}{K} \,,$$

$$K = \max\left\{\frac{(1+e)p'}{\tilde{\kappa}_i(s)}, K_{min}\right\} .$$

The main purpose of K_{min} is to prevent the model to break down at small stresses (net pressures), preventing K to become unreasonable low. For conditions where $K = K_{min}$ the elastic material model becomes linear.

To evaluate if an increase in bulk modulus from 20 MPa to 200 MPa was reasonable the expression,

$$K = \frac{(1+e)p'}{\kappa_i} \,,$$

was used and parameter values evaluated from post-mortem analyses reported in Villar et al. (2017) were inserted, see Figure G-19 and Table G-16. The rightmost column of Table G-16 contains the obtained values for the bulk modulus. As can be seen, the values range from 24 MPa to 480 MPa, which makes K_{min} = 200 MPa seem reasonable.

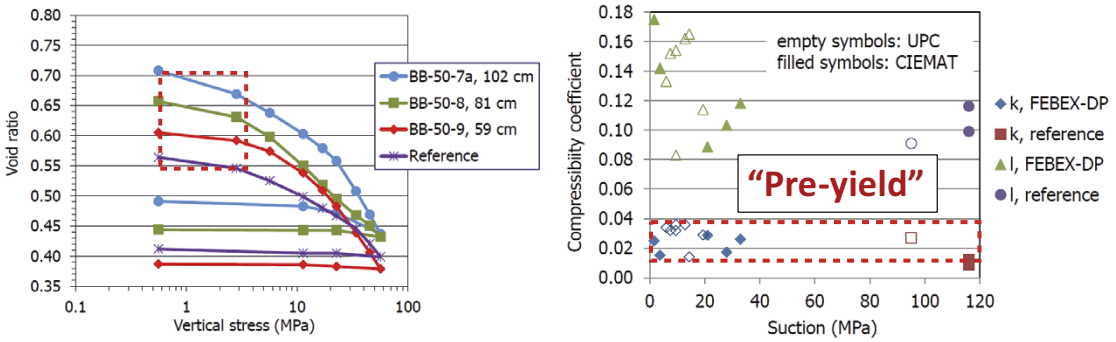

Figure G-19. *Experimental data used for evaluating the bulk modulus. The rectangles with the red hatched outline indicate the relevant ranges.*

Table G-16. Extracted parameter data, for 1 + e, p' and κ_i, used when evaluating the bulk modulus K.

1 + e	p' [MPa]	κ_i	K [MPa]
1.6	0.6	0.01	96
1.6	0.6	0.04	24
1.6	3	0.01	480
1.6	3	0.04	120

G4.2 Buffer material alteration: Decreased p_{ref}

The second buffer material alteration was to decrease a referential pressure p_{ref} present in a mechanically coupled part $f^m(p',e)$ of the modulus κ_s, governing the hydraulically induced strain increment $d\boldsymbol{\varepsilon}^h$. By decreasing p_{ref} the swelling/shrinkage of the material was decreased. In the present work some action which should decrease the heavily swelling outer part of the block at low pressures was sought. This was sought as to obtain higher dry densities at the outer part and also lower dry densities at the inner part (due to less initial compression).

The equations below show the formulation,

$$d\boldsymbol{\varepsilon}^h = -\frac{1}{3} d\varepsilon_v^h \mathbf{1}$$

$$d\varepsilon_v^h = \frac{\kappa_s}{(1+e)(s+p_{atm})} ds$$

$$\kappa_s = \kappa_{s0} f^m(p',e) f^h(s)$$

$$f^m(p',e) = \begin{cases} 1 & \text{if } p' < p_{ref} \\ 10^{-20} & \text{if } p' > p_{swell}(e) \\ 1 - \dfrac{\ln p' - \ln p_{ref}}{\ln(\tilde{p}_{swell}(e)) - \ln p_{ref}} & \text{otherwise} \end{cases}$$

where $\tilde{p}_{swell}(e)$, an experimentally motivated swelling pressure function, will be discussed below.

Figure G-20 shows $f^m(p',e)$ for a constant value of void ratio e (i.e. confined conditions) using p_{ref} = 0.1 MPa and p_{ref} = 1 MPa. The upper vertex of the curves takes place at the chosen value of p_{ref}. The lower value of p_{ref} clearly generates a lower curve which in turn gives a lower swelling modulus and thereby less swelling for the same increment of suction.

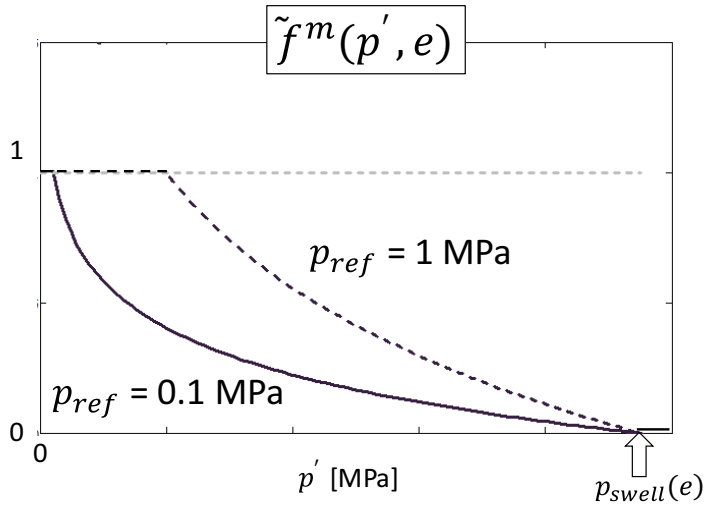

Figure G-20. *The mechanically coupled function $\tilde{f}^m(p',e)$, part of the swelling modulus, when using p_{ref} = 0.1 MPa* or *p_{ref} = 1 MPa. The function $\tilde{f}^m(p',e)$ is made up of three parts being 1 for $p' < p_{ref}$, 1e−20 for $p' > p_{swell}(e)$ and the function generating the curved black lines for the intermediate range.*

For the material model to generate representative swelling and pressure, the ingoing swelling pressure function $\tilde{p}_{swell}(e)$ should be valid for the material which is modelled. In the present case the material is so called ”Febex bentonite”. The parameter setup used in $\tilde{p}_{swell}(e)$, however, was calibrated against so called “MX-80” material data. In order to evaluate the validity of $\tilde{p}_{swell}(e)$using the given parameter set, the curve generated by $\tilde{p}_{swell}(e)$ is shown together with sample data of “Febex bentonite” in Figure G-21. If the somewhat sparse laboratory data is representative at dry densities above 1.6 g/cm^3 $\tilde{p}_{swell}(e)$ will underestimate the swelling pressure at high densities. At lower densities the swelling pressure curve agrees well with data.

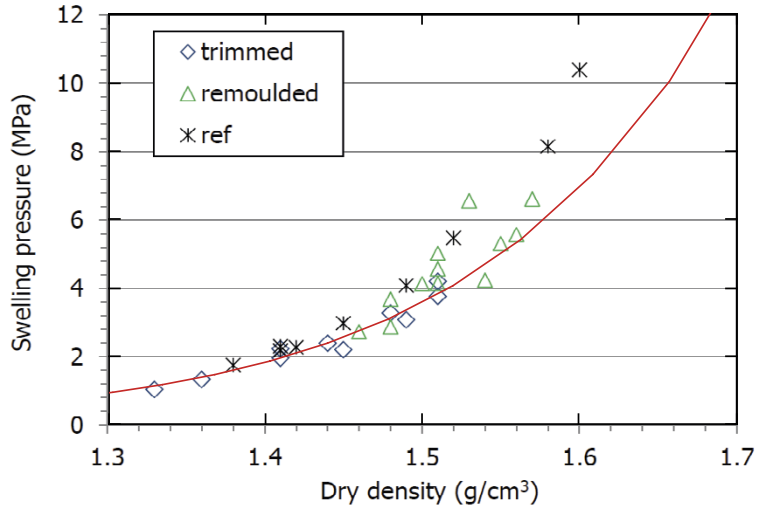

Figure G-21. *Experimental data used for evaluating the bulk modulus. The rectangles with the red hatched outline indicate the relevant ranges.*

G4.3 Testing the new setup

Two systems were simulated to test the performance of the new setup. The first was that of a homogeneous system undergoing free swelling under constant stress followed by pressure build-up under constant volume. The second was a 1D-axisymmetric representation of a buffer section at canister-mid.

G4.3.1 Homogeneous system: free swelling – pressure buildup

As a first study of the performance of the material model a homogeneous system undergoing spatially homogeneous decreasing suction during two steps, free swelling under constant isotropic stress followed by pressure build-up under constant volume, was simulated. The simulation setup is described in Figure G-22 and the results are shown in Figure G-23.

The left diagram in Figure G-23 shows that K_{min}= 200 MPa and p_{ref} = 0.1 or 1 MPa generate final states at full saturation which ends up at the prescribed swelling pressure curve $\tilde{p}_{swell}$. Thus, both setups behave as expected, and based on this quality none can be preferred over the other.

When studying the right diagram in Figure G-23 it can be seen that the path taken to arrive at the final state is different for the setups. p_{ref} = 0.1 MPa generates paths which have gentler pressure buildup as compare to p_{ref}= 1 MPa. This is a consequence of the sought behavior, less amount of initial swelling, when altering the parameter. The difference in paths opens a possibility to evaluate the settings if comparing the responses with experimental data.

Dueck (2004) contain swelling pressure data for MX-80 bentonite obtained from constant volume tests as shown in Figure G-24. The swelling pressure were measured at prescribed RH and the dry density were determined after the tests. The data points indicated with red dots have a dry density (void ratio) relevant for the present analysis. The samples analyzed in the left graph underwent very little swelling from the initial state whereas the samples belonging to the right graph had a significant initial swelling (starting from a void ratio in the range 0.51–0.63). Both data sets, however, indicate the same trend with an initial small increase in pressure with decreasing suction and an increasing derivative of pressure with suction.

If comparing the model responses shown to the right in Figure G-23, and concentrating on the red curves where e = 0.77, the lower curve (where p_{ref} = 0.1 MPa) is in better agreement with the experimental data.

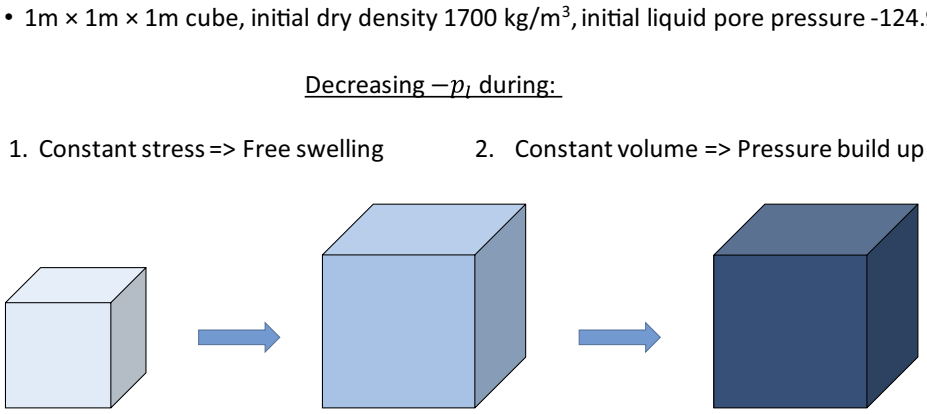

Figure G-22. *Description of the homogeneous system undergoing spatially homogeneous decreasing suction. At top the initial condition is given and below a schematic drawing of the two steps under which suction is decreasing: 1. isotropic constant stress, generating "free" swelling and 2. constant volume generating pressure build-up.*

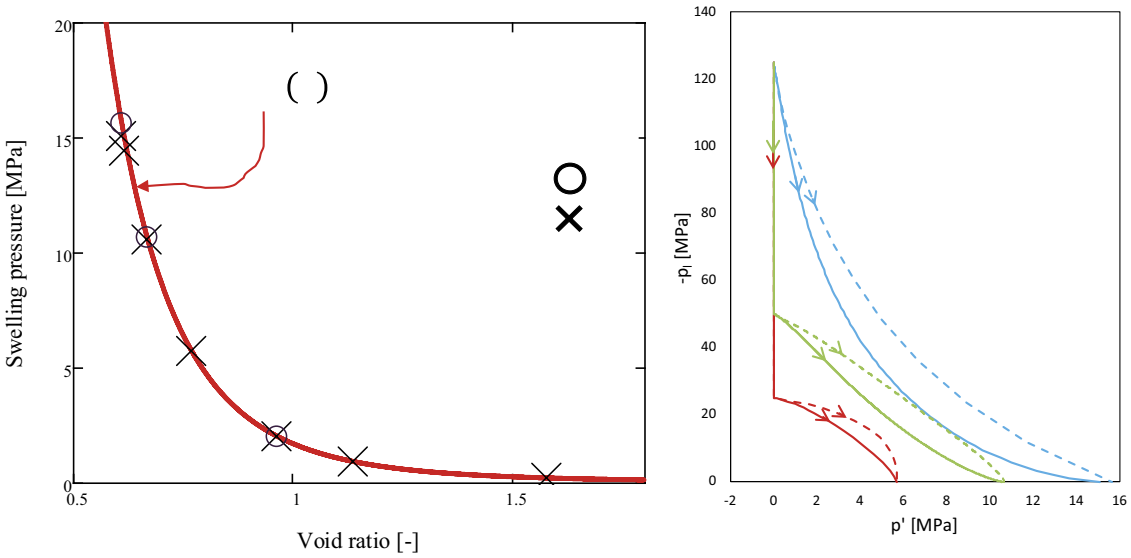

Figure G-23. *Results from the two step homogeneous system using K_{min} = 200 MPa and p_{ref} = 0.1 MPa or p_{ref} = 1 MPa . (Left) Final state in void ratio – swelling pressure space together with the used swelling pressure curve function. (Right) The path travelled in pressure – suction (– gas pressure) space using the two setups for three different prescribed "loading conditions".*

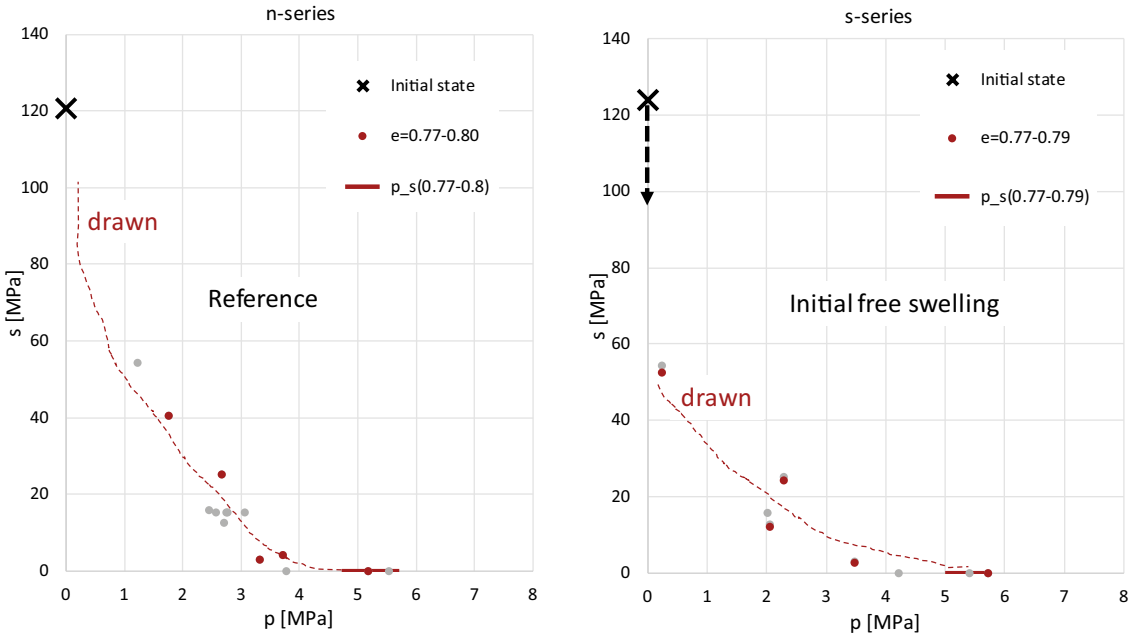

Figure G-24. *Experimental results from evaluating constant volume swelling pressure experiments from Dueck (2004). Samples where the void ratio is relevant for the present analysis are indicated by red dots. The horizontal thick line indicates the range in swelling pressure calculated from using the swelling pressure function given in the model description. The thin hatched line is drawn by hand to indicate a trend in the data. The X indicates the initial state (assuming zero pressure).*

G4.3.2 1D model of a buffer section at canister-mid

In the second study of the material model behavior an axisymmetric 1D geometry of a section through the buffer at canister/heater-mid (of H1) was simulated. In Figure G-25 model results when using different setups can be compared with experimental data obtained at section 27.

The old "base case", using K_{min} = 20 MPa and p_{ref} = 1 MPa, differs significantly when comparing with the case were K_{min} = 200 MPa and p_{ref} = 1 MPa. The overprediction of dry density at the inner part is much less for the higher value of the minimum bulk modulus. When decreasing p_{ref} the inner part of the profile does not change significantly. At the outer part of the buffer, close to the tunnel wall, the underprediction of the dry density becomes significantly less when decreasing p_{ref}.

The simulations show that the effects which were intended by altering the parameter set were obtained. There might be that there could be more to be asked for quantitatively, but qualitatively the intentions are met.

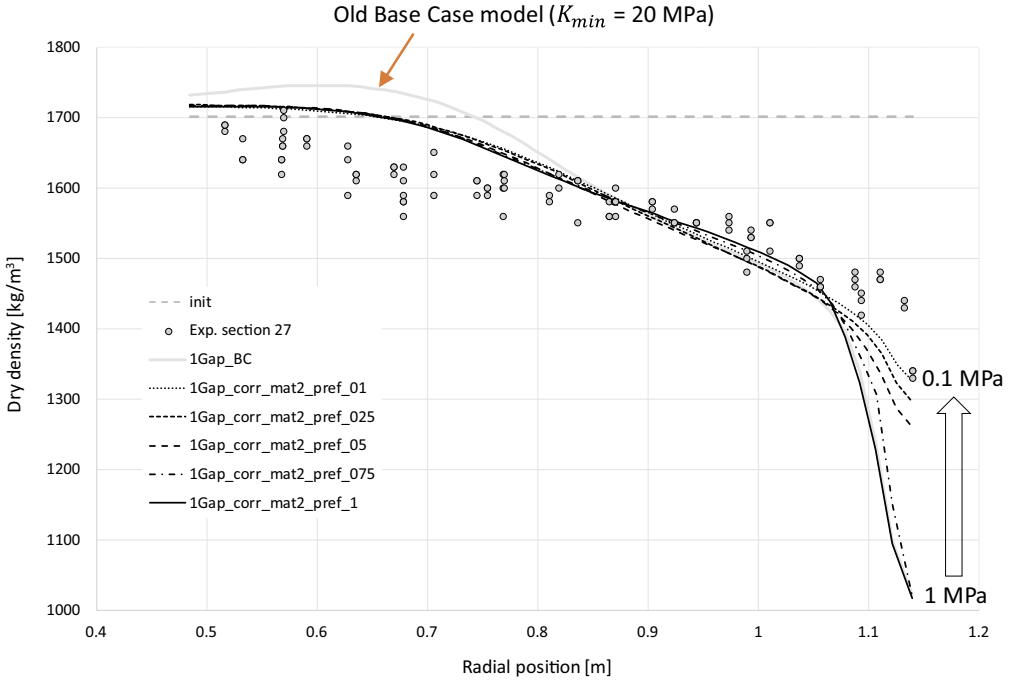

Figure G-25. *Dry density profile about H1 mid (section 27) at excavation. The old base case (K_{min} = 20 MPa and p_{ref} = 1) result is indicated by the thicker gray line and the black curves represents K_{min} = 200 MPa and p_{ref} = 1, 0.75, 0.5. 0.25. 0.1 MPa, in accordance to the legend.*

G5 Comparison with experimental data

In order to get an overview of the performance of the models, some results are here compared with experimental data at three different sections: at H1-center, at H2-center and 0.5 m further in from the inner H2-gable. It was unfortunately not successful to run the simulation of the model with the inner gap until the end of the experiment. The state at the first excavation (H1-center at day 1855) and the sensor data up to day 2595 could however be analyzed for this model.

G5.1 H1-center

Data from both models (with/without inner gap) are here compared with experimental data obtained at the first excavation, 1 855 days after switching on the heaters. Figure G-26 shows profiles of dry density, water content and degree of water saturation at the center of H1.

The model without an inner gap overestimates the experimental dry density data at the inner positions. The model with an inner gap agrees better with the experimental dry density measurements. Since averaged experimental data for this section is about 1 570 kg/m^3, some overestimation is to be expected since the model is assuming an average dry density of 1 600 kg/m^3.

The experiment/model comparison in terms of water content indicates that the mass transport of water is well represented. When introducing an inner slot representation, the water uptake process advances faster. This is probably an effect from a generally lower dry density which gives less water transport resistance.

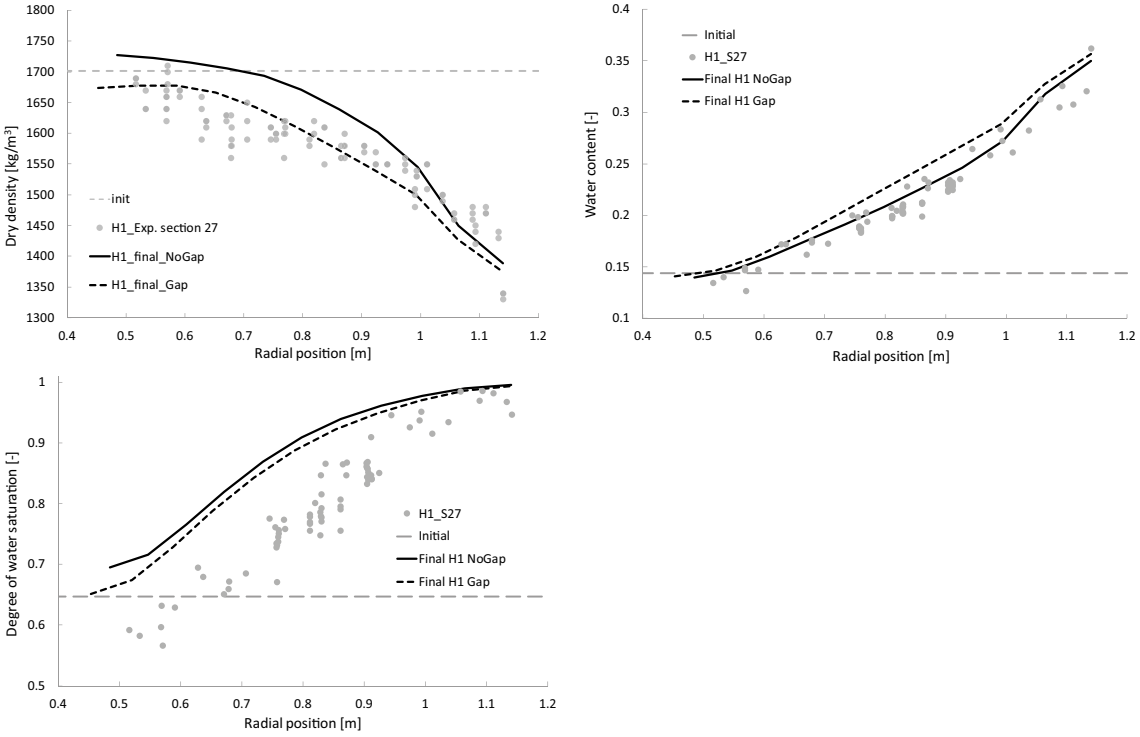

Figure G-26. *Profiles of dry density, water content and degree of water saturation about H1 mid (section 27) at excavation. Experimental data is indicated by the symbols, initial states are indicated by the gray hatched lines, the model results are given by the solid black (model without inner gap) and hatched black (model with inner gap) line, respectively.*

Knowing the dry density ρ_d, water content w, water density ρ_w and solid density ρ_s the degree of water saturation S_l is given by,

$$S_l = \frac{w}{\rho_w} \frac{1}{\frac{1}{\rho_d} - \frac{1}{\rho_s}}.$$

As expected, with w in good agreement with the measurements and ρ_d overestimated, S_l, ends up being overestimated. The model with the inner gap does have slightly less overestimation, but with more water in the clay (higher w) the total effect from obtaining a lower dry density is not entirely enhancing (lowering) the degree of water saturation profile.

G5.2 H2-center

Experimental and model data at the center section of H2 are here studied. First, radial stress evolutions from both models (with/without inner gap) are compared with experimental sensor data. Then profiles of dry density, water content and degree of water saturation from the model without the inner gap are compared with experimental data, obtained at the second excavation, 6 758 days after switching on the heaters.

The simulated radial stress evolution for the model without the inner gap (the upper curve) agrees well with all section E2 and F2-01 sensor data, shown in the upper row of Figure G-27. The model with the inner gap (the lower curve) on the other hand agrees well with all F2 sensor data except F2-01. This could be an indication of that there is some positions where an inner slot is initially present and has an effect on the mechanical process in the buffer.

The appearance of the curve belonging to the model with an inner gap can be understood better when the slot closure evolution is studied, the lower diagram in Figure G-27. At first the outer slot is closing in a similar fashion for both models, this is where the radial stress evolutions coincide. When the outer slot is closed in the two-slot model, the inner slot closure takes over (the buffer swells or being pushed inwards) and no radial stress is generated. About day 2000 the inner slot is closed as well, and the radial stress starts to increase again.

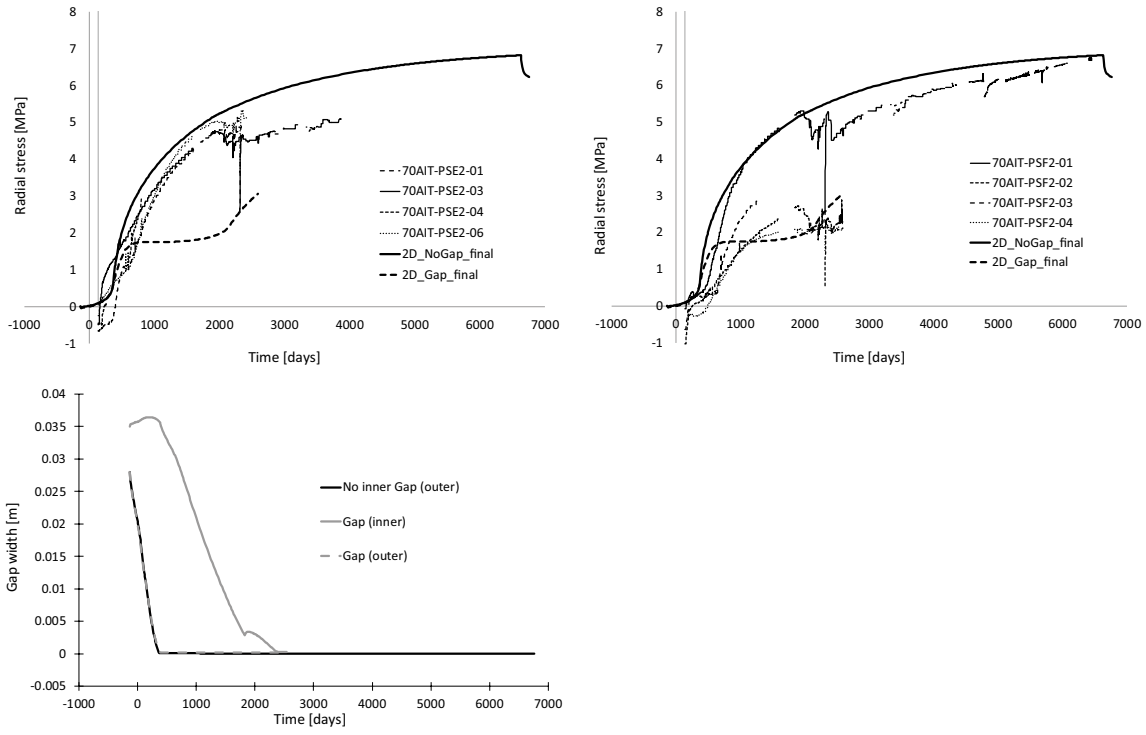

Figure G-27. *evolution of radial stress and gap width about H2 mid (section E2 and F2). Stress sensor data is indicated by the thin lines, and model responses by thick solid (model without inner gap) and thick hatched (model with inner gap) line, respectively.*

Below, in Figure G-28 , experimental data as well as data from the model without the inner gap are shown for sections about the center of H2. Profiles of dry density, water content and degree of water saturation are shown at the time for the second excavation (6 758 days after switching on the heaters).

The comparison of dry density profiles at the H2-section resembles that at the H1-section. The overestimation at the inner positions is now smaller, however, and the underestimation is larger at the outer positions. For this section the averaged buffer densities for the measurements and model agrees well, being about 1 600 kg/m^3.

The water content agrees well in an overall sense, but there is an overestimation at the outer positions.

Since both modelled dry density and water content agree relatively well with experimental data the degree of water saturation also does. At the outer positions however, the under- and overestimation, for the dry density and water content, respectively, work against each other as to generate a degree of water saturation which seem to indicate a better behaving model than is the case.

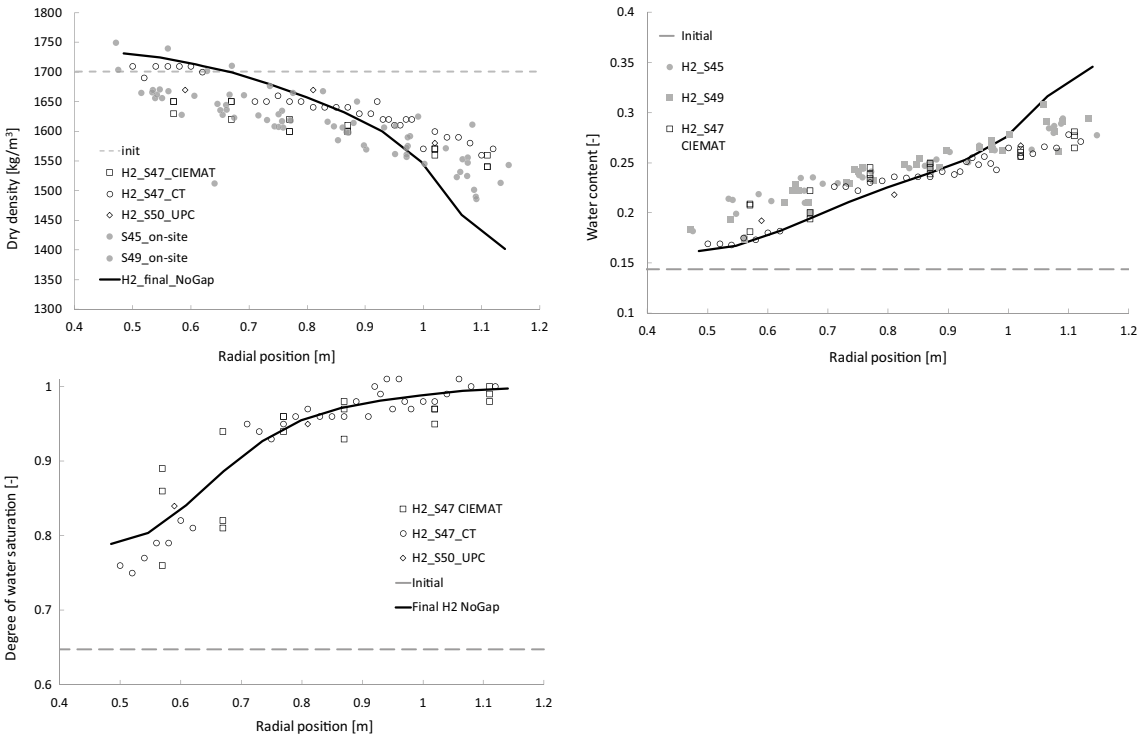

Figure G-28. *Profiles of dry density, water content and degree of water saturation about H2 mid (section 45, 47, 49 50) at excavation. Experimental data is indicated by the symbols, initial states are indicated by the gray hatched lines, the model results are given by the solid black (model without inner gap) and hatched black (model with inner gap) line, respectively.*

G5.3 Cylindrical block section

The third and last section where the model is compared to experimental data is about 0.5 m from the H2 inner gable along the tunnel axis toward the tunnel end. Below, in Figure G-29, experimental data from section 57 and 58 as well as data from the model without the inner gap are shown for the chosen cylindrical-shaped block section. Profiles of dry density, water content and degree of water saturation are shown at the time for the second excavation (6 758 days after switching on the heaters).

The calculated dry density profile is for the most part higher as compared to the experimental measurements. A certain overestimation is not surprising since the average of the experimental measurements is about 1 560 kg/m^3. The model seems to underestimate the swelling and/or overestimate the compression of the block material.

If studying the water content profile, it can be seen that the water mass taken up at this section has been underestimated. This could be one reason for the overestimation in dry density, i.e. lack of swelling due to underestimation of the amount of water being transported into the block.

The degree of water saturation seems to indicate a model which are "right on the spot". As given by the analysis of the dry density and water content, however, the combined under- and overestimation, for the dry density and water content, respectively, work against each other as to generate a degree of water saturation which seem to indicate a better behaving model than is the case.

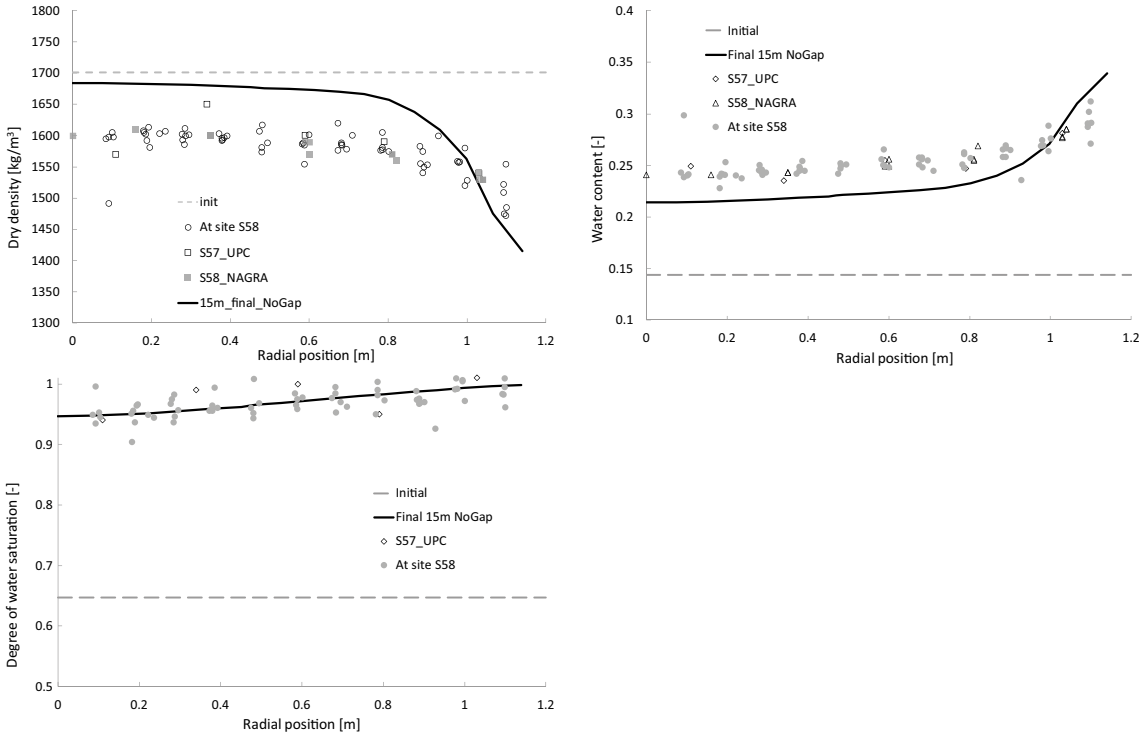

Figure G-29. *Profiles of dry density, water content and degree of water saturation 0.5 m from the inner H2 gable (section 57 and 58) at excavation. Experimental data is indicated by the symbols, initial states are indicated by the gray hatched lines, the model results are given by the solid black (model without inner gap) and hatched black (model with inner gap) line, respectively.*

G6 Final comments

Once more when performing a THM-simulation, the complexity of the mechanical material representation as compared to the other parts of the material model was highlighted. New knowledge in how to set up the mechanical material model of the clay system was gained during this task. This, hopefully, adds one more step towards better possibilities for simulating and predicting the systems we focus on.

The importance of using disqualifying tests and correct evaluation of these when setting up material models was revealed. When first using a homogeneous numerical test, deficiencies of the initially used setup could not be found. Another, 1D axisymmetric, numerical test, on the other hand gave insights what could be done to improve the model. It was then also understood how the first test could, when evaluated differently, disqualify between different setups as well.

It is also important to remember in what sense the model is simplified when evaluating its performance. What effects can be expected/not expected from adopting certain simplifications. Some simplifications/assumptions such as axisymmetry are evident and easy to keep in mind. Another example for the present model is the nonvarying dry density which was assumed to be achieved along the tunnel axis at installation. This must be compensated for when comparing experiment and model, which cannot "outperform" its initial setup. Dry density profiles will for instance not end up at a lower/higher average than assumed and stresses will build up to levels matching the assumed dry densities (if the mechanical material model behaves properly).

One assumption made initially, which had more of a hidden character, was how the clay and steel liner interacted. It was assumed that the steel liner acted as a perfect barrier for the clay. The effect of using this assumption was then tested by assuming the opposite, the clay was not affected by the steel barrier at all.

When studying the results, it became clear that what might seem to be a "perfect" model in some variable can be revealed as "bad" when studying other variables. This was most evident when comparing experimental data and model responses for the cylinder-shaped block. The obtained degree of water saturation profile agrees very well with the measurements, but the dry density and water content show another picture. To obtain a true picture of a model's performance, how well it represents the real system, it is necessary to evaluate its behavior in an overall sense.

It should be noted that the modelling results provided by this team for comparison with other teams and with experimental results considered the start of the isothermal hydration phase as time zero, i.e. 135 days before the beginning of the heating.

G7 Thermal study

This section was part of the first modelling report of SKB1.

Two thermal models, using a 2D axisymmetric geometry shown in Figure G-30 were used for the main purpose as to calibrate the rock thermal conductivity. The difference between the models is the representation of the bentonite buffer, corresponding to a dry or wet state.

The constituents represented in the thermal models are: the Rock (R) surrounding the experiment, the Plug (P) that sealed the experiment during the first phase, the Heaters (H) and the Bentonite buffer (B). The axisymmetric geometry of the model is shown in Figure G-30. Other simplifications besides the axisymmetric assumption are neglecting the steel liner and open gaps present at the installation. These are replaced with bentonite buffer in the model.

The applied **initial conditions** are given in Table G-17.

Table G-17. Initial conditions, porosity and temperature.

Constituent	ϕ_0 [-]	T_0 [°C]
R	0.01	12
P	0.01	12
H	0.01	12
B	0.378	12

The applied **boundary conditions** are:

- T = 12 °C at the outer rock boundary,
- T = 12 °C and γ = 10 W/°C at the tunnel boundary, and
- T = 16 °C at the plug boundary, motivated from measurements.

After the initial 53 days of the experiment the applied heating power to each heater was obtained by using a "feedback loop" of sensor data from a temperature sensor positioned on the outside of the steel liner about the mid-point of the corresponding heater. The heating power was then adjusted as to result in a temperature reading of 100 °C for the selected sensor.

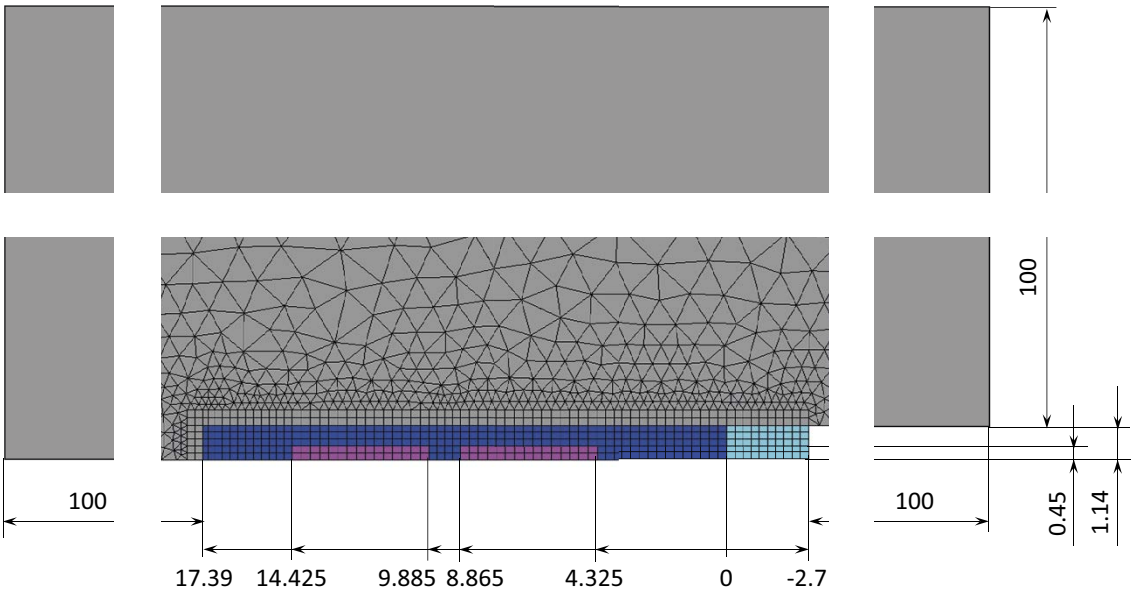

Figure G-30. *Geometry and mesh for the axisymmetric thermal models. Grey =* ***R****ock, Turquoise =* ***P****lug, Blue =* ***B****entonite buffer, Magenta =* ***H****eater.*

This procedure used in the experiment to control the heater power has not been simulated in the models. **Thermal loads**, as given by Table G-18, have instead been applied along the center of the heater representations. The used protocols were obtained by adopting a piecewise linear function to the measured heater powers, see Figure G-31, where also the piece wise linear functions used to describe the heater powers are shown. As can be seen, in the experiment the power of heater 2 was not shut down at day 1827 as was mistakenly prescribed in the models. Thus, the models are only valid up to day 1827 and not to day 1855.

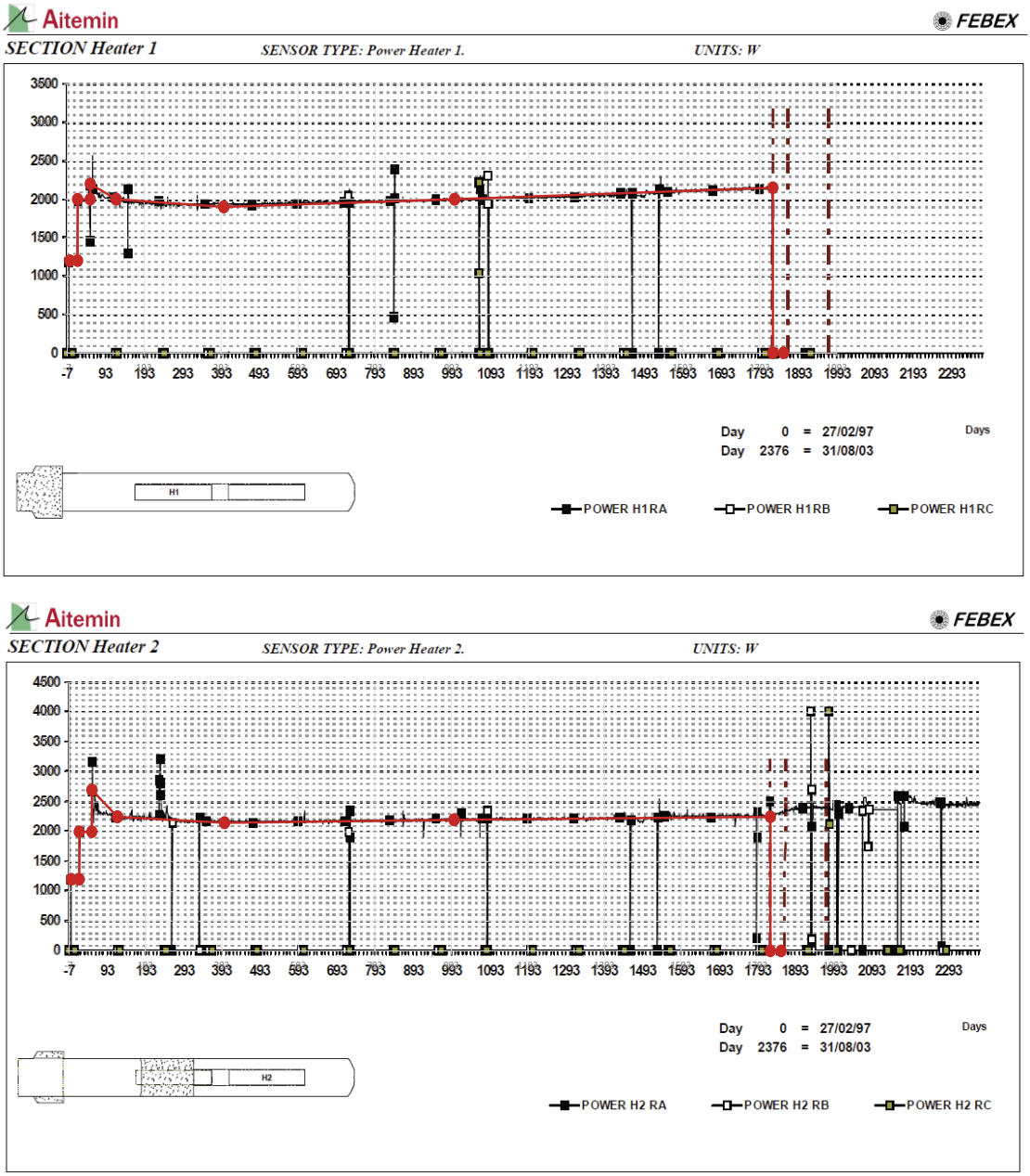

Figure G-31. *Measured heater power and the functions used for prescribing the heater power in the model. Note that the function corresponding to heater 2 is not correct after day 1827.*

Table G-18. Applied thermal load protocol.

Time interval [days]	Heater 1 power [kW]	Heater 2 power [kW]
[0–20]	1.2	1.2
[20–53]	2	2
[53–120]	[2.2–2]	[2.7–2.25]
[120–400]	[2–1.9]	[2.25–2.15]
[400–1 000]	[1.9–2]	[2.15–2.2]
[1 000–1 827]	[2–2.15]	[2.2–2.25]
[1 827–1 855]	0	0, [2.25–2.35] [1]

[1] The non-zero values are the correct ones. Zero was used by mistake.

The constituents have unique material representations as given by the relations below and the parameters given in Table G-19.

Since the mechanical process is excluded the model has constant values of **porosities**, i.e. $\phi = \phi_0$. The **conductive heat flux** is given by Fourier's law,

$$\boldsymbol{h} = -\lambda \nabla T,$$

where the **thermal conductivity** is constant, i.e. $\lambda = \lambda_0$. The **solid phase density** is constant, i.e. $\rho_s = \rho_{s0}$. The **solid phase specific internal energy** is given by the **solid phase specific heat capacity**, according to $e_s = c_s T$.

The used values of the mentioned parameters are given in Table G-19.

Table G-19. Thermal conductivity, solid phase mass density, solid phase specific heat capacity.

Constituent	λ_0 [W/(m·K)]	ρ_{s0} [kg/m^3]	c_s [J/(kg·K)]
R	3.8	2660	920
P	1.7	2000	900
H	45	7800	460
B (dry)	1.0	2735	1091
B (wet)	1.3	2735	1091

G7.1 Results and discussion

Using different values of the rock thermal conductivity, the obtained temperature evolutions in positions within the rock were compared with those measured in corresponding positions in boreholes SF11, SF12, SF13, SF14, SF21, SF22, SF23, SF24, SI1, and SI2 present in the experiment, see Figure G-32 to Figure G-41. The correspondence between the model and experiment for the rock wall temperature evolutions at the axial positions of the heater gables for section D1, G, I, and D2 was also taken into consideration. A value of 3.8 W/(m·K) was found suitable and gave the results presented in Figure G-32 to Figure G-41.

In Figure G-42 to Figure G-47 the solid red and dotted red curves indicate the calculated responses using a buffer thermal conductivity of 1.0 W/(m·K) and 1.3 W/(m·K), respectively. These values correspond to the values expected for bentonite at the initial water saturation about 0.65 (a *dry* state) and at full saturation (a *wet* state), respectively. The effect from including the saturation process can be estimated by imagine temperature evolutions starting close to the solid red curve (dry) and then deviating from this and converge towards the dotted red curve (wet).

The measured temperature evolutions at the outer surface of the steel liner vary between the different orientations. This indicate that the non-axisymmetry of the experiment have a clearly visible effect on the physical processes. In the experiment there is an open gap with varying width in different orientations at the canister surface. Due to the horizontal orientation of the drift, the gap is expected to be zero at the bottom and largest at the top, which in turn would give higher temperature at the bottom. This is the case when studying the measurements.

G7.2 Rock temperatures

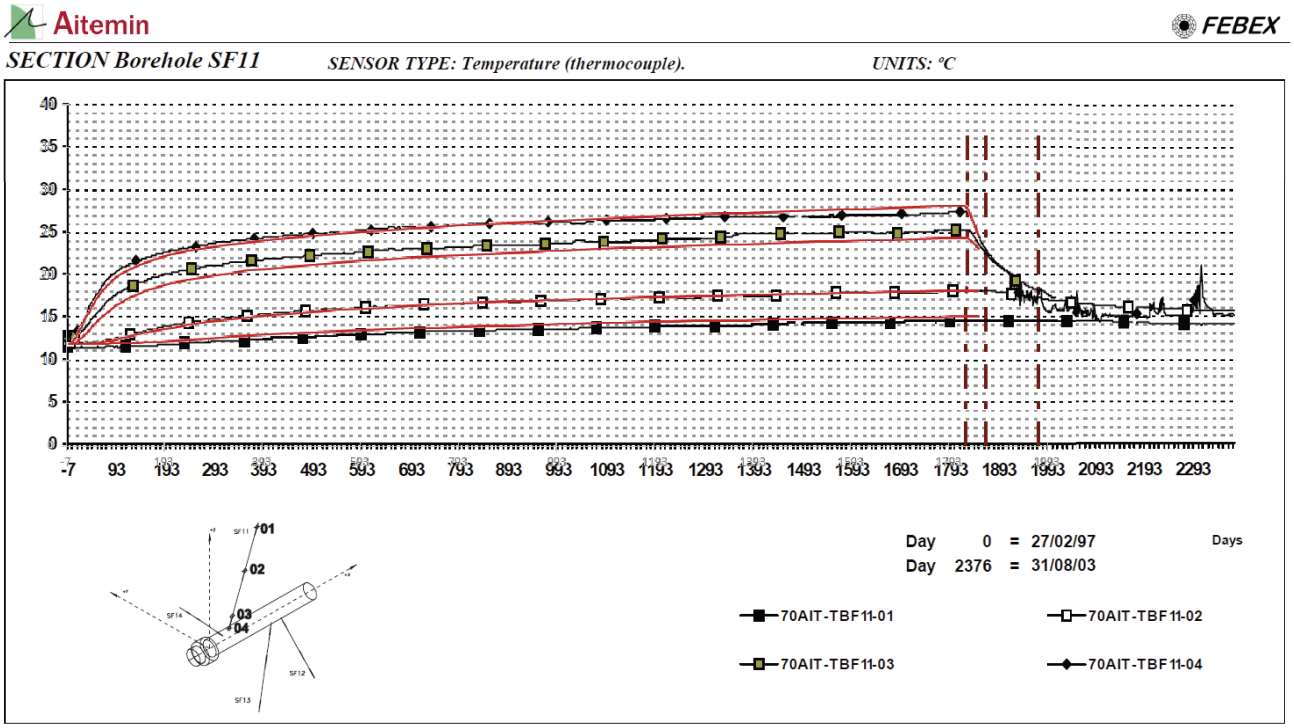

Figure G-32. *Measured and simulated temperatures in SF11.*

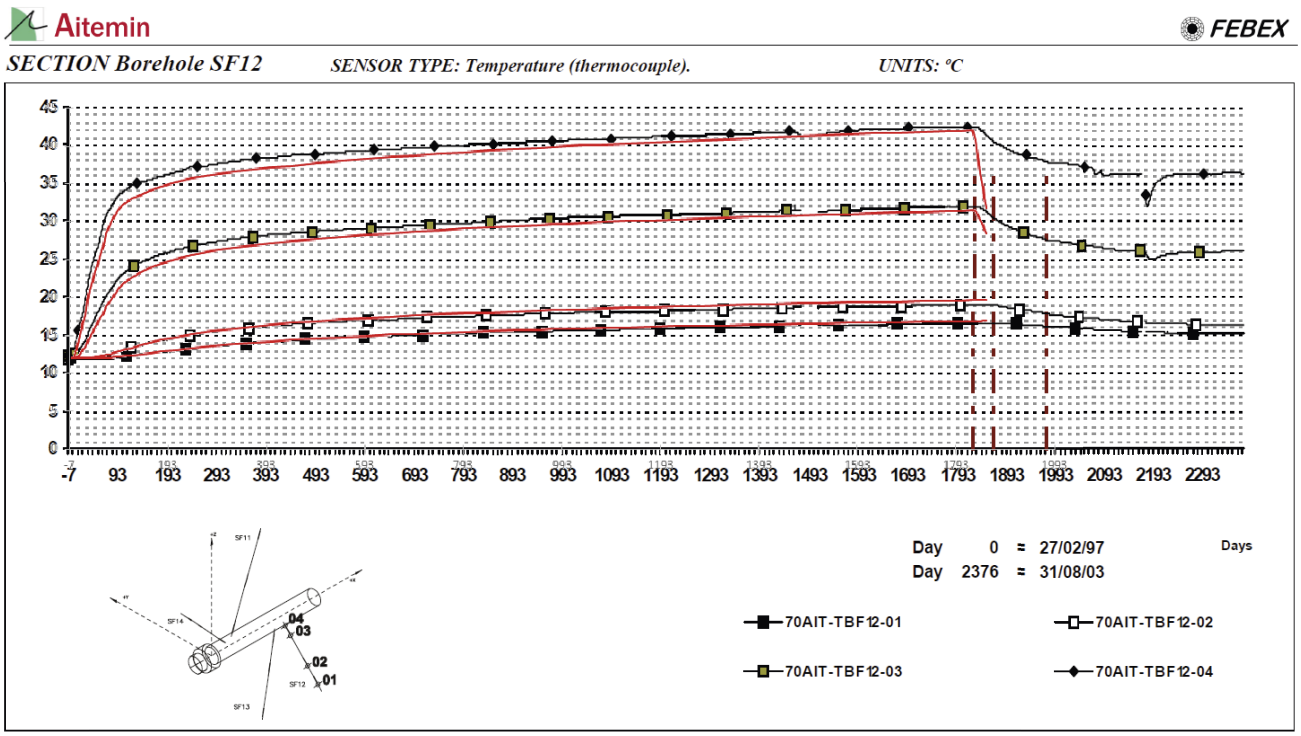

Figure G-33. *Measured and simulated temperatures in SF12.*

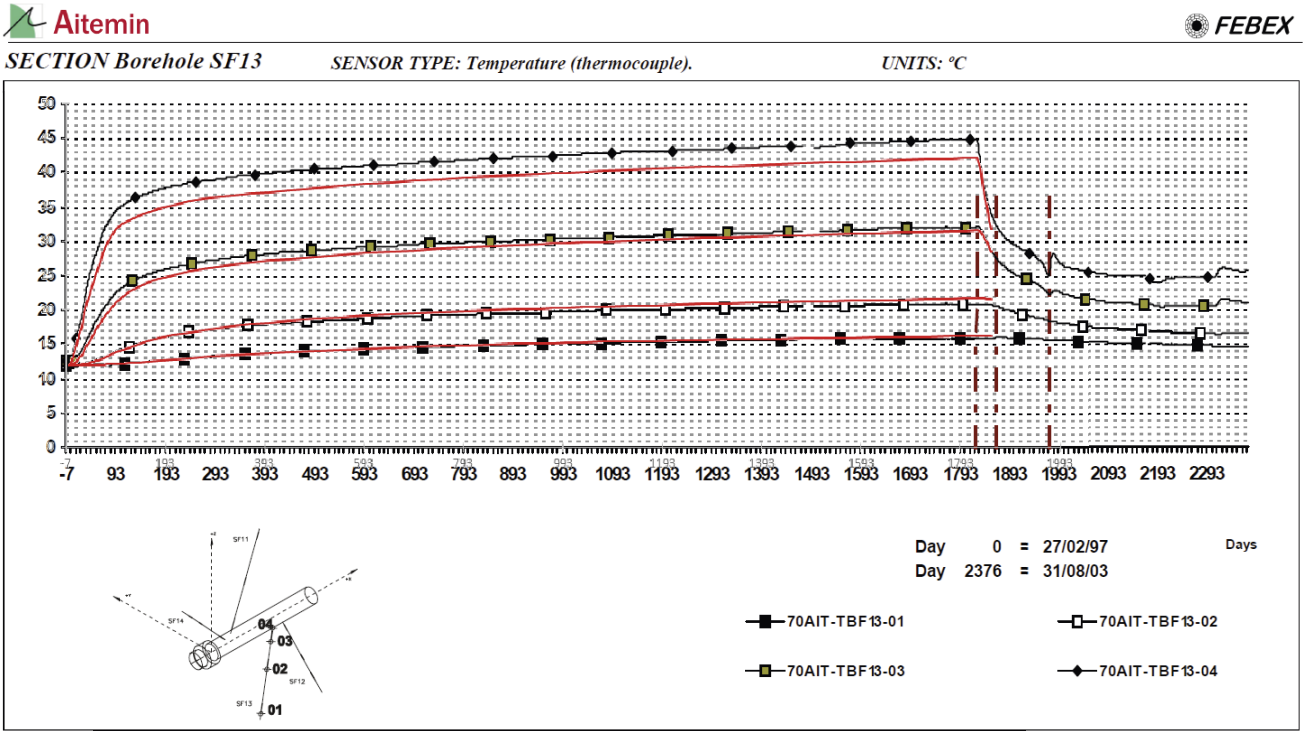

Figure G-34. *Measured and simulated temperatures in SF13.*

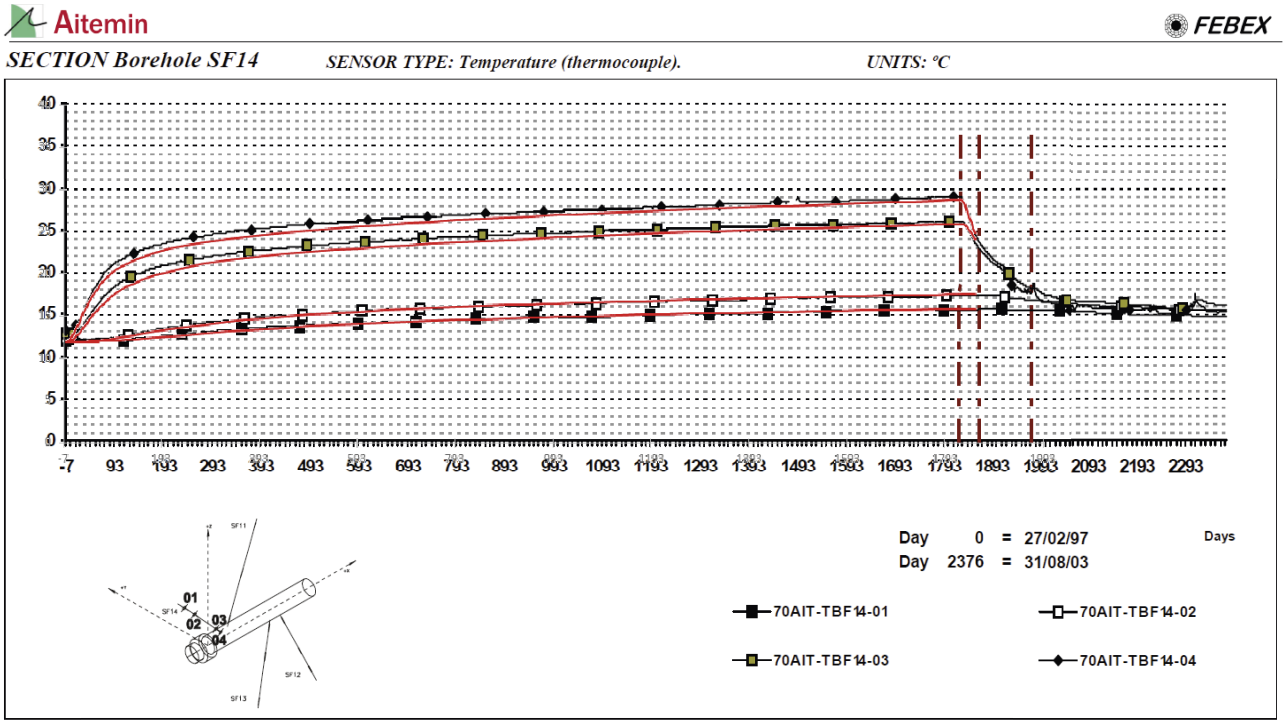

Figure G-35. *Measured and simulated temperatures in SF14.*

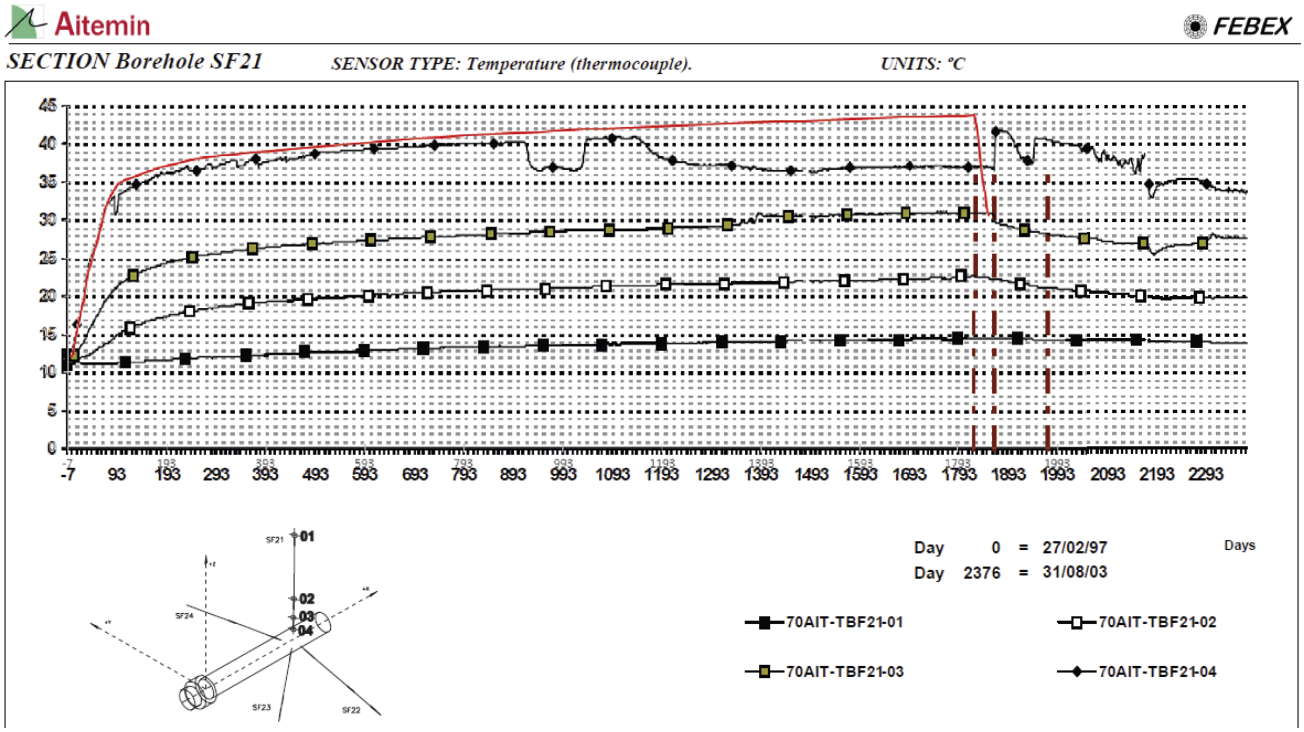

Figure G-36. *Measured and simulated temperatures in SF21.*

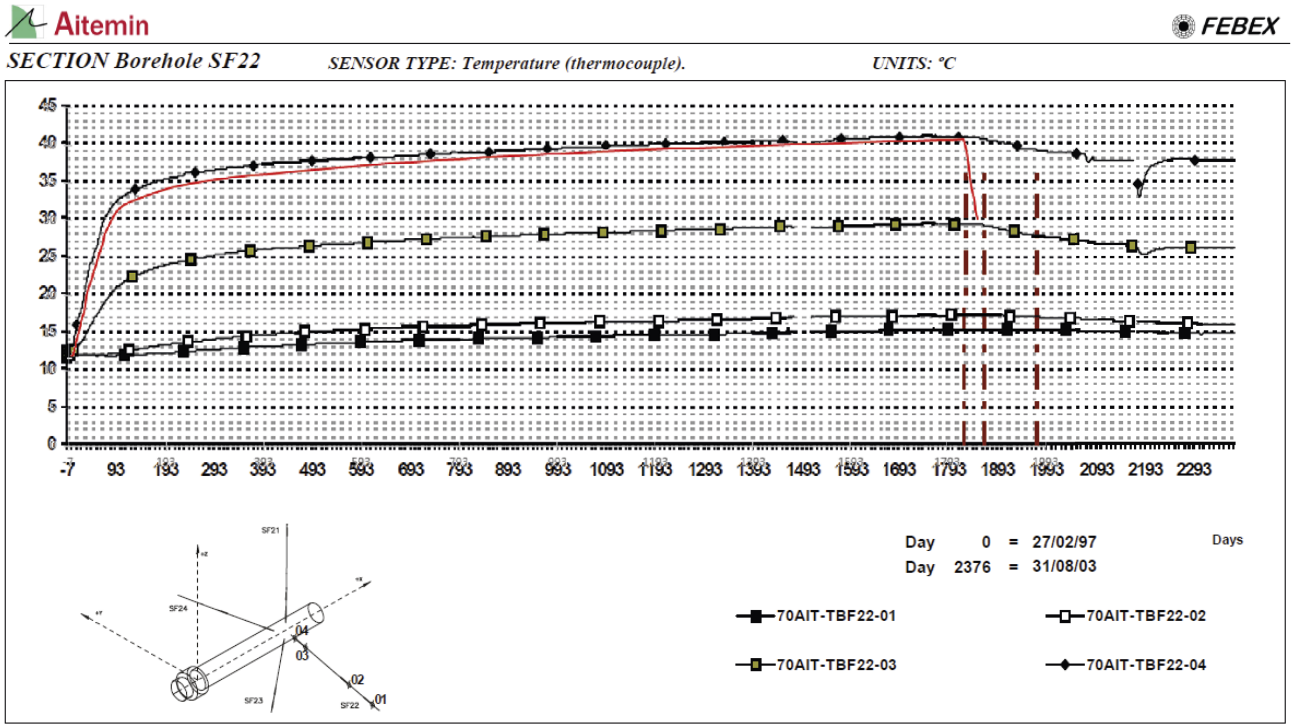

Figure G-37. *Measured and simulated temperatures in SF22.*

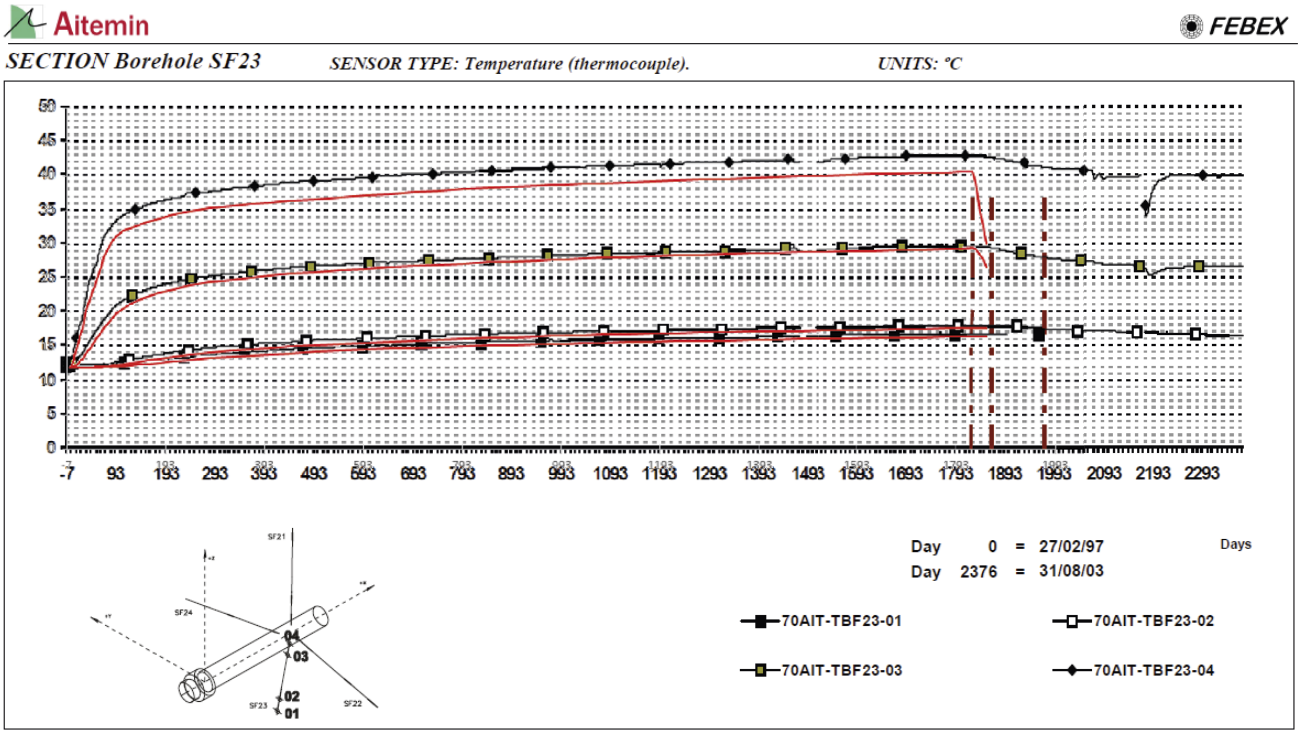

Figure G-38. *Measured and simulated temperatures in SF23.*

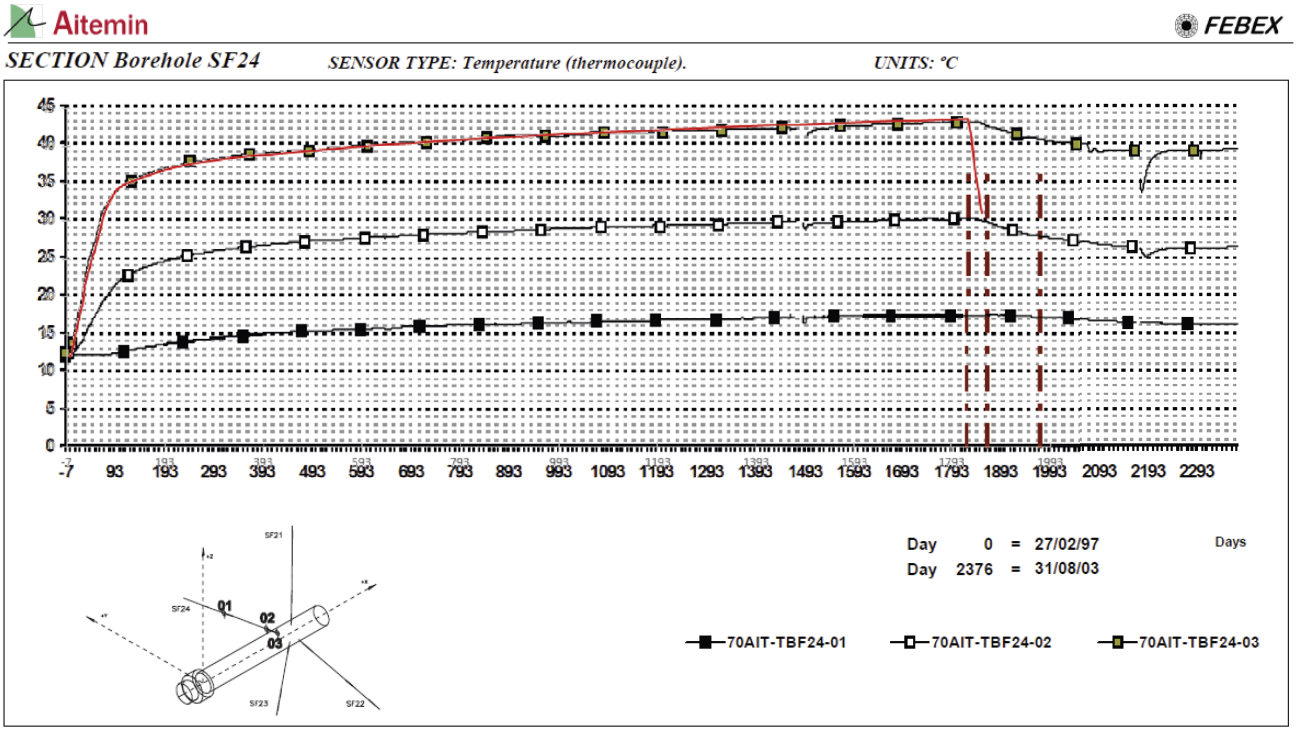

Figure G-39. *Measured and simulated temperatures in SF24.*

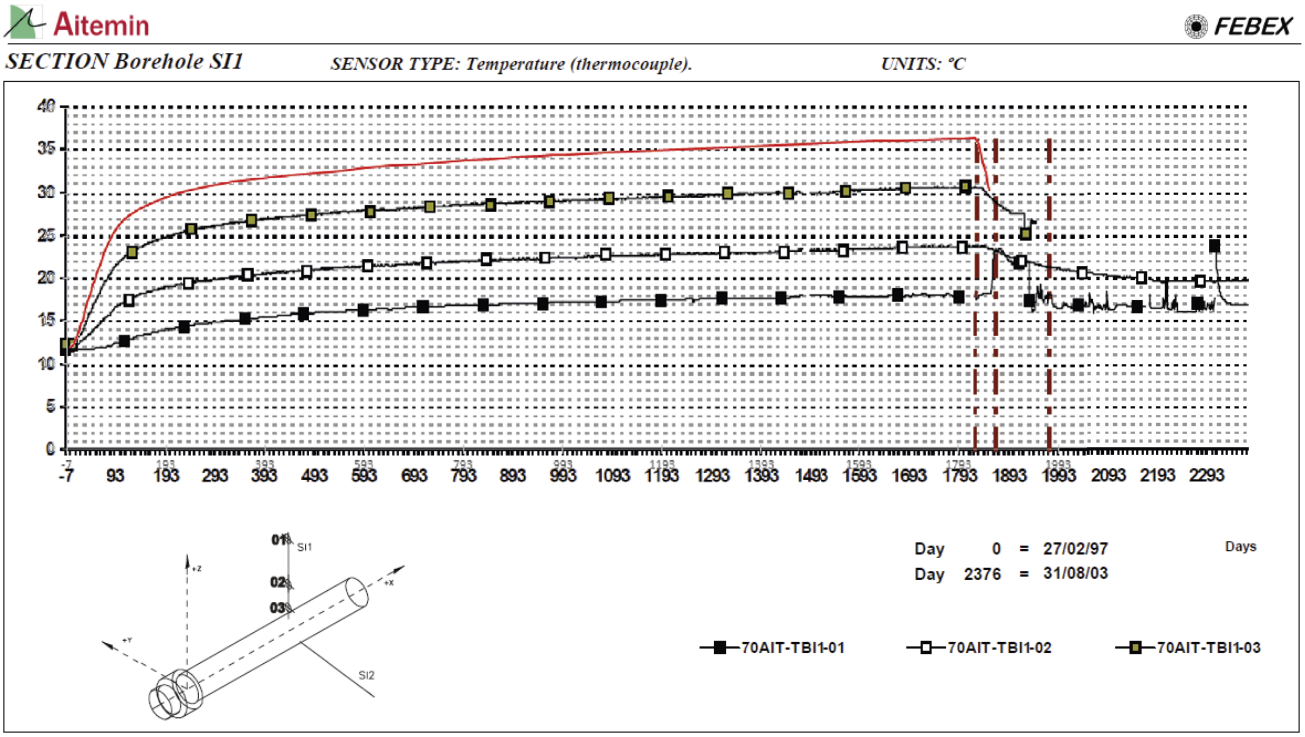

Figure G-40. *Measured and simulated temperatures in SI1.*

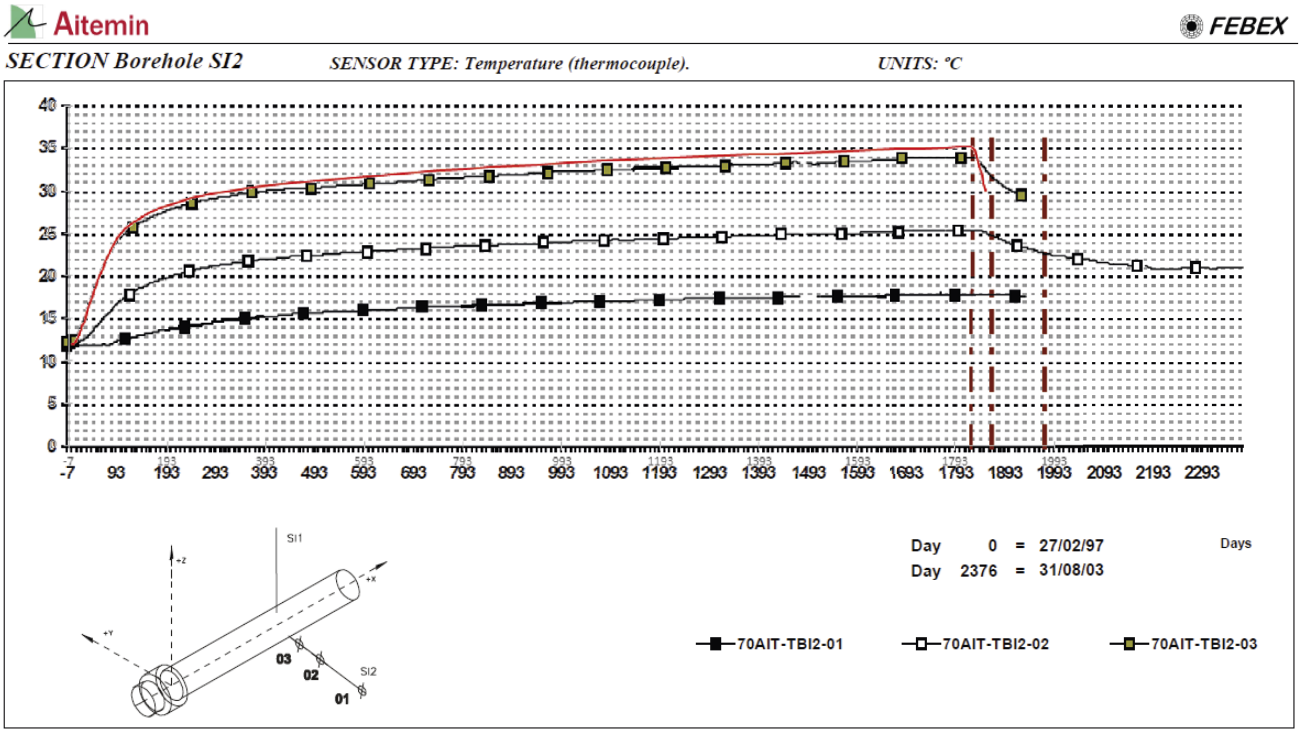

Figure G-41. *Measured and simulated temperatures in SI2.*

G7.3 Buffer temperatures

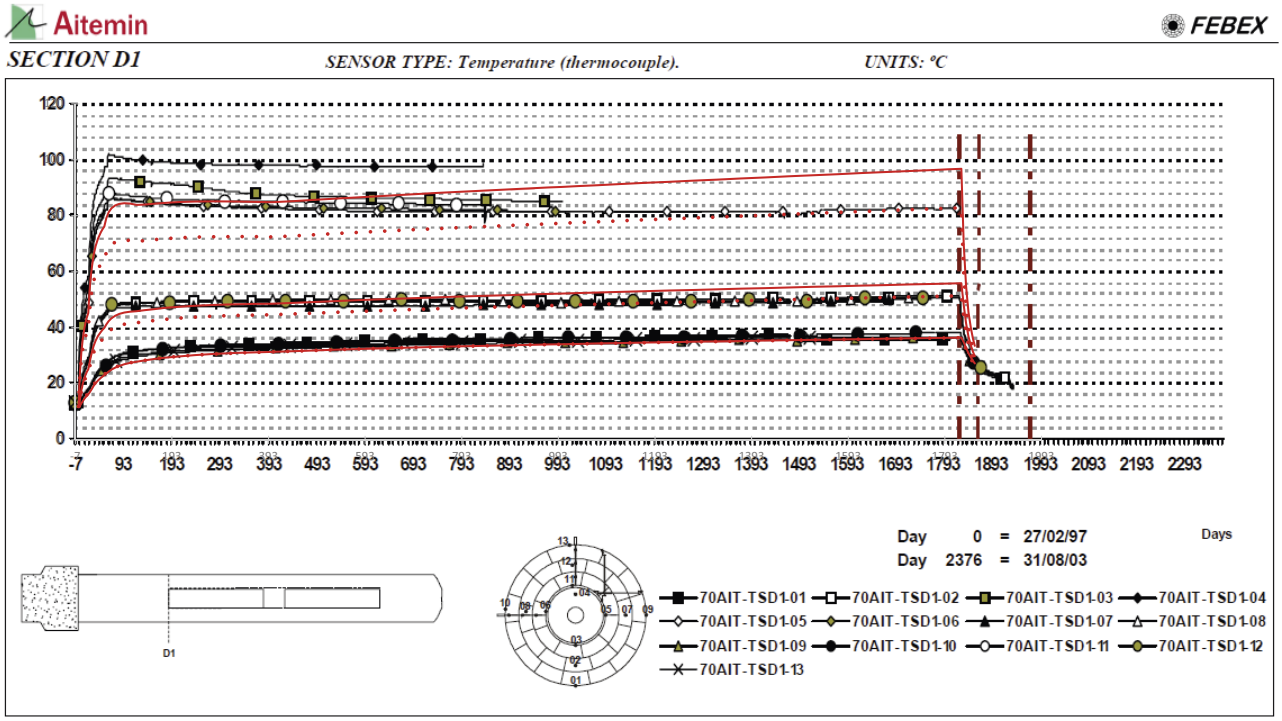

Figure G-42. *Measured and simulated temperatures in the D1-section. Solid line = dry realization, dotted line = wet realization.*

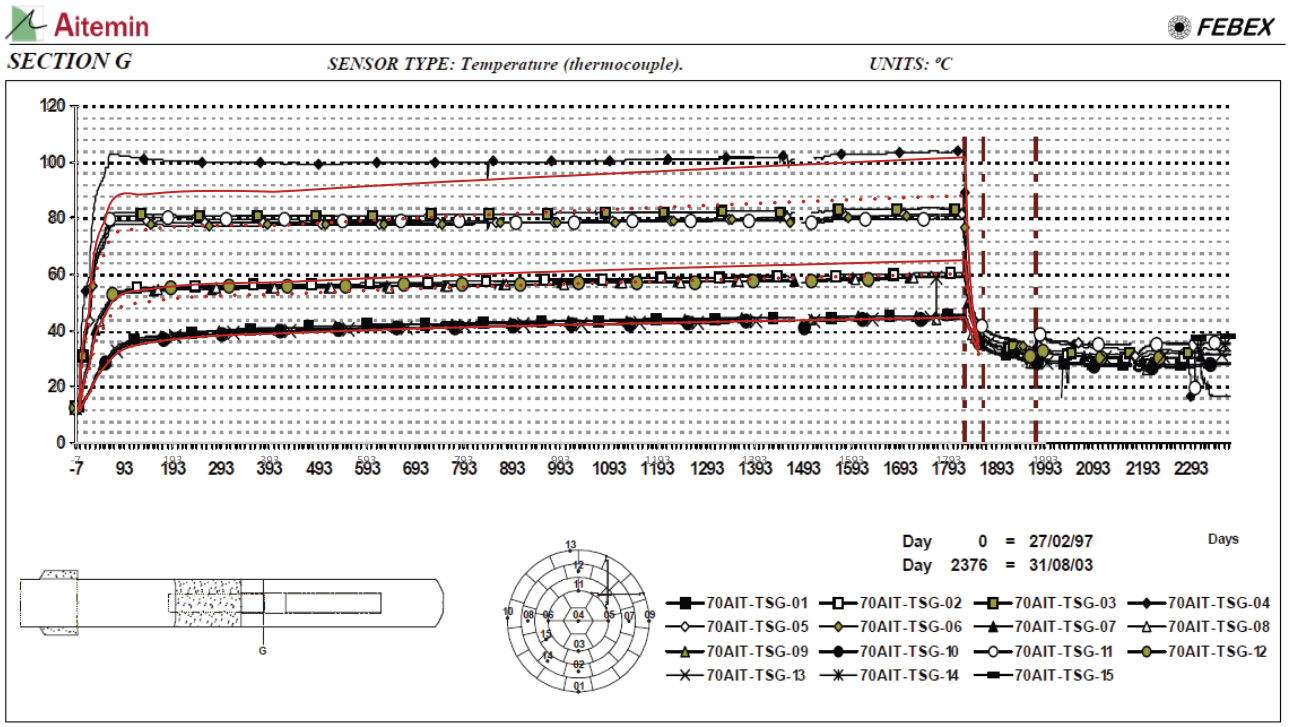

Figure G-43. *Measured and simulated temperatures in the G-section. Solid line = dry realization, dotted line = wet realization.*

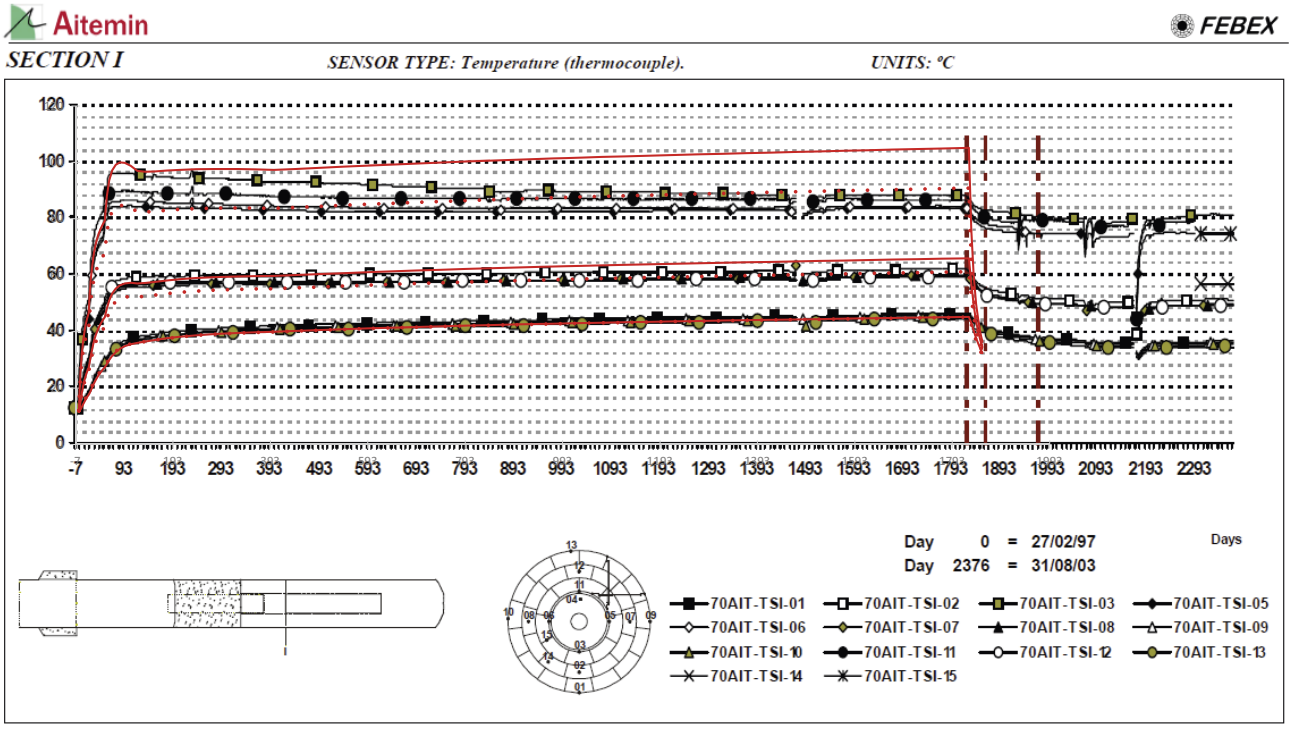

Figure G-44. *Measured and simulated temperatures in the I-section. Solid line = dry realization, dotted line = wet realization.*

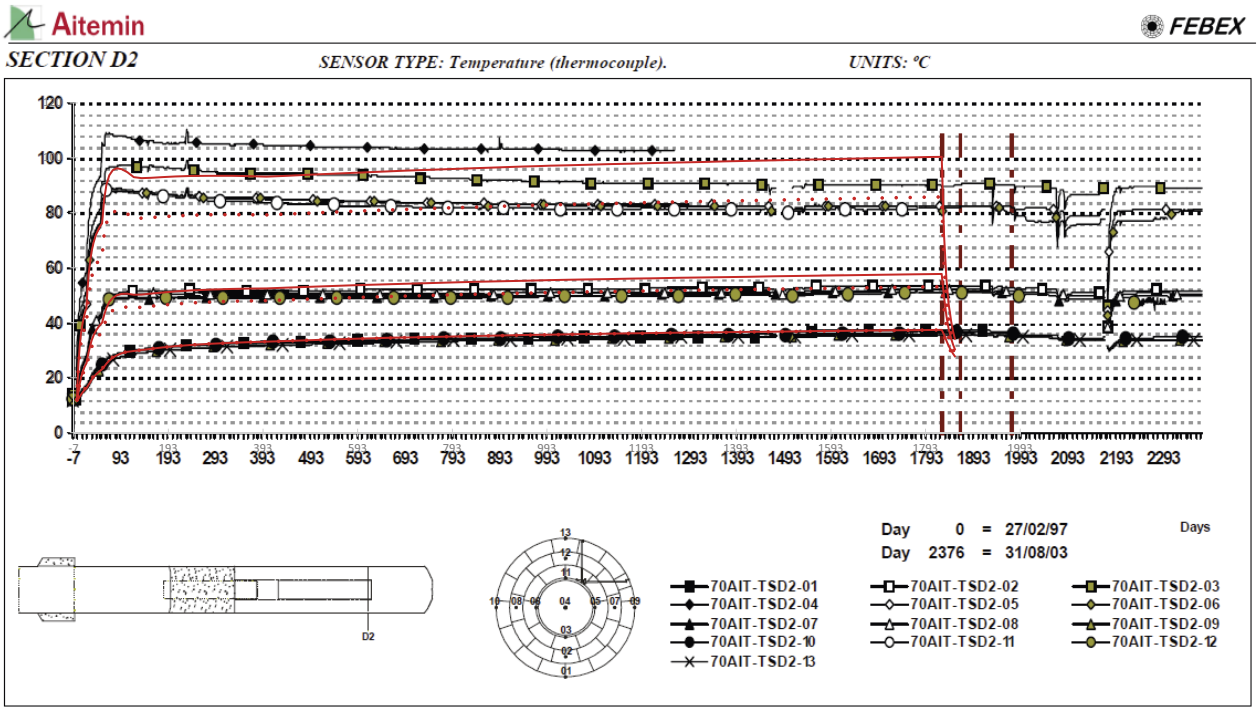

Figure G-45. *Measured and simulated temperatures in the D2-section. Solid line = dry realization, dotted line = wet realization.*

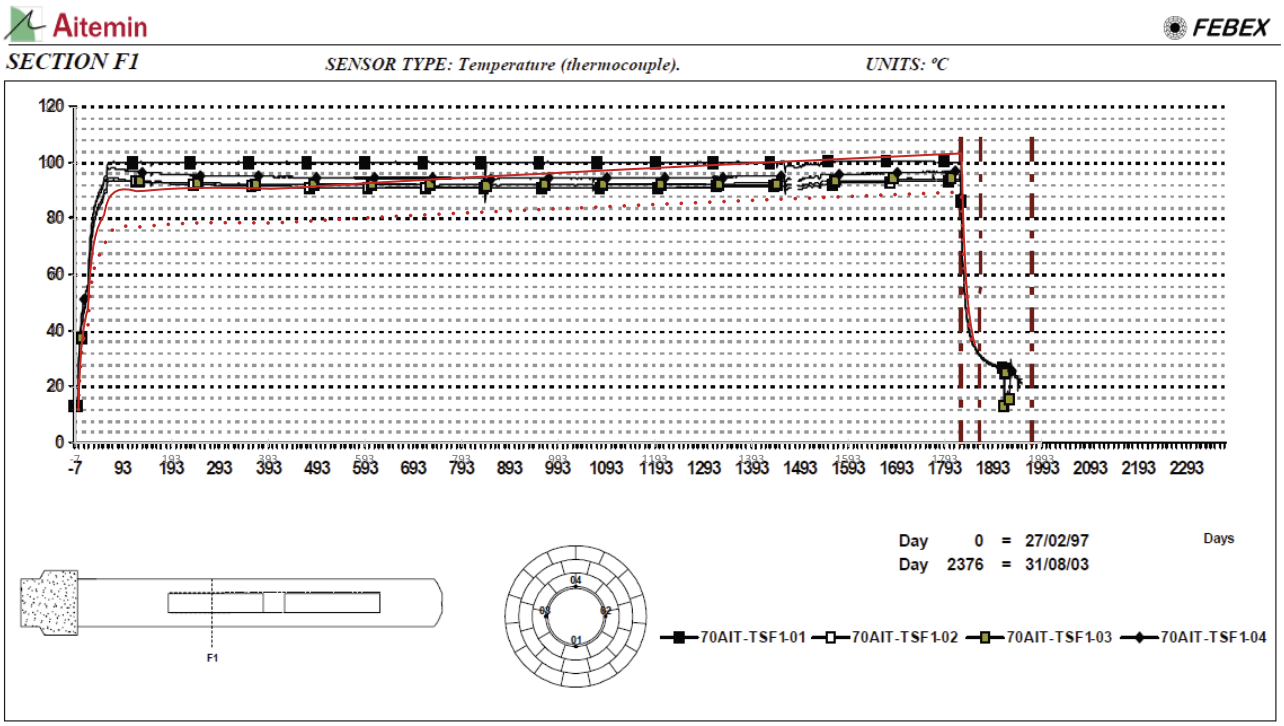

Figure G-46. *Measured and simulated temperatures in the F1-section. Solid line = dry realization, dotted line = wet realization.*

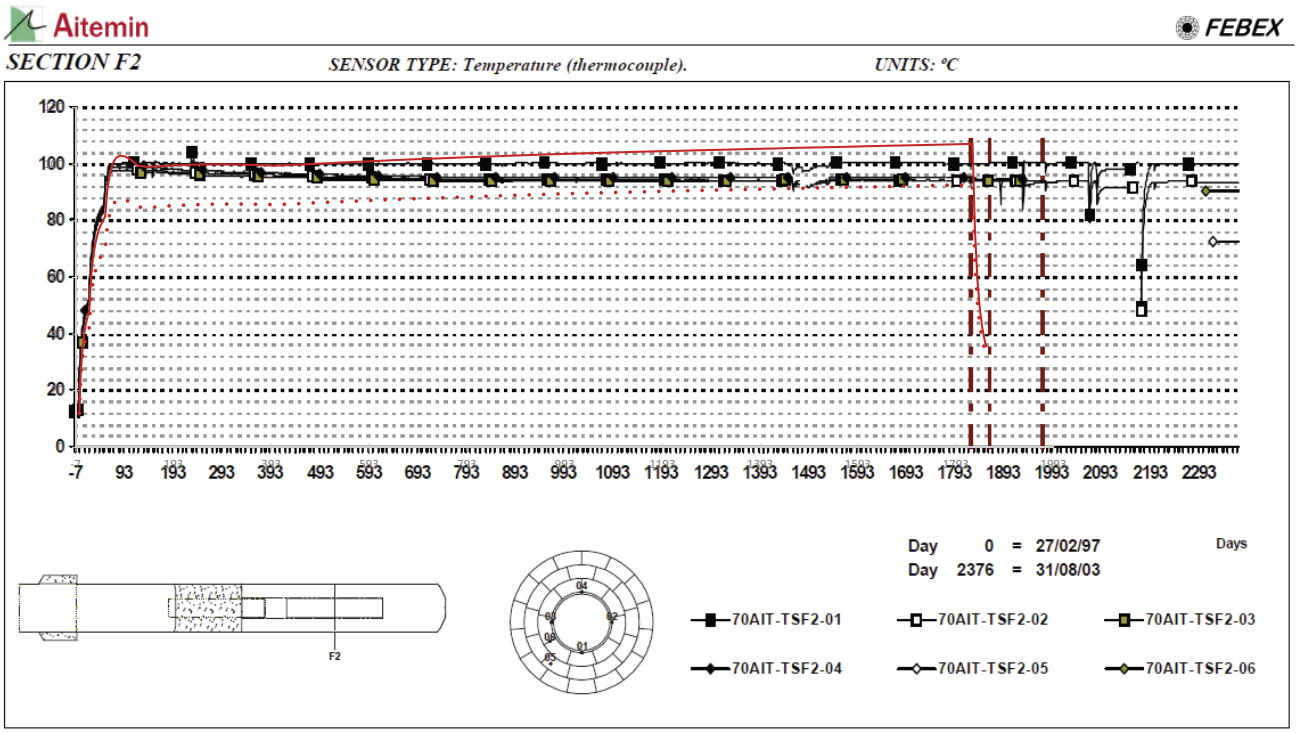

Figure G-47. *Measured and simulated temperatures in the F2-section. Solid line = dry realization, dotted line = wet realization.*

G8 Requested information

General features of the numerical analysis

- Type of analysis: Axisymmetric 2D
- Type of analysis: THM
- Coupled
- Size of the analysis domain: 100 m × 100 m
- Type and number of elements: Two different element types were used, linear quadrilateral elements with 4 integration points and selective integration by means of the "B-matrix" in the inner part of the model and linear triangular elements in the outer part consisting of the rock representation.
- Number of elements across the bentonite barrier: 18
- Number of nodes: 7244

Stages of the analysis

The present model accounts for three phases of the experiment:

– Phase 0 (t = [−135 – 0] days): No heating, water uptake between installation and heating.
– Phase 1 (t = [0 – 1 855] days): Heating from both canisters, water uptake and redistribution.
– Phase 2 (t = [1 855–6 758] days): Heating from the inner canister, water uptake and redistribution.

The excavation process was not represented in the simulations.

G8.1 Initial variables and key parameters for the Rock

Initial conditions of the rock at the start of the analysis (1)

Initial temperature at tunnel axis level (°C)	Initial stresses at tunnel axis level (MPa)	Initial pore water pressure at tunnel axis level (MPa)
12	−0.11	0.1

Initial conditions of the rock at the start of the analysis (2)

Initial density (g/cm^3)	Initial porosity	Initial water content (%)
2660 (solid phase)	0.01	100

Main rock properties (1)

Initial thermal conductivity (W/mK)	Specific heat capacity (J/kgK)	Initial intrinsic permeability (m^2)	Initial hydraulic permeability (m/s)
3.8	920	10^{-10}	10^{-17}

Main rock properties (2)

Linear thermal expansion coefficient (K^{-1})	Young's modulus (MPa)	Poisson's ratio
0	10^5	0.2

Main rock properties: retention curve (3)

Equation used	p_0 (MPa)	λ (-)
$S_l = \left(1 + \left(\frac{p_g - p_l}{p_0}\right)^{\frac{1}{1-\lambda}}\right)^{-\lambda}$	1.74	0.6

Main rock properties: relative permeability (4)

Equation used	λ (-)
$\sqrt{S_l}\left(1 - \left(1 - S_l^{\frac{1}{\lambda}}\right)^{\lambda}\right)^2$	0.6

G8.2 Initial variables and key parameters for the Bentonite

Initial conditions of the bentonite at installation (1)

Initial temperature (°C)	Initial stresses (MPa)	Initial pore water pressure/suction (MPa)	Initial relative humidity (%)
12	−0.11	−124.9	40

Initial conditions of the bentonite at installation (2)

Initial dry density (g/cm^3)	Initial density of the solid phase (g/cm^3)	Initial porosity	Initial water content (%)	Initial degree of saturation (%)
1700	2735	0.378	14.4	0.647

Main bentonite properties (1)

Initial thermal conductivity (W/mK)	Initial thermal conductivity dry bentonite (W/mK)	Initial thermal conductivity saturated bentonite (W/mK)	Initial specific heat capacity of the solid phase (J/kgK)	Thermal expansion coefficient (K^{-1})
0.919	0.571	1.259	1091	0

Main bentonite properties (2)

Initial intrinsic permeability (m^2)	Initial hydraulic permeability (m/s)	Initial intrinsic permeability (saturated) (m^2)	Initial hydraulic permeability (saturated) (m/s)	Swelling pressure under initial conditions (MPa)
0.298×10^{-21}	0.298×10^{-14}	1.1×10^{-21}	1.1×10^{-14}	13.3

Main bentonite properties: permeability dependence on dry density (or porosity) (3)

Equation used (porosity dependent)	κ_0 (m²)	ϕ_0 (-)
$\kappa_0 \frac{\phi^3}{(\phi-1)^2} \frac{(\phi_0-1)^2}{{\phi_0}^3}$	1.1×10^{-21}	0.378

Main bentonite properties: retention curve (4)

Equation used	p_0 (MPa)	λ (-)	p_d (MPa)	λ_d (-)
$S_l = f_d \left(1 + \left(\frac{p_g - p_l}{p_0}\right)^{\frac{1}{1-\lambda}}\right)^{-\lambda}$ $f_d = \left(1 - \frac{p_g - p_l}{p_d}\right)^{\lambda_d}$	22.5	0.09	1 100	2.1

Main bentonite properties: relative permeability (5)

Equation used
S_l^3

Main bentonite properties: thermal conductivity (6)

Equation used
$0.57 + \frac{1.28 - 0.57}{1 + \exp\left(\frac{S_l - 0.65}{-0.1}\right)}$ d

Main bentonite properties: vapour transport (7)

Molecular diffusion coefficient of vapour in free air (m²/s)	Tortuosity
$D_g^w = 5.9 \cdot 10^{-6} \frac{(273.15 + T)^{2.3}}{p_g} = 2.615 \cdot 10^{-5}$	0.5

G8.3 Constitutive functions, graphs

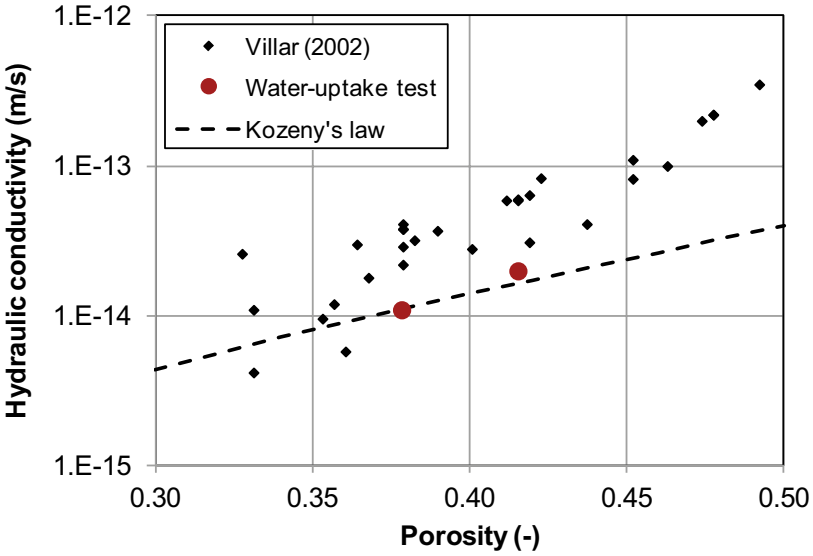

• Hydraulic conductivity vs porosity.

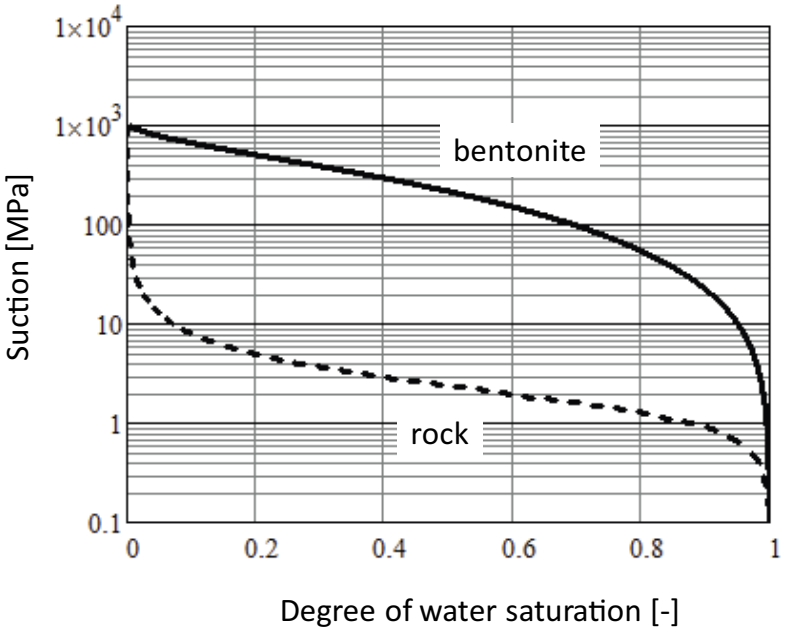

• Retention curve of the bentonite and retention curve of the rock.

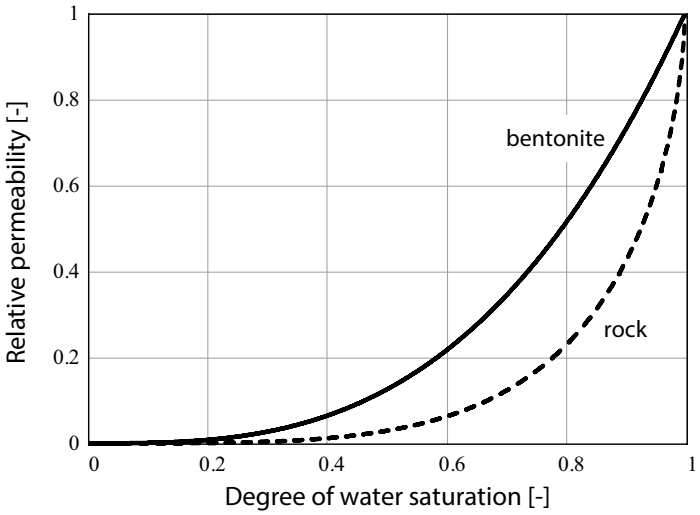

• Relative permeability of the bentonite and relative permeability of the rock.

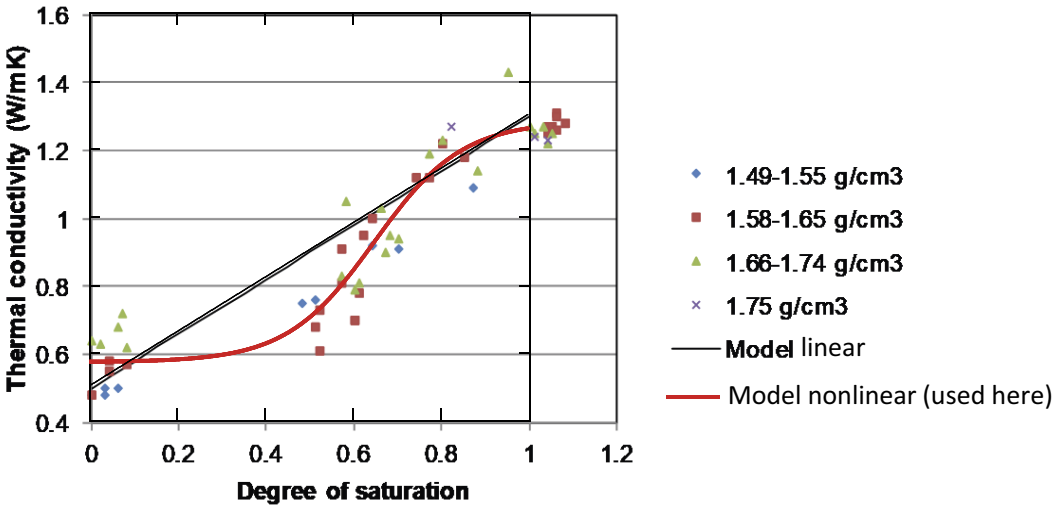

• Thermal conductivity of the bentonite vs degree of saturation.

Appendix H

TUL Report

Technical University of Liberec, Czech Republic (TUL)
Milan Hokr, Petr Rálek, Jiří Landa, Ilona Hančilová

General features of the numerical analysis

- 2D axisymmetric model
- Fully coupled TH (Richards+vapor)
- Nonlinear elasticity with volume expansion from swelling, (postprocessed from TH model results, i.e. only TH-to-M coupling)
- Domain size 35 m × 12 m
- Modified geometry for 2nd stage

Stage number	Brief description	Start time (day)	Duration (days)
1	Pressure stabilizing step	−1	1
2	Heating Power 2 000 W	0	53
3	Heating Temperature 100 °C	53	1 770
4	Heater_2 Temperature 100 °C, Geometry 1	1823	145
5	Heater_2 Temperature 100 °C, Geometry 2	1968	4 500

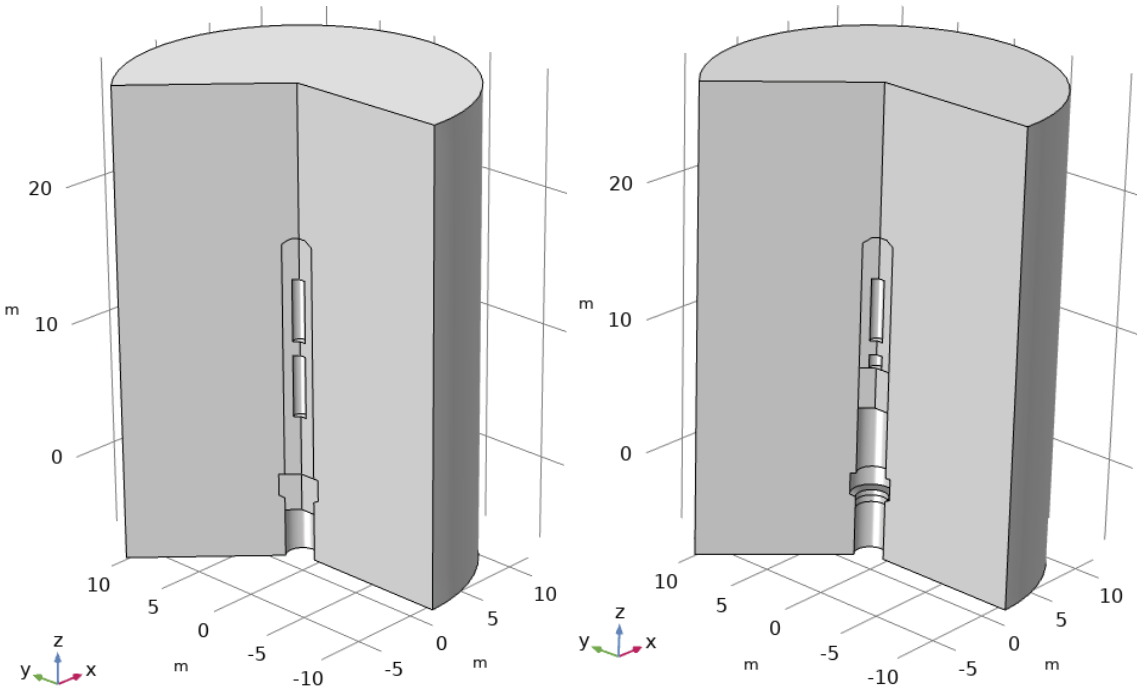

- Geometry 1
  - Stage 1: 1 day simulation with zero pressure on the bentonite/rock interface; no heating
  - Stage 2: both heaters Neumann BC (boundary flux)
  - Stage 3: both heaters Dirichlet BC 100 °C
  - Stage 4: Heater 1 switched off; no special dismantling operation modelling
  - Exporting thermal, pressure and deformation fields (in t = 1 968 d)
- Geometry 2
  - Importing thermal, pressure and deformation fields (in t = 1 968 d) as initial conditions for Stage 5
  - Stage 5: heater 2 100 °C

Geometry

Model 1: Stages 1–4

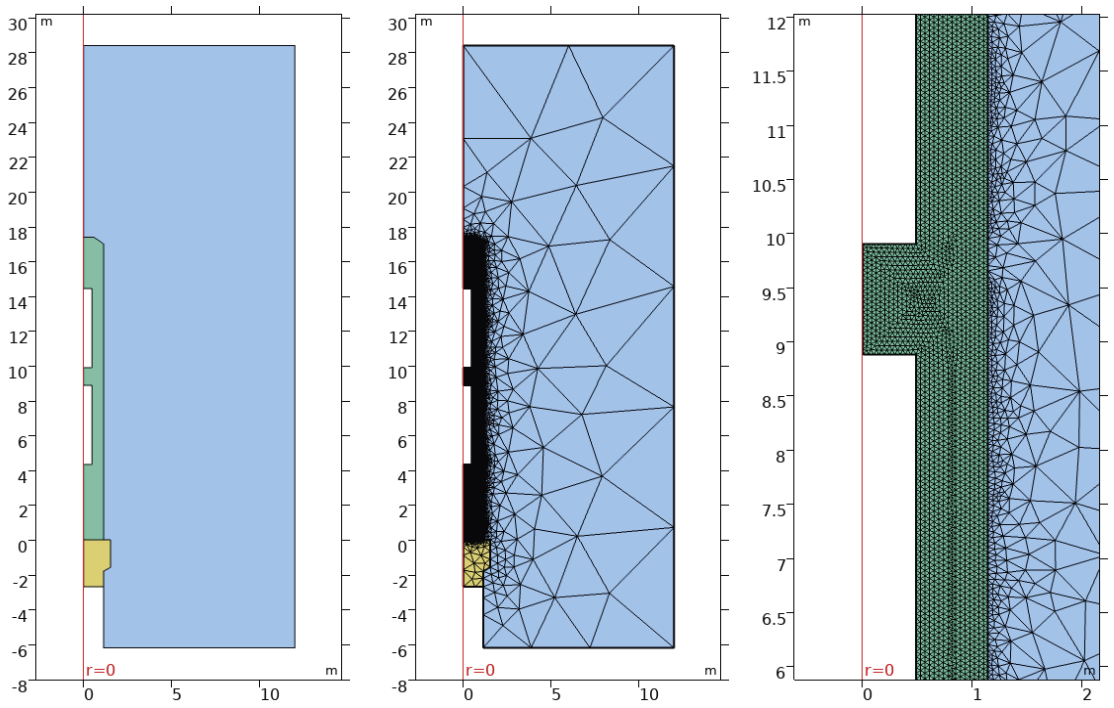

9 396 nodes, 18 372 triangles, 817 boundary elements, 143 632 dof

16 elements across bentonite between heater and rock

Model 2: Stage 5

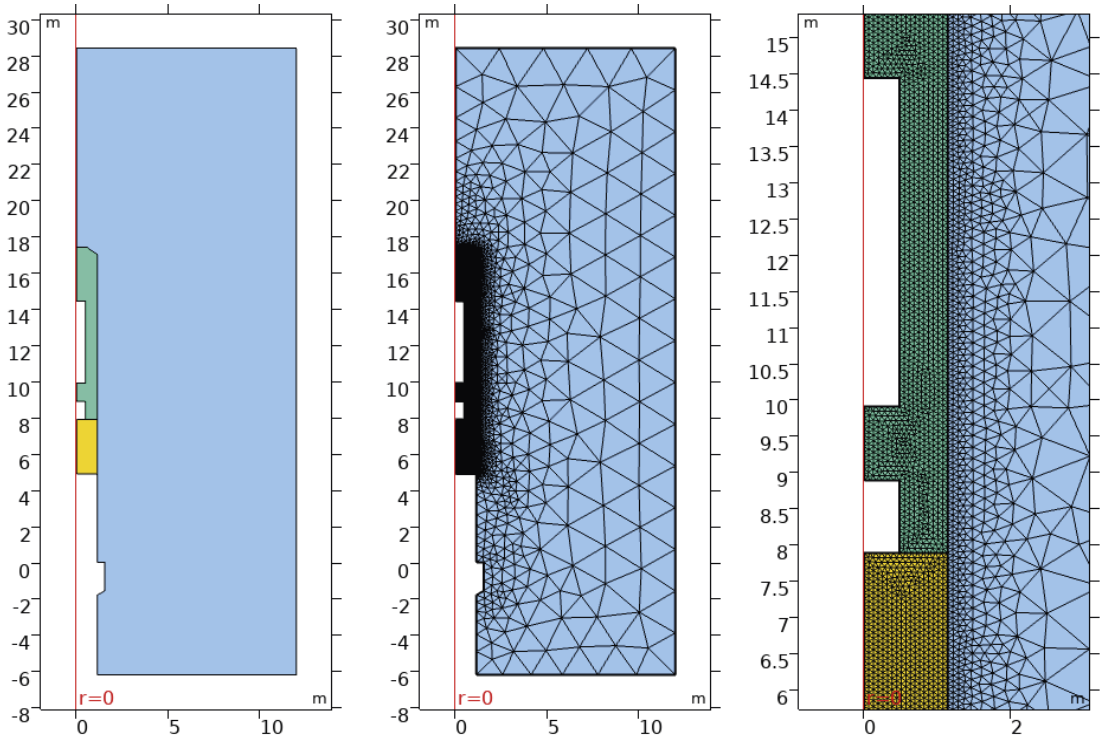

3 744 nodes, 7 220 triangles, 442 boundary elements, 45 534 dof

10 elements across bentonite between heater and rock

Boundary conditions

- Constant temperature 12 deg on outer boundary
- Constant pressure 3×10^6 Pa on outer boundary
- No flow of water elsewhere
- Heater BC (changing according to heating steps):
  - 0–53 days boundary flux
  - 53–1 827 days prescribed temperature 100 deg on the interface heater/bentonite of both heaters
  - 1 827–6 500 days prescribed temperature 100 deg on the interface heater 2 /bentonite
- All bentonite interfaces: zero normal displacement

Initial conditions

- Uniform temperature 12 deg
- Rock pressure uniform 3 MPa
- Bentonite suction −120 MPa
  - Corresponding to 41 % RH and 56 % saturation

Constitutive functions

Initial variables and key parameters

Rock

Initial conditions of the rock at the start of the analysis (1)

Initial temperature at tunnel axis level (°C)	Initial stresses at tunnel axis level (MPa)	Initial pore water pressure at tunnel axis level (MPa)
12	0	3

Initial conditions of the rock at the start of the analysis (2)

Initial density (g/cm^3)	Initial porosity	Initial water content (%)
2.64	0.003	0.1136

Main rock properties (1)

Initial thermal conductivity (W/mK)	Specific heat capacity (J/kgK)	Initial intrinsic permeability (m^2)	Initial hydraulic conductivity (m/s)
3.3	920	10^{-17}	10^{-10}

Main rock properties (2)

Linear thermal expansion coefficient (K^{-1})	Young's modulus (MPa)	Poisson's ratio
---	---	---

Main rock properties: retention curve (3)

Equation used	λ (1)	p_g (MPa)	P_0 (MPa)
$S_l = \left[1 + \left(\frac{p_g - p_l}{P_0}\right)^{\frac{1}{1-\lambda}}\right]^{-\lambda} \; p_l < p_g;\; S_l = 1 \; p_l \geq p_g$	0.595	0.1	1.74

Main rock properties: relative permeability (4)

Equation used	λ (1)
$k_r = \sqrt{S_l}\left[1 - \left(1 - S_l^{\frac{1}{\lambda}}\right)^{\lambda}\right]^2$	0.595

Bentonite

Initial conditions of the bentonite at installation (1)

Initial temperature (°C)	Initial stresses (MPa)	Initial pore water pressure/suction (MPa)	Initial relative humidity (%)
12	0	−120	41.16

Initial conditions of the bentonite at installation (2)

Initial dry density (g/cm^3)	Initial density of the solid phase (g/cm^3)	Initial porosity	Initial water content (%)	Initial degree of saturation (%)
1.6	2.7	0.407	14.22	55.9

Main bentonite properties (1)

Initial thermal conductivity (W/mK)	Initial thermal conductivity dry bentonite (W/mK)	Initial thermal conductivity saturated bentonite (W/mK)	Initial specific heat capacity of the solid phase (J/kgK)	Linear thermal expansion coefficient (K^{-1})
0.936	0.5	1.28	1125.51	---

Main bentonite properties (2)

Initial intrinsic permeability (m^2)	Initial hydraulic conductivity (m/s)	Initial intrinsic permeability (saturated) (m^2)	Initial hydraulic conductivity (saturated) (m/s)	Swelling pressure under initial conditions (oedometric conditions) (MPa)
0.7×10^{-21}	0.7×10^{-14}	4×10^{-21}	4×10^{-14}	5.2

Note: A virtual swelling pressure test (oedometric conditions) may be required to determine the swelling pressure of the bentonite under initial conditions.

Main bentonite properties: permeability dependence on dry density (or porosity) (3)

Equation used	Parameter 1 (units)	Parameter 2 (units)	Parameter 3 (units)	Parameter 4 (units)
---	---	---	---	---

Main bentonite properties: retention curve (4)

Equation used	λ (1)	λ_s (1)	p_g (MPa)	P_0 (MPa)	P_s (GPa)
$S_l = \left[1 + \left(\frac{p_g - p_l}{P_0}\right)^{\frac{1}{1-\lambda}}\right]^{-\lambda} \left[1 - \left(\frac{p_g - p_l}{P_S}\right)\right]^{\lambda_s}$	0.3	1.5	0.1	35	4

Main bentonite properties: relative permeability (5)

Equation used
$k_r = S_l^3$

Main bentonite properties: thermal conductivity (6)

Equation used	α_{dry} (W.m.K^{-1})	α_{wet} (W.m.K^{-1})
$\alpha = \alpha_{\mathrm{dry}}(1 - S_l) + \alpha_{wet} S_l$	0.5	1.28

Main bentonite properties: vapour transport (7)

Molecular diffusion coefficient of vapour in free air (m^2/s)	k_1 (m^{2}s^{-1})	k_2 (K)	k_3 (1)	v_v (1)	τ_v (1)	n_b (1)
$D_{\mathrm{v}} = k_1 v_{\mathrm{v}} \tau_{\mathrm{v}} n (1 - S_l) \left(\frac{T}{k_2}\right)^{k_3}$	2.16 × 10^{-5}	273.15	1.8	0.8	1	0.407

Main bentonite properties: heat capacity (8)

Equation used
C_b = 1.38 T + 732

Additional: Mechanical model

Unlike the equations of the TH model, which are referred to literature (non-isothermal Richards equation – Wang et al. 2011), own relations are used in the model of nonlinear elasticity with swelling, which were derived from the basic theory of continuum mechanics, with the application of constitutive relations from the assignment or from experimental data in the literature. Therefore, the derivation is presented in more detail here.

Using an analog with thermal expansion, it is possible to express the swelling pressure due to saturation in a confined space, under the assumption of isotropic action, as

$\theta = 3K\beta\Delta S$,

where $\theta = \frac{1}{3}(\sigma_x + \sigma_y + \sigma_z)$ is the spherical stress ("hydrostatic pressure") in MPa (corresponds to the measurement of the swelling pressure in any direction), $\sigma_{x,y,z}$ are the normal stresses in individual directions, K is the volume compressibility modulus in MPa, β is the coefficient of expansion (dimensionless) and ΔS is the difference of saturation against the unloaded state. In case the bentonite is only in a closed space and does not change the dry density, only the product $K\beta$, with any combination of the modulus and the expansion factor, would enter as a model parameter (according to measured swelling pressure).

Measured properties of bentonite can be used to derive both parameters (K and β) explicitly. At the same time, the validity of the relationship can also be extended to a case of volume change, i.e. swelling of bentonite into an open space with a change in dry density or, more generally, in conditions of inhomogeneous dry density. The dependence of the swelling pressure on the dry density (Figure H-1) actually indicates the relationship between the pressure (the spherical stress θ in the context of the theory of elasticity) and the change in the volume of the sample, if we consider that the dry bulk density ρ_d is linked to the relative volume expansion $\vartheta = e_x + e_y + e_z$ ($e_{x,y,z}$ are relative elongations in individual directions) by the relation

$$\rho_d(\vartheta) = \rho_d^{(0)} \frac{1}{1 + \vartheta},$$

where $\rho_d^{(0)}$ is the original dry bulk density. From the experimentally obtained dependence $p_{sw}(\rho_d)$, after substitution, it is possible to obtain the dependence $p_{sw}(\vartheta)$ and from it the modulus of compressibility as

$$K(\vartheta) = \frac{\partial p_{sw}}{\partial \vartheta}.$$

The corresponding coefficient of expansion then corresponds to the "distance" on the axis expressing the variable ϑ, i.e.

$$\beta(\vartheta) = \frac{p_{sw}(\vartheta)}{3K(\vartheta)}.$$

A particular expression of the function can be obtained by interpolating the experimental data (for FEBEX processed in subsection 3.2.2).

We assume that the dependence of pressure/expansion on the course of increasing saturation is linear, i.e. we consider β as constant with respect to S – some experimental data confirm this, but there are exceptions (Börgesson et al. 2001).

Another phenomenon included in the model is the change in material properties depending on saturation. Experimental data are available for Young's modulus E (Man and Martino 2009) – this dependence has been also used by the team of Institute of Geonics of the Czech Academy of Sciences, in solving problems within the DECOVALEX project as part of a differently defined model of nonlinear elasticity (Blaheta et al. 2018). The characteristic phenomenon is the reduction of stiffness in the range of saturation values close to $S = 1$. Given that the model described above has volume compressibility as its main parameter, and the change of E can rather be regarded as a manifestation of a change in shear stiffness (change in shape), we introduce the dependencies $E(S, \vartheta)$ and Poisson ratio $\nu(S)$ so that the volume expansion $K = \frac{E}{3(1+2\nu)}$ was only a function of ϑ and not of S. Based on the empirical dependence on S, we denote

$$E(S,\vartheta) = E^{(0)}(\vartheta) \cdot E_{rel}(S),$$

where $E^{(0)}$ is the modulus at initial saturation and E_{rel} is the relative change factor, $E_{rel}(S_0) = 1$. Then there is

$$E(S,\vartheta) = 3K(\vartheta)E_{rel}(S)(1-2\nu(S_0))$$

$$\nu(S) = \frac{1 - E_{rel}(S)\big(1-2\nu(S_0)\big)}{2} \quad .$$

The dependence of the parameters on S extends the link between the coupled H-M phenomena (S also appears directly in the term expressing the swelling), and the dependence on ϑ then defines the nonlinearity of the elastic model.

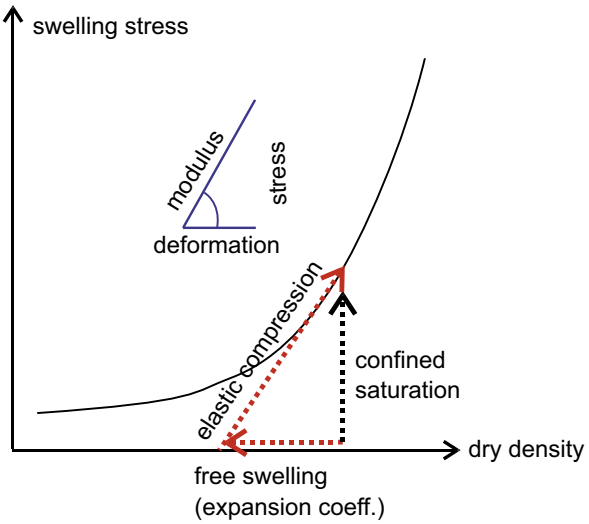

Figure H-1. *Interpretation of the parameters of the nonlinear elastic model from the measured dependence of the swelling pressure on the dry density.*

Appendix I

UPC Report

Universitat Politècnica de Catalunya, Spain (UPC)
Alfonso Rodríguez-Dono

I1 Introduction

The present report contains the description of a model for the large-scale in situ heating test FEBEX (full-scale engineered barrier experiment). In this test, after five years of heating, one of the heaters was switched off and the experiment was partially dismantled, allowing the final state of the barrier to be observed directly. In this way, very valuable information on the state of the bentonite at the end of the test was obtained. The test has received attention during the initial (Gens et al. 1998) and intermediate stages (Alonso et al. 2005). Moreover, Gens et al. (2009) discussed the thermal, hydraulic and mechanical observations in the bentonite barrier and in the host rock, paying special attention to the progress of hydration in the barrier, the effects of heating and vapour transport, and the development of swelling pressures in the barrier.

In the FEBEX experiment, heaters are emplaced in the axis of a tunnel excavated in granite to simulate the heat production of radioactive waste. The test is fully instrumented, and attention is focused on the thermo-hydro-mechanical (THM) behaviour of the near-field region constituted by the compacted bentonite barrier surrounding the heater and the immediately adjacent rock. Interpretation of the test is assisted by the performance of a coupled numerical analysis based on a formulation that incorporates the relevant THM phenomena. Further description of the FEBEX in situ test can be found in Gens et al. (2009).

The model of this test has been developed using CODE_BRIGHT (Olivella et al. 1994, 1996), a Finite Element Method program that enables coupled thermo-hydro-mechanical analysis in geological media. This is a code version that incorporates customized pre- and post- process interfaces so that simulation models that use CODE_BRIGHT – available from https://deca.upc.edu/en/projects/code_bright – can be developed more easily. It allows easy modification of parameters, boundary conditions, excavation protocols, meshing and organization of calculation intervals. The reason is that it has been developed using the GiD interface (http://www.gidhome.com) that permits pre- and post- process of data in a user-friendly way.

The model for FEBEX presented in this report is based on the FEBEX Task 9 specifications document (Annex A) and on the material properties of previous modelling efforts (Gens et al. 2009, Sanchez et al. 2012, Rodriguez-Dono et al. 2020).

Furthermore, Rodríguez-Dono et al. (2020) also developed a model of the well-known FEBEX experiment that was exploited in terms of the implementation of additional processes such as coupled flows and double structure models to investigate their impact of hydration and stress development.

Additional information on the full FEBEX project and its modelling is given in Huertas et al. (2006), Sanchez and Gens (2006), Tadikonda (2014), Bendito and Pintado (2016), Villar (2002), Villar et al. (2018) and Toprak et al. (2018).

Finally, the main objective of this report is to contribute to an enhancing understanding of the interplay between numerical modelling results and the observations of the in situ test. The comparison between modelling results and observations as well as the comparison between the results of the different codes used by different teams are a key tool to achieve this enhanced understanding.

I2 UPC's FEBEX model

I2.1 General features of the numerical analysis

The model developed analyses the **coupled thermo-hydro-mechanical** (**THM**) behaviour of the geological media using Code_Bright v9 and GiD 14. The geometry of the model has been taken from the FEBEX Task 9 specifications document (Annex A) – see Figure I-1. In addition, in this figure, the location of the instrumented sections can be observed.

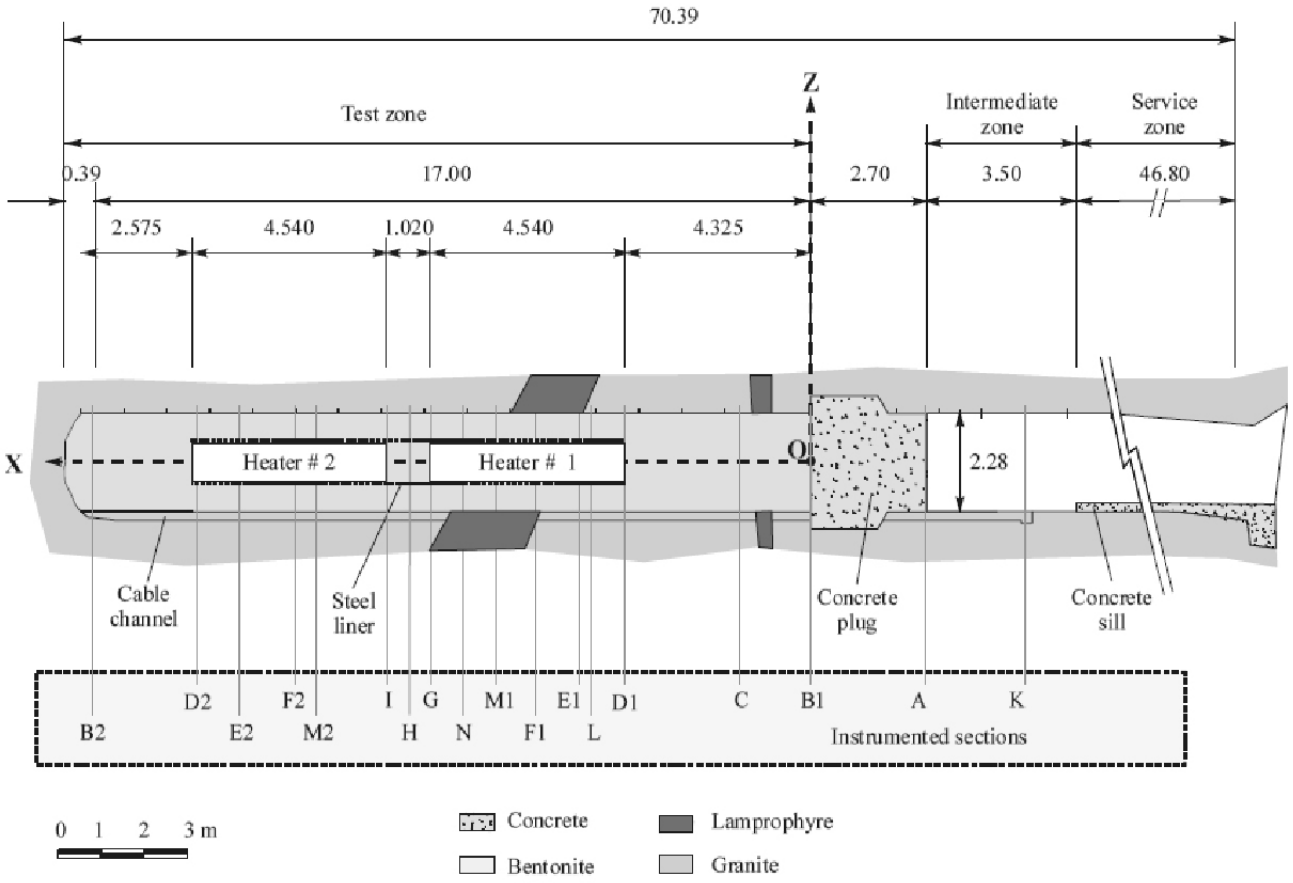

Figure I-1. *FEBEX in situ experiment geometry (Annex A).*

Figure I-2 shows the geometry and materials considered in this model. The host rock (granite), the bentonite buffer (divided in Bentonite and Bentonite2 to allow the partial dismantling of the bentonite buffer), the concrete plug and the canister (heaters #1 and #2) are the materials considered. After the first dismantling, the heater #1 is removed and partially replaced by a dummy. Each heater has a volume of 2.888 m^3. The model is two-dimensional, assuming **axisymmetry** along the tunnel axis. **The dimensions of the model are 30 m by 31.2 m**.

The mesh of the model is composed of **3 049 linear quadrilateral elements and 3 139 nodes**. Unlike the model used in Gens et al. (2009), this model takes advantage of the unstructured mesh development for the discretization of the host rock. With an unstructured mesh, the model will have less elements in the host rock section and thus, it will run faster. However, the buffer is discretized with a structured mesh, as this is more adequate in the zone of interest to reduce numerical errors.

Across the bentonite barrier, there are 10 elements (Figure I-3). The mesh is refined near the heater and near the granite, where the bigger gradients of temperature, pore water pressure, etc are achieved. In fact, the second element – counting from the heater at r = 0.45 m – starts at r = 0.489 m and the penultimate element ends at r = 1.101 m before reaching the granite at r = 1.14 m. Therefore, it would be fair to say that those 10 elements are equivalent to around 17 same-sized elements across the bentonite buffer, at least in terms of the numerical precision.

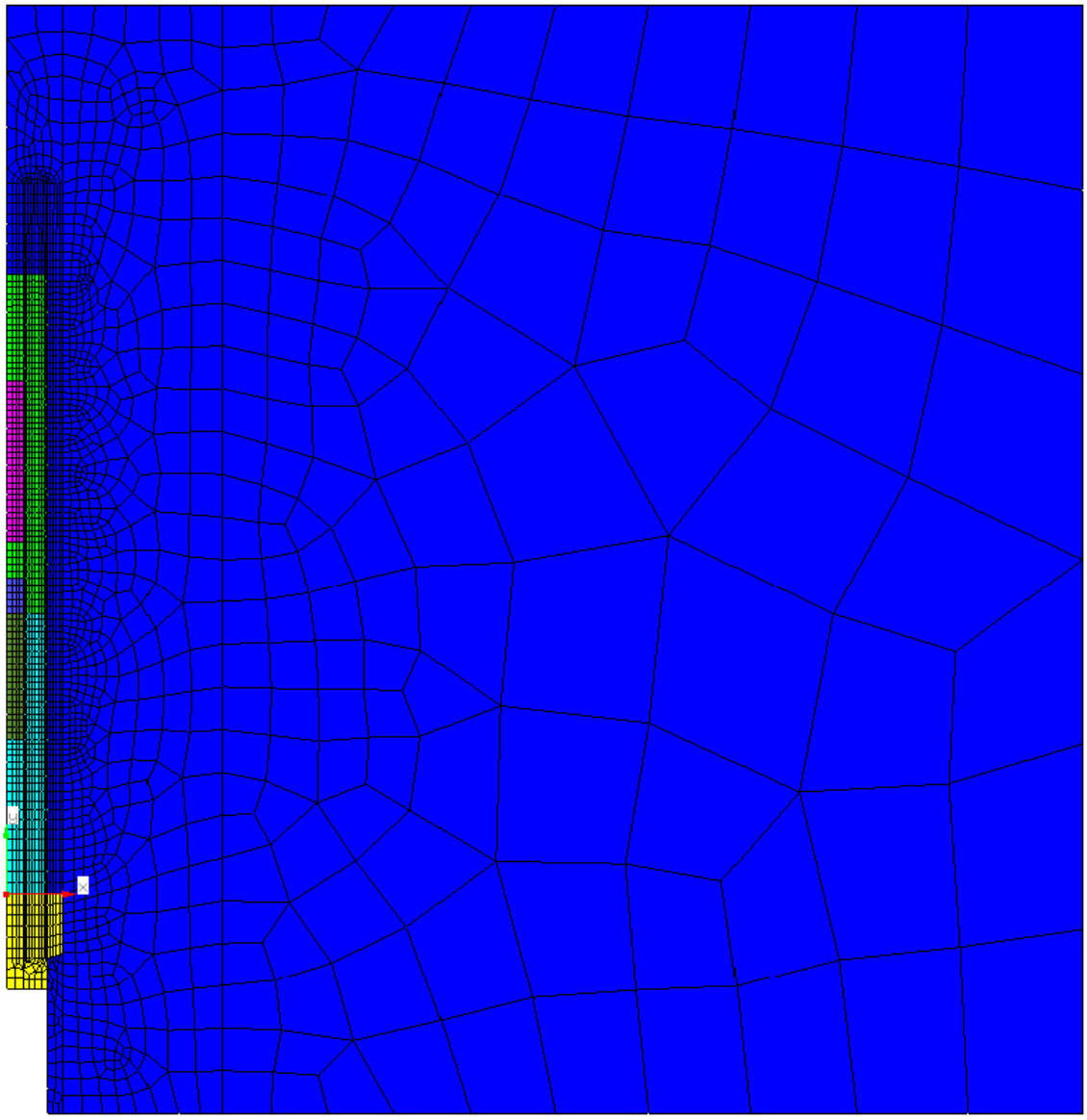

Figure I-2. *Model geometry, materials and mesh considered for UPC's FEBEX model.*

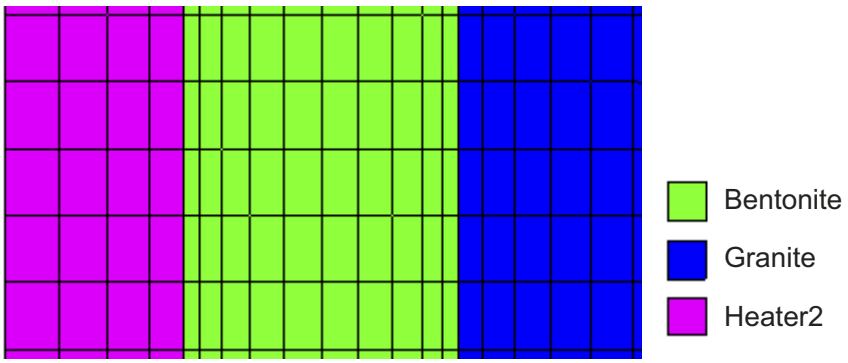

Figure I-3. *Close view of the elements across the bentonite barrier.*

Table I-1 shows the intervals considered in the analysis up to 6758 days, i.e. until the final dismantling of the test. Heaters switch on at day 0 and day 1968 would correspond to the end of the first dismantling.

In order to match the measured evolution of temperature during the experiment (see more details about this in Gens et al. 2009), the heat power was progressively modified (see Table I-1) until the 100 °C target temperature was reached.

Note that the design conditions of the experiment contemplate a maximum temperature of 100 °C at the contact between the heater and bentonite (Villar 2002; Huertas et al. 2006); since it is assumed that engineered clay barriers do not change their properties for temperatures below 100 °C.

From that point on, the temperature was prescribed at the value of 100 °C in both heaters. Later, one of the heaters was removed but the other continued heating until day 6630, in which heater #2 was switched off.

The initial and boundary conditions, as well as the mechanical, hydraulic and thermal parameters used in the model will be described in the sections below.

Table I-1. Time intervals considered for the simulation up to 6758 days.

Stage number	Brief description	Start time (day)	Duration (days)	Prescribed heat flow on heaters $\left(\frac{J}{s\ m^3}\right)$	Prescribed temperature (C)
1	Excavation in granite rock	−200	65	0	12 (far rock)
2	Construction of bentonite, canisters and concrete plug	−135	135	0	12 (far rock)
3	Heaters switch on to 1200 W	0	20	415.5	12 (far rock)
4	Heaters to 2000 W	20	33	692.5	12 (far rock)
5	Heaters at 100 °C	53	1774	0	12 (far rock) 100 (heaters)
6	Heater #1 switch off Heater #2 at 100 °C	1827	39	0	12 (far rock) – (heater #1) 100 (heater #2)
7	Concrete plug demolition	1866	50	0	12 (far rock) 100 (heater #2)
8	First dismantling of bentonite and heater#1	1916	52	0	12 (far rock) 100 (heater #2)
9	Extended transition before final dismantling	1968	4662	0	12 (far rock) 100 (heater #2)
10	Heater #2 switch off	6630	128	0	12 (far rock) – (heater #2)

I2.2 Initial and boundary conditions

I2.2.1 Boundary conditions

A mechanical boundary condition restraining the normal displacements has been applied all along the external boundary for all time intervals (Figure I-4). Also, after the demolition of the concrete plug (interval 7), the normal displacements to the now exposed bentonite have been fixed (Figure I-5a). Similarly, the normal displacements of the exposed bentonite after the first dismantling have also been fixed (Figure I-5b).

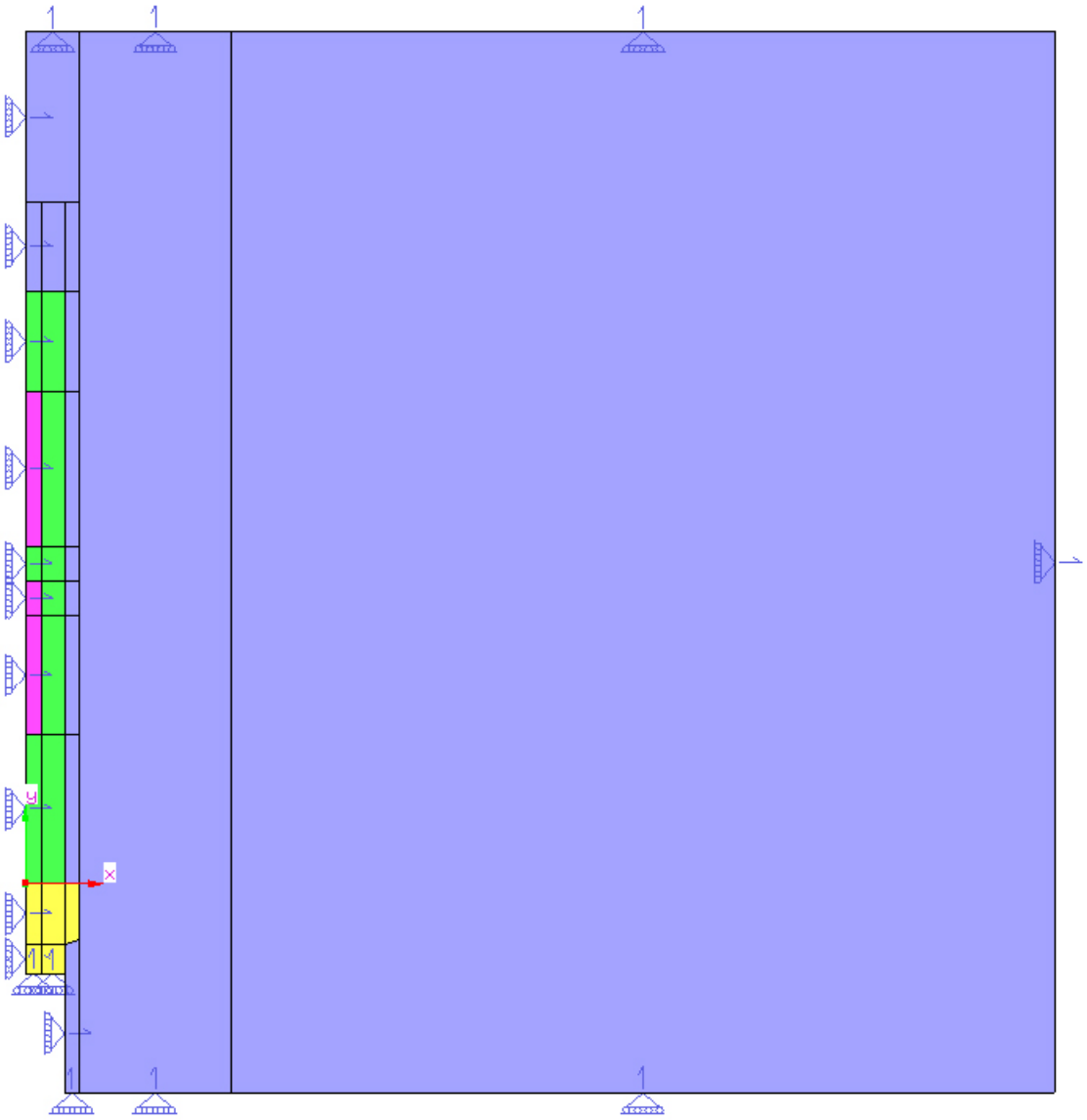

Figure I-4. *Mechanical boundary conditions at the beginning of the simulation.*

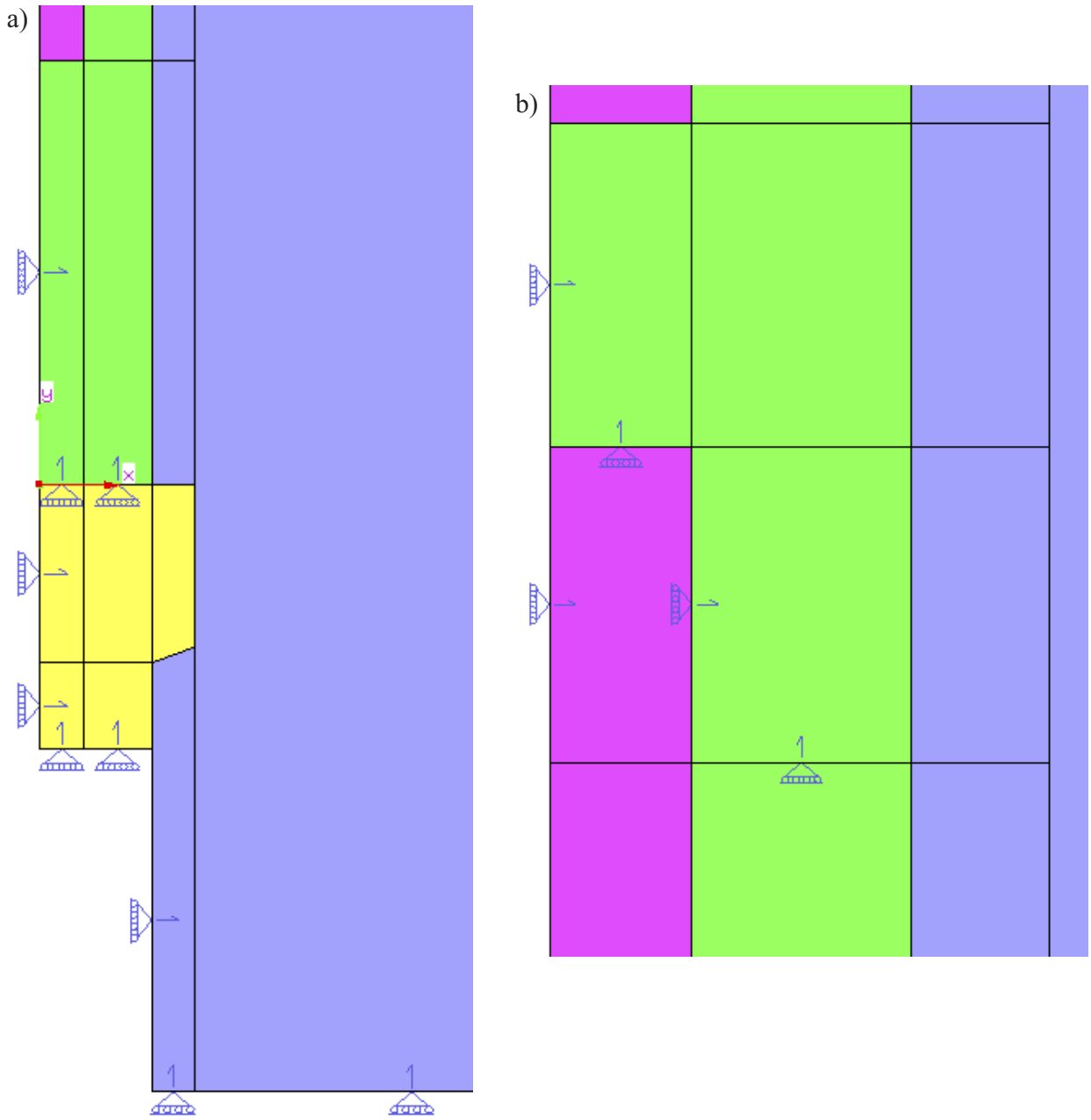

Figure I-5. *Mechanical boundary conditions (a) after the demolition of the concrete plug and (b) after the first dismantling.*

In addition, a constant pore water pressure of 0.9 MPa is imposed on the external boundary, corresponding to the unaltered far host rock (granite). To simulate ventilation, a pore water pressure of −1 MPa has been set in the excavated tunnels before construction of the bentonite buffer (interval 1; Figure I-6) or after dismantling. Moreover, a pore water pressure of −1 MPa has been set on the remaining unconstructed tunnel walls (in front of the concrete plug).

As indicated above (Table I-1), during intervals 3 and 4 the power of the heaters is prescribed and therefore the temperature increases. The power is prescribed using the equivalent volumetric flow rate in both heaters to first 1 200 W (interval 3) and then 2 000 W (interval 4). Once the temperature reaches the target value on the surface canister (100 °C), the boundary condition on the heater is changed from constant power to a constant temperature of 100 °C (interval 5). Then, heater #1 is switched off at day 1827 (interval 6) and heater #2 is switched off at day 6630 (interval 10).

More information about boundary condition implementation in the Code_Bright User's Guide (2018), downloadable from the Code_Bright web page − deca.upc.edu/en/projects/code_bright).

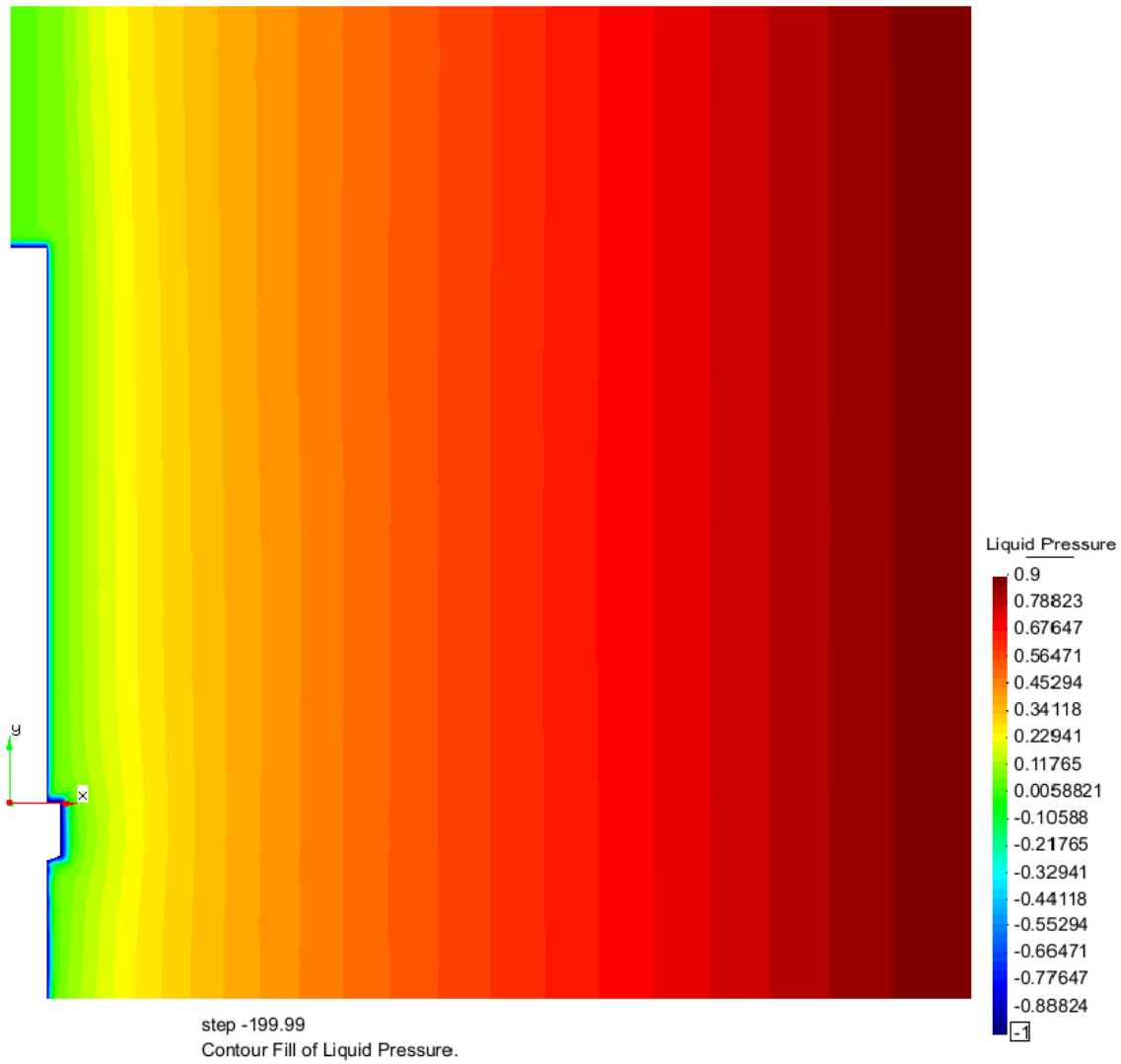

Figure I-6. *Pore water pressure at the beginning of the simulation (interval 1; time = −200 days).*

I2.2.2 Initial conditions

The initial stress has been set to −28 MPa in the granite and to −0.1 MPa in the rest of the materials (negative values correspond to compression). The initial pore water pressure in the rock follows a linear distribution from 0.9 MPa at 30 m from the tunnel axis until 0.1 MPa at 2.28 m from the tunnel axis (Figure I-6). The initial temperature of all materials (including the rock) has been set to 12 °C. Finally, an initial porosity of 0.1 has been set for the concrete plug, and an initial porosity of 0.01 has been set for both the granite and the heaters (Table I-2).

For the bentonite, the initial porosity has been set to 0.42 and the solid phase density has been set as 2.77 g/cm^3. Therefore, the initial dry density of the bentonite is approximately 1.61 g/cm^3. No double porosity has been considered for this model. The initial suction of the bentonite has been set to −135 MPa. Its initial relative humidity is 34 %. Its initial degree of saturation is 65 %.

Table I-2. Initial conditions.

Material	Bentonite	Rock (granite)	Concrete plug	Heaters
Initial temperature (°C)	12	12	12	12
Initial stress (MPa)	−0.1	−28	−0.1	−0.1
Initial pore water pressure (MPa)	−135	0.1—0.9	0	−20
Initial porosity	0.42	0.01	0.1	0.01
Solid phase density (g/cm^3)	2.77	2.75	2.6	8.93
Initial dry density (g/cm^3)	1.61	2.72	2.34	8.84
Initial relative humidity (%)	34	100	100	86
Initial degree of saturation (%)	65	100	80	81

I2.3 Constitutive equations and material parameters

As mentioned above, four different materials have been modelled: the host rock (granite), the canisters (or heaters), the bentonite and the concrete plug. Table I-3 shows a comparison of some relevant thermal and hydraulic parameters for all materials in the model. Table I-4 shows all material parameters used for the granite, the concrete plug and the canister in Code_Bright.

Regarding the hydraulic and thermal constitutive equations, for the retention curve, the Van Genuchten model has been used:

$$S_e = \frac{S_l - S_{rl}}{S_{ls} - S_{rl}} = \left(1 + \left(\frac{P_g - P_l}{P}\right)^{\frac{1}{1-\lambda}}\right)^{-\lambda} \qquad \text{where} \qquad P = P_o \frac{\sigma}{\sigma_o}$$

Figure I-7 shows the graphs corresponding to the retention curves used for bentonite and granite. Tables I-4 and I-5 include the parameters used in Code_Bright corresponding to these curves.

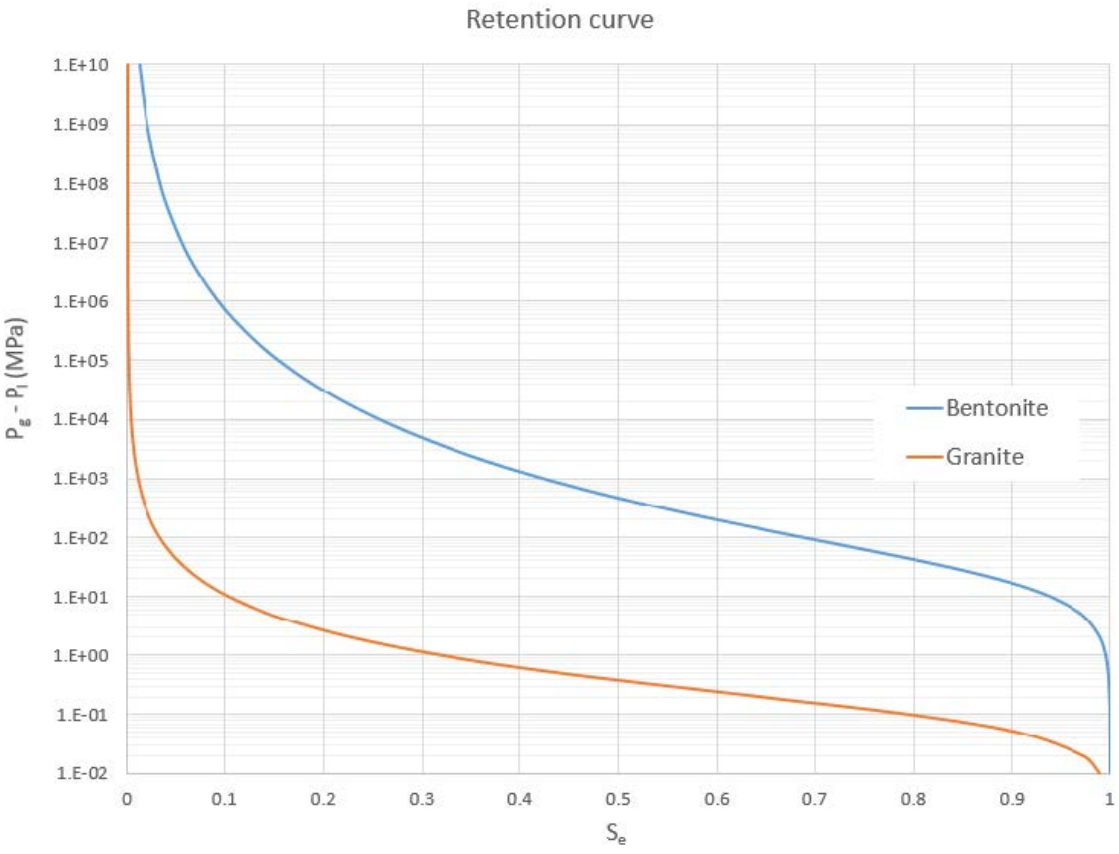

Figure I-7. *Retention curves for bentonite and granite.*

For the granite, the consistent form of relative permeability with van Genuchten model is used:

$$k_{rl} = \sqrt{S_e}\left(1-\left(1-S_e^{1/\lambda}\right)^{\lambda}\right)^2$$

Figure I-8 shows the relative permeability of the granite.

For the liquid flow, Darcy's law has been used: $\mathbf{q}_\alpha = -\dfrac{\mathbf{k}k_{r\alpha}}{\mu_\alpha}\left(\nabla P_\alpha - \rho_\alpha \mathbf{g}\right)$

Where viscosity, density and relative permeability are defined in other laws and where, for a continuum medium (Kozeny's model), the intrinsic permeability **k** (Figure I-9) is defined by:

$$\mathbf{k} = \mathbf{k}_o \frac{\varphi^3}{(1-\varphi)^2}\frac{(1-\varphi_o)^2}{\varphi_o^{\,3}}$$

where: φ_o : reference porosity

$\mathbf{k}_o$: intrinsic permeability for matrix φ_o

To compute the conductive heat flux, the thermal conductivity λ is used in Fourier's law:

$$\mathbf{i}_c = -\lambda \nabla T$$

In this case, the thermal conductivity depends on porosity by a geometric weighted mean:

$$\lambda_{dry} = \lambda_{solid}^{(1-\phi)}\lambda_{gas}^{\phi} \qquad \lambda_{sat} = \lambda_{solid}^{(1-\phi)}\lambda_{liq}^{\phi}$$

$$\lambda_{solid} = (\lambda_{solid})_o + a_1 T + a_2 T^2 + a_3 T^3$$

Where λ_{dry} is the thermal conductivity of the dry porous medium and λ_{sat} is the thermal conductivity of the water saturated porous medium.

Regarding the mechanical behaviour of the granite, a linear expansion law induced by temperature changes has been used:

$$\Delta\varepsilon_v = 3\alpha_s \Delta T \quad (\Delta\varepsilon_v > 0, \text{ extension; } \Delta\varepsilon_v < 0, \text{ compression})$$

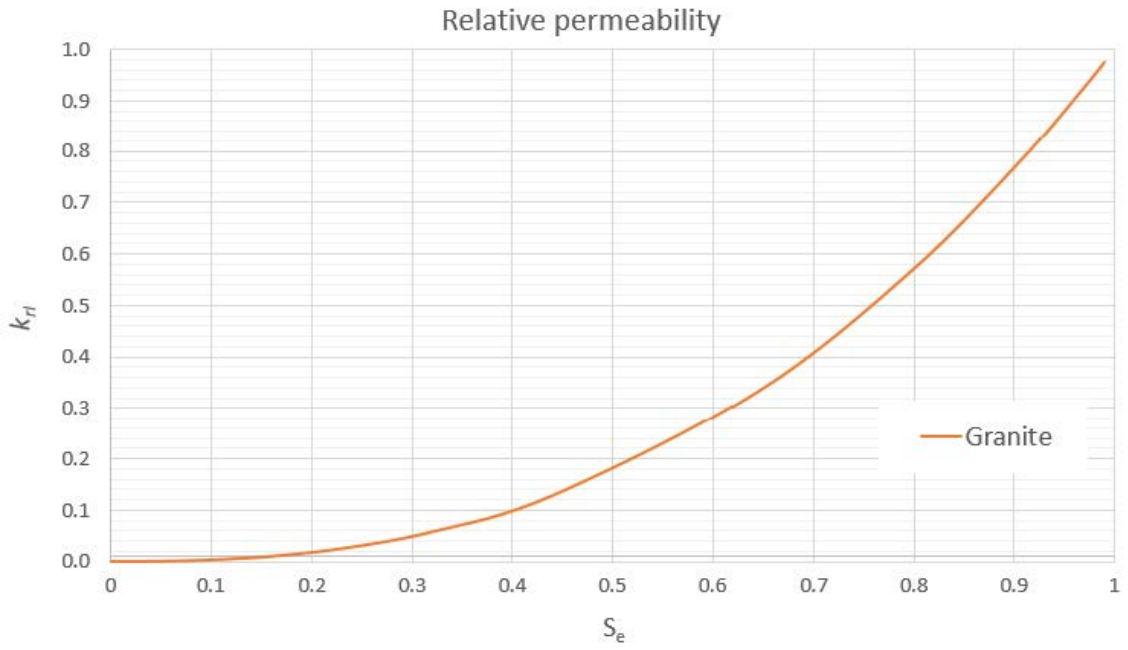

Figure I-8. *Relative permeability of the granite.*

Moreover, a high elastic modulus 100 times bigger than normal has been set for the granite in the first interval (excavation) for the numerical convergence sake, but the normal value has been set in the rest of the intervals. The canister has been modelled as a dense, rigid, impermeable (very low permeability) and very conductive material.

Regarding the liquid phase properties, the water density has been modelled according to the following exponential variation law: $\rho_l = \rho_{l0} \exp(\beta(P_l - P_{lo}) + \alpha T + \gamma \omega_l^h)$

where:

Reference density	ρ_{lo}	1 002.6	kg m^{-3}
Compressibility	β	4.5×10^{-4}	MPa^{-1}
Volumetric thermal expansion coefficient for water	α	-3.4×10^{-4}	C^{-1}
Solute variation	γ	0.6923	
Reference pressure	P_{lo}	0.1	MPa

And the liquid phase viscosity has been modelled according to the following law:

$$\mu_l = A \exp\left(\frac{B}{273.15 + T}\right)$$

where:

Pre-exponential parameter	A	2.1×10^{-12}	MPa s
Exponential parameter	B	1 808.5	K

The intrinsic permeability for the bentonite is considered 3E−21 m^2 for a reference porosity of 0.42 and is considered isotropic. The initial hydraulic conductivity would then be approximately 2.32E−14 m/s for the initial conditions (porosity of 0.42, temperature of 12 °C and pressure of −135 MPa). Note that the intrinsic permeability changes with the porosity of the bentonite (Figure I-9).

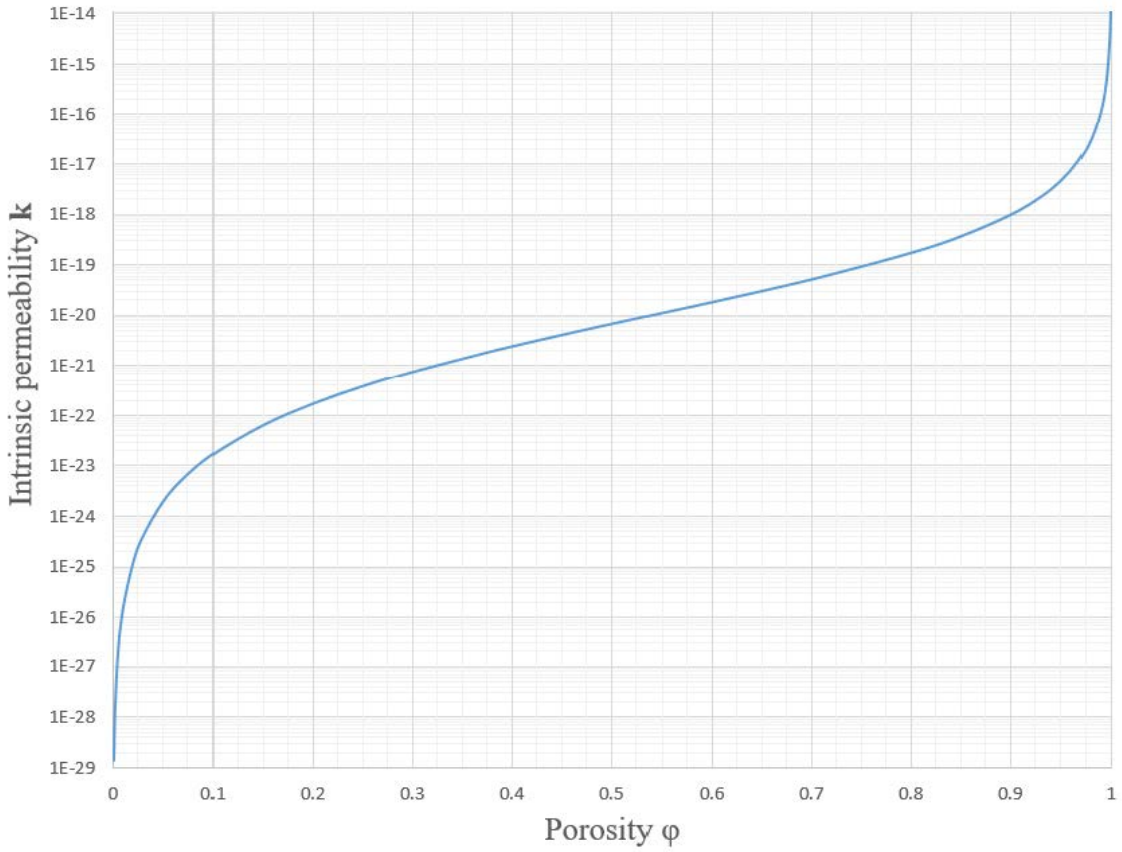

Figure I-9. *Change of the intrinsic permeability of the bentonite with the porosity.*

Regarding the thermal conductivity, 4 W m^{-1} K^{-1} has been assigned for the granite and 2 W m^{-1} K^{-1} for the concrete plug. In the case of the heaters a high thermal conductivity of 390 W m^{-1} K^{-1} has been assign to make sure that the heat is homogeneously distributed throughout the heater. On the other side, different values have been assigned for the bentonite depending on its degree of saturation, according to the following empirical correlation:

$$\lambda = \frac{A_1 - A_2}{1 + e^{\left[(Sr - Sr^*)/b\right]}} + A_2$$

Where A_1 = 1.4 W m^{-1} K^{-1}, A_2 = 0.6 W m^{-1} K^{-1}, b = −0.12 and Sr^* = 0.6.

According to the equation and parameters mentioned above, Figure I-10 shows the change in thermal conductivity of the bentonite with the liquid saturation degree.

Regarding the bentonite, Tables I-5 and I-6 show the constitutive laws used in the model and the properties corresponding to the FEBEX bentonite considered with single porosity. We consider that FEBEX bentonite can be represented with the Barcelona Basic Model or BBM (Alonso et al. 1990), van Genuchten model (van Genuchten 1978, 1980), Darcy's law, power relative permeability (Brooks and Corey 1964) and the aforementioned correlation for thermal conductivity. The parameters are divided in hydraulic and mechanical parameters, which correspond to the Code_Bright materials input window (more information about these parameters in Code_Bright User's Guide).

Furthermore, a virtual swelling pressure test has been performed to determine the swelling pressure of the bentonite from initial conditions, obtaining a value of 5.7 MPa.

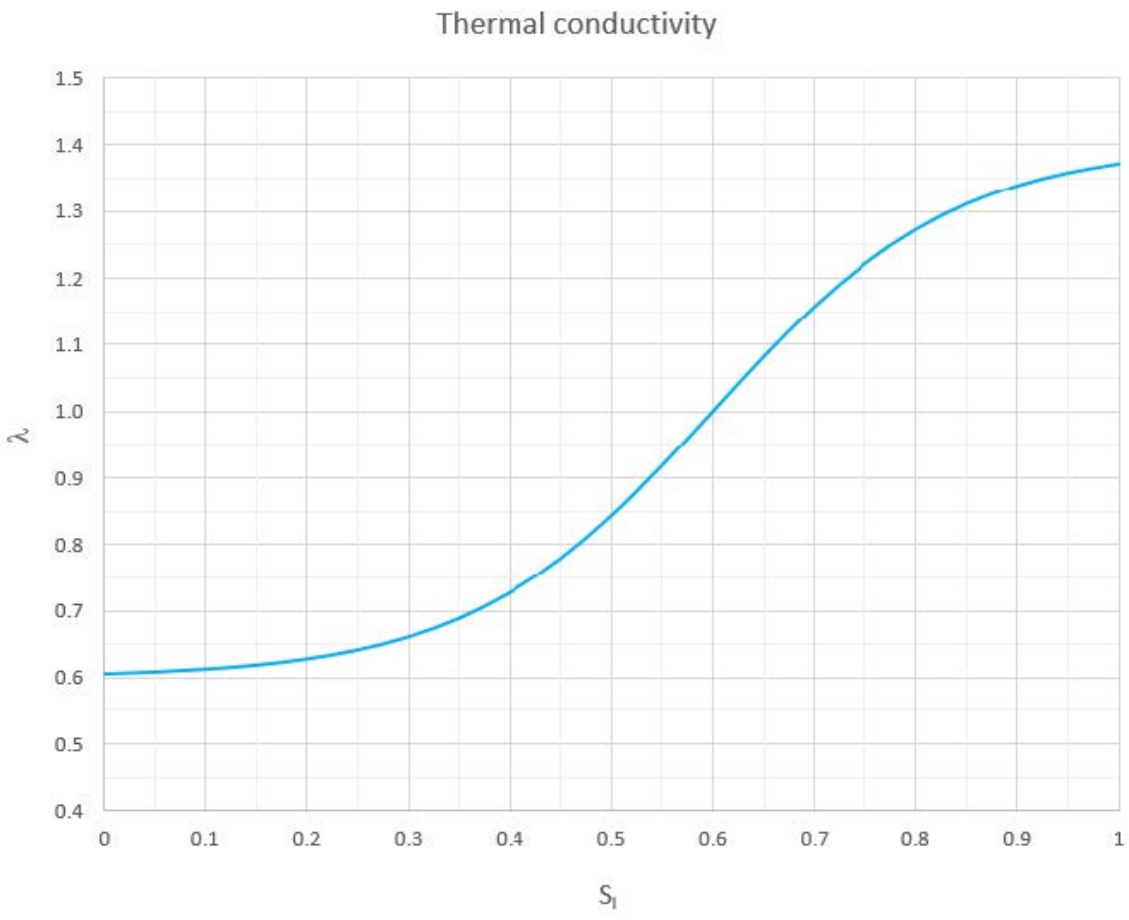

Figure I-10. *Thermal conductivity of the bentonite.*

The different sets of parameters used to represent the properties of bentonite and granite are taken from the calibration work of different researchers (Gens et al. 2009, Villar 2002, Ortuño et al. 2005, Frieg and Vomvoris 1994). Note that in this model we use the standard van Genuchten for the retention curve instead of the modified version proposed in Gens et al. (2009).

Regarding the hydraulic and thermal parameters of the bentonite (Table I-4), the same constitutive laws as for the other materials have been used. Besides that, for the relative permeability of the liquid phase, a generalized power formulation has been used:

$$k_{rl} = AS_e^{\lambda}$$

Figure I-11 shows the relative permeability corresponding to the bentonite.

Table I-3. Thermal and hydraulic parameters.

Material	Bentonite	Rock (granite)	Concrete plug	Heaters
Initial intrinsic permeability (m^2)	3e−21*	8e−18	1e−18	1e−27
Initial hydraulic conductivity (m/s)	2.32e−14*	8e−11	1e−11	1e−20
Thermal conductivity dry (W m^{-1} K^{-1})	0.6	4	2	390
Thermal conductivity saturated (W m^{-1} K^{-1})	1.4	4	2	390
Swelling pressure (MPa)	5.7			

* Intrinsic permeability and hydraulic conductivity corresponding to a bentonite porosity of 0.42. Note that both the intrinsic permeability and the intrinsic permeability of the bentonite change with porosity (Figure I-9).

For the diffusive fluxes of vapour, Fick's law for molecular diffusion has been used:

$$\mathbf{i}_{\alpha}^{i} = -\left(\tau\phi\rho_{\alpha}S_{\alpha}D_{\alpha}^{i}\mathbf{I}\right)\nabla\omega_{\alpha}^{i}$$

Where ϕ is porosity, ρ_{α} is density, S_{α} is degree of saturation, ω is mass fraction and D_{α}^{i} is the diffusion coefficient of species i in phase α in m^2/s.

The non-advective flux of a species in a phase is composed by molecular diffusion and mechanical dispersion (dispersion is defined in another set of parameters).

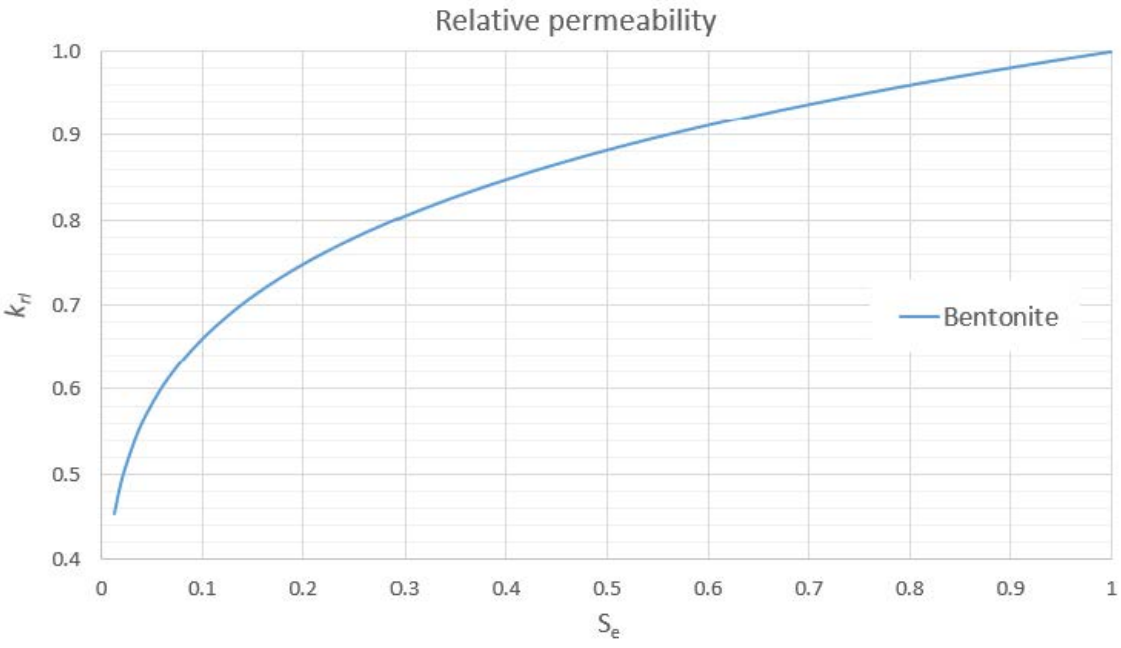

Figure I-11. *Relative permeability of the bentonite.*

Molecular diffusion of vapour or air in the gas phase:

$$D_{\alpha}^{i} = D\left(\frac{\left(273.15+T\right)^{n}}{P_{g}}\right)$$

Where P_g is the gas pressure in Pa, and D and n are parameters. Tortuosity is defined as a constant value in this case:

τ = constant = τ_0

I3 Sensitivity analysis performed

Three sensitivity analysis were performed including the following bentonite parameters: intrinsic permeability, initial porosity and thermal conductivity.

I3.1 Sensitivity to bentonite intrinsic permeability

Three different models have been developed using three different values for the bentonite intrinsic permeability and a sensitivity analysis have been performed over different variables.

For instance, Figure I-12 shows the effect of intrinsic permeability on the degree of saturation at the final dismantling (6 758 days). As it can be observed, slight changes in the intrinsic permeability affect significantly the degree of saturation of the bentonite barrier at the final dismantling. In this figure, we can also see the comparison with real measurements. Moreover, the intrinsic permeability of the bentonite is somewhat uncertain, especially due to the existence of gaps between bentonite blocks and between the blocks and the host rock of the heater. Therefore, in situ intrinsic permeability is expected to have a higher value than that obtained in the laboratory. In any case, note that intrinsic permeability varies with porosity and that the given values are not constant, but referenced to a porosity of 0.4. This analysis have been used to estimate an initial intrinsic permeability of 3e−21 for a reference porosity of 0.42, which is also the initial porosity, considering the aforementioned gaps effect.

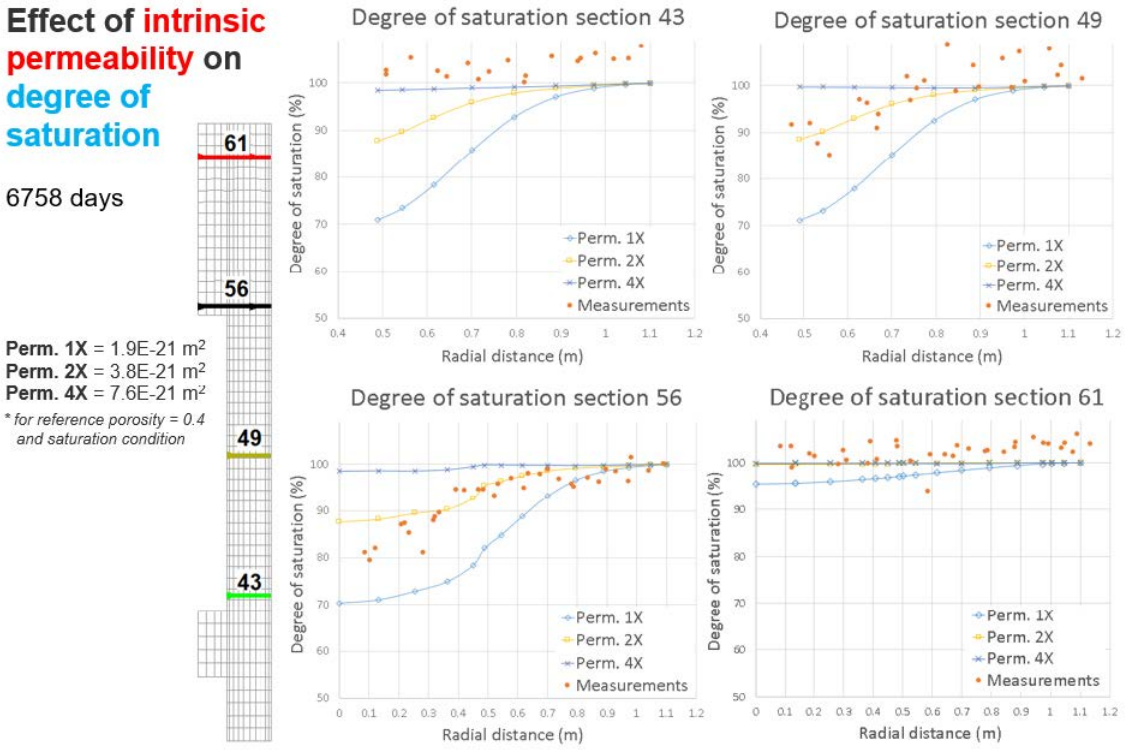

Figure I-12. *Effect of the bentonite intrinsic permeability on the degree of saturation.*

In addition, in Figures I-13 and I-14 it can be observed that the intrinsic permeability has not a significant influence on the dry density or the water content. However, the measurements are quite far for the model results, which motivated the following sensitivity analyses.

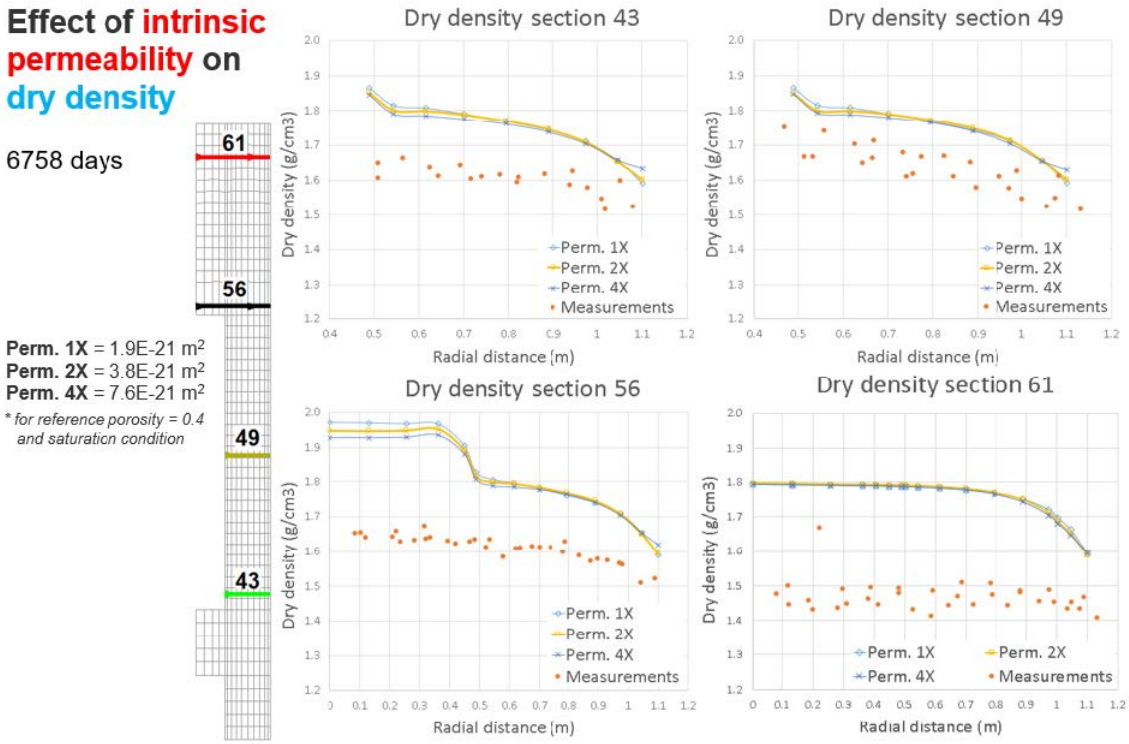

Figure I-13. *Effect of the bentonite intrinsic permeability on the dry density.*

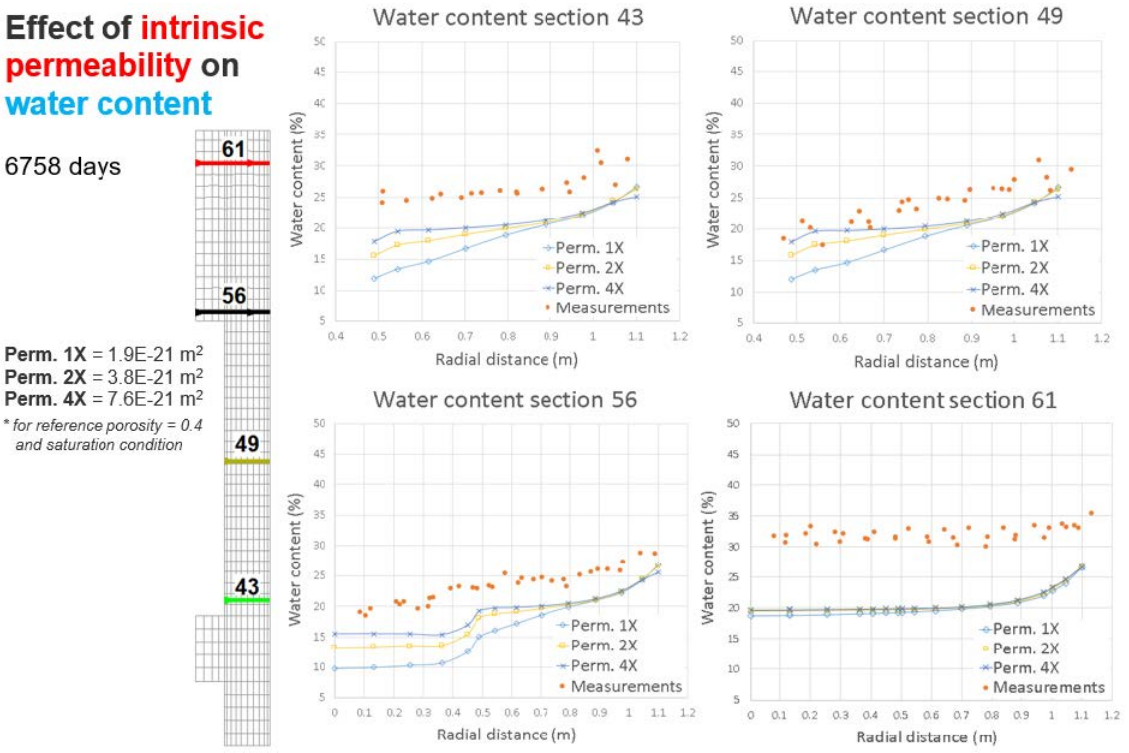

Figure I-14. *Effect of the bentonite intrinsic permeability on the water content.*

I3.2 Sensitivity to bentonite initial porosity

In the last epigraph, we mentioned the possible effect of the gaps on the intrinsic permeability. For the same reason, the initial dry density of a brick of bentonite may not be representative of the whole bentonite barrier. Therefore, we have performed an analysis of the effect of the initial porosity considering both estimated values for the brick and the whole barrier.

In Figures I-15 and I-16, it can be observed that the value of the initial porosity (or, as a consequence, the value of the initial dry density) significantly affects the final values of the dry density and water content for the final state of the bentonite barrier. This means that an initial porosity of 0.42, which gives the estimated value of dry density for the whole bentonite barrier, could be more representative of the initial state of the barrier, so that value for the initial porosity has been taken for the final model. It should also be noted that section 61 is significantly off the measurements, probably due to a big gap between the bentonite barrier end the end of the tunnel excavation. Moreover, in Figure I-17 it can be observed that the initial porosity has also an effect on the final degree of saturation in the same direction as an increase of the permeability.

In addition, it has been tested the effect of these changes on other variables in the model and it can be concluded, in general, that they do not have a significant effect on different variables such as temperature. Although they affect slightly the stresses, it is difficult to state whether these effects take us closer or further from the measurements, due to their uncertainty, being different depending on the section analysed. Finally, there is an effect on the heating power, but it will be analysed in the following section.

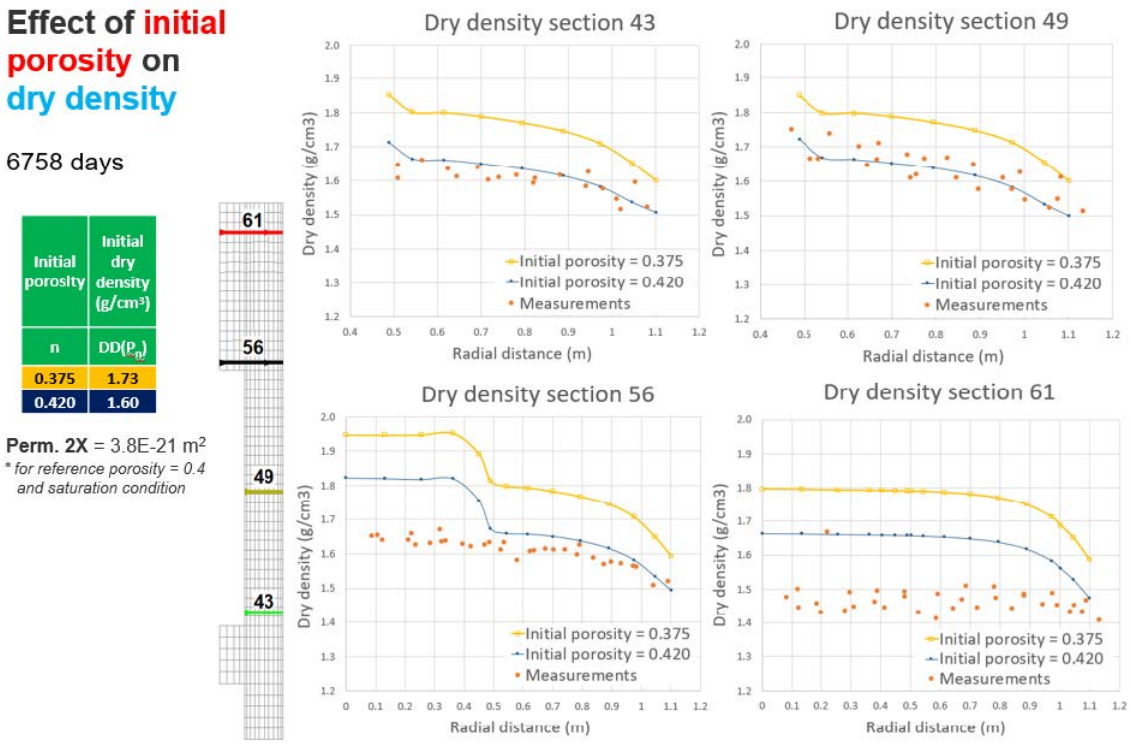

Figure I-15. *Effect of the bentonite initial porosity on the dry density.*

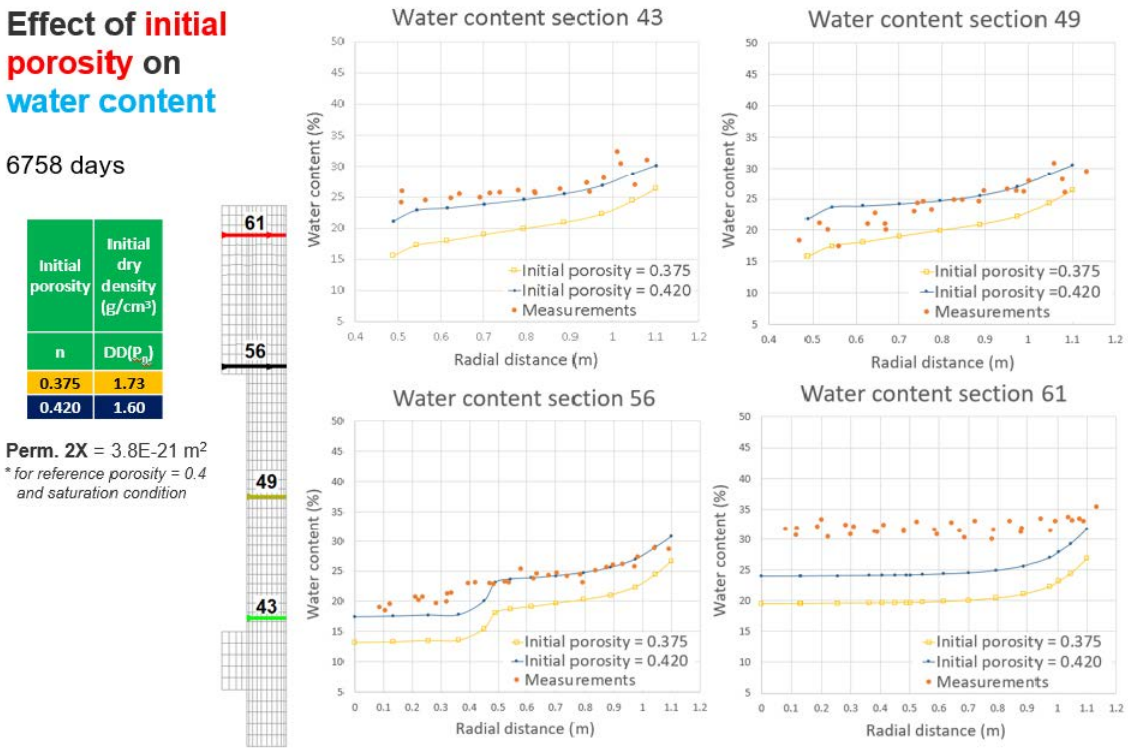

Figure I-16. *Effect of the bentonite initial porosity on the water content.*

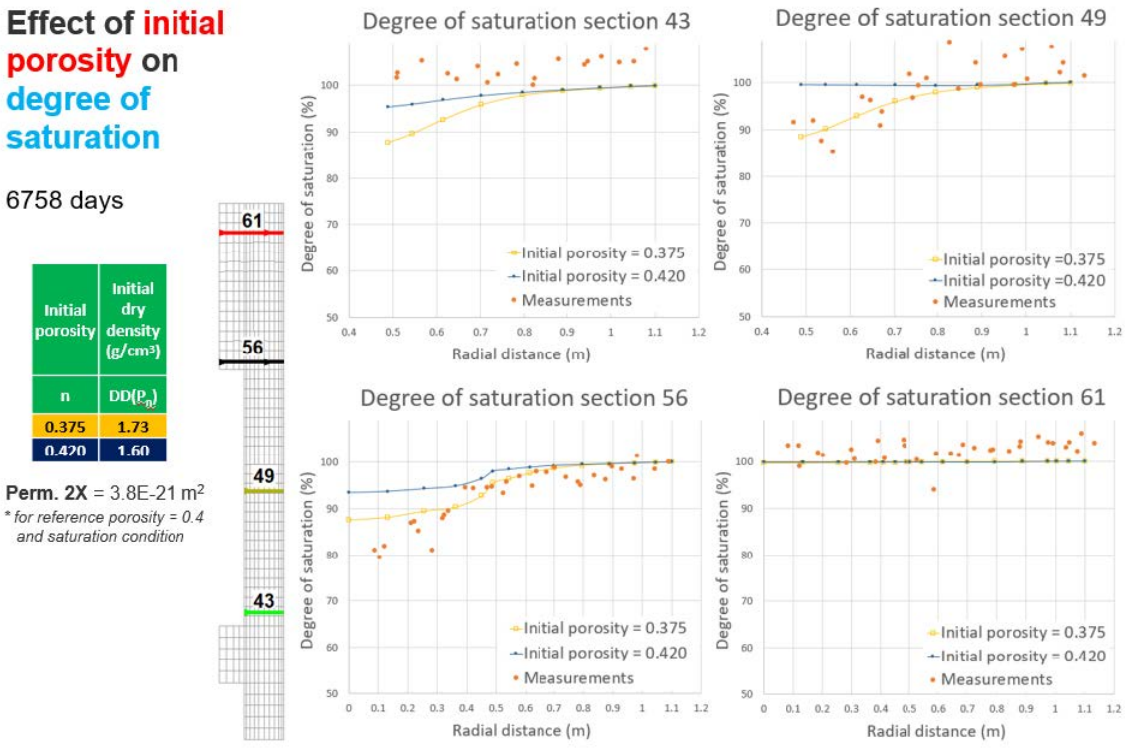

Figure I-17. *Effect of the bentonite initial porosity on the degree of saturation.*

I3.3 Sensitivity to bentonite thermal conductivity

As mentioned in the last section, the sensitivity analyses performed so far have also an influence on the heating power, as shown in Figure I-18, mainly because heat conductivity and liquid advection increase with higher permeability values. Anyway, the results obtained underestimate the in situ measurements. For that reason, we have performed a final sensitivity analysis of the bentonite thermal conductivity.

Figure I-19 shows the different functions and values used for the sensitivity analysis including the s-shaped function corresponding to this final report (Figure I-10). It should be noted that cases R27 and R29 from Figure I-19 give similar results although they use different functions, since most of the bentonite barrier has a degree of saturation higher than 65 % from the beginning, from which point both functions are similar.

Finally, in Figure I-20 it can be observed that the heating power is much closer to the measurements using high thermal conductivity (either case R27 or case R29) than the results obtained from the "base case" (permeability 1X and initial porosity of 0.375) or after the corrections from the previous sensitivity analysis (permeability 2X and initial porosity of 0.42). Therefore, the s-shaped function from Figure I-10 has been taken for the final model.

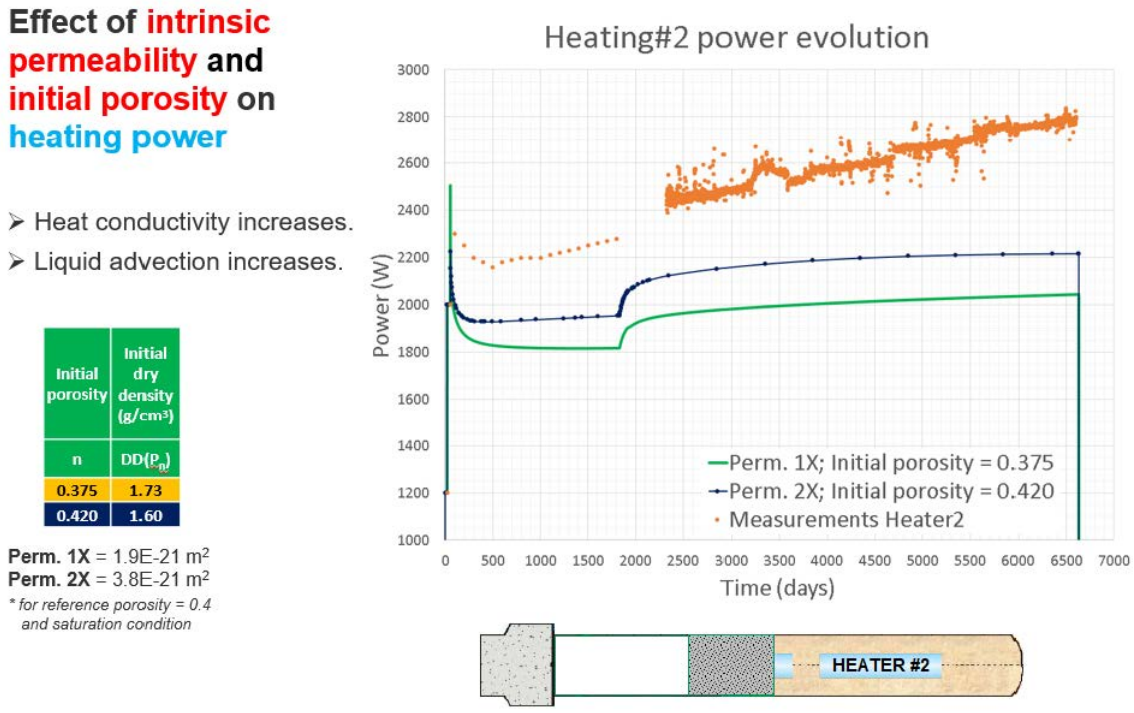

Figure I-18. *Effect of intrinsic permeability and initial porosity on the heating power.*

Effect of thermal conductivity on heating power

$$\lambda = \lambda_{sat}^{S_l} \lambda_{dry}^{(1-S_l)}$$

λ_{dry}	W m^{-1} K^{-1}	0.47
λ_{sat}	W m^{-1} K^{-1}	1.15

λ_{dry}	W m^{-1} K^{-1}	0.6
λ_{sat}	W m^{-1} K^{-1}	1.4

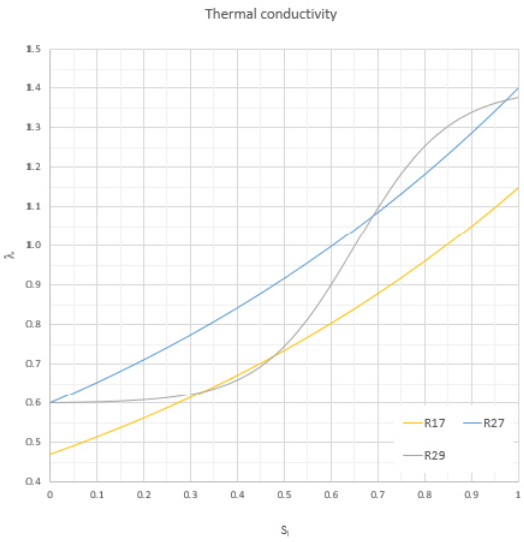

parameter	bentonite S-2	FEBEX bentonite
A_1	0.39 ± 0.08	0.57± 0.02
A_2	1.34 ± 0.06	1.28 ± 0.03
x_0	0.54 ± 0.03	0.65 ± 0.01
d_x	0.15 ± 0.03	0.10 ± 0.02

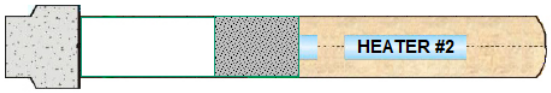

Figure I-19. *Thermal conductivity different functions used in for the sensitivity analysis.*

Effect of thermal conductivity on heating power

Initial porosity	Initial dry density (g/cm³)
n	DD(P_{n0})
0.375	1.73
0.420	1.60

Perm. 1X = 1.9E-21 m²
Perm. 2X = 3.8E-21 m²
** for reference porosity = 0.4 and saturation condition*

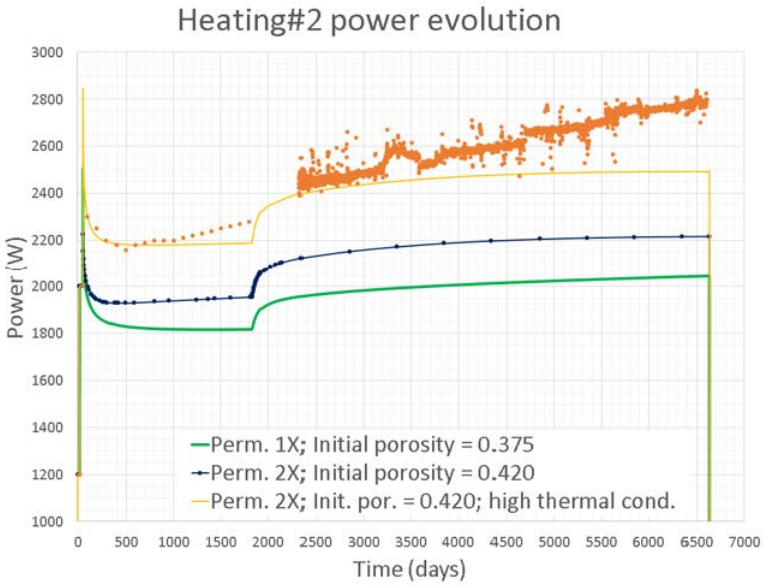

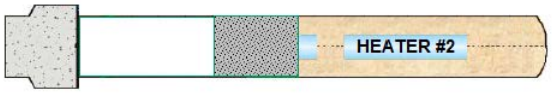

Figure I-20. *Effect of thermal conductivity and initial porosity on the heating power.*

I4 Mechanical, hydraulic and thermal parameters used in Code_Bright

Table I-4. Main material parameters for the granite, the concrete plug and the canister. See Code_Bright User's Guide for further details.

Mechanical data			
	Granite	**Concrete plug**	**Canister**
Linear elasticity (ITYCL = 1)			
P1: E (MPa)	11 697	30 000	21 000
P3: ν	0.3	0.3	0.3
Hydraulic and thermal data			
Retention Curve (ITYCL = 1)			
P1: P_o (MPa)	0.1	0.1	27
P3: λ	0.33	0.33	0.45
P5: S_{ls}	1	1	1
Intrinsic Permeability (ITYCL = 1)			
P1: $(k_{11})_o$ (m^2)	8.e−18	1.e−18	1.e−27
P2: $(k_{22})_o$ (m^2)	8.e−18	1.e−18	1.e−27
P3: $(k_{33})_o$ (m^2)	8.e−18	1.e−18	1.e−27
Conductive flux of heat 1 (ITYCL = 1)			
P1: λ_{dry} (W m^{-1} K^{-1})	4	2	390
P2: λ_{sat} (W m^{-1} K^{-1})	4	2	390
Phase properties			
Solid phase (ITYCL = 1)			
P1: C_s (J kg^{-1} K^{-1})	793	1 000	390
P2: ρ_s (kg m^{-3})	2 750	2 600	8 930
P3: α_s (C^{-1})	7.8e−6	0	1.2e−5

Table I-5. Physical, hydraulic and thermal parameters for bentonite. See Code_Bright User's Guide for further details.

Retention curve (ITYCL = 1)		
P1: P_o (MPa)	20	Van Genuchten model:
P2: σ_o (N m^{-1})	0.072	$S_e = \frac{S_l - S_{rl}}{S_{ls} - S_{rl}} = \left[1 + \left(\frac{P_g - P_l}{P}\right)^{\frac{1}{1-\lambda}}\right]^{-\lambda}$ $\quad P = P_o \frac{\sigma}{\sigma_o}$
P3: λ	0.18	
P4: S_{rl}	0.01	
P5: S_{ls}	1	
Intrinsic permeability (ITYCL = 1)		
P1: $(k_{11})_o$ (m^2)	3e−21	Darcy's law: $\mathbf{q}_l = -\frac{\mathbf{k} k_{rl}}{\mu_l}(\nabla P_l - \rho_l \mathbf{g})$
P2: $(k_{22})_o$ (m^2)	3e−21	
P3: $(k_{33})_o$ (m^2)	3e−21	Kozeny's model: $\mathbf{k} = \mathbf{k}_o \frac{\phi^3}{(1-\phi)^2} \frac{(1-\phi_o)^2}{{\phi_o}^3}$
P4: ϕ_o	0.42	
Liquid phase relative permeability (ITYCL = 6)		
P2: A	1	$k_{rl} = A S_e^{\lambda}$
P3: λ	3	
P4: S_{rl}	0.01	
P5: S_{ls}	1	
Diffusive flux of vapour (ITYCL = 1)		
P1: D (m^2 s^{-1} K^{-n} Pa)	5.9e−6	Fick's law for molecular diffusion:
P2: n	2.3	$\mathbf{i}_g^w = -\left(\tau \phi \rho_g S_g D_m^w \mathbf{I}\right) \nabla \omega_g^w$ $D_m^{vapor} = D\left[\frac{(273.15+T)^n}{P_g}\right]$
P3: τ_o	0.8	$\tau = \text{constant} = \tau_o$
Conductive flux of heat 1 (ITYCL = 1)		
ITYCL	1	Fourier's law: $\mathbf{i}_c = -\lambda \nabla T$
P1: λ_{dry} (W m^{-1} K^{-1})	0.6	$\lambda = \lambda_{sat}^{S_l} \lambda_{dry}^{(1-S_l)}$
P2: λ_{sat} (W m^{-1} K^{-1})	1.4	
Conductive flux of heat 2 (ITYCL = 7)		
P1: b	−0.12	$\lambda = \frac{A_1 - A_2}{1 + e^{\left[(Sr - Sr^*)/b\right]}} + A_2$
P2: Sr^*	0.6	
Solid phase properties (ITYCL = 1)		
P1: C_s (J kg^{-1} K^{-1})	1000	
P2: ρ_s (kg m^{-3})	2770	
P3: α_s (C^{-1})	7.8e−6	

Table I-6. Mechanical parameters for bentonite. Thermo-elasto-plastic (TEP) model. See Code_Bright User's Guide for further details.

Elastic parameters (ITYCL = 1)	
P1: k_{io}	0.05
P2: k_{so}	0.25
P3: K_{min} (MPa)	10
P5: ν	0.4
P8: α_i	−0.003
P9: α_{sp}	−0.161
P10: p_{ref} (MPa)	0.01

$$d\varepsilon_v^e = \frac{k_i(s)}{1+e}\frac{dp'}{p'} + \frac{k_s(p',s)}{1+e}\frac{ds}{s+0.1} + (\alpha_o)dT$$

where:

$$k_i(s) = k_{io}\left(1+\alpha_i s\right)$$

$$k_s(p',s) = k_{so}\left(1+\alpha_{sp}\ln p'/p_{ref}\right)$$

Thermal and other parameters (ITYCL = 1)	
P1: α_o	1.5e−4
P5: T_{ref} (C)	20

Plastic parameters 1 (ITYCL = 1)	
P1: $\lambda(0)$	0.15
P2: r	0.925
P3: β (MPa^{-1})	0.05
P4: ρ (C^{-1})	0.2
P5: k	0.1
P6: p_{so} (MPa)	0.1

$$p_o = p^c\left(\frac{p_o^*(T)}{p^c}\right)^{\frac{\lambda(o)-kio}{\lambda(s)-kio}}$$

$$p_o^*(T) = p_o^*$$

$$\lambda(s) = \lambda(o)\left[(1-r)\exp\left(-\beta s\right)+r\right]$$

Plastic parameters 2 (ITYCL = 1)	
P1: p^c (MPa)	0.5
P2: M	1
P3: α	0.53
P4: e_o	0.6
P5: p_o* (MPa)	12

$$p_s = p_{so} + k\,s\exp(-\rho\Delta T)$$

$$\Delta T = T - T_{ref}$$

Parameters shape yield surf. (ITYCL = 3)	$g_y(\theta)$ = 1
Parameters shape plastic pot. (ITYCL = 3)	$g_p(\theta)$ = 1

Integration control parameters (ITYCL = 1)	
P1: *Tole1*	1e−7
P2: *Tole2*	1e−4
P3: *Tole3*	1e−3
P4: μ	1
P5: *Index*	1
P7: *Itermaxs*	20

I5 EBS Task Force requested tables

I5.1 Rock

Initial conditions of the rock at the start of the analysis (1)

Initial temperature at tunnel axis level (C)	Initial stresses at tunnel axis level (MPa)	Initial pore water pressure at tunnel axis level (MPa)
12	−28	−1*

*At the tunnel boundary, there is an initial pore water pressure of −1 MPa, simulating ventilation, but the far rock mass has an initial pore water pressure of 0.9 MPa (Figure I-6).

Initial conditions of the rock at the start of the analysis (2)

Initial density (g/cm^3)	Initial porosity	Initial water content (%)
2.75	0.01	0.4

Main rock properties (1)

Initial thermal conductivity ($W\ m^{-1}\ K^{-1}$)	Specific heat capacity ($J\ kg^{-1}\ K^{-1}$)	Initial intrinsic permeability (m^2)	Initial hydraulic conductivity (m/s)
4	793	8e−18	8e−11

Main rock properties (2)

Linear thermal expansion coefficient (K^{-1})	Young's modulus (MPa)	Poisson's ratio
7.8e−6	11697	0.3

Main rock properties: retention curve (3)

Equation used	P_0 (MPa)	λ
$S_e = \left(1 + \left(\frac{P_g - P_l}{P_o}\right)^{\frac{1}{1-\lambda}}\right)^{-\lambda}$	0.1	0.33

Main rock properties: relative permeability (4)

Equation used	λ
$k_{rl} = \sqrt{S_e}\left(1 - \left(1 - S_e^{1/\lambda}\right)^{\lambda}\right)^2$	0.33

I5.2 Bentonite

Initial conditions of the bentonite at installation (1)

Initial temperature (C)	Initial stresses (MPa)	Initial pore water pressure/suction (MPa)	Initial relative humidity (%)
12	−0.1	−135	34

Initial conditions of the bentonite at installation (2)

Initial dry density (g/cm^3)	Initial density of the solid phase (g/cm^3)	Initial porosity	Initial water content (%)	Initial degree of saturation (%)
1.61	2.77	0.42	16	65

Main bentonite properties (1)

Initial thermal conductivity ($W\ m^{-1}\ K^{-1}$)	Initial thermal conductivity dry bentonite ($W\ m^{-1}\ K^{-1}$)	Initial thermal conductivity saturated bentonite ($W\ m^{-1}\ K^{-1}$)	Initial specific heat capacity of the solid phase ($J\ kg^{-1}\ K^{-1}$)	Linear thermal expansion coefficient (K^{-1})
1.08	0.6	1.4	1 000	7.8e−6

Main bentonite properties (2)

Initial intrinsic permeability (m^2)	Initial hydraulic conductivity (m/s)	Initial intrinsic permeability (saturated) (m^2)	Initial hydraulic conductivity (saturated) (m/s)	Swelling pressure under initial conditions (oedometric conditions) (MPa)
3e−21*,+	2.3e−14*,+	5.6e−21*,x 5.2e−20*,°	4.3e−14*,x 4e−13*,°	5.7

* Note that both intrinsic permeability and hydraulic conductivity change with porosity (Figure I-9).

+ At an initial relative permeability k_{rl} = 0.925.

x At a porosity = 0.48 (saturated conditions in FEBEX model).

° At a porosity = 0.7 (saturated conditions in oedometer).

Main bentonite properties: intrinsic permeability dependence on porosity (3)

Equation used	$(k_{11})_o$ (m^2)	$(k_{22})_o$ (m^2)	$(k_{33})_o$ (m^2)	φ_o
$\mathbf{k} = \mathbf{k}_o \frac{\varphi^3}{(1-\varphi)^2} \frac{(1-\varphi_o)^2}{\varphi_o^3}$	3E−21	3E−21	3E−21	0.42

Main bentonite properties: retention curve (4)

Equation used	P_0 (MPa)	λ
$S_e = \left(1 + \left(\frac{P_g - P_l}{P_o}\right)^{\frac{1}{1-\lambda}}\right)^{-\lambda}$	20	0.18

Main bentonite properties: relative permeability (5)

Equation used	A	λ
$k_{rl} = AS_e^{\lambda}$	1	3

Main bentonite properties: thermal conductivity (6)

Equation used	A_1 (W m^{-1} K^{-1})	A_2 (W m^{-1} K^{-1})	b	Sr^*
$\lambda = \frac{A_1 - A_2}{1 + e^{\left[(Sr - Sr^*)/b\right]}} + A_2$	1.4	0.6	−0.12	0.6

Main bentonite properties: vapour transport (7)

Molecular diffusion coefficient of vapour in free air (m^2/s)	Tortuosity
2.61e−5*	0.8

*At 12 °C and 0.1 MPa.

Arkitektkopia AB, Bromma, 2023

SKB is responsible for managing spent nuclear fuel and radioactive waste produced by the Swedish nuclear power plants such that man and the environment are protected in the near and distant future.

skb.se